INERTIAL CONFINEMENT FUSION

Lawrence Livermore National Laboratory

UCRL-LR-105821-96

ICF Annual Report *1996*

Work performed under the auspices of the U.S. Department of Energy by
Lawrence Livermore National Laboratory under
Contract W–7405–Eng–48.

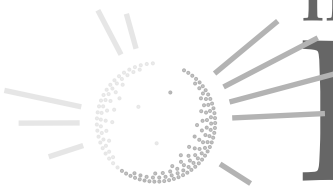

INERTIAL CONFINEMENT FUSION

1996 ICF Annual Report

UCRL-LR-105821-96
Distribution Category UC-712
October 1995–September 1996

Printed in the United States of America
Available from
National Technical Information Service
U.S. Department of Commerce
5285 Port Royal Road
Springfield, Virginia 22161
Price codes: printed copy A03, microfiche A01.

MS Date
June 1997

Lawrence Livermore National Laboratory

FOREWORD

The *ICF Annual Report* provides documentation of the achievements of the LLNL ICF Program during the fiscal year by the use of two formats: (1) an Overview that is a narrative summary of important results for the fiscal year and (2) a compilation of the articles that previously appeared in the *ICF Quarterly Report* that year. Both the *Annual* Overview and *Quarterly Report* are also on the Web at http://lasers.llnl.gov/lasers/pubs/icfq.html.

The underlying theme for LLNL's ICF Program research is defined within DOE's Defense Programs missions and goals. While in pursuit of its goal of demonstrating thermonuclear fusion ignition and energy gain in the laboratory, the ICF Program provides research and development opportunities in fundamental high-energy-density physics and supports the necessary research base for the possible long-term application of inertial fusion energy for civilian power production. ICF technologies continue to have spin-off applications for additional government and industrial use.

LLNL's ICF Program falls within DOE's national ICF program that includes the Nova and Beamlet (LLNL), OMEGA (University of Rochester Laboratory for Laser Energetics), Nike (Naval Research Laboratory), and Trident (Los Alamos National Laboratory) laser facilities. The Particle Beam Fusion Accelerator and Saturn pulsed power facilities are at Sandia National Laboratories. General Atomics, Inc., develops and provides many of the targets for the above experimental facilities. Many of the *Quarterly Report* articles are co-authored with colleagues from these other ICF institutions.

Questions and comments relating to the content of the journal should be addressed to the ICF Program Office, Lawrence Livermore National Laboratory, P.O. Box 808, L-488, Livermore, CA 94551.

Jason Carpenter
Publication Editor

Don Correll
Managing Editor

ACKNOWLEDGMENTS

We thank the 28 authors and their co-authors who contributed to this *Annual Report*. Their work, published in our four *Quarterly Reports*, is compiled here to highlight LLNL's ICF Program accomplishments for the year. We are grateful for their willingness to take time from busy schedules to write the articles that describe their work. We thank the four *Quarterly Report* Scientific Editors Randall McEachern, Deanna Pennington, Alan Burnham, and Michael Marinak for their efforts and diligent review to ensure the quality of each *Quarterly Report*. We thank Roy Johnson for his careful classification reviews. We also thank the secretaries for typing manuscripts, arranging meetings, and offering other invaluable assistance.

We thank Technical Information Department (TID) editors Jason Carpenter, Robert Kirvel, Al Miguel, Peter W. Murphy, Ann Parker, Joy Pérez, Margaret A. Sands, and Dabbie P. Schleich for editing and managing the production cycle; and artists/designers Pamela Davis, Daniel S. Moore, Linda L. Wiseman, and Sandy Lynn for providing expertise in graphic design and layout.

We appreciate the support of Michael Gallardo, the Government Printing Office Coordinator, who worked with the Government Printing Office to obtain high-quality printing; and Mary Nijhuis of TID's Publications Services and TID's Print Plant for making sure that each publication was distributed with dispatch.

The talents and dedication of the ICF Program staff make the *ICF Annual* what it is for so many of its readers.

John Lindl
ICF Science Director

Don Correll
ICF Operations Manager

TABLE OF CONTENTS

ICF Program Overview

Introduction

The continuing objective of the Inertial Confinement Fusion (ICF) Program is the demonstration of thermonuclear fusion ignition and energy gain in the laboratory. The underlying theme of all ICF activities as a science research and development program is the Department of Energy's (DOE's) Defense Programs (DP) science-based Stockpile Stewardship and Management (SSM) Program. The extension of current program research capabilities in the National Ignition Facility (NIF) is necessary for the ICF Program to satisfy its stewardship responsibilities. ICF resources (people and facilities) are increasingly being redirected in support of the performance, schedule, and cost goals of the NIF.

One of the more important aspects of ICF research is the national nature of the program. Lawrence Livermore National Laboratory's (LLNL's) ICF Program falls within DOE's national ICF Program, which includes the Nova and Beamlet laser facilities at LLNL and the OMEGA, Nike, and Trident laser facilities at the University of Rochester (Laboratory for Laser Energetics, UR/LLE), the Naval Research Laboratory (NRL), and Los Alamos National Laboratory (LANL), respectively. The Particle Beam Fusion Accelerator (PBFA) and Saturn pulsed-power facilities are at Sandia National Laboratories (SNL). General Atomics, Inc. (GA) develops and provides many of the targets for the above experimental facilities.

LLNL's ICF Program supports activities in two major interrelated areas: (1) target physics and technology (experimental, theoretical, and computational research); and (2) laser science and optics technology development. Experiments on LLNL's Nova laser primarily support ignition and weapons physics research. Experiments on LLNL's Beamlet laser support laser science and optics technology development.

In addition, ICF sciences and technologies, developed as part of the DP mission goals, continue to support additional DOE objectives. These objectives are (1) to achieve diversity in energy sources through inertial fusion energy (IFE) research and (2) to maintain a competitive U.S. economy through new development of technologies of interest for government and industrial use, including Laboratory Directed Research and Development (LDRD).

This Overview is divided into sections that include Target Physics and Technology, Laser Science and Optics Technology, the National Ignition Facility, and Inertial Fusion Energy/New Technologies. These sections summarize the findings within the individual articles of this *Annual Report*, and also discuss important results from FY 1996 that have not been covered explicitly in the articles.

Many of the articles within this *1996 ICF Annual Report* have been co-authored with colleagues from other national ICF institutions.

Target Physics and Technology

The activities of the Target Physics and Technology (TP&T) Program are directed to ensure the success of achieving ignition on the NIF and supporting the science mission of the DP SSM Program. The activities fall into the following three main areas: Nova target physics, NIF target design and code development, and NIF target area technology development. In the FY 95 annual report overview, we reported that the DOE's Inertial Confinement Fusion Advisory Committee (ICFAC) had achieved its major target physics mission objective. This was a result of the following factors: (1) the Nova Technical Contract (NTC) was essentially completed; (2) there had been significant progress in establishing a robust target design for the NIF; and (3) major progress had been made in achieving adequate target surface finish of cryogenic ignition targets. During 1996, the TP&T Program has shifted its emphasis to better ensure successful ignition on the NIF and expand support for the DP SSM Program. The following is a brief summary of activities in these areas during FY 1996.

Nova Target Physics

Nova Ignition Experiments. Experiments and analyses continued in plasma physics, hohlraum physics, and high-growth-factor implosions. Much of the effort was devoted to extending quantitative understanding of the physics beyond the NTC and to better define the limits in target performance for the NIF. In addition, initial indirect-drive experiments were done on the Omega laser at UR (in collaboration with scientists from LANL and LLE) in order to determine the feasibility of using the facility for indirect drive.

Plasma physics experiments continued to investigate stimulated scattering processes in NIF-like plasmas using "gas-bag" and gas-filled "scale 1" Nova hohlraum targets. An extended set of experiments were done using the f/8 lens in beamline 7 to approximate the NIF focusing geometry. These experiments demonstrated an anticorrelation between stimulated Raman scattering (SRS) and stimulated Brillouin scattering (SBS) as a function of plasma density. This trend is seen in Fig. 1, which shows the SBS and SRS as a function of plasma densities. The data are from gas-bag targets using NIF focusing conditions of 0.35-μm light focused to intensities of 2×10^{15} W/cm^2 using an f/8 lens. Scattering levels have a weak but measurable dependence on smoothing by spectral dispersion (SSD) laser bandwidth as shown in Fig. 1. In addition, a new Thomson scattering diagnostic has been activated during the past year. Initial experiments using the probe during the past year measured temperature and density from gas-filled hohlraums. During the upcoming year, a new 4ω probe will be activated to extend the capability to higher density.

The principal activity for understanding symmetry in gas-filled hohlraums was to manufacture ten kinoform phase plates (KPP) to perform hohlraum coupling and symmetry experiments with ten smooth beams. Experiments in the previous year using one beam with a random phase plate (RPP) showed that the beam performed much closer to expectation than an unsmoothed beam. During this past year, a KPP design was developed to produce approximately round spots on the hohlraum wall. A single KPP was manufactured. Figure 2 shows the improvement of the beam spot at the equivalent plane of the laser entrance hole with a KPP compared to a Nova beam without smoothing. In single-beam experiments, the KPP performed similarly to the RPP in showing SBS and SRS. The thermal x-ray emission is similar to the calculated emission pattern. Manufacture of KPPs for the rest of the Nova beams is in progress and experiments will be done in 1997.

Most of the progress made in high-growth-factor implosions was in the area of analysis to understand the difference in predictions and calculations of the neutron yield for implosions with capsules having a good quality surface finish. Using the new capabilities in the 3-D code HYDRA, the effects of low-mode capsule asymmetry coupling to intrinsic hohlraum asymmetry were investigated. The coupling of these effects was shown to reduce the neutron yield more than if the two effects were assumed to be independent. Work continues to apply these capabilities in understanding the experiments.

We performed two weeks of indirect-drive experiments on the Omega laser at UR in collaboration with UR and LANL scientists. These were the first indirect-drive experiments performed in the facility. The experiments showed that indirect-drive experiments could successfully be fielded on Omega. Drive and implosion symmetry experiments were conducted similar to those conducted on Nova. These demonstrated that Omega can produce similar irradiation conditions as Nova when operated at similar power levels.

Nova Weapons Physics Experiments. The ICF Program and scientists in LLNL's A Division, B Division, V Division, and H Division continued to collaborate on weapons physics experiments on Nova in FY 96.

Nova can produce a range of radiation temperature and pulse length capabilities for driving SSM-based

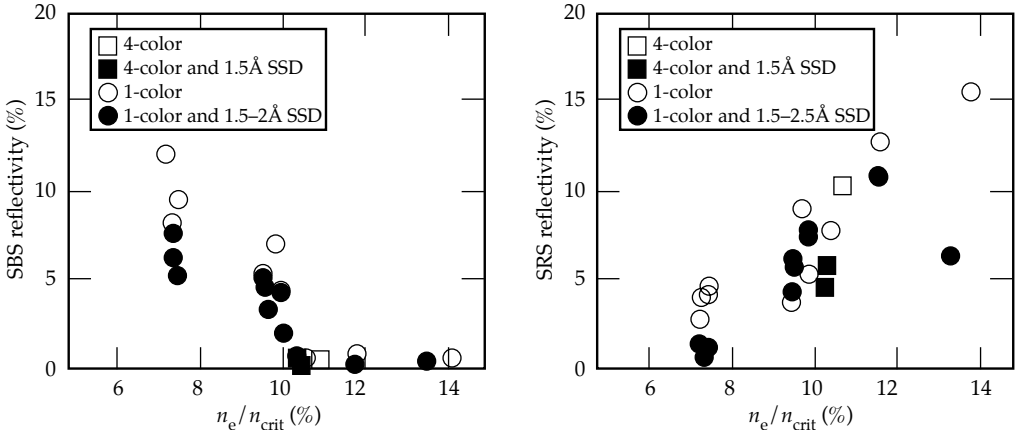

FIGURE 1. A scaling of (a) SBS and (b) SRS reflectivity as a function of plasma density for various laser conditions. The data are taken on Nova with one beam approximating NIF focusing conditions of 2×10^5 W/cm^2 of 0.35-μm light using an f/8 lens.
(02-25-0397-0478pb01)

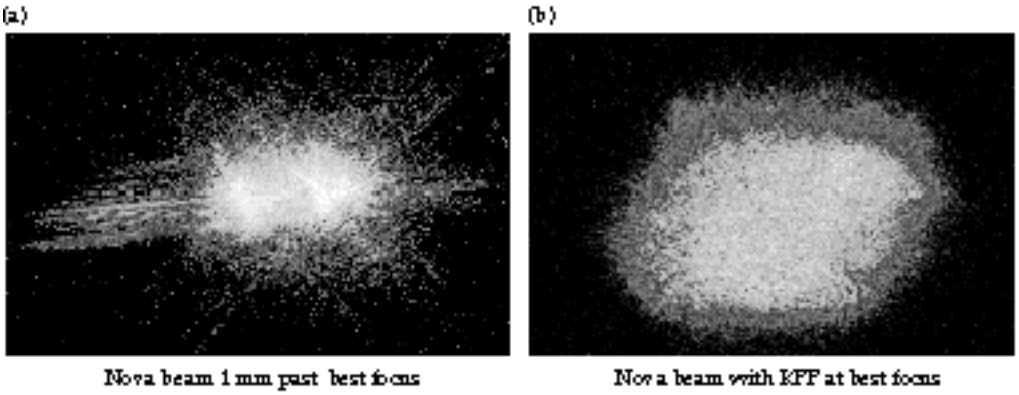

FIGURE 2. Far-field images of a Nova beam comparing the beam structure of a normal Nova beam (a) with one having a kinoform phase plate (b). (02-25-0397-0476pb01)

experiments and these capabilities can be scaled to the NIF. During this period, a collaboration between V & A Divisions and the ICF Program demonstrated that very-high-temperature hohlraums can be produced with hohlraums scaled down to a smaller size than the Nova scale 1, which is 2.6 mm length by 1.6 mm diameter. At the other extreme, a radiation temperature of >80 eV was produced for 14 nsec in a scaled-up hohlraum. The technique used for producing a long laser pulse was to stagger the 2-ns laser pulses. This capability has been used to produce drives for radiation flow experiments down gas-filled tubes where the position of the radiation front was measured by soft x-ray emission. These experiments complement similar experiments at SNL on their z-pinch sources. For the NIF longer pulses, close to 100 ns at 100 eV could be produced. At intermediate pulse lengths, ablation pressures of ~40 Mbar have been produced with 3% uniformity over scale lengths of up to 1 mm.

In collaboration with B Division, experiments have begun on Nova which measure the growth of hydrodynamic instabilities and equations of state in the presence of material strength. At pressures of ~1 Mbar, the melt temperature of metals increases up to 1 eV at compressions of 2–3 in accord with the Lindemann melt model. By carefully shaping the drive pulse on Nova, with a foot/pulse ratio of 50, we have been able (in calculations) to keep the shock heating of metals such as Cu and Mo below their melt temperature. The growth of Rayleigh–Taylor instability at a buried interface has been measured under these conditions, and a reduction in the growth rate because of strength in the solid state has tentatively been identified.

We have developed a plan to further investigate primary physics. We have preliminary data on the Bragg diffraction from a shocked Si witness plate showing lattice compression and subsequent expansion due to the rarefaction wave. The material stayed solid with a clearly defined Bragg diffraction. We have developed a Michelson interferometer to measure the expansion of the rear surface of a witness plate and, importantly, the expansion due to preheat.

For secondary physics, we have worked with A Division and improved our understanding of the physics models used for hydrodynamic mixing in our computer simulations. Passive tracer layers with higher x-ray absorption than the surrounding plastic, so the position of the layer shows up on the radiographs, have been developed to investigate highly vertical flows in the regime between laminar and turbulent flow on Nova. In further hydrodynamic experiments, integrated laser-driven experiments have been used to provide close analogies to thermonuclear secondaries.

In FY 96, Nova was used to make equation-of-state (EOS) measurements of cryogenic deuterium with sufficient precision to distinguish between an old EOS and a new EOS with energy loss from disassociation included. The EOS of hydrogen and its isotopes at high pressure have long been of interest, driven by the need for understanding the physics of high-density matter. Two applications, solar science and inertial confinement fusion (ICF), are critically dependent on hydrogen EOS behavior. The performance of deuterated ICF capsules relies on shock timing and efficient compression which are dependent on the EOS. For these reasons, a number of theoretical models of the EOS of hydrogen have been proposed. An important and outstanding question in the EOS of H_2, as well as D_2, has been the transition from a diatomic to a monatomic fluid. A continuous dissociative transition has been suspected but not observed. Theoretical predictions of molecular dissociation have been complicated by the presence of electronic transitions and possible ionization near pressures required for dissociation (~100 GPa). During this year we performed and published results of the first measurements of density, shock speed, and particle speed in liquid (cryogenic) deuterium, compressed by laser-generated shock waves to pressures from 25 to 210 GPa (0.25 to 2.1 Mbar). The data shown in Fig. 3 indicates that the D_2 compressibility above 50 GPa is significantly greater compared to the existing widely used equation of state. The data strongly indicate a continuous molecular dissociation transition of the diatomic fluid into a monatomic phase.

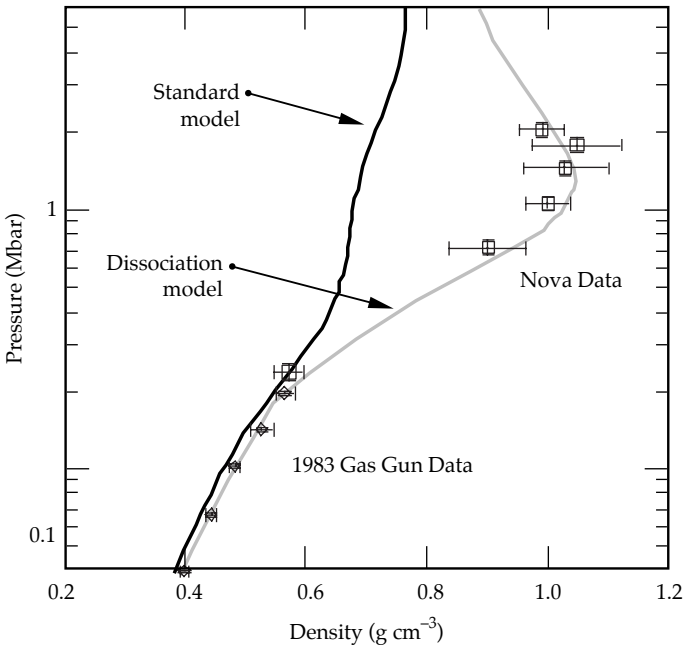

FIGURE 3. Data for the equation of state for liquid D_2 taken using Nova. The data are compared with the standard model (solid line) and the dissociation model (gray line). The previous gas gun data could not discriminate between the two models. (08-00-0996-2169pb01)

Advanced Concepts. The fast ignitor concept uses short-pulse lasers to produce fast electrons to heat a compressed core of DT fuel. Experiments to test the feasibility of this concept were done using the 100-TW laser in the 2-beam chamber of Nova. In 1996, experiments with 0.4-ps pulses at 2×10^{19} W/cm^{-2} demonstrated more than 20% efficiency of coupling laser energy to fast electrons. Modeling indicates that the internal coupling efficiency could be as high as 50%. In parallel, the Petawatt laser was demonstrated (as noted below), and the target chamber is being readied for target experiments in 1997.

NIF Target Design and Code Development

NIF Target Design. Work continued on the NIF point design robustness by direct 2-D simulation (using LASNEX) of inner DT surface and outer CH surface perturbations, coupled with low-mode (ℓ<10) capsule nonuniformities, driven by P_0 through P_8 drive/asymmetry spectrum extracted from integrated (hohlraum + capsule) LASNEX simulations, plus random, time-varying perturbations to that drive and asymmetry. With surface smoothness achieved to date in the laboratory, the capsules in these "everything on it" simulations ignited and burned giving nearly 1-D yields.

We further confirmed NIF robustness by running simulations in 3D using the HYDRA code (including thermonuclear burn physics) that combined inner and outer surface perturbations, with surface smoothness achieved to date in the laboratory. These too ignited and burned, giving nearly 1-D yields.

There was a redesign of the NIF point design to obtain more margin against high-mode (ℓ=100) mode perturbations, which if initially large enough, might break up the shell during the time period prior to achieving maximum velocity. (Current Nova target surface finishes have ℓ=100, smooth enough to meet the NIF specifications even prior to this redesign.) Simulations have also indicated that much higher modes are not an issue.

We designed a wider variety of NIF ignition capsules including lower-energy, lower-intensity 250-eV Be ablator capsules that should be safer from a laser plasma instability point of view. An ignition design was developed using a B_4C ablator.

We identified a beam arrangement on NIF that allows the baseline hohlraum geometry as well as tetrahedral hohlraum and direct-drive, and with LLE, identified a direct-drive ignition target design for NIF.

Code Development and Theory. The capsule-only 3-D radiation hydrodynamics code HYDRA has had a thermonuclear burn package added to it. Thus, in addition to analyzing Nova HEP4 implosions and the effects of low-mode capsule asymmetry coupled to the imposed Nova hohlraum drive asymmetries, it has now been applied to the study of yields for the NIF ignition capsule, subject of the evolution of 3-D inner and outer surface perturbations.

The more general purpose 3-D radiation hydrodynamics ICF design code of the future is HED3D, which will use many of the physics modules that have been developed as part of its precursor project, ICF3D. During this past year, the speed of the ICF3D hydrodynamics has increased considerably. Figure 4 shows an example of its capability in a 3-D calculation of the growth rate of a Rayleigh–Taylor instability. Moreover, its robustness and portability was successfully demonstrated by the fact that it ran on the IBM massively parallel "ASCI Blue Pacific initial delivery" machine within one day of delivery to LLNL. Within two days, a 2-D movie of a finely resolved Rayleigh–Taylor growth simulation was produced using 128 processors. In this past year, 3-D Rayleigh–Taylor growth test problems were successfully performed, with an under 2% error versus the analytic growth rate. PYTHON, a new computer science "shell" well-suited for a C++ object-oriented programming code such as HED3D, has been identified for use in the development of HED3D.

The development phase of the plasma code ZOHAR was completed this year. It is a fluid electron particle ion version of the 2-D fully PIC ZOHAR code. It has already been used to do initial studies of nonlinear saturation behavior of Brillouin scattering including

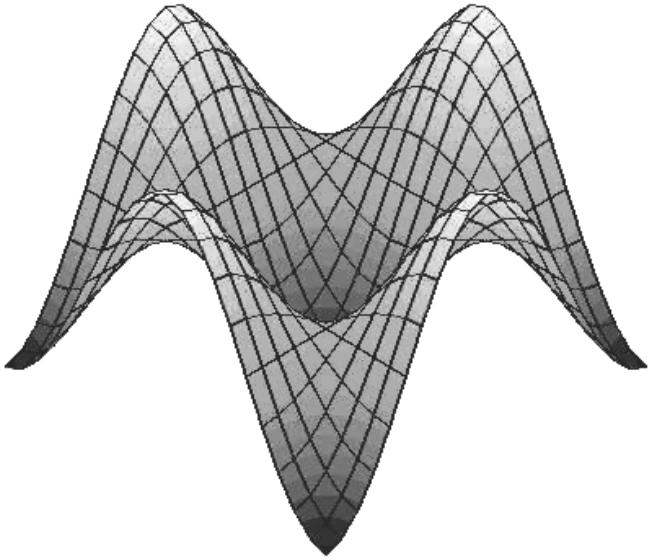

FIGURE 4. Example of the calculation of a Rayleigh–Taylor instability calculation using ICF3D. The figure shows an isodensity contour after perturbation growth. (08-00-0996-2163pb01)

effects of 2-D versus 1-D ion-wave-coherence collapse, as well as revealing interesting physics of the role of separate ions in the development of saturation effects for multispecies plasmas.

The hydrodynamics in the laser filamentation and propagation code F3D was made fully nonlinear. This has been an important development in its use to analyze high-intensity issues encountered in the analysis of high-temperature hohlraums. Figure 5 shows the nonlinear propagation of a laser beam breaking up into multiple filaments. Other developments involve the initial attempts at including into F3D models of the Raman-Brillouin scattering instability competition.

NIF Target Area Technology

NIF Diagnostics. NIF diagnostic developments concentrated on neutron diagnostics compatible with expected NIF yields. A Cherenkov radiation from 16.7 MeV (D,T) fusion gammas was observed as part of a burn history diagnostic capable of operation with NIF yields, requiring a long stand-off distance. An energy-resolved prototype is under construction. Monte Carlo analysis and design of the neutron shield for a proton-recoil neutron yield diagnostic was completed and a prototype is under construction. A charged-particle spectrometer was designed in collaboration with MIT. Preliminary experiments on track detection of charged particles from Nova experiments were completed with assessment of background levels, and a prototype spectrometer is under construction. In addition, a Neutron Time of Flight system was designed and is under construction at LLE (Rochester) for yield and ion-temperature measurement. This instrument will be remotely operable from LLNL. The Neutron Coded Aperture Imager experiment is being moved to LLE for completion.

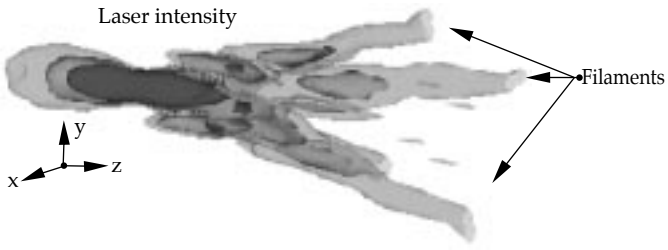

FIGURE 5. Example of a calculation from F3D. The figure shows a constant laser intensity profile for the case where the beam divides into several filaments. (08-00-0896-1888pb01)

NIF Ignition Capsules. Research continued on developing the technology for a variety of NIF ignition capsules. The ability to produce NIF-thickness, gas-permeable, seamless Be ablator coatings on plastic microshells by sputtering was demonstrated, and improvements in surface finish are under development. A technique has been developed and transferred to General Atomics that provides capsules with very small P_1 defects. This technology produces a thin plastic shell that can be decomposed and diffused through an overcoating. This is also the technique for producing all of the thin capsules for the LLE experiments. Optically transparent, 2-mm-diameter, low-density (60 mg/cc) foam shells with 100-μm wall, capable of holding liquid cryogenic D-T, were manufactured as an alternative ignition capsule. An LLNL contract with the Lebedev Institute in Moscow has resulted in the first production of 2-mm-diameter plastic shells by a drop tower technique. Improvements in surface finish are necessary.

Cryogenic Technologies. All NIF target designs require smooth cryogenic layers of DT as the inner capsule layer. In 1996, we completed and demonstrated a self-contained DT source for cryogenic target development experiments at LLNL. We demonstrated the efficacy of heat fluxes on smoothing of solid hydrogen in curved geometries with the same radius of curvature as NIF ignition capsules. For unheated "native" cryogenic layers, surface finishes required for ignition were demonstrated. We demonstrated the efficacy of producing heat fluxes in the interior of enclosed solid D-T cells by microwave heating the free charges in the vapor space and establishing the smoothing properties of this heat flux. We demonstrated the efficacy of infrared heating of bulk solid hydrogen for smoothing the surfaces. In addition, we designed and analyzed thermal characteristics of cryogenic hohlraums for beta-layering fuel in ignition capsules and are nearing completion of a cryogenic test system for development of cryogenic hohlraums.

NIF Target Chamber. Technology is being developed for the survivability and maintainability of the integrity of the NIF target chamber. We confirmed that B_4C can provide for x-ray protection of the chamber wall for up to 20-MJ yield, with only a few grams total ablation and thus minimal impact on debris shields. Figure 6 show the dramatic reduction of material removal for B_4C as a function of x-ray fluence compared to Al, the NIF chamber material. We improved modeling of vapor generation and chamber condensation of materials produced by x-ray ablation from NIF experiments. We obtained good agreement between modeling and Nova experiments and established the viability of lower-cost plasma-sprayed B_4C, compared to the more expensive hot-pressed manufacturing process. We defined a protection scheme for the target positioner using B_4C sacrificial layers coated onto a shock-absorbing aluminum foam. We also defined cryogenic target interfaces and analyzed effects of target emissions on generic cryogenic target support system. We reduced NIF costs through better assessment of activation issues by requiring a smaller neutron shield mass and eliminating most boron content in concrete structures and assessed the efficiency of CO_2 cleaning for first wall panels. Additionally, we established a Target Area System Code for modeling operation off the target area and assessing operational impacts of performing experiments.

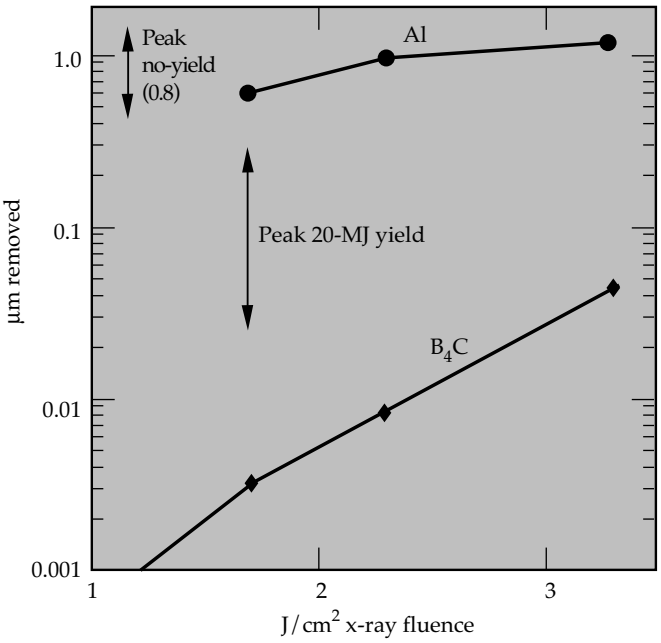

FIGURE 6. Comparison of the material removal as a function of x-ray fluence for Al and B_4C. The solid circles are data taken on Nova verifying that B_4C can be used as a first wall material to mitigate debris. (40-00-0195-0079G)

University Use of Nova

1996 was the first year of an LLNL-operated independently reviewed program for University use of Nova for broad-based SSM experiments. In response to a call for proposals, 18 proposals were received for Nova use. These proposals were reviewed by the Target Physics Program Advisory Committee, which is independent of the staff at LLNL. After review, nine proposals were approved in the fields of astrophysics, atomic physics, high-density physics, plasma physics, diagnostics development, and ICF.

An example of the synergism of ICF with the University use program is the development of the Thomson probe on Nova, which has subsequently been used to characterize hohlraum plasmas. Initial activation and experiments using the probe were done to study the structure of ion acoustic waves in a two-species plasma. An example of the decay waves showing the two ion waves is shown in Fig. 7. This is the first measurement of two-ion-acoustic waves in a two-species plasma with Thomson scattering. This work has resulted in a publication.

To promote the use of large lasers for astrophysics, the ICF Program and V Division jointly hosted a workshop on laboratory astrophysics with large lasers in February. Eighty participants from a broad-based community attended.

Laser Science and Optics Technology

The Laser Science and Technology (LS&T) Program provides laser technology development and validated performance models for NIF and advanced ICF laser systems. LS&T laser developments have spin-offs that are valuable to Stockpile Stewardship, other national programs, and U.S. industry. Many of these spin-offs, which have then been advanced by other sponsors, are now being applied to ICF needs (i.e., spin-backs). Examples include laser diodes in the NIF front-end and zigzag slab laser technology. The ICF Program is strengthened by this synergistic exchange of information between these diverse activities.

LS&T's primary activity in 1996 has been the laser and optics technology developments for NIF. A four-year focused activity for laser technology development started in 1995 and is described in the Core Science and Technology Report (authored jointly with Sandia and Los Alamos National Laboratories). The objectives of the laser developments are to provide validated design packages for the laser components and overall system design and optimization for NIF. The objective of the optics technology developments (formally

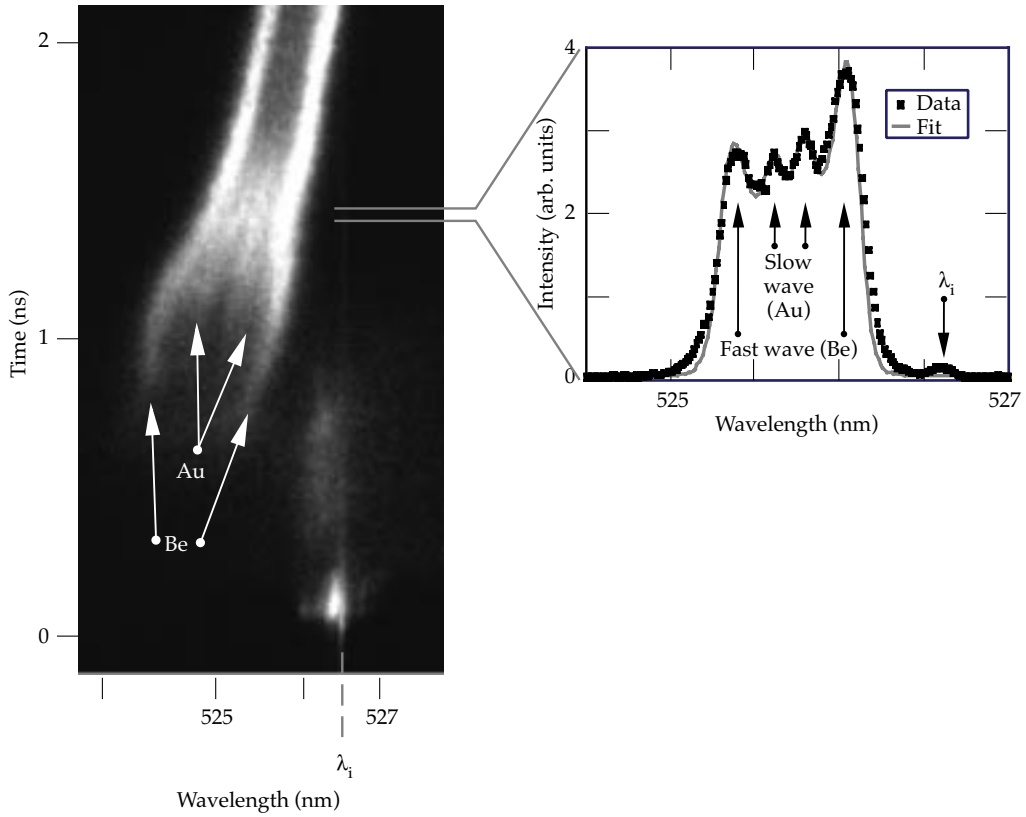

FIGURE 7. Example of results from the Nova University use program. The figure shows results from a Thomson scattering experiment that used Thomson scattering to observe the two ion-acoustic waves from a two-species plasma. This data is taken from a plasma that is 4% Au and 96% Be. (02-25-0397-0477pb01)

managed by the NIF Project) is to develop industrial production methods for the 8000 full-scale NIF optics that meet performance requirements at the required NIF cost and schedule. Both activities are described below.

Laser Science and Optics Technology Highlights

Many major Laser Science and Optics Technology milestones were completed in 1996. The amplifier module prototype laboratory (AMPLAB) was inaugurated, and the first prototype 4 × 2 NIF amplifier and maintenance transport vehicle were designed and fabricated. Re-optimization modeling of the NIF laser design yielded a 11-0-5 configuration of amplifier slabs in each beamline and a myriad of detailed system specifications. Beamlet was used to study the fluence and power limits and focusability of NIF, uncovering issues regarding 3ω damage and potential system failure modes. These discoveries resulted in a NIF design change, placing the frequency converter and 3ω focusing lens inside the target chamber with a 1ω window holding the vacuum. Beamlet studies on the focusability of the 3ω beam on target identified the need for amplifier cooling to increase NIF repetition rate. We have initiated an aggressive effort in this area.

The LS&T Program continued to support target physics experiments on Nova and completed the Petawatt laser beam (10^{15} W) for research on the fast ignition approach to ICF and other ultrahigh irradiance physics experiments. Diffractive optics (kinoform phase plates) were added to the Nova debris shields to provide beam smoothing for both direct- and indirect-drive studies. Hardware for 10-beam smoothing by spectral dispersion was added to Nova to support plasma physics studies.

With respect to spin-off technology, we provided key demonstrations of femtosecond laser cutting for material processing.

1996 was an important year for NIF optics development. We demonstrated the viability of continuous melting of phosphate laser glass at vendor facilities by performing quarter-scale runs at Hoya and full-scale runs at Schott using surrogate glass materials. The KDP rapid growth program matured to produce NIF-size boules (up to 43-cm size) and to yield plates which meet all the NIF 1ω optical requirements. The optics finishing companies have all demonstrated processes which meet NIF cost and performance requirements. An important development in diffractive optics

capability was making a high-efficiency, high-damage-threshold color separation grating to deflect 1ω and 2ω light from the target while maintaining the focusing of 3ω light on target.

Many of our laser and optics technology developments have been done in collaboration with our French Commissariat à l'Énergie Atomique (CEA) colleagues. CEA plans to build the Laser MegaJoule (LMJ) with specifications similar to NIF by 2008 and to test a 4×2 beam bundle in a Ligne d'Integration Laser (LIL) in the year 2000, approximately. This is similar to the schedule for the first NIF beam bundle. Because of our partnership in laser and optics developments, we assisted CEA in organizing a very successful conference on solid-state lasers for ICF in Paris in October 1996, which was attended by 260 participants. This was a follow-up of a previous meeting organized by LLNL and held in Monterey, California, in May 1995.

NIF Laser Component Development

NIF laser component developments include the pulse generator, the amplifier, the pulse power system, the plasma electrode Pockels cell, the beam control system, and the Beamlet test facility. Significant progress has been made in all areas in 1996 with preliminary prototypes and tests of important physics issues.

The NIF front-end design is based on a fiber-optic oscillator, amplifiers, and pulse-shaping systems that deliver nanojoule level inputs to the 192 preamplifier modules (PAMs). During the year, the NIF design was changed from 192 to 48 PAMs. The NIF front-end system has stringent specifications on stability, pulse-shaping, and dynamic range (275). We demonstrated a fiber amplifier with a gain of 300, far exceeding the NIF specification of 36 (see Fig. 8) and converted it into a single-frequency fiber oscillator. We developed an electronic pulse-shaping system, as discussed in 96-2 article on "Temporal Pulse Shaping of Fiber-Optic Beams," that generates a computer-controlled, arbitrary waveform to satisfy NIF requirements. This fiber amplifier and pulse-shaping system are now being transferred to industry, who will manufacture the NIF units. The purpose of the regenerative amplifier (regen) is to amplify nanojoule temporal-shaped pulses up to the millijoule range with pulse-to-pulse stability of <3% rms. To maintain such high stability, the regen rod amplifier is pumped with laser diodes. Output from the regen is further amplified up to 22 J by passing four times through a flashlamp-pumped, 5-cm rod amplifier, or possibly in a 1-Hz repetition-rate zigzag amplifier. The rod amplifier system has demonstrated up to 14 J and is now being redesigned to produce higher output and less temporal pulse distortion. Energy from the four-pass amplifier is split to supply equal input energy to a "quad" of four beams, all of which will focus together on the target after further amplification through the full-aperture amplifiers.

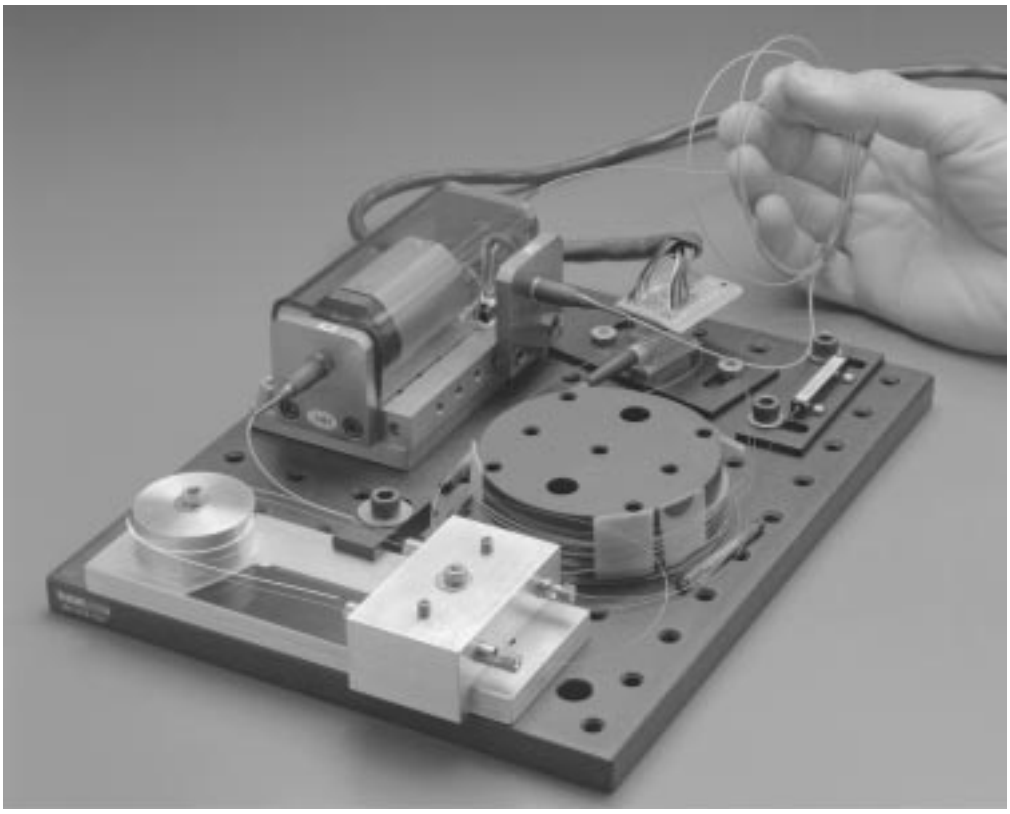

FIGURE 8. The NIF fiber oscillator and fiber amplifier demonstrated a gain of 300, far exceeding the NIF specification of 36.
(70-00-0996-2180pb01)

AMPLAB is the key facility for testing the full-aperture amplifiers. Testing will provide essential information on gain, wavefront performance, cooling recovery, and the degree of cleanliness in assembly and maintenance that affects the lifetime between amplifier refurbishments. AMPLAB construction began in 1996 and will culminate in full-scale amplifier testing in 1997. The 4 × 2 (four slabs high by two slabs wide by one slab long) amplifier module and a cart to load a cassette of amplifier slabs were designed and parts were procured (see Fig. 9). We expect to have the amplifier module and cart assembled and module tests to begin by mid-1997.

Flashlamp cooling will be implemented to increase NIF's shot rate, ideally reducing the wait between shots. The wait is for the thermal distortions of the amplifier slabs to diminish, returning the beam to an adequate quality on target. Without active cooling, adequate beam quality may not return for much more than eight hours. However, by cooling the flashlamps, the wait time can be reduced to eight hours and possibly less. Detailed modeling and tests on Beamlet have greatly increased our understanding of the relationship between amplifier slab temperature and beam wavefront and focusability as discussed later. The 4 × 2 prototype amplifier module in AMPLAB will have gas-cooled flashlamps to test the concept at the NIF scale.

A large-aperture diagnostic system (LADS) will make amplifier gain and wavefront measurements of the AMPLAB module. (LADS is a cooperative development with our French CEA colleagues.) This system consists of a probe laser with large-aperture telescopic beam optics, scientific-grade CCD cameras, and an interferometer.

The reliability of the 7000 NIF flashlamps is very important. The NIF lamps, at 4.3-cm bore and 1800-cm arc length, are the largest commercial lamps ever made and dissipate an unprecedented 36-kJ electrical energy per shot. We have tested prototype lamps from two U.S. makers with a set of six lamps from each company lasting over 20,000 shots. We are also testing lamps from foreign vendors.

The pulsed power system provides the energy for the flashlamps. NIF requires approximately 330 MJ of stored energy. To reduce the cost by approximately a factor of two from previous systems, this large amount of energy will be provided by relatively large, 1.7-MJ modules. NIF pulsed-power development is shared

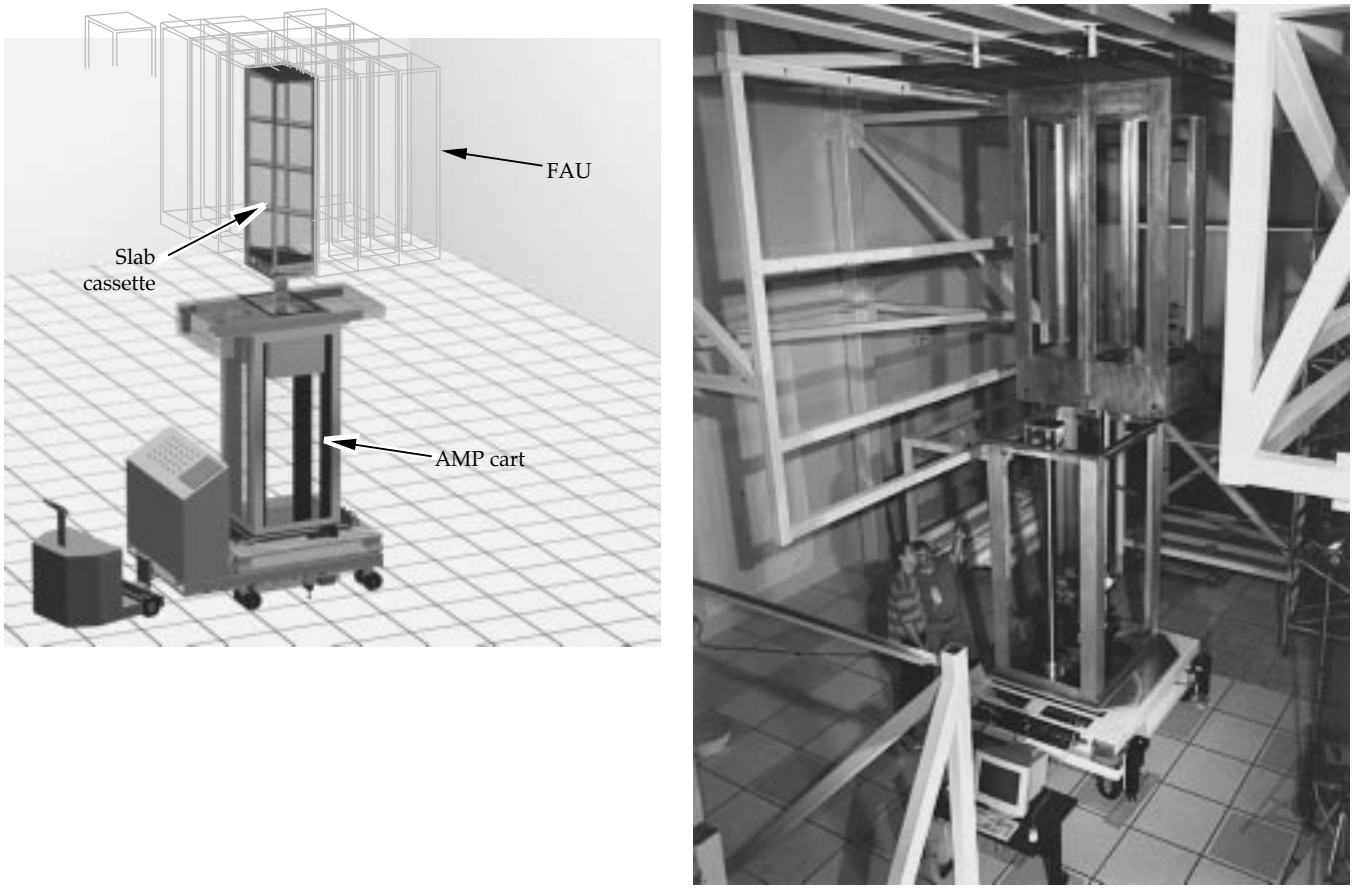

FIGURE 9. A cart inserting amplifier slabs into the 4 × 2 amplifier module. (70-00-0996-2187pb01)

between SNL and LLNL. LLNL is responsible for capacitors, power supplies, and other components, while SNL is responsible for the switch and integrated module testing. During 1996, we tested NIF-like capacitors from two U.S. vendors and several foreign vendors. To reduce fabrication costs, the new capacitors have a higher energy density and more capacitance per can. The NIF switch must reliably handle 500 kA. We have found one commercial switch (high-pressure spark gap) that may meet NIF requirements for at least 1000 shots between refurbishments. We are also working with Russian colleagues on the development of a solid-state silicon switch that has potential for an even longer lifetime. Fault mode testing was done with a commercial partner to verify the viability of the large energy parallel banks planned for NIF.

Significant progess has been made on the plasma electrode Pockels cell (PEPC), with the development of a densely packed prototype for use in a 4×2 beam bundle. The NIF design calls for four PEPCs stacked vertically in a single replaceable unit, but electrically the unit is two 2×1 modules. This year we designed and assembled a 2×1 module to test this concept (see Fig. 10). Initial tests of this prototype appear highly promising. We proved that it is possible to use a metal housing that is optimally biased at the anode potential to produce a uniform discharge and optical switching. One of the key concerns regarding the PEPC was that magnetic coupling between apertures could disrupt discharge uniformity. However, experiments with externally induced magnetic fields showed no adverse effect from having several apertures in close proximity provided the current returns are properly shielded magnetically.

FIGURE 10. A 2×1 prototype of the plasma electrode Pockels cell will test the NIF design. (70-00-0297-0280pb01)

To align and control the large number of NIF beams at an affordable cost, many new concepts and simplifications of previous systems have been implemented. A 1/10 scale optical layout of a NIF beamline was built to test the alignment and control concepts. Both near-field and far-field beam sampling and beam centroiding systems have been tested. The use of a grating beam sampler at the spatial filter pinholes minimizes the required power of the alignment beam. Tests of diagnostic concepts have also been conducted at 1/10 scale, including optical damage monitoring concepts. This concept has also been evaluated on Beamlet. We have also tested a high-energy, far-field measurement system on Beamlet that could measure the performance of each NIF beam.

Development of the NIF control system has focused on the selection of the overall system architecture and supervisory software framework. We are building prototypes of a distributed timing system, auto alignment front-end processors, motor control processors, and integrated energy diagnostics.

Wavefront control is another important aspect of the NIF systems. For efficient frequency conversion and high focusability on target, the NIF beam needs a deformable mirror to correct wavefront aberrations accumulated during the multiple passes through the amplifiers. The NIF specification is for 95% of the focused energy to be contained in a 70-microradian cone (500-micron focal spot). This is consistent with a beam that is 10 times diffraction-limited at 1 micron. Beamlet uses a small 7-cm aperture deformable mirror with 39 actuators to produce the necessary precorrection before injection into the multipass system. We have developed a full-aperture (40-cm square) deformable mirror for use as one of the end mirrors in the multipass cavity. This component will minimize the beam divergence throughout the laser chain, improving alignment accuracy and increasing beam transmission through the spatial filter pinholes. Installation and testing of this prototype on Beamlet is planned for early 1997.

System Integration Tests on Beamlet

The full energy beam diagnostic system constructed for Beamlet in 1995 was used during 1996 to measure the focal energy distribution with and without a KPP. These measurements meet NIF specifications for ICF ignition targets, but confirm the importance of wavefront control for NIF beam focusability. One determinant of beam focusability is amplifier cooling. Figure 11 shows the relationship measured on Beamlet between slab temperature rise and beam divergence. To reduce thermal-driven phase aberrations, in 1996 we installed on Beamlet a "t-1" system to allow the deformable mirror to correct aberrations up to one second before the shot. We also made detailed measurements of beam modulation growth with

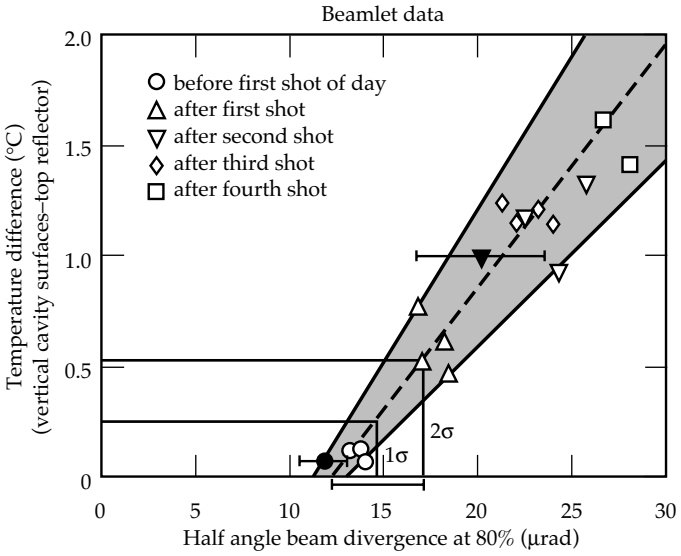

FIGURE 11. Slab temperature rise vs beam divergence, measured on Beamlet. (70-00-0197-0124pb01)

peak power as caused by nonlinear self-focusing. We investigated the effect of spatial filtering on beam modulation and the limits in filtering caused by "pinhole closure" with 20-ns duration ICF ignition pulse shapes. Optimum pinhole shapes and materials are still under investigation.

During Beamlet tests in September, we imploded, for the second time, the input lens to the transport spatial filter. Unlike the first implosion, this accident occurred because of the inadvertent absence of bandwidth on the beam which would have normally prevented transverse stimulated Brillouin scattering in the lens. Because of the implosion threat, we have reduced the stress in the NIF lens design to a level where implosion should not occur (500 psi), and we are now developing a fail-safe bandwidth system. We have also changed the design of the NIF final optics assembly to use a 1ω input window with the frequency conversion crystals and 3ω focusing lens mounted inside the vacuum. This design reduces the damage threat (1ω rather than 3ω) on the atmospheric-pressure-loaded optics. Testing the new final optics configuration on Beamlet will be a major activity in 1997 (the Beamlet "mule" campaign).

NIF Modeling and Optimization

Because of the magnitude of the NIF Project, it is imperative that the design be both cost-optimal and meet the NIF's functional requirements. Numerical modeling and optimization have played a major role this year in fulfilling both of these requirements. Over the past few years, we have developed computer codes capable of simulating the detailed evolution of the beam as it propagates through the chain elements, including effects of optical aberrations, transverse gain variation, multipass gain saturation, nonlinear self-focusing, phase correction with deformable mirrors, and frequency conversion. Separately, we have developed codes that model the propagation of flashlamp light in the pump cavity, the excitation of the laser medium by that light, depumping due to amplified spontaneous emission in the medium, and the prompt thermal loading and ensuing optical distortion in the slabs. Both of these sets of code can run in a parallel-processing mode on our 1-gigaflop cluster of 28 workstations, and can act as the computer engines for large multivariable parametric studies or constrained optimizations. This computational capability was used to examine the predicted performance, cost, and safety of over 100,000 different variations on the NIF configuration—varying such parameters as slab counts in each of the three potential amplifier locations (main, switch, and boost), optical aperture, slab thickness and doping, flashlamp packing and pulse length, pump reflector shapes, pinhole sizes, spatial filter lengths, converter crystal thicknesses, and the detuning angle. The NIF design configuration was chosen as a compromise between cost-effectiveness and performance margin. Subsequent detailed modeling has been used to establish the interface and component specifications and to assess engineering change requests to the baseline design.

NIF Optics Manufacturing Developments

We are following a four-phase program to meet the NIF optics requirements: development, facilitization, pilot production, and production. The *development* phase is used to identify appropriate manufacturing technologies, qualified companies, and to demonstrate prototype production processes by making a small number of full-size optics to NIF specifications. The *facilitization* phase is used to design, build, and install the NIF production equipment, and to modify and/or expand the production facilities as necessary to house the equipment. The *pilot production* phase is used to verify production readiness of the manufacturing facilities and processes. This work includes hiring and training the production staff, manufacturing about 10% of the NIF optics to demonstrate specifications and production rate requirements, and delivering the optics needed for the first bundle. Finally, the *production* phase is used to manufacture the balance of the optics needed to construct the NIF.

Laser materials: Phosphate Laser Glass, KDP/KD*P Crystals, and Fused Silica. We are working with two companies to develop continuous melting technology for platinum-free phosphate laser glass for the NIF—Schott Glass Technologies in Duryea, PA, and Hoya Optics in Fremont, CA. Both companies can also produce this glass using conventional batch processes.

As part of this development effort, the companies have paid considerable attention to determining the optimum composition of the glass. Schott, working closely with LLNL scientists, has developed a new composition, LG-770, for the NIF. In 1996, Schott finalized the composition of LG-770 and batch-melted ten of these slabs for testing on Beamlet. Hoya has elected to melt LHG-8 for the NIF; this is the composition used for Nova. In 1996, Hoya batch-melted nine slabs of LHG-8 at NIF size and specifications for testing in AMPLAB in 1997–8.

Schott and Hoya are taking different routes to the NIF continuous melting technology. Schott is going directly to a full-scale design, while Hoya is doing its development at subscale, and will not build a full-scale melter until the facilitization phase of the NIF Project. In 1996, Schott completed annealing and testing of a NIF-size BK-7 glass analog of laser glass melted in 1995, as shown in Fig. 12.

Forming the glass into a continuous strip is one of the most critical aspects of continuous melting. The BK-7 glass analog met the NIF homogeneity specification, and provides us with greater confidence that the Schott full-scale process will be successful. Also during 1996, Schott completed the detailed design of the full-scale melter and ordered most of the major equipment. Schott also began construction of the building that will house the melter. Installation of the full-scale melter is scheduled to be complete in mid-FY 97, and will be followed by the first full-size continuous melting campaign of phosphate laser glass.

Early in 1996, Hoya operated their subscale continuous melter and formed the phosphate laser glass at about one-fifth NIF scale. Later in the year, the melter and former were reconfigured, and Hoya executed another campaign to form glass at one-half NIF scale (see Fig. 13).

Remarkably, this glass exceeded the NIF platinum inclusion specification, met the IR and UV absorption specifications, and was within a factor of two of the homogeneity specification ($\Delta n \cong 4 \times 10^{-6}$ the specification of 2×10^{-6}). More detailed investigations of the homogeneity at fine spatial scale will be conducted in 1997 to ensure that the glass will meet the transmitted wavefront power spectral density (PSD) specification upon finishing. Hoya will refine their melter design further in 1997 in preparation for designing the full-scale melter that will be constructed in 1998.

The KDP/KD*P rapid crystal growth program produced the first NIF-size KDP boules in 1996 (see Fig. 14). These crystal boules ranged from 43 to 48 cm, and are large enough to yield the <001> "z-plates" needed for the plasma electrode Pockels cell. KDP boules of approximately 51 cm (with a goal of 55 cm) are needed to yield the Type I second harmonic generation crystals

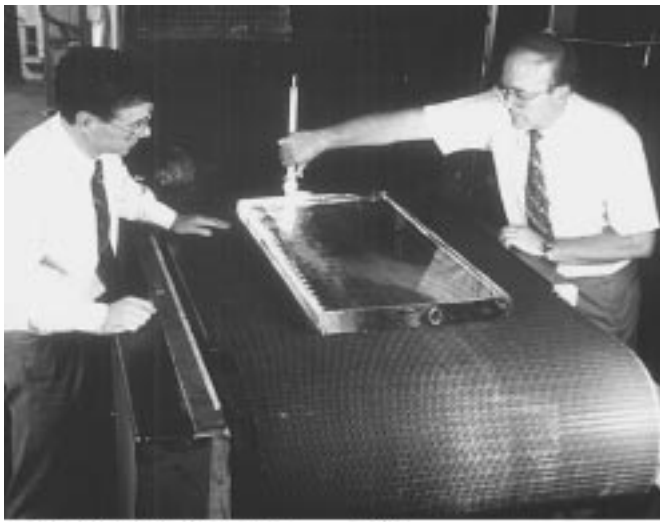

FIGURE 12. NIF-size BK-7 glass analog of laser glass melted in 1995, annealed and tested in 1996 (by Schott). (70-30-1295-2695pb02)

(a)

(b)

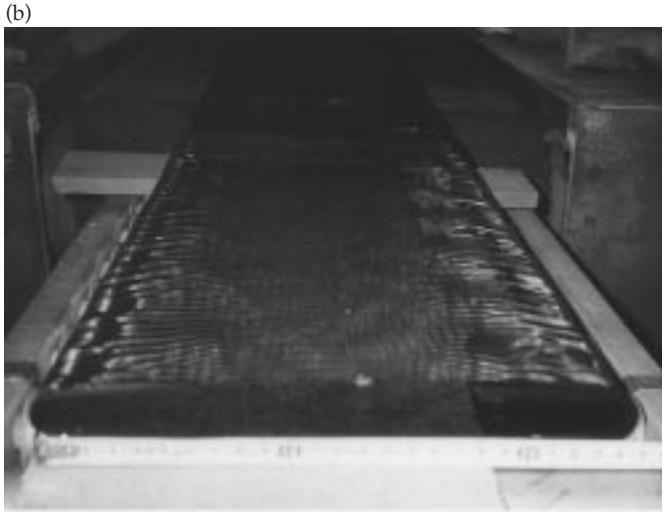

FIGURE 13. Phosphate laser glass formed by Hoya's subscale continuous melter in 1996 at one-fifth NIF scale (a) and at half NIF scale (b). (70-30-0496-0989pb01 top and bottom)

for NIF. Two crystal plates were fabricated from a representative boule and were found to meet all of the NIF optical and damage specifications for 1ω. The growth of these large boules was enabled by stiffening the platform base upon which the crystal grows. All of the growth runs that produced these boules terminated earlier than intended, with spurious crystals appearing in the solution and eventually attaching to the main boule.

The spurious crystals were determined to originate from the main boule, and are created by very slight relative motion between the crystal boule and the platform that breaks off microscopic crystal chips from the boule edges. Efforts in 1997 will be focused on reducing the stresses that produce this relative motion.

Solution inclusions tend to form on the pyramidal <101> faces of rapid growth crystals at the rotation parameters (rotation rate, acceleration, and rotation period) used to grow the large boules to date. These inclusions limit the number of usable plates which can be obtained from these boules. Until the platform was stiffened, we were limited to very low acceleration rates of 50 revolutions per minute per minute (RPM^2); exceeding this acceleration rate led to catastrophic failure by fracturing of the boule. Using a stiffer platform base enabled the use of higher acceleration rates that mitigated the severity of the solution inclusions on the pyramidal faces. An effort was initiated in mid-1996 to understand the nature of the hydrodynamic conditions in the rapid growth system, and of their correlation with morphological instabilities on the growing crystal faces. Scaling analyses relating conditions in the small tanks, where these inclusions rarely occur, and the large tanks, where they frequently occur, indicate that by further increasing the acceleration rates and periods these inclusions can be eliminated. Refinement of this understanding will continue in 1997 in conjunction with the efforts to increase the size of the KDP boules.

Continuous filtration to remove particulate impurities has long been associated with producing high-damage-threshold crystals. A full-scale continuous filtration system was built in 1996, and used successfully to grow a KDP crystal in a subscale crystallizer. The 3ω damage threshold of this crystal was 14 J/cm^2, which marginally meets the NIF requirement for operation at 1.8 MJ. The damage threshold of this crystal is about 30% lower than that of the best conventionally grown crystals. Careful studies in 1996 of damage in both rapidly grown and conventionally grown crystals have indicated the presence of defects in addition to particulates that may ultimately determine the 3ω damage threshold. A primary goal of the KDP group in 1997 is to develop suitable diagnostics for characterizing damage and identifying the critical defects that determine the damage threshold. While continuous filtration is necessary to consistently achieve high damage

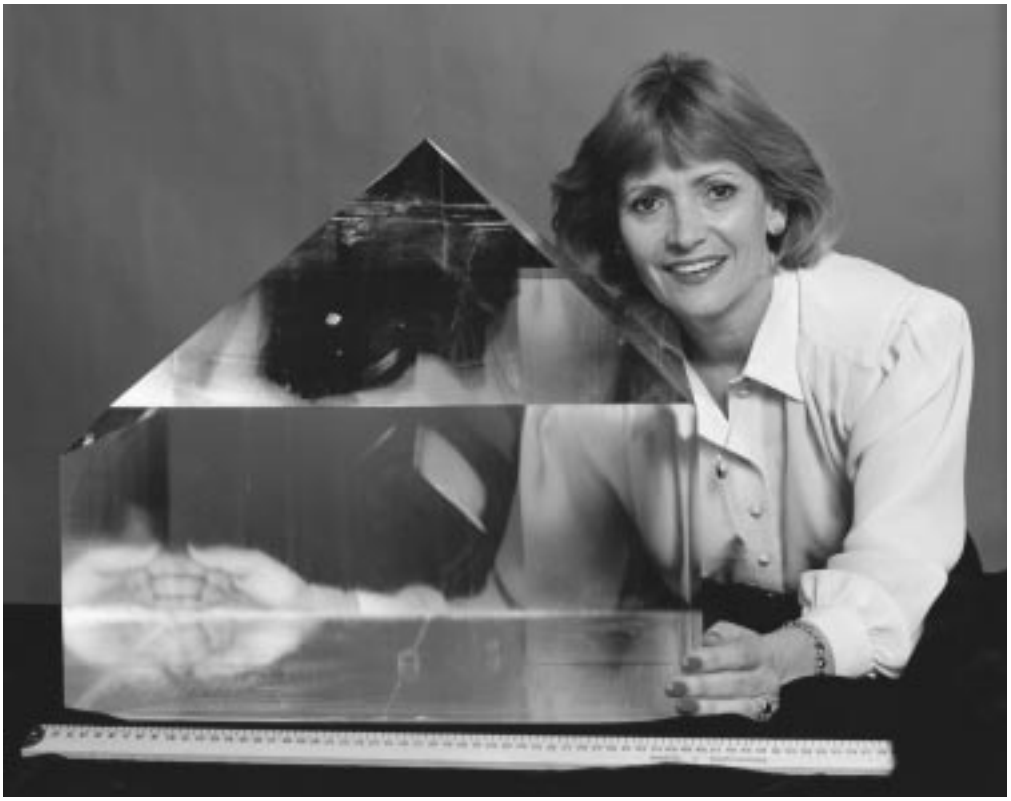

FIGURE 14. Rapid crystal growth technology, which allows growth of KDP crystals at 10-20 mm/day instead of 1-2 mm/day using traditional technology, is being scaled up to produce 55 cm crystal boules needed for NIF. In FY96, we produced the first large boules of KDP which yielded 41 × 41 cm plates needed for the NIF plasma electrode Pockels cell; these crystals met all NIF specifications. FY97 efforts will focus on further scale-up to 55 cm needed for the second harmonic conversion crystal plates, and on the growth of deuterated KDP (DKDP) needed for the third harmonic conversion crystal plates. (70-50-0996-2193pb01)

threshold in KDP, it may not be sufficient by itself. Nevertheless, NIF-size crystals will be grown with continuous filtration in 1997, and evaluated for damage in parallel with the continued, more fundamental studies on KDP bulk damage. The 3ω damage threshold of the boule from which the z-plates were fabricated was 12 J/cm^2, about 10% lower than that of the subscale crystal grown with continuous filtration.

In addition to effort aimed at increasing boule size, reducing inclusions, and understanding damage in 1997, the KDP group will also begin to grow full-size KD*P (deuterated KDP) crystals by rapid growth for the third harmonic generation crystals.

Corning Inc., in Corning, NY, is working to improve its fused silica deposition process and adapt its furnace design to optimize the fused silica boule geometry for the NIF requirements. This work involves increasing the furnace size, the thickness of the boules, and the deposition rate. Significant progress was made on burner modeling and single burner experimental studies, which indicates that the Corning goals for boule thickness and deposition rate can be met. The first implementation of this new design will be tested in mid-1997.

Fused silica boules from Corning tend to have moderately large index inhomogeneities in the center of the boule; this material is generally not used for ICF optics since it fails the homogeneity specification. A careful study of representative samples of this material using phase interferometry was initiated in 1996 to investigate the possibility of using the deterministic finishing processes for lenses and windows (described below) to correct this inhomogeneity, thereby substantially increasing the yield and reducing the cost of fused silica for NIF. The magnitude and gradient of the inhomogeneity was found to be small enough that we, along with the finishing vendors, are confident that this approach will be successful. Hence, the NIF specification for fused silica was relaxed, and the projected cost reduced accordingly.

Optics Fabrication: Flats, Lenses, and Crystals. Plano optics (flats) include amplifier slabs, mirrors, polarizers, windows, diffractive optic substrates, and debris shields. Finishing technology development for all of these optics includes deterministic figuring to minimize the time and cost needed for production. Figuring traditionally contributes about half of the cost of these optics. Other development activities common to these optics are cleaning and surface inspection. Improved cladding technology is required for the amplifier slabs, and finishing processes which produce high 3ω damage threshold surfaces are needed for the diffractive optic substrates and debris shields.

We are working closely with three companies on plano optic fabrication technology—Eastman Kodak in Rochester, NY, Tinsley Laboratories in Richmond, CA, and Zygo in Middlefield, CT. Each company has taken a different route to expand their existing capabilities to meet the NIF requirements.

However, these three companies agreed in 1996 to work together with LLNL and LLE to jointly develop generic technologies outside of their traditionally competitive sphere: edge cladding for amplifier slabs, precision cleaning, and surface inspection. This collaborative effort will minimize the cost of the development program and produce superior results more quickly by capitalizing on the unique strengths of each of the partners. The formal collaboration was initiated in late 1996; the development tasks will be concluded in late 1997.

Kodak has developed small-aperture figuring technology for a variety of defense and astronomy applications. For example, ion-beam figuring was used for final figuring of the hexagonal Keck telescope mirror segments. Kodak first applied their technology using subaperture polishing tools to phosphate laser glass amplifier slabs during the Beamlet Project in 1993. Residual errors caused by overlap of the individual passes of the tool produced ripple that was unacceptable for use on Beamlet. However, by improving the tool design and figuring process, Kodak was able to meet the NIF amplifier PSD specification. This specification is extremely tight to control peak laser fluence due to nonlinear processes limits wavefront aberration in the mm to cm lengthscale of less than one hundredth of a wave. Kodak's process is essentially ripple-free, producing surfaces that meet this specification with only two figuring iterations. Traditional continuous polishing (CP) technology typically requires ten or more iterations to achieve the final figure specification.

Kodak also made substantial progress in improving its CP technology used to polish the plano optics prior to entering its small tool process. Extensive process modeling coupled with real-time diagnostics were applied to a subscale CP machine to demonstrate highly deterministic CP polishing. Kodak will modify their full-scale CP machine in 1997 to demonstrate the process on NIF-size optics.

Tinsley also uses small tool polishing technology for final optical surface figuring. Traditionally, Tinsley has focused on manufacturing high-precision aspheric lenses and other complicated optic shapes. However, Tinsley is adapting this technology to plano optics for NIF. Tinsley designed and built full-scale edging, grinding, and polishing machines in 1996 that are needed for the development program, and can also be used for NIF production.

In 1996, Tinsley used these machines and its improved figuring process to manufacture mirror blanks that met the NIF specifications; these blanks will be coated and tested on Beamlet in 1997. Tinsley,

who had no previous experience with edge cladding, also began an intensive campaign to develop the capability for cladding and finishing NIF amplifier slabs. The company produced its first amplifier slab in 1996. In 1997, Tinsley is scheduled to clad and finish several of the amplifier slabs for AMPLAB.

In contrast to Kodak and Tinsley, Zygo uses its CP machines for final figuring rather than a subaperture polishing tool. To improve the determinism of this process, Zygo has substantially improved the stability (long-term flatness) of the lap surface. In 1996, Zygo demonstrated on a half-scale CP (96-inch diameter) surface form errors of less than one-tenth wave over a fifty-hour period, substantially exceeding their goal for NIF. Zygo will implement this technology on a full-scale CP machine in 1997. The conceptual design of this machine was completed in 1996.

In addition to the figuring development, Zygo has also demonstrated fixed abrasive grinding technology using electrolytic in-situ dressing (ELID) of the grinding wheel at 75% NIF size. This technology is faster than the traditional loose abrasive grinding process, and produces less subsurface damage that reduces the polishing time to remove the damage. In 1996, Zygo also developed and demonstrated at 50% NIF-size rapid and deterministic polishing technology; this step precedes their final figuring CP process. The polishing process will further reduce the time needed and cost for polishing NIF optics.

Tinsley Laboratories has supplied most of the lenses for Nova and all of the Beamlet lenses. Until 1996, these lenses were all round. Maintaining the tight figure tolerances near the edges and corners of square optics is extremely challenging. In addition, the NIF PSD specifications are difficult to achieve using small tool polishing, as discussed above for the plano optics. Tinsley was able to fabricate several square lenses in 1996 that either approached or met the NIF PSD specification. Tinsley has now defined the NIF figuring process for all the spatial filter lenses.

The 3ω damage threshold of the Tinsley lenses is not yet at the NIF specification. Work began in 1996 to develop a more detailed understanding of the determinants of 3ω damage to fused silica surfaces. We developed modified polishing processes and postpolishing processes for two-inch substrates that consistently produced damage thresholds above the NIF requirement. Nevertheless, we do not yet have a diagnostic such as subsurface damage, roughness, or contamination that correlates with damage. In 1997, we will extend the work initiated in 1996 to develop this scientific understanding of surface damage, and work closely with Tinsley to modify their current finishing process to yield high-damage thresholds on full-aperture lenses.

KDP and KD*P crystals are diamond turned rather than polished; this technology was first applied to KDP crystals for the Nova Project at Cleveland Crystals in Cleveland, OH. The flexure coupling was redesigned during the Beamlet Project to meet the Beamlet specifications. The coupling attaches the drive mechanism to the vacuum chuck that supports the crystal on the diamond turning machine used to finish the Nova crystals. This improved flexure coupling reduced the waviness in the one- to ten-millimeter regime, but did not affect the high, frequency surface roughness. The NIF surface roughness specification is two times tighter than Nova and Beamlet to meet the energy and spot size requirements. In 1996, the machine was upgraded by designing and installing a NIF-size flywheel, and the diamond turning process was modified to produce smoother travel along the slideways. The reduced turbulence from the improved flywheel and the smoother travel yielded surface roughness reduced by 2–3× on refinished Beamlet crystals. These crystals meet the NIF specification.

Cleveland Crystals also improved their blank fabrication process in 1996 to produce crystals with significantly better surface flatness. The flatness of the 37-cm Beamlet crystals ranged from 10–15 waves, making alignment very difficult. The NIF specification is 8 waves. Beamlet crystals refinished with this new process had a surface flatness of 3–7 waves. The two 41-cm crystal plates, fabricated from the rapid growth boule described above, were flat to within 3 and 5 waves, respectively.

The diamond turning machine, currently at Cleveland Crystals, produces crystals that meet the NIF specifications, but it is not appropriate to use in NIF production except as a backup machine. The machine is now almost twenty years old, and has tercite pads and steel slideways that are inappropriate for the volume of NIF production (600 crystals over a three year period). The NIF crystal size of 41 cm is also at the extreme of what this machine can handle, and tends to produce moderately high-surface gradients at the tool entry position due to nonstraightness of the slide. In 1996, Moore Tool Company was selected to design and build a new, larger diamond turning machine for NIF using hydrostatic bearings and other improvements over the machine at Cleveland Crystals. The design will be completed in 1997, and the machine built in 1998.

Optical Coatings: Mirrors and Polarizers, and Mirror Substrates. During the advanced conceptual design phase of NIF in 1995, it was suggested that lightweight mirror substrates may be needed to meet structural stability requirements for pointing. To meet this potential requirement, we initiated an effort to polish and coat half-size and full-size lightweight mirror substrates fabricated by Hextek in Tucson, AZ. These substrates were finished at Zygo and will be coated in 1997. They are scheduled to be tested on Beamlet in late 1997.

Both mirror and polarizer coatings require laser conditioning to meet the NIF damage requirement. These coatings are conditioned by exposing them first to a very low fluence, and then to increasing fluences in discrete steps until the damage threshold is approximately twice as high as would otherwise be achieved. This conditioning process is accomplished by rastering a small beam over the coating surface maintaining constant laser fluence, and then starting again at a higher fluence. The current process uses six successive increases to the laser fluence. This process was successfully demonstrated in 1996 on full-aperture turning mirrors installed in Beamlet. The number of steps needed to condition these optics determines the number of conditioning stations for NIF. Tests on small mirrors in 1996 suggest that fewer steps may be used, as few as two or three, which would allow the use of two less conditioning stations. These results will be investigated further in 1997 on full-aperture mirrors.

Also in 1996, the damage threshold of polarizer coatings was increased well above the NIF requirement by modifying the coating design at both Spectra-Physics in Mountain View, CA, and LLE. This work was performed on subscale parts; the results will be confirmed on full-scale coatings in 1997. Substantial progress was made in developing metal hafnium as the source material for the hafnium oxide layers in polarizer and mirror coatings. The hafnium is vaporized in an oxidizing atmosphere so it deposits as HfO_2 onto the substrate. Controlling the deposition rate is far easier with Hf than with HfO_2, the source material traditionally used for high-damage threshold ICF coatings. The improved rate control substantially improves the layer thickness control, thereby increasing the performance and yield. In addition, particulate concentrations are far lower on coatings made from Hf starting material, which also helps improve the damage threshold. NIF-size polarizer coatings will be made in 1997 from metal hafnium to confirm these results.

An automated damage threshold (ADT) system was implemented in 1996 at LLNL for testing coating damage. This system, based on scatter detection, substantially reduces the amount of operator interpretation needed to determine the damage threshold. In addition, much more data is taken over a larger area giving much better statistics for establishing the damage thresholds. Damage test systems installed at the coating vendors in 1996 will be upgraded with the ADT diagnostics as part of the NIF facilitization effort prior to pilot production.

National Ignition Facility

The National Ignition Facility (NIF) is a key component within the proposed facilities for DOE's science-based Stockpile Stewardship and Management Program. The extension of current program experimental capabilities embodied in the NIF is necessary for the ICF Program to satisfy its stewardship responsibilities. The physics and mission of the NIF for stewardship has been thoroughly reviewed by the JASON group and the ICFAC, both of whom strongly support the project.

All NIF Project management and staff positions have been filled to the planned levels. Major commercial contractors were chosen for the conventional facility architectural design, engineering services support, and construction management. Major contracts were placed with commercial vendors for optics facilitization to ensure an adequate optics production capability that meets the NIF cost goals. Work packages that reflect the national scope of the NIF Project were agreed to and implemented with the participating laboratories (Sandia National Laboratories, Los Alamos National Laboratory, and the Laboratory for Laser Energetics at the University of Rochester).

The technical basis of the NIF design was updated through a formal Advanced Conceptual Design (ACD) technical review process. Concurrent with the ACD activity, the documents that provide a hierarchy of the design requirements were reviewed and updated including the *Primary Criteria/Functional Requirements; the System Design Requirements*; and the laser system design/performance baseline. At the request of DOE, Defense Programs and other user requirements were included in the NIF design updates.

Key project controls were developed and implemented including: the *NIF Project Control Manual, the Configuration Management Plan*, and the DOE-approved *Quality Assurance Plan*. Change Control boards were established and are functioning. Cost account plans and authorizations for each work breakdown structure element were established. The commercial Sherpa Product Data Management system was selected and implemented to provide a project-wide centralized document, engineering drawing, and configuration control capability. A detailed Title I design schedule was developed, and regular baseline cost and schedule reviews implemented to track progress. Monthly and quarterly progress reports are prepared and distributed.

Title I design, which was postponed by late release in the Project TEC funding, was begun. An accelerated plan was developed and implemented, and is on schedule. Significant design progress has been made in all areas. The general arrangement of the Laser and Target Area Building (LTAB) was developed and is in configuration control; laser layouts were incorporated into the overall facility layout; and special equipment designs (lasers, etc.) were developed.

The NIF is a part of the Stockpile Stewardship and Management (SSM) Programmatic Environmental Impact Statement (PEIS). The SSM PEIS reaffirms the Secretary's statement at Key Decision One that LLNL is the preferred site for the NIF. In support of the PEIS,

write-ups and supporting analysis have been provided to the DOE, and a *Preliminary Safety Analysis Statement* (PSAR) draft document was completed and submitted to DOE. A final site selection will occur after public review of the SSM PEIS and a formal Record of Decision by the Secretary of Energy.

Inertial Fusion Energy/New Technologies

Inertial Fusion Energy

A new thrust in Heavy Ion IFE research began with the start of construction of an experimental research facility to evaluate recirculating induction accelerators for the acceleration of space-charge-dominated ion beams. This testbed, supported by a variety of DOE funding sources including LDRD and LLNL Engineering Thrust Area initiatives, will develop precise beam control and sensing techniques for all IFE accelerator concepts. The 3-D computational code, WARP3d, was used extensively in the design of the testbed. The recirculator architecture is a leading candidate for major cost reductions in high-current, induction accelerators for IFE.

LLNL's leading candidate for a laser driver is based on a diode-pumped, solid-state laser (DPSSL), for which the gain medium (ytterbium-doped strontium fluorapatite or Yb:SFAP), developed previously at LLNL, is cooled by He gas, known as the gas-cooled slab (GCS) concept. In FY 1996, an experimental campaign to test a small subscale GCS-DPSSL was completed. Results were encouraging enough to propose a 100-J, 10-Hz GCS-DPSSL (called Mercury) for consideration of LDRD funding in FY 1997.

Nova Petawatt Capability

Since 1993, we have been developing a petawatt (10^{15} W) laser capability on a Nova beamline under LDRD support. The Petawatt laser will provide LLNL with the capability to test the fast ignitor approach to fusion and explore other ultrahigh-intensity physics topics. The Petawatt Project reached its goal in May 1996 when we demonstrated the world's first petawatt laser with an output of 500 J in a pulse length less than 0.5 ps. Figure 15 shows the inside of the 20-m-long, 3-m-diameter Petawatt vacuum compressor chamber that contains a pair of 70-cm-diameter pulse compression gratings to produce the subpicosecond output pulse from a spectrally chirped input pulse more than a thousand times longer in duration. A major component of the Petawatt Project was developing the technology necessary to make these large high-damage-threshold gratings, as well as developing an entirely new chirped-pulse master oscillator system for Nova with the mechanical hardware and optical diagnostics necessary for pulse compression. The Petawatt laser received a 1996 *Popular Science* "Best of What's New" award and enabled the developments leading to

FIGURE 15. Inside the Petawatt vacuum compressor chamber. The two pulse-compression gratings produce a subpicosecond output pulse from a spectrally chirped input pulse more than a thousand times longer in duration. (70-60-0796-1538pb01)

a 1996 *R&D 100* award in "Interference Lithography for Patterning Flat Panel Displays." The Petawatt Project has been generally acknowledged to be the Laboratory's most successful LDRD project to date.

Spin-Off Technologies

In FY 1996, we continued to exploit ICF Program expertise and technology of interest to U.S. industrial and government markets in areas such as:

- Health-care technology—Applications of our expertise/technology applied to medicine include (1) modeling laser–tissue interactions, (2) the establishment of a medical photonics laboratory for developing a host of new medical technologies, and (3) the development of user-defined laser diodes and diode-pumped, solid-state lasers for medical procedures (e.g., port-wine stain removal, tattoo removal, and laser surgery).
- Military visualization systems—Pulsed microchannel x-ray imaging technologies are now being applied to developing advanced night- and underwater-vision technologies for the Department of Defense.
- Advanced high-energy particle accelerators—Areas being developed to support advanced accelerator technology include (1) the development of a high-gradient dielectric-wall accelerator to demonstrate transport of electrons at 1 kA with a record gradient of 20 MeV/m using novel insulating materials, and (2) the development of a high-current electron-induction accelerator for LLNL's B-Division Advanced Hydro-Test Facility proposal (a National Radiographic Facility).
- Femtosecond material processing—The use of intense femtosecond laser pulses for precision material processing (cutting) of metals is under development for various government and commercial applications. Processing with ultrashort pulses is qualitatively different from using longer pulses. The energy in an ultrashort laser pulse is deposited in a thin layer at the metal surface. The energy is deposited so quickly that significant thermal conduction or hydrodynamic motion (shock waves) do not have time to occur. Instead, the absorbed energy effectively removes the thin layer of material. Very precise removal of metal has been demonstrated with no modification of adjacent material even at high repetition rates. The laser pulses remove material without significant thermal overlap or bulk heating.

Program Resources and Facilities

Resources

In FY 1996, financial resources for the LLNL ICF Program totaled $83.7M in DOE operating funds and $2.7M in DOE capital equipment allocations. Work-for-Others funding decreased slightly in FY 1996, with $30.1M coming from various sources within the DOE community, other federal sponsors, and international sources. At LLNL, the NIF Project received $21.7M in DOE operating funds and $34M in construction funds for FY 1996. The average LLNL full-time employee equivalent count over the year was 347.6 (excluding the NIF Project). Supplemental contract labor personnel were used in clerical, design, and engineering positions and as Nova operators. The ICF Program employed approximately 61.8 supplemental labor personnel in FY 1996.

Figure 16 shows the resources available to the ICF Program over the past 15 years and compares the operating funds provided by DOE in then-year-dollars vs the same funding discounted to reflect 1982 dollars. The figure illustrates that the real purchasing power for the DOE funding, as related to FY 1982, has remained fairly constant and is expected to remain so in FY 1997.

Figure 17 illustrates Work-for-Others funding, which is becoming a significant part of the total resources available to the ICF Program, but is expected to decrease slightly in FY 1997.

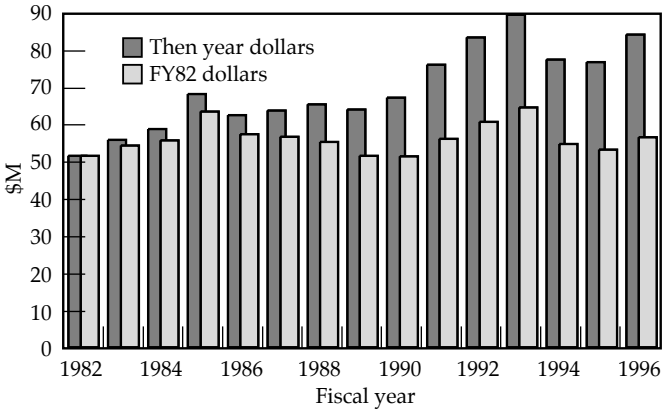

FIGURE 16. ICF program DOE operating funds.
(02-20-0396-0582pb02)

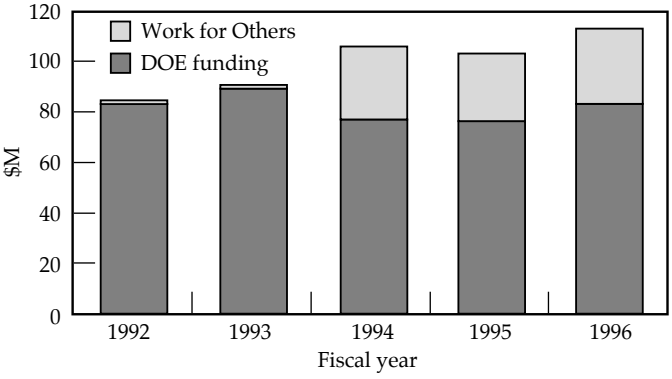

FIGURE 17. LLNL ICF program operating funding.
(02-20-0396-0583pb02)

These resources enabled the ICF Program to continue its support of research and development of high-energy-density physics, laser component development, optics technology, and IFE. A couple of examples of major projects accomplished during FY 1996 are the completion of the Petawatt modification to the Nova laser system and the facilitization of the Amplifier Laboratory in Bldg. 391.

Facilities

In FY 1996, the ICF Program comprised 52 facilities—laboratories, offices, and specialized facilities totaling 636,800 gsf. Figure 18 shows the locations of ICF facilities within the Laser Programs.

The emphasis during the year was supporting NIF activities. This included accommodations for NIF housing, lab modifications, adding support facilities, and developing criteria for a major facility upgrade to the west end of Bldg. 391. Figure 19 shows a location plan for NIF lay-down space to support Laser Target Area Building/Optics Assembly Building (LTAB/OAB) construction and NIF special equipment. In addition, several maintenance projects were completed during the year.

- Detail planning was required to relocate 600 people to meet NIF staffing requirements. Additional office space was obtained during the year to support NIF Title I needs.

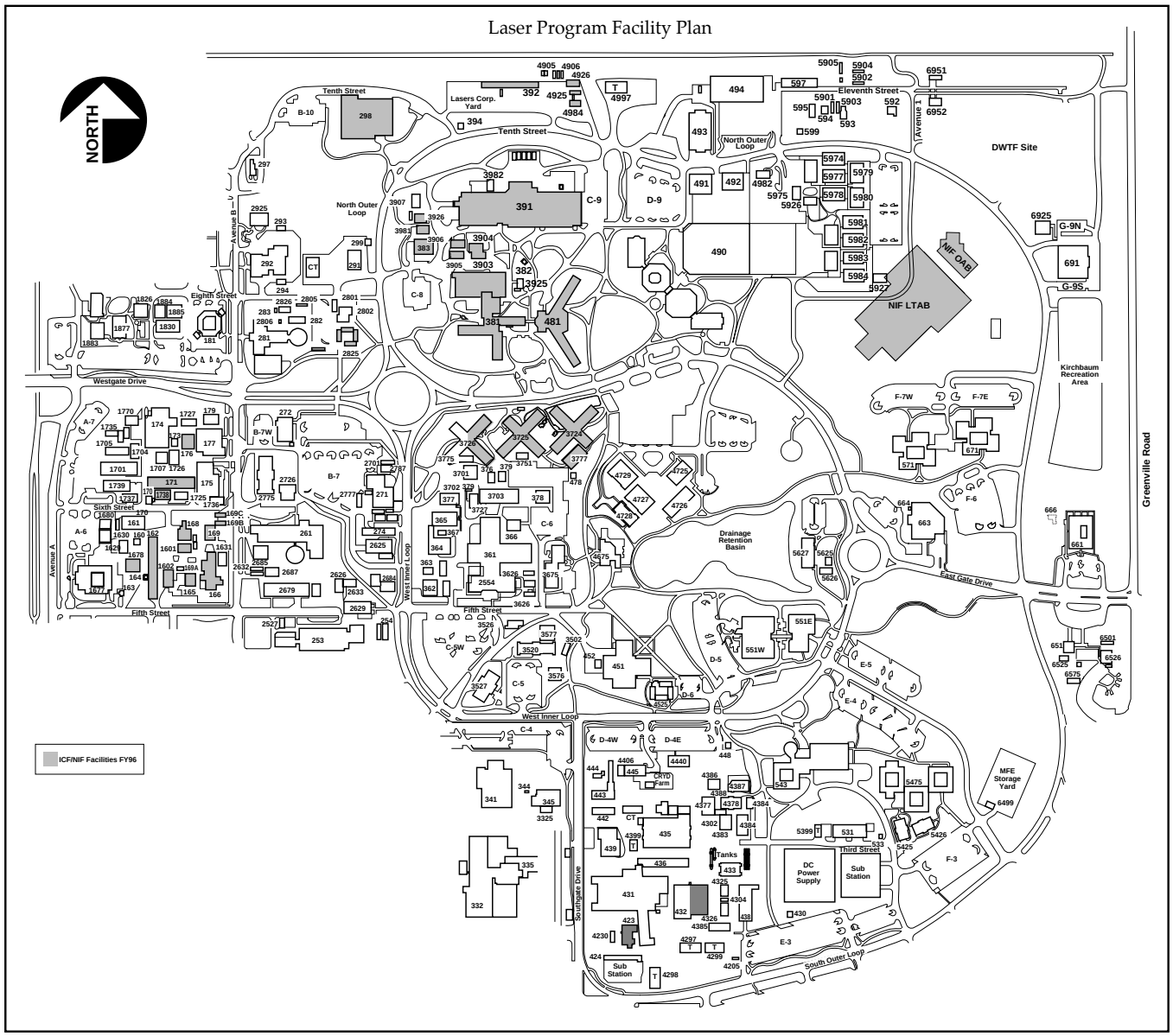

FIGURE 18. Locations of ICF facilities at LLNL site in 1996. (05-00-0497-0547pb01)

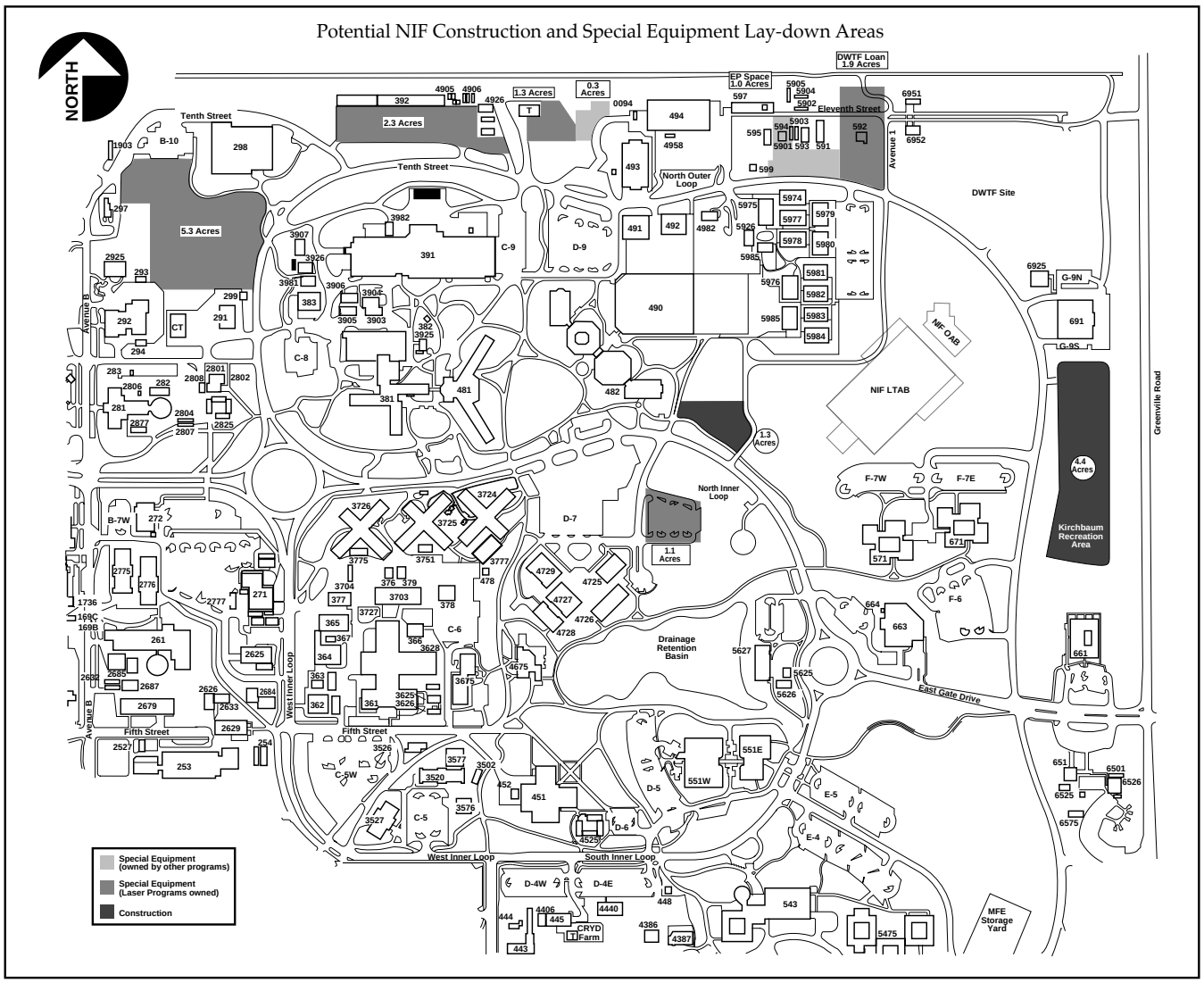

FIGURE 19. Potential NIF construction and special equipment lay-down areas. ((05-00-0497-0546pb01)

- Several major office modifications and upgrades were completed to meet NIF requirements.
- Several A Division/X Division co-location housing plans were developed through the year.
- During FY 1996, ICF facilities successfully carried out $2.3M in facility modifications and major upgrades to key laboratories and buildings.
- Completed Amplifier Development Lab and Flashlamp Test and Research Lab, plus the Control Room for monitoring and controlling both areas.
- Additional space and upgrades were started in Bldg. 432 to support NIF prototype activities.
- Completed upgrades to Bldg. 392 Optical Processing Lab and located support staff into Trailers 4924, 4925, and 4926.
- Developed Bldg. 391 west demolition and upgrades criteria to support NIF optics assembly needs.
- Completed modification to Bldg. 298 for the Laser Cutting Facility.
- Completed Phase I of Bldg. 481 power feeder upgrade.
- Several miscellaneous lab modification and alteration projects were completed during the year.

ES&H

During 1996, ICF continued its emphasis on Environment, Safety, and Health (ES&H) involvement in line operations. This included self-assessment walk-through reviews of labs and specialized facilities throughout the Program.

Special attention was given to ES&H issues, DefTrack deficiencies, and a careful review of safety operations for Beamlet. In addition, ICF Laser/Safety Interlock Systems were given special emphasis and more manpower support for reviews and system upgrades. The following summary highlights many accomplishments:

- Completed Self-Assessment Inspection covering 273 laboratories with 289 noted deficiencies and their subsequent repairs.
- Successfully passed two formal audits by representatives of the Bay Area Air Quality Management District and one by the representatives of the Livermore Water Reclamation District.
- Corrected 119 items from the ICF Def Track system, a laboratory-wide Deficiency Tracking System.
- Contributed to key National Ignition Facility safety documents.
- Assisted in the ICF Lock Out Tag Out implementation plan.
- Provided oversight for the Davis Applied Science student labs.
- Field-tested and proved the economic viability of recovering ethanol from the Sol Gel cleaning process, using a Solvent Recovery Still funded by EPD last year.
- Solved the ES&H issues raised during the LaNSA Pit ground water leak.
- A priority metric was developed, along with an implementation plan, to secure the approximately 188 optical tables, previously identified as potential seismic security problems.
- Relocated the Gas Mixing Lab from B343 to B298.
- Closed an administrative gap in the Incidental Fork Truck Operator's License training requirement by coordinating and documenting the hands-on training section of the course.
- Provided transportation of the ICF salvage hoppers to salvage (this service was discontinued by the transportation group).

Theory and Simulations of Nonlinear SBS in Multispecies Plasmas

S. C. Wilks *D. E. Hinkel* *B. MacGowan*

W. L. Kruer *K. Estabrook* *D. S. Montgomery*

J. Denavit *D. Kalantar* *E. A. Williams*

A. B. Langdon

Introduction

Stimulated Brillouin scattering (SBS) is an instability in which intense laser light incident on a target can decay into a scattered light wave and an ion sound wave. The process requires frequency and wavenumber matching (i.e., $\omega_o = \omega_{sc} + \omega_i$ and $\mathbf{k}_o = \mathbf{k}_{sc} + \mathbf{k}_i$), which corresponds to energy and momentum conservation. Here, ω_o (ω_{sc}) is the frequency of the incident (scattered) light wave and ω_i is the frequency of a sound wave in the plasma, and $\mathbf{k}_o$, $\mathbf{k}_{sc}$, and $\mathbf{k}_i$ are the corresponding wavenumbers. It is important to understand and control this instability to optimize energy deposition in inertial fusion targets.

SBS arises in two distinct places within a gas-filled hohlraum target. First, the gas in the hohlraum is ionized within the first couple of pico-seconds of the laser pulse, so the rest of the nanosecond pulse sees a plasma (~0.1 n_c) as it propagates toward the wall of the hohlraum. At later times, the ablation from the Au wall of the hohlraum becomes underdense and allows for the generation of SBS. It has been proposed that mixed species plasma, both in the gas and the wall of the hohlraum, can minimize the energy transferred to the ion waves and the reflected light, maximizing the amount of laser energy available for conversion to x-rays.

This article presents detailed particle-in-cell simulation studies of SBS in underdense plasmas composed of two and three distinct ion species.[1] Collisionless nonlinear saturation mechanisms are well modeled. For the parameters discussed here, these mechanisms depend critically on plasma composition. The effect of a self-consistently evolved non-Maxwellian distribution for the light ions on the ion-wave amplitude can be observed in detail. Mixtures of H and He are used to illustrate the physics of the situation. Various mixtures of "heavy" ions (carbon) and "light" ions (deuterium–hydrogen) are also studied in these simulations. The reflectivity and ion-wave amplitudes due to the SBS instability show many of the trends seen in experiments with these gases.

Alexeff, Jones, and Montgomery[2] investigated the effects of adding a light-ion species to a plasma composed primarily of a heavier, more abundant ion species. Their experiments show that the damping of the ion wave increases as significant amounts of the lighter species are introduced. This result agrees with a linear ion Landau damping model by Fried and Gould.[3] Clayton et al.[4] used a CO_2 laser to confirm many of the predictions in the linear regime. Although additional research has been done,[5,6] the nonlinear aspects of adding a light species to a plasma have been neglected. Some insight into this state is important since recent experiments[7–9] with intense laser light ($I \approx 3 \times 10^{15}$ W/cm^2, wavelength 0.351 μm, pulse duration $\tau_p \approx 1$ ns) and relatively high plasma density ~0.1 n_c (where n_c is the critical density) are thought to operate in a nonlinearly saturated state.

Computational Technique

We use the electron-fluid, particle-ion code EPIC to study various kinetic nonlinearities for saturation of the ion wave associated with SBS. Kinetic nonlinearities, such as particle trapping and extreme modification of the velocity distribution function arise when individual particle motion becomes important. Bulk "fluid" motion does not resolve individual particle velocities and cannot include single particle effects. An interesting comparison with linear theory is observed; however, there are significant differences. We find that particle trapping can substantially lower the ion-wave amplitude when a light-ion species is present in a predominantly heavy-ion plasma. These results agree with simple

nonlinear theories. Even in the nonlinear state, trace amounts of light ions can substantially reduce the reflectivity arising from SBS in a heavy-ion plasma.

A brief explanation of the simulation code illustrates the physics accessible in this study. EPIC resolves the electromagnetic (EM) wave associated with the laser light, both spatially and temporally, using the Langdon–Dawson advection scheme.[10] In one dimension, the light can be broken up into right- (E_+) and left-going (E_-) waves that advect exactly at the speed of light c:

$$\left(\frac{\partial}{\partial t} \pm c\frac{\partial}{\partial x}\right)E_{\pm} = -\frac{1}{2}J_y = \frac{1}{2}n_e e v_y \quad , \tag{1}$$

where J_y is the transverse current, e is the electron charge, and n_e is the electron plasma density. In the presence of a plasma, the transverse velocity v_y of the electrons serves as the source for the EM waves. The ponderomotive potential $U_p = 1/2\, m v_y^2$, where m is the electron mass, is saved every time step. This is an essential component of the feedback loop in the SBS instability because it couples the reflected light wave to the ion-density fluctuations, which then grow exponentially, according to linear theory. The ion-density fluctuation has a wavenumber $2k_o$ and frequency $\omega_{ia} = 2k_o c_s$, where $c_s = (ZT_e/M_i)^{1/2}$ is the ion sound speed, T_e is the electron temperature, Z is the ion charge state, and M_i is the ion mass. Since the ions move slowly on the time scale of the laser light, they need not be moved every time step. Instead, they are moved every 200th time step or so, by an amount determined by a time average of U_p over this time interval. EPIC handles the ions as particles, and the force on these ions is that due to the electrostatic field obtained from the electron momentum equation [(Eq. (2)], where the electrons are taken to be a massless fluid. Neglecting electron inertia is a good approximation, in that m is much less than M_i, so that the electrons can respond to bulk ion motion instantaneously on the ion time scale. Hence, the electrostatic field felt by the ions is

$$E_x = -\frac{1}{e}\left[\frac{\partial\langle U_p\rangle}{\partial x} - \frac{1}{n_e}\frac{\partial(n_e)T_e}{\partial x}\right] \quad , \tag{2}$$

where $\langle U_p\rangle$ represents the time-averaged value of U_p. Once this electrostatic field is known, the ions are then moved on the grid according to the equation

$$\frac{dv_i}{dt_i} = \frac{Z_i}{M_i}E_x \ ,$$

where

$$\frac{dx_i}{dt_i} = v_i \ . \tag{3}$$

Here, the dt_i denotes the ion time scale. Once the ions are at the new positions, the ion density n_i is computed. This is done for all ion species, usually two or three species with different masses $M_j = A_j M_p$ and charge states Z_j. Here M_p is the mass of the proton and A_j (Z_j) is the atomic number (charge state) of the jth ion. Finally, a new electron density is found by summing the ion density contributions over all species at each grid point, and setting n_e equal to this total ion density. The EM waves are then advected for another 200 time steps, and the process is repeated. (Reference 1 gives further details of the computational model and approximations.)

Experimental Motivation

The motivation for these simulations is a set of recent experimental results obtained on the Nova laser using "gas bags"[7] and gas-filled hohlraums.[8,9,11] Briefly, these experiments measured the reflectivity due to SBS from a number of large-scalelength (~1 mm), low-density (~0.1 n_c) plasmas composed of a variety of gases, such as C_5H_{12}, C_5D_{12}, and CO_2. The simulations presented here attempt to describe some of the trends in the experimental data. For all simulations, $T_e = 3$ keV, and the ratio of T_e to the initial T_i is always in the range $3 \le T_e/T_i \le 10$. The laser wavelength is $\lambda_0 = 0.351\ \mu$m, and the intensity is $I = 2.7 \times 10^{15}$ W/cm^2, as in the experiment. The density is typically either 0.1 n_c or 0.25 n_c, and the system length is usually $L_x = 75$, 150, or $330\lambda_0$. Roughly 1 million particles per ion species are used for the longer systems. Occasionally, the noise was increased to large levels to accelerate the onset of a nonlinear, quasi-stationary state. The reflected wave grows from a noise level I_{noise}, which is set by scattering of the incident wave from ion-density fluctuations. In these simulations, I_{noise}/I_0 is of the order 1%, but can be as low as 0.01%.

A few caveats concerning comparison of these simulations with experimental results are as follows: (1) The ions are constrained to move in one dimension in the simulation. Various two- and three-dimensional results, such as finite speckle width, filamentation, ion transport, and scattering of the ion waves in angle, are expected to reduce the reflectivity observed in the experiments. (2) The system is chosen to be roughly one speckle length long (for an $f/4$ lens), as opposed to the much longer system present in the experiments (~1 mm). (3) The simulations are only run for 10–20 ps, as opposed to a nanosecond for the experiment. However, linear gain calculations of this laser–plasma interaction consistently predict excessive gains, indicating that some nonlinear processes are at work to limit the reflectivities. Despite these differences, we hope to gain insight into some of the nonlinear saturation and damping mechanisms that may be playing a role in current experiments. We concentrate on the trends seen

in the simulations and experiments for various parameters and not on the absolute values of the reflectivity.

Theory

Linear theory predicts that trace amounts of light ions substantially increase the ion Landau damping of the ion wave. There are several reasons for this effect. (1) If we assume that the T_i are the same, the higher thermal velocity for the light-ion species leads to more ions in resonance with the wave. (2) The phase velocity is a function of the plasma composition. To illustrate this, consider the linearized ion continuity and momentum equations for the two fluids:

$$\frac{\partial n_{i1}}{\partial t} + n_{i10}\frac{\partial u_{i1}}{\partial x} = 0 \quad , \qquad \frac{\partial n_{i2}}{\partial t} + n_{i20}\frac{\partial u_{i2}}{\partial x} = 0 \tag{4}$$

and

$$\frac{\partial u_{i1}}{\partial t} = -\frac{Z_1}{M_1}kT_e\frac{1}{n_{e0}}\frac{\partial n_e}{\partial x} \quad , \qquad \frac{\partial u_{i2}}{\partial t} = -\frac{Z_2}{M_2}kT_e\frac{1}{n_{e0}}\frac{\partial n_e}{\partial x} \quad . \tag{5}$$

By combining Eqs. (4) and (5) into one equation for the ion wave, an effective phase velocity v_p for the ion wave is found to be

$$v_p^2 = \frac{n_{i10}\dfrac{Z_1^2 kT_e}{M_1} + n_{i20}\dfrac{Z_2^2 kT_e}{M_2}}{Z_1 n_{i10} + Z_2 n_{i20}} \quad . \tag{6}$$

Figure 1 plots this phase velocity for C and H at $T_e = 3$ keV, as a function of the fraction of H in the gas mixture. The limit in which only C ions are present smoothly connects to the case for only H present. Note that the phase velocity falls rapidly from the pure H case, essentially because the phase velocity is determined by the heavy species when the fraction of H is roughly 50%.

The physics can be clarified by considering the velocity distribution function $f(v)$ of two ion populations with different atomic numbers and charge states. Consider first pure He, as shown in Fig. 2. Notice the small slope and the small number of particles at the phase velocity of the ion wave v_p $(n_H = 0) \equiv c_{sHe}$ available to damp the SBS-generated ion wave. Now consider pure H at the same T_i. The slope at v_p $(n_{He} = 0) \equiv c_{sH}$ is somewhat greater than for pure He, and there are more particles at this phase velocity. Finally, consider a mixture of 20% H and 80% He, where v_p is now given in accordance with Eq. (6) and is approximately equal to c_{sHe} (see Fig. 2). In this case, a large number of H ions can now damp the ion wave even more efficiently than in pure H, because the phase velocity has moved farther into the bulk of the distribution function. Thus, linear theory predicts that the damping for the mixture will actually be greater than for H alone (and thus give the lowest reflectivity), and that pure He will have the least damping (and the highest reflectivity). Simulations bear out this prediction. For simulations with parameters similar to those discussed earlier, pure He gives a reflectivity $R \approx 30\%$, pure H gives $R \approx 10\%$, and the 20% H and 80% He give $R \approx 5\%$.

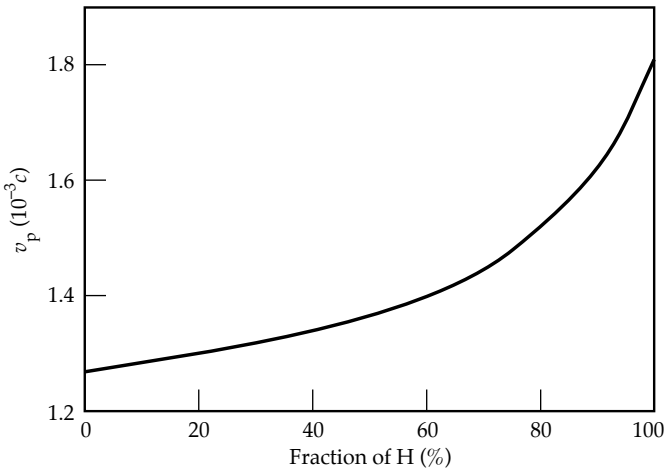

FIGURE 1. Acoustic wave phase velocity vs fraction of H present in a CH plasma. (50-00-0495-1065pb02)

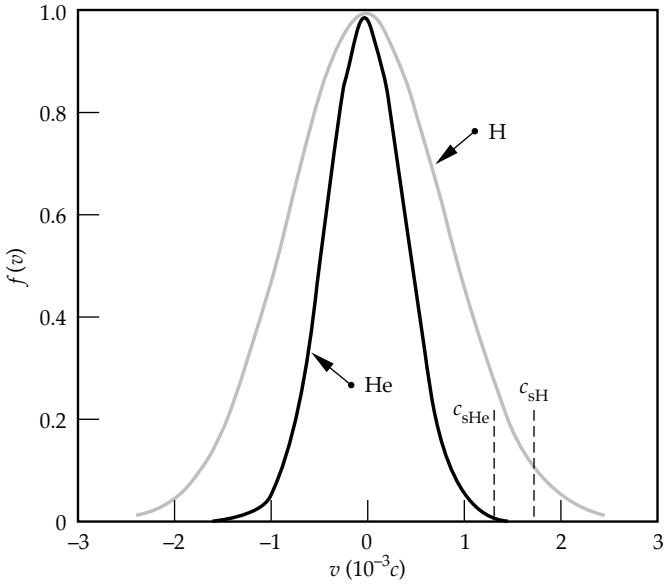

FIGURE 2. Ion distribution functions for a pure He plasma and a pure H plasma, for $T_e = 3$ keV and equal T_e/T_i. (50-01-0695-1418pb02)

Particle Trapping

We have discussed the effect of plasma composition on linear damping of the ion acoustic wave. However, the simulations show that nonlinear effects can be important when the reflectivity is significant. Let us now examine the simplest nonlinear effect, which is ion trapping. When the ion trapping velocity is equal to the phase velocity of the ion wave, the amplitude of the density perturbation associated with the ion wave will saturate. For one species, this limiting amplitude (neglecting temperature effects) is the well-known result $\delta n/n = 1/2$,[1] where δn is the low-frequency fluctuation in n_e associated with the ion wave. For two species, assuming cold ions ($T_i \approx 0$), the limiting amplitude of the density perturbation is found to be $\delta n/n = 0.25$ when the light species is H. This factor-of-2 difference arises from the fact that the H ions are the particles being trapped in a wave with a phase velocity determined by the heavy fluid. The assumption here is that there is only a small amount of the light ions in the mixture. However, when T_i effects are included, the limiting amplitude is considerably reduced to

$$\left(\frac{\delta n}{n}\right)_{tr} \approx \frac{1}{2T_e}\left(\frac{M_1}{Z_1}\right)\left(v_p - \sqrt{\frac{3T_i}{M_1}}\right)^2 \quad , \tag{7}$$

where the phase velocity is found from

$$v_p^4 + v_p^2\left(\omega_{pH}{}^2\lambda_{De}{}^2 + \omega_{pC}{}^2\lambda_{De}{}^2 + 3v_{pH}{}^2\right) + 3v_{pH}{}^2\omega_{pC}{}^2\lambda_{De}{}^2 = 0\,. \tag{8}$$

Here, λ_{De} is the Debye length, ω_{pH} is the plasma frequency of the light-ion species (H), and ω_{pC} is the plasma frequency of the heavy ions (C). For a temperature ratio $T_e/T_i = 10$, Eq. (7) predicts $(\delta n/n)_{tr} \approx 5\%$.

The EPIC simulations show the nonlinear state to be very rich. For example, for the case of C_5H_{12}, the H ion distribution function near v_p initially flattens due to ion trapping, as discussed. However, a number of effects follow. (1) As the ion waves grow and ions are pulled out of the initially Maxwellian distribution, a severe modification of the distribution function near v_p occurs [see Fig. 3(a)]. When a "bump" is present in a distribution function, the distribution function is unstable to ion sound waves near v_p. The ions have a tendency to relax back to a more stable distribution function, sometimes called a "quasilinear plateau." This is essentially a flat slope near v_p. However, it is found that before the distribution function reaches this state, it over-shoots the plateau and re-develops a slope near v_p [see Fig. 3(b)]. Thus, the distribution function will "oscillate" about this point. The distribution function inside the trapping width oscillates at the bounce frequency ω_B, as predicted by O'Neil.[12] As the distribution function evolves, there is a nonlinear frequency shift due to modifications that the trapped ions make on the ion wave, which reduce v_p. This allows the instability to access "fresh" slope on the distribution function. An additional effect that works to widen the plateau region is the transport of the faster,

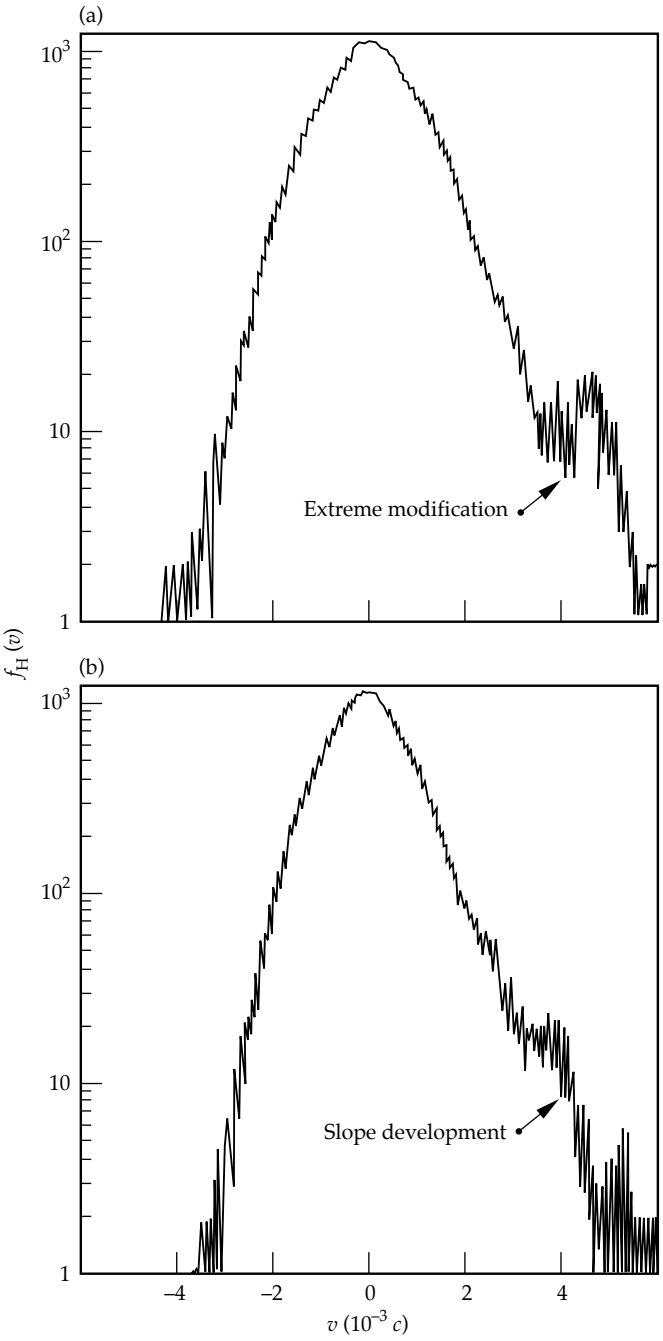

FIGURE 3. Ion distribution for the H component in a C_5H_{12} plasma showing (a) an extreme nonlinear modification early in time and (b) subsequent development of slope later in time near the phase velocity of the ion wave associated with SBS. (50-00-0495-1066pb02)

heated ions. This allows for a redevelopment of the slope, permitting additional damping.

We now compare EPIC simulations with experimental results in which the fraction of light ions (H) in the gas mixture varies, and the reflectivity is measured for two gas mixtures, $CO_2 + C_3H_8$ and $C_5H_{12} + C_3H_8$. By increasing the amount of propane in each mixture, the reflectivity as a function of H present decreased strongly in the gas-bag experiments.[7–9] This agrees with experiments in which this phenomenon was observed using a CO_2 laser.[4] The EPIC simulation results shown in Fig. 4 exhibit a similar trend. In the simulations, the gas starts out as pure C, and H is continuously added (eliminating C to keep the same plasma density) until the gas is pure H. Clearly, varying the plasma composition by adding H is an important technique for reducing the level of SBS.

SBS in Gas-Filled Hohlraums

Current hohlraums are filled with a low-density gas, which slows the inward motion of the Au walls and improves the time-dependent symmetry of the x-ray flux on the capsule. As discussed, SBS in the low-density gas is reduced by the presence of H. (An H–He mixture is planned for ignition hohlraums.) However, it is necessary to avoid significant SBS from the low-density Au near the walls, where the ion wave is weakly damped. Indeed, this SBS could be a seed that is further amplified in the low-density gas.[8]

A series of simulations has been conducted to understand the Au wall–gas interface. Figure 5 shows the variation of plasma density along the direction of the laser beam when the reflectivity has saturated (≈20 ps). In this simulation, four-fifths of the plasma is a C_5H_{12} gas at 0.1 n_c, and the last fifth of the plasma is Au at 0.12 n_c. Initial values are $T_e = 3.0$ keV, $T_e/T_i = 2.0$ for Au, $T_e/T_i = 5$ for H, and $T_e/T_i = 5$ for C. The laser $I = 2.7 \times 10^{15}$ W/cm^2. As shown in Fig. 5, a substantial ion wave develops in the Au. However, because of the H in the gas, the ion density perturbation in the C_5H_{12} is quite low. In this simulation, $R \approx 6.0\%$. In a similar simulation using identical parameters but without the Au wall, $R \approx 2.0\%$. Clearly, the presence of low-density Au near the hohlraum wall can significantly affect the reflectivity.

One proposed solution is to use Be-doped Au for the hohlraum wall.[13] However, there is an additional complication when one attempts to model Au–Be; namely, collisions between the Au and Be ions. Simply, estimates of collision times are roughly equal to the time it takes to flatten the slope (see the discussion associated with Fig. 3). This introduces yet another enhanced damping mechanism—collisional damping. This is due to the fact that collisions can "keep the slope," thus increasing the range of validity of linear theory since the distribution function can remain more or less Maxwellian. Therefore, further study of the Au–Be wall requires that collisions be included in the simulation code. Preliminary studies with a collisional code[14] have shown that the addition of Be does in fact reduce SBS in the Au-wall blow-off. This is in agreement with recent experiments on the Nova laser.[14,15]

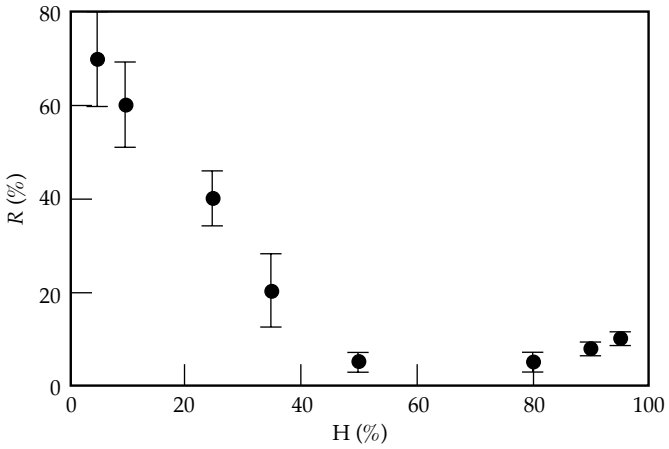

FIGURE 4. Simulation results of reflectivity vs percentage of H present in the plasma. Clearly, the inclusion of small quantities of H can significantly reduce the SBS reflectivity in the nonlinear state. (50-01-0695-1421pb01)

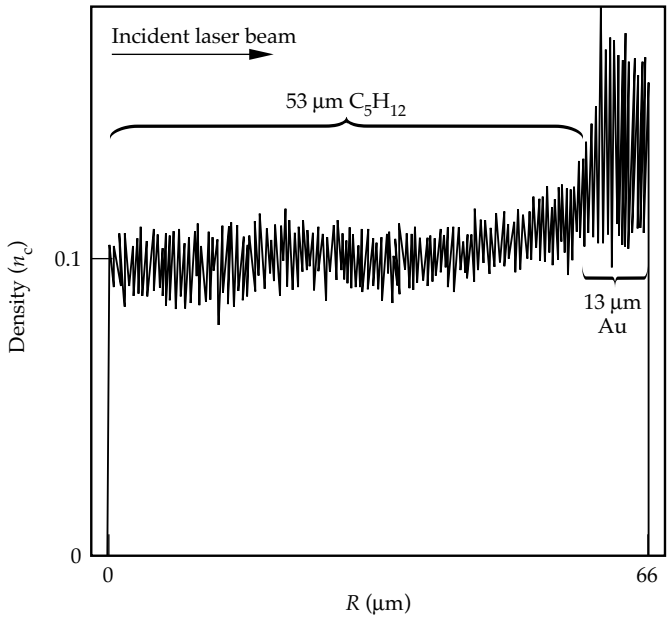

FIGURE 5. Density profile of an EPIC simulation modeling the interface between a low-density gas and the Au wall blow-off of a hohlraum. Note that the Au is initially in the last one-fifth of the plasma. (50-01-0695-1422pb01)

Summary

This article presents a detailed study of nonlinear processes associated with SBS in a multi-ion-species plasma. We theoretically estimate and compare a number of these nonlinear effects with EPIC kinetic multi-ion-species simulations results and with recent experiments. EPIC results for reflectivities are consistent with the trends observed in experiments. We provide a physical argument for the linear damping in a multispecies plasma, obtaining a simple physical picture of the role light ions play in the damping of the ion waves associated with SBS. We also address the modifications to ion trapping, an inherently nonlinear process, when two species are present and find that the addition of a light species could greatly decrease the amplitude of the ion wave where trapping will occur. These simulations show that distortion in the ion distribution functions can play an important role in determining the amount of reflectivity due to SBS observed in recent experiments. We illustrate a solution to the possible problem of significant SBS due to the low-density Au in gas-filled hohlraums.

Notes and References

1. S. C. Wilks, W. L. Kruer, D. E. Hinkel, E. A. Williams, et al., *Phys Rev. Lett.* **74**, 5048 (1995).
2. I. Alexeff, W. D. Jones, and D. Montgomery, *Phys. Rev. Lett.* **19**, 422 (1967).
3. B. Fried and R. W. Gould, *Phys. Fluids* **4**, 139 (1961).
4. C. E. Clayton, C. Joshi, A. Yasuda, and F. F. Chen, *Phys. Fluids* **24**, 2312 (1981).
5. E. A. Williams, et al., *Phys. Plasmas* **2**, 129 (1995).
6. H. X. Vu, et al., *Phys. Plasmas* **1**, 3542 (1994).
7. B. MacGowan, et al., *Bull. Am. Phys. Soc.* **39**, 1662 (1994).
8. J. Fernandez, et al., *Bull. Am. Phys. Soc.* **39**, 1663 (1994).
9. R. Turner, et al., *Bull. Am. Phys. Soc.* **39**, 1662 (1994).
10. A. B. Langdon and J. M. Dawson, *Proc. First Conf. Num. Sim. Plasmas*, College of William and Mary, Williamsburg, VA. 39–40, 19–21 (1967).
11. G. F. Stone, C. J. Rivers, M. R. Spragge, and R. J. Wallace, *ICF Quarterly Report* **5**(3), 151, Lawrence Livermore National Laboratory, Livermore, CA, UCRL-LR-105821-95-3 (1995).
12. T. M. O'Neil, *Phys. Fluids* **8**, 2255 (1965).
13. K. Estabrook, et al., *Bull. Amer. Phys. Soc.* **40** (1995).
14. P. Rambo, W. L. Kruer, and S. C. Wilks, *Bull. Amer. Phys. Soc.* **40** (1995).
15. R. Kirkwood, et. al., *Bull. Amer. Phys. Soc.* **40** (1995).

Modeling of Self-Focusing Experiments by Beam Propagation Codes

W. H. Williams *P. A. Renard*

K. R. Manes *D. Milam*

J. T. Hunt *D. Eimerl*

Introduction

Computer codes that model the propagation of intense laser beams through laser systems have played key roles in the design and analysis of all the ICF lasers built at Livermore.[1] These codes treat, at various levels of sophistication, the effects of linear diffraction, loss, amplification, and beam perturbation by self-focusing.

Laser designs for the National Ignition Facility (NIF)[2] are being analyzed using two recently developed comprehensive, *ab initio* computer simulation codes, PROP1 and PROP2, which treat one and two transverse dimensions, respectively. The codes use fast-Fourier-transform (FFT) propagators on a rectangular grid and treat only one polarization of the field. The effects of linear propagation and nonlinear refraction are calculated separately at each step along the propagation (z) axis. Within the limit of grid resolution, they calculate the electric field experienced by each component in a laser during a shot. To model typical NIF laser operations realistically, we use beam aberrations obtained from measurements on actual optical components, gain profiles from existing testbed amplifiers, adaptive optics models, and characterizations of various optical defects observed in tests of the Beamlet laser.

It is important that these codes be validated, because staging and architecture decisions, which often involve significant cost consequences, are driven by risk-of-damage assessments made using them. Over the past year, PROP1 and PROP2 have been benchmarked against analytical propagation cases, nonlinear perturbation analyses, earlier-generation FFT codes, and, most important, against the results of specially designed experiments. This article describes two comparisons of the code with results of self-focusing experiments conducted in the Optical Sciences Laser (OSL) facility.[3]

Self-focusing has always been a significant problem in fusion lasers, and beam photographs often show intensity ripple generated by self-focusing. Figure 1 demonstrates the seeding of intensity ripple by scattering from obscurations in the chain. These three photographs of the output beam in the Novette laser, the two-beam predecessor of Nova, were taken during shots at 10, 11, and 13 TW. The three intense regions in the right sides of the beams were caused by millimeter-sized imperfections on a turning mirror about two-thirds of the way through the chain. The nonlinear origin of the resulting intensity ripple is apparent from the rapid growth of ripple amplitude with increasing laser power. (The dark band in the center of each beam is the shadow of an absorbing region that separates the

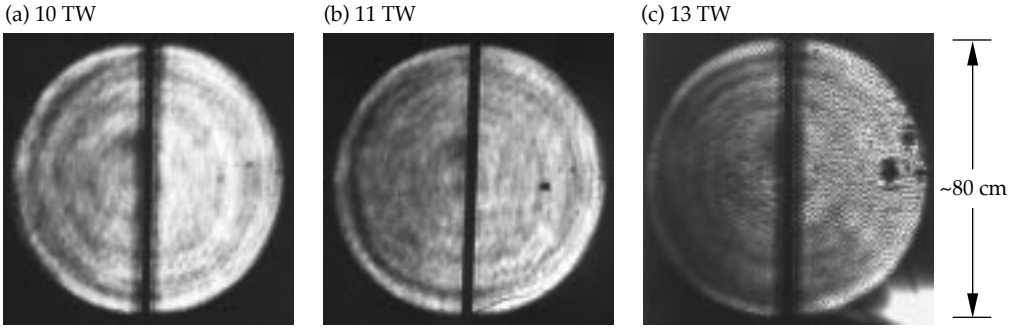

FIGURE 1. Photographs of the output beam of the Novette laser for output powers of 10, 11, and 13 TW. The growth of ripple depth at the three small areas in the right side of the beam illustrates the seeding of self-focusing by imperfections on components in the chain. (70-00-0196-0155pb01)

two halves of the largest amplifier disks to prevent parasitic losses.)

A correct treatment of nonlinear refraction is one of the most difficult aspects of the modeling of beam propagation. The refractive index of most optical materials has a small but important nonlinear (intensity-dependent) contribution that typically limits the high-power performance of fusion lasers. The "nonlinear index coefficient" γ is defined by the expression for the total refractive index,

$$n = n_0 + \gamma I, \tag{1}$$

where n_0 is the linear index and I is the intensity. The optical propagation distance z is related to n_0 and γ and the physical path length d by the rule

$$z = \frac{d}{n_0 + \gamma I} \approx \frac{d}{n_0} - \frac{B}{k}, \tag{2}$$

where $k = 2\pi / \lambda$ is the wave number and B is the intensity-dependent phase retardation, given by

$$B(x, y) = k\gamma \int_0^L I(x, y)\, dz; \tag{3}$$

the integral is taken along a particular ray path through the laser. Intense regions of the beam induce more retardation, causing the wavefront to lag and focus just as a positive lens does.

Localized self-focusing can produce very high intensities. In most simple calculations, the self-focusing at local intensity maxima is treated in Fourier-transform space. The input intensity ripple is described by a Fourier distribution; the self-focusing in a segment of the beam path is described by a multiplication factor, or gain, for each spatial-frequency component in the distribution.[4] Transforming the amplified frequency distribution back to physical space yields the intensity ripple at the output of the path segment. The gain for individual frequency components of the electric field can be as high as $\exp(B)$, and the total induced phase retardation in a laser operated at high intensity can exceed 2π. Therefore, for ripple of the physical scale that corresponds to greatest gain, the power of those components can be increased by a factor of $\exp(2B)^2 \approx 300{,}000$.

A major contribution to our ability to build high-power lasers was the realization that a spatial filter could be used to block the Fourier components of intensity ripple that experienced highest gain.[5] Lenses in the spatial filters also correct for linear diffraction through image relaying.[6,7] The filters are interspersed in the chain so as to "clean" the beam after each accumulation of ΔB in phase retardation; the present NIF design point is $\Delta B = 2.2$ rad. The apertures used in the spatial filters segregate the beam perturbations into high-frequency components, which are blocked, and low-frequency components, which are transmitted.

There remains the problem of understanding the issues that result from modest self-focusing of $\Delta B = 2$–2.3 in sections of the chain between filters. The most serious of these issues is optical damage. Optical damage in the near IR is presumed to depend on the local strength and duration of the optical field and on the condition of the optical component, which in actual systems may depend on its usage history. In most instances, the damage threshold of optical surfaces and coatings is less than that of the bulk material. One task in evaluating a proposed design is to determine the damage thresholds of the various components. A second task is to use a code such as PROP2 to determine the risk of damage for the proposed design. Self-focusing must be considered during this determination. During transmission of a beam at a high (but nominally safe) intensity through an optical component, self-focusing within the component at local regions of high intensity can cause enough intensification to damage the exit surface. In extreme cases, the induced focusing can break the beam into intense filaments that cause internal bulk damage called angel-hair tracking.[8]

Figure 2 illustrates an interesting special case of self-focusing, called hot-image formation. Light diffracted by an obscuration or defect on one component spreads across the beam in a second component. Nonlinear refraction in this second component, driven by the sum of the scattered and primary beams, creates a lensing effect that deflects some of the energy from the beam into a downstream focus, which appears as a bright image of the obscuration. A third component, in the plane of this induced "hot" image, might be damaged even when the system was operating at a nominally safe intensity that did not damage the first two components.

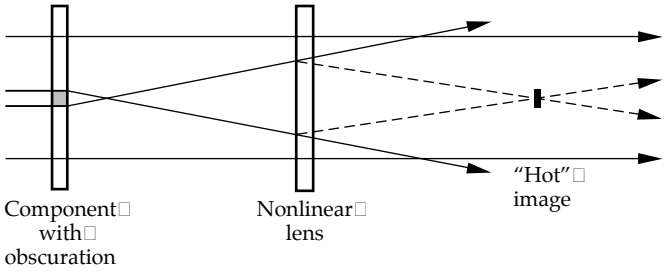

FIGURE 2. Nonlinear refraction induced by the sum of a scattered wave and the intense background wave produces a conjugate wave that is focused to an intense ("hot") image. (70-00-0196-0142pb01)

Hot-image formation by a thin "lens" has been treated analytically for low-intensity ripples in a

high-intensity beam.[9] The scattering sources treated were opaque disks and circular obscurations with Gaussian-distributed opacity. The analysis is readily extended to the case of an opaque linear obscuration (e.g., a wire). Neglecting some details, the model predicts that opaque obscurations cause the formation of hot images with intensity that is greater by a factor of $\sim(1 + B^2)$ than the mean intensity in the beam. For $\Delta B = 2.3$ rad, the predicted relative intensity is ~6.

In contrast to analytic perturbation models, which can easily treat only shallow modulation, PROP1 and PROP2 were designed to treat self-focusing of a beam containing deep intensity ripples. Validation of these codes by modeling the performance of large lasers is difficult, because it is difficult to identify all the source terms for amplitude ripple. We have therefore conducted self-focusing experiments in the OSL facility and compared the results with the predictions of the codes. We used the hot-image configuration for the experiments, since we could induce either a hot image or track damage in the "lens" by varying the obscuration.

Arrangement of the OSL Experiments

The OSL is a 100-J class Nd:glass laser staged to produce 0.5–100-ns pulses that are minimally disturbed by nonlinear refraction in the laser itself. In a typical shot, the fluence is below 0.5 J/cm^2 everywhere in the chain, and the induced phase retardation is less than 0.1 wave ($B = 0.6$). The beam diameter is reduced from 80 to 20 mm at the laser output to increase its intensity.

Figure 3 shows the arrangement used for the self-focusing experiments. The beam was passed through a 25-cm-long silica rod. Obscurations (wires with diameter of 175 or 500 μm) were placed in the beam in a plane 100 cm upstream of the rod. The energy, waveform, and spatial distribution of the beam were measured in the plane of the obscuration. Energy was measured to within 1% by an absorbing-glass calorimeter, and the spatial distribution was recorded by a CCD camera. The waveform was recorded by a Hamamatsu diode and a Tektronix SDC5000 oscilloscope and by a streak camera.

The experiment was arranged to allow recording of the spatial distribution of the beam in planes at a suitable range of distances downstream from the silica rod; the hot images were predicted to lie about 100 cm downstream. Because the area of a CCD camera is about 5 × 6 mm, the entire 20-mm beam could not be recorded without demagnification, which might have limited the resolution in the records of the small, hot images. Two records were therefore made. One camera, placed directly in the 20-mm-diam beam, recorded a 1:1 image of a 5-mm-diam beam segment isolated by an iris. A second camera recorded an image of the same plane, but with a demagnification of about 2:1. Changing the plane of observation without disturbing the cameras was accomplished by mounting the pick-off optics on a slide rail.

Selection of Wire Diameters

Wire diameters were selected on the basis of calculations done with PROP1. We wanted one wire that produced beam ripple of modest depth, which could be regarded as a perturbation, and another that produced very deep modulation. The experimental results confirm that these calculations give a good overall view of the intensity variation along the entire beam path. Figure 4 shows the predicted evolution of intensity with propagation distance z when a 175-μm-diam wire is placed in a 1053-nm plane-wave beam. The wire was at $z = 0$, and the silica rod was positioned between $z = 105$ and $z = 130$ cm. The input pulse waveform was a 0.5-ns linear ramp with a peak intensity of

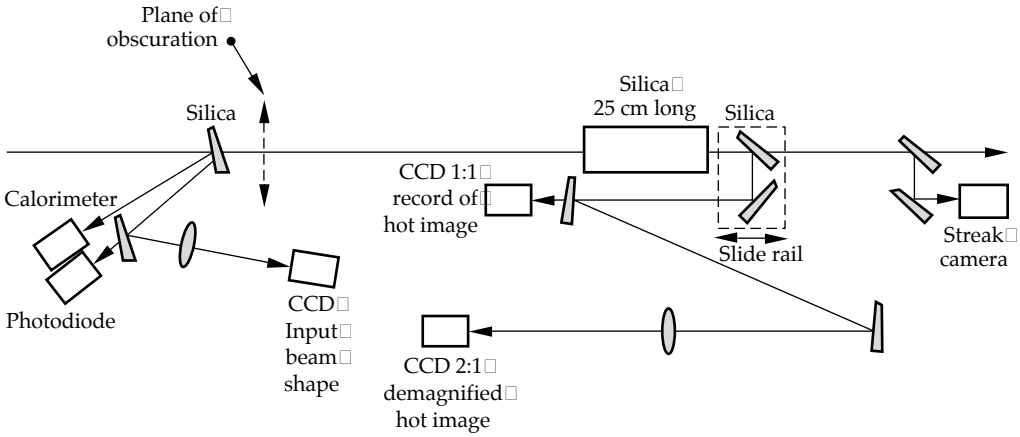

FIGURE 3. Experimental arrangement for characterizing input pulses and recording hot images formed by nonlinear refraction. (70-00-0196-0143pb01)

6.0 GW/cm^2. The waveform was sliced into five equal-fluence segments (with average intensities of 1.3, 3.2, 4.3, 5.0, and 5.6 GW/cm^2), which were independently propagated through the system. The intensity was calculated in planes separated by 5 cm. In each plane, the beam contained the diffraction pattern of the wire; the curve in Fig. 4 simply connects the calculated values of the highest intensity anywhere within the beam.

The calculated intensity increased rapidly in the region immediately beyond the wire as the diffraction ripples formed, and then decreased slightly as the beam propagated to the entrance of the silica rod. Over this zone, intensity changes arose solely from linear diffraction. Self-focusing in the rod produced two effects: the diffraction fringes were narrowed and intensified, and an induced "whole-beam" lensing occurred as a result of the intensity gradients in the superposition of the diffracted light and the main beam. Fringe intensification accounts for the higher intensity at the output end of the rod; high intensity at z = 230 cm was caused by lensing. In this case, the calculated intensity is higher in the hot image than in the rod, and the rod can be regarded as the "lens."

Figure 5 shows the results of a corresponding calculation with a 500-μm-diam wire. The intensity variation within the beam is very high at the entrance of the rod, because the diffracted light has not yet spread across the dark shadow of the wire. It is predicted that fringe intensification will produce a higher intensity at the output surface of the rod than that produced downstream by induced lensing. In this case, it is expected that avoidance of damage to the rod will limit input intensity to values below that required to produce an intense image.

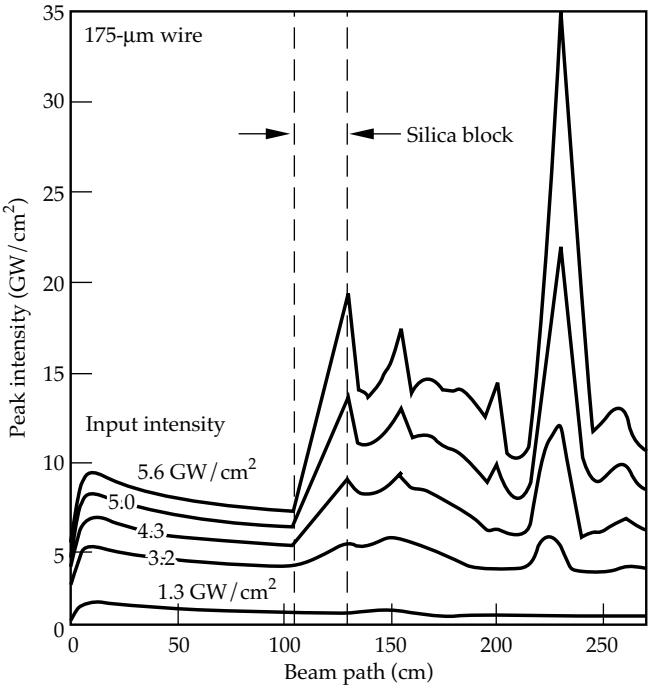

FIGURE 4. Predicted variation of intensity with propagation distance when a plane-wave beam is intercepted by 175-μm-diam wire placed in the beam path and is then propagated through a 25-cm-long silica rod. PROP1 calculations predicted formation of an intense image of the wire. (70-00-0196-0146pb01)

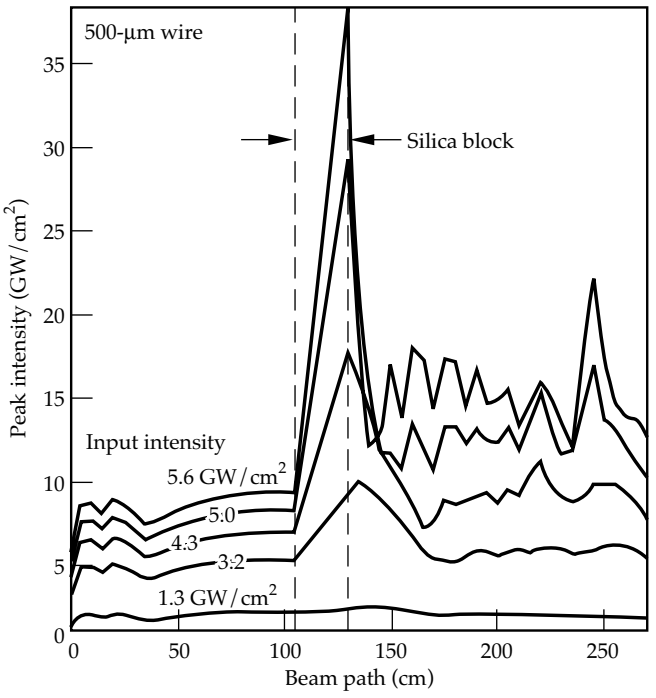

FIGURE 5. Plane-wave PROP1 calculations for a 500-μm-diam wire. The predicted intensity at the output surface of the silica rod is higher than that in the hot image. (70-00-0196-0147pb01)

Results and Analysis

Experiments with each wire diameter were conducted in two stages. In the first series of shots, we held the input intensity approximately constant and recorded the spatial distribution in several planes behind the rod to locate the most intense hot image. In the second series, the plane with the most intense image was recorded as the input intensity was ramped from 1 to 6 GW/cm^2. The duration of the input pulses was about 0.5 ns. The experiments with the 175- and 500-μm-diam wires were modeled with PROP1 and PROP2, respectively.

Experiments with 175-μm Wire

Figures 6–8 show representative data from the experiments with the 175-μm-diam wire. The spatially averaged input fluence was 2.1 J/cm^2. Figure 6 shows the spatial distribution of fluence in the plane containing

the wire. The beam was shaped by apodization and image relaying. It contained weak residual diffraction from the apodization, and random ripple caused by its passage through the many components in the laser. The wire was placed 103 cm in front of the silica rod. Figure 7 shows the 1:1 and 2:1 recordings of the beam in a plane 102 cm behind the rod. The image of the wire is clearly visible. The spatial nonuniformity of the images was caused by intensification due to self-focusing of random intensity fluctuations on the beam. Figure 8 shows the pulse waveform recorded by the streak camera for this shot.

We modeled this experiment with PROP1, using an input beam constructed from the CCD record of the actual input beam. To build an input spatial distribution for the code, we averaged a 4-mm-wide swath across the CCD image of the 20-mm input beam. The wire was modeled as a 175-μm obscuration with four-point smoothing at the edges to minimize Gibbs ringing. The resulting field was propagated across the 103-cm air gap to the rod, through the rod, and through the 102-cm air gap to the plane that was recorded by the output CCD camera. The spatial grid on the field was 8192 points across the 3-cm beam. The rod was divided into ten

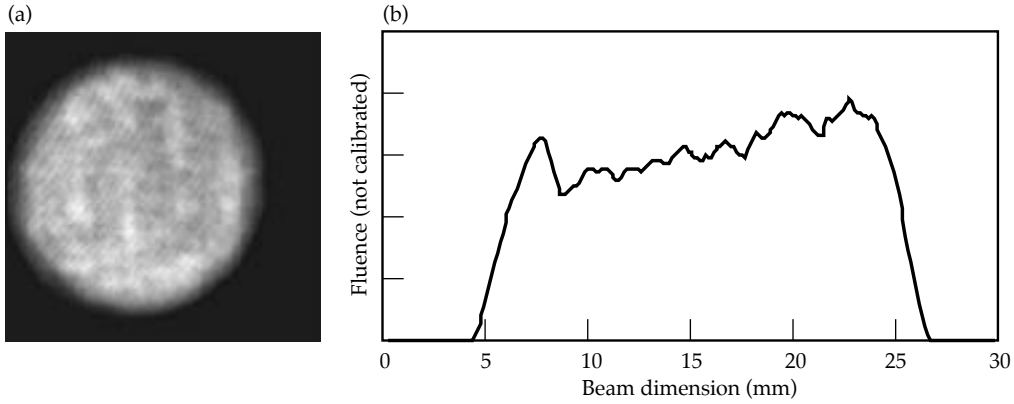

FIGURE 6. (a) CCD record of fluence distribution in the 20-mm-diam beam in the plane of the obscuration. (b) Vertical lineout through the beam. (70-00-0196-0148pb01)

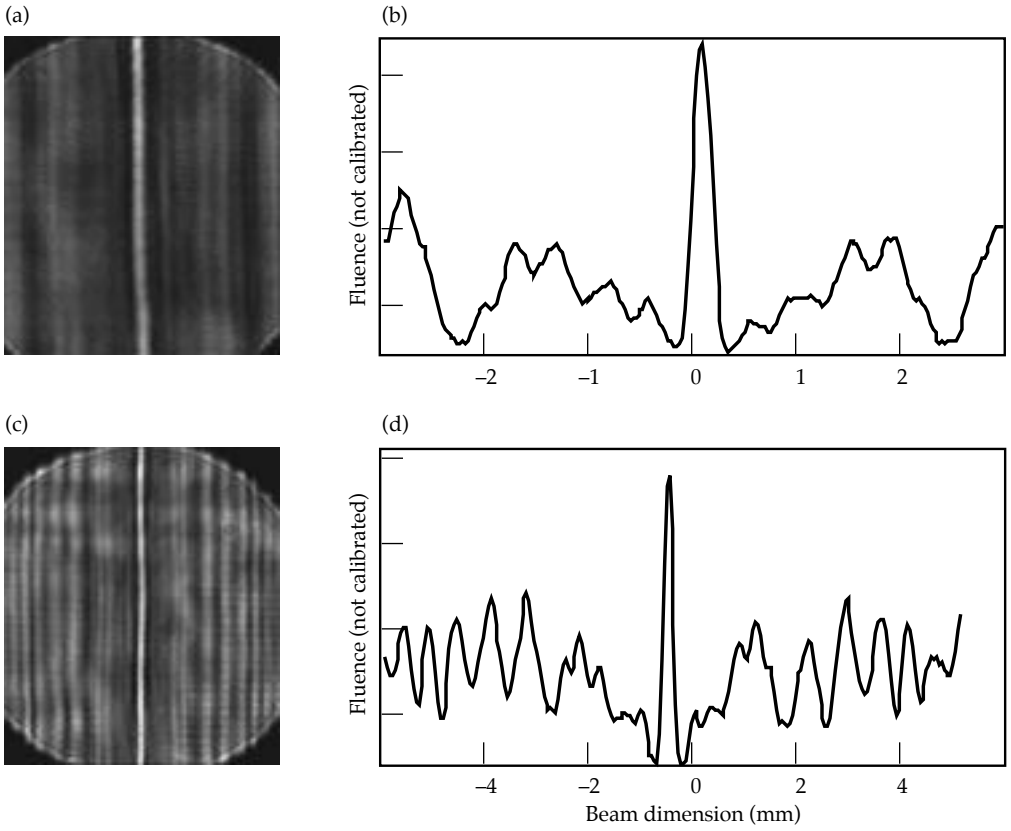

FIGURE 7. Fluence distribution in the hot image of the 175-μm wire, and corresponding horizontal lineouts. Peak input intensity 5 GW/cm^2. (a) and (b), 1:1 record for a central 5-mm-diam area of the beam. (c) and (d), 1.95:1 demagnified image. (70-00-0196-0149pb01)

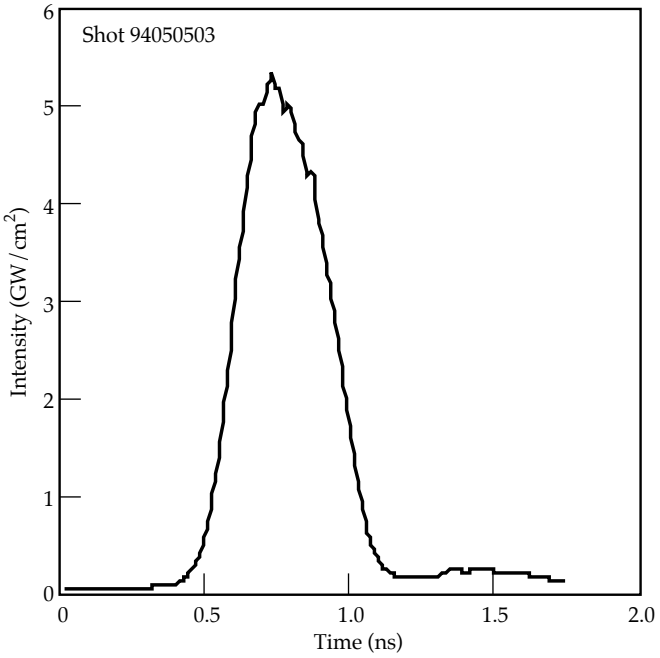

FIGURE 8. Waveform of the input laser pulse. (70-00-0196-0144pb01)

2.5-cm-thick slices, with propagation and self-focusing effects calculated serially in each slice. The value $n_0 = 2.7 \times 10^{-7}$ cm^2/GW was used for the silica.[10] The pulse was divided into 39 time segments of equal duration, which were independently propagated and summed to provide an integrated calculation that could be compared with the relevant 4-mm swath across the time-integrated output CCD image. Figure 9 shows the swaths through the experimental data.

Figure 10 shows the calculated and measured lineouts. To compare the calculation, which yielded a one-dimensional profile with absolute units of J/cm^2, with the relative fluence in the CCD hot-image record, we rescaled the calculated result using a simplex multivariable routine to minimize the rms point-to-point difference between the measured and calculated lineouts. The central peak of the hot image was not included in this minimization. It was necessary to make a small horizontal expansion of the modeled data to bring it into agreement with the measured result. We believe that the horizontal mismatch arose from a small error in the measured 2:1 demagnification of the experimental data.

The intensities in the hot image agree with theory to within 15%. This uncertainty is acceptable, because the resolution of the image of the wire is limited (three pixels at the peak), because the uncertainty in the nonlinear refractive index of the silica is about 10%, the uncertainty in the measurement of spatially averaged

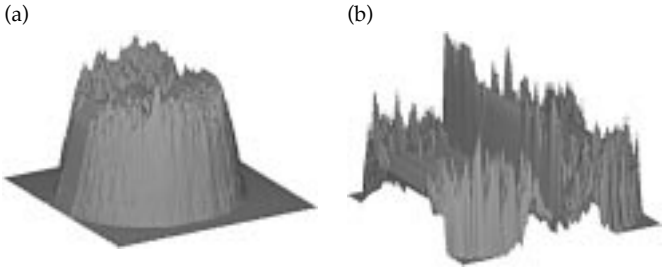

FIGURE 9. Averaged 4-mm-wide swaths across the CCD records of (a) the input beam and (b) the hot image used in PROP1 modeling of the experiments with the 175-μm wire. (70-00-0196-0145pb01)

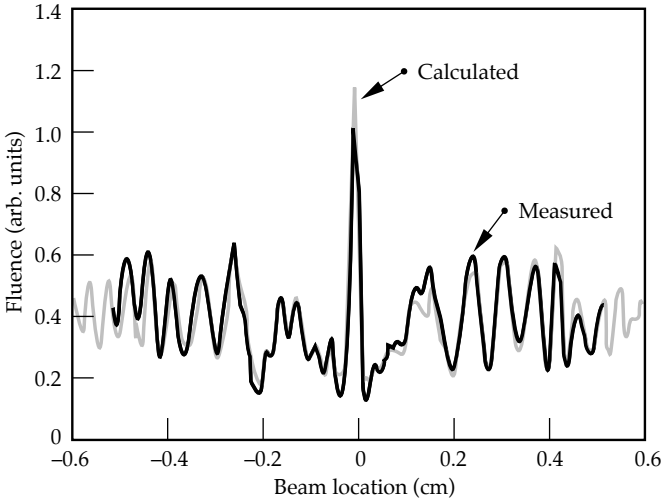

FIGURE 10. Calculated and measured fluence distributions in the hot image of the 175-μm wire. (70-00-0196-0150pb01)

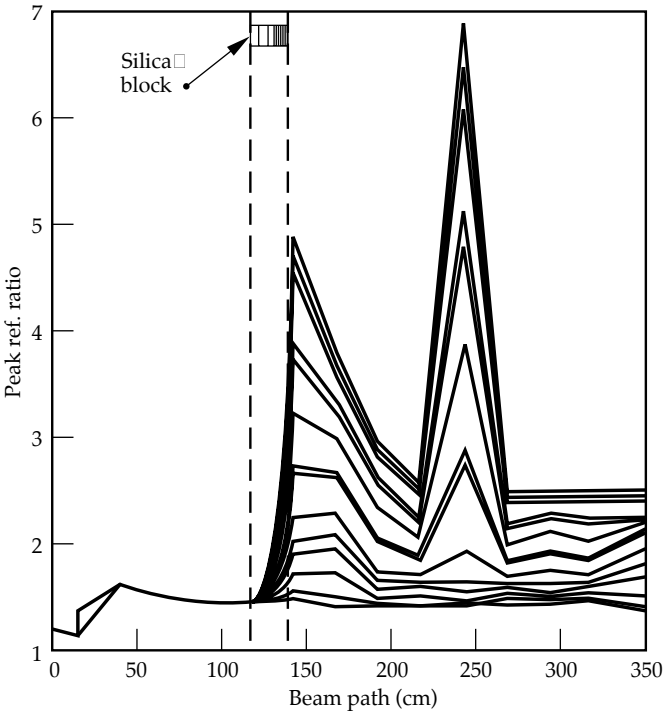

FIGURE 11. Calculated intensity vs propagation distance for time slices for the experiment with the 175-μm wire. (70-00-0196-0151pb01)

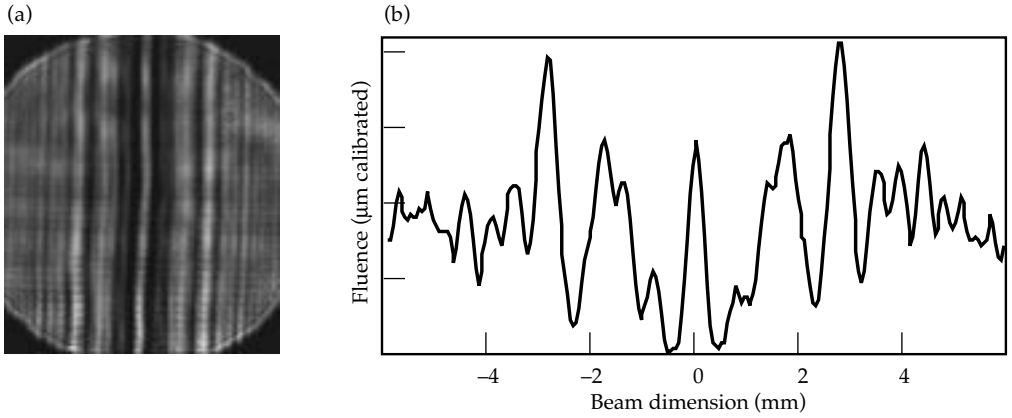

FIGURE 12. Fluence distribution in the image plane for a 500-μm wire. Intensity in the image was less than that in adjacent diffraction fringes. (70-00-0196-0152pb01)

intensity is at least 5%, and the hot-image intensity scales approximately as B^2. Further, the output CCD record contains random intensity variations as well as the image of the wire. We conclude that experiment and theory are in excellent agreement.

It should be noted that time-integrated records such as those in Fig. 10 do not show the hot-image intensity generated at the temporal peak of the pulse. Figure 11 shows the calculated intensity vs z for about half of the time slices. During the most intense slice, the intensity in the hot image was 7 times the mean intensity in the main beam. The intensity for this slice was about 5 GW/cm^2, and the phase retardation was $B = 2.0$ rad. Thus the intensification for this slice was greater than the factor of $1 + B^2 = 5$ predicted by the analytic perturbation models for shallow ripple.

Experiments with 500-μm Wire

The experiment was repeated with a 500-μm wire 105 cm in front of the rod. Figure 12 shows one of the images of a plane 103 cm behind the rod, recorded during a shot with a fluence of 2.3 J/cm^2 . The image of the wire is visible, but its intensity is less than that of the adjacent diffraction ripples. This was the case for shots at lower fluence and for images in other planes. Track damage was induced in the rod by this shot. The spatially averaged intensity at the temporal peak of the pulse was 5 GW/cm^2, and the intensity was higher by 10–15% at isolated places in the beam.

PROP 2 was used to model the tracking induced in this experiment. The CCD image of the input beam was placed on a 3×3 cm grid of 2048×512 pixels, with the higher resolution in the direction orthogonal to the obscuring wire. The rod was broken into three 5-cm slices and ten 1-cm slices, with ten propagation steps in each slice. The thicker 5-cm slices were acceptable at the entrance of the rod, because the intensity increased slowly there. Because track induction is a response to instantaneous intensity, we did not integrate over the intensity range in the temporal waveform. Instead, several runs were made with the input beam scaled to yield spatially averaged intensities between 1.9 and 7.5 GW/cm^2.

Figure 13 shows the results of the calculations as plots of the highest intensity in the rod, anywhere in the beam, vs distance through the rod. For high input intensity, there is a value of z for which the intensity increases abruptly. The apparent stabilization of intensity at high values after the abrupt rise is an artifact of the calculation that occurs when the area of individual intense filaments in the beam is less than the area of the grid sectors.

Damage should occur in the rod where intensities are above the bulk damage threshold. The nonzero rise time of the temporal waveform and the value of the damage threshold both play roles in shaping the damage. As the intensity increases during the rise of the pulse, the z value for the abrupt increase in intensity decreases, so the zone of high intensity starts at the rear surface of the rod and moves toward the front. If the intensity in the self-focused filaments in the beam

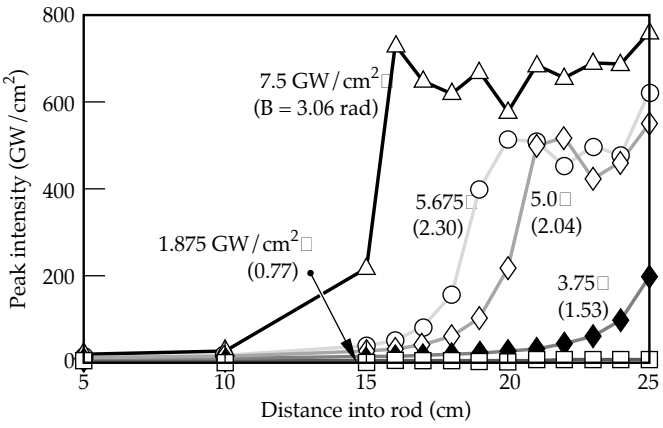

FIGURE 13. Calculated intensity vs propagation distance within the silica rod for the experiment with the 500-μm wire. The intensity distribution in the input beam was scaled to have spatially averaged values of 1.9 to 7.5 GW/cm^2; that for the experiment was 5 GW/cm^2. (70-00-0196-0153pb01)

exceeds the damage threshold, the result is the familiar angel-hair track damage. The value of the bulk damage threshold would play a significant role in determining the length of the track if one were attempting to determine the minimum input intensity for track induction, because of the slow variation of intensity with z at relatively low input intensities (see the calculation for 3.75 GW/cm^2 in Fig. 13). At input intensities well above the minimum for tracking, however, the intensity rises so abruptly that the value of the damage threshold is almost irrelevant. For 0.5-ns pulses, the damage threshold is between 300 and 500 GW/cm^2 (Ref. 11), so the calculated intensities are adequate to cause damage.

There is remarkable agreement between the length of the tracks induced in the rod and corresponding features of the PROP2 calculations. The tracks begin 18 cm from the entrance face; the calculations predict that the abrupt increase in intensity occurs 18–20 cm from the entrance of the rod for intensities of 5.0 to 5.6 GW/cm^2, which is a reasonable representation of the variation of input powers in the experiment. There is also good agreement between the predicted shape of the beam at the output of the rod (Fig. 14) and the pattern of damage on that face. The most intense spikes in Fig. 14 are in two rows separated by 2.3 mm and concentrated in the top of the beam. The damage in the rod shows the same top-to-bottom spatial asymmetry in the magnitude of the damage, and it contains two principal rows of spikes separated by 2.5 mm.

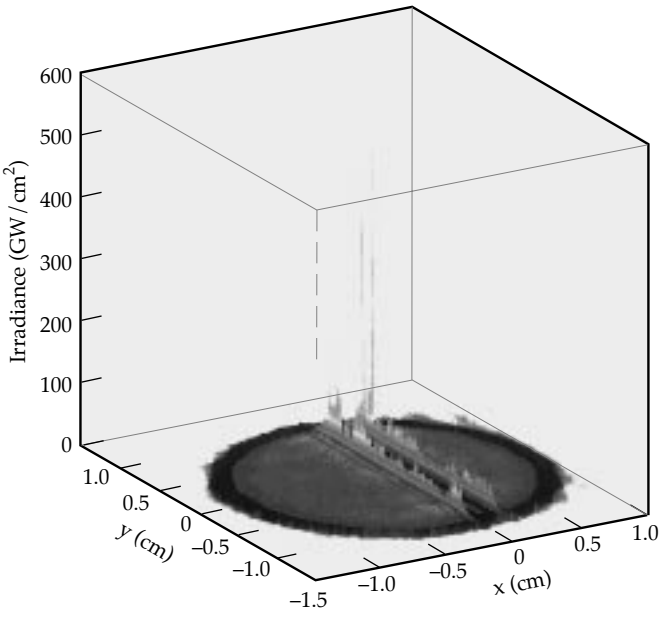

FIGURE 14. Calculated flux distribution at the output face of the rod for B = 2 rad and for spatially averaged intensity 5 GW/cm^2 at the plane of the 500-μm wire. The top-to-bottom asymmetry in spike intensity correlates with the fluence variation in the input beam (see Fig. 6). (70-00-0196-0154pb01)

Summary

We have used the PROP1 and PROP2 codes to model self-focusing experiments conducted in the OSL facility. The source terms, both native beam ripple and that induced by obscurations, were measured and used in the codes. We accurately calculated the shape of an induced "hot" image formed by placing a thin wire in the beam, and the length of self-focusing tracks induced by placing a thicker wire in the beam. These results provide a significant validation of the codes.

Acknowledgments

We are indebted to John Trenholme and Clay Widmeyer for valuable input during the design of the experiment and the reduction of the data, and to Walter Sell, who maintained and operated the OSL facility during the experiments.

Notes and References

1. The earlier codes BTGAIN, ZAX, SNORT, LAMP, ARTEMIS, and MALAPROP, which were developed at Livermore, are reviewed in W. W. Simmons, J. T. Hunt, and W. E. Warren, "Light Propagation Through Large Systems, " *IEEE J. Quantum Electron.* **QE-17**, 1727–1743 (1981). Liberal use was also made of the code OASIS, originally developed by Rockwell Rocketdyne, Inc. under contract with the U.S. Air Force.
2. J. A. Paisner, E. M. Campbell, and W. J. Hogan, "The National Ignition Facility Project," Lawrence Livermore National Laboratory, Livermore, CA, UCRL-JC-117379 Rev. 1 (June 1994).
3. D. Eimerl, R. Boyd, and D. Milam, "The OSL: A New Facility for Laser Research," *ICF Quarterly Report* **1**(3), 108–113, Lawrence Livermore National Laboratory, Livermore, CA UCRL-LR-105821-91-3 (1991).
4. V. I. Bespalov and V. I. Talanov, "Filamentary Structure of Light Beams in Nonlinear Liquids," *JETP Lett.* **3**, 307–312 (1966).
5. W. W. Simmons, S. Guch, F. Rainer, and J. E. Murray, "High-Energy Spatial Filter for Removal of Small-Scale Beam Instabilities in High-Power Lasers," *IEEE J. Quantum Electron.* **QE-11**, 300 (1975).
6. J. T. Hunt, P. A. Renard, and W. W. Simmons, *Appl. Opt.* **16**, 779–782 (1977).
7. J. T. Hunt, J. A. Glase, W. W. Simmons, and P. A. Renard, *Appl. Opt.* **17**, 2053–2057 (1978).
8. J. A. Fleck, Jr., and C. Layne, *Appl. Phys Lett.* **22**, 467–469 (1973).
9. J. T. Hunt, K. R. Manes, and P. A. Renard, *Appl. Opt.* **32**, 5973–5982 (1993).
10. D. Milam and M. J. Weber, *J. Appl. Phys.* **47**, 2497–2501 (1976).
11. E. W. Van Stryland, M. J. Soileau, A. L. Smirl, and W. E. Williams, *Phys. Rev. B* **23**, 2144–2151 (1980).

Gas-Filled Target Designs Produce Ignition-Scale Plasma Conditions with Nova

L. V. Powers *B. H. Failor* *B. J. MacGowan* *R. E. Turner*

P. A. Amendt *S. W. Haan* *D. S. Montgomery* *E. A. Williams*

R. L. Berger *J. A. Harte* *D. H. Munro* *B. H. Failor*

C. A. Back *D. H. Kalantar* *S. M. Pollaine* *J. C. Fernandez*

T. P. Bernat *R. L. Kauffman* *T. D. Shepard* *W. W. Hsing*

K. G. Estabrook *B. F. Lasinski* *L. J. Suter* *B. H. Wilde*

Introduction

In current hohlraum target designs for the National Ignition Facility (NIF), low-*Z* gas fills are used to reduce radial expansion of the gold hohlraum wall.[1] In vacuum, the expansion of the hohlraum wall during the NIF laser pulse (~18 ns) would produce unacceptable levels of asymmetry in the radiation field. The gas, once heated, provides enough pressure to tamp the radiating gold surface. In current designs, the H/He gas fill produces a plasma with an electron density of nearly 10^{21} cm^{-3} and an electron temperature in excess of 3 keV at the peak of the laser pulse. The laser beams propagate efficiently through the weakly absorbing hot gas and deposit most (~90%) of their energy in the gold wall near the initial radius of the target, thus maintaining the high radiation symmetry required for imploding high-convergence capsules.

Even for low-density ($n_e \approx 0.1 n_c$) fills, however, the linear gain for stimulated Brillouin scattering (SBS) in the gas is high. In smaller-scale exploding-foil targets,[2] flow velocity gradients typically limit the SBS gain to modest values. At the peak of the NIF laser pulse, the laser beam must propagate through 2–3 mm of gas plasma with a calculated velocity-gradient scalelength of $L_v \approx 10$ mm. Velocity-gradient stabilization is ineffective at this scale, and the (linear) SBS gain is set by ion Landau damping. For the peak (single beam) NIF intensity of 2×10^{15} W/cm^2 and the calculated plasma conditions, the linear SBS gain coefficient in the gas plasma is ~20. Although nonlinear effects are likely to limit the SBS reflectivity,[3] the scaling of such mechanisms is not quantitatively understood.

Although numerous experimental studies of scattering instabilities in laser-produced plasmas have been performed,[4] plasma conditions of NIF target designs are not easily accessible with current lasers. Further, difficulty in quantitatively modeling SBS in past experiments casts doubt on theoretical extrapolation. The objective of the work reported here is to design targets for interaction experiments that match as closely as possible the conditions of the NIF gas plasma in the path of the laser beams. To assess SBS scaling to NIF parameters, we have designed Nova targets that closely mimic the NIF gas plasma parameters and that allow scaling studies in density, temperature, and laser conditions. Gas-filled targets are heated with nine beams of the Nova laser to produce large, hot, nearly static plasmas. These plasmas have been extensively characterized using x-ray imaging and spectroscopy to verify the plasma conditions.[5–7] Calculations of the plasma conditions compare favorably with these measurements. In interaction experiments,[8,9] the qualitative features of the backscattered spectra[10] from the tenth Nova beam are also consistent with the calculated plasma conditions and temporal evolution of the target parameters that influence SBS.

Although the primary focus of this work was to design and field targets that reproduce NIF underdense plasma parameters important to SBS, the target designs have also proven useful for ongoing studies of other parametric processes that could affect NIF. The gains for stimulated Raman backscattering (SRS) in these plasmas are also high and comparable to calculated SRS gains in NIF hohlraums. New diagnostic capabilities have led to experiments to study the scaling

of SRS backscattering with electron temperature, electron density, and beam conditioning.[11] Broadening of SRS spectra from unsmoothed beams is interpreted as evidence that filamentation is above threshold but is suppressed by beam smoothing in agreement with calculations.[12] In other experiments, Brillouin forward scattering in crossed beams is being investigated using these target designs.[13]

NIF Target Analysis

We have analyzed detailed simulations of various NIF target designs[1] using the LASNEX ICF design code[14] to define desirable conditions for Nova preformed-plasma experiments. To assess the potential levels of scattering instabilities in NIF plasmas, we have calculated the linear gain and the resultant reflectivities by assuming no nonlinear saturation effects other than pump depletion and by assuming that the reflection is confined within the solid angle of the incident light.

Figure 1 shows the target geometry and a typical laser pulse shape for the baseline NIF hohlraum design. In NIF indirect-drive target designs, the hohlraum wall is illuminated by two pairs of symmetrically placed rings of laser beams. The hohlraum is filled with He or H/He mixtures at an initial density of 0.0013 g/cm^3, which corresponds to an electron density $n_e = 4 \times 10^{20}$ cm^{-3} at full ionization. The density of the low-Z fill plasma evolves throughout the pulse because of wall expansion, plasma blowoff from the capsule, and material loss though the laser entrance holes. We have analyzed simulations for a range of NIF target designs at times throughout the laser pulse. The highest linear gains for SRS and SBS occur at the peak of the pulse, when the maximum intensity of a single beam is $I = 2 \times 10^{15}$ W/cm^2. Figure 2 shows the calculated profiles for laser intensity I_L, electron density n_e, electron temperature T_e, ion/electron temperature ratio T_i/T_e, and flow velocity component parallel to the beam path $v_{||}$, along the propagation path for the baseline NIF hohlraum design. Alternative designs with lower peak power and correspondingly lower plasma densities at the peak of the pulse result in lower gains for scattering instabilities.

The laser intensity in the NIF point design is well below the threshold for absolute SBS at the calculated densities and temperatures, so only the convective instability is a concern. To obtain the small-signal intensity gain coefficient $G(\omega_s)$ for SBS, we integrate the local intensity spatial gain rate[15] $\kappa(\omega_s,z)$ over the path of the scattered light. Using plasma profiles from LASNEX simulations, we evaluate

$$n = n_0 + \gamma I, \tag{1}$$

on a fine mesh along the propagation path of the laser beam. Here z is the position along the ray path, $\omega_{0,s}$ and $k_{0,s}$ are the frequency and wavenumber of the pump and scattered light waves, respectively, $v_0 \equiv eE_0/m\omega_0$ is the laser pump strength parameter, $v_g \equiv c_s^2 k_s/\omega_s$ is the group velocity of the ion acoustic wave (c_s is the sound speed in the plasma), and $\chi_{e,i}$ are the electron and ion susceptibilities, respectively. The gain calculation includes a multi-species treatment of ion Landau damping.[16] The intensity variation along the ray path due to beam divergence and inverse bremsstrahlung absorption is also included.

The propagation length through the ~0.1n_c gas plasma is longer for the inner beam cone, resulting in higher integrated SBS gain. At NIF scale, flow velocity gradients are weak in the direction of beam propagation ($L_v \approx 10$ mm) and do not effectively limit SBS. On the other hand, the ions and electrons are near equilibrium ($T_i/T_e = 0.4$) at the high-intensity peak of the pulse, leading to efficient ion Landau damping by the light

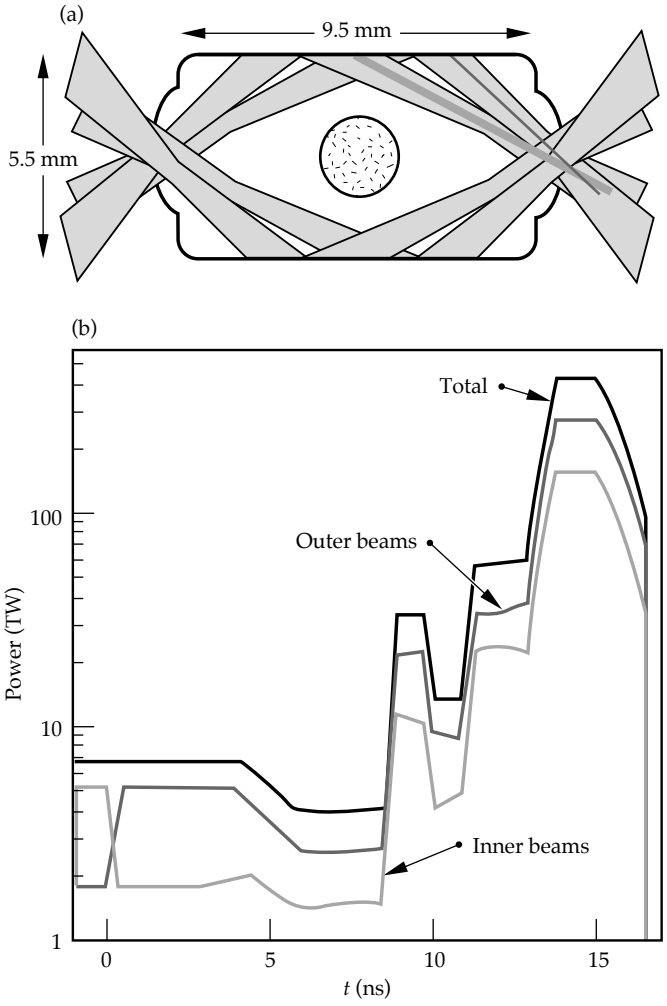

FIGURE 1. NIF target design. (a) Target and illumination geometry for baseline NIF target design. (b) Typical laser pulse shape. (50-04-1095-2377pb02)

ions in the gas. In this parameter regime, the linear gain exponent for SBS is approximately

$$z = \frac{d}{n_0 + \gamma I} \approx \frac{d}{n_0} - \frac{B}{k}, \qquad (2)$$

where I is the laser intensity in W/cm^2, λ is the laser wavelength in micrometers, T_e is the electron temperature in keV, n_e/n_c is the electron density normalized to critical density, and ω_a and ν_i are the ion-acoustic-wave frequency and amplitude damping rate, respectively. Landau damping increases further when the He fill is replaced by a H/He mixture with the same electron density.[16] For pure He fill, the calculated linear gain exponents for SBS for the inner and outer beams are 28 and 9, respectively; for an equimolar H/He mixture, the corresponding values are 21 and 6. The longer gas path length and lower electron temperature in the inner cone also lead to higher SRS gain.

For the high gain exponents calculated for the inner beam cone, linear theory is not adequate to assess

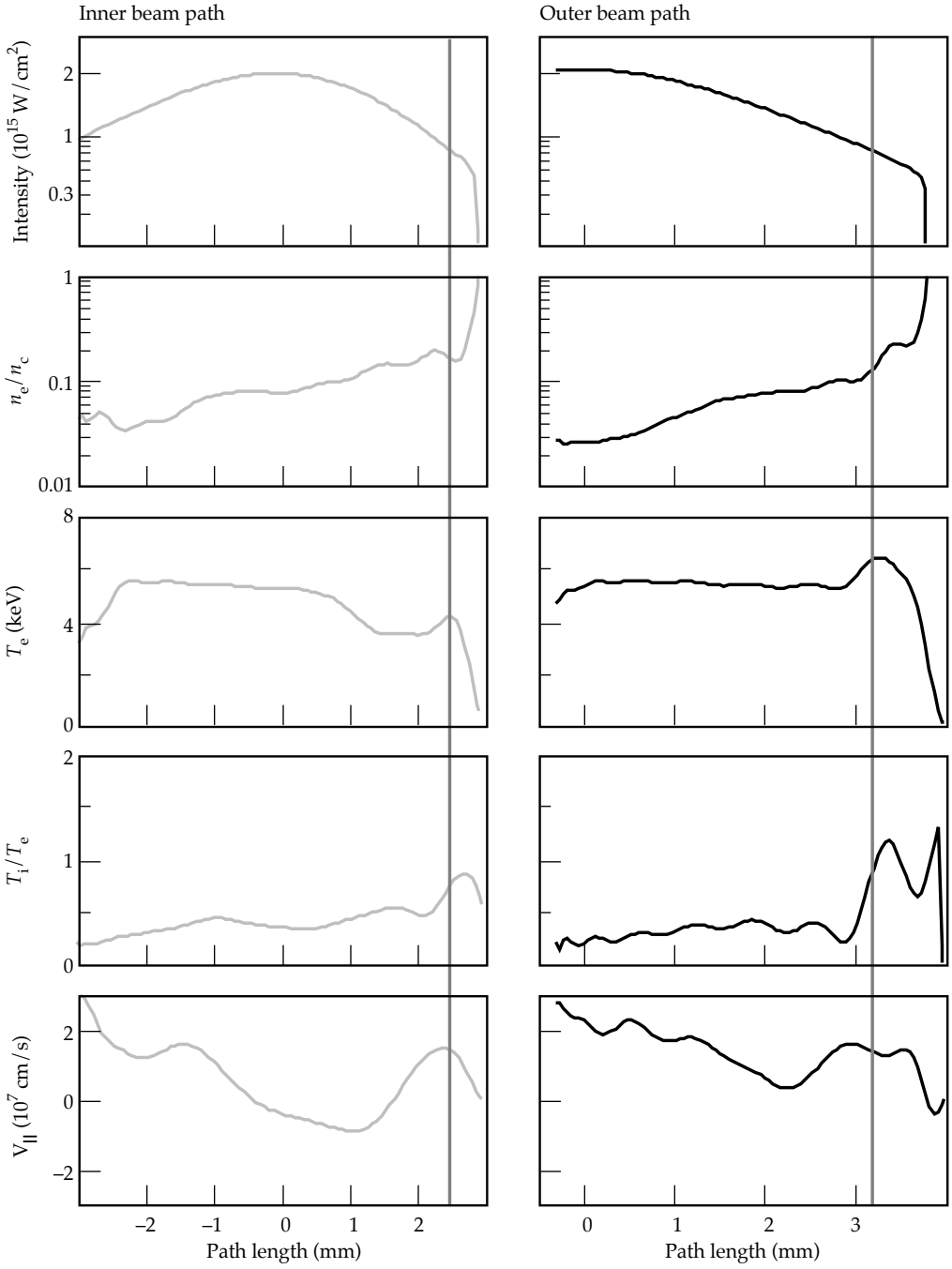

FIGURE 2. NIF plasma parameters: lineouts of intensity, electron density, electron temperature, ion/electron temperature ratio, and flow velocity parallel to the laser path for the inner (left) and outer (right) beam cones along the paths indicated by gray lines in Fig. 1. The laser entrance hole is at the left limit of the plots; the gas/gold interface is marked by light shaded vertical lines. The path length is defined such that the position of best focus of the laser beam is at zero. (50-04-1095-2378pb02)

scattering levels. Nonlinear damping or detuning of SBS-produced ion waves is likely to limit the instability growth to much lower levels.[3] However, the intensity structure of spatially smoothed laser beams, although an improvement over that of unsmoothed Nova beams, increases the effective gain above that for a uniform beam.[17] Temporal beam smoothing is therefore necessary to reduce the expected gain.[18] Although all these effects are expected to be important, quantitative predictions of scattering levels including these effects is beyond the scope of current simulation techniques. Interaction experiments using the Nova targets described below have provided a means for quantifying scattering levels in plasmas similar to the low-Z fill plasma in NIF hohlraum designs and for verifying that scattering levels in such plasmas are acceptable.

Nova Target Designs

The thermal energy content of the gas plasma in the baseline NIF hohlraum design is >70 kJ at the peak of the pulse, so it is not possible to create a comparable plasma with the ~30 kJ available with Nova. Instead, we have endeavored to identify and reproduce the essential parameters of the NIF inner beam path in Nova experiments. First, a large, nearly uniform test plasma is required to provide a comparable plasma path length in which SBS gain is not limited by flow gradients. Second, a relatively hot plasma is required to access the strong damping regime for SRS. Third, the relevant plasma conditions must be maintained for much longer than the growth times for instabilities to assess asymptotic scattering levels. Based on these criteria we set electron density $n_e \approx 10^{21}$ cm^{-3}, electron temperature $T_e > 3$ keV, interaction length $L \approx 2$ mm, flow velocity gradient scalelength $L_v > 6$ mm, and plasma lifetime ≥0.5 ns as desirable parameters for Nova target designs.

Various target options were investigated in simulations and evaluated against these criteria. The gas targets were selected for three reasons. First, and perhaps most important, is the consideration that the underdense NIF plasma is formed by heating a low-density gas; hence we expect gas targets to closely parallel the NIF plasma formation processes. Second, a substantial amount of Nova's energy would be required to expand a solid target to achieve the long-scalelength plasma required. Third, the initially homogeneous gas fill suggests less uncertainty and temporal variation in the plasma density than plasmas formed by expansion. Two principal target types were used (Fig. 3), both containing neopentane (C_5H_{12}) gas at 1 atm pressure ($n_e = 10^{21}$ cm^{-3} at full ionization): (1) gas balloons ("gasbags") ~2.5–3 mm in diameter with a ~5000-Å thick polyimide ($C_{22}H_{10}N_2O_5$) membrane, and (2) cylindrical gold hohlraums with length and diameter ~2.5 mm with polyimide windows ~6000 Å thick to contain the gas. Denavit and Phillion[19] proposed similar gas target geometries. An alternative hohlraum geometry was used in complementary experiments fielded on Nova by Los Alamos National Laboratory.[20] Using nine Nova beams, which deliver ~30 kJ of 0.351-μm light, we heat the gas to preform plasmas with the desired parameters. The tenth beam, an interaction beam whose intensity, pulse shape, f/number, and spatial and temporal intensity structure ("smoothness") are varied, is delayed until the gas target is expected to be uniformly heated.

The behavior of the two targets is similar, although details differ because of the different geometries and pulse shapes. In both targets the laser beam burns through the polyimide in ~200 ps; the gas becomes transparent by $t \approx 500$ ps. The calculated electron density (10^{21} cm^{-3}) and temperature (~3 keV) of the preformed plasma are uniform over a length of $L \approx 2$ mm. The maximum calculated flow velocity in this region is $<10^7$ cm/s. The path length of the $0.1n_c$ density plateau decreases to ~1.5 mm at $t = 1$ ns because of rarefaction.

In the gasbag targets, heater beams are arranged to symmetrically illuminate nearly the entire target surface [Fig. 3(a)]. The temperature and density in the center of the target is very uniform after the initial plasma formation. In the hohlraum targets, laser access is limited to laser entrance holes in the ends of the cylinder. The beams are therefore more tightly focused than in the gasbag geometry [Fig. 3(b)], and the laser directly heats only a portion of the contained gas. The gas plasma created in the hohlraum targets exhibits a weak density gradient along the beam path, with density decreasing towards the laser entrance hole. The presence of underdense gold blowoff in the hohlraum may, on the other hand, produce additional SBS. Because most of Nova's energy is required to heat the gas, however, the gold plasma evolution does not approximate

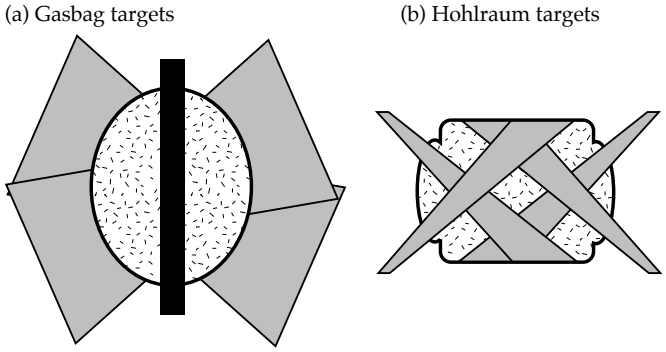

FIGURE 3. Nova target geometries for (a) gasbag and (b) hohlraum targets. For the gasbag target, the dark band indicates the position of the washer. Speckled regions represent gas fill; gray shading shows the illumination geometry for the heating beams. (50-04-1095-2379pb01)

the NIF gold blowoff. SBS from the underdense gold plasma in gas-filled hohlraums is the subject of separate ongoing experiments.

Extensive characterization was carried out to ensure that predicted plasma conditions were achieved. Spectroscopic measurements are consistent with the calculated underdense plasma temperatures.[5] Imaging techniques confirm the plasma size, homogeneity, and temporal evolution.[6] Streaked and gated images show that the heater beams propagate through the gas as calculated without significant breakup.[7] Optical spectra are consistent with expected target parameters and evolution.[10]

Comparison of Nova and NIF Target Parameters

Figure 4 shows selected plasma parameters from LASNEX simulations of Nova gas-filled targets and from the baseline NIF hohlraum design. For the Nova targets, quantities are plotted at the time when the peak SBS is observed in interaction experiments (0.9 ns for gasbag targets and 1 ns for hohlraums). For the NIF targets, quantities are plotted at the peak of the pulse (t = 14.5 ns), when the calculated SBS gain is highest. At the time of peak SBS, the Nova targets have a >1.5 mm region of plasma with electron density ~0.1n_c, flow velocity gradient scalelengths $L_v > 6$ mm, electron temperatures $T_e > 3$ keV, and ion/electron temperature ratios Ti/Te ≈ 0.15–0.2. These parameters match the NIF gas plasma conditions within a factor of two.

The calculated linear gain exponents for SBS and SRS backscattering are similar for the Nova targets and the NIF baseline design. Table 1 shows gain exponents for peak laser intensity $I = 2 \times 10^{15}$ W/cm^2 and $f/8$ focusing, with best focus as defined in Fig. 4. Gains are shown for targets without hydrogen in the fill gas (C_5D_{12} for Nova and pure He for NIF) and for the baseline designs (C_5D_{12} for Nova and equimolar H/He for NIF). The gasbag targets have somewhat higher peak gains than the Nova hohlraum targets for similar fill conditions, primarily because the plasma density is more homogeneous in the gasbags. Both Nova targets have calculated gain exponents comparable to those for the NIF inner cone. Gains for SRS and SBS

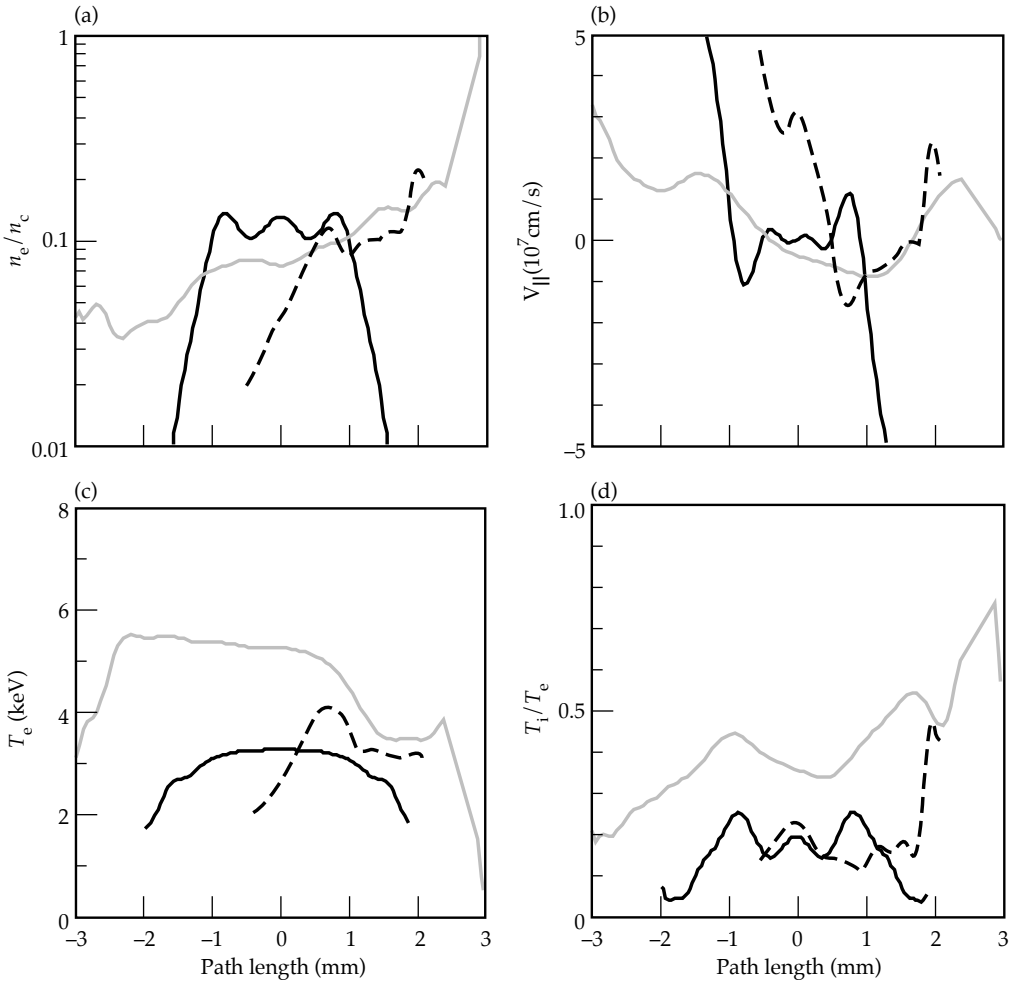

FIGURE 4. Calculated parameters of the low-Z gas plasma along a beam path for the inner cone of NIF beams (gray line), Nova hohlraums (solid line), and gasbags (dashed line). The path length is defined such that the nominal position of best focus of the interaction beam in Nova experiments coincides with best focus of the NIF laser at zero. (50-04-1095-2380pb01)

backscattering are lower for the NIF outer beam cone because of a shorter laser path length through the gas fill plasma. For both instabilities, the longer path length of plasma in the NIF target is compensated for by increased Landau damping to give comparable gains to the Nova targets. For SBS, the higher value of T_i/T_e in the NIF targets leads to increased ion Landau damping. Ion Landau damping is most effective when light (H) ions are present, as shown in Table 1 and as discussed in detail in Refs. 10 and 16. For SRS, electron Landau damping is predicted to be more effective in the NIF target because of the higher electron temperature. Additional scaling experiments have been performed on Nova with higher intensity ($>5 \times 10^{15}$ W/cm^2) interaction beams,[8,9] for which the calculated gain exponents exceed NIF values by more than a factor of two.

Calculated backscattering spectra from the Nova targets show features that are signatures of large, static plasmas. Comparisons with observed spectra[7,10] provide further verification that the calculated plasma conditions have been achieved. Figure 5 shows a typical calculated SBS spectrum from a gasbag target. The interaction beam in the calculations (and in typical interaction experiments) is a 1-ns flat-topped pulse with 200 ps rise time, delayed 400 ps relative to the plasma formation laser beams. The brightest feature is red-shifted by ~10 Å from the incident wavelength $\lambda_0 = 0.351$ μm. This corresponds to scattering from the hot, static density plateau in the middle of the target. By contrast, SBS spectra from exploding foils or disks are typically blue-shifted, indicating that the signal is dominated by plasma regions in which $v_{||} > c_s$. The calculated gain decreases after ~1 ns because of the gradual disassembly of the density plateau and because of energy transfer from the electrons to the ions, which increases the ion Landau damping. These qualitative features are seen in experiments in which significant scattering is observed,[10,11] although peak scattering occurs somewhat later (~200 ps) than calculated. Figure 6 shows a typical calculated SRS spectrum. The dominant feature at $\lambda \approx 5700$ Å is indicative of scattering from the $0.1n_c$ density plateau formed by the gas. The longer-wavelength feature that appears at $t \approx 1$ ns is associated with a compression shock generated by the expanding polyimide membrane; this feature appears in some of the measured spectra.[7,10] Again the scattering level decreases after ~1 ns, although the interaction beam is at full intensity until $t \approx 1.4$ ns, in qualitative agreement with observations.

Although qualitative features of the backscattered spectra are consistent with the calculated plasma evolution, linear theory is clearly inadequate to model

TABLE 1. Calculated linear gain exponents for Nova and NIF target designs.

Target design	SRS	SBS	SBS (no hydrogen)
Nova gasbag	20	35	64
Nova gas hohlraum	16	19	27
NIF (inner cone)	30	21	28
NIF (outer cone)	7	6	9

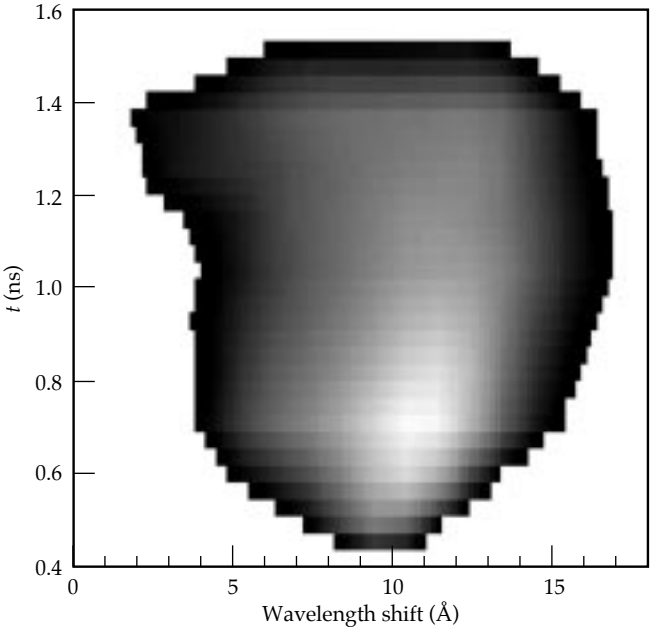

FIGURE 5. Calculated SBS backscattered spectra from a neopentane-filled gasbag target with $f/8$ interaction beam intensity $I = 2 \times 10^{15}$ W/cm^2. (50-04-1095-2386pb02)

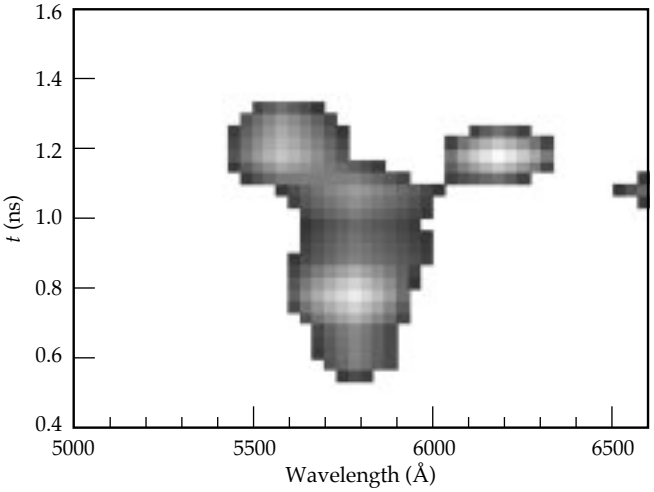

FIGURE 6. Calculated SRS backscattered spectra from a neopentane-filled gasbag target with $f/8$ interaction beam intensity $I = 2 \times 10^{15}$ W/cm^2. (50-04-1095-2382pb02)

these experiments quantitatively. The measured SBS reflectivities for these plasmas are well below the scattering levels predicted by linear theory. For the SBS gain exponents of >20 calculated for these conditions, the calculated reflectivity is limited by pump depletion to ~30% in the absence of other nonlinear saturation mechanisms, whereas the measured reflectivities are <3% in neopentane-filled targets.[8,9] For these high gains, however, nonlinear saturation mechanisms that limit the amplitude or coherence of the ion waves driven by SBS[3,21] are likely to be important. Theoretical and experimental efforts are under way to quantify these effects. Further, scattering from high-*Z* blowoff from the gold wall in NIF hohlraums is not well modeled in these Nova targets. Although gold plasma in the Nova gas-filled hohlraums may contribute to the SBS signal, tamping of the wall expansion reduces the extent of the high-*Z* blowoff, and strong absorption in the gas fill reduces the laser intensity in the high-*Z* plasma to below NIF-relevant levels. Scattering from high-*Z* plasmas is the subject of continuing research.

Conclusion

Using gas-filled targets on Nova, we have produced plasmas that closely match the calculated low-*Z* plasma environment in NIF hohlraums in electron density and temperature, density and velocity scalelengths, and calculated SBS gain. These plasmas were extensively characterized using x-ray and optical diagnostics. The plasma parameters and target evolution predicted by LASNEX design calculations are consistent with these observations. These comparisons verify that the desired parameters for SBS experiments were attained and corroborate important aspects of our modeling of NIF hohlraum conditions. SBS reflectivity is <3% from an interaction beam that mimics the NIF laser beam intensity, focusing, and beam smoothing.

Acknowledgments

We acknowledge valuable discussions with J. D. Kilkenny, J. D. Lindl, and M. D. Rosen, and the support of the LASNEX group in performing simulations required to design and analyze these experiments.

Notes and References

1. S. W. Haan, S. M. Pollaine, J. D. Lindl, L. J. Suter, et al., *Phys. Plasmas* **2**, 2480 (1995).
2. J. M. Moody, H. A. Baldis, D. S. Montgomery, R. L. Berger, et al., *Phys. Plasmas* **2**, 4285 (1995).
3. W. L. Kruer, *Phys. Fluids* **23**, 1273 (1980).
4. H. A. Baldis, D. S. Montgomery, J. D. Moody, C. Labaune, et al., *Plasma Phys. Controlled Fusion* **34**, 2077 (1992), and references therein.
5. C. A. Back, D. H. Kalantar, R. L. Kauffman, R. W. Lee, et al., "Measurements of electron temperature by spectroscopy in millimeter-size hohlraum targets," Lawrence Livermore National Laboratory, Livermore, CA, UCRL-JC-122046; submitted to *Phys. Rev. Lett* (1996).
6. D. H. Kalantar et al., *Phys. Plasmas* **2**, 3161 (1995).
7. L. V. Powers, R. L. Berger, R. L. Kauffman, B. J. MacGowan, et al., *Phys. Plasmas* **2**, 2473 (1995).
8. B. J. MacGowan, C. A. Back, R. L. Berger, K. S. Bradley, et al., *Proceedings of the IAEA 15th International Conference on Plasma Physics and Controlled Nuclear Fusion Research* (International Atomic Energy Agency, Vienna, 1994), p. 16.
9. L. V. Powers, R. E. Turner, R. L. Kauffman, R. L. Berger, et al., *Phys. Rev. Lett.* **74**, 2957 (1995).
10. D. S. Montgomery et al., *Bull. Am. Phys. Soc.* **39**, 1952 (1994).
11. B. J. MacGowan, R. Berger, J. Fernandez, B. Afeyan, et al., *ICF Quarterly* Report **5**(4), 305, Lawrence Livermore National Laboratory, Livermore, CA, UCRL-LR-105821-95-4 (1995).
12. R. L. Berger, B. F. Lasinski, T. B. Kaiser, E. A. Williams, et al., *Phys. Fluids B* **5**, 2243 (1993); R. L. Berger, T. B. Kaiser, B. F. Lasinski, C. W. Still, *ICF Quarterly Report* **5**(3), 200–207, Lawrence Livermore National Laboratory, Livermore, CA, UCRL-LR-105821-95-3 (1995).
13. R. K. Kirkwood, B. B. Afeyan, W. L. Kruer, B. J. MacGowan, et al., "Observation of energy transfer between frequency mismatched laser beams in large scale plasma," Lawrence Livermore National Laboratory, Livermore, CA, UCRL-JC-122102; submitted to *Phys. Rev. Lett.* (1996).
14. G. Zimmerman and W. Kruer, *Comments Plasma Phys. Controlled Fusion* **2**, 85 (1975).
15. D. W. Forslund, J. M. Kindel, and E. L. Lindman, *Phys. Fluids* **18**, 1002 (1975); R. L. Berger, E. A. Williams, and A. Simon, *Phys. Fluids B* **1**, 414 (1989).
16. E. A. Williams, R. L. Berger, A. V. Rubenchik, R. P. Drake, et al., *Phys. Plasmas* **2**, 129 (1995); H. X. Vu, J. M. Wallace, and B. Bezzerides, *Phys. Plasmas* **1** (11), 3542–3556 (1994).
17. H. A. Rose and D. F. DuBois, *Phys. Rev. Lett.* **72**, 2883 (1994).
18. R. L. Berger, B. F. Lasinski, A. B. Langdon, T. B. Kaiser, et al., *Phys. Rev. Lett.* **75**, 1078 (1995).
19. J. Denavit and D. W. Phillion, *Phys. Plasmas* **1**, 1971 (1994).
20. J. C. Fernandez, J. A. Cobble, B. H. Failor, W. W. Hsing, et al., **53** *Phys. Rev. E.* (1996).
21. S. C. Wilks et al., *Phys. Rev. Lett.* **75**, 5048 (1995); B. I. Cohen et al., *Bull. Am. Phys. Soc.* **40**, 1778 (1995).

Stimulated Brillouin Scattering in Multispecies Plasmas

E. A. Williams

Introduction

Stimulated Brillouin scattering (SBS) is a plasma instability in which laser light, propagating through an underdense plasma, is scattered by self-excited ion-acoustic waves.[1]

In inertial confinement fusion (ICF) applications, backscattered laser light is wasted energy that is not absorbed by the target. It is neither converted to x rays by the laser-heated hohlraum (indirect drive) nor used to directly implode the target (direct drive). Energy lost in this manner has to be replaced by a compensating increase in the power of the laser.

Scattering in directions other than backward, or near backward, gives rise to a different concern. This obliquely scattered light may be absorbed elsewhere in the hohlraum, or by the capsule, changing the spatial distribution of absorbed energy and affecting implosion symmetry. Although scattering adds to the effective "spot motion" it can, within limits, be tuned away in the target design. The real concern is that the shot-to-shot variation of the scattering might exceed the tolerance of the design.[2–4]

Because of this consideration, it would be highly desirable to limit SBS scattering to not more than a few percent of the incident power. Limiting laser intensity and the hohlraum gas density, for instance, are possibilities. In this article, we discuss the possible benefits of choosing hohlraum gases[5] and/or hohlraum wall materials[6] that contain multiple-ion species to increase the ion Landau damping of the SBS ion waves.

Under cryogenic constraints, the only candidate for a mixed species gas is a hydrogen–helium (H–He) mixture, currently used in the National Ignition Facility (NIF) designs.[2,3] Gases such as methane, propane, pentane, and carbon dioxide[7] have been used in Nova hohlraum and gas-bag experiments. Recent Nova experiments have used Au hohlraums with multilayers of Au and Be to coat the inside walls.

Landau Damping of Ion-Acoustic Waves

Theoretically, increasing the linear damping rate of the SBS ion waves, all else equal, should reduce the amplitude to which they grow, and consequently reduce the amount of scattered light. If the reduction of linear growth rate is sufficient to force the instability to remain in a linear regime, there is a quantitative relation between growth rate and reflectivity. Conversely, if the relevant rates are reduced, but the ion waves are nevertheless driven nonlinear, then the connection between increased damping and reduced scatter is less direct. A connection is anticipated, however, and is the subject of current research.

To our benefit, nature provides the natural phenomenon of (ion) Landau damping. This is a kinetic (as opposed to fluid) effect, in which ions in the distribution function whose (thermal) velocities match the phase speed of the ion acoustic wave, "surf" on the wave, thereby extracting energy and damping it. More precisely, ions slightly slower than the wave are accelerated, those slightly faster are decelerated. Because, in a thermal distribution, the number of ions decreases with increasing velocity (i.e., the distribution function has negative slope), the net effect is damping.

When the ion acoustic velocity greatly exceeds the characteristic thermal velocity, the number of ions available on the tail of the distribution is very small, and the damping is weak. In the opposite limit, where the ion thermal velocity greatly exceeds the acoustic velocity, the damping is again weak because the distribution function is locally almost flat. Maximum damping occurs in the intermediate case where the ion acoustic velocity is two to three times the thermal velocity. Because, at a given ion temperature, the ion thermal velocity varies inversely with the square root of the atomic mass, the ion Landau damping can be controlled by judicious choice of material composition.

In a single-ion-species underdense plasma, the ratio of the ion acoustic speed to the ion thermal velocity $\kappa(\omega_s, z) = \frac{v_s}{v_{th}}$ is large for both mid- and high-Z plasmas,

UCRL-LR-105821-96-1

both because $Z>>1$ and because electron-ion collisions are insufficient for the ion temperature T_i to equilibrate with the laser-heated electrons, where T_e is the electron temperature. In Nova hohlraums, $T_i/T_e \approx 0.2$; for the longer pulse lengths in NIF hohlraums, we anticipate $T_i/T_e \approx 0.5$. Because of this, the fraction of ions in such a plasma near the phase velocity of the ion wave is very small, making ion Landau damping very weak.

Typically, adding a low atomic number component, such as H, to a plasma modestly changes the ion acoustic frequency, but greatly increases the number of high-thermal-velocity ions, thereby dramatically increasing the Landau damping. This multispecies effect was first examined in the early days of magnetic fusion research and was experimentally tested in a variety of experiments,[8] including an observation of reduced SBS in a microwave plasma.[9] This work has been extended to consider plasmas of interest to ICF[5] and is summarized here.

We consider the kinetic treatment of ion acoustic waves in a plasma, consisting of an arbitrary number of ion species. We assume Maxwellian velocity distributions, with common ion temperature T_i and electron temperature T_e. The electrostatic normal-mode frequencies of the plasma are then given by the zeroes of the plasma dielectric function ε, which relates the frequency ω to the wavenumber k, of any given mode, written as follows:

$$\varepsilon(k,\omega) = 1 + \chi_e + \sum_\beta \chi_{i\beta} = 0\,, \tag{1}$$

where the electron susceptibility is χ_e and the ion susceptibility for species β is $\chi_{i\beta}$. The susceptibilities can be expressed as derivatives of Fried and Conte's Z function[10]

$$\chi_e = -\frac{\omega_{pe}^2}{2k^2 v_e^2} Z'\left(\frac{\omega}{\sqrt{2}k v_e}\right)$$

and

$$\chi_{i\beta} = -\frac{\omega_{pi\beta}^2}{2k^2 v_{i\beta}^2} Z'\left(\frac{\omega}{\sqrt{2}k v_{i\beta}}\right), \tag{2}$$

in which the plasma frequency and thermal speed are ω_{pe} and v_e for the electrons and $\omega_{pi\beta}$ and $v_{i\beta}$ for the ion species. The thermal speed of species β is defined here by $v_\beta = \sqrt{T_\beta / A_\beta M_p}$ (consistent with the practice in the laser–plasma literature but in contrast, for example, to Swanson[10]), where M_p is the proton mass, and T_β and A_β are the temperature, in energy units, and the atomic mass of species β. We ignore flow. If the component species were to all flow with velocity **u**, ω would be replaced in all of the above by $(\omega - \mathbf{k}\bullet\mathbf{u})$.

The theoretical discussion is more straightforward if we convert to normalized units: $K \equiv k\lambda_{De}$, $\Omega = \omega/\omega_{pe}$, and $V_\beta = v_\beta/v_e$, with electron Debye length $\lambda_{De} \equiv v_e/\omega_{pe}$. We take the ionic charge and the number fraction of the β species to be Z_β and f_β. The total ion density n_i and the electron density n_e are related through the average charge $\overline{Z}$, as $n_e = n_i\overline{Z}$. The average charge and ion number densities are then related by

$$\overline{Z} \equiv \sum_\beta f_\beta Z_\beta \quad \text{and} \quad n_\beta = f_\beta n_e / \overline{Z} = f_\beta n_i \quad . \tag{3}$$

In these units,

$$\chi_e = -Z'\left(\Omega/\sqrt{2}K\right)/2K^2$$

and

$$\chi_{i\beta} = \frac{f_\beta Z_\beta^2}{\overline{Z}} \frac{T_e}{T_i} \frac{1}{2K^2} Z'\left(\Omega/\sqrt{2}KV_\beta\right) \quad . \tag{4}$$

Although this dispersion relation has an infinite number of roots, $\omega(k)$, only a small number of them have $\omega_i << \omega_r$, corresponding to freely propagating waves (where i and r denote the imaginary and real parts of the complex mode frequency). For these, their phase velocity $\mathrm{Re}(\omega)/k$ is such that it is either much larger than or much less than the thermal velocity of each species. The Landau damping contribution of each species is then small because the number of particles at the phase velocity, or the slope of the particle distribution function, is small.

For high enough electron temperature [approximately when $T_e/T_i > 3\langle Z\rangle/\left(\langle Z^2/A\rangle A_l\right)$], there is a "fast" ion acoustic wave that is weakly damped. The $\langle\ \rangle$ denote averages weighted by the ion fractions. A_l is the atomic number of the lightest component. The condition implies that the sound speed is much greater than the thermal velocity of the lightest ion species. The sound speed is approximated by

$$\left(\frac{\Omega_r}{K}\right)^2 = \frac{m_e}{M_p}\left(\frac{\langle Z^2/A\rangle}{\overline{Z}(1+K^2)} + \frac{\langle Z^2/A^2\rangle}{\langle Z^2/A\rangle}\frac{3T_i}{T_e}\right) \quad , \tag{5}$$

where m_e is the electron mass.

In un-normalized quantities,

$$\left(\frac{\omega_r}{k}\right)^2 = \frac{\langle Z^2/A\rangle T_e/\overline{Z}M_p}{1+k^2\lambda_{De}^2} + \frac{\langle Z^2/A^2\rangle}{\langle Z^2/A\rangle}\frac{3T_i}{M_p}\,. \tag{6}$$

The sound speed is of course much slower than the electron thermal velocity. The electron damping puts a lower limit on the total ion wave damping, which is approximately given by

$$\frac{\Omega_i}{\Omega_r} = -\sqrt{\frac{\pi}{8}}\frac{1}{1+\mu+K^2}\left(\frac{\Omega_r}{K} + \sum_\beta \frac{\alpha_\beta\Omega_r}{KV_\beta} e^{-\Omega^2/2K^2V_\beta^2}\right), \tag{7}$$

which gives a minimum damping decrement of 0.01–0.015 in cases of interest.

The "fast" mode is the direct analog of the usual single-species ion wave. However, in a multi-ion species plasma there are possibilities for additional "slow" modes. These modes have sound speeds intermediate between the thermal velocities of a light group of ion species and a heavy group. In these modes, the light ions act like the electrons in the fast mode. They, together with the electrons, react so as to charge–neutralize the heavy ions. Unlike the electrons, the light ions are repelled by the regions of heavy-ion concentration. Their motion is thus out of phase with the heavy ions. This contrasts with the fast mode where the electron and ion species motions are in phase, so that the plasma is effectively a single fluid.

A weakly damped fast mode always exists for sufficiently large T_e/T_i, whereas slow modes exist for at most a finite range of T_e/T_i. Detailed criteria for the existence of these modes have been published elsewhere.[12] Asymptotic kinetic and multifluid approximations for the frequency and damping decrement of the slow modes are readily derived, but are only modestly quantitatively accurate, essentially because the ratios of the sound speed to the ion thermal velocities are neither particularly large nor small.

Figures 1 and 2 show the sound speed and damping decrement as a function of T_i/T_e for equal mixtures of H with He and C—mixtures of interest for the NIF and current Nova experiments. In each case, there are fast and slow modes. The fast mode is less damped when T_i/T_e is <0.2 or 0.32, respectively, with the slow mode becoming the lesser damped mode at higher values of T_i/T_e. One consequence of this is that the sound speed of the dominant mode increases less rapidly with T_i than would be anticipated from the fluid result [see Eqs. (5) and (6)].

Also shown in Figs. 1 and 2 are the thermal velocities of the two ion species, which can be compared with the respective sound velocities. In contrast with the CH mixture, the H thermal velocity in the H–He mixture does not actually exceed the slow mode phase speed. Because of this, the ion acoustic damping for H–He mixtures is very strong at the T_i/T_e ratios anticipated for NIF hohlraums (~0.5).

SBS in Multispecies Plasmas

The kinetic dispersion relation for SBS is

$$\frac{1+\chi_e+\sum_i \chi_i}{\left[\chi_e\left(1+\sum_i \chi_i\right)\right]}\left[(\omega_0-\omega)^2-\omega_{pe}^2-(k_0-k)^2\right]=\frac{k^2v_0^2}{4}. \quad (8)$$

The frequency and wave number of the pump and ion wave are (ω_0, k_0) and (ω, k), respectively. The simplest linear model to assess the effect of ion acoustic damping on SBS is to take the plasma to be a homogeneous slab and the laser beam to be uniform. The time development of the SBS instability in such a model has been analyzed in detail.[13] The instability grows as if the

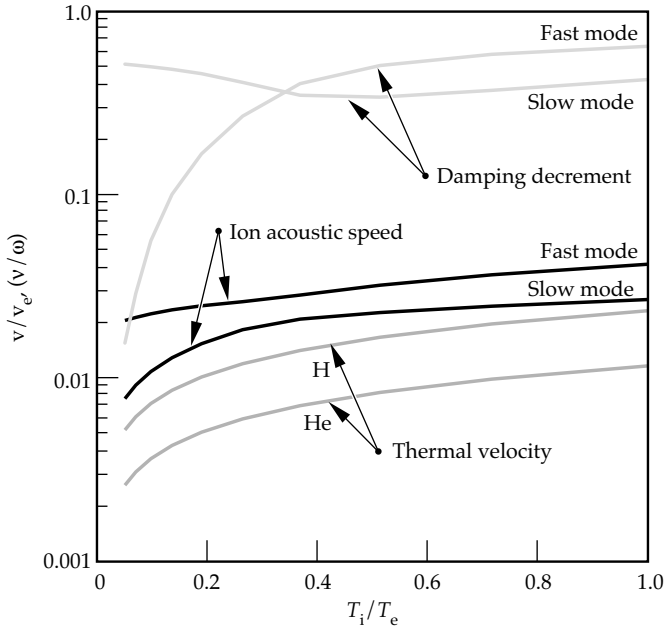

FIGURE 1. A plot of the damping decrement ν/ω and the ion-acoustic and thermal velocities normalized to the electron thermal velocity vs the ion-electron temperature ratio T_i/T_e. The H–He plasma has T_e = 3 keV and $n_e = 10^{21}$ cm^{-3}. (50-01-1195-2518pb01)

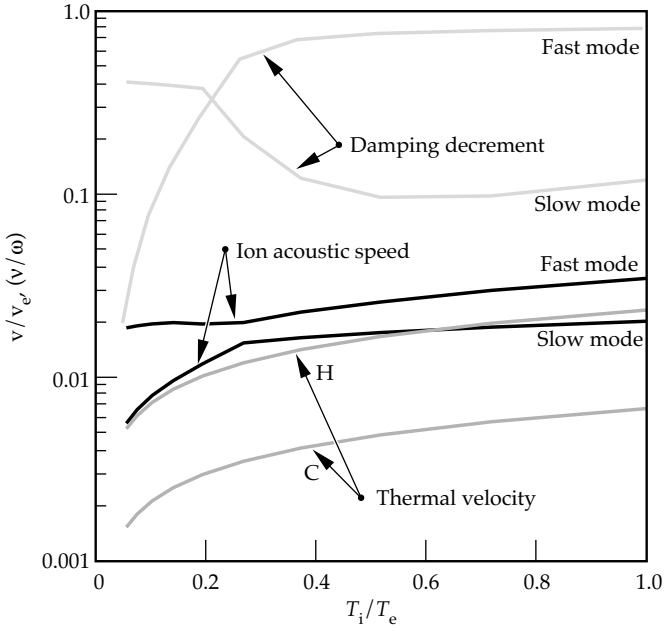

FIGURE 2. A plot of the damping decrement ν/ω and the ion acoustic and thermal velocities normalized to the electron thermal velocity vs the ion-electron temperature ratio T_i/T_e. The CH plasma has T_e = 3 keV and $n_e = 10^{21}$ cm^{-3}. (50-01-1195-2519pb01)

medium were infinite for the first few light transit times. The appropriate growth rate is given by the root of Eq. (8) for complex ω maximized over (real) k.

In a reduced mode-coupling description, this temporal growth rate is given by

$$\gamma = -\nu/2 + \left[\gamma_0^2 + (\nu/2)^2\right]^{1/2} \qquad (9)$$

where γ_0 is the growth rate in the absence of damping, and ν is the ion-acoustic damping rate. One therefore anticipates that the initial growth rate is unaffected by damping whenever $\gamma_0 >> \nu$. This result is borne out by solutions of the full kinetic dispersion relation [see Eq. (8)]. Unless the intensity is relatively low (less than $\sim 10^{14} W/cm^2$) and the damping is high (decrement >0.1), the kinetic temporal growth rate is essentially independent of material composition.

However, provided the damping is strong enough to prevent absolute instability, which in the mode-coupling model requires $\gamma_0 < (\nu/2)(c/c_s)^{1/2}$, where c_s is the sound speed, the instability evolves into a steady state in which the scattered wave amplifies exponentially from noise across the plasma. The spatial growth rate is given by the imaginary part of the solution of the dispersion relation [see Eq. (8)] for (complex) k, maximized over the frequency shift ω.

Below the absolute threshold, it is a good approximation to neglect the imaginary part of k in evaluating the susceptibilities, giving the following expression for the spatial growth rate:

$$\kappa = \frac{k^2 v_0^2}{4c^2} \frac{\left|1 + \sum_i \chi_i\right|^2 \mathrm{Im}(\chi_e) + |\chi_e|^2 \mathrm{Im}\left(\sum_i \chi_i\right)}{\left|1 + \chi_e + \sum_i \chi_i\right|^2}, \qquad (10)$$

which is directly proportional to the Thomson cross section.

It might be expected that whenever two weakly damped ion acoustic waves are present, the SBS (and Thomson) spectra would exhibit two peaks. In fact, except for special choices of material and electron-ion temperature ratio, a single peak is observed. This is because it is not easy to satisfy the Rayleigh criterion that the separation of the peaks has to exceed their combined widths.

Figure 3 shows the spatial amplification rate for backward SBS from a 10^{15} W/cm^2, 0.35-μm laser in a fully-ionized CH plasma, with $T_e = 3$ keV and $n_e = 10^{21}$ cm^{-3}, plotted against the wavelength shift of the scattered light in Angstroms. Curve A in Fig. 3 shows $T_i/T_e = 0.075$. At this temperature, in comparison with Fig. 2, the fast mode is weakly damped and the slow mode is nonresonant. The growth rate curve shows a sharp peak, with a shift corresponding to the fast wave ion-acoustic frequency. Curve B shows $T_i/T_e = 0.2$, where both modes are modestly (and equally) damped, but only a single broad peak is seen in the spectrum, with an inferred ion-acoustic velocity between that of the two ion modes. In curves C and D where T_i/T_e increases, the peak shifts and narrows, reflecting a contribution only from the slow mode.

Figure 4 plots the spatial growth rate (maximized over scattered frequency) for SBS backscatter vs T_i/T_e

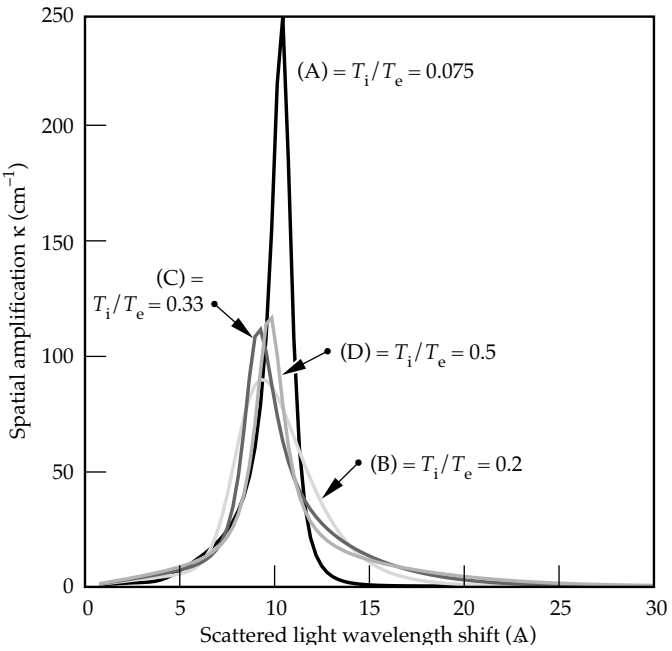

FIGURE 3. A plot of the SBS backscatter spatial amplification rate in a CH plasma vs the wavelength shift of the scattered light. The 0.35-μm $I_L = 10^{15}$ W/cm^2, and the plasma has $T_e = 3$ keV and $n_e = 10^{21}$ cm^{-3}. (50-01-1195-2520pb01)

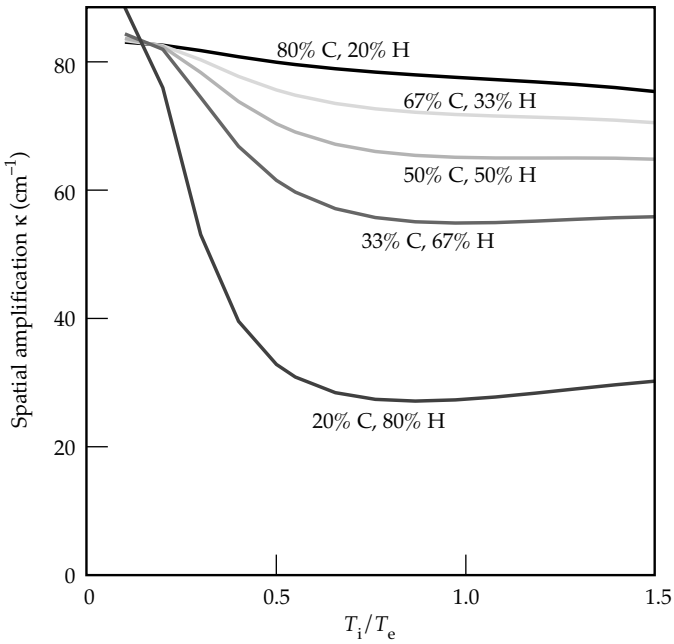

FIGURE 4. A plot of the maximum (over wavelength) SBS backscatter spatial amplification rate vs T_i/T_e for various CH mixtures for the conditions of Fig (3). (50-01-1195-2521pb01)

for various C–H mixtures. Here, adding increasing fractions of light H ions to the C plasma decreases the spatial amplification rate for SBS. In these calculations, the laser intensity $I_L = 10^{14}$ W/cm^2, $T_e = 3$ keV, and $n_e = 10^{21}$cm^{-3}. Below the absolute threshold, the kinetic growth rates scale as its fluid approximation, namely as $I_L n_e / T_e$, keeping the material variation intact.

Conclusion

The Landau damping of ion-acoustic waves can be substantially higher in plasmas that contain mixtures of ionic species than that encountered in single-species plasmas. In multispecies plasmas, the linear spatial growth rate of stimulated Brillouin scattering is substantially reduced. Despite the big gap between linear models of SBS in a uniform plasma and the realities of nonlinear saturation, structured laser beams, and nonuniform plasmas, the simplicity of the physics suggests that the tailoring of material compositions to maximize Landau damping will be a powerful tool to control undesired SBS in ICF applications.

Notes and References

1. W. L. Kruer, *The Physics of Laser–Plasma Interactions* (Addison–Wesley, Redwood City, CA, 1988), p. 99.
2. S. W. Haan, S. M. Pollaine, J. D. Lindl, L. J. Suter et. al., *Plasma Physics* **2**, 2480 (1995).
3. J. D. Lindl, *Plasma Physics* **2**, 3933 (1995).
4. J. D. Lindl, "Time Dependent Asymmetries in Laser–Fusion Hohlraums: a Response," Lawrence Livermore National Laboratory, Livermore, CA, UCRL-JC-122654; submitted to *Comments in Plasma Physics and Controlled Fusion*.
5. E. A. Williams, R. L. Berger, R. P. Drake, A. M. Rubenchik, et al., *Phys. Plasmas* **2**, 129 (1995).
6. K. Estabrook, Lawrence Livermore National Laboratory, Livermore, CA, personal communication (1996).
7. L. V. Powers, R. L. Berger, R. L. Kaufman, B. J. McGowan et. al., *Plasma Physics* **2**, 2473 (1995).
8. I. Alexeff, W. D. Jones, and D. Montgomery, *Phys. Rev. Lett.* **19**, 422. (1967); A. Hirose, I. Alexeff, and W. D. Jones, *Phys. Fluids* **13**, 1290 (1970).
9. C. E. Clayton, C. Yoshi, A. Yasuda, and F. F. Chen, *Phys. Fluids* **24**, 2312 (1981).
10. B. D. Fried and S. D. Conte, *The Plasma Dispersion Function* (Academic, New York, NY, 1961).
11. D. G. Swanson, *Plasma Waves,* (Academic, San Diego, CA, 1989).
12. I. M. A. Gledhill and M. A. Hellberg, *J. Plasma Phys.* **36**, 75 (1986).
13. D. E. Hinkel, E. A. Williams, and R. L. Berger, *Plasma Physics* **2**, 129 (1995).

Optical Scatter—A Diagnostic Tool to Investigate Laser Damage in KDP and DKDP

B. W. Woods *J. J. De Yoreo*

M. Runkel *M. R. Kozlowski*

M. Yan

Introduction

Single crystals of KH_2PO_4 (KDP) and $K(D_xH_{1-x})_2PO_4$ (DKDP) will be used for frequency conversion and as part of a large aperture optical switch[1] in the proposed National Ignition Facility (NIF) at the Lawrence Livermore National Laboratory (LLNL). These crystals must have good optical properties and high laser damage thresholds. Currently, these crystals have a lower laser damage threshold than other optical materials in the laser chain, forcing designers to limit the output fluence of the NIF to avoid damaging the crystals. In addition, minimum acceptable laser fluences can be safely employed only after the crystals have been treated in a procedure known as laser conditioning,[2] which has been shown to dramatically improve their damage thresholds. Furthermore, while more efficient frequency conversion schemes are being explored both theoretically and experimentally, the advantages of these schemes cannot be fully realized unless the damage thresholds of the conversion crystals are increased. Over the past decade, LLNL has generated an extensive data base on laser damage in KDP and DKDP crystals both at the first and third harmonics of Neodymium-doped yttrium-aluminum-garnet (Nd-YAG).[3] Over this time period, the damage thresholds of these crystals have increased, due in part to better filtration of the growth solution;[4] nevertheless, the damage thresholds of the best crystals are still far below the theoretical limits calculated from the band structure of perfect crystals. Thus, damage in KDP and DKDP is caused by defects in the crystals. Unfortunately, little is understood about the mechanism of laser-induced damage, the conditioning process in the crystals, or the defects that are responsible for damage.

Recently, we began an investigation aimed at understanding and improving laser damage and conditioning in KDP and DKDP. Our strategy is to use a range of characterization techniques to profile defects in crystals of both types and to perform damage and conditioning experiments on these well-characterized crystals to identify the defects that are responsible for damage and conditioning. The techniques include ultraviolet absorption measurements for profiling the distribution of impurities, x-ray topography for mapping the locations of structural defects such as dislocations and crystal sector boundaries, and light scattering for detection of inclusions of the growth solution and of foreign particles. This paper focuses on the development and use of light scattering to investigate laser-induced damage in KDP and DKDP. Both types of crystals are very similar in terms of defects and damage thresholds; therefore for clarity in this article, references to KDP include DKDP.

Laser Damage in KDP

Laser damage in KDP typically progresses with increasing laser fluence from pin-point damage characterized by individual 1- to 10-μm-diam damage sites, often with fractures radiating along specific crystallographic directions, to massive damage in the form of a continuous track of 10- to 100-μm diam scatterers visible to the naked eye. Historically, better solution preparation and growth processes have improved the laser damage thresholds in KDP and DKDP. Figure 1 is

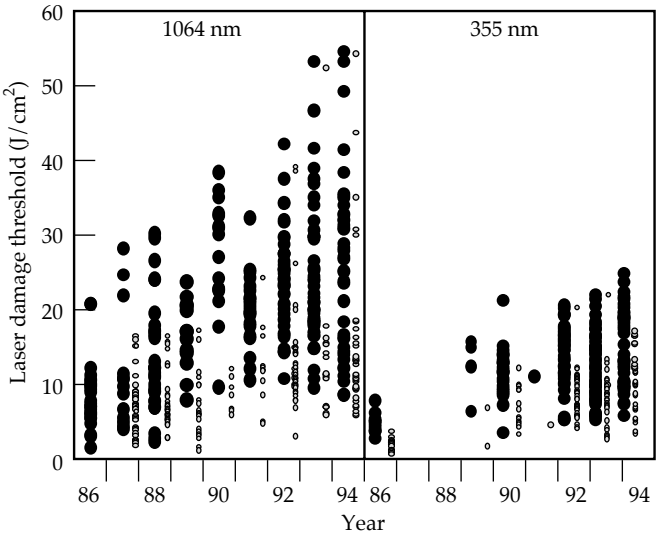

FIGURE 1. Measured bulk damage thresholds vs time for KDP and DKDP, scaled to 3 ns values by $\tau^{0.5}$ and measured at 1ω (1064 nm) and 3ω (355 nm). Note the general improvement in damage thresholds over the 8-year period is shown, as well as the beneficial effect of laser conditioning. Solid circles are conditioned; open circles are unconditioned. (70-50-0296-0307pb01)

a plot of laser-damage thresholds as a function of year measured at 1ω and 3ω for both conditioned (R-on-1) and unconditioned (S-on-1) test conditions. Because damage thresholds are generally measured shortly after growth and fabrication are complete, it is evident that the damage thresholds have improved over time. This plot includes all damage tests on all crystals, so the median values one can deduce are not representative of the best damage thresholds that are currently achieved. For example, the nominal damage threshold for 3-ns pulses at the third harmonic of Nd:YAG in KDP crystals that vendors have produced for the Beamlet laser system[5] are 10 and 20 J/cm^2 for S-on-1 and R-on-1, respectively. While these thresholds could be controlled by typical defects in high-quality crystals such as point defects (impurity atoms) or dislocations, the well-documented improvement in damage thresholds in response to continuous filtration[4] of the growth solution during crystal growth suggests that inclusions play a significant role in damage.

Scatter Measurement

We chose light scattering as a means of characterizing inclusions in KDP. Figure 2(a) is a schematic of the scatter measurement we implemented to view both defects and bulk damage in the crystals. We installed the scatter diagnostic in the ZEUS laser-damage facility at LLNL—a system capable of delivering a usable high-fluence beam of 100 J/cm^2 at 1ω and 75 J/cm^2 at 3ω in an 8-ns pulse. The crystal is mounted in an X–Y translation stage to allow positioning of the damage beam at any point on the crystal. The translation stage is also attached to a rotary stage that allows the test region of the sample to be viewed under an optical microscope, using Nomarski or backlighting techniques to detect damage. This is a typical method used to damage test samples. With the aid of an alignment camera, a probe laser is positioned collinear to the damage beam. To obtain an image of the scattered light from the probe laser, we use a high-dynamic-range 1024 × 1024 pixel, 14-bit CCD camera with appropriate imaging optics to look through the edge of the crystal, horizontally. Current system magnification is approximately 2×, resulting in each pixel mapping to approximately a 10-μm^2 area in the crystal.

Figure 2(b) is a schematic diagram of the illumination and imaging geometry, where the beam propagation is oriented from top to bottom. The nominal beam diameter for the ZEUS damage laser is 1 mm at 1/e^2 of its peak intensity, and the diameter of the probe beam is 2 mm at 1/e^2. We estimate that the two beams are coaligned to approximately ±250 μm at the sample plane. The scatter from the surface has to be avoided because it is much brighter than the bulk scatter and will saturate the camera. Signals we observe consist of several components: Rayleigh scatter, Brillouin scatter, Mie scatter, and fluorescence. Notch filters are used to eliminate the fluorescence and Brillouin signals. The primary focus of this study are Mie scatter sites and scattering off of index variations. The Becke line test[6] has shown that all of the large (Mie) scattering sites we have observed are regions with an index of refraction that is less than the bulk crystal. We have been able to detect many more defects with this scatter diagnostic than with conventional optical microscopy and have seen dramatic differences between different vintages and types of crystals.

Results and Development of Light Scattering

Current studies include four types of crystals with different growth histories. Figure 3 shows the scatter

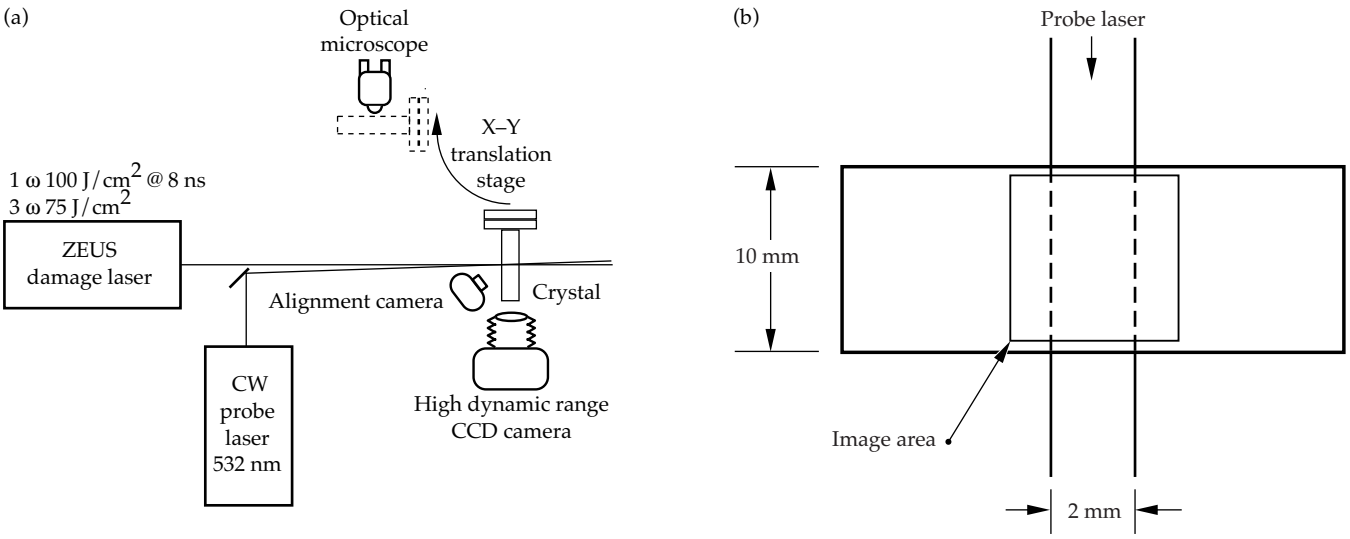

FIGURE 2. Schematic of (a) scatter measurement system and (b) orientation of scatter image. (70-50-1195-2524pb02)

signal from each of these different types—note the gray-scale adjustments for each image to emphasize the important features. Figure 3(a) shows the scatter signal from a crystal grown before continuous filtration increased the damage thresholds.[4] Many large (Mie) scatterers are visible in this type of crystal (currently in use on the Nova laser at LLNL). Figure 3(b) shows a crystal grown later, following improvements in solution processing techniques. These crystals, which are also in use on Nova, have significantly fewer large Mie scattering sites and have a higher laser-damage threshold. Figure 3(c) shows one of the most recently grown crystals used on the Beamlet laser system both in the Pockels cell and as frequency converters. These crystals have very few large (Mie) scattering sites and have the highest laser-damage thresholds of any crystals tested, to date. Figure 3(d) shows a crystal grown at LLNL as part of a program to develop an innovative process for growing KDP and DKDP crystals with excellent optical properties at growth rates up to 10× faster than conventional techniques.[7] This process includes filtration of the solution prior to the start of crystal growth. These crystals have fewer scattering sites than the early Nova crystals, but the sites are typically larger.

During laser-damage tests, we see increases and decreases in the scattering intensity from Mie scatterers. Figure 4 shows a sequence of images in which most of the initial scatter sites diminish in intensity or disappear while one scatter site increases dramatically in intensity, generating what we would traditionally refer to as damage. These images may represent our first glimpse at both the defects that induce damage and the process of laser conditioning. However, while we typically see that nearly all pre-existing scatter sites diminish in intensity or disappear during damage testing, when laser damage occurs, it often does not initiate at an obvious pre-existing scatter site (illustrated in Fig. 5). This unexpected result has four possible explanations: (1) Defects other than inclusions, such as dislocations and point defects, may induce damage. (2) The damage may initiate at features that are below our spatial or intensity resolution. To address this possibility, our detection system currently incorporates microscopy,

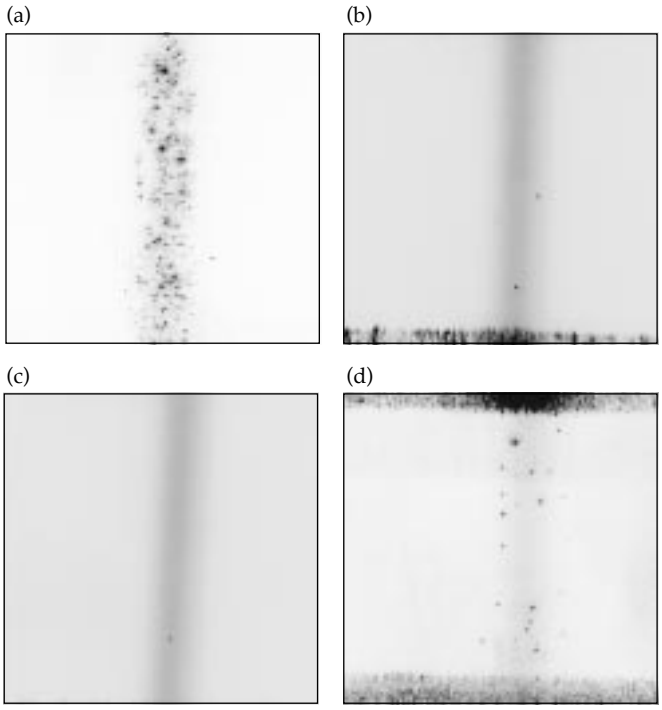

FIGURE 3. Scatter signals from (a) Nova pre-continuous filtration (b) post-Nova, (c) Beamlet, and (d) rapidly grown crystals. (70-50-1195-2525pb01)

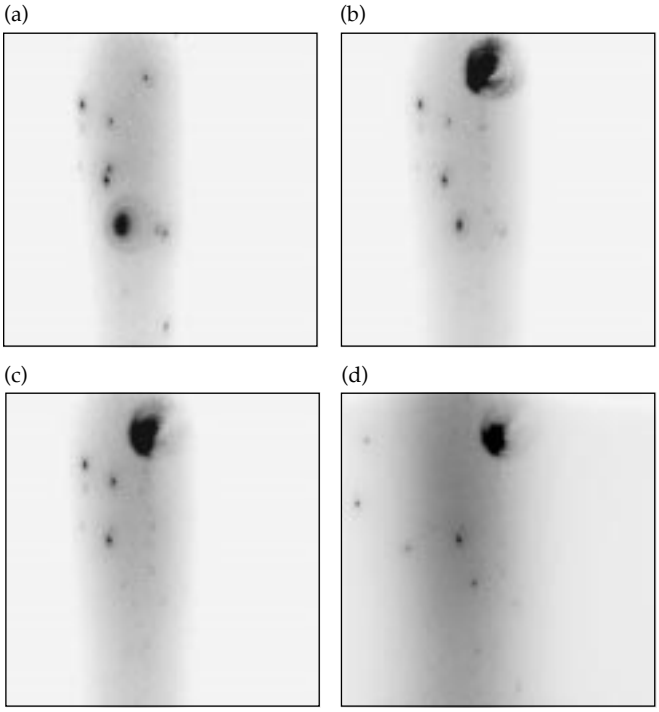

FIGURE 4. Scatter signal from KDP crystal (a) before exposure to the damage beam and after, (b) at one 10.2-J/cm^2 pulse, (c) at one 11.1-J/cm^2 pulse, and (d) at 600 10-J/cm^2 pulses. (70-50-1195-2523pb01)

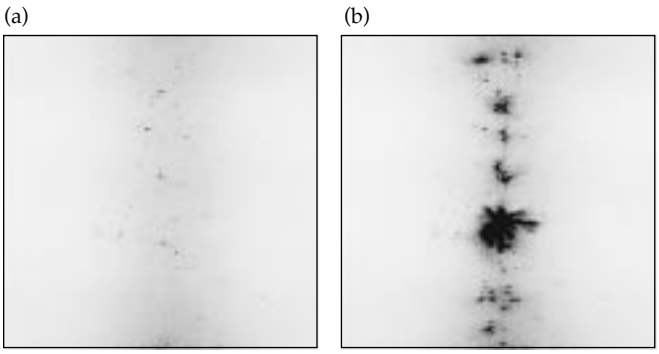

FIGURE 5. Images showing (a) the scatter signal before illumination and (b) heavy laser damage initiated in areas that had no initial scatter sites. (70-50-1195-2526pb01)

allowing us to obtain magnifications of up to 900×. Using these higher magnifications should also help us develop insight into the conditioning process and determine why the amplitude of some scatter sites decreases dramatically when subjected to a high-fluence beam. (3) Damage may be caused not by defects per se but rather initiates in regions that have high stress fields due to defects. Therefore, we plan to develop micrometer-size strain maps for the crystals and to correlate them to optical damage. (4) The illumination angle, viewing angle, or polarization direction of the probe beam might not be optimal to detect the sites where damage initiates.

We investigated item (4) above and found scatter to be quite sensitive to both the angle at which we illuminate the sample and the angle at which we view the scatter signal. Figure 6 shows the scatter signal from a crystal under illumination at normal incidence and at 5° off of normal incidence. The scatter signal from the region near the center of the image nearly disappeared when the crystal was tipped by 5°. This result suggests that there were planar scatterers in the crystals that could only be detected at certain angles. Because KDP grows as a faceted crystal, one might expect to find planar features in the crystals known as growth stria, which lie parallel to the growth front and correspond to variations in growth rate, inhomogeneities in impurity incorporation or sporadic incorporation of particles, and/or solution inclusions. We found that this effect is pronounced in crystal plates cut from the upper portion of KDP boules when the normal to the plate lies along the <001> axis of the crystal, as shown in Fig. 7(a). Such crystals typically contain four separate sectors to which material was added during growth, corresponding to the four {101} faces of the crystal. If the laser is incident normal to the face of the crystal and the camera views the crystal along the normal to one of the edges [see Fig. 7(b)], then the normal to the growth front will be at 45° to both of these directions in one and only one sector. As Fig. 7(c) shows, under these conditions we observed strong scattering with a lineation parallel to the growth front. In other words, we observed scattering from planar variations in the crystal. At the boundary between two adjacent growth sectors, this scattering suddenly disappears and in the adjacent sectors, only Rayleigh and Mie scattering can be observed [see Fig. 7(d) and 7(e)]. Successive rotations of the crystal by 90° result in the same progression of scattering across each of the four growth sectors. Figure 8 shows the scatter

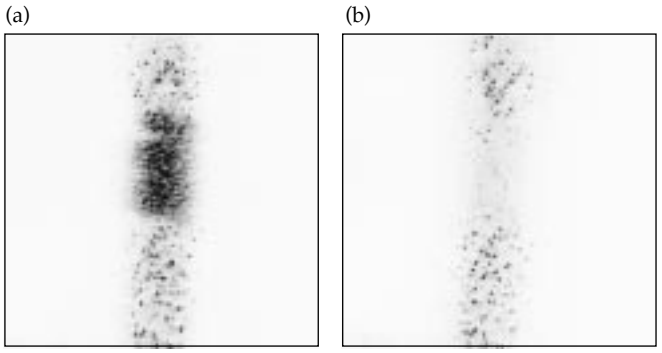

FIGURE 6. Scatter signal from crystal (a) at normal incidence and (b) at 5° from normal. (70-50-1195-2527pb01)

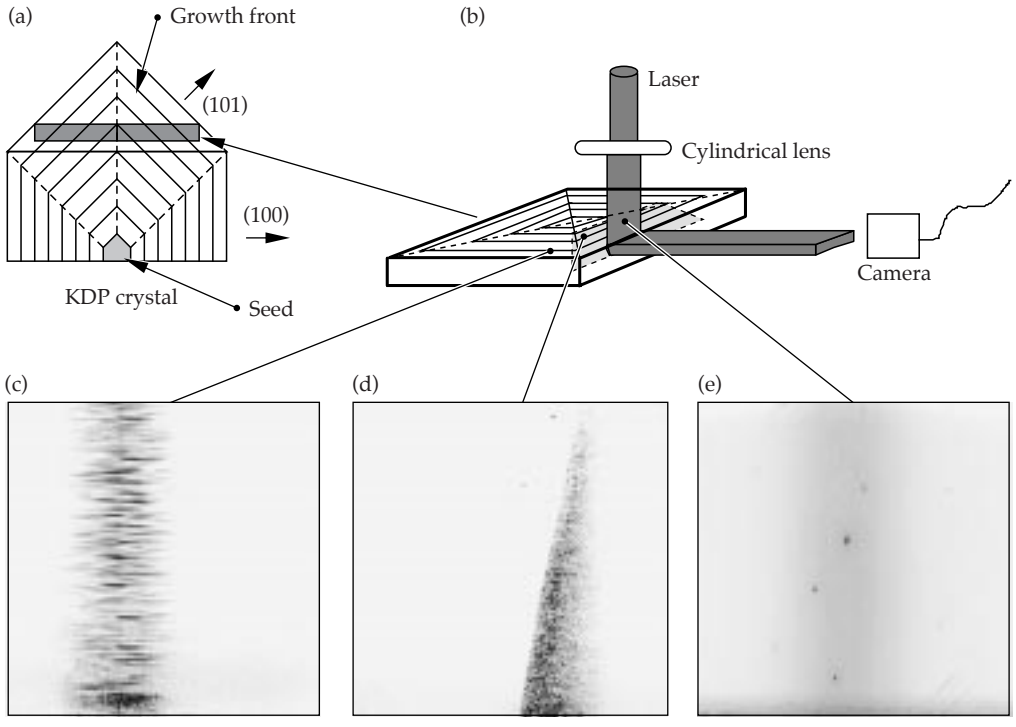

FIGURE 7. Schematic of KDP crystal showing (a) orientation of the growth front relative to plates cut for damage testing, (b) arrangement of laser, crystal, and camera which generates (c) strong scattering from growth planes (d) scattering at sector boundaries, and (e) Rayleigh and Mie scattering only. (70-50-1195-2528pb01)

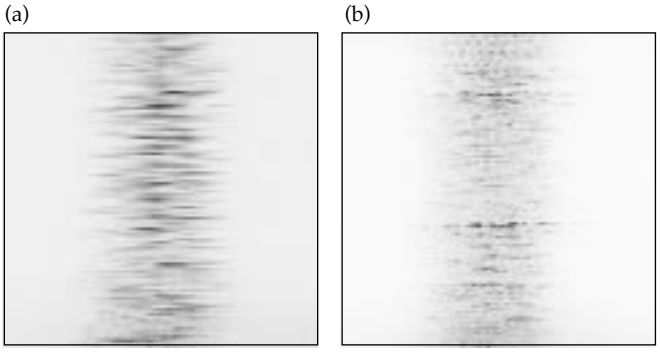

FIGURE 8. Comparison of scattering from growth stria in (a) rapidly grown and (b) Beamlet-vintage crystals. The most intense scattering in (a) is about 20× that in (b). (70-50-1195-2462pb01)

signal generated by these features in a fast-grown crystal as well as one grown for Beamlet. The intensity of the brightest features are about 20 times greater in the fast grown crystal than in the Beamlet crystal. At this time, we do not know if these features consist of planar arrays of inclusions or are simply variations in refractive index which produce a series of dielectric mirrors within the crystal. We also do not know how these features affect the damage threshold of the crystals.

Conclusion

The scatter diagnostic installed on the ZEUS laser-damage facility at LLNL allows us to view scatter and optical damage in bulk KDP. The historical record of damage shows a correlation between the level of filtration and solution processing, number of scattering sites, and optical damage. However, damage often initiates in regions where no initial scatter site is observed. The amplitude of the scatter signal from large (Mie) scatter sites often decreases when subjected to a laser pulse. These sites may be providing our first glimpse into the conditioning process. When the crystals are properly oriented relative to the probe beam and the camera, we observe strong scattering with a lineation perpendicular to the growth direction. We interpret this to be scatter from growth stria—planar variations in crystal homogeneity produced at the growth front of the crystal during growth. Positive identification of the defects that cause laser damage in KDP is crucial to improving damage thresholds for the NIF.

Acknowledgments

We gratefully acknowledge the contributions of Frank Rainer for many helpful discussions regarding laser damage in KDP and for developing an extensive data base on laser-damage measurements at LLNL. We also thank Peter Thelin, Jose Vargas, and Ron Vallene for providing the optical finishing on our many test samples.

Notes and References

1. M. A. Rhodes, B. Woods, J. J. DeYoreo, D. Roberts, and L. J. Atherton, *Appl. Opt.* **34**, 5312 (1995).
2. J. E. Swain, S. E. Stowkowski, and D. Milam, *Appl. Phys. Lett.* **41** (1982).
3. F. Rainer, L. J. Atherton, and J. J. DeYoreo, "Laser Damage to Production-and Research-Grade KDP crystals," in *Laser-Induced Damage in Optical Materials*, H. E. Bennett et al. Eds., (SPIE—International Society for Optical Engineering, Bellingham, WA, 1992; *Proc. SPIE*, **1848**).
4. K. E. Montgomery and F. P. Milanovich, *J. Appl. Phys.* **68** , 15 (1990).
5. J. Campbell, L. J. Atherton, J. J. DeYoreo, M. R. Kozlowski, et al., *ICF Quarterly Report* **5**(1), 52–61, Lawrence Livermore National Laboratory, Livermore, CA, UCRL-LR-105821-95-1 (1994).
6. An Introduction to the Methods of Optical Crystallography, F. D. Bloss, Ed., (Saunders College Publishing, San Francisco, 1989).
7. N. P. Zaitseva, I. L. Smol'skii, and L. N. Rashkovich, *Sov. Phys. Crystallogr* **36**, 113 (1991).

SOFT X-RAY INTERFEROMETRY

L. B. Da Silva *J. C. Moreno*

T. W. Barbee, Jr. *J. E. Trebes*

R. Cauble *A. S. Wan*

P. Celliers *F. Weber*

Introduction

In the study of laser-produced plasmas, optical interferometry plays a key role in accurately measuring electron density profiles for a variety of target conditions. Attwood et al.[1] were the first to quantify profile steepening due to radiation pressure using a short pulse 2650-Å optical interferometer. This method was used to measure electron density profiles in exploding foils under conditions relevant to x-ray lasers.[2] Young et al.[3,4] also used optical interferometry to investigate the filamentation instability in laser-produced plasmas. Nevertheless, the size of the plasma and the peak electron density accessible in all these cases were severely restricted by absorption and refraction. Inverse bremsstrahlung absorption becomes significant for optical probes at electron densities exceeding 10^{20} cm^{-3}. Refraction of the probe beam is sensitive to electron density gradients and ultimately affects spatial resolution and data interpretation.[5] These problems are particularly significant as we progress in producing and studying large (3 mm) and high-density (10^{22} cm^{-3}) plasmas relevant to Inertial Confinement Fusion (ICF) and astrophysics. Therefore, we need to develop interferometry techniques at soft x-ray wavelengths where absorption and refraction effects can be mitigated.

This article describes the use of interferometry at soft x-ray wavelengths to probe laser-produced plasma. We discuss the properties and characteristics of existing soft x-ray lasers that make them well suited to probe laser-produced plasma. The design and performance of a multilayer-optic-based interferometer is presented along with results of its use to probe millimeter-size plasmas.

Advantages and Properties of Collisional X-Ray Lasers

Worldwide[6] research demonstrates soft x-ray lasers that operate from 400 to 35 Å (30 to 350 eV). These systems use high-power optical lasers to produce a hot and uniform plasma suitable for laser amplification and propagation. Recently, the efficiency and range of collisionally pumped systems has been increased using multipump pulse techniques.[7] Although recombination schemes have also been used, the highest gain-length products, and consequently output powers, have been observed for neon-like collisionally pumped lasers. Saturated output has been reported in selenium,[8] germanium,[9] and yttrium[10] using optical pumping and in argon using capillary discharges.[11] The high brightness and comparatively routine operation of existing soft x-ray lasers offer an opportunity to use these systems for a variety of applications. These applications include the use of a Ni-like tantalum x-ray laser for biological imaging,[12] which allows us to study biological specimens in a natural environment with resolutions far exceeding those possible with optical techniques. The high brightness of saturated x-ray lasers also makes them an ideal tool for probing high-density and large plasmas relevant to astrophysics and ICF. In addition, the wide range of available x-ray laser wavelengths (Fig. 1) now makes it possible to take advantage of absorption edges to enhance contrast.

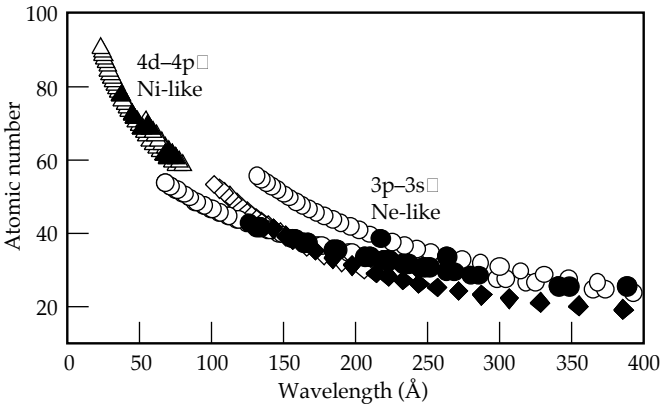

FIGURE 1. Measured (filled symbols) and calculated (open symbols) wavelengths as a function of atomic number for primary neon- (3p–3s) and nickel-like (4d–4p) collisionally pumped x-ray laser lines. (08-00-1295-2637pb01)

This article focuses on the use of soft x-ray lasers to study laser-produced plasmas.

Absorption and Refraction Effects

Two main effects ultimately limit the plasma condition that can be probed with any laser source. The first is absorption, which limits the density of the plasma; the second is refraction, which limits the density gradients. In a plasma with electron density n_e, the index of refraction n_{ref} is related to the critical electron density $n_c = 1.1 \times 10^{21}\ \lambda^{-2}$ (cm^{-3}) (λ in μm) by $n_{ref} = \sqrt{1 - \frac{n_e}{n_c}}$. In an interferometer, the number of fringe shifts, N_{Fringe}, is then given by

$$N_{Fringe} = \frac{\delta\phi}{2\pi} = \frac{1}{\lambda}\int_0^L (1 - n_{ref})\,dl \approx \frac{n_e}{2n_c}\frac{L}{\lambda} = 4.54 \times 10^{-22} n_e L \lambda ,$$

where the integral is along ray trajectories through the plasma. dl is the differential path length, L is the plasma length, and we assume refraction effects are negligible. Experimentally, the maximum number of fringe shifts measurable is usually constrained by detector resolution and is rarely greater than ~50. This imposes a constraint on the product $n_e L$ for a given wavelength. However, absorption is a more significant constraint on the accessible plasma density and size. We can estimate this parameter space by considering only free-free absorption. For most high-temperature plasmas of interest, the level of ionization is sufficient to eliminate any bound-free absorption in the soft x-ray region. Resonant line absorption is possible but very unlikely given the narrow bandwidth (~10 mÅ)[13] of the x-ray laser. Under these conditions the absorption coefficient α is approximately given by[14]

$$\alpha \approx 2.44 \times 10^{-37} \frac{\langle Z^2 \rangle n_e n_i}{\sqrt{T_e}(h\nu)^3}\left[1 - \exp\left(\frac{-h\nu}{T_e}\right)\right] \text{cm}^{-1} . \qquad (1)$$

Here, the electron temperature T_e and photon energy $h\nu$ are in electron volts, and n_e and ion density n_i are in cm^{-3}. The strong scaling with photon energy shows the advantage of probing with soft x-ray sources. Using Eq. (1) if we consider only free-free absorption in a plasma with 1-keV temperature and average ionization of 30 (mid-Z plasma), we obtain $\alpha \approx 2.6 \times 10^{-43}\ n_e^2$ for λ = 155 Å. If we allow for one optical depth (i.e., $\alpha L = 1$) of absorption, we obtain $n_e^2 L = 3.8 \times 10^{42}$. Figure 2 compares the electron density and plasma dimension accessible with a soft x-ray laser source (155 Å) and an optical laser source (2500 Å). Clearly, the strong wavelength scaling ($\propto \lambda^2$) shows the advantage of probing with shorter wavelengths. The parameter space accessible with a 155-Å probe easily covers the plasmas normally produced in the laboratory.

Refraction of the probe beam is sensitive to electron density gradients and ultimately affects spatial resolution and data interpretation.[5] At 155 Å, $n_c = 4.6 \times 10^{24}$ (cm^{-3}), which is well above that of most plasmas of interest. For a simple plasma with a linear density gradient $n_e = n_0\,[1 - (y/y_0)]$, the deflection angle θ scales as $\theta \propto \lambda^2 L/y_0$. This strong scaling supports the advantage of using a short wavelength probe. Figure 3 compares the deflection angle after propagating through a 3-mm plasma for an optical (2650 Å) and soft x-ray (155 Å) probe source. At a fundamental level, large deflection angles imply significant spatial blurring and reduced spatial resolution. In addition, since probe rays propagate through a range of electron densities, interpretation is more difficult.

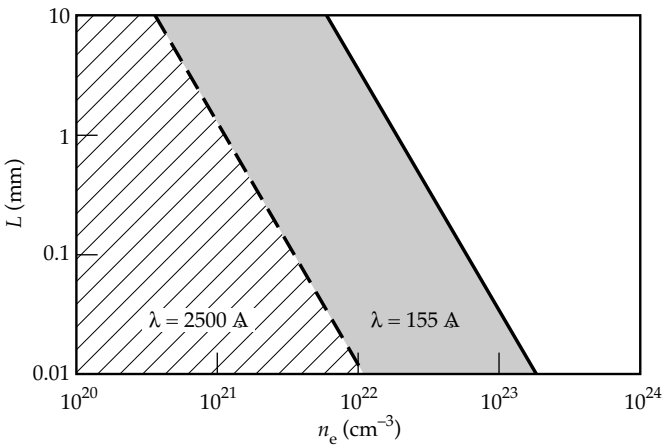

FIGURE 2. Parameter space accessible for plasma probing, using an optical laser (2500 Å) and a soft x-ray laser (155 Å). Only free-free absorption is considered. (08-00-1295-2638pb01)

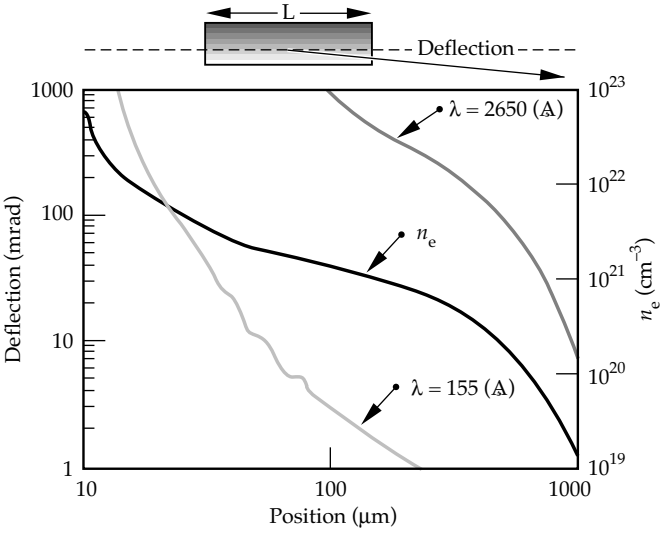

FIGURE 3. Calculated deflection vs path displacement normal to the target surface for an optical (dark gray line) and an x-ray laser (light gray line) probe traversing 3 mm of plasma (produced by driving a 50-μm thick CH target with a 1-ns square 0.53 μm laser pulse at 2.0×10^{13} W/cm^2). The target surface was at 25 μm prior to the pulse. Also shown is the calculated electron density (solid line). (08-00-1295-2639pb02)

The strong wavelength scaling of absorption and refraction ($\propto \lambda^2$) counters the loss in sensitivity caused by the linear scaling of fringe shift with probe wavelength. This difference in scaling makes the soft x-ray regime an attractive area in which to operate. To date, all our experiments for probing plasmas have used the yttrium x-ray laser. This neon-like collisionally pumped x-ray laser is well suited to this application by virtue of its high output power (Fig. 4) and monochromatic output (i.e., dominated by a single line at 155 Å).[10] The wavelength is also well suited to existing multilayer mirror technologies, which have demonstrated reflectivities of ~60%. At Lawrence Livermore

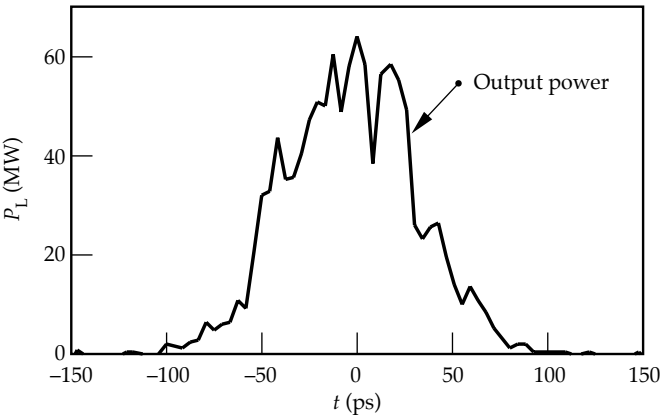

FIGURE 4. Measured output power of 3-cm-long yttrium exploding foil x-ray laser. (08-00-1295-2640pb01)

National Laboratory (LLNL), we use this system to image accelerated foils[15] and measure electron density profiles in a laser irradiated target using moiré deflectometry.[16] More importantly, we have developed the necessary technology to perform x-ray laser interferometry. In contrast to other techniques, interferometry offers the possibility of directly measuring the two-dimensional (2-D) electron density profile.

Interferometry Using Soft X-Ray Lasers

Extending conventional interferometric techniques into the soft x-ray range has been difficult because of the problems with designing optical systems that operate in the range of 40–400 Å. Reflective/grating systems have been used successfully at 1246 Å.[17] Svatos et al.[18] have demonstrated a purely reflective Fresnel bimirror setup at 48 Å. Both techniques, however, lack some of the advantages of standard interferometer geometries. Fortunately, multilayer mirror technology now allows us to have artificial structures that can be routinely fabricated with reflectivities as high as 65% at 130 Å[19] and with the overall uniformities required by more conventional interferometers.

Figure 5 is a schematic of the experimental setup used to probe plasmas. The system consists of a collimated x-ray laser source, an imaging mirror, and an interferometer. For our experiments, we chose to employ a skewed Mach–Zehnder interferometer, consisting of two flat multilayer mirrors and two multilayer beamsplitters (the most critical element in the system). The polarizing properties of multilayer mirrors, when operated at 45°, prevented us from using a more conventional Mach–Zehnder geometry. Each multilayer mirror consisted of a superpolished (<1 Å rms roughness) fused silica blank coated with 30 layer pairs of Si at 55.9 Å and Mo at 23.9 Å. The mirrors had a peak reflectivity of 60 ±5% at 155 Å. Although soft x-ray beamsplitters with small apertures have previously been used in x-ray laser cavities,[20] comparatively large open areas were necessary for our application. The *active* region of the beamsplitters used in the interferometer was 1.2 × 1.2 cm and consisted of 1000 Å of Si_3N_4 overcoated with 8 to 12 layer pairs of Mo/Si. The beamsplitters were fabricated from polished Si wafers overcoated with 1000 Å of Si_3N_4. The Si substrate thickness was varied from 0.4–0.8 mm, with the best results at thicker samples. The coated wafers were annealed to achieve maximum tension in the Si_3N_4. Anisotropic Si etching techniques were used to remove the Si substrate from a 1.2- × 1.2-cm area. The flatness

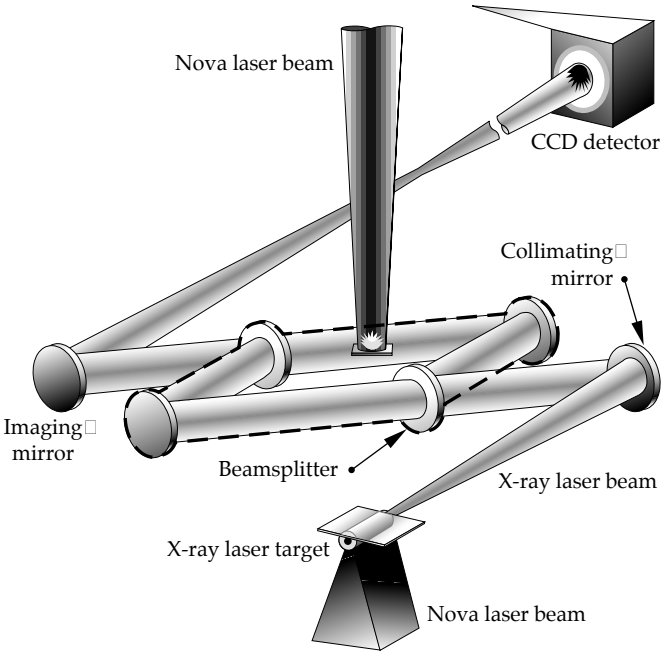

FIGURE 5. Experimental setup showing the optical components for plasma probing using a soft x-ray Mach–Zehnder interferometer. (08-00-1295-2641pb01)

of the beamsplitters was subsequently measured with an optical interferometer. Over the clear aperture, the figure error was typically less than 5000 Å for high-quality Si substrates but could be significantly worse (10000 Å) for conventional thin (0.4 mm) Si wafers. The figure quality was also extremely sensitive to the tension of the Si_3N_4 membrane. The best results were obtained with high-stress membranes (~200 MPa), which had a manufacturing yield of approximately 30%. The measured reflectivity and transmission for these beamsplitters at 155 Å were 20% and 15%, respectively. The overall throughput of each arm, accounting for the mirror and beamsplitter (one transmission and one reflection), was $\sim 0.6 \times 0.20 \times 0.15 = 0.018$.

The probe source consisted of a collisionally pumped neon-like yttrium x-ray laser, operating at 155 Å. The x-ray laser was produced by irradiating a solid 3-cm-long yttrium target with one beam from Nova ($\lambda_{laser} = 0.53$ μm, 600 ps square) at an intensity of 1.5×10^{14} W/cm^2. In this pumping geometry, the x-ray laser has an output energy of 3 ±2 mJ, a divergence of approximately 10–15 mrad (FWHM), and an output pulse width of 250 ps. The short pulse width allowed us to obtain an interferogram in a single 250-ps exposure, thereby reducing the effects of vibrations. A spherical multilayer mirror, placed 50 cm from the x-ray laser, collimated the beam and injected it into the interferometer. The transverse coherence length, after beam collimation, was calculated to be $L_s \approx 50$–100 μm, and the longitudinal coherence length was measured to be $L_t \approx 150$ μm. The limited transverse and longitudinal coherence constrains us to match the two paths of the interferometer to maximize fringe visibility. The interferometer was prealigned on an optical bench, using a 200-μm optical fiber and a white light source. Observation of white light fringes matched the optical path lengths to better than 2 μm.

The plasma to be probed was imaged onto a charge-coupled device (CCD) using a 100-cm radius of curvature multilayer mirror with an effective *f* number of 25. The CCD was a back illuminated TEK1024B with 1024×1024 24-μm pixels and a measured quantum efficiency of 40 ±10% at 155 Å. A filter consisting of 1000 Å of Al and 2000 Å of lexan directly in front of the CCD eliminated stray optical light. To reduce background self-emission, a series of three multilayer mirrors reduced the bandpass of the system. The effective bandpass of this system was 4 Å, which is significantly broader than the 10-mÅ spectral width of the x-ray laser source. The image magnification was 19, giving a pixel limited resolution of ~1.3 μm. Figure 6 shows a typical interferogram obtained using this system. In this figure, there is no target plasma; the dark band is an alignment reference positioned at the object plane of the imaging optic. Analysis of the fringe pattern gives a maximum figure error of 300 Å over the full 3-mm field of view and a fringe visibility of 0.7 ±0.2.

Figure 7 shows the interferogram of a plasma produced by irradiating a Si wafer overcoated with 10 μm of CH. The triangular shaped target allows a range of plasma lengths to be probed simultaneously. The Si substrate was polished to ~7 Å rms roughness to

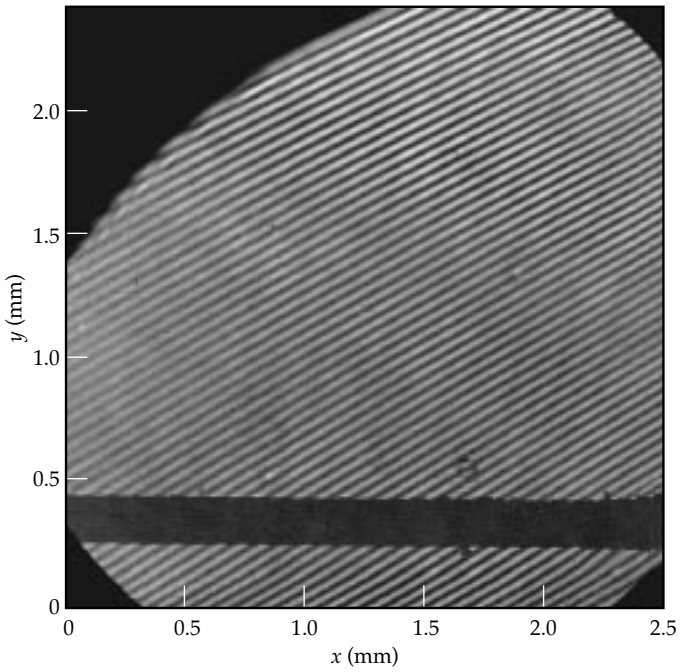

FIGURE 6. Soft x-ray (155 Å) interferogram showing a fringe visibility better than 0.5. The horizontal bar is an alignment reference at the object plane. (08-00-1295-2642pb01)

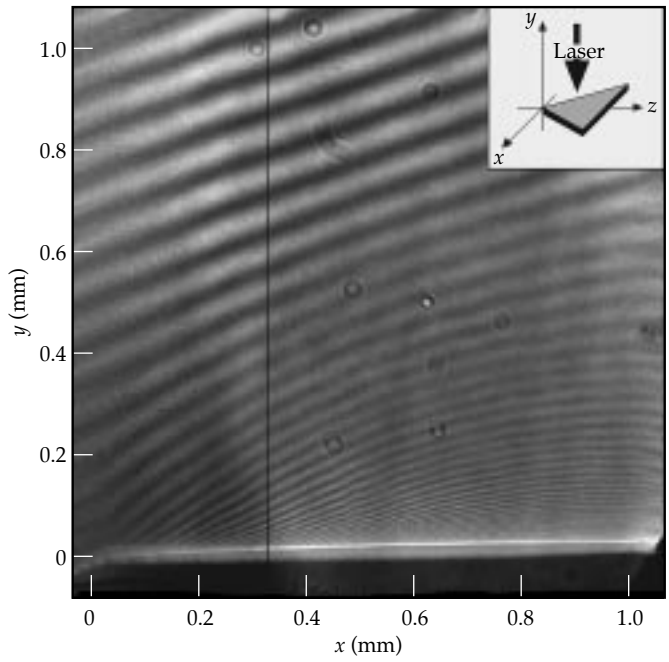

FIGURE 7. Interferogram of CH target irradiated at 2.7×10^{13} W/cm^2. The vertical line shows the position of the lineout in Fig. 8. The inset shows the target geometry. (08-00-1295-2643pb01)

produce a clean flat surface. The CH side was irradiated by a beam smoothed with random phase plates (RPPs) and segmented with wedges to produce a flat-top intensity distribution over a 0.7-mm-diam spot.[21] A 1-ns square laser pulse with a wavelength of 0.53 μm produced an intensity on target of 2.7×10^{13} W/cm^2. The target was backlit edge-on by the x-ray laser beam 1.1 ns after the start of the laser pulse. The image shows excellent fringe visibility and very little self emission from the plasma.

Figure 8 shows the measured electron density as calculated from the interferogram at a distance of 0.35 mm from the tip of the target where the probe length is 0.7 mm. Fringes are clearly resolved as close as 0.025 mm from the initial target surface. The fast evolution of the density profile, close to the critical surface, causes motion blurring of the fringes within the 250-ps x-ray laser frame time. Figure 8 also shows the calculated electron density profiles obtained from a one-dimensional (1-D) LASNEX simulation. The simulation results predict higher electron densities than measured with the discrepancy, increasing as we move away from the surface. This trend is consistent with the plasma expansion not being 1-D, which leads to significant lateral expansion and lower electron densities. We chose a triangular target geometry to illustrate the range of plasma lengths that can be easily probed with a soft x-ray laser. Unfortunately this geometry leads to a three-dimensional expansion, which is difficult to simulate. In the near term, we plan to improve both the target geometry and laser uniformity to generate a truly 2-D profile, which can be accurately compared with simulations. However, the magnitude of the discrepancy we observe between the experiment and simulations is similar to that measured using soft x-ray deflectometry.[16]

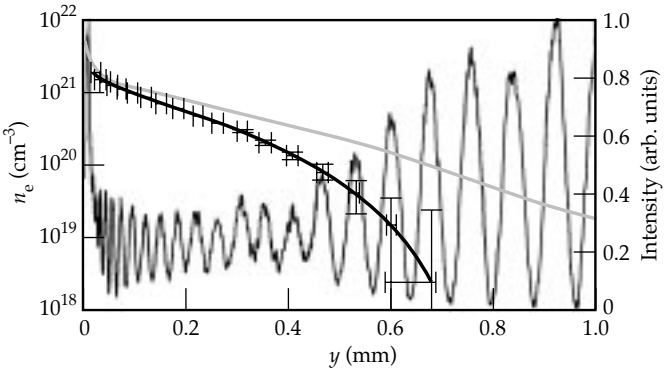

FIGURE 8. The thin solid line is a lineout through the interferogram of Fig. 7 at a position x = 0.35 mm. The thick solid line shows the calculated electron density profile and estimated error bars. The gray line is the electron density profile as calculated by one-dimensional LASNEX simulation. (08-00-1295-2644pb01)

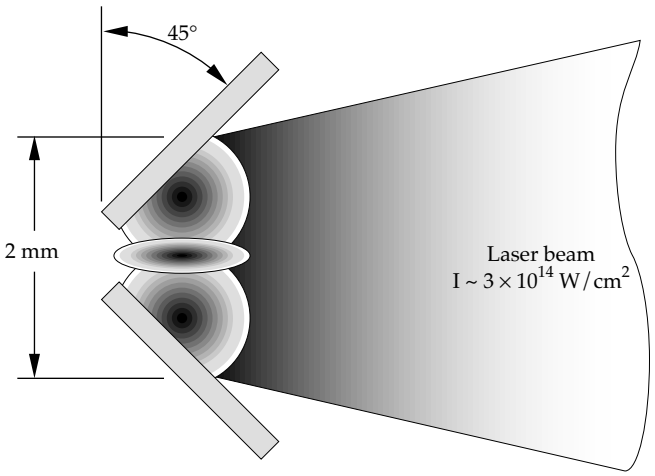

FIGURE 9. Target geometry for studying colliding plasmas. (08-00-1295-2645pb01)

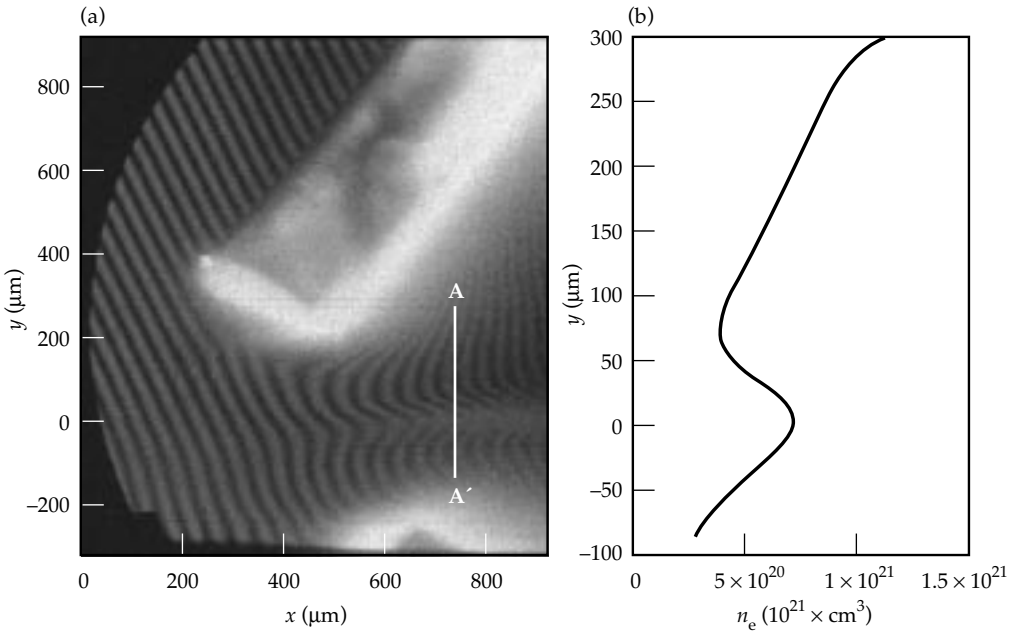

FIGURE 10. (a) Interferogram obtained of Au colliding plasma. (b) Electron density calculated from interferogram along line A–A′. (08-00-1295-2646pb01)

More recently, we used this interferometer to probe colliding plasmas that have relevance in ICF hohlraum experiments. The target consisted of two pieces of 3- × 2-mm polished Si, which were coated with 2 μm of Au and positioned as shown in Fig. 9. The target was irradiated at an intensity of 3×10^{14} W/cm^2 (λ_{laser} = 0.53 μm, 1 ns square), with a focal spot 2 mm high and 0.5 mm wide produced by combining cylinder lenses and RPPs. Figure 10 shows an interferogram at a time 1.0 ns after the start of the drive—providing clear evidence of interpenetrating plasmas. Figure 10(b) shows the measured electron density profile along the line A–A' in Fig. 10(a). The region of plasma stagnation and interpenetration is ~100 μm, which is larger than predicted by simple fluid codes. We are currently modeling this experiment, and we plan to publish the results in the future.

Conclusion

The high brightness and short wavelength of x-ray lasers make them ideally suited for studying long scalelength and high-density plasmas. Our results illustrate the importance of soft x-ray interferometry in diagnosing laser-produced plasmas by reducing the effects of absorption and refraction. Detailed comparisons of 2-D electron density profiles obtained from the x-ray laser interferogram and profiles obtained from radiation hydrodynamics codes, such as LASNEX, will allow us to study the physics of laser–plasma interactions in more detail. Ultimately, our motivation for developing x-ray laser interferometry is to provide a mechanism to probe the deficiencies of our numerical models in areas such as laser deposition by both resonance and inverse bremsstrahlung absorption, flux-limited heat conduction, hydrodynamics, and non-LTE (local thermodynamic equilibrium) atomic kinetics. In the near future, this technique will be used to diagnose the plasmas produced in ICF hohlraum targets, which has been impossible with conventional optical interferometry. In addition to probing laboratory plasmas, an x-ray interferometer can be used to characterize the figure and phase properties of multilayer mirrors near the intended operating wavelength. Measurement of spectral lineshapes with unprecedented resolution is also possible.[17,22]

Notes and References

1. D. T. Attwood, D. W. Sweeney, J. M. Auerbach, and P. H. Y. Lee, *Phys. Rev. Lett.* **40**, 184–186 (1978).
2. M. D. Rosen, P. L. Hagelstein, D. L. Matthews, E. M. Campbell, et al., *Phys. Rev. Lett.* **54**, 106 (1985); G. Charatis, G. E. Busch, C. L. Shepard, P. M. Campbell, and M. D. Rosen, *Journal De Physique* **C6**, 89 (1986); M. K. Prasad, K. G. Estabrook, J. A. Harte, R. S. Craxton, *Phys. Fluids B* **4**, 1569 (1992).
3. P. E. Young, *Phys. Fluids B* **3**, 2331–2336 (1991).
4. S. Wilks, P. E. Young, J. Hammer, M. Tabak, and W. L. Kruer, *Phys. Rev. Lett.* **73**, 2994–2997 (1994).
5. L. B. Da Silva, B. Cauble, G. Freiders, J. A. Koch, et al., (SPIE–International Society for Optical Engineering, Bellingham, WA, 1994; *Proc. SPIE* **2012**, 158).
6. *X-Ray Lasers 1994* , D. C. Eder, and D. L. Matthews, Eds., (American Institute of Physics, Williamsburg, VA, 1994) vol. 332; *X-Ray Lasers 1992*, E. E. Fill, Ed., (IOP Publishing Ltd, Schliersee, Germany, 1992) vol. 125.
7. H. Daido, R. Kodama, et al., *Opt. Lett.* **20**, 61–63 (1995); L. B. Da Silva, R. A. London, B. J. MacGowan, S. Mrowka, et al., *Opt. Lett.* **19**, 1532–1534 (1994); J. Nilsen, B. J. MacGowan, L. B. Da Silva, and J. C. Moreno, *Phys. Rev. A* **48**, 4682–4685 (1993). E. E. Fill, Y. L. Li, G. Preztler, D. Schlogl, et al., *Physica Scripta* **52**, 158–161 (1995); T. Hara, K. Ando, and Y. Aoyagi, *AIP Conference Proceedings* **332**, 181–185 (1995).
8. B. J. MacGowan, L. B. Da Silva, D. J. Fields, C. J. Keane, et al., *Phys. Fluids* **4**, 2326–2337 (1992).
9. A. Carillon, H. Z. Chen, P. Dhez, L. Dwivedi, et al., *Phys. Rev. Lett.* **68**, 2917–2920 (1992).
10. L. B. Da Silva, B. J. MacGowan, S. Mrowka, J. A. Koch, et al., *Opt. Lett.* **18**, 1174–1176 (1993).
11. J. J. Rocca, V. Shlyaptsev, F. G. Tomasel, O. D. Cortazar, et al., *Phys. Rev. Lett.* **75**, 1236–1236 (1995) and *Phys. Rev. Lett.* **73**, 2192–2195 (1994).
12. L. B. Da Silva, J. E. Trebes, R. Balhorn, S. Mrowka, et al., *Science* **258**, 269–271 (1992).
13. C. W. Allen, *Astrophysical Quantities*, (Oxford University Press, New York, NY 1963).
14. J. Koch, B. J. MacGowan, L. B. Da Silva, D. L. Matthews, et al., *Phys. Rev. Lett.* **68**, 3291 (1992).
15. R. Cauble, L. B. Da Silva, T. W. Barbee, P. Celliers, et al., *Phys. Rev. Lett.* **74**, 3816–3819 (1995).
16. D. Ress, L. B. Da Silva, R. A. London, J. E. Trebes, et al., *Science* **265**, 514–517 (1994).
17. S. Chakrabarti, D. M. Cotton, J. S. Vickers, and B. C. Bush, *Appl. Opt.* **33**, 2596–2602 (1994).
18. J. Svatos, D. Joyeux, D. Phalippou, and F. Polack, *Opt. Lett.* **18**, 1367–1369 (1993).
19. T. W. Barbee Jr., J. C. Rife, W. R. Hunter, M. P. Kowalski, et al., *Appl. Opt.* **32**, 4852–4854 (1993); D. G. Stearns, R. S. Rosen, and S. P. Vernon, *J. Vac. Sci. Technol. A, Vac. Surf. Films* **9**, 2662–2669 (1991).
20. A. M. Hawryluk, N. M. Ceglio, D. G. Stearns, K. Danzmann, et al., (SPIE–International Society for Optical Engineering, Bellingham, WA, 1987; *Proc. SPIE* **688**, 81–90).
21. S. G. Glendinning, S. V. Wever, P. Bell, L. B. Da Silva, et al., *Phys. Rev. Lett.* **69**, 1201–1204 (1992).
22. M. R. Howells, K. Frank, Z. Hussain, E. J. Moler, et al., *Toward a Soft X-Ray Fourier Transform Spectrometer*, LBL-34798, (1993).

Metastable Crystal Structures of Solid Hydrogen

G. W. Collins

W. G. Unites

E. R. Mapoles

T. P. Bernat

Introduction

All current ignition target designs for inertial confinement fusion (ICF) require a uniform cryogenic (liquid or solid) deuterium–tritium (DT) fuel layer. However, it is difficult to support a uniform liquid DT layer inside a capsule in the presence of gravity.[1] Fortunately, a solid DT layer is stable in the presence of gravity and self-symmetrizes due to the natural heating from tritium beta decay (beta-layering).[2] Recent experiments show that beta layering can produce a surface roughness of 1 μm rms, which is smooth enough for current National Ignition Facility ignition target designs. The surface roughness of these polycrystalline DT layers is determined by the way crystal facets stack up to conform to the 1-mm radius of curvature. If we could produce a stable amorphous DT layer, the surface roughness could be reduced significantly. Alexandrova et al. claim to have observed such an amorphous layer of H_2.[3] In this article, we describe the equilibrium and metastable structures of solid hydrogen. Since the crystal structure of all the hydrogen isotopes is the same, we work with H_2 and D_2 instead of DT.

We begin by reviewing some basic properties of solid hydrogen. Because the interaction between hydrogen molecules is weak, the rotational quantum number is well defined in the low-pressure solid at temperatures above $0.2T_{tp}$, and most of the molecules are either in the ground ($J = 0$) or first excited ($J = 1$) rotational state. T_{tp} is the triple-point temperature for a particular hydrogen isotope or mixture: T_{tp} ($J = 0$ H_2) = 13.8 K and T_{tp} ($J = 0$ D_2) = 18.7 K.[4] All the hydrogens typically form an hcp structure near their respective T_{tp},[5,6] however, at low enough temperature and large $J = 1$ concentration ([$J = 1$] > 55%), the lattice transforms to fcc with the molecules oriented. This phase transition lowers the electric quadrupole–quadrupole energy for $J = 1$ molecules by about 5 K/molecule, which is much greater than the ~1 mK/molecule energy difference between disordered hcp and fcc structures. In $J = 0$ hydrogen, the free energy difference between hcp and fcc is not well understood, but the equilibrium crystal structure at all temperatures and pressures below ~100 GPa is hcp.[7]

Rare gas solids also form simple molecular solids with lattice potentials similar to hydrogen. However, Ne, Ar, Kr, and Xe crystallize into fcc at low pressure, while the lightest rare gas, ^{4}He, primarily forms an hcp structure at low temperature and pressure, and fcc only at high temperature and pressure. The hcp structure forms in low pressure ^{4}He and possibly $J = 0$ hydrogen because the dispersion interaction for the closed shell S state orbital is comparatively small.[8]

While hcp is the equilibrium structure at low $J = 1$ concentrations, nonequilibrium hydrogen fcc structures have been observed.[9] In this article, we describe the temperature dependence and crystal morphology of metastable phases of $J = 0$ H_2 and D_2.[10] We also show that (1) the metastable fcc phase is separated from hcp by a spectrum of energy barriers, (2) the fcc phase is less stable in H_2 than in D_2, (3) the structural symmetry decreases as the deposition temperature T_d decreases, and (4) the crystallite length scale decreases with decreasing T_d. However, we find no evidence that an amorphous phase of hydrogen can be produced at temperatures as low as $0.18T_{tp}$.

To determine lattice structure, we detect the $J = 0 \rightarrow 2$ signal of the rotational Raman spectrum. In pure $J = 0$ solids, this signal produces a multiplet that can be a unique signature of the crystal lattice. A triplet is unique to hcp, whereas fcc symmetry produces a doublet. Van Kranendonk[7] outlines the calculational procedure for determining the spectral positions and intensity ratios. Some of our observations may be related to those of Silvera and Wijngaarden[11] and Durana and McTague,[12] who observed a four-peak

spectrum in rapidly pressurized hydrogen. Four peaks are expected if the Raman signal results from both hcp and fcc crystals because the high-energy shifted peaks for both hcp and fcc are close together and the low-energy shifted fcc signal is at lower energy than the other hcp lines.

Experimental Details

For these experiments, a Cu sample cell is fitted with two opposing vertical MgF_2-coated sapphire windows that serve as the hydrogen substrate and permit optical access. The cell is connected to the cold tip of a He flow cryostat. Both a 30-K radiation shield and the outer vacuum jacket contain sapphire windows for optical access. A calibrated germanium resistance thermometer (GRT) is fitted on the Cu sample cell and checked against T_{tp} of D_2 and H_2. At $T > 0.5\ T_{tp}$, we compare the thermometer temperature with the temperature calculated from the hydrogen vapor pressure,[13] as measured by a capacitance manometer. The agreement between the vapor pressure and the GRT shows the accuracy of the temperature measurement to be better than 0.05 K.

The H_2 and D_2 gas were high-purity research grade, with an isotopic purity of 99.9% and 99.8% respectively. The samples studied contained a $J = 1$ concentration less than ~1%. The rotational and isotopic concentrations are determined by comparing the Raman line intensities for the $J = 0 \rightarrow 2$ and $J = 1 \rightarrow 3$ transitions. The hydrogen gas was cooled to ~20–30 K just before deposition. The deposition rates are determined from the layer thickness, measured by interferometry, vs time. All the samples were between 30 and 300 μm thick.

We measured the Raman shift of the 488-nm line of an Ar ion laser in a back scattering geometry with a modified 0.5-m SPEX 1870 spectrograph fitted with a liquid-nitrogen-cooled CCD having a 22.5-μm pixel width. We used $f/3$ optics to couple light in and out of the sample. Our spectral resolution was ~0.4 cm^{-1}. Line positions were determined from both a calibrated Th lamp and the triplet structure of H_2 or D_2 crystallized through the triple point, with their line positions as measured by Bhatnagar et al.[14] The laser power level (~1 to 100 mW in ~40 μm^2) did not influence the lattice structure or visually change the layer morphology.

Raman Data

Figure 1 shows several different Raman spectra for vapor-deposited H_2 or D_2 layers. The spectra on the left and right are from H_2 and D_2 respectively. The three-peak spectrum in Fig. 1(a) is typical of H_2 or D_2 at $T_d > 0.3 T_{tp}$. The four-peak spectra in Fig. 1(b) and 1(e) are typical of $3.5\ K \leq T_d\ (H_2) < 4\ K$ and $4\ K < T_d\ (D_2) \leq 6$ K, and of deposition rates of $0.1 < R\ (\mu m/min) < 40$. Figure 1(d) is typical for $3.5 \leq T_d\ (D_2) < 4$ K, where it appears that the peaks in Fig. 1(e) shift toward an unresolved lineshape with two main branches. Figures 1(c) and 1(f) show the signals several minutes after rapidly warming H_2 and D_2 respectively. The quadruplet in Fig. 1(b) and 1(e) and the unresolved "doublet" in Fig. 1(d) transform to a triplet within minutes upon warming the sample rapidly through ~0.5 T_{tp}. At constant temperature the Raman spectra in Fig. 1 are stable for at least two days, the maximum duration of observation. Figure 2(a) shows the temperature dependence of the Raman spectrum of D_2 for $T_d = 5.3$ K. The steady decrease in the relative intensity of the first and fourth peaks with increasing temperature is not reversible upon cooling. There is a slight shift in the spectrum of ~–0.45 cm^{-1} upon warming from 5 to 7 K. The high-energy peak is shifted slightly more (~–0.70 to –0.90 cm^{-1}) than the other, low-energy peaks. The quadruplet signal in H_2 also transforms to a triplet upon slowly raising T to ~5.5 K.

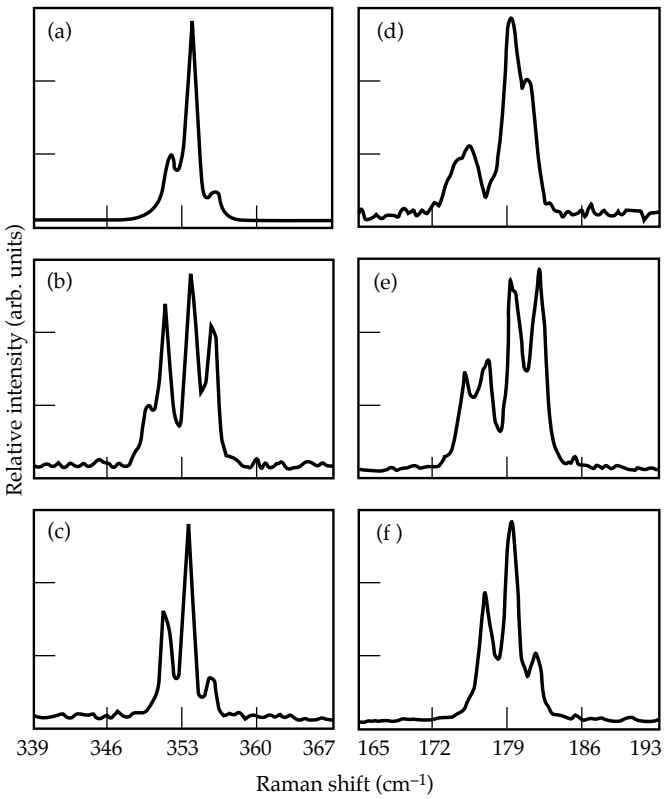

FIGURE 1. $J = 0 \rightarrow 2$ Raman signal for (a) H_2 deposited at 5.5 K and 5 μm/min, (b) H_2 deposited at 3.5 K and 2 μm/min, (c) same sample as Fig. 1(b) after warming from 3.5 K to 7 K, (d) D_2 deposited at 3.5 K and 0.2 μm/min, (e) D_2 deposited at 5.2 K and 0.4 μm/min, (f) same sample as Fig. 1(e) after warming from 5.2 K to 11.4 K.
(10-06-0296-0312pb01)

In Fig. 2(b) we plot the intensity ratio of the low-energy Raman peak of the quadruplet divided by the average of the other three peaks, $R_{fcc/hcp}$, vs temperature (all values, not just the steady state value) from two different experiments. The large scatter of points at each temperature is due primarily to the complicated time dependence at constant temperature. The lowest value for $R_{fcc/hcp}$ is the steady state value. The plot is approximately linear from 6 K to 11 K. For D_2 deposited between 5.1 K and 5.5 K and held at constant temperature for about two days, there is no change in $R_{fcc/hcp}$. Thus, after relaxation, $R_{fcc/hcp}$ is roughly constant at constant temperature and decreases with increasing temperature.

The Raman spectrum of D_2 deposited at 3.5 K [see Fig. 1(d)] behaves differently. As T is increased from T_d to 7 K, the two overlapping lines in the right branch separated slightly, but the general structure still consisted of two main branches. Upon increasing T to ~10 K, the structure transformed into a well resolved triplet, similar to that shown in Fig. 1(f), within ~10 min.

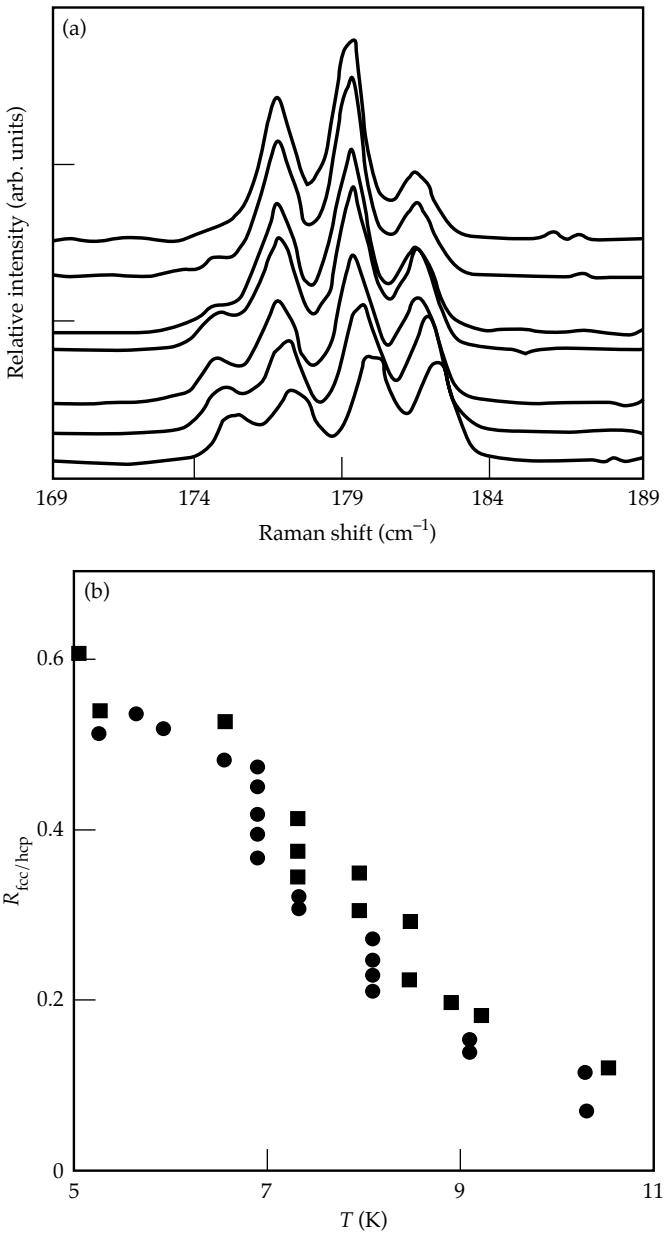

FIGURE 2. Temperature and time dependence of the $J = 0 \rightarrow 2$ Raman spectrum, upon warming solid $J = 0$ D_2. (a) D_2 deposited at 5.3 K and 2.2 μm/min (from bottom to top) (i) after deposition at 5.3 K, (ii) after raising T to 6.9 K, (iii) after waiting at 6.9 K for 34 min, (iv) after raising $T$to 7.4 K and waiting 8 min, (v) after 13 min at 8.1 K, (vi) after 5 min at 9.1 K, and (vii) after 2 min at 10.4 K. (b) The low-energy Raman peak divided by the average of the other three peaks ($R_{fcc/hcp}$) vs T from two different experiments. The circles show the same experiment as in Fig. 2(a). The squares show a similar experiment with $J = 0$ D_2 deposited at 5.1 K and 0.4 μm/min. After deposition, the sample sat at ~5.3 K for 23 h, and then we began raising T at ~0.5 K/20 min. (10-06-0296-0312pb01)

Discussion of Raman Data

In Table 1 we list the theoretical and measured line positions for the Raman multiplet for both hcp and fcc crystal structures. We calculate the theoretical values from Van Kranendonk.[7] The measured values are from the present work and Bhatnagar et al.[14] The calculated values for the hcp lattice are close to the measured values. The calculated low-energy line of an fcc structure is at the same position as the low-energy line of the quadruplet spectra in Fig. 1(b) and 1(e). The calculated high-energy line of the fcc lattice would be unresolved from the high-energy hcp line given our resolution. Because of the low-energy line position in the quadruplet spectrum and the change in intensity of the high-energy line upon warming to $T = 0.5T_{tp}$, we interpret the quadruplet spectrum to be the signature of a mixed hcp and fcc lattice. Thus, the narrow-line resolved spectra of Fig. 1(b) and 1(e) reflect the presence of both hcp and fcc crystallites.

TABLE 1. Calculated and measured $J = 0 \geq 2$ Raman line positions (in cm^{-1}) for H_2 and D_2 in hcp and fcc phases.

	H_2			D_2		
	Calculated	Ref. 15	Fig. 1	Calculated	Ref. 15	Fig. 1
hcp						
$m_j = 2$	354.5	353.85	354	179.6	179.4	179
$m_j = 1$	352.0	351.84	352	176.5	176.8	177
$m_j = 0$	357.0	355.83	356	182.7	182.0	182
fcc						
E_1	349.6		350	173.6		175
E_2	356.9		356	182.6		182

The relative $m_j = 1, 2, 0$ intensity ratios for Fig. 1(a), 1(c), and 1(f) are 0.33:1:0.15, 0.55:1:0.21, and 0.64:1:0.34. The relative m_j intensities depend on crystal orientation with respect to the incident and scattered electric field

polarizations.[7,15] Assuming the incident light is collimated, a powder average of hcp crystallites yields 1:1:0.5, and a crystal with its c axis perpendicular to the substrate yields 0:1:0. Thus, there is a preferential c-axis alignment perpendicular to the substrate. Although a preferential growth along the c axis has been observed near the triple point, it is unclear why these small crystals would grow in a preferred direction or transform from fcc to hcp in a preferred orientation.

As T_d decreases in the range $0.2 < T_d/T_{tp} < 0.3$, the intensities of the low- and high-energy peaks increase relative to the two central peaks. After deposition, as T is increased towards $0.5\ T_{tp}$, the low- and high-energy peaks decrease. This is expected if an fcc component occurs at $T_d/T_{tp} < 0.3$ and increases with decreasing T_d. Thus, the ratio $R_{fcc/hcp}$ is a relative measure of fcc to hcp structure in the sample. The irreversible decrease in $R_{fcc/hcp}$ with increasing temperature suggests that the fcc component, once formed, is metastable at $T<0.5\ T_{tp}$. The equilibration of $R_{fcc/hcp}$ after each temperature increase suggests that the fcc phase is separated from the lower-energy hcp phase by many different barrier energies. At constant T_d, we also see a slight increase in the fcc component with decreasing R. This implies that the fcc component may be found at $T_d/T_{tp} > 0.3$ if we deposited at lower R. This effect may be due to sample heating.

Relative to their triple points, the temperature at which the mixed fcc + hcp structure is formed is lower in H_2 (~4 K) than in D_2 (~6 K). Also, the mixed phase transforms to pure hcp at a relatively lower temperature in H_2 (~5.5 K) than in D_2 (~10.5 K). Thus the fcc phase is less stable in H_2 than in D_2. If the fcc phase is metastable and separated from the hcp phase by a spectrum of energy barriers, and if tunneling is a dominant mechanism for molecular motion at these low temperatures, then H_2 would be able to cross the energy barriers to reach the lower-energy hcp phase more rapidly than D_2. Although tunneling diffusion has been observed for hydrogen atoms in solid hydrogen,[16] tunneling of molecules in solid hydrogen has not been clearly observed.[17]

The unresolved lineshape of Fig. 1(d) is significantly different than the other narrow line spectra in Fig. 1. This broad lineshape indicates that the lattice structure of samples deposited at $T_d < 0.2\ T_{tp}$ have less symmetry than pure hcp or fcc. The broad lineshape may result from a randomly stacked close-packed lattice or very small crystallites, but probably not an amorphous structure, which would give rise to a single broad line similar to that of the liquid phase.

Crystal Morphology

Figure 3(a) and 3(b) show shadowgraph images of H_2 crystallites deposited at $R = 40\ \mu m/min$ and $T_d = 3.6$ K and 7.0 K. These and similar experiments qualitatively show that the average crystal size decreases rapidly with decreasing temperature and increasing deposition rate between $3.6 < T_d < 11$ K and $0.1 < R\ (\mu m/min) < 40$. Figure 4 shows the change in the average crystal diam vs different T_d. The smallest crystal diam is at the limit of our optical resolution (~3 μm) and is thus a very rough estimate.[18]

Since the deposition temperatures used here are below the roughening transition temperatures for the low-energy crystal facets,[19] the lowest-free-energy configuration is in the form of faceted crystallites. The appearance of smooth rounded crystallites as in Fig. 3(b) implies that the crystal morphology is nonequilibrium and is determined by kinetics. To qualitatively understand the dependence of crystal size on temperature and deposition rate, we assume that the temperature controls the rate at which molecules relax from a high-energy to low-energy configuration. We expect the

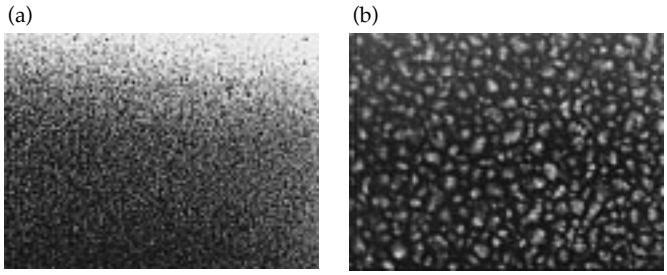

FIGURE 3. Shadowgraph images of H_2 deposited at 40 μm/min and (a) 3.6 K and (b) 7.0 K. The horizontal field of view is 1.7 mm. (10-06-0296-0312pb01)

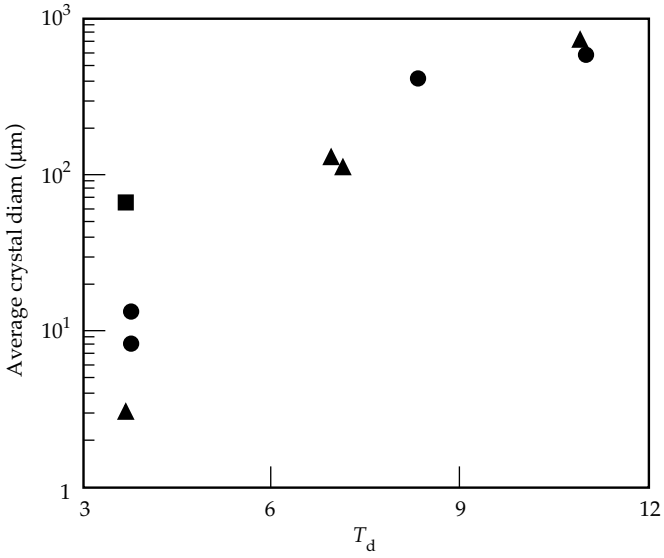

FIGURE 4. Average crystallite diam vs T_d for H_2 deposited at 0.2 μm/min (squares), 2 μm/min (circles), and 40 μm/min (triangles). (10-06-0296-0312pb01)

lowest-energy site to be that with the maximum number of neighboring bonds, such as a step edge of a crystal. As the temperature decreases or the deposition rate increases, there is less chance of finding a low-energy site before the next layer of material covers the substrate.

Summary

In summary, using Raman spectroscopy we find that $J = 0$ D_2 or $J = 0$ H_2 forms a mixed fcc/hcp structure when deposited at $0.2 < T_d/T_{tp} < 0.3$. The fcc phase is less stable in H_2 than D_2. This fcc component transforms continuously and irreversibly to hcp upon increasing the temperature through $0.5T_{tp}$, suggesting that the fcc phase is separated from the lower-energy hcp phase by a spectrum of barrier energies. As T_d decreases below ~0.2 T_{tp}, the lattice structure has less symmetry than fcc or hcp and possibly resembles a randomly stacked close-packed phase. Finally, the crystallite size decreases with decreasing T_d from millimeter scale at a few degrees below T_{tp} to micrometer scale at ~0.3 T_{tp}.

The metastable hydrogen structure described here may elucidate several recent experiments. D atoms in solid deuterium deposited from the gas phase at ~3 K have a significantly different activation energy than expected for the equilibrium hcp structure.[17,20] Also, surface-state electron mobility[21] shows an increased conductivity after annealing vapor-deposited films. These observations can be at least qualitatively explained by the metastable structures described here and those that may be found at lower deposition temperatures.

Notes and References

1. J. J. Sanchez et al. *ICF Quarterly Report* **4**(3), 117, Lawrence Livermore National Laboratory, Livermore, CA, UCRL-LR-105821-94-3 (1994).
2. A. J. Martin, R. J. Simms, and R. B. Jacobs, *J. Vac. Sci. Technol. A* **6**(3), 1885 (1988); J. K. Hoffer and L. R. Foreman, *Phys. Rev. Lett.* **60**, 1310 (1988); T. P. Bernat, E. R. Mapoles, and J. J. Sanchez, *ICF Quarterly Report* **1**(2), 57, Lawrence Livermore National Laboratory, Livermore, CA, UCRL-LR-105821-91-2 (1991); G. W. Collins et al., *ICF Quarterly Report* **3**(2), 81, Lawrence Livermore National Laboratory, Livermore, CA, UCRL-LR-105821-93-2 (1993).
3. I. V. Aleksandrova, E. R. Koresheva, and I. E. Osipov, Russian Academy of Sciences, P. N. Lebedev Physical Institute, Report No. 57, Moscow (1992).
4. Isaac F. Silvera, *Rev. Mod. Phys*. **52**, 80 (1980).
5. Isaac F. Silvera, *Rev. Mod. Phys*. **52**, 393 (1980).
6. P. C. Souers, *Hydrogen Properties for Fusion Energy* (University of California, Berkeley, 1986), Ch. 6.
7. Jan Van Kranendonk, *Solid Hydrogen* (Plenum Press, New York, 1983), p. 226.
8. K. F. Niebles and J. A. Venables in *Rare Gas Solids*, M. L. Klein and J. A. Venables, Eds. (Academic Press, New York, 1976), vol. 1, Ch. 9.
9. R. L. Mills, J. L. Yarnell, and A. F. Schuch, *Proceedings of the Low Temperature Physics Conference 13*, Boulder (Plenum, NY) vol. II, p. 202; O. Bostanjoglo and R. Kleinschmidt, *J. Chem. Phys.* **46**, 2004 (1967); A. E. Curzon and A. J. Mascall, *Brit. J. Appl. Phys*. **16**, 1301 (1965); C. S. Barrett, L. Meyer, and J. Wasserman, *J. Chem. Phys*. **45**, 834 (1966).
10. The substrate was an amorphous or nanocrystalline film of MgF_2 vapor deposited onto a sapphire window that was cleaved normal to the c axis.
11. I. F. Silvera and R. J. Wijngaarden, Phys. Rev. Lett. **47**, 39 (1981). R. J. Wijngaarden, Ph.D. thesis, Harvard University, University Microfilms, Ann Arbor, MI, 1982.
12. S. C. Durana and J. P. McTague, *Phys. Rev. Lett*. **31**, 990 (1973).
13. Isaac F. Silvera, *Rev. Mod. Phys*. **52**, 49 (1980).
14. S. S. Bhatnagar, E. J. Allin, and H. L. Welsh, *Can. J. Phys*. **40**, 9 (1962).
15. J. P. McTague, I. F. Silvera, and W. N. Hardy, *Proceedings of the 7th AIRAPT Conf. on Light Scattering in Solids*, Paris, France, 1971 (Flammarion Sciences, Paris) p. 456.
16. G. W. Collins et al., *Phys. Rev. B* **45**, 549 (1992); A. S. Iskovskikh et al., *Sov. Phys. JETP* **64**, 1085 (1986).
17. J. R. Gaines, P. A. Fedders, G. W. Collins, J. D. Sater, and P. C. Souers, *Phys. Rev. B*. **52**, 7243 (1995).
18. Crystals left at constant temperature, even near 3.5 K, appeared to increase with time, although we did not study this phenomenon in detail. The crystal size for $T > 0.7$, T_{tp} also depends on layer thickness. For the data in Fig. 4, the layers are about 50 μm thick. Layers thinner than 10 to 20 μm have smaller crystals.
19. G. W. Collins, E. R. Mapoles, W. Unites, T. P. Bernat, "*Roughening Transition in Solid Deuterium*," Lawrence Livermore National Laboratory, Livermore, CA, UCRL-JC-117390 (1994).
20. A. V. Ivliev et al., *JETP Lett*. **38**, 379 (1983); E. B. Gordon et al., *JETP Lett*. **37**, 282 (1983).
21. M. A. Paalanen and Y. Iye, *Surface Science*, **170**, 80 (1986); K. Kono, U. Albrecht, and P. Leiderer, *J. Low Temp. Physics*, **82**, 279 (1991).

X-Ray Production in Laser-Heated Xe Gas Targets

R. L. Kauffman

L. J. Suter

H. N. Kornblum

D. S. Montgomery

Introduction

High-powered lasers focused to high intensities can generate bright x-ray sources. When they directly irradiate high-*Z* planar targets, more than 50% of the incident laser energy can be converted to soft, or thermal, x rays.[1,2] Enclosed targets, or hohlraums, can confine the x rays for inertial confinement fusion (ICF) and other radiation-heating experiments.[3–5] Laser-heated plasmas can also be a bright source of keV x-ray emission.[6,7] These x rays are produced by bound–bound and bound–free transitions in the hot, underdense plasmas. The spectrum is highly structured and depends on the target material.

To date, most studies of x-ray production from laser-produced plasmas have used solid or overdense targets whose initial density, when ionized, is above the critical plasma density, n_c, for absorption.[1,8] In such targets, the laser energy is absorbed at, or near, critical densities producing a hot plasma. Electron conduction from the hot plasma efficiently heats the higher-density matter while the hot plasma expands to form a lower-density plasma, or corona. This establishes an ablation process in which the denser matter flows through the critical density region and is heated by the laser and then exhausted into the corona. X rays are produced primarily in the region around critical density that is heated by the laser, a region called the conversion layer. For high-*Z* targets, x rays from the conversion layer can produce a thermal wave into the dense target material, which also can contribute to the production of thermal x rays. Although this heating and x-ray production process has been shown experimentally to be efficient, a significant amount of energy is coupled to hydrodynamic motion of the expanding plasma.

We present results from a new type of target that does not rely on ablation for heating the plasma. In the new targets, the density is less than n_c when ionized. The plasma is initially cold and opaque to the laser. The laser is absorbed efficiently by inverse bremsstrahlung heating of the plasma. As the plasma is heated, inverse bremsstrahlung becomes less efficient, making the plasma more transparent. The supersonic heat wave that is established ionizes the underdense plasma. The process has the advantage of being more efficient for radiation production, compared with overdense targets, because laser energy heats the plasma without ablation, and less energy is wasted on hydrodynamic motion. The plasma subsequently disassembles as it expands, producing hydrodynamic motion; however, this occurs after the plasma is already heated. The higher plasma temperatures can potentially produce brighter sources for both thermal and multikilovolt x rays. In addition, the higher plasma temperatures can produce higher ionization states, which may result in higher-energy x rays than those attainable using overdense targets. More efficient targets for x-ray production have several applications, including use as a bright x-ray source for backlighters and for radiation-effects experiments.

Experiment

The experiments were performed using the Nova laser[9] to investigate underdense targets and to demonstrate their efficiency for both thermal and multi-keV x-ray production. The targets, called gasbags[10], are nearly spherical thin membranes filled with gas similar to those developed for large plasma experiments. The thin membranes are made of 4000-Å polyimide ($C_{14}H_6N_2O_4$) stretched over a support washer.[11] Figure 1(a) is a picture of the target mounted in the Nova target chamber and viewed from the west by the polar target alignment viewer (TAV1). The striped, nearly hemispherical objects are the membranes. The stripes are caused by interference patterns of the optical illumination system in the membrane. The large black stripe in the center is a support washer for the

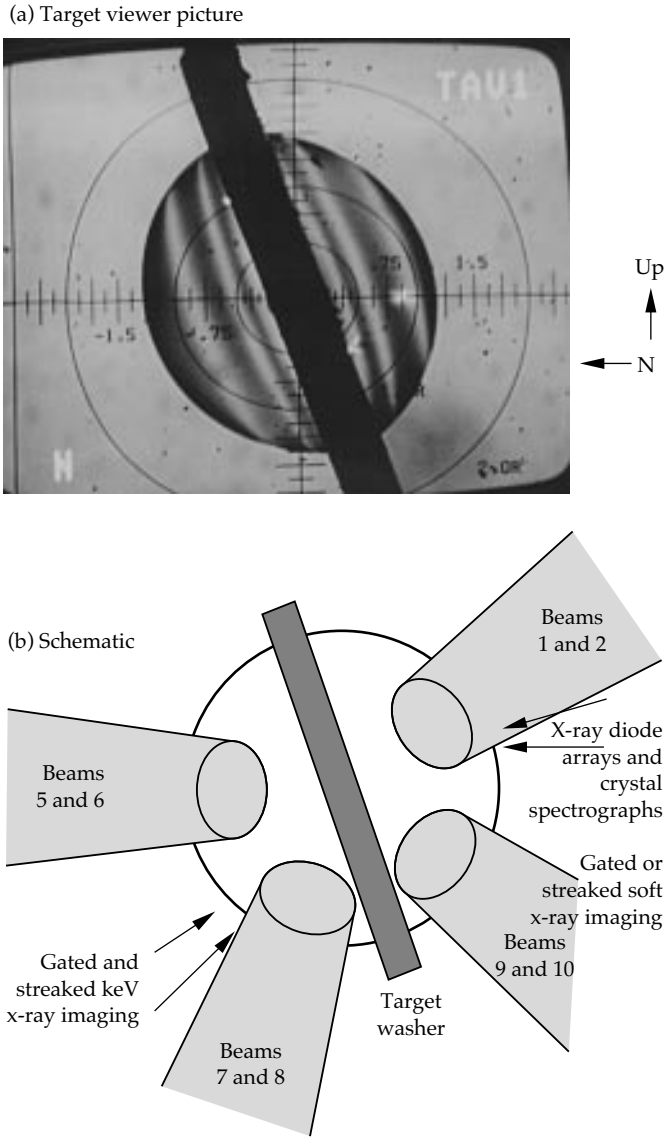

FIGURE 1. Experimental geometry. (a) Image of the target in the target alignment viewer. (b) Schematic of focusing geometry on the target surface and view of the diagnostics. This view is from the west on Nova along the axis of symmetry of the beam cones. (08-00-0296-0438pb01)

membranes. The target is rotated 90° to the normal configuration for the large plasma experiments to allow optimal viewing by x-ray diagnostics.

The targets are filled with a gas mixture of Xe and C_3H_8 (propane) at 1 atm of pressure. We chose Xe because it is a relatively high-atomic-number gas that is easily handled. When ionized to a Ne-like configuration, Xe has x-ray line emission in the 4–6-keV range, which is of interest for x-ray radiography and x-ray exposure experiments. Xe is mixed with C_3H_8 to supply H ions to the plasma. Mixing of light ions, such as H, with heavy ions helps suppress stimulated Brillouin scattering (SBS), which could be a source of energy loss.[12] We chose C_3H_8 because it produces 32 free electrons per molecule when fully ionized. This number is similar to the 44 free electrons per molecule produced when Xe is ionized to a Ne-like configuration. Thus, the relative concentration of the two gases could be varied without significantly changing the plasma electron density while maintaining the same initial fill pressure.

Table 1 lists the experimental parameters for a total of four Nova shots performed in this first set of scoping experiments. All targets were filled to 1 atm. The varying gas concentrations and approximate diameter of the targets for each shot are listed in the table.

TABLE 1. Summary of Xe-filled gas targets.

Shot number	Gas mixture	E_{Laser} (kJ)	Target diam (mm)	Defocus (mm)	I_{Laser} (W/cm^2)
24061417	25% Xe/ 75% C_3H_8	22.1	2.75	2/5	$1.6/5.5\times10^{14}$
24061419	75% Xe/ 25% C_3H_8	20.7	2.75	2/5	$1.5/5.3\times10^{14}$
24072917	75% Xe/ 25% C_3H_8	22.1	2.5	1.8	6.7×10^{14}
24072919	90% Xe/ 10% C_3H_8	22.1	2.5	1.8	6.3×10^{14}

The targets are irradiated with eight of Nova's ten beams. Figure 1(b) is a schematic showing the beam positions on the target membrane. The other two Nova beams were not used because they would have hit the target washer support. The beams are pointed at the center of the target. Beams 1, 2, 5, and 6 are at an angle of 43° to the washer normal; beams 7, 8, 9, and 10 are at 63°. The beams irradiate the membrane surface in converging focus. The average intensity on the membrane for each of the shots is listed in Table 1. For the first two shots, the focusing is chosen to provide the lowest intensity irradiation on the membrane and still miss the washer. The average intensity for the beams at 43° is the lower intensity value listed in Table 1; the higher intensity is for the beams incident at 63°. For the second two shots, the focusing is the same for all eight beams so that the average intensity for all beams on the membrane is the same. The laser energy is 21 to 22 kJ of 0.35-μm light in a 1-ns square laser pulse.

We measured x-ray production from the targets using several diagnostics shown in Fig. 1(b). Absolute x-ray production in the range of 0.1 to 1.8 keV is measured using Dante, a broadband, multichannel soft-x-ray spectrometer.[13] X-ray spectra in the range of 1.8 to 7.0 keV is measured using time-integrated x-ray crystal spectrographs. Absolute yields are obtained by normalizing these spectra to a broadband, filtered x-ray diode on Dante as described below. Beam heating and propagation is measured using gated x-ray imaging.[14] In addition, back-reflected light near the incident wavelength from SBS is measured on beam 7 using the Full Aperture Backscatter Station (FABS).[15,16]

Results

We studied the heating dynamics of the gasbag using time-resolved, x-ray pinhole camera imaging. Figure 2 is an example of the images taken with the west axial x-ray imager (WAX).[14] This view is the same as that shown in Fig. 1(a), although the images are inverted in the pinhole camera. The time sequence of events run from the upper right to the lower left. The time difference between images is ~50 ps, and the first image is ~100 ps after the start of the laser pulse.

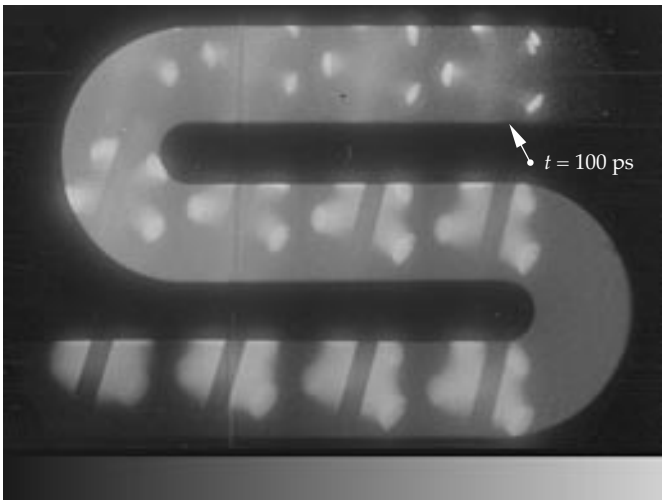

FIGURE 2. Time-resolved x-ray images. The sequence of events is from upper right to lower left. The first image is 100 ps after the beginning of the 1-ns laser pulse. The images are of x-ray emission above 2 keV. Each image is time-resolved to about 80 ps, and time between images in a row is 40 ps. The time interval between the last image in a row and the first image in the next row is 80 ps. (08-00-0296-0439pb01)

The images show the dynamics of the gasbag heating. Initially, the heating is highly localized at the surface of the gasbag. As the plasma is ionized, the beams penetrate the gasbag until all of the beams reach the center. This event appears to occur in the seventh image, or ~400 ps from the beginning of the laser pulse. The beams continue to propagate to the other side of the target. The plasma is still relatively cold since it is not heated by the beams. Later in time, the plasma appears to become more uniformly heated, either by electron or radiation conduction. Late time images viewed from normal to the washer indicate that the entire plasma is heated nearly uniformly by the end of the 1-ns laser pulse.

An interesting feature occurs in the region near the position that the lasers initially irradiate the membrane. This region continues to be brighter even after the laser has penetrated into the center of the gasbag. This appears to be higher-density plasma from a blast wave launched when the initial solid membrane explodes.[10] The high-density region persists long after the membrane has been ablated, but it should not significantly affect the present experiments.

We measured absolute x-ray production in the 0.1–1.8-keV range using Dante.[13] Figure 3 shows time-integrated spectra from the three different fill mixtures. The spectra show two distinct features, one at about 270 eV, and the other between 700 eV and 1.5 keV. The highly modulated spectra suggest that the emission is generated mostly by line or band transitions from ionized Xe. High-resolution spectra were not obtained

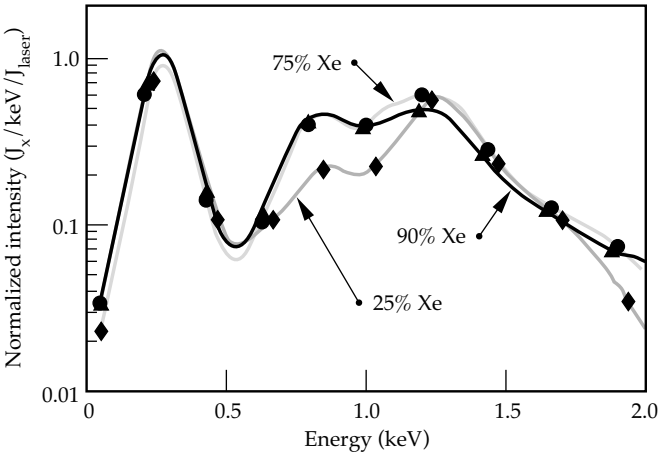

FIGURE 3. Time-integrated x-ray spectrum from 0.1 to 1.8 keV for different concentrations of Xe. (08-00-0296-0440pb01)

below 2 keV, so positive identification of the atomic configurations producing these modulations is not possible. High-resolution spectra of Xe from Tokamak plasmas have identified two spectroscopic regions of line production.[17] In the region from 21 Å (590 eV) to 12 Å (1030 eV), lines and unresolved transition arrays (UTAs) have been identified from Xe^{+26} (Ni-like) to Xe^{+30} (Cr-like) ions. This is approximately the spectral region for the higher-energy feature observed in the present spectrum. The present spectrum is shifted to slightly higher energy probably due to higher plasma temperatures. Reference 17 also reports observing a number of lines from 55 Å (225 eV) to 40 Å (310 eV) and identifies them as $\Delta n = 0$ (3d–3p) transitions from Xe^{+27} (Co-like) and Xe^{+28} (Fe-like). This is the same energy range as the lower-energy feature in the present spectrum. More work is needed to better understand the spectrum below 1.5 keV.

Time-dependent total x-ray power is derived by spectrally integrating time-resolved Dante spectra. Figure 4(a) shows results of the integrals. Time resolution is ~180 ps. A typical incident laser pulse summed over all eight beams is also shown. The most distinctive feature in the data is that significant x-ray power

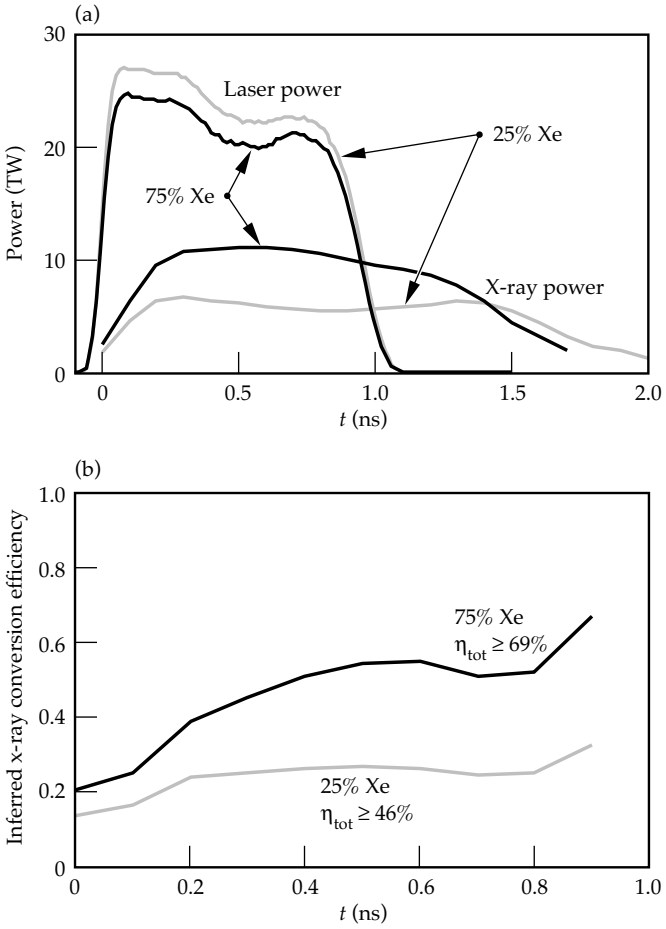

FIGURE 4. X-ray power emitted from 0.1 to 1.8 keV. (a) X-ray and laser power as a function of time. (b) Instantaneous conversion efficiency, defined as the x-ray power divided by the laser power. Data are for 25% and 75% concentrations of Xe. (08-00-0296-0441pb01)

continues 300 to 600 ps after the end of the laser pulse. Errors in timing are estimated to be ~100 ps. This observation is consistent with the laser heating the gas as a supersonic heat wave and the cooling occurring later in time due to radiative cooling and hydrodynamic expansion.

Instantaneous x-ray conversion efficiency is derived by dividing the x-ray power by the laser power. Figure 4(b) shows these results. The instantaneous conversion efficiency is ~25% for the 25% Xe fill and varies from 40 to 60% for the 75% Xe fill over most of the laser heating pulse. The instantaneous conversion efficiency begins rising as the laser pulse turns off. Of course, this quantity does not have any significance after the laser pulse ends because the laser power in the denominator is zero. It does, however, indicate that potentially longer pulses can be used, and such pulses can still maintain efficient conversion because there does not seem to be a drop in efficiency during the heating pulse. X-ray production times will ultimately be limited by the disassembly of the target.

Figure 4(b) also shows the total conversion efficiency for x-ray power emitted below 2 keV. These values are higher than the instantaneous conversion efficiency because they include x-ray power emitted after the end of the laser pulse. These efficiencies compare quite favorably with x-ray conversion efficiencies measured from Au disks, as shown in Fig. 5. Here, the Xe data are plotted at the incident intensity on the membrane of the target. The large uncertainty for one of the intensities for the gasbag indicates the range of intensities used with the two different focusings on the membrane. The Au data points are measured conversion efficiencies using single Nova beams irradiating disk targets. The data include the thermal emission from 0.1 to 2 keV and the Au M-band emission from 2 to 5 keV. When contributions are included for the Xe L-shell emission, as discussed below, the Xe gasbags are more efficient emitters than Au disks.

Significant x-ray emission is also observed from $\Delta n = 3$–2 transitions from Xe. Figure 6 shows a typical time-integrated spectrum. The most prominent features are from Xe^{+44} (Ne-like configuration) in the wavelength (energy) range of 2.3 to 3.0 Å (4 to 5 keV). These transitions are identified in Fig. 6. Line emission is also observed between 1.8 and 2.2 Å from $\Delta n = 4$–2 transitions.

Absolute emission levels are obtained by normalizing the spectrum in Fig. 6 to a high-energy channel from Dante. In general, this normalization is within a factor of 2 of the intensity predicted using calibrations of the various spectrograph components. Results of the normalization are plotted in Fig. 7, comparing them with data from various Z disks.[18] The gasbags are significantly more efficient at x-ray production in the 4–5-keV range

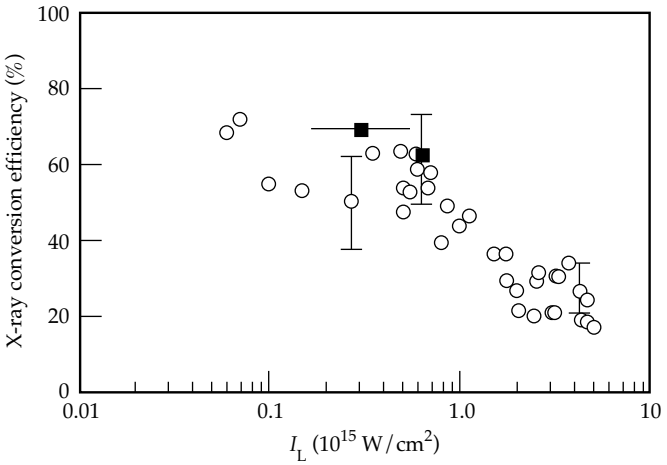

FIGURE 5. Time-integrated x-ray conversion efficiency as a function of intensity for x-ray production in the region of 0.1 to 1.8 keV. Xe data are shown as the closed squares (■). Also shown are data from Au disk experiments (○). Xe experiments are plotted at the average intensity on the initial gasbag surface. (08-00-0296-0442pb01)

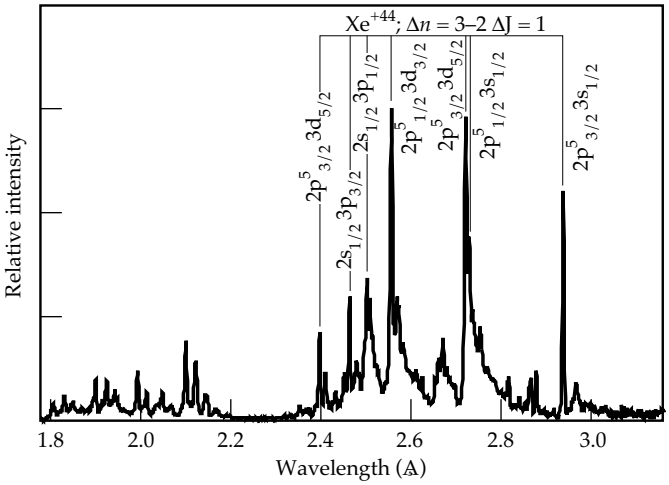

FIGURE 6. X-ray spectrum of Xe for the 4–6-keV region. Resolution is ~7 mÅ. Transitions for Ne-like Xe are denoted. (08-00-0296-0443pb01)

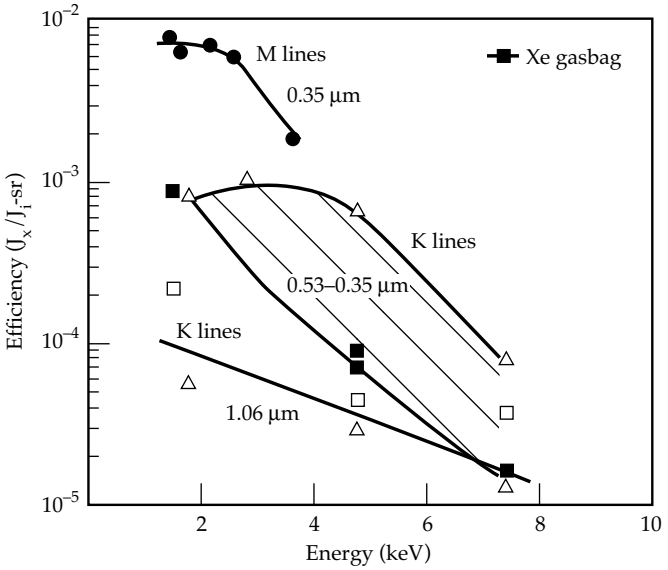

FIGURE 7. X-ray conversion efficiency into multi-keV x rays for Xe gasbags. Data are integrated from 4 to 7 keV. The efficiency is plotted in joules of x rays (J_x) per steradian (sr) divided by the incident laser energy in joules (J_i). The efficiencies are compared with conversion efficiencies measured on solid targets. (08-00-0296-0444pb01)

than disk targets. Only M-shell x-ray production for elements emitting below 3 keV are as efficient.

We monitored backreflected SBS from the gasbags using FABS on beamline 7. As mentioned previously, Xe is mixed with propane to provide hydrogen for enhancing Landau damping of the ion wave produced by SBS.[12] This mechanism has been shown to be effective for suppressing SBS in large-scale plasma experiments.[15] Low levels of SBS are observed for all targets. SBS levels of ~2% are observed for the 25% and 75% Xe fills at intensities of 4 and 6×10^{14} W/cm^2, respectively. SBS light scattered outside of the lens was not measured for these experiments, but it has generally been comparable to the light scattered into the lens. These scattering levels are similar to levels seen from hohlraum targets using normal Nova beams.

For the 90%-Xe-filled target, the focus of beamline 7 was placed at the center of the gasbag, and the focal spot on the membrane is ~300 μm in diameter. The intensity of this beam varies from ~3.5×10^{15} W/cm^2 on the membrane to >1×10^{16} W/cm^2 at the center of the gasbag. SBS from this shot is ~6%, suggesting that SBS will not necessarily be a limiting factor in optimizing the targets for irradiation intensity.

Light produced by stimulated Raman scattering (SRS) was not measured in these experiments. Fast electrons produced by SRS is monitored by measuring the x-ray bremsstrahlung. Inferred fast electron levels are low, typically less than 0.1%. Of course, this does not include fast electrons that escape the target or lose their energy to plasma expansion instead of collisional stopping in the Xe.

Summary

These experiments have demonstrated that underdense targets can be a bright source of both sub-keV and multi-keV x rays. The brightness is greater than that measured in high-Z solid target experiments. Increased x-ray production is attained by reducing the energy coupled to hydrodynamic motion and increasing the internal energy in the plasma. More efficient targets for x-ray production have several applications. One is as a brighter x-ray backlighter source. We have shown that x-ray production is enhanced by a factor of 3 or more above that from conventional solid targets. This factor of 3 directly correlates with lower laser energy requirements for backlighter beams. Spectra at different x-ray energies could be attained by changing the gas or using low-density foams doped with high-Z elements. As long as the ionized electron density of the material is below ~0.25 n_c, the foam targets should perform similarly to gas-filled targets. At higher density, laser–plasma instabilities become more significant, and at densities above n_c the targets become ablative, performing more like disk targets. Another application is as a bright x-ray source for radiation-effects experiments. In addition, such features could be incorporated into hohlraum designs for ICF to increase radiation production and heating efficiency. Significant work in calculations and experiments is still needed to optimize underdense sources for any of these applications. Nevertheless, these initial experiments demonstrate the significant advantages that underdense target have over solid disk targets as a bright laser-produced x-ray source.

Notes and References

1. W. C. Mead, E. K. Stover, R. L. Kauffman, H. N. Kornblum, and B. F. Lasinski, *Phys. Rev. A* **38**, 5275–5288 (1988).
2. F. Ze, D. R. Kania, S. H. Langer, H. Kornblum, et al., *J. Appl. Phys.* **66**, 1935–1939 (1989).
3. R. Sigel, R. Pakula, S. Sakabe, and G. D. Tsakiris, *Phys. Rev. A* **38**, 5779 (1988).
4. H. Nishimura, Y. Kato, H. Takabe, T. Endo, et al., *Phys. Rev. A* **44**, 8323–8333 (1991).
5. R. L. Kauffman, L. J. Suter, C. B. Darrow, J. D. Kilkenny, et al., *Phys. Rev. Lett.* **73**, 2320–2323 (1994).
6. B. Yaakobi, P. Bourke, Y. Conturie, J. Delettrez, et al., *Opt. Commun.* **38**, 196 (1981).
7. D. L. Matthews, E. M. Campbell, N. M. Ceglio, G. Hermes, et al., *J. Appl. Phys.* **54**, 4260 (1983).
8. R. Sigel, K. Eidmann, F. Lavarenne, and R. F. Schmalz, *Phys. Fluids B* **2**, 199 (1990).
9. E. M. Campbell, J. T. Hunt, E. S. Bliss, D. R. Speck, and R. P. Drake, *Rev. Sci. Instrum.* **57**, 2101 (1986).
10. D. H. Kalantar, B. J. MacGowan, T. P. Bernat, D. E. Klem, et al., *Rev. Sci. Instrum.* **66**, 782 (1995).
11. Luxel Corp., P. O. Box 1879, Friday Harbor, Wash. 98250.
12. E. A. Williams, R. L. Berger, R. P. Drake, A. M. Rubinchik, et al., *Phys. Plasmas* **2**, 129 (1995); H. X. Vu, J. M. Wallace, and B. Bezzerides, *Phys. Plasmas* **1**, 3542 (1994).
13. H. N. Kornblum, R. L. Kauffman, and J. A. Smith, *Rev. Sci. Instrum.* **57**, 2179 (1986).
14. D. K. Bradley, P. M. Bell, J. D. Kilkenny, R. Hanks, et al., *Rev. Sci. Instrum.* **63**, 4813–4817 (1992); P. M. Bell, J. D. Kilkenny, G. Power, R. Bonner, and D. K. Bradley, *Ultrahigh Speed and High Speed Photography, Photonics, and Videography '89* (SPIE, Bellingham, WA, 1989; Proc. SPIE, **1155**), pp. 430–444.
15. R. K. Kirkwood, C. A. Back, K. S. Bradley, D. H. Kalantar, et al., *Bull. APS* **39**, 1753 (1994).
16. B. J. MacGowan, et al., *ICF Quarterly Report* **5**(4), 4–220, Lawrence Livermore National Laboratory, Livermore, CA, UCRL-LR-105820-95-4 (1995).
17. F. J. Wyart, C. Bauche-Arnoult, E. Luc-Koenig, and TFTR Group, *Phys. Scr.* **32**, 103–106, (1985).
18. R. Kauffman, *Handbook of Plasma Physics; Vol. 3 Physics of Laser Plasmas*, Eds., A. M. Rubenchik and S. Witkowski (North Holland, Amsterdam 1991), p. 123.

Measurement of 0.35-μm Laser Imprint in a Thin Si Foil Using an X-Ray Laser Backlighter

D. H. Kalantar
*M. H. Key**
L. B. DaSilva
S. G. Glendinning
*J. P. Knauer***
B. A. Remington
F. Weber
S. V. Weber

Introduction

High-gain direct-drive inertial confinement fusion (ICF) requires very uniform irradiation of a hollow spherical shell with a layer of fusionable deuterium–tritium (D-T) on its inner surface. The intensity of laser irradiation builds up in several nanoseconds from an initial "foot" at 10^{13} W/cm^2 to more than 10^{15} W/cm^2 during the main drive pulse. Laser ablation of the capsule surface produces a high pressure that accelerates the shell radially inward in a spherical implosion. During the main drive phase, there is Rayleigh–Taylor (RT) growth of surface perturbations due to two factors: the initial surface roughness of the capsule and imprint from spatial nonuniformities in the laser drive intensity early in the laser pulse. With the completion of the Omega upgrade laser at the University of Rochester,[1] the Nike laser at the Naval Research Laboratory,[2] and proposals for the National Ignition Facility (NIF),[3] there is considerable interest in studying the physics of direct-drive ICF, and particularly in the imprinting process.[4–6]

On a large scale, the uniformity of illumination on a direct-drive implosion capsule is determined by the multibeam irradiation geometry, and on a small scale, by beam smoothing techniques. Large-scale nonuniformities are minimized by using a large number of beams (such as the 60 beams of the Omega Upgrade laser or 48 beam clusters of the proposed NIF). The small-scale spatial variations of intensity due to the speckle pattern of individual laser beams are effectively smoothed with smoothing by spectral dispersion (SSD),[7] where a random phase plate (RPP)[8] is illuminated by the spectrally dispersed frequency components of a broad-band laser beam giving a rapidly fluctuating speckle pattern on the target.

Our interest is in studying the imprinting of nonuniformities due to a direct-drive laser beam under conditions simulating the low-intensity foot of a pulse designed for an ignition target such as might be used on the NIF. By studying the reduction of optical and imprinted hydrodynamic perturbations with SSD smoothing, we will be able to assess the effectiveness of SSD bandwidth in suppressing imprint for direct-drive experiments. To demonstrate the effect of beam smoothing on laser imprint, we have obtained extreme ultraviolet (XUV) radiographs (at 15.5-nm radiation) of the imprinted modulation at shock breakout due to (1) a static laser speckle pattern and (2) a one-dimensional (1-D) SSD smoothed speckle pattern.

Experiment

We irradiated a 3-μm-thick Si foil with a 3×10^{12}-W/cm^2, 400-ps pulse of 0.35-μm laser light in the Nova two-beam target chamber.[9] The speckle pattern from this beam imprinted modulations in the Si foil, which we measured by XUV radiography. We used an Y x-ray laser with a wavelength of 15.5 nm as the XUV backlighter,[10,11] and we imaged the Si foil in two dimensions onto an XUV-sensitive charge-coupled device (CCD) camera by using XUV multilayer optics[12] as shown in Fig. 1.[13–15] The XUV imaging system uses an off-axis spherical optic for imaging at about 25× magnification. The angle of incidence on the imaging optic was only 1.25°, minimizing astigmatism, and providing a spatial resolution of about 3 μm.

The XUV image is a two-dimensional (2-D) image of the modulation in optical depth of the foil at 15.5 nm due to imprint of the laser speckle pattern. We used the x-ray laser as a backlighter since the optical depth of most materials is high at 15.5 nm, which allows us to make a sensitive measurement of the optical depth variation in the foil. Si was used because it has the lowest

*Rutherford Appleton Laboratory, UK, and University of Oxford, UK.
**University of Rochester, Laboratory for Laser Energetics, Rochester, New York.

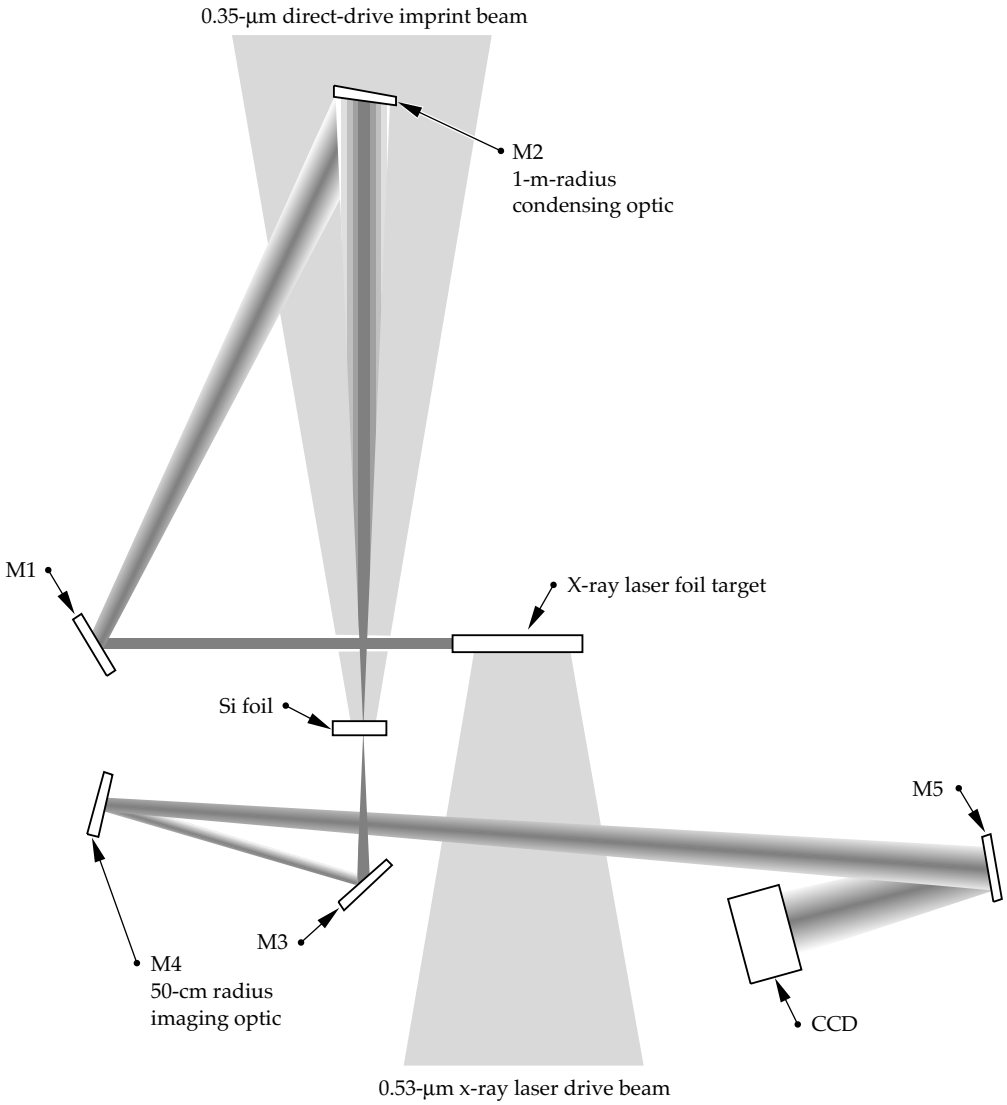

FIGURE 1. X-ray laser imaging system for measuring direct-drive imprinted modulation on a thin Si foil. The imaging optics are Mo/Si multilayer optics. (08-00-0296-0363pb01)

opacity at 15.5 nm. It is still highly attenuating at this wavelength, which limits the thickness of foils that we can probe to <4 μm. Because it is highly attenuating, a 50-nm thickness variation in the Si foil results in a 10% change in the backlighter intensity in the XUV radiograph.

To measure the effect of laser imprint on a directly driven foil, we probe the foil before significant RT growth occurs at the time of shock breakout. Computer simulations of the Si foil done with the LASNEX computer code[16] indicate that with a laser intensity of 3×10^{12}-W/cm^2, a ~2-Mbar shock propagates through a 3-μm-thick foil and breaks out the back side at about 260 ps. At this time, the Si foil is compressed by a factor of 1.5. We timed the 80 ps duration x-ray laser pulse to radiograph the optical depth modulation of the foil at shock breakout, namely at t = 260 ps, and we turned the optical laser drive pulse off at 400 ps.

Laser Imprint

In Fig. 2, we show time-integrated far-field images of the drive beam that were recorded photographically at an equivalent focal plane diagnostic station. These are shown as modulation in the intensity pattern of the RPP focal spot. Figure 2(a) shows the static RPP speckle pattern for a 100-μm-square region at the object plane obtained with zero bandwidth. The theoretical root mean square (rms) fractional modulation of the exposure due to a static RPP speckle pattern is 1.0.[17] We measured a modulation of 0.6, but our measurement may be affected by the finite resolution of the far field imaging system, the film calibration, and the fact that the beam has a time-skew of about 100 ps. Note that the time skew is introduced by the grating used to disperse the bandwidth for SSD. It results in a

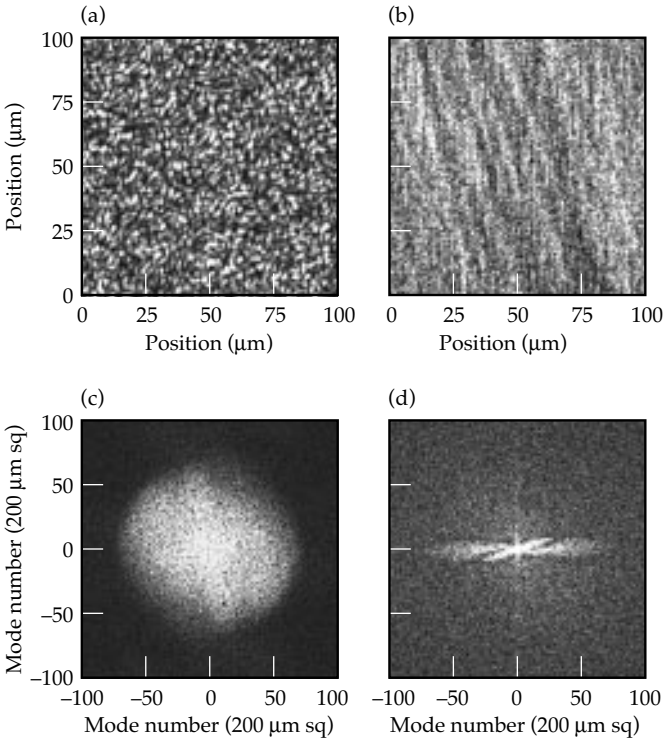

FIGURE 2. Time-integrated optical far-field images of the 0.35-μm laser intensity modulation in a 100-μm-square region at the equivalent focal plane for (a) a static speckle pattern with an intensity of 2.3×10^{12} W/cm^2 and (b) an SSD-smoothed speckle pattern with 0.33 THz of bandwidth at 0.35 μm and an intensity of 3.3×10^{12} W/cm^2. Two-dimensional Fourier transforms of (c) the static speckle pattern and (d) the SSD-smoothed speckle pattern shown for a 200-μm-square region of the object plane. (08-00-0296-0364pb01)

speckle pattern that changes during the initial portion of the laser pulse as the laser beam fills in to the full aperture, even for the case with no bandwidth.

The optical far-field image shown in Fig. 2(b) for the case of 0.33-THz bandwidth at 0.35 μm has an rms modulation of 0.15. This is the time-integrated modulation in exposure. This value is reduced from a theoretical value of 1.0 for the static speckle pattern by the SSD. It reaches an asymptotic value of 0.15 after about 100 ps. One-dimensional streaks in the vertical direction are due to the 1-D dispersion from the grating, and additional streaks at a small angle relative to the vertical are attributed to chromatic aberration in the focus lens, resulting in a multidirectional SSD pattern.

We characterize the far-field speckle pattern by Fourier analysis. Figures 2(c) and 2(d) show 2-D Fourier transforms of the far-field intensity modulation. The transform of the static laser speckle pattern shows azimuthal symmetry due to the isotropy of the speckle pattern [Fig. 2(c)]. The transform of the SSD-smoothed speckle pattern, however, has a distinct "propeller" shape that dominates in the horizontal direction [Fig. 2(d)]. This indicates that there is short-wavelength structure in the horizontal direction [i.e., perpendicular to the vertical streaks in Fig. 2(b)], while short-scale laser nonuniformities are suppressed in the vertical direction due to the SSD smoothing. The transform also shows a feature that is tilted at about 20°. This is due to the slightly rotated additional streaks in Fig. 2(b), mentioned above.

Figure 3 shows face-on radiography images of the imprinted modulation in thin Si foils due to both a static speckle pattern and an SSD-smoothed speckle. The imprint appears as a modulation in the optical depth of the foil, given by the natural logarithm of the ratio of transmitted XUV intensity to a smoothed fit of the overall x-ray laser profile. Figure 3(a) shows a 100-μm-square region from the radiograph of a 3.05-μm-thick Si foil irradiated by the static speckle pattern shown in Fig. 2(a). Figure 3(b) shows a 100-μm-square region from the radiograph of a 3.15-μm-thick Si foil irradiated by the SSD-smoothed speckle pattern shown in Fig. 2(b).

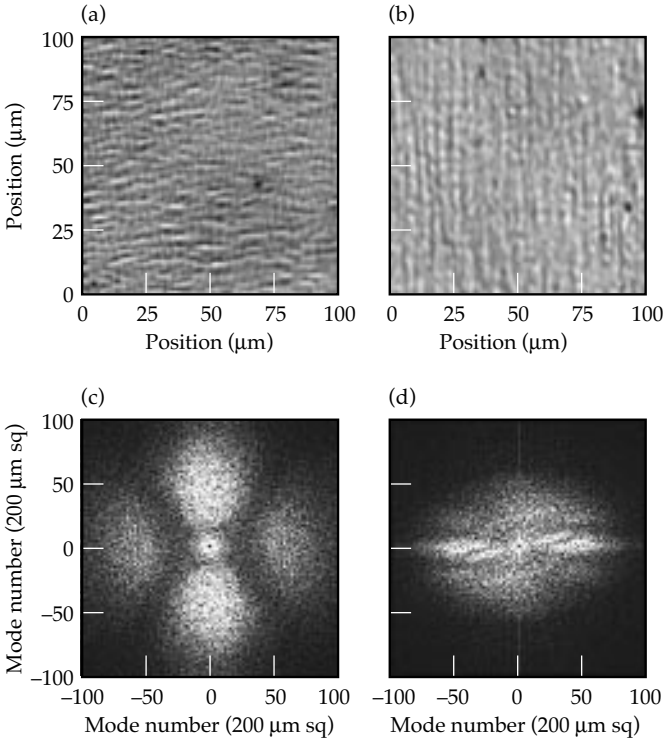

FIGURE 3. XUV radiographs showing the imprinted modulation in optical depth in a 100-μm-square region at the object plane of (a) a 3.05-μm Si foil irradiated by the speckle pattern shown in Fig. 2(a) and (b) a 3.15-μm Si foil irradiated by the SSD-smoothed speckle pattern shown in Fig. 2(b). These radiographs were obtained at t = 260 ps. Two-dimensional Fourier transforms of the imprint due to (c) a static speckle pattern and (d) an SSD-smoothed speckle pattern shown for a 200-μm-square region of the object plane. (08-00-0296-0365pb01)

The rms modulation in optical depth of the foil imprinted with a static speckle pattern is 0.37 ± 0.06. We translate this to an rms modulation in foil thickness using the cold opacity, μ, times the density of Si, ρ. The shocked density of the Si foil is about 1.5 times solid density at shock breakout, which gives us a product $\mu\rho = 3.21\ \mu m^{-1}$. Therefore, this modulation in optical depth corresponds to an rms thickness modulation of only 115 nm in the foil at shock breakout.

The rms modulation in optical depth of the Si foil imprinted with the 0.33-THz SSD-smoothed beam is 0.23 ± 0.04, which corresponds to a 72-nm rms modulation. The error bars quoted above correspond to the standard deviation obtained from calculating the rms from multiple lineouts of the 2-D radiographs.

Figures 3(c) and 3(d) show 2-D Fourier transforms of the face-on XUV radiographs. The Fourier transform corresponding to the static speckle pattern [Fig. 3(c)] shows a lobe structure with the vertical direction dominating. This is a result of the slight horizontal anisotropy in the radiograph image [Fig. 3(a)], and is consistent with the astigmatism of the imaging system when the foil is about 100 μm away from best focus,[15] which is the limit of our ability to position the Si foil. Note that the uncertainty in the measured rms optical depth modulation due to locating the target to within 100 μm of best focus of the imaging system is ±20%.

Figure 3(d) shows the Fourier transform of the optical depth modulation imprinted with the SSD-smoothed speckle pattern. One-dimensional SSD suppressed the short-wavelength structures in the direction of dispersion. As a result, the 2-D Fourier transform shows structures similar to the Fourier transform of the intensity modulation of the laser speckle intensity pattern [Fig. 2(d)]. The transform has a strong directionality, and the tilted structure due to chromatic aberrations of the Nova lens is reproduced in imprint almost identically.

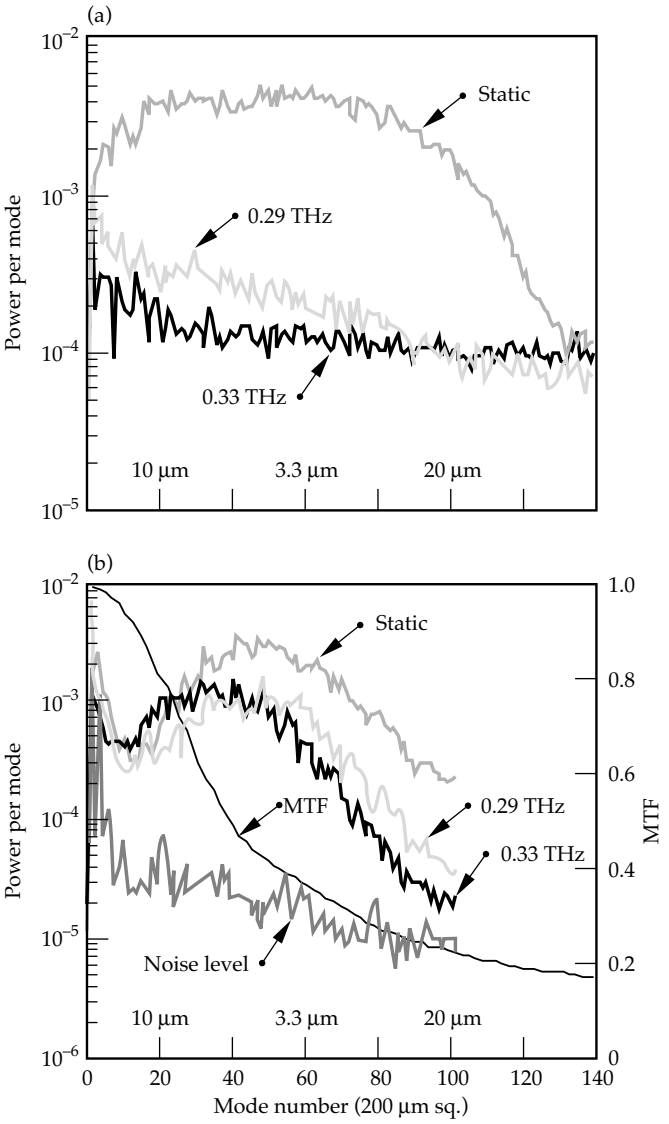

FIGURE 4. Power per mode for a 200-μm region measured from (a) the optical far-field images and (b) the XUV radiographs of 0.35-μm laser imprint. The MTF for the imaging system is shown overlaid in (b). (08-00-0296-0366pb01)

Discussion and Simulations

We compare the modulations imprinted in the Si foil with and without SSD bandwidth by performing radial lineouts of the square of the 2-D Fourier transforms (Fourier power) of the optical speckle patterns and the XUV radiographs of the imprinted foils, as shown in Fig. 4. We azimuthally integrated the Fourier power so that the sum over mode number gives us the square of the rms. Figure 4(a) shows the Fourier power per mode calculated for the static and 0.33-THz SSD band width cases. We also show the result for an intermediate case of 0.29-THz (at 0.35 μm) SSD bandwidth, obtained on a separate shot. Figure 4(b) shows the Fourier power per mode for the XUV radiographs recorded at the time of shock breakout with zero, 0.29-THz, and 0.33-THz SSD bandwidth. The noise in the radiograph measurement is shown as a power spectrum calculated from the XUV radiograph of an undriven Si target. The noise is primarily due to the surface finish of the polished Si foils, which we characterized by scanning with an atomic force microscope. Note that we have also plotted a modulation transfer function (MTF) for the imaging system in Fig. 4(b) to illustrate the resolution at short wavelengths. The calculated value of the MTF is about 0.3 for a 3-μm wavelength modulation.

The modulation of optical depth at 15.5 nm in the Si foil has an rms of about 0.37 ± 0.06 when it is imprinted with a static 0.35-μm laser speckle pattern. The rms is reduced by 40% to 0.23 ± 0.04 when we apply 0.33-THz SSD beam smoothing on the imprint beam. The reduction in power per mode is greatest for the short wavelength modes ($n \geq 40$, $\lambda < 5\ \mu m$). For a mode number of 67 ($\lambda = 3\ \mu m$), the power is reduced by a factor of six. For

a mode number of 20 (λ = 10 μm), the power is nearly the same with and without bandwidth, differing by at most 50%. The time-integrated modulation in fractional exposure of the speckle pattern shows a much greater reduction in power per mode when SSD bandwidth is introduced. The rms modulation is reduced by a factor of about four, between the static and 0.33-THz cases from a measured rms of 0.6 to 0.15. For a mode number of 67, the optical power per mode is reduced a factor of 30 to 35, and it is reduced a factor of 20 to 25 at mode 20 with 0.33-THz SSD.

We used the 2-D LASNEX computer code to simulate the imprint of a thin Si foil in a 2-D approximation. We simulated imprint on a target 60 μm wide in the transverse direction with reflection boundary conditions. The laser intensity and pulse shape were taken from the experiments, but the drive pattern was calculated from a speckle model[18] at each time step. For the example of zero bandwidth, the lineout was static, whereas for the case with the SSD-smoothed imprint beam, the speckle pattern was calculated at each time step in the simulation, and this time-varying lineout across the dispersion direction was used as the laser intensity profile for the simulation.

The rms modulation in optical depth was calculated and averaged over 80 ps, centered at t = 260 ps. As shown in Fig. 5, the result was convolved with a 1-D MTF for the imaging system for comparison with the experiment. The rms modulation of the optical depth of the Si foil calculated for the static speckle pattern imprint is 0.36. For the 0.33-THz SSD smoothed speckle pattern, the imprinted rms modulation from the simulation is 0.072, about a factor of five lower than the static case. This is consistent with the reduction in rms modulation of the asymptotic optical intensity distribution, shown in Fig. 5 for comparison. (We have not included the effect of the 100-ps skew in the imprinting laser beam in the simulation. Results from applying the skew parallel or perpendicular to the dispersion direction indicate that it reduces the rms modulation by a factor less than two for each case.)

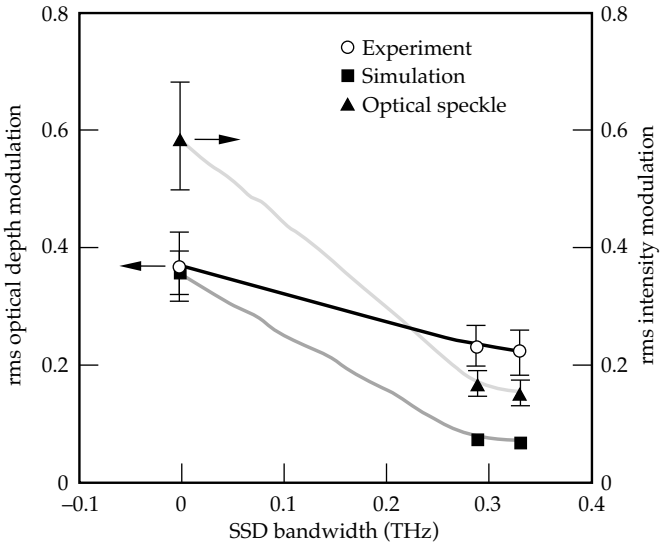

FIGURE 5. Simulated rms modulation in optical depth imprinted in the Si foil. Optical rms and experimental results are included. (08-00-0296-0367pb01)

Figure 5 also plots the measured rms modulation of the Si foil. The simulated imprint decreases more rapidly with SSD bandwidth than we measured using XUV radiography. To test whether the conclusion is affected by noise in the measurement at high mode number, we impose a high-mode cutoff in calculating the rms modulation. The result does not change significantly. By integrating only over modes with mode numbers less than 24 (λ < 5 μm), the measured rms modulation of the imprint is reduced by a factor of 1.7 when we apply SSD bandwidth. The simulated rms is reduced by a factor of 4.5 by the addition of SSD smoothing.

The difference between reduction of optical and imprinted hydrodynamic perturbations through SSD smoothing is important in assessing the effectiveness of SSD bandwidth for suppression of imprint. We expect that the hydrodynamic response of the Si target should be linear with the optical intensity modulation, but the temporal weighting of the optical speckle may be more complex than is indicated by just the time-averaged speckle pattern. This may be due to the presence of the skew in the beam and the finite rise time of the laser pulse shape. The fact that the measured imprint is reduced less than the asymptotic laser smoothing level suggests that the observed imprint is dominated by the early time intensity modulation in the optical speckle pattern, before the asymptotic limit is reached. This limit is reached for the SSD-smoothed beam by about 100 ps,[18] which implies that the imprinting time for the short spatial scales measured here is significantly shorter than 100 ps. One possible reason is that the effect of thermal smoothing may be progressively overwhelming the effect of the optical smoothing, though the 2-D modeling implicitly includes thermal smoothing.

The simulations also show less reduction in the imprint than the optical smoothing level. A similar experimental conclusion has been obtained in parallel measurements using conventional x-ray radiography.[19]

Summary

We measured laser imprint as the modulation in optical depth of a thin Si foil that is irradiated by a low-intensity 0.35-μm beam on Nova. We recorded images of imprint due to a beam with and without SSD bandwidth by using an x-ray laser backlighter, and we demonstrated the effect of beam smoothing on laser imprint at the time of shock breakout.

The imprinted rms modulation in optical depth is reduced by a factor of two when the time-integrated rms modulation in exposure of the optical drive pulse is reduced by a factor of seven from 1.0 to 0.15 with 0.33-THz bandwidth. Simulations of the imprint in two dimensions show about a factor of four reduction in the rms optical depth modulation, also less than the reduction of the optical modulation rms.

Acknowledgments

We gratefully acknowledge the support from the Nova Operations group for their assistance and patience during these experiments. S. Alvarez and J. R. Mazuch assembled the XUV laser targets. J. C. Moreno provided assistance in measuring the absolute x-ray laser timing.

Notes and References

1. J. M. Soures, *J. Fusion Energy* **10**, 295 (1991).
2. J. D. Sethian et al., *Fusion Technology* **26**, 717 (1994).
3. S. W. Haan et al., *Phys. Plasmas* **2**, 2480 (1995).
4. J. D. Kilkenny et al., *Phys. Plasmas* **1**, 1379 (1994).
5. M. H. Desselberger et al., *Phys. Rev. Lett*. **68**, 1539 (1992).
6. M. H. Emery et al., *Phys. Fluids B* **3**, 2640 (1991).
7. S. Skupsky et al., *J. Appl. Phys*. **66**, 3456 (1989).
8. Y. Kato et al., *Phys. Rev. Lett*. **53**, 1057 (1984).
9. E. M. Campbell et al., *Rev. Sci. Instrum*. **57**, 2101 (1986).
10. L. B. DaSilva et al., *Opt. Lett*. **18**, 1174 (1993).
11. L. B. DaSilva et al., *Rev. Sci. Instrum*. **66**, 574 (1995).
12. T. W. Barbee, Jr., et al., *Appl. Opt.* **32**, 4825 (1993).
13. M. H. Key et al., *J. Quant. Spectrosc. Radiat. Transfer*, **54**, 221 (1995).
14. M. H. Key et al., *XUV Lasers and Applications* 2520 279 (SPIE, Bellingham, WA, 1995).
15. D. H. Kalantar et al., *Rev. Sci. Instrum*. **67**, 781 (1996).
16. G. B. Zimmerman and W. L. Kruer, *Comments Plasma Phys. Controlled Fusion* **2**, 51 (1975).
17. J. W. Goodman, "Statistical Properties of Speckle Patterns," in *Laser Speckle and Related Phenomena*, J. C. Dainty, Ed. (Springer, New York, 1990), Ch. 2, pp. 9–75.
18. S. N. Dixit, Lawrence Livermore National Laboratory, Livermore, CA, private communication (1995).
19. S. G. Glendinning et al., "Measurements of Laser Speckle Induced Perturbations in Laser Driven Foils," Lawrence Livermore National Laboratory, Livermore, CA, UCRL-JC-123082; accepted for publication in *Phys. Rev. E* (1996).

Absorption of Laser Light in Overdense Plasmas by Sheath Inverse Bremsstrahlung

T. Y. B. Yang

W. L. Kruer

R. M. More

A. B. Langdon

Introduction

In recent years, there has been increasing interest in the interaction of short laser pulses with overdense plasmas.[1–12] For sufficiently short laser pulses, the hydrodynamic motion of the heated target does not play a dominant role, and the production of high-density plasmas with sharp density gradients becomes feasible. One topic of great interest is the dependence of the light absorption on the laser intensity and plasma temperature in such plasmas.

In the Fast Ignitor concept[13] of inertial confinement fusion, the core is ignited with super-thermal electrons generated by the high-intensity ignition laser. It is expected that the absorption of the laser energy occurs at a steep gradient produced by the hole-drilling laser. Furthermore, the absorption is mainly due to collisionless mechanisms such as the one discussed in this article. Although the intensity of the ignition laser is expected to be so high that the assumption of the present linear analysis is no longer valid, certain aspects of the present analysis still hold true. For example, the transverse electron temperature is invariant for normal incidence case, unless surface rippling happens. Also, the comparison between the analytical and numerical results provides some criteria in determining parameters (e.g., grid size and time step) used in numerical simulations, which will be heavily relied on in the regime of the Fast Ignitor where analytical analysis may not be tractable.

It has been observed in laser absorption experiments[1–3] that, starting from a sufficiently low intensity, the absorption rate of light in overdense plasmas increases as a function of laser intensity until it reaches the "resistivity saturation,"[1] a condition in which the electron mean-free path in the plasma reaches a minimum value. Further increase of the laser intensity and the plasma temperature will then cause an increase in the electron mean-free path and a decrease in the absorption rate. When the electron mean-free path is longer than the skin depth, theoretical studies[14–16] suggest that collisionless absorption mechanisms such as the sheath inverse bremsstrahlung[14] and the anomalous skin effect[15–19] become important.

In this article, we modify the original sheath inverse bremmstrahlung model[14] by including the $\mathbf{v} \times \mathbf{B}$ (velocity and magnetic field, respectively) term in the Lorentz force equation, since the evanescent magnetic field in an overdense plasma is greater than the corresponding electric field. Our results are significantly different from those derived without the $\mathbf{v} \times \mathbf{B}$ term, except when the distribution function is isotropic $[f_0(\mathbf{v}) = f_0(|\mathbf{v}|)]$. For an isotropic distribution function, identical results will be obtained whether or not the $\mathbf{v} \times \mathbf{B}$ term in the equation of motion is included in the derivation. However, if the $\mathbf{v} \times \mathbf{B}$ term were neglected, the absorption of the light would be incorrectly interpreted as an increase in the transverse electron temperature, while the conservation of the transverse components of the canonical momentum requires that, after leaving the interaction region ($|x| \lesssim \delta$), an electron should have the same transverse momentum as it did before it entered the interaction region.

By deriving the absorption coefficients for both the sheath inverse bremsstrahlung and the anomalous skin effect from the same set of equations, we show that both phenomena are limiting cases of the same collisionless absorption mechanism. The sheath inverse bremsstrahlung corresponds to the limit where $\omega^2 c^2 >> \omega_p^2 v_e^2$, while the anomalous skin effect corresponds to $\omega^2 c^2 << \omega_p^2 v_e^2$.

We have carried out numerical simulations of the light absorption in overdense plasmas using the particle-in-cell (PIC) plasma simulation code ZOHAR.[20] The absorption coefficients observed in the simulations are in reasonable agreement with the values calculated from the linear theory. We have investigated the effects of finite density gradients with ZOHAR simulations.

Theoretical Model for the Sheath Inverse Bremsstrahlung Absorption and the Anomalous Skin Effect

The model consists of an overdense plasma filling the half-space $x > 0$, and electric and magnetic fields of the following forms, respectively:

$$E_y(x,t) = \mathrm{Re}\left\{E_0 \exp\left[i(kx \pm \omega t)\right]\right\} \quad ,$$

$$B_z(x,t) = \mathrm{Re}\left\{\frac{ck}{\omega} E_0 \exp\left[i(kx \pm \omega t)\right]\right\} \quad . \qquad (1)$$

Here, x is the propagation direction, E_0 and ω are real-valued constants, and k is the wave vector. Immobile ions, with zero density for $x < 0$ and a constant density for $x > 0$, are assumed to form the neutralizing background. The plasma is assumed to be highly overdense ($\omega_p^2 >> \omega^2$) and the fiducial thermal velocity v_e, which characterizes the electron distribution, is sufficiently small ($\omega^2 c^2 >> \omega_p^2 v_e^2$). Except in the sheath regime near $x = 0$, the electron density n_e is equal to n_0 for $x > 0$ and is zero for $x < 0$. When an electron hits the sheath ($x = 0$) from the right ($x > 0$), instantaneous specular reflection is assumed, i.e., the y and z components of the momentum remain unchanged while the x component reverses with the amplitude unchanged. Since the typical time scale to reverse electron momentum in the sheath region is $1/\omega_p$, which is much shorter than both the wave period ($2\pi/\omega$) and the transit time in the skin depth ($c/v_e\omega_p$) in an overdense nonrelativistic plasma, instantaneous reflection is a reasonable assumption. Here, $\omega_p = (4\pi n_0 e^2/m_e)^{1/2}$ is the electron plasma frequency. The assumption of specular reflection requires that the sheath be one-dimensional (1-D), i.e., that the scale length of the transverse variation be much longer than the width of the sheath (approximately equal to the Debye length). The present analysis also assumes that the quiver velocity $v_{os} = eE_0/m_e\omega$ is much smaller than the fiducial thermal velocity v_e, so that the perturbation analysis is applicable.

In a recent paper,[21] the power transferred from the laser to the plasma per unit area of laser–plasma interface was derived from the equation of motion, giving

$$P_{ab} = \frac{2n_0 e^2 E_0^2 \delta^2}{m_e} \int d^2 v_\perp \int_0^\infty dv_x \frac{v_x v_y^2 \left(\omega^2\delta^2 \pm v_x^2\right)}{\left(\omega^2\delta^2 \pm v_x^2\right)^3} f_0(\mathbf{v}) \quad , \qquad (2)$$

where $\delta = i/k$. A similar derivation without the $\mathbf{v} \times \mathbf{B}$ term in the equation of motion will give

$$P_{ab} = \frac{n_0 e^2 E_0^2 \delta^2}{m} \int d^2 v_\perp \int_0^\infty dv_x \frac{v_x^3}{\left(\omega^2\delta^2 + v_x^2\right)^2} f_0(\mathbf{v}) \quad . \qquad (3)$$

For an isotropic distribution function [$f_0(\mathbf{v}) = f_0(|\mathbf{v}|)$], Eq. (3) is equivalent to Eq. (2). For general distribution functions, however, Eq. (3) gives an absorption rate significantly different from Eq. (2).[21] Moreover, if the $\mathbf{v} \times \mathbf{B}$ term had been neglected, the absorption of the light would be incorrectly interpreted as an increase in the transverse (y-direction) electron temperature, while the conservation of the transverse components of the canonical momentum requires that, after leaving the interaction region ($|x| \lesssim \delta$), an electron should have the same y-momentum as it did before it entered the interaction region.

To show the relation between the sheath inverse bremsstrahlung and the anomalous skin effect, we follow the usual treatment of the anomalous skin effect[15–19] and extend the plasma and the electromagnetic fields in the present model to the half space $x < 0$ with

$$E_y(\pm x) = E_y(x), \quad B_z(\pm x) = \pm B_z(x) \quad . \qquad (4)$$

The discontinuity in B_z requires a current sheet $\mathbf{J} = \hat{e}_y J_0 \delta(x) \exp(-i\omega t)$, whose amplitude is determined by

$$B_z\left(x = 0^+\right) \pm B_z\left(x = 0^\pm\right) = 2B_z\left(x = 0^+\right). \qquad (5)$$

Since an electron with $x > 0$ in the extended model will have the same orbits as the corresponding electron in the original model, the two models are equivalent as far as the region $x > 0$ is concerned. In the extended model, the electric field satisfies the equation

$$\left(c^2 \frac{\partial^2}{\partial x^2} + \omega^2\right) E_y(x) = \pm 4\pi i\omega \left[j_y(x) + J_0\delta(x)\right] \quad , \qquad (6)$$

where $j_y(x)$ is the current density induced by the electromagnetic fields. Performing the Fourier transform on Eq. (6), and making use of the well known relation[22] between the induced current density j_y and the electric field E_y, it follows that

$$\hat{E}_y(k) = \frac{\pm 4\pi i\omega J_0}{D(\omega, k)} \quad , \qquad (7)$$

and

$$D(\omega, k) = \omega^2 \pm c^2 k^2 \pm \omega_p^2 \left[1 \pm \int d^3 v \frac{k v_y^2}{\omega \pm k v_x} \frac{\partial f_0}{\partial v_x}\right] \quad . \qquad (8)$$

Here, $\hat{E}_y(k)$ is the Fourier transform of $E_y(x)$.

In the regime of the anomalous skin effect ($\omega^2 c^2 << \omega_p^2 v_e^2$ and $\omega_p^2 >> \omega^2$), and for an isotropic distribution function [$f_0(\mathbf{v}) = f_0(|\mathbf{v}|)$], making the

appropriate approximation[21] of the function $D(\omega,k)$ gives the absorption coefficient

$$\eta_{as} = \frac{8\omega\delta_{as}}{3\sqrt{3}c} \quad . \tag{9}$$

It was also shown in Ref. 21 that the appropriate approximation of the function $D(\omega,k)$ in the $\omega^2c^2 >> \omega_p^2 v_e^2$ limit reproduces the power absorption of the sheath inverse bremsstrahlung given in Eq. (2). The corresponding absorption coefficient is

$$\eta_{sib} = \pm\frac{8\omega^2\omega_p^2\delta^4}{c\left(\omega^2\delta^2 + c^2\right)}\int d^2v_\perp v_y^2\int_0^\infty dv_x\,\frac{v_x^2}{\left(\omega^2\delta^2 + v_x^2\right)^2}\frac{\partial f_0}{\partial v_x}$$

$$= \frac{16\omega^2\delta^2}{c}\left[\int d^2v_\perp v_y^2\int_0^\infty dv_x\,\frac{v_x\left(\omega^2\delta^2 \pm v_x^2\right)}{\left(\omega^2\delta^2 + v_x^2\right)^3}f_0(\mathrm{v})\right]$$

$$\times\left[1 \pm \int d^3v\,\frac{v_y^2(\omega^2\delta^2 - v_x^2}{\left(\omega^2\delta^2 + v_x^2\right)^2}f_0(\mathrm{v})\right]^{\pm1} \quad . \tag{10}$$

The sheath inverse bremsstrahlung and the anomalous skin effect are two limiting cases of a more general collisionless absorption mechanism described by Eqs. (7) and (8). The sheath inverse bremsstrahlung corresponds to the limit where $\omega^2c^2 >> \omega_p^2 v_e^2$, while the anomalous skin effect corresponds to $\omega^2c^2 << \omega_p^2 v_e^2$. In the intermediate regime ($\omega^2c^2 \approx \omega_p^2\, v_e^2$), the absorption coefficient can be obtained by performing the inverse Fourier transform of Eqs. (7) and (8).

For a plasma with Maxwellian distribution function

$$f_0(\mathbf{v}) = \frac{1}{\left(2\pi v_e^2\right)^{3/2}}\exp\left(\pm\frac{|\mathbf{v}|^2}{2v_e^2}\right) \quad , \tag{11}$$

Eq. (10) reduces to a closed analytic form

$$\eta_{sib} = \frac{8}{\sqrt{2\pi}}\frac{v_e}{c}\,a\left[(a+1)\exp(a)E_1(a) \pm 1\right]$$

$$\times\left[\frac{1}{2} + \frac{\sqrt{\pi a}}{2}\exp(a)\mathrm{erfc}\left(\sqrt{a}\right)\right]^{\pm1} \quad , \tag{12}$$

where

$$a = \frac{\omega^2\delta^2}{2v_e^2}, \quad E_1(a) = \int_0^\infty \frac{\exp(\pm t)}{t}\,dt \quad ,$$

and

$$\mathrm{erfc}(z) = \frac{2}{\sqrt{\pi}}\int_z^\infty \exp\left(\pm t^2\right)dt \quad . \tag{13}$$

As can be seen from Eq. (12), the quantity $\eta_{sib}c/v_e$ depends on the system parameters only through the dimensionless parameter $\omega\delta/v_e$, which is approximately the ratio of the transit time in the collisionless skin depth over the period of the incident light. This result will be compared with the more accurate result calculated from Eqs. (7) and (8), i.e.,

$$\eta_{ab} = \frac{8\sqrt{2}}{\pi}\frac{v_e}{c}\,\mathrm{Im}\left(\int_0^\infty d\xi\,\frac{1}{1 \pm \frac{\xi^3}{b^2}Z(\xi)}\right) \quad , \tag{14}$$

where $b^2 = \omega_2c_2/2\,\omega_p^2 v_e^2$ and $Z(x)$ is the plasma dispersion function.[23] Equation (14) was derived in Ref. 21.

Figure 1 plots the quantities $\eta_{ab}c/v_e$ (Exact) calculated numerically from Eq. (14), $\eta_{sib}c/v_e$ (SIB) calculated from Eq. (12), and $\eta_{as}c/v_e$ (ASE) defined in Eq. (9). The curves are plotted versus $\omega^2c^2/\omega_p^2v_e^2$ in Fig. 1. It can be seen that both $\eta_{sib}c/v_e$ and $\eta_{as}c/v_e$ are in good agreement with $\eta_{ab}c/v_e$, in their respective regimes of validity. It is worth reiterating that, for an isotropic distribution function [$f_0(\mathbf{v}) = f_0(|\mathbf{v}|)$], such as the one in Eq. (11), an identical absorption coefficient would be obtained whether or not the $\mathbf{v}\times\mathbf{B}$ term in the equation of motion was included in the derivation. However, neglecting the $\mathbf{v}\times\mathbf{B}$ term will lead to an incorrect interpretation of the absorption mechanism.

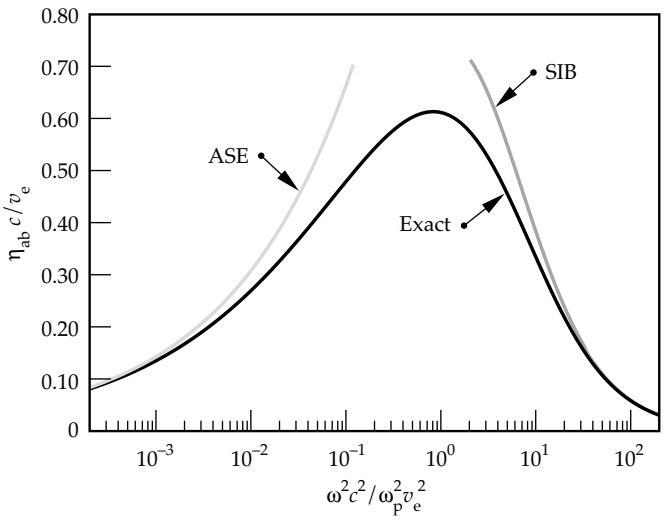

FIGURE 1. The quantities $\eta_{ab}c/v_e$ (Exact) calculated numerically from Eq. (14), $\eta_{sib}c/v_e$ (SIB) calculated from Eq. (12), and $\eta_{as}c/v_e$ (ASE) defined in Eq. (9). The curves are plotted versus $\omega^2c^2/\omega_p^2\,v_e^2$. (08-00-0296-0388pb01)

Numerical Simulations of the Light Absorption in Overdense Plasmas

To examine the validity of the absorption coefficient derived in the previous section, we have carried out several runs of numerical simulations using the PIC plasma simulation code ZOHAR.[20] In all the simulations, the electric field of the incident light E_{in} satisfies $E_{in}^2 << \pi n_0 m_e v_e^2$ so that the quiver velocity of electrons in the overdense plasma is smaller than the thermal velocity, as was assumed in the analytical derivation of the absorption coefficient. The 1-D simulations are set up as follows:

1. The electromagnetic fields can vary only in the x direction. The length of the simulation region is $l_x = 40c/\omega_p$.
2. The boundary conditions of the electromagnetic fields at $x = 0$ correspond to a normally incident circularly polarized plane wave. The amplitude of the wave gradually increases from zero at the beginning of the simulation ($t = 0$) to a value E_{in} at the end of the fifth wave period. The amplitude of the incident wave remains constant thereafter.
3. The wave impedances of the boundaries are chosen such that the outgoing waves will be completely reflected at $x = l_x$ and completely transmitted at $x = 0$.
4. The initial electron density n_e is zero for $0 < x < 3l_x/4$, and is equal to a constant value n_0 for $3l_x/4 < x < l_x$. Immobile neutralizing background charge density with the same profile as that of n_e is imposed to ensure charge neutrality at $t = 0$.
5. At $t = 0$, simulation particles are loaded uniformly in the region $3l_x/4 < x < l_x$, with Maxwellian distribution in the velocity space.
6. During the simulation, particles that hit the right boundary at $x = l_x$ are re-emitted according to the Maxwellian distribution, with the same thermal velocity v_e as the initial distribution function.
7. For particles moving to the left, we have used two types of reflection conditions, as will be described later.

Three sets of simulations have been carried out, with the initial thermal velocity v_e equal to $0.1c$. Each set consists of simulations with different values of ω/ω_p. The simulation parameters are (i) 800 equally spaced grid points for the electromagnetic fields; (ii) 409,600 simulation particles; (iii) the time step $\Delta t = 0.04/\omega_p$. The total numbers of time steps N_t are $N_t = 80{,}000/\omega_p$ for the simulations with $(\omega c/\omega_p v_e)^2$ equal to 0.1 or 0.2, and $N_t = 40{,}000/\omega_p$ for the rest. There are three differences between the three sets of simulations: (1) For the first set of simulations, the particles that reach the laser–plasma interface at $x = 3l_x/4$ are reflected specularly, and the longitudinal electric field (E_x) is purposely turned off to mimic the idealized model of the linear theory. (2) For the second and the third sets of simulations, the self-consistent longitudinal electric field (E_x) remains on, and the particles that reach the left simulation boundary at $x = 0$ are specularly reflected. However, only a few particles ever reach the left boundary—most of the particles are reflected by the sheath electric field in the vicinity of $x = 3l_x/4$. (3) The steady-state value of laser intensity for the first and second sets is $(eE_{in}/\omega_p m_e c)^2 = \wp_{in} = 10^{-5}$, and that for the third set is $\wp_{in} = 2.5 \times 10^{-4}$.

Figure 2 compares the absorption coefficients observed in the simulations with those calculated numerically from Eq. (14). The absorption coefficients

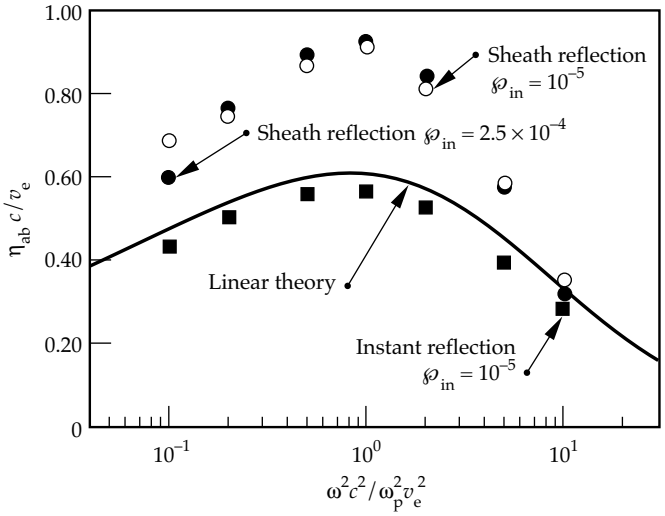

FIGURE 2. A comparison of the absorption coefficients times c/v_e observed in the PIC simulations with those from the linear theory. (08-00-0296-0389pb01)

from the first set of simulations (solid squares) agree quite well with the linear theory, while those from the second set (open circles) and the third set (solid circles) are significantly greater than predicted by the linear theory, except those with $(\omega c/\omega_p v_e)^2 = 10$. A plausible explanation of the discrepancy is that the linear theory assumes instant reflection in the sheath region, while the finite reflection time may play an important role in those simulations. This explanation is supported by the agreement between the linear theory and results from the first set of simulations, where instant specular reflection condition is imposed at the laser–plasma interface at $x = 3l_x/4$. The comparison between the second and third sets of simulations indicates that most of the simulations are in the linear regime, since the absorption coefficients are not very sensitive to the intensity of the incident laser light. The exceptional cases are those with $(\omega c/\omega_p v_e)^2 = 0.1$, for which the nonlinear effects may have set in when $\wp_{in} = 2.5 \times 10^{-4}$.

In the simulations, the flows of the electromagnetic energy and the electron kinetic energy through the boundaries at $x = 0$ and $x = l_x$ are taken into account, therefore corresponding to the net transfer of the electromagnetic energy into the electron kinetic energy as shown in Fig. 2. The total (electromagnetic plus kinetic) energy is conserved very well in the simulations, with the change in the total energy (ΔE_{total}) no more than 1% of the net increase in the electron kinetic energy (ΔE_e).

As mentioned earlier, the transverse components of the canonical momentum are the constants of the motion in the present 1-D model. This is confirmed by the distributions of the momentum observed in the simulations, which show hardly any changes in the distributions of p_y and p_z. The absorption of the electromagnetic energy, therefore, must be accompanied with the change in the distribution of the longitudinal momentum p_x.

Figure 3 compares the distributions $N(/m_e c)$ of the normalized longitudinal momentum $p_x/m_e c$ at the ends of three PIC simulations (black line) with those at the beginnings of the simulations (gray line). We obtain the distributions by sorting the simulation particles into bins of width $\Delta p_x/m_e c = 0.02$. Only particles located in the interval $7l_x/8 \le x \le l_x$ are counted, so that all the particles counted are at least $5c/\omega_p$ away from the laser–plasma interface. Figures 3(a) and 3(b) correspond to the solid squares in Fig. 2, with $(\omega c/\omega_p v_e)^2$ equal to 0.1 and 1.0, respectively. Figure 3(c) is obtained from a simulation similar to the one corresponding to the solid square with $(\omega c/\omega_p v_e)^2$ equal to 10, except that $\wp_{in} = 10^{-3}$ so that the difference between the initial and the final distributions can be seen easily. The absorption coefficient observed in the simulation for Fig. 3(c) is 0.0327, which is very close to the value 0.0324 for $\wp_{in} = 2.5 \times 10^{-4}$ shown in Fig. 2 (the solid square at $\omega^2 c^2/\omega_p^2 v_e^2 = 10$).

In Figs. 3(a) and 3(b), significant differences between the initial and the final distributions can be seen clearly for $p_x > 0$. Because the parameters ω_p and v_e are the same for all three simulations, the comparison between the three final distributions in Figs. 3(a) and 3(b) indicates that as ω becomes smaller, the change in $N(p_x/m_e c)$ shifts to smaller p_x. A possible implication of this trend is that the breakdown of the linear theory, which assumes that the unperturbed velocity is greater than the quiver velocity $v_{os} = eE_0/m_e\omega$, may set in at a smaller E_0 when ω decreases. For the case in Fig. 3(a), sizable changes in $N(p_x/m_e c)$ can be seen even for negative p_x. This can explain the considerable decrease in the absorption coefficient, for the cases with $(\omega c/\omega_p v_e)^2 = 0.1$ in Fig. 2, as $\wp_{in}$ increases from 10^{-5} (open circle) to 2.5×10^{-4} (solid circle).

The results described so far are obtained from simulations with the sharpest density gradient possible, i.e., the densities of the immobile ions increase from zero to the maximum values within one grid separation, $\Delta x = 0.05c/\omega_p$. To study the effects of finite density gradients, we have also carried out three sets of simulations consisting of runs all having a linear ramp in their ion density profile. The width of the ramp L varies over a wide range of values. The initial n_e profile in each run coincides with the ion density profile. The laser intensity corresponds to $(eE_{in}/\omega_p m_e c)^2 = \wp_{in} = 10^{-5}$, and the thermal velocity is $v_e = 0.1c$. The rest of the simulation parameters are similar to those described earlier in this section.

In Tables 1(a)–(c), absorption coefficients η obtained from these simulations are shown versus the widths L of the density ramp. Each of the three panels corresponds to a set of simulations with a fixed $(\omega_p/\omega)^2$ (100, 50, or 20). For $(\omega_p/\omega)^2 = 100$, panel (a) clearly shows that η, as a function of L, has a maximum value approximately equal to 11.5% with $L\omega_p/c$ between 2 and 3. Panel (b) shows a similar dependence of η on L for $(\omega_p/\omega)^2 = 50$, with the maximum η of 9.5% occurring around $L\omega_p/c = 1.5$. For $(\omega_p/\omega)^2 = 20$, panel (c) shows no increase in η for small $L\omega_p/c$. Although we might have caught the increasing trend in η for $(\omega_p/\omega)^2 = 20$ had we run more simulations with finer grid separations, we do not expect to see much increase in η.

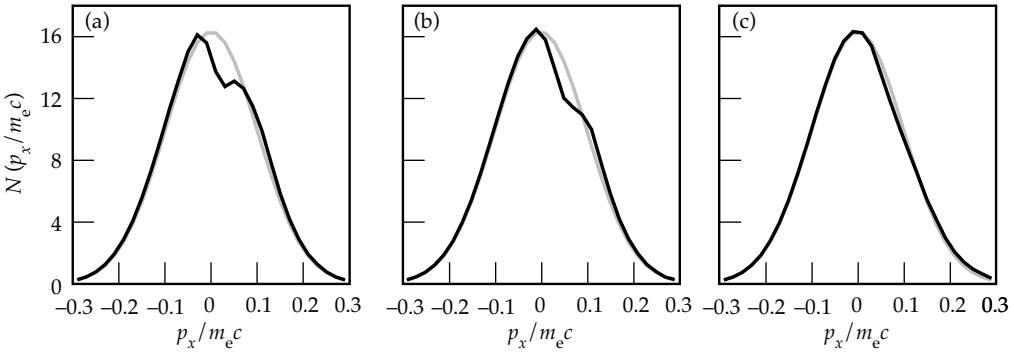

FIGURE 3. The initial (gray) and the final (black) distributions of the normalized longitudinal momentum $p_x/m_e c$, observed in three PIC simulations. The panels (a), (b), and (c) correspond to $\omega^2 c^2/\omega_p^2\ v_e^2 = 0.1$, 1.0, and 10.0, respectively.
(08-00-0296-0390pb01)

TABLE 1. Absorption coefficients η obtained from simulations with $v_e = 0.1\,c$ and various density ramp widths L. The panels (a), (b), and (c) correspond to $(\omega_p/\omega)^2$ = to 100, 50, and 20, respectively.

(a) Absorption coefficient η for $(\omega_p/\omega)^2 = 100$

$L\omega_p/c$	0.05	0.5	1	2	3	4	5	10	15	20
η (%)	9	9.5	10.5	11.5	11.5	11	10.5	7.8	5.5	4.2

(b) Absorption coefficient η for $(\omega_p/\omega)^2 = 50$

$L\omega_p/c$	0.05	0.5	1	1.5	2	2.5	3	3.5	5	7
η (%)	8	8.8	9.3	9.5	9.3	8.9	8.5	7.8	6	4.2

(c) Absorption coefficient η for $(\omega_p/\omega)^2 = 20$

$L\omega_p/c$	0.05	0.5	1	1.5	1.8	2	3
η (%)	6	6	5.5	5	4.2	4	2

For $L\omega_p/c$ sufficiently greater than unity, we expect that the absorption coefficient η will be a function of $c(\omega_p/\omega)^2/(\omega L)$. The results in Table 1 reflect such a dependence. For example, the runs of $L\omega_p/c = 20$ in panel (a), $L\omega_p/c = 7$ in panel (b), and $L\omega_p/c = 1.8$ in panel (c) all correspond to $c(\omega_p/\omega)^2/(\omega L) = 50$, and they all have η = 4.2%. The runs of $L\omega_p/c = 10$ in panel (a) and $L\omega_p/c = 3.5$ in panel (b) also have the same η of 7.8% as they both correspond to $c(\omega_p/\omega)^2/(\omega L) \approx 100$.

Summary

We modified the original sheath inverse bremsstrahlung model[14] by including the $\mathbf{v} \times \mathbf{B}$ term (velocity × magnetic field) in the Lorentz force equation. We showed that the present results are significantly different from those derived without the $\mathbf{v} \times \mathbf{B}$ term. The $\mathbf{v} \times \mathbf{B}$ term is also important in interpreting the absorption mechanism: if the $\mathbf{v} \times \mathbf{B}$ term were neglected, the absorption of the light would be incorrectly interpreted as an increase in the transverse electron temperature, which would violate the conservation of the transverse components of the canonical momentum (in the case of a normally incident laser light). We also showed that both the sheath inverse bremsstrahlung and the anomalous skin effect are limiting cases of the same collisionless absorption mechanism. We compared results from PIC plasma simulations with the absorption coefficient calculated from the linear theory and investigated the effects of finite density gradients with PIC simulations.

Acknowledgments

We are grateful for inspiring discussions with T. W. Johnston, J. P. Matte, S. C. Wilks, R. S. Walling, Z. Zinamon, and M. E. Foord.

Notes and References

1. H. M. Milchberg, R. R. Freeman, S. C. Davey, and R. M. More, *Phys. Rev. Lett.* **61**, 2364 (1988).
2. J. C. Kieffer, P. Audebert, M. Chaker, J. P. Matte, et al., *Phys. Rev. Lett.* **62**, 760 (1989).
3. R. Fedosejevs, R. Ottmann, R. Sigel, G. Kühnle, et al., *Applied Phys. B* **50**, 79 (1990).
4. R. Fedosejevs, R. Ottmann, R. Siegel, G. Kühnle, et al., *Phys. Rev. Lett.* **64**, 1253 (1990).
5. M. M. Murnane, H. C. Kapteyn, and R. W. Falcone, *Phys. Rev. Lett.* **62**, 155 (1989).
6. D. Kühlke, U. Herpes, and D. von der Linde, *Appl. Phys. Lett.* **50**, 1785 (1987).
7. C. H. Nam, W. Tighe, S. Suckewer, J. F. Seely, et al., *Phys. Rev. Lett.* **59**, 2427 (1987).
8. D. G. Stearns, O. L. Landen, E. M. Campbell, and J. H. Scofield, *Phys. Rev. A* **37**, 1684 (1988).
9. G. Kühnle, F. P. Schäfer, S. Szatmari, and G. D. Tsakiris, *Appl. Phys. B* **47**, 361 (1988).
10. J. A. Cobble, G. A. Kyrala, A. A. Hauer, A. J. Taylor, et al., *Phys. Rev. A* **39**, 454 (1989).
11. H. W. K. Tom and O. R. Wood II, *Appl. Phys. Lett.* **54**, 517 (1989).
12. S. E. Harris and J. D. Kmetec, *Phys. Rev. Lett.* **61**, 62 (1988).
13. M. Tabak, J. Hammer, M. E. Glinsky, W. L. Kruer, et al., *Phys. Plasmas* **1**, 1626 (1994).
14. P. J. Catto and R. M. More, *Phys. Fluids* **20**, 704 (1977).
15. J. P. Matte and K. Aguenaou, *Phys. Rev. A* **45**, 2588 (1992).
16. W. Rozmus and V. T. Tikhonchuk, *Phys. Rev. A* **42**, 7401 (1990).
17. E. M. Lifshitz and L. P. Pitaevskii, *Physical Kinetics* (Pergamon, Oxford, 1981).
18. S. Ichimaru, *Basic Principles of Plasma Physics* (Benjamin, Reading, MA, 1973).
19. E. S. Weibel, *Phys. Fluids* **10**, 741 (1967).
20. A. B. Langdon and B. F. Lasinski, *Methods Comput. Phys.* **16**, 327 (1976).
21. T.–Y. B. Yang, W. L. Kruer, R. M. More, and A. B. Langdon, *Phys. Plasmas* **2**, 3146 (1995).
22. R. C. Davidson, *Handbook of Plasma Physics* **1**, Eds., A. A. Galeev and R. N. Sudan (North–Holland, New York, 1983). pp. 521–585.
23. B. D. Fried and S. D. Conte, *The Plasma Dispersion Function* (Academic, New York, 1961).

Radiation-Effects Testing for the National Ignition Facility Final Optics

C. D. Marshall *S. A. Payne*

J. A. Speth *M. Borden**

L. D. DeLoach *S. Karr***

Introduction

The principal technical goal of the National Ignition Facility (NIF) is to achieve thermonuclear ignition in a laboratory environment by means of inertial confinement fusion (ICF). Such ignition will enable the NIF to service the Department of Energy Stockpile Stewardship Management Program, to achieve inertial fusion energy goals, and to advance scientific frontiers.[1] All three applications will make use of the extreme conditions created in the target chamber. For a predicted 20-MJ yield scenario, the NIF will produce ~10^{19} neutrons with a characteristic deuterium–tritium (D–T) fusion energy of 14 MeV per neutron. The ICF process will also directly or indirectly produce x rays, gamma rays, secondary neutrons, and solid, liquid, and gaseous target debris. Thus, a critical design issue is protecting the final optical components and sophisticated target diagnostics in the harsh environment.

Figure 1 shows the basic geometry of the NIF target chamber. The final optics package is located 6.5 m from the target and chamber center. The debris shields, which are designed to absorb x rays and target debris, are likely to require frequent replacement. The target chamber wall, ~1-m-thick concrete shielding, and target area concrete shield wall (not shown in Fig. 1) will absorb virtually all of the radiation and target debris and protect most of the laser system from direct line-of-sight irradiation. However, penetrating radiation, such as neutrons and gamma rays, will propagate through the ~1-cm-thick debris shields to interact with the relatively expensive fused-silica focus lenses and potassium-dihydrogen-phosphate (KDP) frequency-conversion crystals.

This article focuses on potential degradation of the NIF final-focus lenses and frequency-conversion crystals, which must last for many years. Furthermore, an ICF-based power plant may become possible in the next century, when it will likely be necessary to maintain SiO_2 final optics at an elevated temperature to anneal the radiation-induced defects that are formed.[2]

Review of Fundamentals

Fused silica (synthetic SiO_2) or fused quartz (natural SiO_2) are among the optical materials of choice for situations involving ultraviolet transparency, precision quality, large size, or harsh environments. Issues surrounding the radiation hardness of SiO_2 have been studied for many decades,[3–6] and the recent emergence

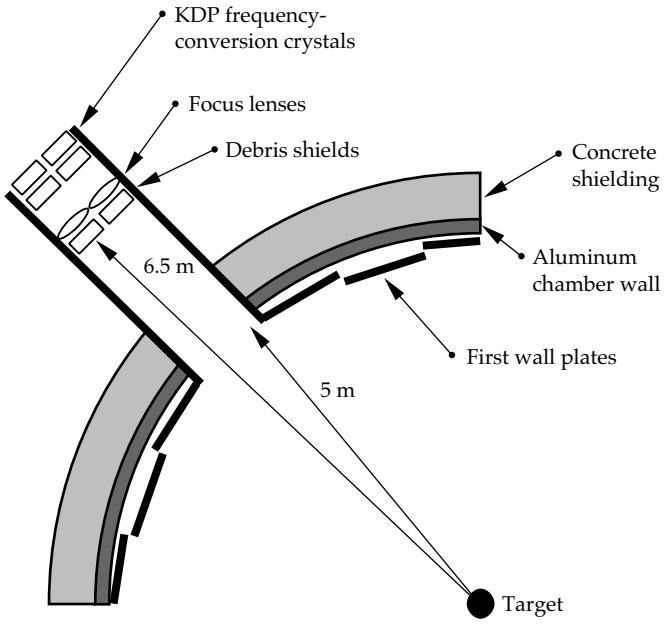

FIGURE 1. Geometry of the NIF target chamber and position of the final optical components. (50-02-0694-2720pb02)

*Los Alamos National Laboratory, Los Alamos, New Mexico.
**Sandia National Laboratory, Albuquerque, New Mexico.

of deep-ultraviolet (DUV) lithography has prompted renewed interest.[7–9] Many defects have been characterized and elucidated, and this report builds on that foundation.[3–6] However, substantial uncertainty remains in the literature, partly as a consequence of the often unclearly specified radiation conditions and different types of SiO_2 that have been used. We tested a wide variety of commercial fused silica and fused quartz samples with a wide variety of specified irradiation conditions, leading to an improved understanding of the issues important for SiO_2 radiation hardness.

Far less is known about the radiation resistance of KDP.[10,11] Our work is intended to assess radiation hardness and to unravel some of the basic material physics issues when SiO_2 and KDP encounter gamma-ray or neutron irradiation.[12]

In general, when electromagnetic radiation of sufficient energy is used to irradiate an optical material, solarization or optical darkening occurs. Absorption or scattering of photons leads to the generation of energetic electrons and holes that eventually react with pre-existing structural defects (precursors) or the intrinsic material itself to create the electronic defects associated with solarization.[5,13]

A ~1-MeV gamma ray, typical of the energy range to be produced on the NIF, is, in principle, capable of yielding about 10^5 electron–hole (e–h) pairs per photon. The process begins by the production of energetic Compton electrons, which produce secondary electrons and e–h pairs. The action of neutrons differs from that of gamma-ray photons because of their uncharged nature. Neutrons initially collide with nuclei and can induce nuclear reactions that produce other types of radiation, such as gamma rays and alpha particles. However, some momentum transfer always occurs. The resulting "knock-on-collision" displacement damage can lead to precursor sites that later encounter electrons and holes and become converted to other types of defects. Precursors can also result from manufacturing processes, including oxidizing or reducing conditions.

Many different defects can be created in irradiated SiO_2 and KDP. Here, we review those most prominently observed in our studies. In perfect SiO_2 glass, silicon is tetrahedrally bonded by four oxygens in a continuous, random glass network. The Si–O–Si bonds can be strained, which is believed to render the site more susceptible to electronically induced displacements.[14] An oxygen-deficient center (ODC), which gives rise to an absorption band at 5 eV can be created as a result of collisions with neutrons.[15] The ODC can be converted to an E' defect center by losing an electron.[5,16,17] The E' absorption occurs at 5.8 eV. The precise absorption spectra associated with all defect species have not yet been fully resolved. For example, the B_1 band, with an absorption at 4 eV, is only observed in fused quartz, and a definitive defect site has not been correlated with this band.[5,15] An Al impurity[15,18] is known to give rise to absorption at 2.0 eV. We found evidence of the Al impurity, B_1, D_0, and E' absorption bands during our work as a result of gamma-ray electronic excitations, and we believe that neutron collisions produce the ODC.

Many different absorption bands have been identified with impurities and gamma-ray irradiation in KDP. For example, transition metals, such as Al, Fe, As, Cr, Pb, and V, can lead to significant radiation-induced absorption in KDP, all with absorptions in various portions of the ultraviolet spectrum. In general, these absorptions arise from electrons that are promoted by means of irradiation to the KDP conduction band in ways similar to those described above for SiO_2. The electrons are then trapped at impurity sites in the band gap between the conduction and valence band. The energy gap between the impurity site and the lower edge of the conduction band determines the wavelength of induced absorption.

Penetrating Radiation Characteristics

NIF

Most of the penetrating radiation from the NIF target will emanate directly from 14-MeV monochromatic neutrons (the flux of 17.6-MeV gamma rays from D–T fusion is less by a factor of 10^4). However, significant neutron-induced nuclear reactions will also arise from various structures in the target area.[19] These secondary reactions produce penetrating radiation consisting of neutrons that range from $<<0.01$ to ~10 MeV in energy, and gamma rays that range from 0.01 to 10 MeV. Depending on whether the radiation is prompt (directly from the target) or secondary, the pulse duration is in the range of 5 to 100 ns, respectively.

The time-integrated dose over an expected 30-year lifetime of the NIF is expected to be 1.1 Mrad from neutrons (n^o) and 0.6 Mrad from gamma rays in the SiO_2 focus lenses; in KDP, the time-integrated dose is 1.1 Mrad from n^o and 0.5 Mrad from gamma rays. These doses correspond to ~2 and ~1 krad of n^o and gamma rays, respectively, for each of the 20-MJ yield shots with a total 385-MJ/year yield.[19] For reference, 1 rad is defined as 10^{-5} J of absorbed energy per gram of material. Of course, variations in both the transverse and longitudinal doses arise from absorption and shadowing, but the ±10% variation is not significant compared to other issues, such as the NIF gain and shot rate, which may be accelerated.

Sources for Radiation Testing

No radiation test sources currently in operation can produce the necessary spectrum and temporal format of neutrons and gamma rays that is exactly equivalent for direct accelerated life tests of the NIF final optics.

Thus, we used a variety of radiation sources that bracket the problem to interpolate results and predict what will happen on the NIF. Table 1 lists the radiation sources we used and their relevant temporal and spectral characteristics. Modeling exercises benchmarked against the accumulated data provided a realistic view of the radiation damage to optics that may be expected from the NIF.

The Los Alamos Neutron Science Center (LANSCE) shown in Fig. 2 is a kilometer-long, proton-accelerator, neutron-spallation source that provides a hard neutron and gamma-ray spectrum extending from thermal energies <<0.01 MeV to several hundred MeV. The pulse format of the accelerator furnishes a long (ms) train of 300-ps pulses with a macrorepetition rate of 10 Hz. This facility allowed us to obtain both neutron and gamma-ray pulsed irradiations with energies and doses spanning the relevant range for the NIF.

The Sandia National Laboratory Pulsed Reactor facility No. III (SPR-III) shown in Fig. 3 is an enriched ^{235}U pulsed nuclear reactor that provides a relatively hard (for a reactor) neutron spectrum extending from thermal energies to ~3 MeV.[20] The reactor is nominally operated with 100-μs pulses at a repetition rate of once

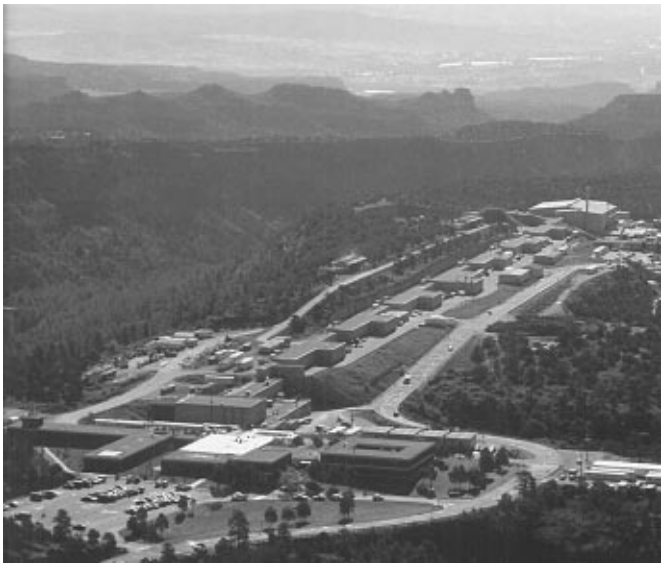

FIGURE 2. The Los Alamos Neutron Science Center (LANSCE) was the pulsed, high-energy (>10-MeV) neutron-irradiation facility used in our studies. (70-17-1095-2274pb04)

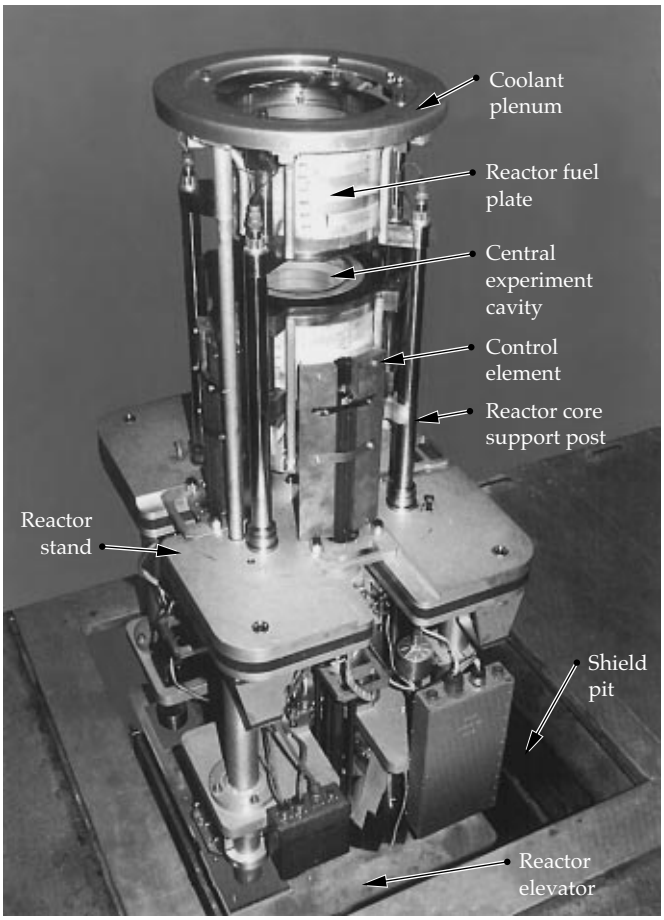

FIGURE 3. The Sandia National Laboratory Pulsed Reactor No. III (SPR-III) was the pulsed nuclear reactor used in our studies. (70-17-1095-2274pb03)

TABLE 1. Summary of radiation source characteristics that were collaboratively used for accelerated life testing of NIF final optics components at LANL, SNL, LLNL, and French Commissariat Energie Atomique Laboratories.

		NIF	LANL LANSCE	SNL SPR-III	LLNL RTNS-II	CEA Sames	LLNL ^{60}Co	LLNL e^- LINAC
Neutrons	Spectra (MeV)	14 primary <0.01–1 low dose	<0.01–100	<0.01–1	14	14	None	None
	Pulse format	5 ns	ps trains	100 μs	continuous (or 5 ns)	continuous		
	NIF 30-yr dose (Mrad)	1	4	4	4	N/A	N/A	N/A
Gamma rays	Spectra (MeV)	0.01–10	1–100	0.01–1	0.01 to 1	0.01 to 1	1	0.01–50
	Pulse format	20 ns	ps trains	100 μs	continuous	continuous	continuous	20 ns
	NIF 30-yr dose (MRad)	0.5	4	4	N/A	N/A	4	4

every 2 hr. The neutron energy spectrum is peaked at 1 MeV but is broad, with 99% of the neutron energy bracketed within 0.01 to 10 MeV. This facility allowed us to obtain gamma-ray irradiations with energies close to the relevant range for the NIF, along with n^o irradiation with energies near that of the NIF (see Table 1).

The French Commissariat Energie Atomique (CEA) Sames neutron source and LLNL RTNS-II neutron source are D accelerators with T targets that provided a continuous source of direct, 14-MeV, D–T fusion neutrons. These facilities provided us with the best match to the neutron energies on the NIF; however, the continuous temporal format is dissimilar. Gamma-ray irradiation is also present in these sources due to secondary reactions.

At LLNL, an electron accelerator spallation source (0.01 to 50 MeV) and a ^{60}Co source (1 MeV) also provided pure gamma-ray radiation in ns pulsed and continuous formats, respectively. These gamma-ray facilities, together with the mixed-neutron and gamma-ray sources, allowed for the separation of effects that arose from gamma rays and neutrons.

Experimental Results

We have developed a physical model of the primary radiation-damage pathways for silica glass and KDP in the penetrating radiation dose range of interest for the NIF. The primary consideration was the induced optical absorption in the glasses as a function of absorbed radiation dose. The temporal format of the radiation pulses was of interest because potential thermal annealing at room temperature could affect radiation damage of subsequent pulses. The radiation spectral shape was also of concern because neutrons of different energy have differing percentages of elastic and inelastic scattering.

We studied as many as 25 sources and grades of SiO_2 to understand the impact of manufacturing methods on precursors to damage. In addition, we studied many different impurities in deliberately doped KDP to understand the impacts of purity and process control in the starting material.

Radiation Effects in Silica Glass

Figure 4 is an example of eight types of SiO_2 we tested following irradiation, including fused silica and fused quartz from different vendors and manufacturing processes. All samples were simultaneously irradiated with 3.7 Mrad of gamma rays from a ^{60}Co source. The results varied widely.

Despite the wide variation in radiation resistance, these samples led to only four radiation-induced absorption spectral shapes, as shown in Fig. 5. From this information and data obtained on other radiation sources, it was possible to determine the origin of the prominent spectral shapes. The peak at 246 nm arises from direct-neutron, collision-induced displacements creating a localized ODC that is intrinsic to all SiO_2. The absorption peak at 300 nm in Fig. 5(b) arises from the conversion of 241-nm defect absorption that is present

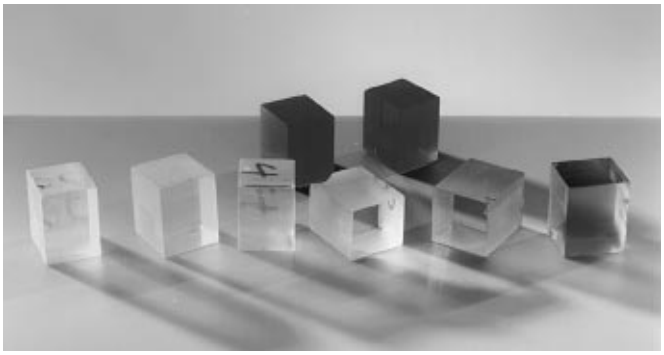

FIGURE 4. Eight different types of fused silica and fused quartz from several different manufacturers. All were irradiated with 3.7 Mrad of gamma rays from a ^{60}Co source. (70-15-1094-3620pb02)

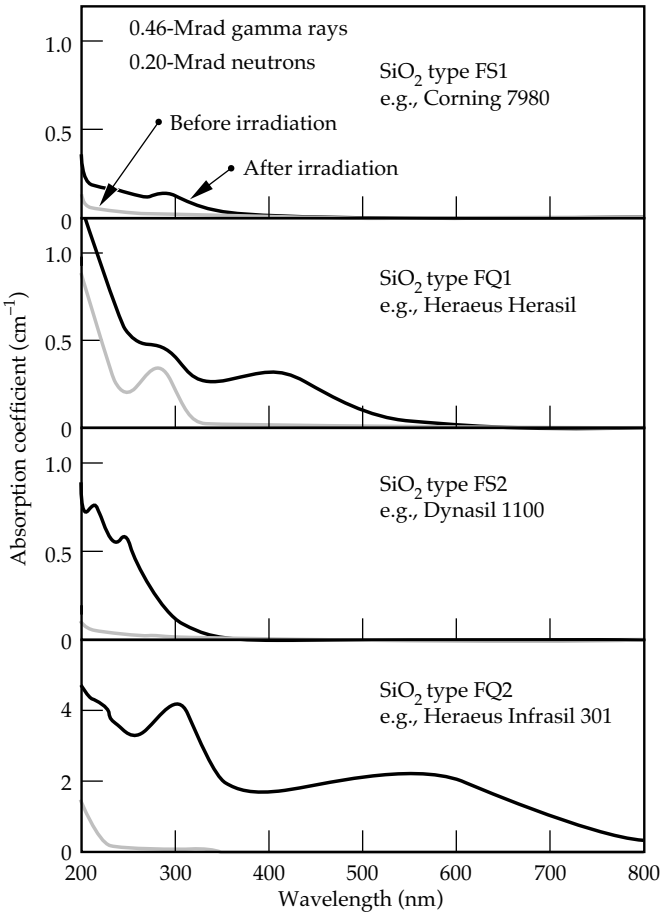

FIGURE 5. Under identical doses of 200-krad neutron and 460-krad gamma irradiation, the absorption spectra of all 25 types of SiO_2 that we studied fell into four distinct classes. (70-17-0596-1038pb01)

prior to irradiation, which is likely due to a Ge impurity center originating from the manufacturing process. The peak at 210 nm (E′ defect) is due to a two-step process of first creating the 246-nm ODC defect and then converting it into an E′ center with gamma rays. The peak centered at 550 nm is most likely due to Al impurities in the SiO_2, as suggested in the literature.[5,16,17] The four spectra shown in Fig. 5 correspond to the four classes of SiO_2 in Table 2. The most radiation-hard variants are synthetic fused silicas, such as Corning 7980 and Heraeus Suprasil grades.[12]

To benchmark the effective lifetime of the NIF optics, it was necessary to use a mixed neutron and gamma-ray source because synergistic neutron and gamma pathways lead to radiation-induced damage. The SPR-III reactor was a versatile radiation source for our purposes, with 100-μs pulse operation, a mixed neutron and gamma dose ratio similar to the NIF (within a factor of 5), and a gamma spectrum very close to that of the NIF (see Table 1). The neutron spectrum from this largely unmoderated ^{235}U fission reactor, however, extends over a broad energy range, with a peak flux at 1 MeV. This is low compared to the direct D–T 14-MeV neutrons that will dominate the NIF spectrum. As a consequence, these results must be extrapolated to higher neutron energies (more damage per individual collision cascade created by a single neutron) to make NIF predictions. The SPR-III data are intended to provide insight into the impact of the gamma-ray and nº mix of radiation.

Figure 6 shows the results of a dose-dependent study on the SPR-III over two experimental days. One year on the NIF, with 385 MJ of fusion yield assumed in the NIF conceptual design report (CDR), is predicted to produce ~40 krad of neutron dose and ~20 krad of gamma-ray dose, hereafter referred to as a "NIF year." One shot on the SPR-III corresponds to one neutron NIF year and 5 gamma-ray NIF years.

Figure 6(a) shows the cumulative effect of up to eight pulses from the SPR-III for FS1 glasses, revealing absorptions at both 213 and 246 nm. On closer inspection, the E′ center at 213 nm grows at an accelerated rate compared to the 246-nm feature. This observation suggests that neutrons first create the ODCs, which are then converted to E′ centers by gamma rays. A critical test to confirm this synergistic gamma-ray/nº effect is

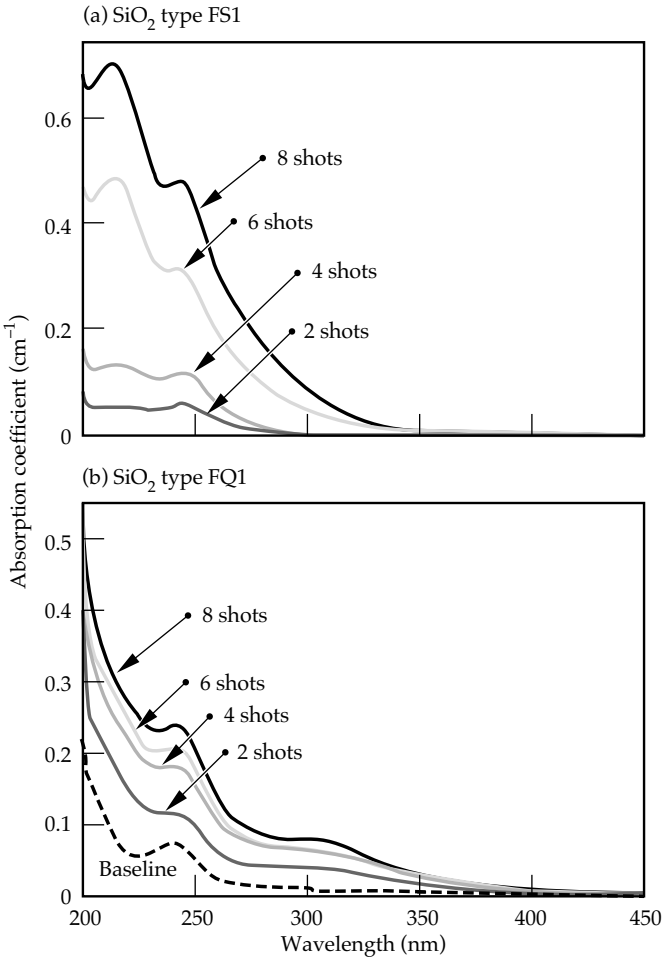

FIGURE 6. Optical absorption spectra of (a) fused silica and (b) fused quartz taken after successive shots on the SPR-III. One shot has 40 kRad nº and 100 krad of gamma-ray dose. (70-17-0596-1040pb01)

FS1 silica most rad-hard type	FS2 silica rad-soft type	FQ1 silica rad-hard type	FQ2 quartz rad-soft type
Corning 7980	Dynasil 1100	Heraeus Herasil-1top	Heraeus Infrasil-301
Corning 7940	Dynasil 1101	Heraeus Herasil-1	Dynasil QIR
Heraeus Suprasil-1		Heraeus Herasil-2	Nippon OZ
Heraeus Suprasil-2		Heraeus Herasil-3	Nippon OX1
Heraeus Suprasil-3		Heraeus Homosil	
Dynasil 4100		Heraeus Infrasil-302	
Dynasil 4101		Heraeus TO8	
Nippon ES		Dynasil QUV	
		Nippon OY	

TABLE 2. All of the SiO_2 sample types studied fell into four groupings of radiation response designated as FS1, FS2, FQ1, and FQ2, where FS = synthetic fused silica, and FQ = natural fused quartz.

shown in Fig. 7. Here the FS1-type sample is first irradiated in the SPR-III to create the ODCs, and then in a separate irradiation, it is subjected to pure gamma rays from the ^{60}Co source to show that the ODCs are converted to E′ centers. Recall that irradiation by gamma rays alone has no effect; that is, the neutrons first "soften" the material by generating ODCs.

For a pulsed radiation source, annealing of the induced defects generally follows the radiation pulse; i.e., some of the defects are self-healing at room temperature with relaxation times (inverse rate constants) ranging from nanoseconds to hours. The defects discussed in this paper are primarily long-lived defects that show no further decay after many days to months following irradiation at room temperature. The temporal format of the radiation pulse could, in general, affect the number of "permanent" defects observed, since annealable defects could be further affected by a subsequent radiation burst before they had a chance to decay. To test this possibility (i.e., to explore the dose-*rate* dependence), we performed an experiment on the SPR-III in which the radiation dose rate was varied over eight orders of magnitude. Figure 8 summarizes the results.

In the first experiment shown at the top of Fig. 8(a), the reactor was run in a steady-state mode for 30 minutes with relatively low radiation flux. In the second experiment at the bottom of Fig. 8(a), a 100-μs pulsed-neutron format was used. The total time-integrated neutron (and gamma-ray) dose during the 30-minute runs and the 100-μs pulses was measured to be approximately the same, 1.5×10^{15} n°/cm^2 to within 10%. The neutron and gamma-ray spectra are virtually identical for these two experiments because the reactor has the same degree of moderation inside the core region. Nearly the same overall experimental time elapsed between pulses.

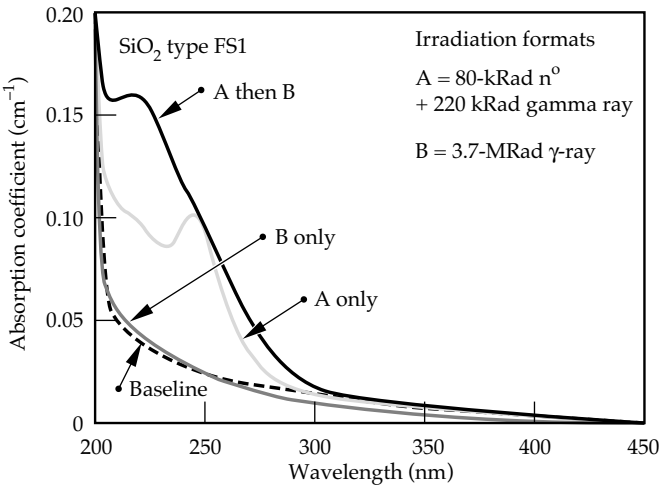

FIGURE 7. Optical absorption spectra of FS1 glass reveal that the oxygen-deficient center created by neutrons can be converted to E′ center absorption at 213 nm with gamma rays. (70-17-0596-1041pb01)

Figure 8(b) shows the results of this analysis. The data show little dose-rate dependency over the range studied in this experiment. This can be rationalized by showing that the number density of defect centers is less than the number density of atoms by four orders of magnitude. Consequently, one would expect that multiple collisions and interactions on a single physical site would be infrequent (i.e., two neutrons striking the same nucleus or damaged region) and that the system behaves as if single, isolated collisional impact sites are present.

Figure 9 is a reduction of the data in Fig. 6, which resulted from exposing fused silica and fused quartz for up to eight shots on the SPR-III reactor. The data in Fig. 7 were fit to a sum of Lorentzians, $L(\lambda)$, to account for the absorption arising from each species:

$$\alpha_i(\lambda) = \sum_i \alpha_i N_i L_i(\lambda) , \qquad (1)$$

where

$$L_i(\lambda) = \frac{\Delta\lambda_i^2}{\Delta\lambda_i^2 + (\lambda_i - \lambda)^2} \quad , \qquad (2)$$

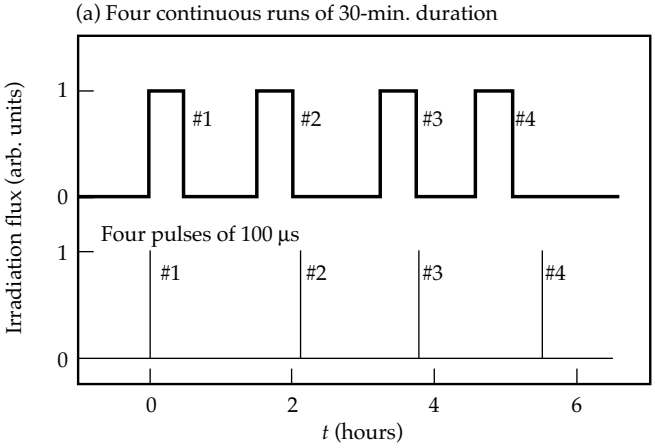

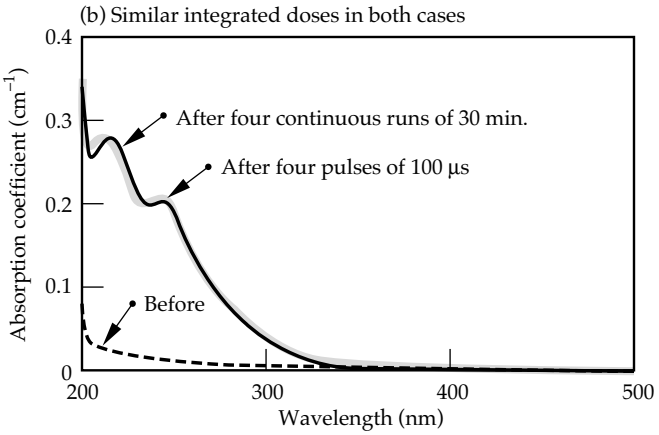

FIGURE 8. Experiment to study the effect of room-temperature annealing with short-pulse vs continuous irradiation. (a) Temporal format of radiation flux from the SPR-III. (b) The experimental results. Similar time-integrated doses were used in both experiments. (70-17-0596-1042pb01)

λ_i is the peak wavelength, and $\Delta\lambda$ is the half width at half maximum of the absorption spectrum for i = E′, ODC, Ge, or B_1. The data points in Fig. 9 give the peak defect absorption coefficients obtained from the Lorentzian curve fits to the spectra in Fig. 6. With fused silica, shown in Fig. 9(a), the absorption peak at 246 nm grows as a function of dose most rapidly at first; at higher doses, the 210-nm absorption peak growth rate overtakes it. This qualitative observation is consistent with the model described in Fig. 10.

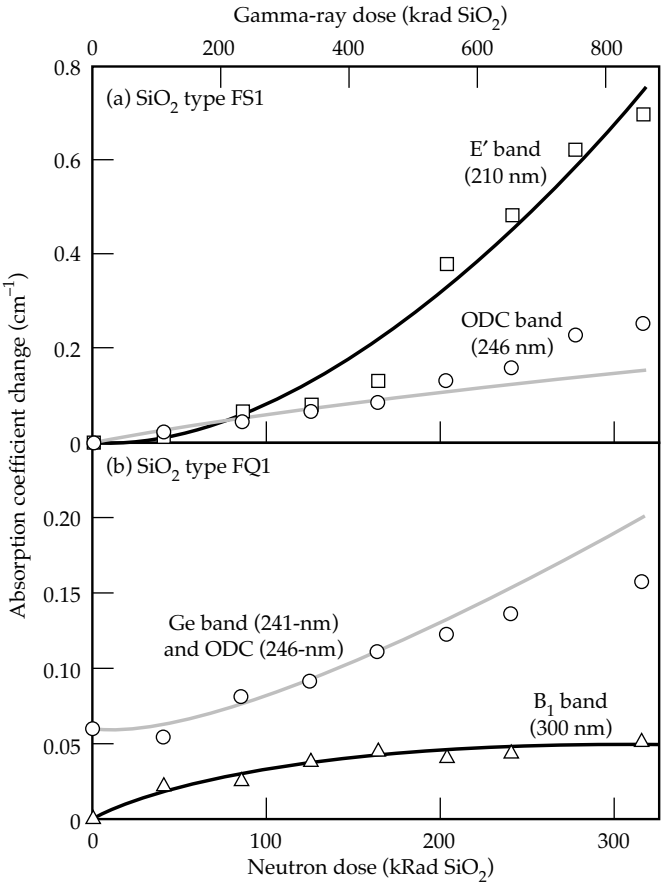

FIGURE 9. Radiation-induced absorption of E′ (210-nm), ODC (246-nm), Ge (241-nm), and B_1 (300-nm) bands in SiO_2 for (a) fused silica type FS1 and (b) fused quartz type FQ1. Data points were obtained from the SPR-III experiments. Solid lines show the numerical modeling using Eqs. (1) through (3). (70-17-0596-1043pb01)

Quantitative modeling of the defect absorption peaks shown in Fig. 9(a) for fused silica can be performed by applying rate equations derived from the model in Fig. 10 for the number density of neutron-induced ODC and subsequent gamma-ray-induced E′ defects, denoted as N_{ODC} and $N_{E'}$, respectively. The rate equations can be written as

$$\frac{dN_{ODC}}{dt} = M_{col}\sigma_{col}(E)\, N_{SiO_2}\, \frac{dF_n}{dt} - \beta_{E'}\, \frac{dD\gamma}{dt} N_{ODC} \quad (3)$$

and

$$\frac{dN_{E'}}{dt} = \beta_{E'}\, \frac{dD_\gamma}{dt} N_{ODC} \quad . \quad (4)$$

The first term in Eq. (3) describes the formation of ODC defects due to direct neutron collisions, where F_n is the neutron fluence, σ_{col} is the neutron collision cross section, N_{SiO2} is the silica number density, and M_{col} is a collision multiplier that denotes the number of cascade-collision-induced defects due to a single, primary neutron collision, as shown in the first step of Fig. 10. Equation (4) and the last term in Eq. (3) account for the second step in Fig. 10, where ODC defects are transformed into E′ defects with gamma rays. Here, $\beta_{E'}$ denotes a phenomenological conversion coefficient, and D_γ is the gamma-ray dose in krad. Defect optical absorption cross sections (σ_{ODC} and $\sigma_{E'}$) are then multiplied by the number densities obtained from Eqs. (3) and (4) to obtain the absorption coefficients in Fig. 9.

For the modeling of the defect absorption peaks in fused quartz shown in Fig. 9(b), the direct conversion of pre-existing Ge impurity into B_1 defects, with number densities N_{Ge_m} and N_{B1}, respectively, can be written as:

$$\frac{dN_{B1}}{dt} = -\frac{dN_{ODC_m}}{dt} = \beta_{B1}\, \frac{dD\gamma}{dt} N_{ODC_m} \quad , \quad (5)$$

where β_{B1} is the gamma-ray conversion coefficient. The pre-existing Ge concentration, determined from absorption spectra and mass spectra copy of individual

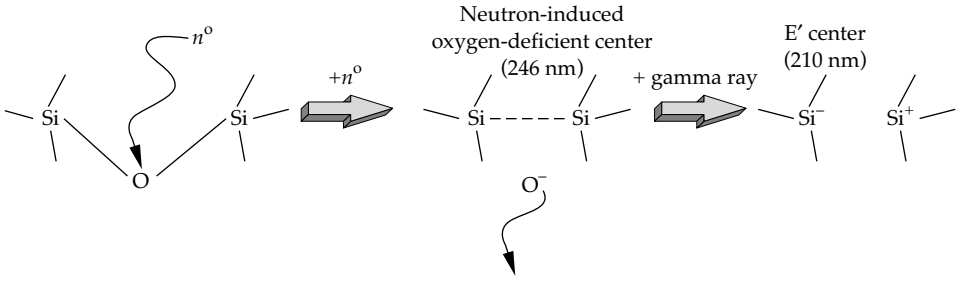

FIGURE 10. Mechanistic model of primary radiation damage mechanisms in SiO_2 that lead to changes in optical transmission. Both neutrons and gamma rays, either separately or in combination, can lead to radiation-induced damage. (70-17-0596-1039pb01)

samples, results in a nonzero initial condition. The solid lines in Fig. 9 are fits generated from Eqs. (1) through (5). Table 3 gives the parameters obtained from these curve fits.

The data-fitting parameters lead to an overdetermined system, which may not be evident from first glance at Table 3. To first order, the two unknown optical cross sections, σ_i, and the neutron multiplier, M_n, determine the height of the four curves; the two conversion coefficients, β_i, determine the shape of the data curves.

From this interpretation, the collision multiplier can be estimated by the Kinchin–Pease expression[21]

$$M_n = \frac{0.8E_{\text{dam}}}{2E_{\text{def}}}\eta_{\text{anneal}} \quad , \tag{6}$$

where E_{dam} is the average kinetic energy of the atom, which receives the initial direct collision, given as[22]

$$E_{\text{dam}} = E_n \frac{2}{A+\frac{2}{3}} \quad , \tag{7}$$

where A is the atomic mass (average of Si and two O), and $E_n \approx 1$ MeV is the neutron energy, yielding $E_{\text{dam}} \approx 0.1$ MeV. We estimate the defect formation energy of the ODC, E_{def}, as 40 eV from calculations of SiC, a related, covalently bound material.[23] An additional factor, η_{anneal}, is included by Diaz de la Rubia and others to account for the rapid (< 1-ns) annealing that occurs from the enormous local-energy deposition following a neutron–nucleus collision. Estimates from simulations place η_{anneal} at ~0.2 for fast neutrons.[21,24] Substitution into Eq. (6) yields M_n at ~200, a value that is reasonably close to our experimental assessment of 105 given the level of approximation in Eqs. (6) and (7).

To apply this model to NIF-like conditions, the neutron multiplier obtained at 1-MeV average neutron energy must be extrapolated to 14 MeV for D–T fusion neutrons present on the NIF. For this extension, we analyzed several experiments from three different high-energy neutron sources. Two experiments were performed on 14-MeV D–T fusion neutron sources (CEA Sames and LLNL RTNS-II), and one set of experiments was performed on the LANSCE high-energy (>100-MeV) proton-spallation neutron source.

Figure 11 shows the results of irradiating type FS1 fused silica (e.g. Corning 7980) with 2×10^{14} n^o/cm^2 in the Sames neutron source. The neutron multiplier, M_n, required to fit the data set was 70. The induced-absorption spectral shape is similar to that shown in Fig. 7(a) for the fission-reactor-induced absorption, indicating that no fundamentally new defects are created. The number of defects per collision is expected to be higher for 14- vs 1-MeV neutrons, however. Data taken on the RTNS-II in 1987 by Singh et al. (unpublished) at much higher doses (10^{16} n^o/cm^2) implied a neutron multiplier of 200. Data taken on the LANSCE were roughly consistent with this neutron multiplier range, although detailed dosimetry of neutron fluence as a function of neutron energy for the broad spectrum on the LANSCE is still being analyzed elsewhere. The overall spread of up to a factor of 3 in neutron-damage effectiveness (M_n) is large, depending on the experiment. The neutron multiplier inferred from these experiments varied over the range of 70 to 200, depending on the dose and

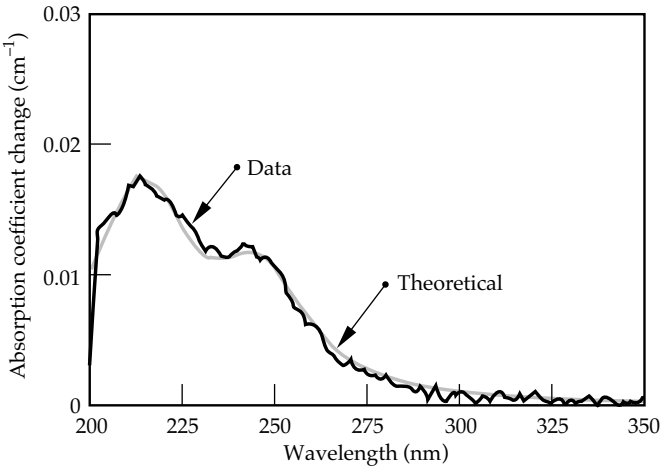

FIGURE 11. Absorption induced by the CEA Sames 14-MeV D–T fusion neutron source with 2×10^{14} n^o/cm^2 fluence at room temperature. Both data and the theoretical curve are shown. (70-17-0596-1044pb01)

TABLE 3. Parameters used to model data from the SPR-III reactor (Figs. 7–10) and to predict NIF fused silica final optics performance in Fig. 12.

Parameter	Value	Units	Source
Neutron absorption coefficient, $N_{SiO2}\sigma_{col}$	0.35	cm^{-1}	Literature
ODC to E′ gamma-ray conversion coefficient, $\beta_{E'}$	0.0007	s/krad	Data fit
Collision multiplier for 1-MeV neutrons, M_n	105	Unitless	Data fit
Collision multiplier for 14-MeV neutrons, M_n	200	Unitless	Data fit
ODC to B1 gamma-ray conversion coefficient, β_{B1}	0.004	s/krad	Data fit
Optical cross section for ODC defect, σ_{ODC}	2.1×10^{-18}	cm^2	Data fit
Optical cross section for E′ defect, $\sigma_{E'}$	3.2×10^{-17}	cm^2	Literature
Optical cross section for B_1 defect, σ_{B1}	9.4×10^{-18}	cm^2	Data fit
Optical cross section for Ge impurity, σ_{Ge}	1.1×10^{-17}	cm^2	Ge concentration

neutron source. The range may be due to differences in neutron dosimetry calibration or to other uncertainties in the radiation environment, such as the ratio of neutron to gamma dose. To be conservative, we use $M_n = 200$ to predict the NIF final-optics performance.

Predictions for Silica Glass on NIF

The predicted transmission of silica glass as a function of time on NIF is plotted in Fig. 12 for both fused silica type FS1 and fused quartz type FQ1, with an initial condition of $N_{Ge} = 5.7 \times 10^{15}$ cm^{-3} determined from data. The final-focus lens is assumed to be 4.5 cm thick. Thicker lens designs would be expected to have larger absorbance (–log transmission) that is proportional to the thickness. From the predictions in Fig. 12, FS1 is significantly more radiation-resistant than FQ1 at 3ω. Fused silica is expected to have >99% transmission over the 30-year facility lifetime. Fused quartz, however, is expected to drop to a 99% lens transmission within one year, which is undesirable. Fortunately, FS1 is the current baseline material that was assumed in the CDR.

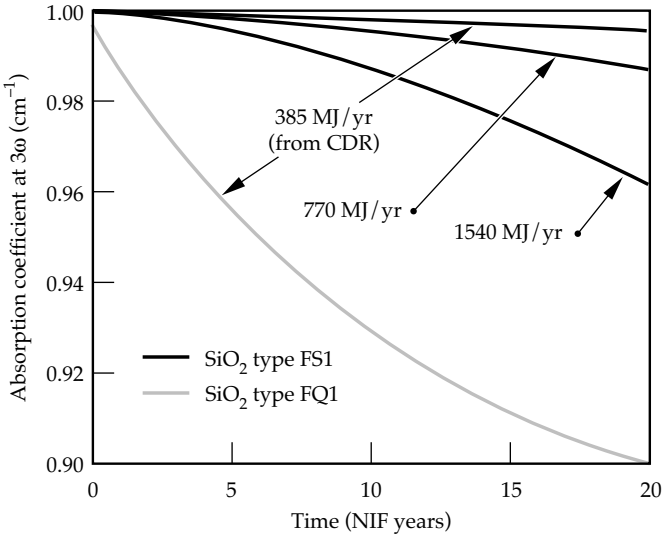

FIGURE 12. Predicted transmission of NIF final-focus lens vs time for fused silica type FS1, such as Corning 7980 or Heraeus Suprasil, and fused quartz type FQ1, such as Heraeus Herasil 1-SV. Predictions for the NIF CDR fusion yield of 385 MJ/year, and for 2 and 4 times that shot rate, are shown for FS1. (70-17-0596-1045pb01)

If the shot rate or target yields on NIF were increased by 2 to 4 times over that assumed in the NIF CDR, (yield rates of 770 and 1540 MJ/yr), the lifetime of the silica final-focus lenses would be reduced. Figure 12 shows our predictions for these shots rates, which lower the effective lifetime to 18 and 9 years for a 2× and 4× increase in yield rate, respectively. This would present an incrementally small increase in the NIF operational cost over the 30-year facility lifetime.

KDP Impurity-Related Radiation Effects

The results of irradiation experiments with both gamma rays and neutrons indicate that only gamma rays have a measurable impact on the UV transmission spectra of KDP at integrated doses relevant to the NIF. Figure 13 shows the spectral results of two representative KDP and KD*P crystals for samples irradiated on the SPR-III (n° and gamma-ray source) and LLNL ^{60}Co (gamma-ray source only). The spectral features observed after similar gamma-ray doses from the two sources are nearly identical in shape and magnitude, demonstrating that the presence of ~1 MeV n° in the SPR-III does not produce observable optical damage in KDP. Direct knock-on neutron collisions will introduce noncrystalline defects; however, they do not appear to introduce optically absorbing species. No changes in refractive index were experimentally observed to within the experimental precision of 10^{-5}. The different spectra in Fig. 13 appear to correlate to the presence of impurities detected by wet chemical analyses of several of the crystals. Most KDP samples give rise to relatively featureless spectra, which show a slight overall increase in absorption (<0.03 cm^{-1} at 3ω). These samples are shown in Fig. 13(a) and (b). The strong absorption band at ~263 nm is typical of As-containing KDP and KD*P, as seen in Figs. 13(c) and (d). Other radiation-sensitive impurities have also been identified and are discussed below.

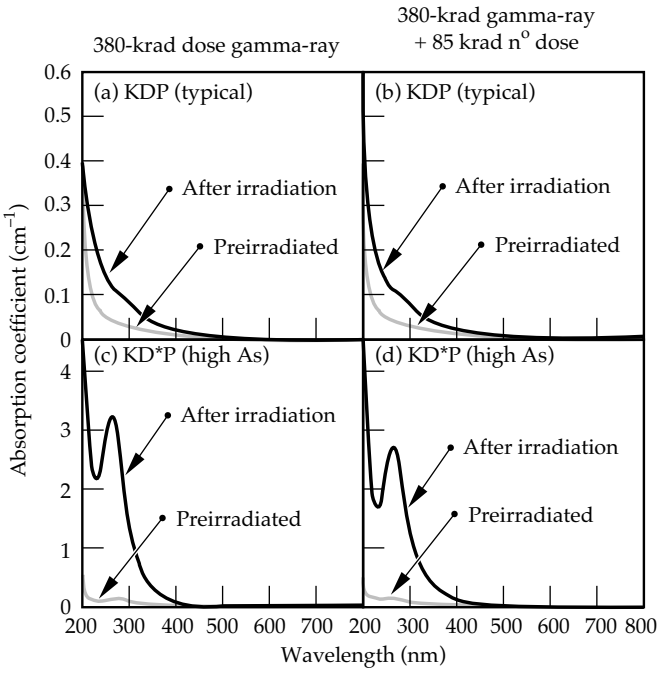

FIGURE 13. KDP and KD*P spectra before and after irradiation with (a) and (c) 380-krad gamma rays, or (b) and (d) 380-kRad gamma rays and 85 krad n°. Spectra are virtually identical with or without the 85-krad neutron dose indicating that gamma-ray damage is expected to dominate the radiation effects for NIF KDP and KD*P. Differences between samples types are due to impurities. All spectra are σ-polarized. (70-17-0596-1046pb01)

In the case of As, where the readily incorporated $(AsO_4)^{3-}$ substitutes isomorphically for the $(PO_4)^{3-}$ group, irradiation by gamma rays turns the anion complex into a color center with a peak absorption at 263 nm, which is presumably $(AsO_4)^{4-}$ based on evidence in the literature.[10,11] To test the correlation of As with the strongly absorbing peak at ~263 nm, we analyzed five samples using inductively coupled plasma (ICP) mass spectroscopy. Figure 14 shows the absorption coefficient of the 263-nm peak as a function of As concentration. In this case, the absorption coefficient was taken from spectra collected after irradiation on the SPR-III (for a gamma-ray dose of 380 krad). A linear regression to the data appears to be a good fit, indicating that As is responsible for the absorbing defect center.

Because As impurities appear to play the most important role in radiation-induced damage in all of the materials studied to date, we recently completed a study to understand the dose dependence of this phenomena. This study allows for predictions of NIF performance based on the integrated gamma-ray dose present in the final optics package as a function of time. Figure 15 is a compilation of results from the SPR-III pulsed nuclear reactor, the LLNL ^{60}Co continuous gamma-ray source, the LLNL pulsed-spallation gamma-ray source (LINAC), and the LANL pulsed spallation n^o and gamma-ray source (LANSCE). All of the data fall onto one curve, indicating that pulse length and radiation spectra do not play a primary role in modifying the radiation-induced damage in KDP. This result can be explained as follows. Gamma rays impart energy to the electronic portion of the atomic structure via Compton scattering. This first produces a ~100-keV electron, for each 1 MeV of initial gamma-ray energy, that then rapidly scatters via cascade e^-–e^- reactions to form multiple ~10-eV electrons. As a consequence, the initial energy of the gamma ray determines the number, rather than the damage characteristics, of final energetic electrons. The ~10-eV electrons next form defects in the material by trapping at precursor sites (e.g., impurities). This simple mechanism is linearly related to the time-integrated, radiation-induced electron density in the conduction band of the material, and does not depend on the initial gamma-ray spectrum or temporal pulse length to first order.

Based on the As precursors described above, we propose a simple mechanism, where

$$\left(AsO_4\right)^{3-} \xrightarrow{\text{gamma rays}} \left(AsO_4\right)^{4-} \xrightarrow{\text{gamma rays}} \left(AsO_3\right)^{2-} + O^{2-} \quad . \tag{8}$$

The $(AsO_4)^{4-}$ species causes the 263-nm absorption shown in Fig. 13(c), whereas the $(AsO_3)^{2-}$ species is believed to have minimal observable absorption. Initial conditions are determined from the concentration of As in the crystal, and all of the As is assumed to be of the form $(AsO_4)^{3-}$. A simple set of coupled rate equations for the concentration of $(AsO_4)^{3-}$, $(AsO_4)^{4-}$, and $(AsO_3)^{2-}$:O^{2-} lead to an analytic solution for the absorption coefficient at 3ω of the form:

$$\alpha = \frac{A_3^0 \sigma_{As} s \beta_{32}}{\left(\beta_{21} - \beta_{32}\right)} \left[\exp\left(-D'\beta_{32}t\right) - \exp\left(-D'\beta_{21}t\right)\right] \quad . \tag{9}$$

The parameters used to fit the data in Fig. 15 using Eq. (9) are defined and quantified in Table 4.

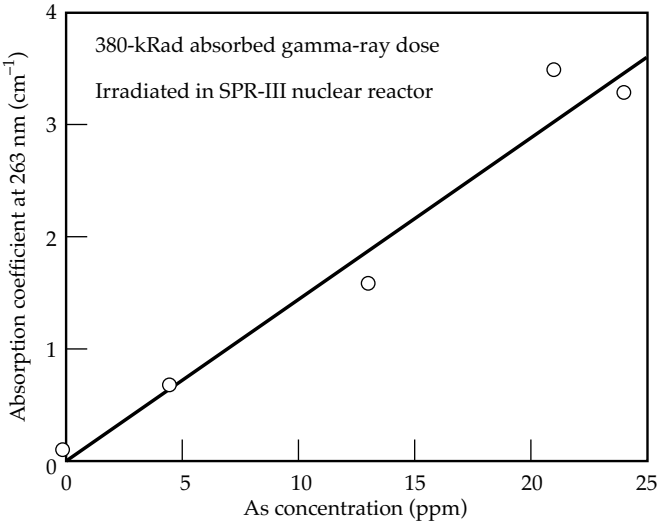

FIGURE 14. Arsenic concentration in ppm by weight vs 380-krad gamma-ray-induced σ-polarized absorption coefficient at 263 nm for several different KDP and KD*P samples. The good linear correlation suggests that As is a precursor for the radiation-induced 263-nm absorption. (70-17-0596-1047pb01)

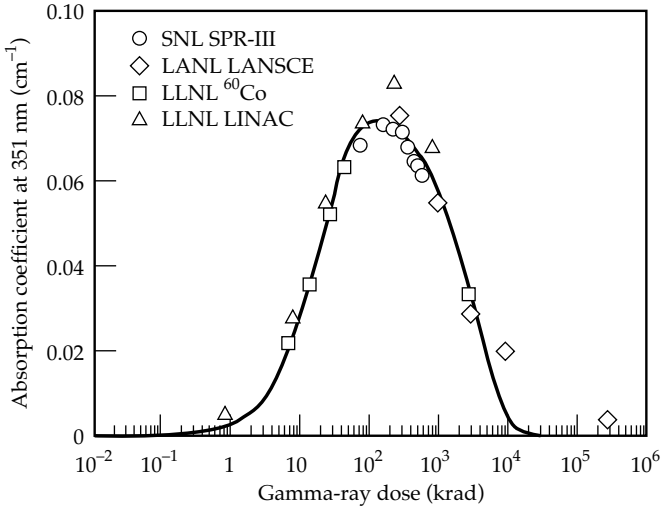

FIGURE 15. Gamma-ray-induced absorption at 3ω (351 nm) as a function of gamma-ray dose. For reference, the NIF is expected to have 160 krad for each decade of operation. Independent data from the source characteristics suggests that the total integrated dose, independent of gamma-ray spectral or temporal characteristics, is adequate for phenomenologically modeling radiation damage in the NIF. (70-17-0596-1048pb01)

From Table 4, we can predict the 3ω transmission of a NIF tripler KD*P crystal, taken to be 0.95 cm thick, for different D–T fusion yields and As impurity concentrations. Figure 16 shows predictions for three different fusion-yield scenarios on the NIF, ranging from a baseline operation of 385 MJ/year to four times this rate (higher gain per shot and/or higher shot rate) for crystals with the same amount of As as a recent crystalline boule grown for the NIF prototype Beamlet Laser System (4.5-ppm As). In any of these cases, the transmission of the tripler drops gradually to 93% within ~1 year. It is clearly undesirable to have this level of loss routinely on the NIF following the first year of full-yield operation. The dotted line in Fig. 16 shows the predicted transmission of a tripler KD*P crystal for 0.5-ppm As. The transmission of this crystal is expected to exceed 99% for the lifetime of the facility. Consequently, 0.5 ppm is the maximum level of As that would be desirable in NIF KD*P triplers. It should be possible to hold the As concentration below this value by using high-purity starting materials.[25]

Impurities other than As could also cause problems in KDP at ppm levels. To test this hypothesis, we irradiated 15 KDP crystals using 14 different impurity dopants and one undoped sample. Results using the SPR-III are summarized in Table 5 and Fig. 17. We found that other impurities—most notably metals, such as Al, Fe, As, Cr, Pb, and V—can lead to significant radiation-induced absorption in KDP. We obtained the concentrations of all the dopants in the crystals, using inductively-coupled plasma mass spectroscopy, in the growth solution and spectra before and after a dose of 1.4×10^{15} n^o/cm^2 and 473 krad of gamma rays. Even thought it is clear that many impurities can cause problems, it is not practical to test the entire periodic table. Consequently, a testing procedure, that uses a readily available radiation source, such as the ^{60}Co source at LLNL, will likely be used on actual starting materials that have been grown into test pieces prior to growth of large boules.

Figure 18 presents typical σ-polarized spectra used to obtain the results in Table 5. The spectra in Fig. 18(a) is for a crystal grown with no deliberate doping, and the resulting change in transmission is minimal in the wavelength region of interest. Figures 18(b) through (d) are for samples doped with Al, Cr, and Pb, respectively. Many of the spectra have absorptions peaked at 266 nm, both before and after irradiation, that look

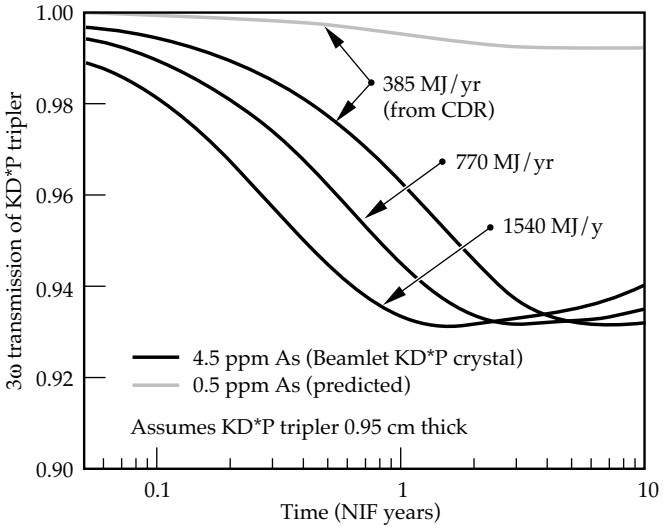

FIGURE 16. Predicted transmission of the NIF KD*P tripler crystal as a function of time for different fusion-yield assumptions and levels of As impurities. (70-17-0596-1049pb01)

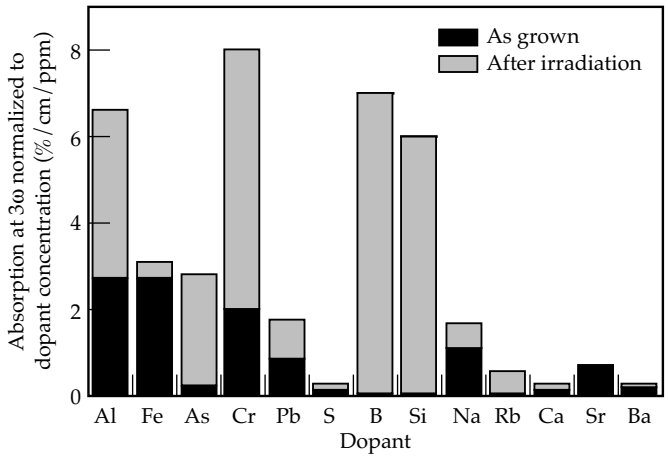

FIGURE 17. Experimental results of irradiating impurity-doped KDP with 473 krad of gamma rays. Absorption coefficients are weighted for concentration in ppm by weight. (70-17-0596-1050pb01)

Parameter	Value	Units	Source
As concentration in Beamlet KD*P boule (LL3LG), A_3°	8.3×10^{16}	cm^{-3}	Measured
Defect optical absorption cross section, σ_{As}	9.3×10^{-19}	cm^2	Data fit
Rate constant for first step in Eq. (8), β_{32}	0.047	1/krad	Data fit
Rate constant for second step in Eq. (8), β_{21}	3.0×10^{-5}	1/krad	Data fit
Gamma ray dose rate, D'	15.9	krad/yr	Ref. 1,19

TABLE 4. Parameters used to model data in Fig. 15 and to predict NIF fused silica final optics performance in Fig. 16.

TABLE 5. Experimental results of deliberately doping KDP with various impurities and irradiating with 1.4×10^{15} n^o/cm^2 at 1 MeV equivalent, or 84 krad of neutrons and 473 krad of gamma-rays (Si equivalent). The absorption coefficients are weighted for concentration and were background corrected with a blank sample that showed induced absorptions of 0.0%/cm and 5.9%/cm before and after irradiation, respectively.

Impurity	Concentration in growth solution/crystal (ppm by weight)[25]	Peak absorption wavelength (nm)	Concentration weighted absorption at 3ω before irradiation (%/cm/ppm)	Concentration weighted absorption at 3ω after irradiation (%/cm/ppm)
Al	11/5	266	2.7	6.6
Fe	10/21	<290	2.7	3.1
As	1000/18	263	0.2	2.8
Cr	9/<4	358 and 270	>2	>6
Pb	50/10	<230 and 268	0.8	1.8
V	10/0.9	266	~20	~40
S	250/14	266	0.1	0.3
B	250/<1	266	>7	>7
Si	250/<1	266	>6	>6
Na	1000/15	266	1.1	1.7
Rb	250/26	218	0.6	0.6
Ca	250/34	266	0.1	0.3
Sr	100/0.8	276	0.7	0.7
Ba	100/20	266	0.2	0.3

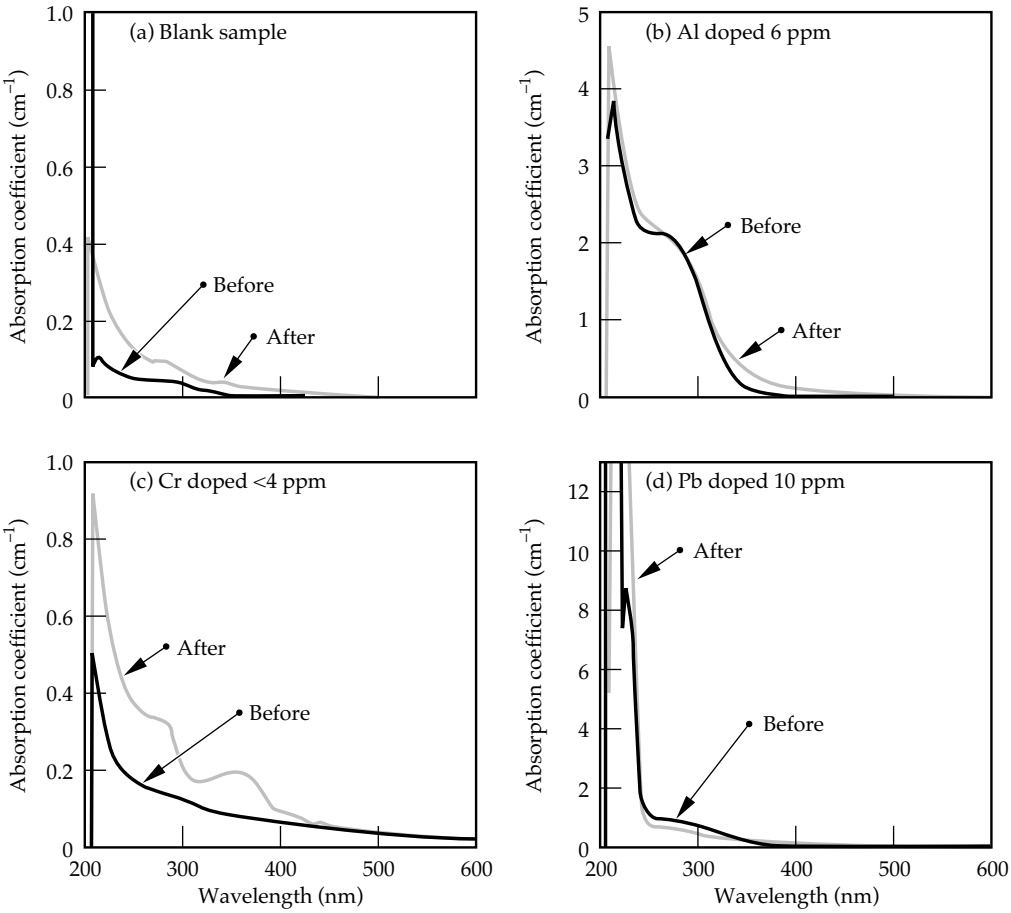

FIGURE 18. Absorption spectra of (a) control sample, and KDP doped with (b) Al, (c) Cr, and (d) Pb before and after irradiation with 1.4×10^{15} n^o/cm^2 and 464 krad of gamma rays.
(70-17-0596-1051pb01)

virtually identical to that in Fig. 18(b). This transition was observed to be only weakly polarized. Because many different dopants provide the same absorption spectra, this peak appears to be due to an intrinsic vacancy or F center in the KDP lattice induced by the presence of a nearby impurity. [11,26] Some of these dopants have measurable increases in 3ω absorption after irradiation. For example, Al-doped KDP appears to initially have ~3%/cm loss; but following irradiation, it has ~6%/cm loss due to the peak lowering and broadening as shown in Fig. 18(b). This behavior is also observed in general for V, S, B, Si, Na, Rb, Ca, Sr, and Ba dopants, although the magnitude of the effect normalized for concentration seems to vary. Other common impurities in KDP are metals such as Fe, Cr, and Pb. These lead to different absorption features, as noted in Table 3, with varying degrees of impact on 3ω transmission. The transition metals also appear to be more sensitive, in general, to gamma irradiation.

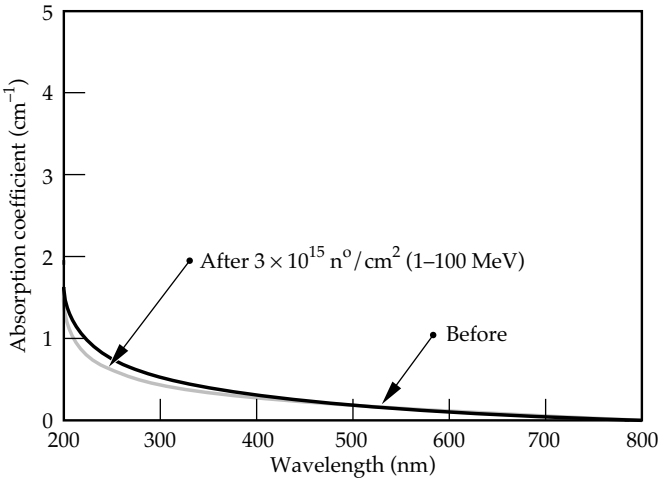

FIGURE 19. Fast-grown KDP sample (LLNL boule LNL-58) before and after irradiation at LANSCE with ns-pulsed, 1- to 100-MeV neutrons and gamma rays with up to ~100 years of the NIF dose at CDR shot rates and assumed yields. (70-17-0596-1052pb01)

High-Energy Neutron Irradiation Experiments

A remarkable outcome of our experiments is the lack of absorption in KDP following irradiation with neutron energies of ~1 MeV. The NIF is expected to produce neutrons that are primarily at 14 MeV directly from the D–T fusion reaction. Consequently, we performed experiments at CEA Sames with 14-MeV n^o irradiation and at LANSCE with 1- to 100-MeV n^o irradiation. Neutron fluxes ranged from 2×10^{14} n^o/cm^2 on Sames to as high as 3×10^{17} n^o/cm^2 on LANSCE. These high-energy neutron irradiations agree with the previous 1-MeV SPR-III neutron-irradiation results in that there are no observable neutron-induced effects in the absorption of the material. Figure 19 shows a typical result for very high-purity KDP irradiated to 3×10^{17} n^o/cm^2. This neutron flux is equivalent to ~100 years of operation on the NIF at 385 MJ/year thermonuclear yield, as assumed in the CDR. The increase in absorption at 3ω was only 5.6 %/cm even after such a large dose. KDP showed significantly less change in UV absorption than fused silica, which is normally assumed to be the "optimal" radiation-resistant optical material. As discussed above, KDP with impurities can have significantly larger induced absorption.

This sample serves as important proof that, with sufficient purity, KDP can withstand the radiation environment on the NIF and have minimal radiation-induced absorption losses at 3ω (<1% per decade of NIF yield). There must, of course, be displacements induced in the crystals from direct-neutron knock-on collisions, but they do not appear to manifest themselves optically at doses relevant to the NIF. This situation may arise from either the lack of natural color centers capable of near-UV or visible absorption, as opposed to vacuum-UV, or possibly from rapid self-annealing of the local displacements at room temperature. Our data suggest that secondary gamma irradiation appears to induce virtually all of the observed damage in KDP.

Summary

We performed a variety of neutron and gamma-ray irradiation experiments in the SNL SPR-III, LANL LANSCE, CEA Sames, and LLNL ^{60}Co and LINAC facilities. These facilities provide complementary sources of gamma rays and neutrons with various energy and pulse formats. We focused on high-energy, penetrating radiation (gamma rays and neutrons) that will propagate through the debris shield and supply a 3-krad dose from neutrons and gamma rays to the NIF final optics for each 20-MJ-equivalent NIF shot. From our experiments and modeling, fused silica (such as Corning 7980 and Heraeus Suprasil) is expected to have <1% loss at 3ω in the final-focus lens after 30 years of use at baseline NIF D–T fusion-yield levels. The optical absorption is due both to neutron-induced displacements and gamma-ray-induced color center formation. Neutrons induce an absorption peak centered at 246 nm, whereas gamma rays introduce absorption peaks centered at 210 and 300 nm in high-purity fused silica and fused quartz, respectively. Increasing the shot rate or yield by 4 times over CDR assumptions is expected to decrease the effective lifetime of the focus lens to 8 years for a ~1% loss. If fused quartz (such as Heraeus Herasil 1)

is used, 1% losses are reached within 1 year for CDR-level fusion yields. Therefore, it is advisable that only radiation-resistant, synthetic fused silica be used for the final-focus lenses.

Neutron collisions do not appear to degrade the optical properties of KDP at NIF-relevant fluences. Gamma rays can cause significant problems if impurities, such as As, are present at ppm levels. For As, which appears to be a common impurity, we constructed a physical picture and measured the quantitative parameters necessary to model the radiation-induced losses expected for KDP and KD*P. We also found that other impurities, such as Al, Fe, As, Cr, Pb, and V, can cause significant problems at ppm concentrations. Assuming these impurities are at acceptable levels, the neutron and gamma-ray damage to KDP arrays should not present a significant problem for more than one decade of NIF operation. Using the LANSCE facility, which has a more severe radiation environment than that expected on the NIF, the purer growths of KDP at LLNL showed virtually no observable degradation (<1%/cm losses) at up to the equivalent dose of ~100 NIF years.

Acknowledgments

We especially thank D. Berry and P. Griffin of SNL for their invaluable efforts in coordinating and performing the SPR-III experiments, and S. Sterbenz and W. Sommer of LANL for their enabling support and insight at LANSCE. W also gratefully thank E. Beriot and P. Schneider of CEA for their coordination of the Sames experiments in France. At LLNL, we thank C. Orth for discussing the neutronic cross sections with us, M. Tobin and J. Latkowski for calculating the radiation source characteristics, T. Diaz de la Rubia for sharing his insights into the neutronic defect mechanisms, and J. Marion, M. Yan, N. Zaitseva, J. Atherton, J. Campbell, and J. DeYoreo for providing the KDP samples and impurity concentrations and for their interest and guidance. We also thank R. Torres for the ICP mass spectroscopy work, and T. Cowan for performing and enabling the e^- spallation experiments. We also thank M. Singh for sharing his RTNS-II data taken in 1987 and more recent insights, and R. Vallene and P. Thelin for sample fabrication.

Notes and References

1. W. A. Bookless and D. Wheatcraft, *Energy & Technology Review*, Lawrence Livermore National Laboratory, Livermore, CA, UCRL-52000-94-12 (1994).
2. C. D. Orth, S. A. Payne, and W. F. Krupke, *Nuclear Fusion* **36** (1), 75–115 (1996).
3. A. Smakula, *J. Opt. Soc. Am.* **40**, 266 (1950).
4. R. A. Weeks and C. Nelson, *J. Am. Ceram. Soc*. **43**, 399 (1960).
5. D. L. Griscom, *J. Ceram. Soc. Japan* **99**, 923 (1991).
6. D. L. Griscom, "Nature of Defects and Defect Generation in Optical Glasses," (SPIE—International Society for Optical Engineering, Bellingham, WA, 1986; *Proc SPIE*, **541**) p. 38–59.
7. M. Rothschild and D. J. Ehrlich, *J. Vac. Sci. Technol. B* **6**, 1 (1988).
8. M. Rothschild, R. B. Goodman, M. A. Hartney, et al., *J. Vac. Sci. Technol. B* **10**, 2989 (1992).
9. D. J. Krajnovich, I. K. Pour, A. C. Tam, et al., *SPIE Proceedings* **1848**, 544 (1992).
10. A. N. Levchenki, V. M. Shulga, and A. O. Doroshenko, *Sov. Phys. Solid State* **32**, 1432 (1990).
11. G. N. Pirogova, Y. V. Coronin, V. E. Kritskaya, et al., *Inorg. Materials* **22**, 97 (1986).
12. C. D. Marshall, J. A. Speth, and S. A. Payne, "Induced Optical Absorption in Gamma and Neutron Irradiated Fused Quartz and Silica," Lawrence Livermore National Laboratory, Livermore, CA, UCRL-JC-122652; submitted to *J. Non-Crystalline Solids* (1995).
13. W. U. Condon and H. Odishaw, *Handbook of Physics* (McGraw-Hill, New York, 1967).
14. D. H. Levy, K. K. Gleason, M. Rothschild, et al., *Appl. Phys. Lett*. **60**, 1667 (1992).
15. M. Guzzi, M. Martini, A. Paleari, et al., *J. Phys. Condensed Matter* **5**, 8105 (1993).
16. H. Imai, K. Arai, J. Isoya, et al., *Phys. Rev. B* **44**, 4812 (1991).
17. R. A. Weeks, *J. Non-Cryst. Solids* **179**, 1 (1994).
18. R. A. Weeks, *J. Am. Ceram. Soc*. **53**, 176 (1970).
19. J. Latkowski, Lawrence Livermore National Laboratory, Livermore, CA, personal communication (1995).
20. *Sandia National Laboratories Radiation Facilities*, (1985), Third Edition, SAND83-0598, Eds. G. A. Zawadzkas, P. A. Kuenstler, and L. M. Choate, available from National Technical Information Service, U. S. Department of Commerce, Springfield, VA.
21. T. Diaz de la Rubia and W. J. Phythian, *J. Nucl. Materials* **191**, 108 (1992).
22. M. S. Livingston and J. P. Blewet, *Particle Accelerators* (McGraw-Hill, New York, 1962).
23. J. Wong, T. Diaz de la Rubia, M. W. Guinan, et al., *J. Nucl. Materials* **212**, 143 (1994).
24. T. Diaz de la Rubia, M. W. Guinan, A. Caro, et al., *Radiation Effects in Solids* **130**, 39 (1994)
25. J. Atherton and J. DeYoreo , Lawrence Livermore National Laboratory, Livermore, CA, personal communication (1995).
26. M. Yang, Lawrence Livermore National Laboratory, Livermore, CA, personal communication (1996).

Temporal Pulse Shaping of Fiber-Optic Laser Beams

S. C. Burkhart

F. A. Penko

Introduction

Precise temporal pulse-shaping of the laser beams for inertial confinement fusion (ICF) experiments has become increasingly important over the last 15 years, as better understanding has been made of optimal target drive conditions.[1] ICF targets have been shown to reach higher temperatures and better convergence when the laser drive is increased in a controlled manner during the drive pulse duration, which mitigates premature heating of the capsule interior. Computer simulations and experimental campaigns have confirmed the advantages of such a shaped laser drive. Another consideration is that small asymmetries in the initial laser drive imprint on the capsule, preventing implosion symmetry and limiting capsule convergence. This puts high value upon balancing the power for the multiple beams of lasers like Nova, Omega, or the National Ignition Facility (NIF). Since each beamline behaves somewhat differently, temporal shaping capability for each beam is planned for the NIF to achieve power balance. Finally, temporal pulse shaping is required to correct for pulse distortion due to gain saturation in the main amplifiers, which can cause the end of an initially square temporal pulse to droop by factors of up to 15:1 at the laser output. To achieve independent pulse shaping on the NIF, an integrated electrooptic modulator driven by a ~ 5-V arbitrary pulse shape generator will be used for the front end of the laser system,[2] when each laser beam is at low energy ($< 1\ \mu J$), as shown in Fig. 1. This article discusses the design and performance of this device.

Background

To date the Nova, Omega, Phebus, and Shiva lasers have all used conventional optical oscillators and amplifiers for laser-pulse generation, requiring bulk KDP Pockels cells for temporal pulse shaping.[3] Depending on the design, these Pockels cells have a half-wave voltage of either 4 or 8 kV, which places severe demands on the electrical waveform generation due to the high voltages. For Nova, the shaped pulse is derived from a square high-voltage pulse, generated by a photoconductive silicon switch[4] that discharges an initially charged 25-Ω transmission line. The square pulse is injected into a section of nonuniform transmission line designed to reflect an electrical pulse shape, generating the desired optical pulse shape through the Pockels cell. On Nova, the transmission line initially consisted of a microstrip line, but this was soon replaced by a variable impedance transmission line (VITL),[5] a manually adjustable nonuniform line. In 1989, Nova abandoned the VITL and returned to the microstrip transmission lines due to the difficulty in retuning the VITL to previously generated pulse shapes. Also in 1989, a numerical method for calculating the required stripline impedance was developed,[6] a

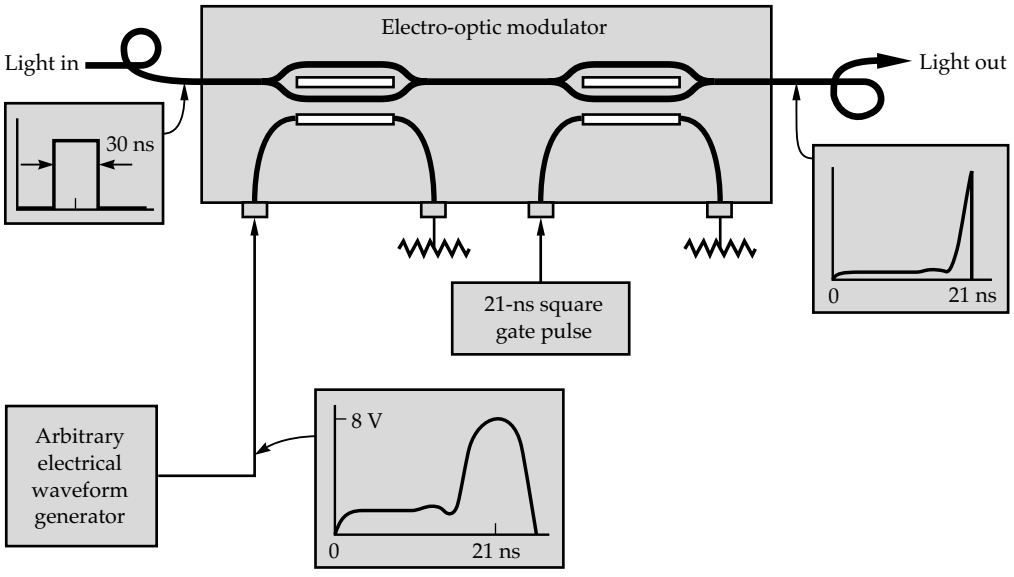

FIGURE 1. The NIF pulse-shaping system, comprised of an electrooptic modulator, a square pulse generator, and an arbitrary electrical waveform generator. The electrooptic modulator (two Mach–Zehnder interferometers) modulates the fiber-provided laser light using electrical pulses from the arbitrary waveform generator (AWG) and the square pulse generator. The second Mach–Zehnder interferometer is necessary to achieve > 10^5 on/off contrast. (70-50-0195-0185pb01)

technique now implemented on Omega and Phebus. The limitation of this technique is that each different pulse shape requires a new microstrip transmission line to be fabricated, similar to that shown in Fig. 2.

One major development from the Beamlet project[7] is a new type of laser master oscillator and pulse shaping system based on 1.053-μm fiber-optic lasers and components.[8] In this new system, beam intensity is controlled by an integrated optic Mach–Zehnder interferometer (electrooptic modulator), which has an extinction voltage of only 10 V. This advance opened up new approaches to pulse shaping, which on Beamlet was originally accomplished using transmission lines periodically coupled by potentiometers. This arrangement provided pulse-adjustment capability for monotonically increasing pulses, but was still was not amenable to computer control.

In 1994, we began to develop a fully computer-controllable electrical pulse shaping system capable of driving the Beamlet-style electrooptic modulator. Haner and Warren[9,10] set precedence for this approach by developing an electrical technique based on microwave GaAs field-effect transistors (FETs) to generate subnanosecond shaped pulses for laser beam modulation and subsequent compression to subpicosecond duration. Their circuit consisted of six GaAs-FETs connected in parallel through coupling capacitors to construct short shaped pulses. The method of Haner and Warren demonstrated the speed needed for ICF lasers, but the parallel connection approach was not extendable to large numbers of GaAs-FET sections. The arbitrary waveform generator (AWG) we developed bypassed these limitations by using a traveling wave architecture and a reflection-free trigger system. We have modeled[11] the circuit, performed device characterization experiments, and fabricated a 14-element unit.

Waveform Generator Principles

The waveform generator is based on the summation of short (250-ns) pulses sequenced in time and with differing amplitudes. This is similar to the digital-to-analog converter in a compact disc player, but at a speed beyond the state of the art. In the following two sections, we describe the wave-summing approach and discuss some of the practical issues with the electrical circuitry.

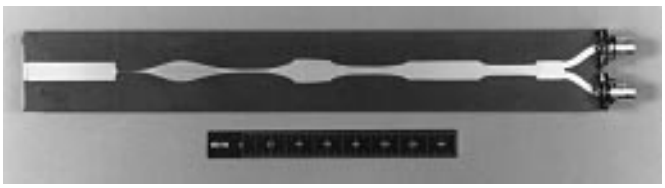

FIGURE 2. An example of the nonuniform transmission lines synthesized for pulse shaping on the Nova laser. This particular nonuniform transmission line generates a "picket-fence" pulse, consisting of two small prepulses followed by a main drive pulse, for Nova target experiments. (70-50-0396-0503pb01)

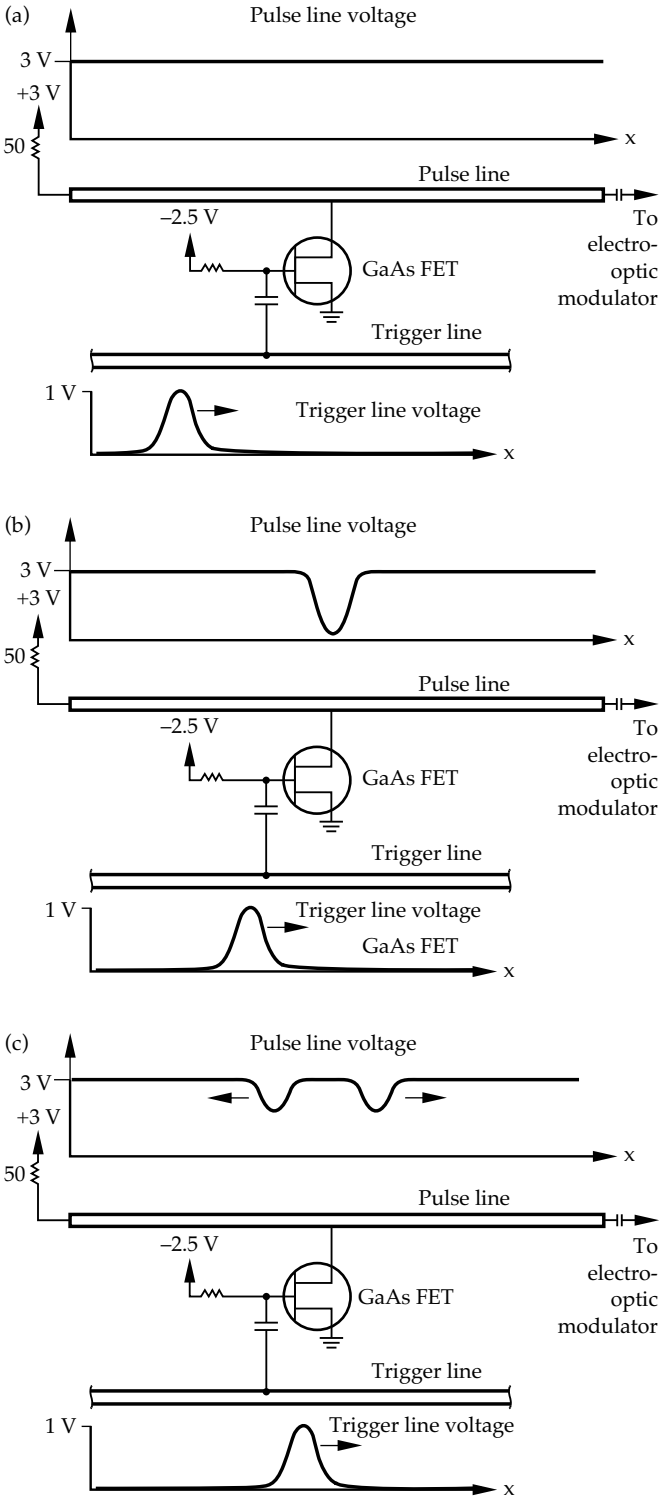

FIGURE 3. The AWG concept in three stages: (a) A 1-V trigger pulse is launched onto the trigger transmission line. The initially quiescent pulse transmission line is tied to +3 V through a termination resistor. (b) The trigger pulse turns on the GaAs field-effect transistor (FET) as it propagates past the coupling capacitor. This creates a dip in the pulse line voltage proportional to the initial GaAs-FET bias voltage (–2.5 V). (c) The voltage dip is really composed of two counterpropagating pulses: the pulse traveling to the right becomes part of the shaped pulse, and the pulse propagating to the left is absorbed by the termination. The trigger pulse propagates to the next GaAs-FET stage. (70-50-0396-0504pb01)

Impulse Generation and Traveling Wave Summation

Arbitrary waveforms are assembled using a large number of the basic circuit sections shown in Fig. 3. Each section consists of a power GaAs-FET connected between the charged transmission line and ground, activated by the impulse from the trigger line. When 1 V of the trigger impulse is coupled to the GaAs-FET gate, it turns on, conducting current in proportion to the initial bias pulse on the gate, as shown in Fig. 3(b). An opposite polarity replica of the trigger pulse is generated onto the pulse line, composed of two counterpropagating pulses each containing half the amplitude. The left-going pulse is absorbed by a terminator shown on the left side of Fig. 3, but the right-going pulse becomes part of the overall shaped pulse. The amplitude of the generated pulse is dependent upon the initial bias (V_{b1}, V_{b2}, etc.), because the GaAs-FET does not turn on until the gate voltage exceeds approximately –2.2 V relative to the source (the grounded terminal in this circuit). If the bias is initially set to –4.0 V, the 1-V trigger pulse does not turn on the GaAs-FET and no impulse is generated on the pulse line. On the other hand, if the bias is initially –2.2 V, it turns on strongly, making an impulse in excess of 1 V. For bias voltages intermediate between these two extremes, the impulse amplitude follows a square law, $I_{ds} \propto (V_{gs} - V_{TO})^2$ where V_{gs} is the gate-to-source voltage due to the bias plus the trigger voltages and V_{TO} is the gate cutoff voltage (nominally –2.2 V).

Each of the elemental impulses traveling to the right becomes a time-slice of the overall shaped pulse (Fig. 4). The timing between the trigger line and the pulse line is set to generate impulses at a specific rate. We chose four gigasamples per second (GS/s) based on an analysis of the temporal resolution required to synthesize NIF pulse shapes. For this data rate, the trigger delays shown in Fig. 4

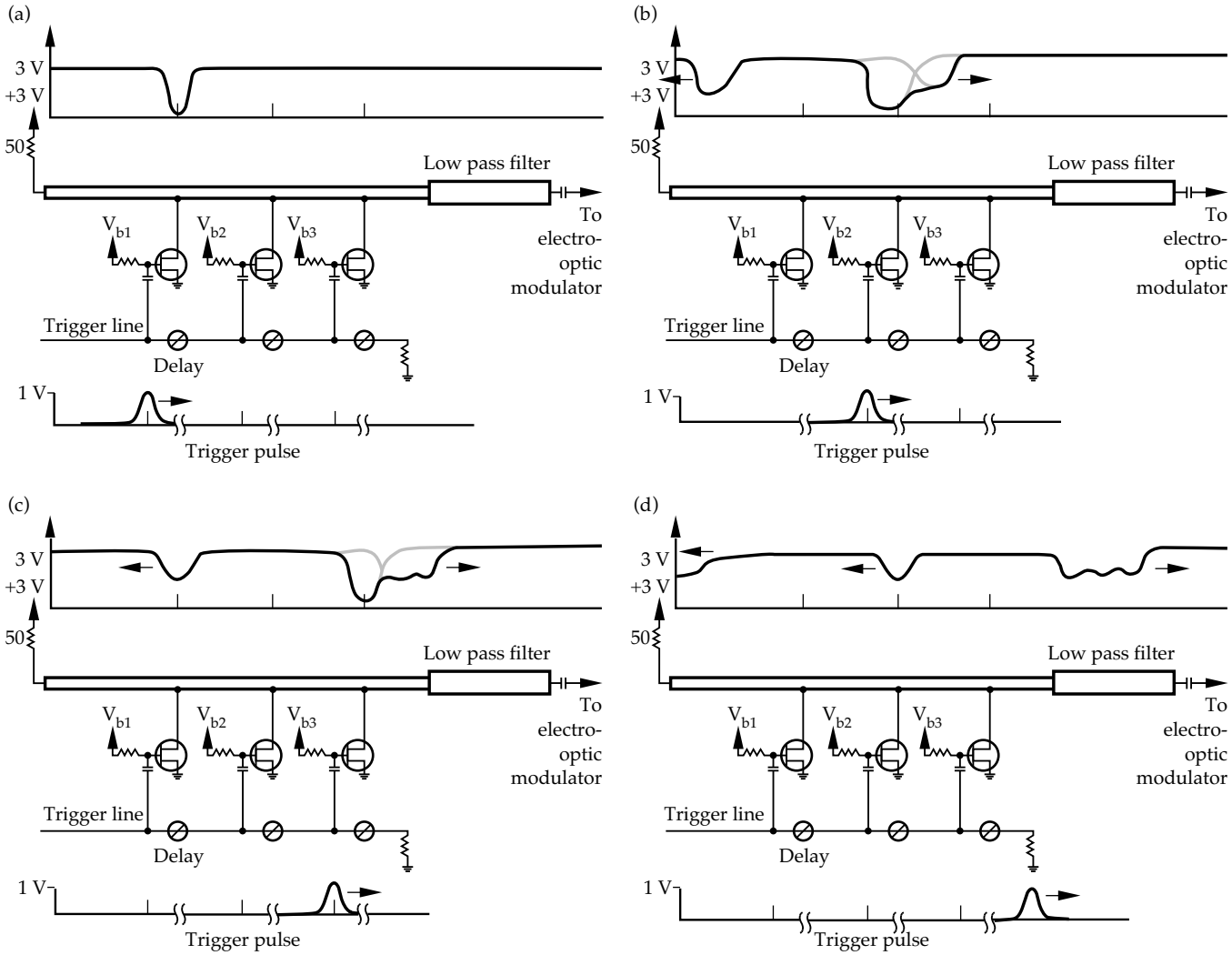

FIGURE 4. A square pulse generated from three pulses. (a) The first pulse is generated by the first GaAs-FET, with the pulse amplitude set by the bias voltage V_{b1}. For this drawing, $V_{b1} = V_{b2} = V_{b3}$. (b) The trigger pulse delay makes the second GaAs-FET turn on just after the first pulse propagates past, summing the second impulse (set by V_{b2}) to the shaped pulse. (c) A third impulse (set by V_{b3}) is added onto the end of the shaped pulse. (d) The final, shaped, square pulse remains after the left-propagating pulses have traveled towards the termination. The 4-GHz sinusoid on the top of the square pulse is strongly suppressed by the 1-GHz low-pass filter (not shown). (70-50-0396-0505pb01)

are set to 250 ps plus the FET-to-FET delay along the pulse line. Also, the trigger pulse full width at half maximum (FWHM) is set to between 250 and 350 ps to overlap each subsequent elemental pulse onto the tail end of the previous one. The elemental pulses are summed with each amplitude independently set by the computer-controlled gate-bias voltages. The harmonics at multiples of the sampling frequency (4 GHz for our design) are suppressed by a 1.0-GHz maximally linear phase (Bessel) low-pass filter at the generator output. This constitutes a 4-GS/s AWG, with a 1-GHz bandwidth, and a pulse length limited only by the number of GaAs-FETs sequenced along the transmission line. Presently, commercial waveform generators are limited to 1 GS/s, with a bandwidth of 200 Mhz, at a cost unacceptable to the NIF Project.

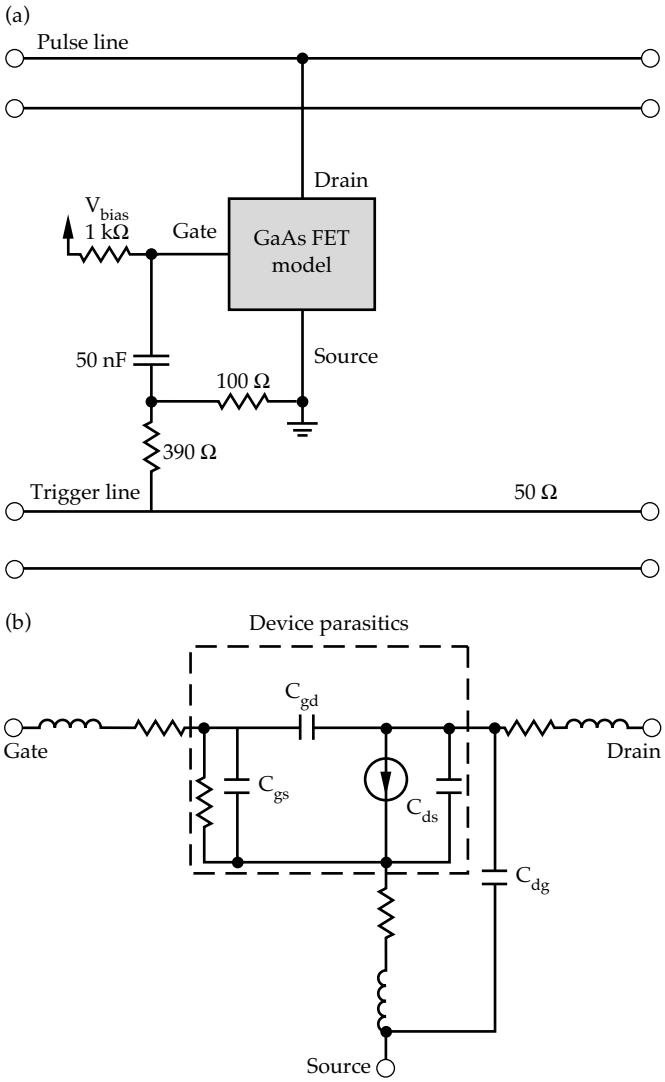

FIGURE 5. Circuit representation of each GaAs-FET section. (a) Bias is provided through a 1-kΩ resistor, and the trigger pulse propagates through the 50-nF capacitor to the GaAs-FET gate. The 100-Ω resistor to ground speeds up the switching. (b) Detailed model of the GaAs-FET parasitic elements. The key elements are C_{gd} and C_{ds}, which cause discontinuities (and reflections) on the pulse line. We compensate for the capacitive load by decreasing the line impedance. (70-50-0396-0506pb01)

Transmission Line Compensation and Trigger Distribution

Figure 5 shows the complete circuit model for the "building block" described above. Ideally, the GaAs-FET acts as a voltage-controlled current source when on and as an open circuit when off. This ideal behavior is modified by the stray inductance, capacitance, and lead resistance inherent in the GaAs-FET structure and the packaging, as shown in Fig. 5(b). Circuit modeling and experiments demonstrated that 4-GS/s operation is possible if the gate node impedance is less than 240 Ω. Going to higher speeds (more than 4 GS/s) requires a lower gate impedance with a commensurate increase in trigger-pulse attenuation.

The other significant parasitics are C_{gd} and C_{ds}. [Fig. 5(b)]. These capacitances effectively load the pulse line with distributed capacitance, lowering the transmission line impedance. This is shown by the measured time domain reflectometer (TDR) trace looking into a 14-element AWG in Fig. 6. The unloaded line impedance of 56 Ω decreased to 38.5 Ω when loaded with the GaAs-FETs. We found that we could compensate for GaAs-FET loading by increasing the line impedance such that it became 50 Ω when loaded. This requires precise knowledge of the parasitics, which we obtained by de-embedding[12] them using the manufacturer's S-parameters. We applied the de-embedding technique to the Mitsubishi MGF1801B GaAs-FET and obtained an equivalent shunt capacitance of 0.63 pF. This compares quite well to 0.56 pF calculated from the TDR data in Fig. 6.

Trigger pulse distribution is another important consideration for a long series of GaAs-FET sections. The trigger pulse is attenuated as it triggers each GaAs-FET in sequence, so we developed a technique for maintaining its amplitude. We accomplished this by matching the parallel combination of tap resistor and output trigger line to the input trigger line. This minimized reflective losses and

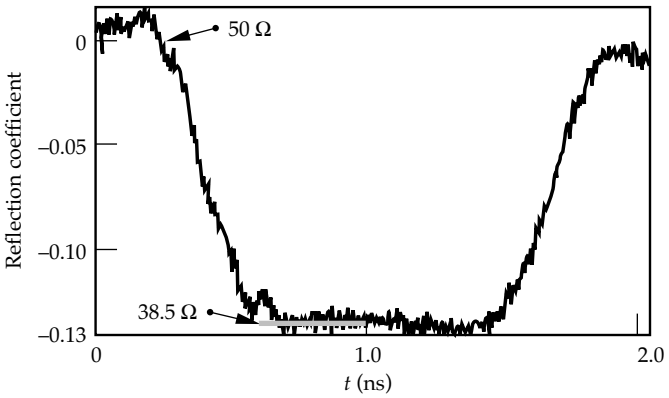

FIGURE 6. Time domain reflectometer (TDR) trace from a 14–GaAs-FET pulse-shaping transmission line. The capacitive loading of the GaAs-FETs reduces the line impedance from 55 to 38.5 Ω. Increasing the line impedance to approximately 80 Ω unloaded results in near 50-Ω performance after the FETs are installed. (70-50-0396-0508pb01)

maintained trigger amplitude within 5% along the 14-section distribution line. We found that it was always advantageous to start the line at the lowest realizable impedance, despite the discontinuity loss where the 50-Ω input cable connected to the printed circuit board. We used 25 Ω as a starting impedance in our prototype because a lower impedance would require an excessively wide transmission line.

Circuit Realization

A 14-stage arbitrary waveform generator was designed and fabricated using the printed circuit shown in Fig. 7.

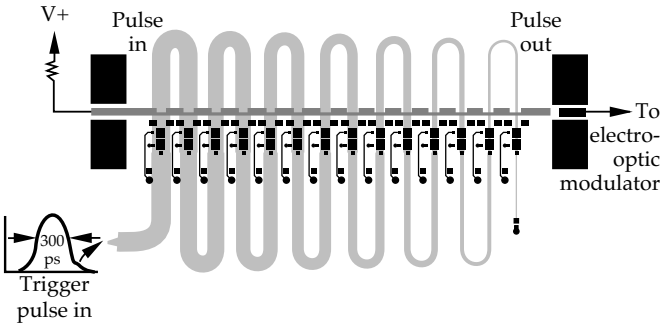

FIGURE 7. Circuit realization of a 14-section AWG. The pulse line is initially charged to voltage (V+), and a 300-ps FWHM trigger pulse is injected into the 25-Ω trigger line. Each GaAs-FET is mounted with its associated circuitry where the pulse lines and trigger lines cross. The printed circuit is constructed from teflon/glass precision microwave circuit board. (70-00-0895-1895pb02)

The circuit board material is a teflon/fiberglass matrix substrate, manufactured to tight tolerances for dielectric constant and substrate thickness, commonly used in microwave circuitry. It is designed as a four-layer board, three layers of 31-mil substrate sandwiched between four layers of copper plating. The first and third layers (starting from the bottom) are ground planes stitched together by numerous plated via holes. The second layer contains the trigger line, which involves a total of 3.5 ns of delay, and the top layer is printed with the pulse line circuit along with mounting pads for all the surface mount components. We used stripline construction for the trigger line to avoid modal dispersion inherent in microstrip, which tends to distort fast pulses. To reduce stray capacitance in the printed circuit, we soldered the GaAs-FETs directly to the edge of the pulse line with a minimum of lead length. Small sections of transistor leads on the board can have large fractions of a picoFarad of stray capacitance, enough to markedly affect the pulse line impedance. The transmission line was manufactured to have a loaded line impedance of $50 \pm 4\ \Omega$. A 4-Ω impedance mismatch causes ~ 4% voltage reflection. In comparison, the highest quality microwave SMA connectors are specified to $50 \pm 2.5\Omega$. We also measured the trigger line performance and verified that the trigger pulse maintains its shape and amplitude as it propagates past the 14 GaAs-FETs. There were reflections due to the capacitance of each GaAs-FET gate, but the circuit design mitigated the effect of these reflections.

We built a 28-stage, 7-ns pulse shape generator, consisting of two of the 14-stage circuits, and installed it in the Beamlet laser system. Figure 8 shows the system.

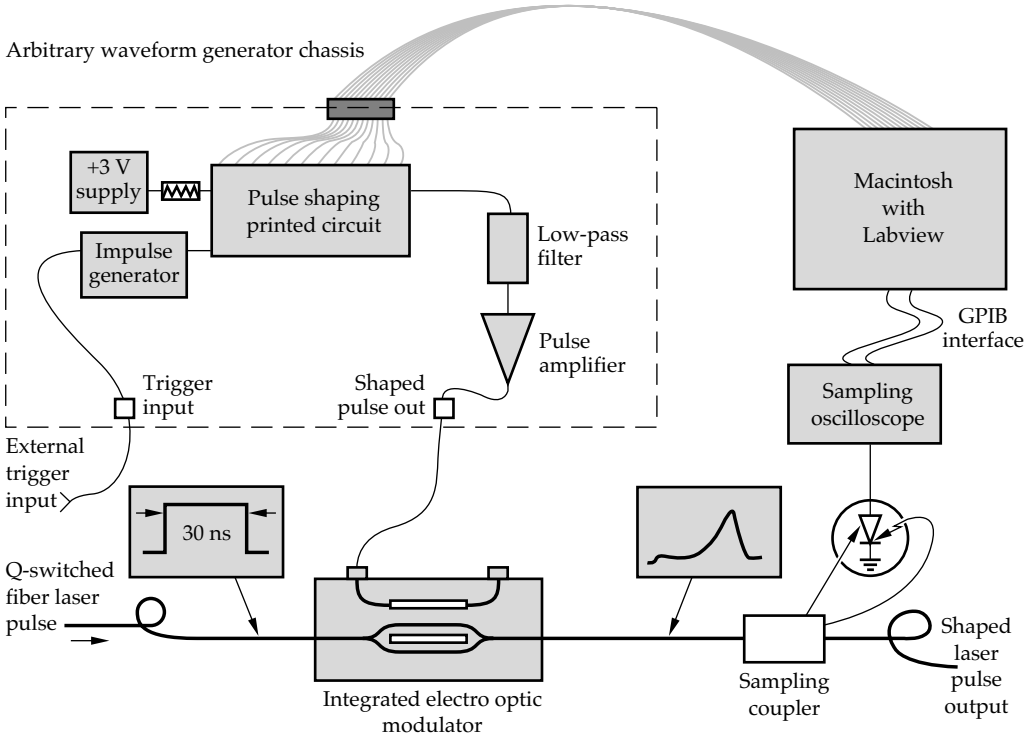

FIGURE 8. Prototype arbitrary optical waveform generation system for the NIF. A 30-ns pulse from the laser oscillator is amplitude-modulated by a Mach–Zehnder electrooptic modulator (only one of the two modulators on the chip is shown). The shape of the optical pulse is measured by a sampling oscilloscope, and the GaAs-FET bias voltages are adjusted until the desired pulse shape is achieved. (70-50-0396-0511pb01)

The AWG circuit is connected to the other supporting electronics. One of the key electronics is the impulse generator that generates the 300-ps trigger pulse. Originally we used an expensive, commercially available generator, but we found that a fixed-width impulse generator consisting of an avalanche diode and a chain of step recovery diodes, originally developed for impulse radar,[13] worked just as well for a small fraction of the price. The impulse generator as designed had a 170-ps FWHM pulse width at 28 V, which we stretched to 300 ps and attenuated to 4 V. The pulse shaping circuit is connected to a control computer that has 32 channels of 12-bit digital-to-analog output for setting the bias on each of the GaAs-FET stages. The shaped electrical pulse, nominally 1 V peak, is low-pass–filtered to remove the 4-GHz sampling noise and is amplified to 5 V to drive an integrated electrooptic modulator. The modulator is an integrated Mach–Zehnder interferometer, similar to that used in the Beamlet front end. The shaped optical pulse is sampled and diagnosed by a fast diode detector and sampling scope, and software written in Labview adjusts the pulse-shaping bias voltages to set and maintain the required optical pulse shape.

Experimental Results

The pulse-shaping system installed on Beamlet has been used to generate a number of relevant pulse shapes that are used (or planned to be used) in Nova, Beamlet, and NIF. Figure 9 shows the generation of a NIF-like pulse: it has the general shape of a NIF-like pulse, but the contrast is reduced to accommodate the diagnostics, and the overall pulse length is shortened to 7 ns to accommodate the subscale waveform generator. Generating this and other pulses is quite simple using feedback software written in Labview, which works in closed loop to minimize the error between the desired pulse and the pulse measured by the diagnostics. Generating a new pulse shape requires only that the user make a (time,intensity) text file, consisting of unequally spaced X-Y pairs in a two-column format. To attain the pulse peak, the feedback control system is not required to fit to the ideal pulse beyond the peak, instead the precipitous drop at the end of the pulse is handled by a pulse slicer. The contrast necessary for NIF has been demonstrated by this system where the electrical pulse was measured directly, instead of the optical pulse being measured. The electrooptic modulator has a $\sin^2(V/V_1)$ response, so for 500:1 optical contrast we need only 25:1 electrical contrast. This is easily measured by the system. However, practical operation with a 500:1 dynamic range demands two transient digitizer channels interfaced to the control system to accurately measure the foot and the peak. This task will be accomplished by mid-1997.

The pulse shape shown in Fig. 10 is the laser pulse required to produce a 3-ns FWHM temporally gaussian laser pulse at the frequency converted (351-nm) wavelength of Beamlet. The temporal shape was calculated by back propagating the tripled light through the frequency converters and the laser chain, back to the AWG. This pulse was useful for benchmarking previous small-spot laser damage experiments[14] against large-aperture Beamlet damage tests.

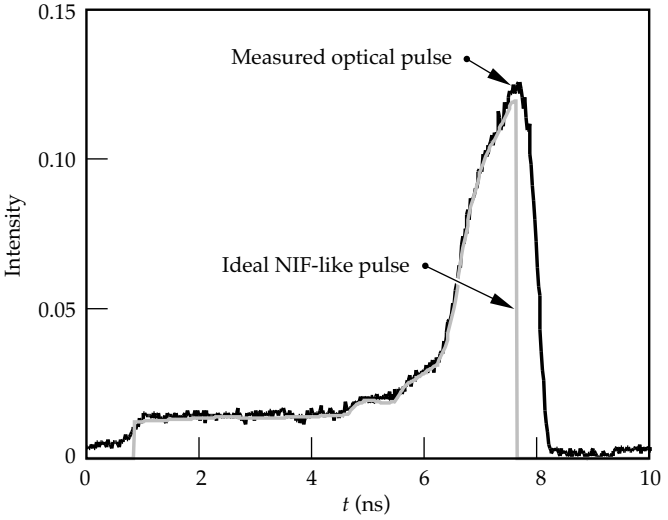

FIGURE 9. NIF-like pulse generated on a 7-ns (28-section) AWG. The NIF pulse is characterized by a long foot followed by a relatively short drive pulse. (70-50-0396-0512pb01)

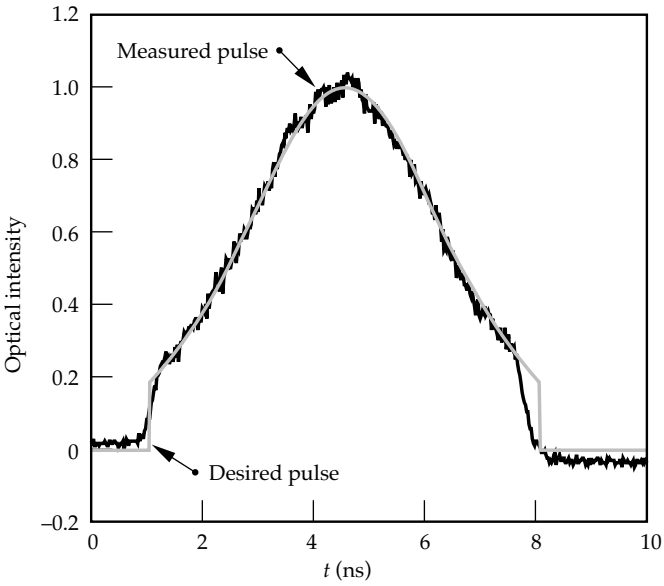

FIGURE 10. Optical pulse used for optics damage experiments. The object of this pulse was to generate a Gaussian-shaped 3-ns-FWHM 3ω pulse from Beamlet. (70-50-0396-0544pb01)

Alternative Applications

In addition to pulse shaping for ICF lasers, precision pulse shaping has several other notable applications that are being pursued. One application is its obvious use as a high-speed modulator of lasers for fiber-optic communications. We have been investigating the possibility of directly connecting the GaAs-FET stages to bit lines of a high-speed computer bus and clocking the data at multigigahertz speeds onto fiber-optic networks. For such a system, the AWG would be operated in the digital mode, in essence as a high-speed multiplexer. The present state of the art is up to 10 GB/s using very expensive GaAs chip-sets. Our AWG technology presents the possibility to operate in excess of 20 GB/s while offering significantly reduced costs relative to the other systems. This system also shows potential for preshaping data communication pulses to compensate for path-pulse distortion in long-haul telecommunications transmission.

Another application currently being pursued is a localized wave-mode generator. Localized wave modes are a form of radar pulses requiring precisely temporally shaped basis modes that, when a reconstructed in the far field, have been shown to stay localized in excess of ten times beyond that predicted by classical diffraction theory. To date, owing to the difficulty in producing subnanosecond shaped electromagnetic pulses, the only demonstration of such modes has been done using acoustic waves in water. Using the AWG to generate electrical pulses, we have already propagated individual 300-MHz localized wave-basis modes from a broadband antenna. The next step is to construct a 5×5 array of such radiators and verify the existence of localized wave modes in free space.

Conclusions

We have developed a computer-controlled arbitrary waveform generator that satisfies the NIF requirements for flexible laser pulse shaping. Technical advancements in a GaAs-FET–based wave summing architecture, element compensation, and efficient trigger-pulse distribution have been very successful in this demonstration. The 7-ns version of the arbitrary waveform generator fielded on the Beamlet laser has produced a number of challenging pulses for Beamlet experiments. Vendor development and production of a full NIF-length generator has begun, with the first prototype due for testing in the first half of fiscal year 1997. The NIF will require 192 such arbitrary waveform generators to be fielded by the year 2000.

Notes and References

1. J. Lindl, *Phys. Plasmas*, **2** (11), 3955–3957 (1995).
2. *National Ignition Facility Conceptual Design Report,* Lawrence Livermore National Laboratory, 7000 East Avenue P. O. Box 808, Livermore, CA 94550, UCRL-PROP-117093 Vol. 3.
3. E. Storm, *Laser Program Annual Report 84*, Lawrence Livermore National Laboratory, Livermore, CA, UCRL-50021-84, p. 2-13.
4. R. B. Wilcox, *Lasers and Particle Beams*, **4**,141–143 (1986).
5. G. M. McWright, *Rev. Sci. Instrum.* **56**(11), 2151–2153 (1985).
6. S. C. Burkhart and R. B. Wilcox, *IEEE Trans. on Microwave Theory Tech*., Vol. 38, pp. 1514–1518, 1990.
7. J. H. Campbell et. al., *ICF Quarterly Report* **5**(1), 1–85, Lawrence Livermore National Laboratory, Livermore, CA, UCRL-LR-105821-95-1 (1995).
8. B. M. Van Wonterghem et. al., *ICF Quarterly Report* **3**(1), 1–9, Lawrence Livermore National Laboratory, Livermore, CA, UCRL-LR-105821-93-1 (1993).
9. M. Haner and W. S. Warren, *Applied Optics*, **26**, 3687–3694 (1987).
10. M. Haner and W. S. Warren, *Appl. Phys. Lett.* **52**, 1458–1460 (1988).
11. S. C. Burkhart, *Voltage-Controlled MESFET Pulse Shape Generator*, LLNL internal report, Lawrence Livermore National Laboratory, Livermore, CA, UCRL-ID-116054 (1994).
12. J. M. Golio, *Microwave MESFETs 1/2 HEMTs*, Norwood, MA, Artech House, 1991, pp. 219–229.
13. T. E. McEwan, R. L. Hanks, and J. D. Kilkenny, *High-Voltage Picosecond Pulse Generation Using Avalanche Diodes*, LLNL internal report, Lawrence Livermore National Laboratory, Livermore, CA, UCRL-102565 (1990).
14. L. Sheehan et. al., *Proc. 25th Annual Boulder Damage Symposium*, **2114**, 559–568, SPIE, Bellingham, Washington (1993).

Studies of Energy Transfer Between Crossing Laser Beams in Plasmas

R. K. Kirkwood *B. B. Afeyan* *K. G. Estabrook*
W. L. Kruer *B. J. MacGowan* *J. D. Moody*
D. S. Montgomery *D. M. Pennington* *T. L. Weiland*
S. C. Wilks

Introduction

The amplification of light by the parametric decay of a laser beam propagating in a plasma has been studied since the inception of the inertial confinement fusion (ICF) program, primarily because it is a mechanism for scattering and loss of the laser's energy. Recent studies[1] show that the resonant nonlinear processes which excite plasma waves and lead to stimulated Raman and Brillouin scattering (SBS and SRS)[2] can also lead to the transfer of energy between laser beams under the right conditions. This stimulated energy transfer is analogous to four-wave mixing in nonlinear media,[3] although standard optics treatments do not include the propagation velocity of the plasma waves which affect the frequency matching conditions and limit the energy transfer. In past ICF experiments, symmetric illumination of the target has worked to prevent energy transfer between beams. In the National Ignition Facility (NIF), however, laser beams with different intensities and different angles of incidence will cross at the hohlraum entrance, where energy transfer may occur. Such energy transfer would be detrimental to the implosion symmetry and fusion yield. We have performed a series of experiments using the Nova facility to understand and control these effects.

The process by which light is transferred between two beams is the same as the process by which stimulated scattering grows from thermal noise. In both cases, the incident laser beam decays into an electrostatic wave, propagating in the plasma, and a scattered electromagnetic wave. The decay is initiated when it is "seeded" by a source of one of the decay waves. For stimulated scattering experiments, the seed wave is a very low amplitude electrostatic or electromagnetic wave that is generated by thermal noise, while in crossing beam experiments the seed wave is a second laser beam. The interaction of crossing beams is obviously favored over stimulated scattering because the initial seed is large and only a small amplification factor will result in substantial transfer of energy. However, the symmetry of the crossed beam interaction has suppressed the effect in previous ICF experiments in which the crossing laser beams had identical intensities, as well as identical incident angles. With identical beams in a stationary plasma, there can be no net energy transfer. Furthermore, the stimulated process can only occur when the incident and seed waves have different frequencies in the frame of the plasma, with fastest growth occurring when the difference frequency is equal to that of the resonant plasma wave. Thus, either a frequency difference between the incident and seed waves, or a plasma flow that Doppler shifts the frequency of one of the waves relative to the other, can allow the stimulated process to occur and transfer significant energy. In the NIF, the beams will be required to have different intensities and different incident angles, which results in different frequences in the frame of the flowing plasma, thus allowing for the possibility of resonant energy transfer between the beams.

To simulate the interaction of the four-color beams in NIF, we performed a series of experiments on Nova to study the transfer of energy between beams with slightly mismatched frequencies in a nearly stationary but otherwise NIF-like plasma. In these experiments, the frequency mismatch was achieved by tuning the frequency of the incident beam rather than relying on Doppler shifts from plasma flows. For the first time, the amplification of a probe laser beam by interaction with a second frequency shifted (pump) beam and a stimulated ion acoustic wave was observed. The amplification of the long wavelength (probe) laser beam reaches a maximum of 2.8 when the frequency difference $\Delta\omega$ of the two beams is in the vicinity of the ion acoustic resonance ($\Delta\omega = c_s\,|\Delta\mathbf{k}|$). Here, c_s is the acoustic speed and $\Delta\mathbf{k}$ **is** the difference in wave vectors between the two beams. The amplification is steady state in that it persists for many (~10^3) ion acoustic

periods and is resonant in that it is largest at a particular frequency difference. In addition, in the large, mixed species plasmas that are used in these experiments, we find that the amplification of the probe beam is independent of its intensity (up to a maximum average scattered intensity of 1.0×10^{15} W/cm^2). This indicates that the ion wave response n_1 remains unsaturated up to $n_1/n_0 \sim 1\%$, where n_0 is the unperturbed density.

Experimental Setup

The experiments were performed in an approximately spherical plasma[4] produced by eight $f/4.3$, $\lambda = 351$ nm beams. These heater beams have a 1 ns, square pulse shape with a total power of 20 TW (2.5 TW each beam) and pass through a 1 atm C_5H_{12} gas contained in a 500-nm-thick spherical polyimide shell with radius $r_0 = 1.3$ mm. Each heater beam is centered at the target center with a converging focus. The beam spot size at the target center is approximately equal to the target diameter, allowing spatially uniform heating. Two dimensional (2-D) numerical simulations using LASNEX[5] indicate that after $t = 400$ ps, a stationary plasma is formed (velocity $\leq 0.15\, c_s$), with a uniform density plateau ($\Delta n/n \leq 0.1$) in the region between $r = 250$ and 900 μm. By 1.4 ns after the beginning of the heater beam pulse, the outer edge of the plateau region has shrunk to approximately $r = 450$ μm by an incoming shock wave created by the ablation of the polyimide shell. The plasma parameters calculated by the simulation, and in agreement with measurements[4] are: electron density of $n_e = 10^{21}$ cm^{-3} (0.1 n_c, where n_c is the critical density for $\lambda = 351$ nm light) and electron temperature $T_e = 3.0$ keV.

The high-intensity pump beam and low-intensity probe beam are also $f/4.3$ and $\lambda_o = 351$ nm, and are aligned to cross at $r = 400$ μm near best focus for both beams. As a result, the interaction between the two electromagnetic waves occurs in the plateau region of the plasma, as shown in Fig. 1. This allows the ion wave that is driven by the beating of the two beams to propagate in a plasma in which gradients are minimized. The interaction beams have random phase plates (RPPs) which smooth the intensity profile and limit the spot size to 177 μm full-width half maximum (FWHM) (345 μm between first Airy minima) and the peak pump intensity to 1×10^{16} W/cm^2 (2×10^{15} W/cm^2 average inside the Airy minima) in vacuum. The beams have their polarizations aligned within 25° of parallel. The simulations indicate that the presence of the focused probe beam increases the temperature only slightly (~6%) in the vicinity of best focus.

The probe beam is adjusted to have a wavelength slightly longer than that of the pump with the wavelength separation ranging between 0.0 and 0.73 nm. The pump beam frequency is 10,527.7 Å (1ω). The technique used to provide the tunable frequency probe beam is based on nonlinear mixing of the two frequencies in

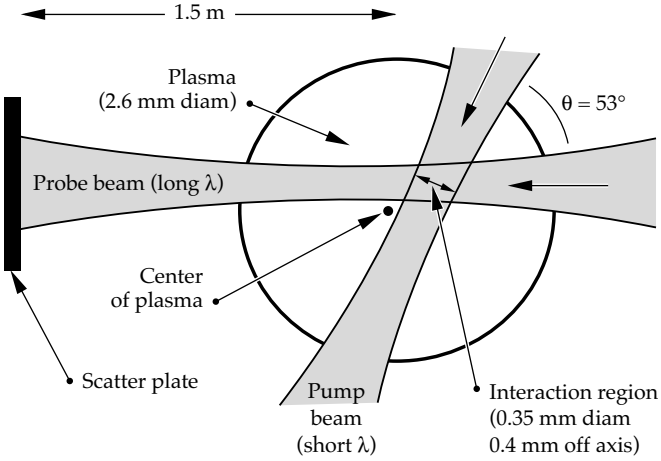

FIGURE 1. Experimental configuration showing an approximately spherical plasma and two interaction beams crossing in a homogeneous region off the plasma center. The two beams are detuned by $\Delta\lambda = 0.0$ to 0.73 nm to excite the ion acoustic resonance. The transmitted power vs time of the long wavelength probe beam is measured. (08-00-0296-0343pb01)

an optical fiber prior to injection into the laser chain.[6] Two photons at different pump frequencies mix together to create a comb of single frequency sidebands separated by the difference frequency between the two initial pump frequencies. The pump frequencies are produced by two Q-switched neodymium-doped yttrium lithium fluoride oscillators. The difference frequency is variable from 0.1–4.5 Å by tuning one of the oscillator frequencies via an intracavity etalon. The total number of frequencies produced is controlled by varying the oscillator intensities into the fiber. The probe frequency of interest is selected with a grating monochrometer located in the Nova preamplifier section and is frequency tripled (3ω) by potassium dihydrogen phosphate crystals after amplification. While up to 260 Å of bandwidth (FWHM) can be generated with the fiber-optic technique at 1ω, the maximum usable frequency range is ~32 Å due to gain narrowing in the laser amplifier chain, limiting the maximum frequency separation of the converted beam to 10.7 Å at 3ω.

The probe beam has a square pulse shape lasting 2.0 ns, which begins at the same time as the heaters ($t = 0$). The pump beam has a 1.0 ns square pulse shape that is delayed 0.4 ns so that the plasma in the interaction region is relatively homogeneous during the interaction period. The transmitted power of the probe beam is collected by a fused silica plate 1.5 m from the target, which is roughened to scatter the light over a broad angle.[7] This scattered light is imaged onto a fast photodiode and a gated optical imager. The photodiode is calibrated to provide a histogram of the probe beam power, which is transmitted through the plasma and onto the scatter plate. The imager captures a 2-D image of the light on the scatter plate during the 0.6 ns period when all beams are on and provides a measure of the directionality of the transmitted power during the period of the interaction.

Demonstration of Energy Transfer

The transmitted probe power waveforms, with and without a pump beam, are shown in Fig. 2, for the case of $\Delta\lambda = 0.43$ nm, and a normalized probe intensity of $I_{probe}/I_{pump} = 0.06$. The total transmitted energy without a pump beam is $49 \pm 7\%$ of the incident energy which is in agreement with a calculation of inverse bremsstrahlung absorption and refraction by the plasma.[7] This transmission is reproducible within $\pm 15\%$. The shape of the waveform in the pump-off case in Fig. 2 shows that the transmission first increases in time when the plasma temperature is increasing and then decreases in time after the heaters turn off at 1.0 ns and the plasma radiatively cools. Comparison of the waveforms in Fig. 2 shows an increase in the probe's transmitted power during the time the pump beam is on ($0.4 \le t \le 1.4$ ns). The pump on waveform is corrected to account for a small variation in the energy of the probe beam between the two shots. The transmitted probe power is nearly the same in the two experiments before the arrival of the pump. After $t = 0.4$ ns, the transmitted probe power rises in about 150 ps to nearly 1.7 times the level observed without the pump, indicating amplification of the probe by the pump. After the pump turns off, the probe power drops rapidly to equal the value observed without the pump. The amplification is determined from the ratio of the two traces and is found to vary between 1.6 and 1.8 during the 1-ns duration of the pump pulse. The average amplification A is determined by averaging over the 1 ns that the pump is on plus an additional 0.3 ns to include the signal delayed by the response of the detector, and is found to be 1.7 in this case.

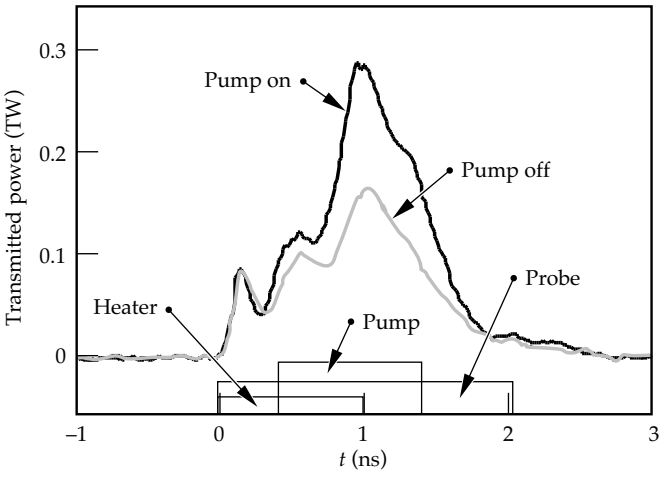

FIGURE 2. Measurement of the probe beam power transmitted through the plasma for the case $\Delta\lambda = 0.45$ nm and $I_{probe}/I_{pump} = 0.06$. In the pump on case, a 2×10^{15} W/cm^2 pump beam intersects the probe between 0.4 and 1.4 ns causing the probe to be amplified by a factor of 1.7 above the pump off case. (08-00-0296-0344pb01)

The amplification observed in Fig. 2 can be explained by scattering from an ion wave produced by the beating of the incident and pump beams. The interaction of the beams creates an ion wave in the plasma, as shown in Fig. 3(a), that scatters energy from the pump so that it propagates parallel to the probe beam, as shown in Fig. 3(b). The ion wave forms in response to the interference of the two beams, which generates a ponderomotive force that is periodic in space and time, and proportional to the product of the amplitude of the two beams. The initial ion wave amplitude is then proportional to the probe beam incident amplitude.

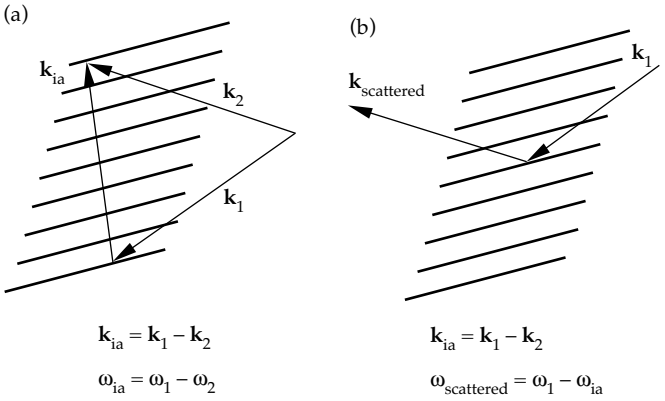

FIGURE 3. (a) Interference of the pump and probe beams creates an ion acoustic wave in the plasma with wave ventor $\mathbf{k}_{ia} = \mathbf{k}_1 - \mathbf{k}_2$ and frequency $\omega_{ia} = \omega_1 - \omega_2$, where $|\mathbf{k}_1| = 2\pi/\lambda_1$ is the wave vector of the pump beam and $|\mathbf{k}_2| = 2\pi/\lambda_2$ is the wave vector of the probe beam. (b) Diffraction of the pump beam off the traveling ion acoustic wave generates a scattered wave with wave vector $\mathbf{k}_{scattered}$ and frequency $\omega_{scattered}$ that is equal to $\mathbf{k}_2$ and ω_2. (08-00-0796-1581pb01)

As a result, the energy scattered from the pump is also proportional to the probe intensity, and an amplification of the probe results. This amplification is defined to be the ratio of the transmitted power measured in an experiment with the pump beam, to that measured in an essentially identical experiment without the pump beam. Resonant interaction requires that the ion wave have a wave vector $\mathbf{k}_{ia}$ which satisfies wave vector matching $\mathbf{k}_{ia} = \Delta\mathbf{k} = \mathbf{k}_1 - \mathbf{k}_2$, where $\mathbf{k}_1$ is the wave vector of the pump and $\mathbf{k}_2$ is the wave vector of the probe. An ion wave with this wave vector will cause energy to be diffracted in the direction of the probe beam. In addition, the scattered wave has its frequency down shifted by the ion wave frequency $\omega_{ia} = c_s\,|\Delta\mathbf{k}|$. Experimental evidence of the wave number matching is obtained from the 2-D image of the transmitted probe beam on the scatter plate. To eliminate the spatial structure in the transmitted beam that is due to the inhomogeneity of the incident beam, the 2-D image is averaged over azimuthal angle to

obtain a measure of the beam intensity as a function of the angle from the beam axis, as shown in Fig. 4. The amplified beam has an azimuthally averaged angular profile which is largest inside the $f/4.3$ cone of the incident beam (±6.6°) and similar to the profile of the probe beam obtained when it is transmitted through the plasma with the pump beam off. The fact that the intensity of the amplified beam falls rapidly outside of the $f/4.3$ cone (FWHM = 12°) indicates that the scattering is caused by ion waves with wave numbers near the phase-matched value $\Delta\mathbf{k}$. The profile of the unamplified beam intensity outside the cone is similar to that for the amplified case, indicating that in these experiments the observed spreading of the beam is not caused by the two beam interaction but rather by refraction and scattering from the unperturbed plasma.

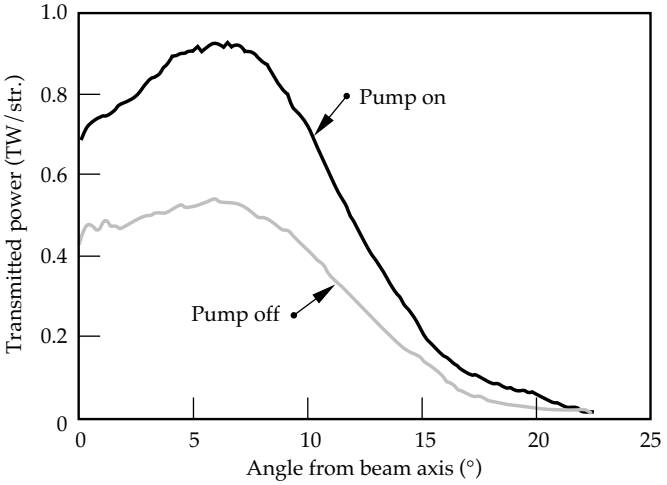

FIGURE 4. The angular distribution of the transmitted power of the probe beam is shown for the experiment in Fig. 2. The similar profiles in the two cases indicate that the amplified light is collimated and coincident with incident laser beam. (08-00-0296-0345pb01)

Determination of the Wavelength Dependence and Maximum Gain

Experiments to determine the average energy amplification as a function of the frequency mismatch were performed for six different pump/probe wavelength separations between 0.0 and 0.73 nm with the normalized probe intensity I_{probe}/I_{pump} between 0.06 and 0.32. The amplifications for these cases are shown in Fig. 5 and exhibit significant gain only when there is a frequency separation between the two beams. The largest amplification is 2.8 when the wavelength separation is $\Delta\lambda = 0.58$ nm. The resonant ion wave frequency is calculated as $\omega_{ia} = c_s |\Delta\mathbf{k}|$ and the half width of the resonance as $\nu_i/2$, where ν_i is the intensity damping rate of the ion wave.[1,8,9] The predicted position of the resonance is $\Delta\lambda = 0.46$ nm with a width of ± 0.04 nm

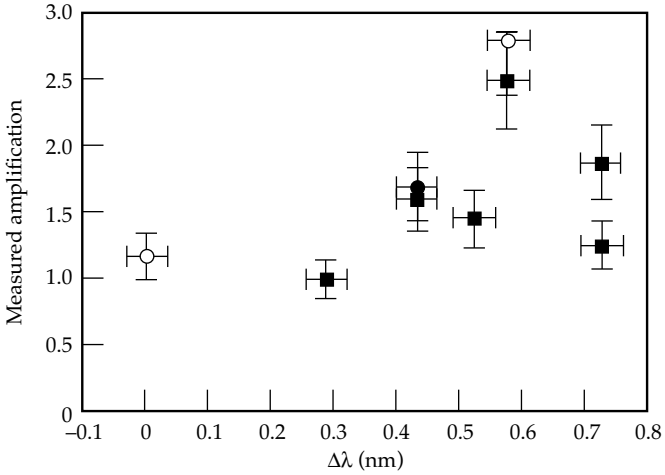

FIGURE 5. A series of experiments measured the amplification of the probe beam as a function of the wavelength separation of the two beams, as shown. The amplification is greatest when the frequency separation is in the vicinity of the unshifted ion wave resonance, $\Delta\lambda = 0.46 \pm 0.04$ nm. Data is shown for I_{pump}/I_{probe} equal to 0.06 (●), 0.13 (■), and 0.32 (○). (08-00-0296-0346pb01).

for the plasma parameters found in the vicinity of the focused beam. This indicates that the observed maximum measured gain is near the ion wave resonance, but may be Doppler shifted by weak plasma flows produced by heater beam and target inhomogenities that are not included in the 2-D simulations. The observation of a maximum amplification near the ion wave frequency combined with the observation of reduced amplification at both larger and smaller frequencies ($\Delta\lambda = 0.3$ nm and 0.73 nm) indicates that resonant excitation of an ion acoustic wave is necessary for amplification.

To compare with theory, we adopt the model of a steady state, convectively saturated instability leading to the amplification A of the probe by a gain coefficient or exponent g such that $g = \ln(A)$. This interpretation is applied in this case for two reasons: (1) the beam crossing angle is < 90° (forward scattering) so that the instability will be convectively saturated in the linear regime, and (2) the duration of the experiment (1 ns) is long compared with the time to reach a steady state, which, in the strong damping limit, is the ion wave damping time (~1.0 ps). The convective saturation of the gain results from the scattered electromagnetic wave propagating out of the interaction region and the ion wave energy being absorbed by Landau damping. The model is extended beyond the standard formulation of nonlinear optics[3] by adding ion wave damping and gain saturation. In the strong damping limit the saturated gain exponent in a homogeneous plasma scales as $nLI_{pump}/(T_e\nu_i)$, where L is the length of the interaction region.[1] According to this model, the pump wave scatters its power in the direction of the probe wave, and the transmitted amplitude is proportional to both the incident pulse wave amplitude

and an exponential proportional to the pump wave intensity. The measured amplification is also affected by small scale inhomogeneities both in the incident beam and in the plasma, for which accurate characterization and analysis is presented elsewhere.[1,10] These inhomogeneities make a calculation of the gain of the instability based on the simple model of coherent laser beams in uniform plasmas an over estimate of the actual gain. In fact, under the conditions of this experiment, the ideal model indicates a gain coefficient of $g \approx 20$ when the probe beam is perfectly tuned,[1,8,9] while the maximum observed gain coefficient is $g = 1.0$. This difference can be substantially reconciled by considering calculations, including the two types of inhomogeneities, and recognizing that the set of discrete measurements in Figure 5 may miss the exact resonance and underestimate the peak gain. (1) Because the shape of the resonance is $g \propto 1/[1+4(\Delta\omega/\nu_i)^2]$,[1] a frequency detuning of as little as $\Delta\omega = \nu_i$ (or $\Delta\omega \approx 0.2\ \omega_{ia}$) can decrease g locally by a factor of 5. This frequency detuning can result from Doppler shifting by small amplitude velocity fluctuations in the plasma or by inhomogeneous steady flows, both of which are produced by structure in the laser beam or target. For example, velocity fluctuations as small as $\delta v/c_s \approx 0.2$ rms in the interaction region reduce the gain at resonance by a factor of 3 by Doppler shifting the resonance to different frequencies in different regions of space as discussed in Ref. 1. As shown in Ref. 10, the combination of a spectrum of velocity fluctuations and linear gradients lead to reductions in g by a factor > 5. (2) The gain is reduced by laser beam incoherence. These experiments use RPPs that eliminate large scale structure in the beams, but necessarily create a speckle pattern of small high intensity regions surrounded by large regions of low or zero intensity. The gain of two intersecting beams with RPPs is largely determined by the overlap of the spatial profiles of the two beams. This can lead to a reduction of gain coefficient by an additional factor of 2 or more, depending on details of the beam structure.[10] Clearly, these crossing beam experiments provide a valuable test-bed for motivating and testing improvements to the theory.

Demonstration of Linearity

To investigate the dependence of the scattered power on the incident probe power, experiments were performed at both high- and low-scattered power at the frequency separation of maximum observed gain, $\Delta\lambda = 0.58$ nm. The high-probe intensity was $I_{probe}/I_{pump} = 0.32$ and the low probe intensity was $I_{probe}/I_{pump} = 0.13$. The measured amplification of the probe at high intensity was 2.8 ± 0.42 and at low intensity was 2.5 ± 0.37, indicating that the gain is nearly independent of the probe intensity up to this level and that the ion wave is unsaturated. Under these conditions, a maximum of 52% ± 12% of the pump energy was transferred to the probe. This large an energy transfer should lead to a 23% reduction in the spatially averaged amplification due to pump depletion. This effect was not observed, but it is comparable with the combined shot-to-shot variation in the transmission coefficient (± 15%) and amplification in these measurements.

The amplitude of the ion wave is estimated by considering the amplitude necessary to scatter one half the probe energy in a volume of dimension L, according to the formula $n_1/n_0 = 2/\pi\,(2)^{1/2}\,(\omega/\omega_p)^2\,(L/\lambda_0)$. A lower limit to the maximum ion wave amplitude observed in this experiment is $n_1/n_0 = 1\%$, assuming the scattering occurs uniformly over the region in which the beams intersect ($L = 345$ μm). The actual wave amplitude may be higher if inhomogeneities localize the scatter to a region smaller than L.

The data in Figure 5 indicate a linear dependence of transmitted power on the incident probe power over a wide range if the experiments done at $\Delta\lambda = 0.45$ nm and 0.6 nm are considered. The transmitted power measured with values of I_{probe}/I_{pump} different than 0.13 are normalized to the transmitted power measured at the same $\Delta\lambda$, but with $I_{probe}/I_{pump} = 0.13$. These normalized values are plotted in Fig. 6 and show that the transmitted power is proportional to the incident probe power over a range of 5:1, in good agreement with Ref. 1. At the highest probe intensity, $I_{probe}/I_{pump} = 0.13$, the transmitted power is sufficiently large that a reduction of the gain of approximately 25% is expected due to pump depletion. Although this effect is not apparent in the data in Fig. 6 it is about the same order of magnitude as the indicated error bars and is probably not observable in these experiments.

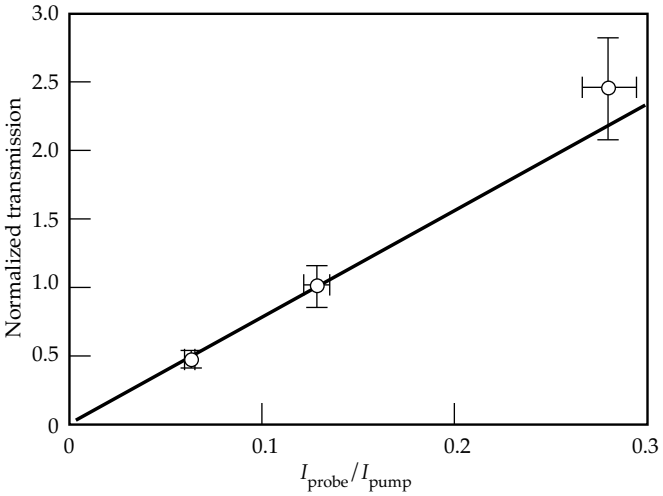

FIGURE 6. The measured transmitted power is shown to be proportional to the probe intensity over the range of $I_{probe}/I_{pump} = 0.06$ to 0.32, using data obtained at disparate separation frequencies by normalizing to the amplification measured with $I_{probe}/I_{pump} = 0.13$. (08-00-0296-0347pb01)

Conclusions

We report the first observation of energy transfer between frequency-mismatched laser beams in the presence of a stimulated ion acoustic wave. The effect is shown to be linear with probe beam intensity, indicating that there is no saturation of the ion wave up to a maximum of 52% energy transfer in these conditions. We also show that energy transfer occurs only when the beams are not symmetric and is maximized when the difference in the wave frequencies in the plasma frame is near the frequency of the resonant ion acoustic wave. Although it is expected that the flowing plasmas present in NIF targets may Doppler shift the frequencies of the incident beams so that they satisfy the resonance conditions, this experiment demonstrates that the transfer of energy may be controlled by adjusting the wavelengths of the incident beams.

Notes and References

1. W. L. Kruer, S. C. Wilks, B. B. Afeyan, and R. K. Kirkwood, *Phys. of Plasmas* **3**, 382 (1996).
2. W. L. Kruer, *The Physics of Laser Plasmas Interactions* (Frontiers in Physics, Addison–Wesley Publishing Company, The Advanced Book Program, 1988).
3. N. Bloembergen, *Nonlinear Optics* (Frontiers in Physics, W. A. Benjamin, Inc., Advanced Book Program, 1965).
4. D. H. Kalantar et al., *Phys. of Plasmas* **2**, 3161 (1995).
5. G. Zimmerman and W. Kruer, *Comments in Plasma Phys. and Controlled Fusion* **2**, 85 (1975).
6. D. M. Pennington, et al., *ICF Quarterly Report* **5**(1), 130–141, Lawrence Livermore National Laboratory, Livermore, CA, UCRL-LR-105821-95-1 (1995).
7. J. D. Moody et al., *Bull. Am. Phys. Soc.* **39**, 1753 (1994).
8. E. A. Williams et al., *Phys. of Plasmas* **2**, 129 (1995).
9. H. X. Vu, J. M. Wallace, and B. Bezzerides, *Phys. of Plasmas* **1**, 3545 (1994).
10. B. B. Afeyan et al., *Bull. Am. Phys. Soc*. **40**, 1822 (1995) and to be published (1996).

Ion-Beam Propagation in a Low-Density Reactor Chamber for Heavy-Ion Inertial Fusion

D. A. Callahan

A. B. Langdon

Introduction

Heavy-ion fusion (HIF) is an attractive candidate for inertial fusion energy (IFE) production. In HIF, beams of heavy ions (mass ~100 to 200 amu) are accelerated and focused on an indirectly driven inertial confinement fusion (ICF) target. At the target, the ion energy is converted in a hohlraum into x rays, which implode the capsule. Accelerator drivers have the long lifetime (~30 years), high repetition rate (~5 Hz), and high efficiency (~30%) needed for commercial energy production. In addition, final focusing is accomplished via magnetic fields, which are not damaged by the blast.

The accelerator requirements are set by the target. In order to get efficient coupling of ion energy into x rays, the amount of radiator material in the target (Fig. 1) that needs to be heated must be kept reasonably small. Because the ions must be stopped in the target, the ion range (equal to the stopping distance times the material density) is related to the amount of material necessary. In order to keep the target mass reasonably small, an ion range of 0.1 g/cm^2 is used. For ions of mass 100 to 200 amu, this corresponds to an ion energy of 3 to 10 GeV. To get the required beam power on target (5 to 10 MJ in 10 ns = 0.5–1.0 $\times$ 10^{15} W), the beam current must be greater than 50 kA. This current is broken into several beams to keep the space-charge forces manageable. In most conventional ion accelerators, space-charge plays only a small role; in a HIF accelerator, space-charge is very important.

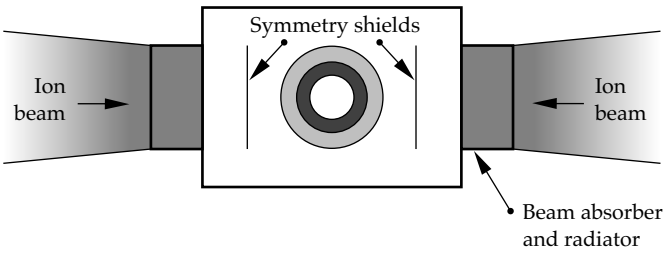

FIGURE 1. Schematic IFE heavy-ion indirect-drive target with end radiators. (40-00-1096-2401pb01)

The gain of a heavy-ion target generally increases as the size of the beam focal spot decreases. In order to get a small spot (radius ~2 to 5 mm), the beam emittance must be kept small. The beam emittance (a term used in accelerator physics) is proportional to the phase space area occupied by the beam and is related to the beam temperature. Keeping the emittance small throughout the accelerator in the presence of nonlinear fields (resulting from imperfect accelerator elements, misalignments, fringe fields, etc.) while preforming the necessary beam manipulations (beam bending, beam combining, etc.) is a challenge. Recent *Quarterly* articles by W. M. Sharp[1] and A. Friedman[2] discuss issues and progress towards understanding the accelerator needed for a HIF power plant.

Once the beams leave the accelerator, they must be focused and transported through the reactor chamber to the target. Transporting the heavy-ion beams from the accelerator to the target is extremely important for a successful HIF reactor. Chamber transport (along with the target) sets the requirements on the accelerator driver.[3] As a result, improvements in chamber transport and final focus can significantly reduce the cost of electricity. Relaxing the requirements on the accelerator reduces the cost of the driver, which directly impacts the cost of electricity; reducing the beam spot size at the target allows a larger target gain, which also reduces the cost of electricity. Improvements in beam transport and final focusing can be exploited in optimizing the end-to-end HIF system.

The main-line approach to chamber transport is low-density, ballistic or nearly ballistic transport. The HYLIFE-II reactor[4] uses a low-density chamber with a pressure of a few millitorr. Even at the low density of the HYLIFE-II chamber (5 $\times$ 10^{13} cm^{-3} ≈ 0.003 torr), partial beam-charge neutralization is needed to overcome

the effects of beam stripping. In this case, beam stripping refers to collisional ionization of the beam ions to a higher charge state by the background gas. Beam stripping and neutralization have been recognized as important issues in chamber transport for many years.[4, 5] Low-density transport is the most conservative option, but puts strict requirements on the beam quality out of the accelerator.

In this article, we first discuss different effects that impact the beam spot size at the target. We then show that ballistic transport in a near vacuum is possible, but puts undesirable constraints on the reactor chamber design. We then discuss simulations of partially neutralized beam transport in a low-density chamber. Finally, we discuss calculations of multiple beam effects in the chamber. Partial neutralization allows chamber operation at higher pressures, and the use of ions with higher charge-to-mass ratio which are easier to accelerate. Both increases in flexibility allow for lower reactor cost.

Total Beam Spot Size at the Target

In this section we describe the different effects that lead to the final beam spot size at the target. The beam spot size is increased by the beam's space charge and emittance, chromatic aberrations in the final focusing system, and errors in aiming the beams at the target. These sources are roughly independent and add in quadrature,[6]

$$r_{\text{target}}^2 \approx r_s^2 + r_c^2 + r_a^2 \quad , \tag{1}$$

where r_{target} is the final spot radius at the target, and r_s, r_c, and r_a are the spot radius due to space charge and emittance, chromatic aberrations, and aiming, respectively. The simulation results presented in the sections below do not include chromatic aberrations or aiming errors; Eq. (1) is used to estimate the total spot radius. The spot radius necessary for a high gain ($\leq$40) ranges from 2 to 6 mm depending on the details of the target design.

In the HYLIFE-II reactor concept, the targets are injected into the chamber at a rate of six per second using a gas gun. Petzoldt[7] estimates that the spot radius due to errors in aiming the beams at the target is 0.4 mm. This estimate takes into account translational positioning errors and rotations of the target.

Chromatic aberrations occur in the final focusing system because particles with different longitudinal momenta are focused at different distances. This causes a radial spread in the particles at target, which is proportional to $\delta p/p$, the longitudinal momentum spread divided by the longitudinal momentum. For a focusing system of four thin lenses, single-particle calculations (neglecting space charge) show that $r_c = 8F\theta\delta p/p$, where F is the focal distance, and θ is the half convergence angle of the beam. Including space charge reduces the chromatic aberrations by about a factor of 3/4, so

$$r_c \approx 6F\theta\frac{\delta p}{p} \quad . \tag{2}$$

Generally F is set by the reactor geometry and has a value of ~5 m. The convergence angle θ is generally limited to ~15 mrad to avoid geometric aberrations in the final focusing magnets. It is possible to use larger angles and correct the geometric aberrations using an octupole correction.[8] A larger convergence angle results in a larger aperture for the final focusing magnets, however, which increases the cost of those magnets. For the purposes of these calculations, we will keep $\theta \leq 15$ mrad.

Limiting the spot radius from chromatic aberrations to 1 to 1.5 mm sets a limit on the allowable momentum spread in the final focusing system. Using $F = 5$ m and $\theta = 15$ mrad, we find $\delta p/p \leq 2.2 - 3.3 \times 10^{-3}$ in the final focusing system. In the conventional HIF driver scenario, the beam is drift compressed by a factor of 10 or more between the end of the accelerator and the final focusing system. This is accomplished by giving the beam a velocity "tilt" so that the beam tail is moving faster than the beam head. After the tilt is applied, the beam is allowed to drift and it compresses as the tail catches up with the head. This drift compression increases the longitudinal momentum spread, and, as a result, $\delta p/p \leq 2.2 - 3.3 \times 10^{-4}$ at the end of the accelerator if the beam is to be drift-compressed by a factor of 10 prior to focusing.

If $r_a = 0.4$ mm, and $r_c = 1.5$ mm, then 2.57 mm are left for space charge and emittance (r_s) in a total spot (r_{target}) of 3 mm. An optimization needs be done to weigh the relative costs of each of the spot size contributions. We need to assess the cost of increasing $\delta p/p$ at the expense of beam emittance, for example.

The beam-spot radius from space charge and emittance can be estimated using the envelope equation

$$a'' = \frac{K}{a} + \frac{\varepsilon^2}{a^3} \quad , \tag{3}$$

where each ' indicates a derivative with respect to z, K is the perveance (which is a measure of the beam's space charge), ε is the unnormalized emittance, and a is the beam edge radius. Multiplying by a' and integrating gives

$$\left(a_f'\right)^2 - \left(a_0'\right)^2 = 2K\ln\left(\frac{a_f}{a_0}\right) - \varepsilon^2\left(\frac{1}{a_f^2} - \frac{1}{a_0^2}\right) \tag{4}$$

where 0 and f denote the initial and final values. At the beam waist $a_f = r_s$ and $a_f' = 0$. At the entrance,

$a_0' = \theta$ and $a_0 \approx F\theta$. Using these substitutions and assuming $a_0 \gg r_s$, Eq. (4) becomes

$$\theta^2 = 2K \ln\left(\frac{a_0}{r_s}\right) + \frac{\varepsilon^2}{r_s^2} \quad . \tag{5}$$

In the absence of space charge (i.e., a perfectly neutralized beam), $K = 0$ and the spot radius due to emittance r_e is given by

$$r_e = \frac{\varepsilon}{\theta} \quad . \tag{6}$$

If $r_e = 1$ mm and $\theta = 15$ mrad, then transverse beam emittance is restricted to $\varepsilon \leq 15$ mm-mrad.

Using Eq. (5), we can estimate the maximum beam perveance allowed for a given r_s. Using $\theta = 15$ mrad, $a_0 = 7.5$ cm, $r_s = 2.5$ mm, and $\varepsilon = 15$ mm-mrad, Eq. (5) gives a maximum perveance of $K = 2.8 \times 10^{-5}$. The perveance is related to the beam current by

$$K = \frac{2Z}{(\gamma\beta)^3 A} \frac{I_b}{I_0} \quad , \tag{7}$$

where Z is the ion charge state, β is the beam velocity over the speed of light, γ is the Lorentz factor, I_b is the beam current, A is the ion mass in amu, and $I_0 = m_{amu}\, c^3/e = 31$ MA. For $K = 2.8 \times 10^{-5}$, this leads to a maximum current per beam of 2.3 kA for a mass-200 ion and 1.6 kA for a mass-135 ion, both at $\beta\gamma = 0.3$. Neutralization is needed if the current per beam is larger than these values.

Ballistic Transport in a Near Vacuum

Using the equations introduced in the previous section, we can show that a beam of 10-GeV, singly charged, heavy (~200-amu) ions can be ballistically transported with a reasonable spot size provided the chamber density is low enough to avoid beam stripping. The target requires a main pulse with 4 MJ of energy in 10 ns (an additional 1 MJ is carried by a low-power prepulse). The total current necessary in the main pulse is 4 MJ / (10 GeV × 10 ns) = 40 kA. Without neutralization, the maximum current per beam found in the previous section was 2.3 kA, so 17 beams are needed for the main pulse. This provides a reasonable, conservative scenario for transporting the beam to the target.

Beam stripping is an issue, however. Estimates of the cross section[9–11] for stripping the beam ions by the background gas in HYLIFE-II (BeF_2 from the molten LiF-BeF_2 chamber wall) range from 1.3 to 4.0×10^{-16} cm^2. Stripping only about 1% of the beam ions requires a chamber density $\leq 10^{11}$ cm^{-3}. This density is two orders of magnitude below the chamber density in the HYLIFE-II reactor ($\sim 5 \times 10^{13}$ cm^{-3}). Since a HIF reactor has a repetition rate of about 5 Hz, it is difficult to achieve densities lower than used in HYLIFE-II after each shot. Thus, purely ballistic transport puts an undesirable restriction on the chamber density.

Low-Density, Nearly Ballistic Transport

One option for improving the beam focus at the density of HYLIFE-II is to partially charge neutralize the beam. At the density of the HYLIFE-II chamber, the stripping mean-free-path is 0.5 to 1.5 m. In the HYLIFE-II design, the chamber radius from "first wall" to the target is 3 m (from target to the center of the last focusing magnets is about 5 m, as used in the "Total Beam Spot Size at the Target" section). Therefore, the beam will strip 2 to 6 times during chamber transport. Simulations with the BICrz code[12–15] show that most of the stripped electrons tend to stay with the beam. However, in the higher charge state, the ions respond more strongly to the electric fields and the spot size increases. Simulations with a stripping mean-free-path of 1.2 m in a 3-m chamber show an increase in the beam spot radius from 2.6 mm (vacuum transport) to 8 mm. This is an unacceptably large spot, and partial beam neutralization must be used to offset this increase.

While beam stripping makes chamber propagation more difficult, ionization of the background gas by the beam ions can partially neutralize the beam and aid transport. Cross sections for collisional ionization of BeF_2 by the beam have a larger uncertainty than stripping cross sections because calculating molecular cross sections is more difficult than calculating atomic cross sections. Estimates of the mean-free-path for ionizing the background gas range from 0.7 to 25 m. For BeF_2, the ratio of stripping to gas ionization cross sections is not favorable (i.e., more stripping than gas ionization). Other chamber gases, such as Li, may have a more favorable cross section ratio.[16]

Simulations show that including a stripping mean-free-path of 1.2 m and a gas ionization mean-free-path of 3.0 m reduced the spot radius from 8 to 5.4 mm. Neutralization by gas ionization occurs "for free" since we do not have to add anything to the reactor for it to occur; however, gas ionization neutralizes the beam slowly, so radial velocities develop before neutralization occurs. The solid

curve in Fig. 2 shows the neutralization fraction as a function of distance from the chamber wall for a simulation without beam stripping. The beam is more than 70% neutralized, but it takes about 2.5 m of propagation distance to reach this level of neutralization. To get a smaller spot, additional neutralization is needed.

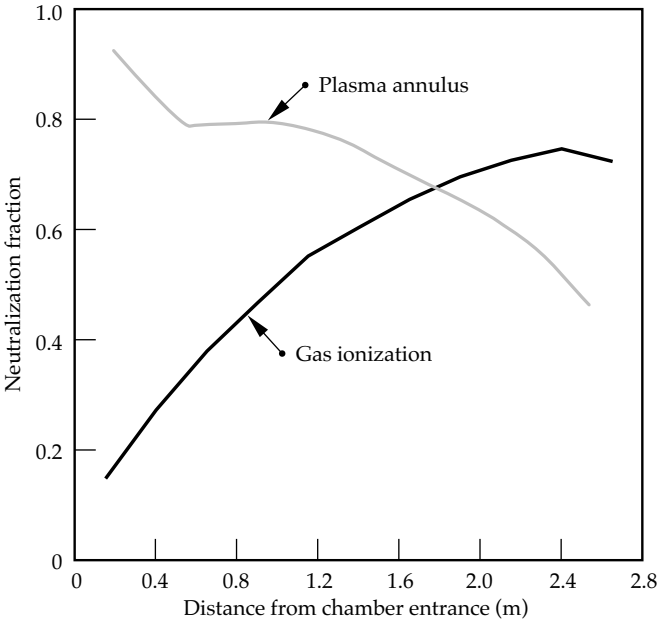

FIGURE 2. Neutralization fraction as a function of distance from the chamber entrance for neutralization using collisional ionization of the background gas (black curve) and neutralization using a preformed plasma annulus in the chamber (gray curve). (50-00-0696-1362pb01)

Neutralization Using a Preformed Plasma Annulus

Neutralizing an ion beam is more difficult than neutralizing an electron beam. When an electron beam passes through a plasma, the plasma electrons are moved out of the beam path, and the beam is neutralized by the immobile ions. For an ion beam, however, electrons must be pulled in from outside the beam path in order to reduce the net charge.

One method for neutralizing the beam quickly is to create a preformed plasma in the chamber before the beam enters. Simulations used a small (0.3-m = 40% of the beam length) annulus of plasma just inside the chamber entrance. A 4-kA beam of Pb^+ ions entered the chamber through the annulus. The annulus had a total electron charge of four times the beam charge.

As the beam entered the chamber, electrons were pulled from the inner surface of the annulus by the large radial electric field of the beam (E_r = 16 MV/m at the beam edge for a 4-kA beam of radius 5 cm). The electrons are accelerated longitudinally by the z electric field of the beam and oscillate back and forth across the beam in both the radial and longitudinal direction. The details of the acceleration and deceleration of the electrons in the longitudinal direction will depend on the shape of the beam. These simulations used a beam with a current profile that was parabolic in z.

Because the BICrz code is axisymmetric, particles cannot gain or lose angular momentum. The only angular momentum a particle has is the momentum it is created with. For the plasma annulus, we used an initial isotropic temperature of 100 eV. The particles can heat in r and z, but not in θ. As a result, a temperature anisotropy develops, which causes an excess of electrons near the axis. This causes the radial fields to become nonlinear. Figure 3 shows the radial velocity

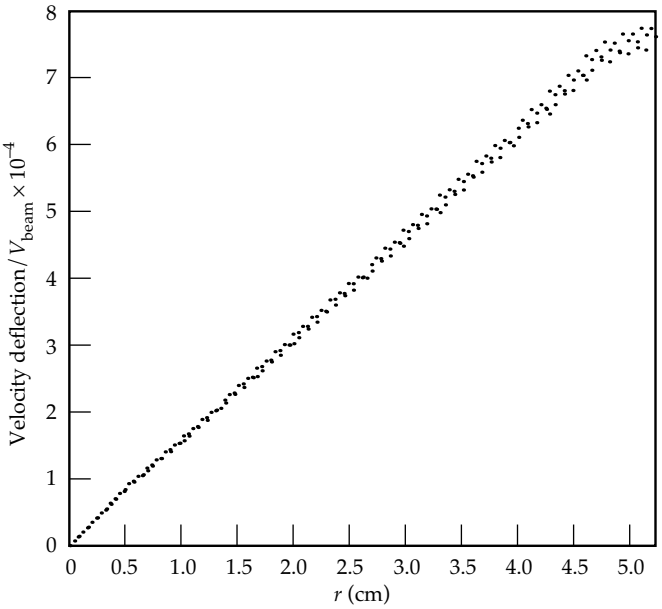

FIGURE 3. The radial velocity deflection of particles near the axial center of the beam as a function of radius shows the electric field is linear when no electrons are present. (50-00-0696-1363pb01)

deflection of particles near the center of the beam as a function of radius when no electrons are present. As expected, the field is linear. Figure 4 shows the same plot when the beam has passed through a plasma annulus (but with no beam stripping). The field is greatly reduced from the previous case, but the nonlinearity is also apparent. Because of the abundance of electrons near the axis, the field is negative at small radii. We can compensate for linear fields by increasing the focusing angle at the final optic. We cannot compensate for the nonlinear fields in this way; as a result the nonlinear fields can make it more difficult to focus the beam.

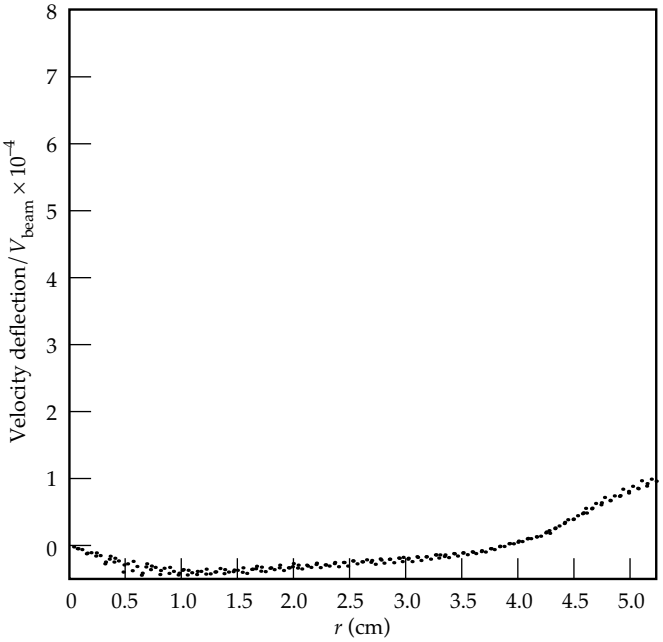

FIGURE 4. When electrons are present, the radial velocity deflection of particles near the axial center of the beam as a function of radius shows that the electric field is reduced, but nonlinear. (50-00-0696-1364pb01)

The charge neutralization fraction can be estimated using the Child–Langmuir space-charge-limited current from the inner surface of the annulus. For the 0.5-cm gap between the beam radius and the inner edge of the annulus used in this simulation, this estimate yields a neutralization fraction of 90%. Simulations are in agreement with this estimate, and the gray curve in Fig. 2 shows that the beam is quickly neutralized to slightly more than 90% while inside the annulus. As expected, neutralization reduces the beam spot size at the target. In a simulation with a stripping mean-free-path of 1.2 m and a plasma annulus, the final spot was 3.5 mm. This is a significant decrease over the 8-mm spot found without neutralization, but is not as good as the pure vacuum transport result of 2.6 mm.

The gray curve in Fig. 2 shows that while the beam is well neutralized near the chamber entrance, it does not remain well neutralized. The electrons pulled in from the plasma annulus are hot ($v_{th} \approx 0.3\ c$). As the beam compresses, the electrons do not compress as readily as the beam, and the neutralization fraction falls off as the beam approaches the target. The fact that these electrons are hot and as a result do not neutralize well near the target was seen in earlier studies.[17,18] Electrons created by collisional ionization of the background gas are cooler than those pulled in from the plasma annulus, and we expect the smallest spot when both collisional ionization and a plasma annulus are included. Simulations confirm this, and the spot is reduced from 3.5 to 3.0 mm when a gas ionization mean-free-path of 3 m is added to the simulation.

Neutralization Using a Plasma Column

In the case of the plasma annulus, neutralization was quite good (>90%) inside the annulus, but the neutralizing electrons did not compress with the beam. As a result, neutralization got worse as the beam got closer to the target. One method to remedy this problem is to put the plasma throughout the entire chamber so the beam can continually pull in new electrons as it compresses.

The plasma density required in the plasma column is not large. Simulations show that ionizing just 0.44% of the background gas ($n_e = 2.5 \times 10^{11}$ cm^{-3}) in a cylinder of radius $\sqrt{2r_{beam,\,initial}}$ is enough to eliminate the effects of beam stripping when the stripping mean-free-path is 1.2 m. In this case, the electron density was six times the initial beam density. As the beam compressed, the beam density became much larger than the electron density.

One method for reducing the cost of the driver is to use a lighter, lower-energy ion such as 5.3-GeV Cs^+. The cost of using the lighter, lower-energy ion is that more current is necessary to deliver the same energy to the target. For 5.3-GeV Cs^+, 75 kA of current is needed to provide 4 MJ of energy in the 10-ns main pulse. We found in the second section that the maximum current we can transport in the chamber for a mass-135 ion without neutralization is 1.6 kA per beam. This means we would need more than 45 unneutralized Cs beams. With about 80% neutralization, we can transport the 75 kA of Cs in 10 beams.

In the simulation, the low-density plasma column neutralized the Cs beam quite well. A simulation with a 7.5-kA beam of 5.3-GeV Cs^+ ions (without beam stripping) and a low-density plasma column ($n_e = 2.3 \times 10^{11}$ cm^{-3}) produced a spot of 1.2 mm. This simulation used a smaller emittance (15 mm-mrad) than was used in some of the previous cases (33 mm-mrad). For these parameters , the unneutralized beam spot radius was 9 mm and the perfectly neutralized spot radius (from emittance only) was 0.9 mm. Figure 5 shows

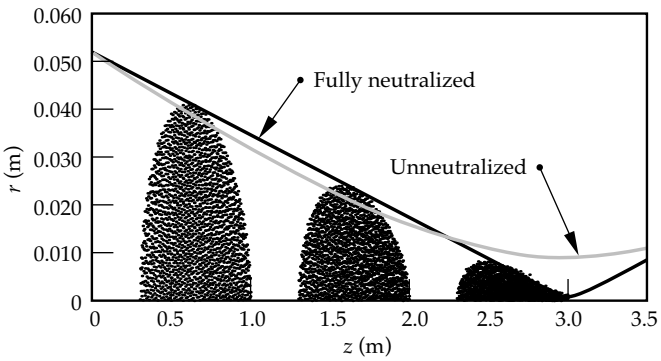

FIGURE 5. A particle-in-cell simulation shows that a 7.5-kA beam of 5.3-GeV Cs^+ ions is well neutralized by a low-density plasma column. The gray curve shows the envelope solution with no neutralization while the solid curve shows the envelope solution with perfect neutralization. (50-00-0696-1365pb01)

the simulation particles at three times plus the envelope solution for the unneutralized beam (gray curve) and the fully neutralized beam (black curve). The particles follow the fully neutralized envelope solution quite well indicating a high degree of neutralization.

Adding a beam stripping mean-free-path of 3.2 m to the Cs beam simulation produced a spot of 2 mm. This mean-free-path would correspond to a decrease of about a factor of two in the chamber density from the standard HYLIFE-II case.

Producing the plasma column in the HYLIFE-II chamber still needs to be addressed. Some methods under consideration are using an electrical discharge or a laser to ionize some of the chamber vapor and using a plasma gun to create the plasma and inject it in the chamber. Any equipment used to create the plasma (lenses, insulators, etc.) must be protected from the blast. This work is in progress.

Interactions Between Neighboring Beams

Most indirect-drive, HIF target designs have two radiation converters (one located at either end of the hohlraum). However, many beams (i.e., more than two) are necessary to reduce the space-charge forces. This means that half the beams will be aimed at each radiation converter, and these beams will be fairly close to one another in the chamber (see Fig. 6). As a result, each beam will be affected by the fields from neighboring beams, which can result in an increase in the beam spot size.

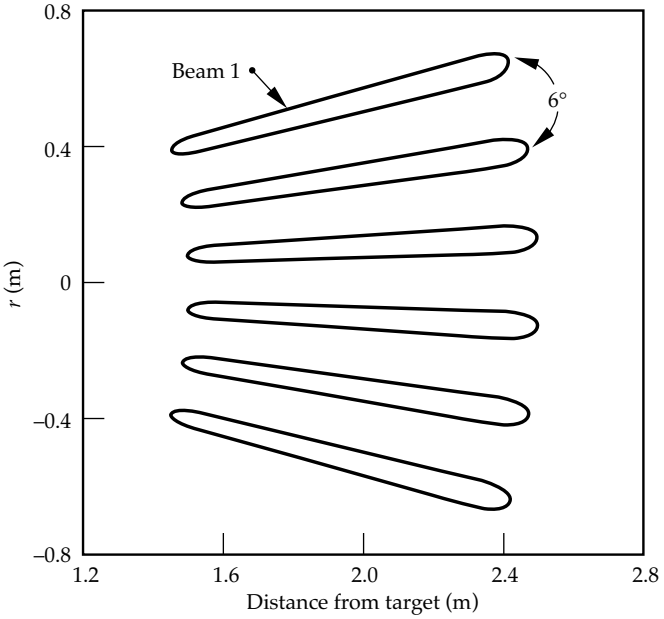

FIGURE 6. One option for multiple beam transport in the HYLIFE-II reactor is to place six beams in a "fan" aimed at one radiation converter. (50-00-0696-1366pb01)

If the fields due to the neighboring beams were constant along the beam length, we could compensate for them by increasing the focusing angle slightly. The fields are not constant, however, and vary along the pulse because of variations in the beam current as a function of z and the finite length of the beams. These two effects cause the field at the ends of the beam to be smaller than the field at the beam center. Since we cannot adjust the focusing angle on the time scale of the beam pulse duration (10 ns for the main pulse), the beam ends will be overfocused if the beam center is focused.

Hofmann, Hasse, and Reiser studied this problem for a cone of beams produced by an RF Linac with storage rings.[19] In the RF Linac approach to HIF, beam compression is done by a phase rotation and results in a beam with a roughly Gaussian current profile. The variation in current along with the finite length of the beams causes a large variation in the electric field between the beam center and the beam ends. Hofmann et al. found that the increase in spot size due to the neighboring beams was tolerable for a charge state +1 beam, but scaled as the charge state squared, so that it was not acceptable for higher-charge-state ions.

This problem is less severe for beams produced by an induction linac. With careful longitudinal beam control, the induction linac can produce a nearly flat topped current pulse so that variations in the electric field come almost exclusively from the finite length of the beams. Calculations show 5% beam loss for a "fan" of either six unneutralized, 4-kA beams of 10-GeV Pb^+ ions or six 70% neutralized, 7.5-kA beams of 5.3-GeV Cs^+ ions.[20]

Complete simulations of the neighboring beams problem will require a fully three-dimensional, electromagnetic code. Such a code is under development by J.-L. Vay and C. Deutsch at University of Paris-Orsay.[21]

Summary

Transporting the heavy-ion beam through the reactor chamber to the target is a critical step in a HIF power plant. We have simulated low-density, nearly ballistic transport in a chamber that is consistent with the HYLIFE-II reactor design. Our simulations show that even at the relatively low densities of HYLIFE-II, beam stripping plays an important role. We have found that we can overcome the effects of beam stripping by charge neutralizing the beam using a low-density plasma column in the chamber.

Charge-neutralized transport has also opened up new accelerator regimes by allowing lower-mass, lower-energy ions to be used. Using lower-energy ions should reduce the cost of the accelerator driver, which in turn reduces the cost of electricity. Using

lower energy ions requires a larger beam current to deliver the same amount of energy to the target; transporting this large current requires either a very large number of beams or charge-neutralized transport. Our simulations showed that ionizing less than 0.5% of the background gas in the HYLIFE-II chamber is sufficient to transport a 7.5-kA beam of Cs^+ ions.

Experiments are needed to verify the results of the simulations. We believe that experiments to study beam neutralization can be done using existing facilities at LBNL or Sabre at Sandia National Laboratories.

Beam neutralization thus far has concentrated on "passive" neutralization using plasmas in the chamber. "Active" neutralization by co-injecting an electron beam along with the ion beam is another possibility for beam neutralization. Further study in this area is needed.

Notes and References

1. W. M. Sharp, *ICF Quarterly Report* **4**(2), 70–77, Lawrence Livermore National Laboratory, UCRL-LR-105820-94-2 (1994).
2. A. Friedman et al., *ICF Quarterly Report* **5**(3), 179–186, Lawrence Livermore National Laboratory, UCRL-LR-105821-95-3 (1995).
3. V. O. Brady, A. Faltens, D. Keefe, E. P. Lee, J. Hovingh, *Heavy Ion Fusion System Assessment: Final Focus and Transport Model*, LBL-23040, July 1987.
4. R. W. Moir et al., *Fusion Technology* **25**, 5 (1994).
5. W. A. Barletta, W. M. Fawley, D. L. Judd, J. W-K. Mark, and S. S. Yu, "Heavy-Ion Inertial Fusion, Interface between Target Gain, Accelerator Phase Space, and Reactor Transport Revisited," *Proc. of International Symposium of Heavy Ion Accelerators*, Tokyo, Japan, January 23–27, 1984 (UCRL-90246).
6. E. P. Lee, *Heavy Ion Inertial Fusion*, M. Reiser, T. Godlove, and R. Bangerter, Eds., *AIP Conference Proceedings*, American Institute of Physics, New York, NY, p. 461 (1986).
7. R. W. Petzoldt, Ph. D. Thesis, University of California at Davis, 1995.
8. D. D.-M. Ho, I. Haber, K. R. Crandall, S. T. Brandon, *Particle Accelerators* **36**, 141 (1991).
9. N. Barboza, U.C. Berkeley, private communication (1994).
10. W. R. Meier et al., *Osiris and Sombrero Inertial Confinement Fusion Power Plant Designs*, WJSA-92-01, DOE/ER/54100-1 (1992).
11. B. Badger et al., *HIBALL-2, An Improved Conceptual Heavy Ion Beam Driven Fusion Reactor Study*, UWFDM-625, U. of Wisconsin (1984).
12. C. K. Birdsall and A. B. Langdon, *Plasma Physics via Computer Simulation*, McGraw-Hill, New York, 1985.
13. A. B. Langdon, *Computer Physics Communications* **70**, 447 (1992).
14. A. B. Langdon, *Bull. Am. Phys. Soc.* **35**, 2415 (1991).
15. D. A. Callahan and A. B. Langdon, *Proc. of the 1995 Particle Accelerator Conference*, pp. 3238–3240, Dallas, TX, May 1–5, 1995.
16. N. Barboza, submitted to *Fusion Engineering and Design*.
17. G. R. Magelssen and D. W. Forslund, *Heavy Ion Inertial Fusion*, *AIP Conference Proceedings*, p. 330, M. Reiser, T. Godlove, and R. Bangerter, Eds., American Institute of Physics, New York, NY (1986).
18. D. S. Lemons, M. E. Jones, *Heavy Ion Inertial Fusion*, M. Reiser, T. Godlove, and R. Bangerter, Eds., *AIP Conference Proceedings*, American Institute of Physics, New York, NY, p. 287 (1986).
19. I. Hofmann, R. W. Hasse, and M. Reiser, *J. Appl. Phys.* **73**, 7061 (1993).
20. D. A. Callahan, *Appl. Phys. Lett*. **67**, 27 (1995).
21. J.-L. Vay, accepted for publication in *Fusion Engineering and Design*.

Efficient Production and Applications of 2- to 10-keV X Rays by Laser-Heated "Underdense Radiators"

L. J. Suter *M. S. Maxon*

R. L. Kauffman *J. F. Davis**

Introduction

Within the next decade, very-high-power, high-energy laser facilities may be constructed in Europe[1,2] and the United States.[3] Two-dimensional (2-D) numerical simulations with the LASNEX code[4] at Lawrence Livermore National Laboratory (LLNL) indicate that this next generation of lasers offers the prospect of producing multi-keV x rays with unprecedented efficiency: as much as 14% above 10 keV, 30% above 4 keV. Such efficiencies, coupled with the intrinsically high energy of these facilities, should allow us to produce great quantities of multi-keV x rays—as much as several hundred kilojoules. This, in turn, may allow us to perform experiments and field diagnostics we could never consider with current facilities. Applications of high-energy, multi-keV sources with the proposed National Ignition Facility (NIF) include volume preheating of experimental targets; bright, multi-keV backlighting; pumps for fluorescent imaging of capsule dopants and Doppler velocimetry; and uniform irradiation of large test objects for Nuclear Weapons Effects Testing (NWET).

Projections of Efficiency

Conventional slab targets irradiated by current lasers produce multi-keV x rays with relatively low efficiency. At photon energies >3 keV, the typical efficiency for converting laser light into multi-keV x rays is less than 1%.[5] Multi-keV efficiencies well in excess of those commonly obtained today are predicted to be achieved with "underdense radiators," a nontraditional source of laser-generated x rays (so called because the density of these targets is less than critical density of the laser light). Figure 1 shows two examples of such sources. Figure 1(a) is a column of gas (or foam) irradiated from one end by a single 0.35-μm (blue) laser beam. In simulations using 0.01 g/cm^3 of Xe gas irradiated by a 2-ns flattop pulse at an intensity of 10^{15} W/cm^2, we find

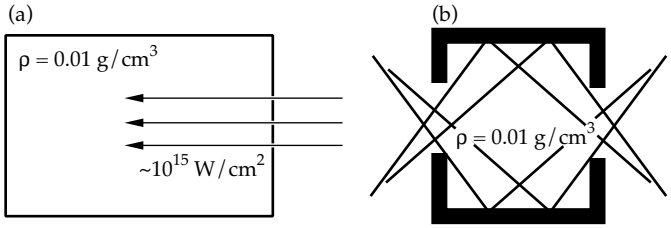

FIGURE 1. Two types of "underdense radiators." (a) is a gas (or foam) column irradiated from one end with a single, large-*f*-number beam. (b) is a transparent container, filled with underdense gas or foam, irradiated with several beams. NIF target type (a) can be irradiated with, at most, 10 TW. Target type (b) can accept several beams, so it can be irradiated with higher total power. (20-03-0696-1296pb01)

efficiencies into photons of energy >4 keV (L-shell Xe and continuum) to be 19% with a 10-TW beam. Since a cluster of four "beamlets" of the proposed National Ignition Facility (NIF)[3] will deliver 10 TW in the geometry of Fig. 1(a), good efficiency may be achievable with such gas-column sources. However, simulations indicate that higher efficiencies and higher photon energies with such a target will require more than 10 TW. This would be incompatible with the 10-TW/beam maximum of the NIF. Figure 1(b) shows a higher power source compatible with the NIF. It is a low-*Z* container, transparent to x rays of interest, filled with an appropriate-Z, low-density gas or foam. Since it is heated by more than one beam, it can be irradiated at much more than 10 TW. In simulations where the can is filled with Xe gas at 0.01 g/cm^3, we find near-optimal performance for containers 2 mm diameter and 1.6 mm long with 1-mm-diam laser entrance holes. For 2-ns pulses, simulated, >4-keV efficiencies range from 17% at 20 TW to 30% at 60 TW.

We have efficient 2-D designs of target type (b) at photon energies up to ~10 keV. Table 1 summarizes our LASNEX study. In all cases, the densities are 0.01 g/cm^3, and the rest of the laser energy appears as either thermal emission (<1 to 2 keV) or plasma energy.

*Alme Associates, Alexandria, VA.

Figure 2 plots the highest source efficiencies in the third column of Table 1 vs photon energy and compares them with current disc backlighter efficiencies.[5] The figure forcefully illustrates how much more efficient underdense radiators, heated by powerful lasers, can be compared to current backlighters.

TABLE 1. Summary of LASNEX study results.

Material	Power (TW)	Fraction of laser energy > $h\nu$ (keV)
Kr	60	4% > 13; 30% > 2
Ge	60	14% > 10; 26% > 2
Ge	50	10% > 10; 26% > 2
Ge	30	7% > 10; 20% > 2
Cu	40	11% > 8.5; 26% > 2
Cu	30	10% > 8.5; 24% > 2
Dy	60	9% > 8; 24% > 2
Xe	60	30% > 4; 48% > 1
Xe	50	26% > 4; 48% > 1
Xe	30	22% > 4; 40% > 1
Xe	20	17% > 4; 37% > 1

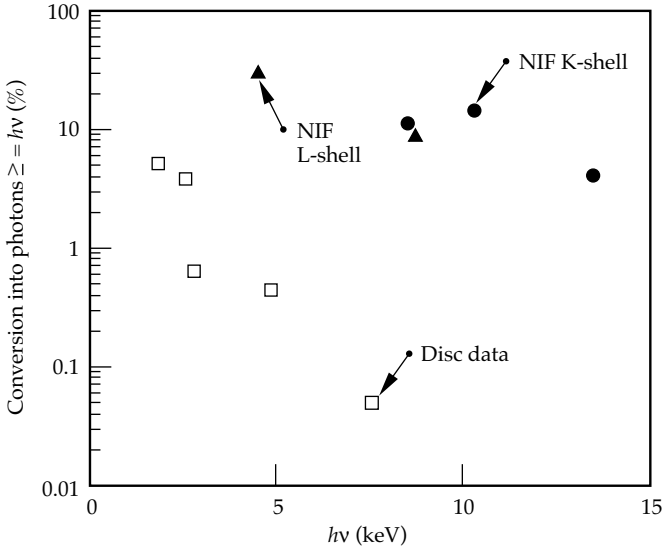

FIGURE 2. The projected multi-keV efficiencies for sources like those of Fig. 1(b) are much higher than current disc efficiencies. K-shell refers to the Ge, Cu, and Kr sources of Table 1. L-shell refers to the Dy and Xe sources. (20-03-0696-1301pb01)

Physics of Efficient Production

Analysis of LASNEX simulations leads to a simple understanding of such high efficiencies in the multi-kilovolt regime and tells us why these are qualitatively different from standard discs. In the following discussion, we use Xe as an example, although the arguments are valid for other materials as well.

Good Multi-KeV Efficiency Is Intrinsically Possible

First, we show how high, multi-keV efficiency is possible with an underdense radiator. Figure 3 illustrates the first component of high, multi-keV efficiency. It shows theoretical estimates of Xe emission at electron temperatures of 2 keV and at 5 keV. The Xe density is 0.01 g/cm^3. This plot makes a widely known but essential point: x-ray emission shifts to higher energy as plasma is made hotter. Figure 4, which plots radiation production/cm^3 vs electron temperature, contains the next step in the argument. This is from an optically thin LASNEX simulation. The black line is total emission vs T_e. The gray line is the emission >4 keV (see Fig. 3). This plot shows that the overall radiation production does not change greatly with plasma temperature. However, at higher temperatures almost all the emission will be multi-keV (see Fig. 3). Figure 4 illustrates an important point: a material that efficiently produces x rays in the softer, "thermal" region may also efficiently

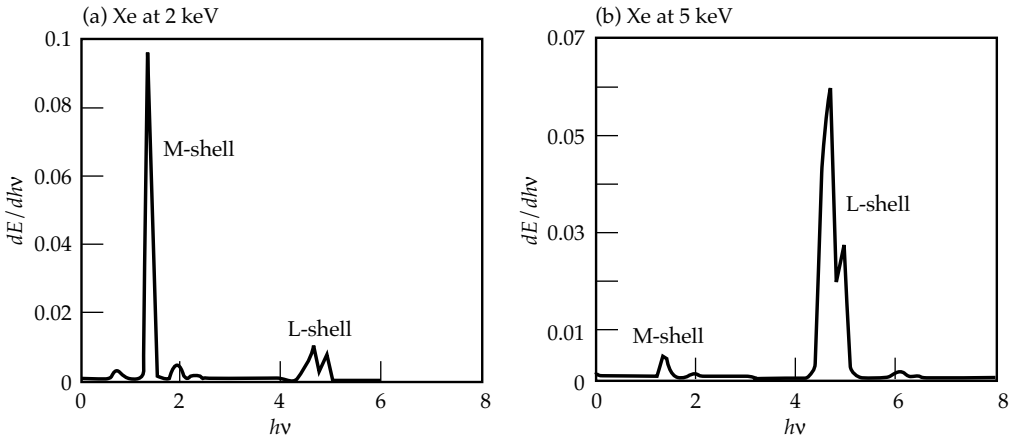

FIGURE 3. Emission from 0.01 g/cm^3 Xe at electron temperatures of (a) 2 keV and (b) 5 keV, simulated by XSN. Heating a material causes more of its total emission to be produced at higher photon energies. (20-03-0696-1302pb01)

produce x rays in a much more energetic region if it is made hotter.

Figure 5 is the plot needed to reach a simple, quantitative understanding of efficient multi-keV production. It shows Xe L-shell radiation production vs electron density for material at electron temperatures of 3, 4 and 5 keV. The Xe volume is that of a 1.4-mm-radius standard "gasbag"[6] similar to ones we have shot on Nova for studies of laser–plasma instabilities.[7] Figure 5 shows that at densities ~1 to 1.5×10^{21}/cm, a 4- to 5-keV Xe-filled gasbag would produce ~5 to 12 TW of L-shell emission. Thus, if we can heat such a gasbag to these temperatures with a 30-TW, 1-ns Nova pulse (30 kJ energy), and if it remains together for ~1 ns, we might expect to produce ~5 to 10 kJ of L-shell emission, or 16 to 33% multi-keV efficiency.

That we can both heat the bag and that it does not disassemble too quickly follow from simple arguments. If all the material in the gasbag is at constant temperature, then its thermal energy in kJ is approximately $2.75T_e$ (in keV) $\times n_e$ (in units of 10^{21}/cm^3). For the temperature and density regimes of interest (4 to 5 keV, 1 to 1.5×10^{21}), this corresponds to 10 to 20 kJ. Moreover, the sound speed of Xe gas at 4 keV is ~6×10^7 cm/s, so the rarefaction takes more than 1 ns to propagate to the center of the 1.4-mm-radius bag.

The Xe emission calculations just discussed were made with a non–local-thermodynamic-equilibrium average-atom model known as XSN.[8] Better theoretical estimates using a detailed configuration approximation model[9] give essentially the same result. Our estimates above also assume the radiation can get out. Detailed simulations with radiation transport of the lines indicate that the radiation can escape.

Hydrodynamics for Good Efficiency

Above we reasoned that efficient multi-keV radiation production is possible. It also indicates that the achievement of good multi-keV efficiency requires a hydrodynamic system that converts most of the laser energy into hot plasma at sufficient density that it can radiate a considerable fraction of the energy before it disassembles. Underdense plasmas can provide such a hydrodynamic system. Moreover, they do this better than discs, which is the main reason underdense plasmas can be considerably more efficient multi-keV sources than discs (see Fig. 2).

We can see the hydrodynamic differences by analyzing three simulated Xe gas-column sources of different densities (0.01, 0.02 and 0.1 g/cm^3) but irradiated by the same laser. Figure 6 shows the total L-shell radiation escaping 1-D simulations of these gas columns vs time. (1-D analogs of the 2-D gas column of Fig. 1[a]. The 1-D efficiency is higher than 2-D efficiency because there is no radial hydrodynamic disassembly.) The gas column that started at 0.01 g/cm^3 (~$0.2n_c$ when fully ionized) has the highest efficiency. At the

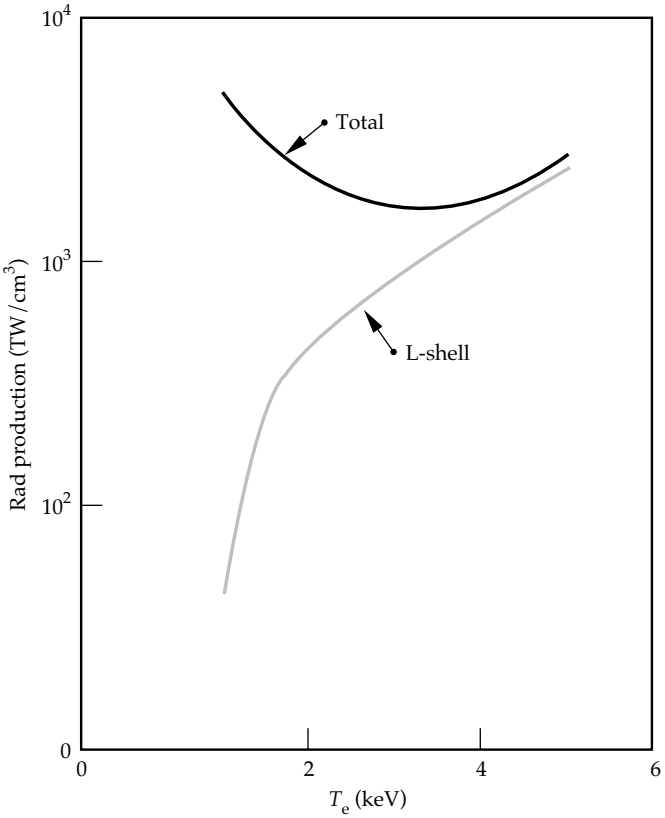

FIGURE 4. Total emission per cm^3 vs electron temperature and L-shell emission (Xe at 0.01g/cm^3). A material that is an efficient source of thermal x rays can also be a good source of multi-keV x rays, if we can make it hot enough. (20-03-0696-1303pb01)

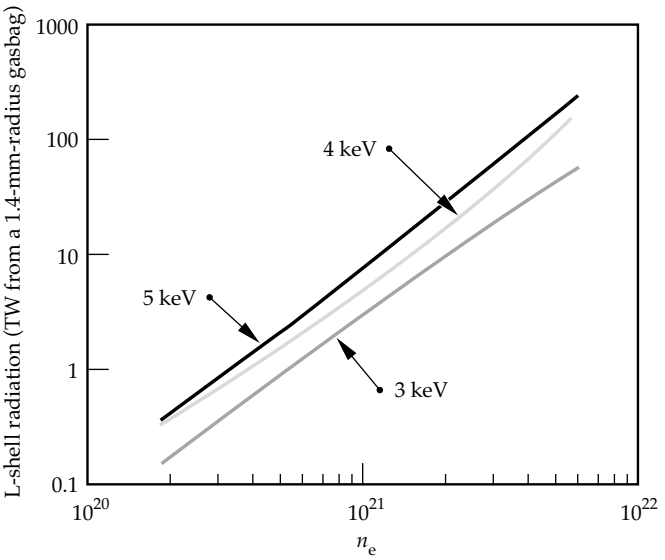

FIGURE 5. L-shell emission from the volume of a 1.4-mm-radius, Xe-filled gasbag, vs electron density. (20-03-0696-1304pb01)

end of the 2-ns pulse, more than half of the incident 48-TW laser power is escaping this column as L-shell emission. The column that started at 0.02 g/cm^3 behaves like the lower density one for ~1 ns, but then its efficiency drops notably. The 0.1-g/cm^3 gas column has comparatively low efficiency the whole time. We call it disc-like since its simulated L-shell radiation production is the same as a frozen Xe slab's (not shown).

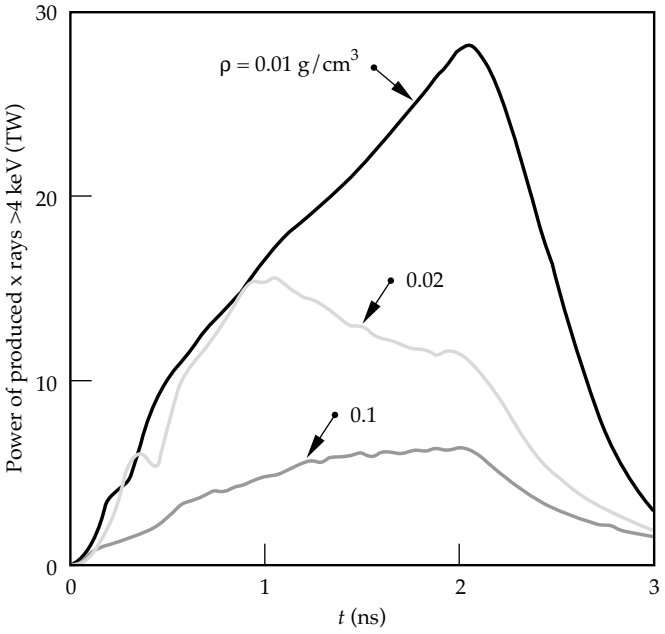

FIGURE 6. Time dependence of L-shell emission escaping 1-D LASNEX simulations of Xe gas columns of different densities. The three columns were all irradiated with 48 TW of blue laser light. (20-03-0696-1305pb01)

Now we can pass on to the next level of understanding. Figure 7 plots electron density and temperature, at 1 ns, vs length along the gas columns. The three 1-D gas columns clearly have very different hydrodynamics. In Fig. 7(a), in the 0.01-g/cm^3 gas column, the heating front moves nearly supersonically (also known as a bleaching front). However, in the poorest-efficiency, 0.1-g/cm^3 gas column, Fig. 7(b), the heating front moves subsonically (also known as an ablative front). Unlike the bleaching front, the ablative front drives a shock of dense material ahead of itself. The 0.02-g/cm^3 gas column is a transitional case; early in time it was heating in an approximately supersonic manner. However, residual hydrodynamics caused a density bump ahead of the front to accumulate, finally causing a transition, at ~1 ns, to completely ablative heating. The transition from bleaching to ablative coincides with the efficiency drops at 1 ns seen in Fig. 6.

Further analysis shows that a bleaching front creates far hotter plasma than an ablative front, hotter plasma that is denser and therefore more efficient in producing multi-keV x rays. In particular, we find the following:

- In producing a given mass of hot plasma, more energy is lost to low-photon-energy radiation when the heating occurs in a dense ablation front than when the matter is heated in the uncompressed bleaching front. The ablative front's dense material, which is being heated by conduction from the laser-deposition region, has a very high radiation production rate. However, since it is relatively cold, the emission is not multi-keV. This emission is energy lost from the system that cannot contribute to heating plasma and, since it is low-photon energy, does not contribute to multi-keV production. From the viewpoint of multi-keV radiation production, it is a parasitic loss.

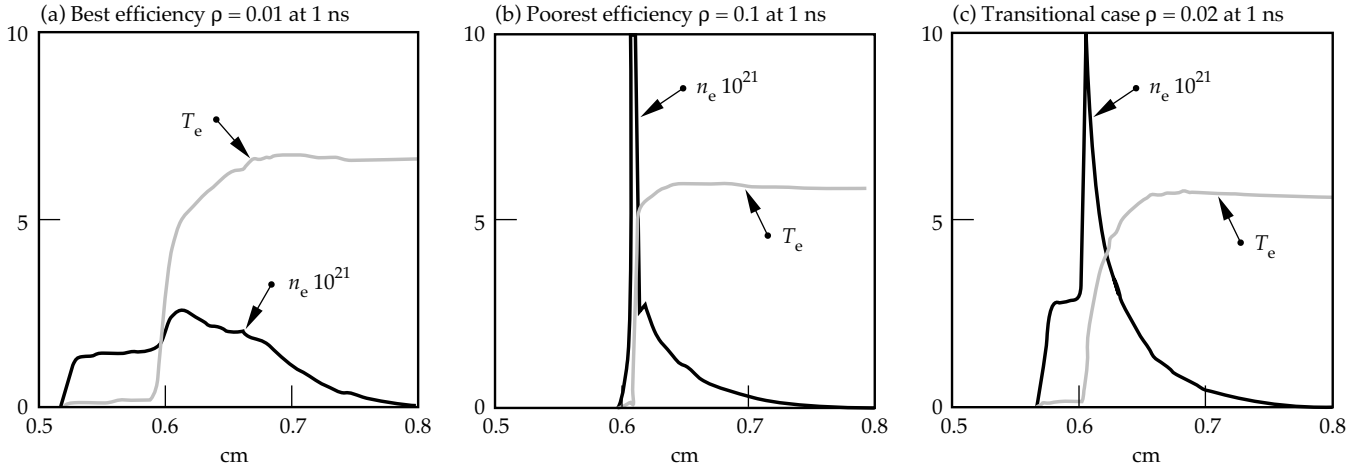

FIGURE 7. Electron temperature (keV) and electron density (× 10^{21}) at 1 ns vs axial position (cm) for the three 1-D gas-column sources in Fig. 6. (20-03-0696-1306pb01)

- Because of the higher density, the material in the ablation front rises to higher pressure. This ends up as more kinetic energy per unit of mass heated.
- More kinetic energy causes the hot blowoff behind an ablative heating front to be less dense than behind a bleaching front; compare electron density profiles of Fig. 7(a) and 7(b). Consequently, the blowoff behind the bleaching front produces more coronal, multi-keV x rays per unit mass because such emission scales approximately as $(n_e)^2$ (see Fig. 5).

Experimental Validation of Modeling

Calculations similar to those above provided the first indication that we might be able to very efficiently produce multi-keV x rays with laser-heated underdense sources.[10] Following these initial findings, we performed theoretical and experimental work to examine the validity of these predictions. This involved testing our ability to properly estimate the multi-keV efficiencies of published slab data,[11–13] as well as efficiencies from Xe-filled gasbags[6] specifically shot at Nova to test these predictions.[14] Figure 8 compares simulated and experimental absolute multi-keV efficiencies for all these experiments. Except for two low-intensity (1.4×10^{14} W/cm^2) slab targets, there is general agreement between the experiment and simulations. In particular, the >4 keV, L-shell production from our Xe gasbag experiments[14] agrees satisfactorily with the 2-D LASNEX estimates. They are actually slightly higher than the simulations. This favorable comparison seems to lend credibility to the predictions discussed above.

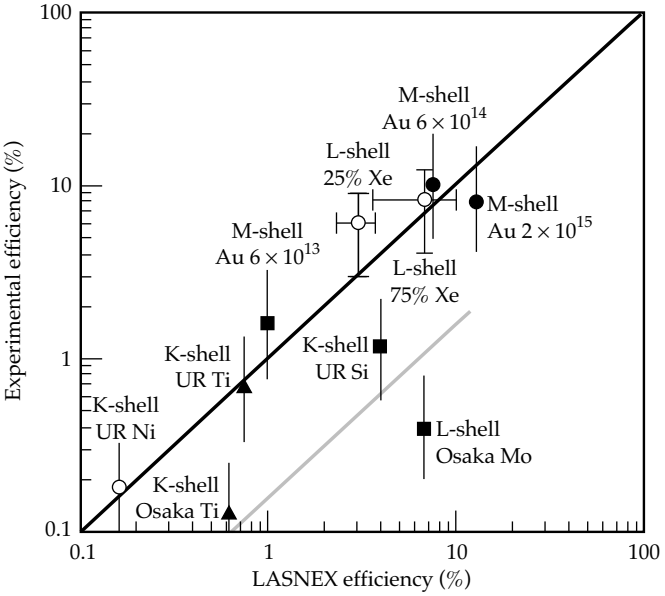

FIGURE 8. Comparison of simulated and experimental multi-keV conversion efficiencies from several databases. (20-03-0696-1307pb01)

In addition to this comparison with experiment, there is a fairly extensive and documented database indicating that LASNEX reasonably models the electron temperature in gasbags and gas-filled hohlraums.[15] The capacity to properly estimate underdense plasma electron temperatures is an essential component of believable, multi-keV predictions.

Applications of Efficient Multi-KeV X-Ray Sources

Below we discuss four applications of high-energy, multi-keV sources with the NIF:

1. Volume preheating of experimental targets.
2. Bright, multi-keV backlighting.
3. Pumping for fluorescent imaging of capsule dopants and doppler velocimetry.
4. Uniform irradiation of large test objects for NWET.

Preheat Sources

Multi-keV x rays can be used to preheat experimental packages. The preheat temperature T_e produced in a package located distance d away from a multi-keV source can be found by balancing x-ray deposition with internal energy. Neglecting ionization energy, this balance is approximately

$$\frac{\eta_x E_L}{4\pi d^2 \ell} = \left(\frac{3}{2}\right)\frac{\rho(Z+1)T_e}{A}\left(9\times 10^4\right) \quad . \tag{1}$$

Here η_x is the multi-keV efficiency; E_L is the laser power; ℓ is the scale length over which x-ray absorption occurs in the experimental package; ρ, Z, and A are the density, atomic number, and weight of the experiment we are preheating. Using $\eta_x = 30\%$, $E_L = 10^6$ J, $d = 0.5$ cm, $\rho = 1$ g/cm^3, and $(Z+1)/A = 0.33$ gives $T_e = 2$ eV-cm/ℓ. Depending on ℓ, it may be possible to preheat large $\rho = 1$ samples to ~5 eV and thinner ones up to several tens of eV, possibly approaching 100 eV. NIF applications for preheat sources like this include off-Hugoniot equation-of-state measurements and low-temperature hydrodynamics.

Backlighter Sources

Sources like these could serve as the bright, high-photon-energy, large-area backlighters needed for bigger targets. Consider, for example, the 60-TW Ge source listed in Table 1 scaled up to 100 TW (14% > 10 keV). Viewed from the end of the 2-mm-diam cylinder, the >10-keV emission/cm^2/sr will be 3.5×10^{13} W/cm^2/sr. This is equivalent to viewing a 10-keV hemi-isotropic

disc source of 1% efficiency irradiated by 700 TW at an intensity of ~2.2×10^{16} W/cm^2.

Pumps for Fluorescence-Based Diagnosis

Efficient multi-keV sources and high-power lasers may allow us to field fluorescence-based diagnostics—a qualitatively new way of studying hydrodynamics. The principle is simple: a multi-keV source at distance d pumps a dopant in a capsule. In imaging, the number of photons collected from a resolution element r is given by

$$\#\ \text{of photons} = \frac{\eta_x P_L}{4\pi d^2} r^2 \left(\frac{r}{\ell}\right) \frac{\frac{\eta_F}{4\pi}\delta\Omega\eta_{det}\delta\tau}{E_x} \quad . \qquad (2)$$

Here, P_L is the laser power; E_x, the source's average photon energy; η_F, the dopant's fluorescent efficiency; and $\delta\Omega$, η_{det}, and $\delta\tau$, the camera's solid angle, efficiency, and time resolution. Using r = 10 μm, P_L = 60 TW, η_x = 10%, E_x = 10 keV, d = 0.5 cm, $\delta\tau$ = 100 ps, and η_F = 0.2 (i.e., Cu-K at 8 keV has η_F = 0.2 in Ref. 16) gives

$$\#\ \text{of photons} = \left(3.2 \times 10^9\right)\left(\frac{10\,\mu\text{m}}{\ell}\right)\delta\Omega\eta_{det} \quad . \qquad (3)$$

For a 10-μm pinhole at 1 cm and the dopant concentration arranged so that $10\,\mu\text{m}/\ell$ = 0.01 to 0.1, we collect 40 to 400 photons from each 10-μm resolution element. For a curved crystal/Rowland circle system, the number of photons could be ~300 to 3000, at 1% crystal reflectivity.

A compelling possibility is using doppler spectroscopy of fluorescent lines to measure pusher velocity and, possibly, show the evolution of turbulence (via line broadening) at stagnation. Figure 9 indicates how the fluorescent lines may be shifted when the pusher starts to move, during final acceleration, and during stagnation. A requirement for this will be an efficient spectrometer which sees only diametrically opposed parts of a doped capsule. Related to this, fluorescence might produce cutaway pictures of capsule mix, perhaps similar to those used to visualize mixing in 3-D simulations. At a velocity of 10^7 cm/s or more, narrowband Doppler imaging with a camera of spectral resolving power 1500 or greater[17,18] could image only one side of the imploding pusher.

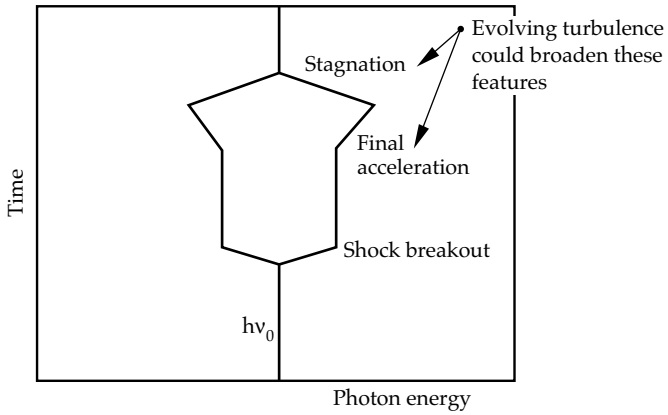

FIGURE 9. Doppler spectroscopy of fluorescing dopants in a capsule could measure pusher velocity and, possibly, show the evolution of turbulence, via line broadening, at stagnation. Efficient multi-keV sources could pump such fluorescence. (20-03-0696-1308pb01)

Large Fluence-Area Products with Good Uniformity

A requirement for NWET is that the flux over a test object be uniform to ±10%. This allows us to describe an NWET simulator by the fluence × area product that it can produce with that uniformity. In general, the fluence × area product in a given spectral region will be

$$\text{fluence} \times \text{area} = \left(\frac{E_L \eta}{4\pi}\right) T_{\text{debris-shield}}\left(\delta\Omega_{10\%}\right) \quad . \qquad (4)$$

The first term ($E_L\eta/4\pi$) is the source output per steradian in the spectral range of interest. It is determined by multi-keV source efficiency and total laser energy. $T_{\text{debris-shield}}$ is the debris shield transmission. It will be ~unity at 5 keV and higher, but may be significantly <1 at lower energies. The last term $\delta\Omega_{10\%}$ is the solid angle we can collect from each source and still get ±10% uniformity. It is a strong function of geometry. If all the emission is concentrated at a single point, as in typical pulse-power NWET simulators, we can collect only 0.45 sr with ±10% uniformity. However, if we produce x rays in a number of properly distributed sources, the useful solid angle increases. With four distributed sources, we can collect up to 1.6 sr from each source, and with 25 distributed sources, 4.5 sr. Thus, with proper facility capabilities, it is possible for 1 J of laser-produced multi-keV energy to be worth up to 10 J produced by a more conventional NWET simulation source. However, this improvement comes at a facilitization price. The sources need to be distributed over an area comparable to the size of the test object. For objects ~1 m across, this requires steering beams to irradiate sources much as 50 cm from chamber center.

On the NIF, the estimated fluence × area products with four distributed sources and 100% debris-shield transmission are as follows: 1 to 5 keV, 50,000 J-cm^2; 5 to 15 keV, 14,000 J-cm^2. With 25 distributed sources: 1 to 5 keV, 140,000 J-cm^2; 5 to 15 keV, 40,000 J-cm^2. This prospect for simulation capacity has led to the formation of a joint U.S. Department of Defense–Department of Energy working group (NIF Radiation Sources Users Group[19]) that works with the NIF Project aiming to optimize the NIF's NWET capabilities.

Acknowledgments

This work was supported by the Defense Nuclear Agency (Department of Defense) and the U.S. Department of Energy. We would like to acknowledge very useful discussions with Mike Tobin and Greg Simonsen of LLNL, C. P. Knowles of JAYCOR, and William Summa and Ralph Schneider of DNA.

Notes and References

1. M. Andrè, M. Novaro, and D. Schirmann, "Technologie pour un Laser Megajoule," *Review Scientifique et technique de la Direction des applications militaires*, Chocs, Numèro 13, 73, April 1995.
2. J. MacMordie, private communication (AWE, Aldermaston, UK, 1995).
3. J. T. Hunt et al., *A Design Basis for the National Ignition Facility*, Lawrence Livermore National Laboratory, Livermore, CA, UCRL-JC-117399 (1994).
4. G. B. Zimmerman and W. L. Kruer, *Comments Plasma Phys. Controlled Fusion* **2**, 51 (1975).
5. R. L. Kauffman, *Handbook of Plasma Physics, Vol. 3: Physics of Laser Plasma*, p. 123, Eds. M. N. Rosenbluth and R. Z. Sagdeev, Elsevier Science Publishers B. V. (1991).
6. R. L. Kirkwood et al., "Effect of Ion Wave Damping on Stimulated Raman Scattering in High Z Laser Produced Plasmas," *Phys. Rev. Lett*., accepted for publication.
7. B. J. MacGowan et al., *Phys Plasmas* **3**, 2029 (1996).
8. D. E. Post, R. V. Jensen, C. B. Tarter, W. H. Grasberger, and W. A. Lokke, *At. Data and Nuclear Data Tables* **20**, 397 (1977); G. B. Zimmerman and R. M. More, *J. Quant. Spectros. Radiat. Transfer* **23**, 517 (1980).
9. P. L. Hagelstein, *Physics of Short Wavelength Laser Design*, Lawrence Livermore National Laboratory, Livermore, CA, UCRL-53100 (1981).
10. L. J. Suter et al., "NIF will be a very useful DNA simulation facility just using laser produced x rays," *Proceedings of the NWET Applications for NIF Workshop*, G. Simonsen, Ed., Lawrence Livermore National Laboratory, Livermore, CA, March 15–17, 1994.
11. Kondo et al., *J. Appl. Phys*. **67**, 2693, (1990).
12. Yaakobi et al., *Opt. Commun*. **38**, 196 (1981).
13. R. L. Kauffman et al., *Laser Program Annual Report, 1986*, Lawrence Livermore National Laboratory, Livermore, CA, UCRL-50021-86 (1986).
14. R. L. Kauffman et al., *ICF Quarterly Report* **6**(2), Lawrence Livermore National Laboratory, Livermore, CA, UCRL-50021-96 (to be published fourth quarter, 1996).
15. L. V. Powers et al., *Phys. Plasmas* **2**, 2473 (1995).
16. S. T. Perkins et al., *Tables and Graphs of Atomic Subshell and Relaxation Data Derived from the LLNL Evaluated Atomic Data Library (EADL), z=1-100*, UCRL-50400 Vol. 30, Lawrence Livermore National Laboratory, Livermore, CA, October 31, 1991.
17. F. J. Marshall and J. Ortel, "A Framed Monochromatic X-Ray Microscope for ICF," *11th Topical Conference High Temperature Plasma Diagnostics*, Monterey, CA, May 12–16, CONF-960543-Absts., E-1, submitted to RSI.
18. S. A. Pikuz et al., "High-Luminosity Monochromatic X-Ray Backlighting Using Incoherent Plasma Source to Study Extremely Dense Plasma," *11th Topical Conference High Temperature Plasma Diagnostics*, Monterey, CA, May 12–16, CONF-960543-Absts., E-2, submitted to RSI.
19. Wendland Beezhold (SNLA), George Ulrich (DNA), and Greg Simonsen (LLNL), private communication (December, 1994).

Laser–Tissue Interaction Modeling with the LATIS Computer Program

R. A. London *M. E. Glinsky*

D. S. Bailey *G. B. Zimmerman*

D. C. Eder

Introduction

The development of new instruments and procedures for use in laser medicine typically involves extensive experimental and clinical studies. Computational modeling of the laser–tissue interaction process can be used to explore and reduce the experimental parameter space (e.g., laser wavelength, pulse length and pulse energy), and to gain a deeper understanding of specific laser-medical processes. In this way, modeling can lead to more rapid development of new instruments and protocols and to the genesis of new ideas. In addition, modeling will be useful in the future for patient-specific treatment planning and for physician training. Modeling will only be useful, however, if it is closely linked to experiments; a project to develop a specific instrument or protocol must involve iteration between modeling and experiment, converging on a set of optimized design parameters. Figure 1 shows a likely iterative process using LATIS, a computer program we have recently developed at the Lawrence Livermore National Laboratory to treat a wide range of laser–tissue interaction phenomena.

The therapeutic uses of lasers fall into three broad classes, depending on the physical mechanism by which the laser interacts with and alters the living tissue: photothermal, photochemical, and photomechanical. The physical processes involved in these three laser–tissue interactions include laser light propagation, thermal heat transport, thermal coagulation, and other material changes; photochemistry; and hydrodynamic motion, respectively. An excellent introduction to many aspects of these processes can be found in a recently published textbook in which chapters have been written by several of the experts in this field.[1] In this article, we present the structure and contents of the LATIS program. We also present a brief discussion of several applications, and a detailed discussion of one application: the problem of laser-light dosimetry with dynamic optical properties.

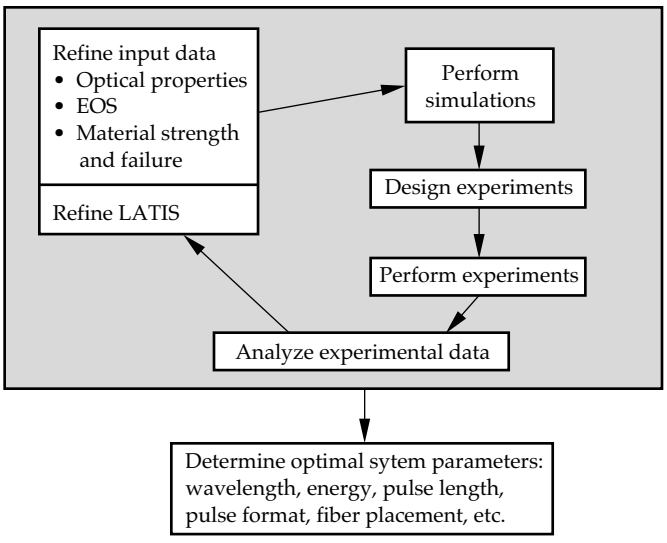

FIGURE 1. LATIS is used in an iterative method along with experiments to design a laser-medicine system. The cycle eventually converges on optimized experiment design parameters. (50-03-0796-1584pb01)

The LATIS Program

LATIS is a two-dimensional, time-dependent simulation program. It is based on the experience gained during 25 years of modeling high-intensity laser–matter interactions for fusion research, particularly with the LASNEX code.[2] LATIS uses cylindrical geometry, with spatial positions described by radial and axial coordinates, r and z. The spatial domain of a calculation is defined by a connected mesh of line segments containing quadrilateral zones. Each line segment intersection is called a mesh point. Positions and velocities are defined at the mesh points, while most material properties, such as temperature and density, are defined at the zone centers. Physical properties are modeled mathematically by analytic formulas, table interpolations, and both ordinary and partial differential equations. Partial differential equations are solved by finite-difference or finite-element methods. In addition, the Monte Carlo method is also used for laser transport, as described below. LATIS is written in

FORTRAN and controlled by a computer-science backplane called Basis.[3] Basis is an interpreter that allows the user considerable flexibility in setting up problems, adding user-defined functions without recompiling the code, and mathematical and graphical post-processing.

The physical processes considered by LATIS are grouped into four categories, as illustrated in Fig. 2: laser propagation, thermal response, material response, and hydro response. For most applications, laser propagation is calculated in the radiation-transfer approximation, although for certain situations, such as ultrashort laser pulses, a wave treatment is needed. Reference 1 describes the radiation transfer approximation in the context of laser–tissue interaction and the associated calculational methods.

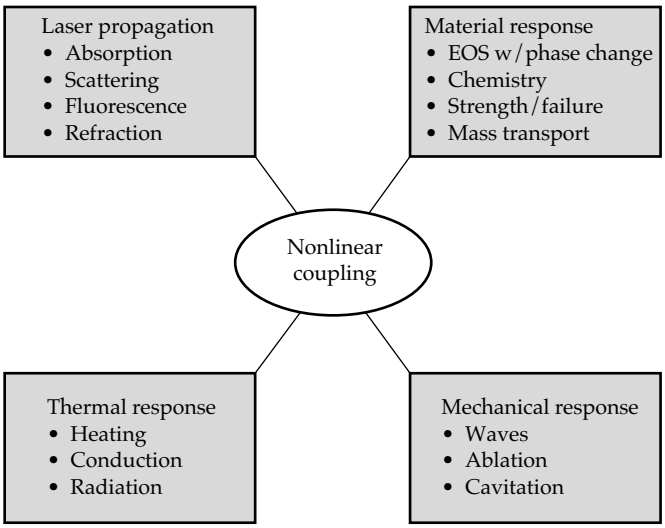

FIGURE 2. LATIS models laser–tissue interactions considering four areas of coupled physical processes. Features such as the hydro response are being developed for future use in tissue ablation applications. (50-03-0796-1585pb01)

Laser Propagation

To model the laser propagation portion of a simulation, we mainly use the time-dependent Monte Carlo method, in which light is represented by a finite number of "super photons"—typically 10^3 to 10^4. Since a typical problem involves on the order of 1 J of laser energy, each super photon represents on the order of 10^{15} real photons. (Henceforth we refer to the super photons simply as photons.) The propagation of the photons is treated in a probabilistic manner. In LATIS, laser photons are created along one or several line segments of the numerical mesh with specified spatial energy distribution and angular distribution relative to the segment normal. A fixed number of photons is introduced at the first time step of the simulation. The photons are then tracked time-dependently through the spatial domain of the calculation. When they cross material interfaces with unequal indices of refraction, such as an air–tissue interface, Fresnel reflection and refraction are calculated. Scattering is calculated probabilistically along a photon's path, according to the scattering coefficient, which may vary in space and time. An anisotropic angular phase function is used to select the scattering angle. We currently use the Henyey–Greenstein phase function, which has been found to be a good approximation to tissue scattering.[4,5] Absorption is calculated analytically along each photon path according to the absorption coefficient, without destroying the photons. Each photon is assigned a weight, which decreases with absorption. When the weight drops below a specified value, typically 1%, the photon is retired from the Monte Carlo calculation. The energy absorbed along the photon path is tabulated in spatial zones, where it is added to the material internal energy. At the end of a time step, a certain number of photons are still "alive" within the spatial domain of the simulation, and a certain number have been removed, either by leaving the domain or by having dropped below the minimum weight. At the beginning of the next time step, new photons are injected if the laser source is still turned on. In order to keep the total number constant at the user-specified value, and to ensure the best statistics, an attempt is made to make the ratio of the number of source photons to the source energy for that particular time step equal to the ratio of the number of living photons to their total energy. If the number of photons that were removed during the time step is not enough to create the desired number of new photons to do this, we use a technique called "combing." Combing reduces the number of photons in zones having two or more photons in a statistical but energy-conserving manner.

In addition to the Monte Carlo method, we have the ablility to invoke the diffusion approximation for laser transport, which is generally faster, but not as accurate near the surface of the material and for complicated geometries. For ultrashort pulses, we are adapting a wave equation solver to calculate the laser propagation and absorption.[6] This is necessary because the absorption occurs via an evanescent wave extending into a high-density plasma, which cannot be described in the radiation transfer approximation.

Thermal Response

Absorption of the laser light primarily goes into raising the tissue temperature according to its specific heat. (For soft tissues this quantity is approximately that of water.) Heat is then carried away from the laser deposition region by thermal conduction and other processes. This is modeled with the well known "bio-heat" equation—essentially a diffusion equation with cooling and heating terms due to blood perfusion and boundary effects (see Refs. 7 and 8 for a basic discussion of the bio-heat equation). The effects of blood perfusion are

important for relatively long pulses (>1 s), which are used mainly for photothermal therapies. Heat exchanges between blood and tissue occurs most effectively in the smallest vessels (the arterioles, venules, and capillaries). In these vessels, the blood and tissue come to the same temperature very rapidly. (In larger vessels, there is little heat transfer between the blood and the tissue due to the rapid flow rate and lower surface-to-volume ratio.) Because the small vessels are generally short (≈1 mm or less) compared to other scales of interest, such as the laser spot size, the blood thermal effects are assumed to be local. By further assuming that the blood coming into the arterioles has a temperature equal to the body core temperature (37°C), we represent the blood–tissue exchange as local heating and cooling rates that are linear in temperature and that drive the tissue towards body temperature. In the models discussed below, we assume specific temperature and damage dependence to the blood perfusion, representing increases due to vessel dilation at slightly elevated temperatures and a decrease due to coagulation at long exposures to high temperature.

Material Response

The material response portion of the LATIS simulation includes calculation of the equation of state (EOS) that specifies the internal energy and pressure of a material as functions of the density and temperature. We usually use steady-state, equilibrium models; however, time-dependent models can be incorporated. It is important to accurately describe phase changes in the EOS, such as the liquid–vapor change in water. In the primary implementation, the EOSs are generated in the form of tables and placed in a simple library format for easy access by LATIS. The tables are produced by the Livermore EOS generator HQEOS,[9,10] which is a global model including solid, liquid, vapor, and plasma states over a wide range of temperatures and densities. Models for chemical processes, such as protein denaturation and tissue coagulation, are included. We have also implemented an "Arrhenius" model, which describes such chemical processes by a single temperature-dependent rate equation.[11] Henceforth these processes are generically called damage. The rate equation is integrated to give a "damage integral"

$$\Omega = \int k\, dt \quad , \tag{1(a)}$$

where the damage rate is

$$k = \frac{k_b T}{h} \exp\left[\frac{\Delta S}{R} - \frac{\Delta H}{RT}\right] \quad . \tag{1(b)}$$

In these equations, k_b, h, and R are the Boltzmann, Planck, and gas constants, T is temperature, and ΔS and ΔH are the entropy and enthalpy of the reaction. This formula applies formally only to ideal first-order reactions. Although in reality the damage processes in tissue are likely to be more complicated, we still use Eq. (1) as a convenient fitting formula to experimental data for such highly temperature-sensitive reactions. The undamaged fraction of the tissue $f_u = \exp(-\Omega)$, while the damaged fraction $f_d = 1 - f_u$. The damage integral is used to alter both the blood perfusion and the scattering coefficient. Other chemical processes, such as those responsible for tissue fusion in a welding procedure or photochemical processes during photodynamic therapy can be modeled in a similar manner. Another set of important material properties are the strength and failure characteristics under mechanical forces. We currently use simple prescriptions, such as a stress-strain relation, but more sophisticated time-dependent models are under development.

Hydrodynamic Response

The fourth category of physical process considered by LATIS is the hydrodynamic response of the tissue. These effects include acoustic waves, elastic and plastic deformations, and large motions such as cavitation and ablation. LATIS solves partial differential equations describing mass and momentum conservation using the Lagrangian method. In this method, the spatial zones represent small mass elements. The mesh points move in response to pressures generated in neighboring zones. The mass stays in each zone, moving with the mesh. The hydro equations are solved by a finite difference method and advanced in time via a second-order differencing scheme. The method is explicit, so that a maximum time step is set by a numerical stability criterion (the "Courant limit"). Other criteria, such as changes in the temperature and density, are also used to set a maximum time step to ensure an accurate and stable solution of the hydro equations.

Coupling

The four areas of interactions are all coupled together allowing for nonlinear effects, such as alteration of the optical and thermal properties by time-dependent variations of temperature. This coupling is done explicitly by the operator splitting method, in which the time advance of each process is calculated using the most recent data from the other processes. The accuracy of this procedure is fixed with time-step controls, ensuring a converged solution.

Applications of LATIS

To date, LATIS has been used to simulate both photothermal and photomechanical laser–tissue interactions. Photochemical applications are planned for future

work in the areas of cancer and arthritis treatment. In the photothermal area, we have used LATIS to study the effects of dynamic optical properties on laser dosimetry[12] (which we summarize below as a detailed example of LATIS in action), welding of intravascular patches,[13,14] and the thermal environment for general tissue welding.[15] In the photomechanical area, we have applied LATIS to study high-precision tissue ablation with ultrashort pulses[16] and laser thrombolysis for stroke therapy.[17]

Laser Dosimetry with Dynamic Optics

Many laser applications are based on raising the temperature of a localized region of tissue for a certain period of time to cause necrosis or other alterations, such as tissue fusion. In these photothermal applications, the local energy dose (energy/unit mass) delivered to the tissue is a critical parameter.

Dynamic optics is defined as the alteration of tissue optical properties by laser irradiation. The effects of dynamic optics on the total dose to the tissue, the size of the damaged region, and the reflected light pattern are very important for photothermal applications of lasers, such as tumor treatments.[18] In this section, we illustrate the application of LATIS to a problem in which the laser scattering coefficient and the blood perfusion change due to thermal damage. We focus on the size of the damage region, and we study how dynamic optics effects vary with the laser-irradiation and tissue parameters.

We chose characteristic, but "generic," tissue properties to demonstrate the capabilities of LATIS and to illustrate the physical effects involving dynamic optics. The optical properties were those of dog myocardium at a laser wavelength of 630 nm. The dynamic scattering coefficient was a linear combination of an undamaged and a damaged coefficient: $\mu_s = \mu_u f_u + \mu_d f_d$, where the tissue f_u and f_d are calculated as described in the paragraph following Eq. (1). The scattering coefficients were $\mu_u = 50\ \text{cm}^{-1}$ and $\mu_d = 350\ \text{cm}^{-1}$. The absorption coefficient was fixed at $\mu_a = 0.3\ \text{cm}^{-1}$. Such parameters are also typical of many other soft tissues in the 630–800-nm range. Thermal properties (heat capacity and conductivity) were taken to be those of water, accurate to 30% for most tissues.[19] Damage rate coefficients were fit to average data for whitening of several tissues: dog prostate, dog heart, and rat and pig liver. The coefficients used in Eq. (1) were $\Delta S = 68.2$ cal/deg/mole and $\Delta H = 45.79$ kcal/mole. With these coefficients, the damage time scale $(1/k)$ varies rapidly with temperature from 100 s at 65°C to 0.5 s at 90°C. In the simulations, the temperature was kept near 72.5°C, at which the damage time scale was 20 s. We also included temperature and damage effects on the blood perfusion.[20] The temperature-dependent coefficient increased linearly by a factor of four between 37°C and 42°C to model increased perfusion due to vessel dilation. It was constant at temperatures above 42°C. The damage-dependent coefficient was an exponential cutoff of the perfusion with the damage integral to account for vessel coagulation.

A standard case was defined with the following parameters: laser pulse length 60 s, laser spot size (radius) = 1 mm, scattering anisotropy factor = 0.9, and blood perfusion rate = 0.4 mL/g/min. The laser irradiation pattern was assumed circular with a constant intensity distribution, and the tissue was assumed initially homogeneous. The irradiation geometry and problem zoning are shown in Fig. 3. Fine zones were placed near the laser spot,

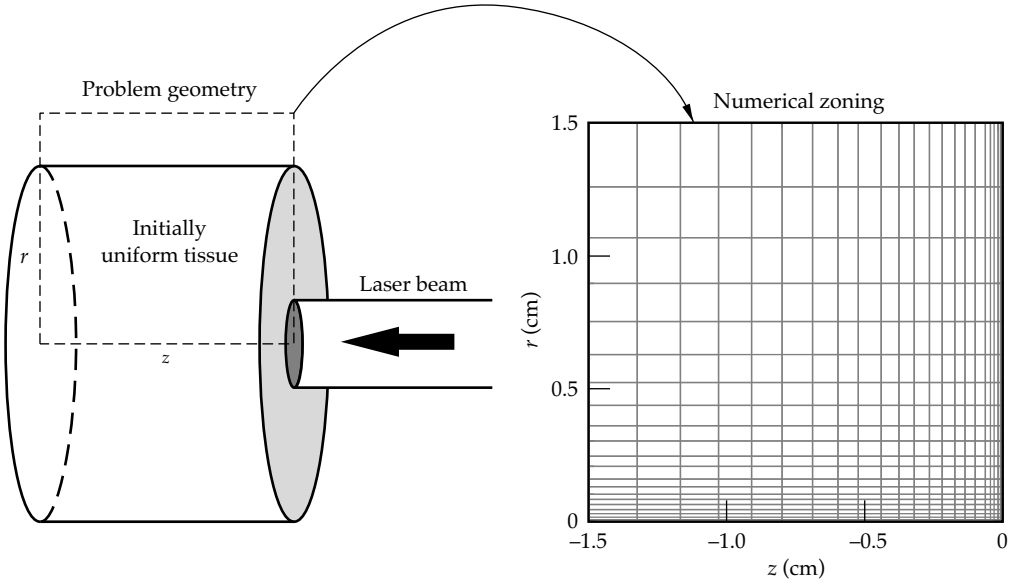

FIGURE 3. The laser–tissue interaction is modeled in cylindrical geometry, with fine zoning near the laser spot and course zones far from the spot. (50-03-0796-1586pb01)

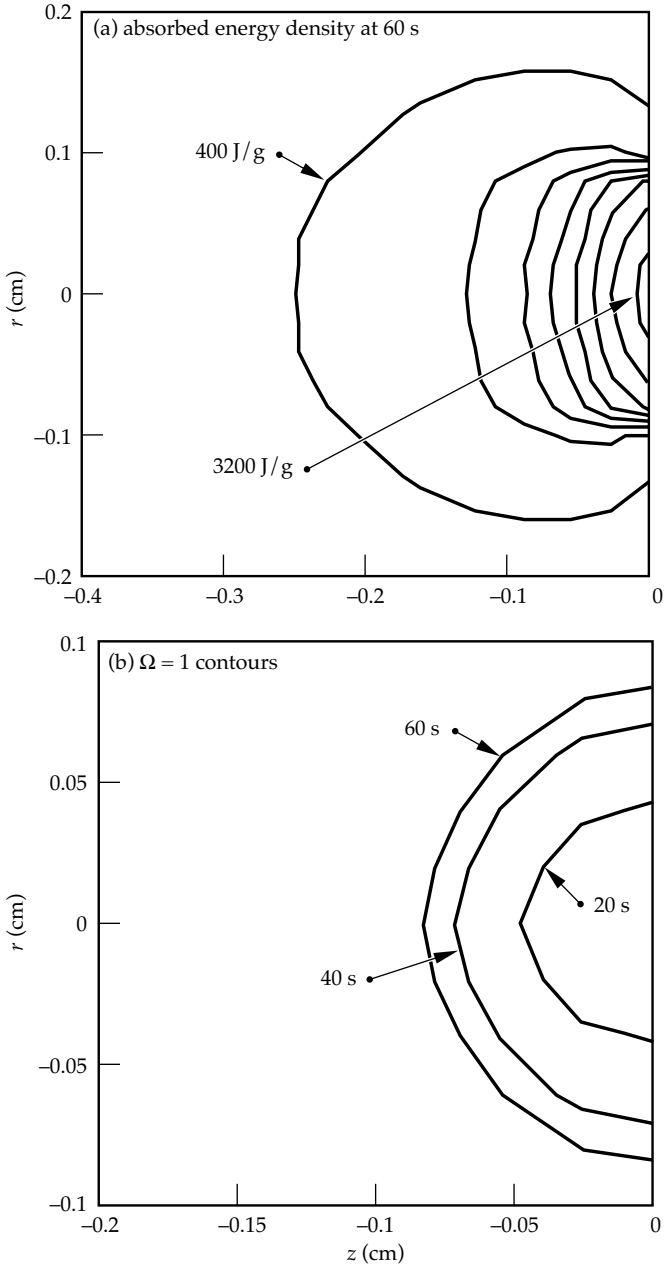

FIGURE 4. The total absorbed energy density integrated over the 60-s pulse is shown in (a). The contour intervals are equal. Laser and tissue conditions are for the standard case. This pattern reflects the light distribution. The damage region ($\Omega = 1$) is shown at various times during the pulse in (b). It grows due to heat diffusion and time-accumulation of damage. (50-03-0796-1587pb01)

where the highest resolution was desired, while courser zones were used far from the laser deposition region. This zoning technique increased the problem resolution while maintaining a relatively small number of zones.

The laser intensity was controlled by a thermostat function that keeps the surface temperature of the directly irradiated region within a desired range. This type of control is motivated by clinical considerations, such as achieving a maximum damage rate over a specified volume without approaching temperatures near 100°C at which tissue dehydration might occur. We actively controlled the laser intensity by monitoring the average temperature in a 3×3 set of tissue zones within the laser spot. We turned the laser off when the temperature exceeded the desired maximum and then turned it back on when the temperature dropped below the desired minimum. We chose a minimum of 70°C and maximum of 75°C. This technique enabled a very good control of the damage progress and avoided adverse effects associated with dehydration or vaporization as temperatures approached 100°C. Such a temperature-control technique has recently been demonstrated experimentally using infrared radiometry by several groups.[21,22]

Results for the distribution of absorbed laser energy and the damage zone for a simulation of the standard case are shown in Figs. 4(a) and 4(b). The absorbed laser light reflects the time-average light distribution, since the absorption coefficient is constant. Due to heat diffusion, the temperature distribution (not shown) extended further from the laser focal region than the laser deposition. The size of the damage zone, as indicated by the $\Omega = 1$ contours of Fig. 4(b), grew in time, due to both heat diffusion beyond the energy deposition region and the increasing time for accumulation of damage.

We now compare the damage zone ($\Omega \geq 1$) for the standard case with dynamic optics to that with static optics in Fig. 5. By static optics we mean a simulation in which the scattering coefficient was kept fixed at its undamaged value even though the tissue became damaged. It is clear that the inclusion of dynamic optics reduces the size of the damage zone. To measure this reduction, we defined a damage ratio as the depth of the damage zone with dynamic optics relative to that without dynamic optics:

$$D \equiv \frac{z(\Omega = 1)\ \text{dynamic}}{z(\Omega = 1)\ \text{static}} \qquad (2)$$

For the standard case, as shown in Fig. 5(a), we found $D = 0.67$. For a larger spot size ($r = 0.5$ cm), shown in Fig. 5(b), the effect of dynamic optics was somewhat less than for the standard case—$D = 0.77$.

We performed a parametric study that quantified the reduction in the damage zone caused by dynamic optics. For each parameter variation, we performed two simulations—one with dynamic optical coefficients and one with static coefficients. We then formed the damage ratio as defined above. The parameter variations and resultant damage ratios are listed in Table 1.

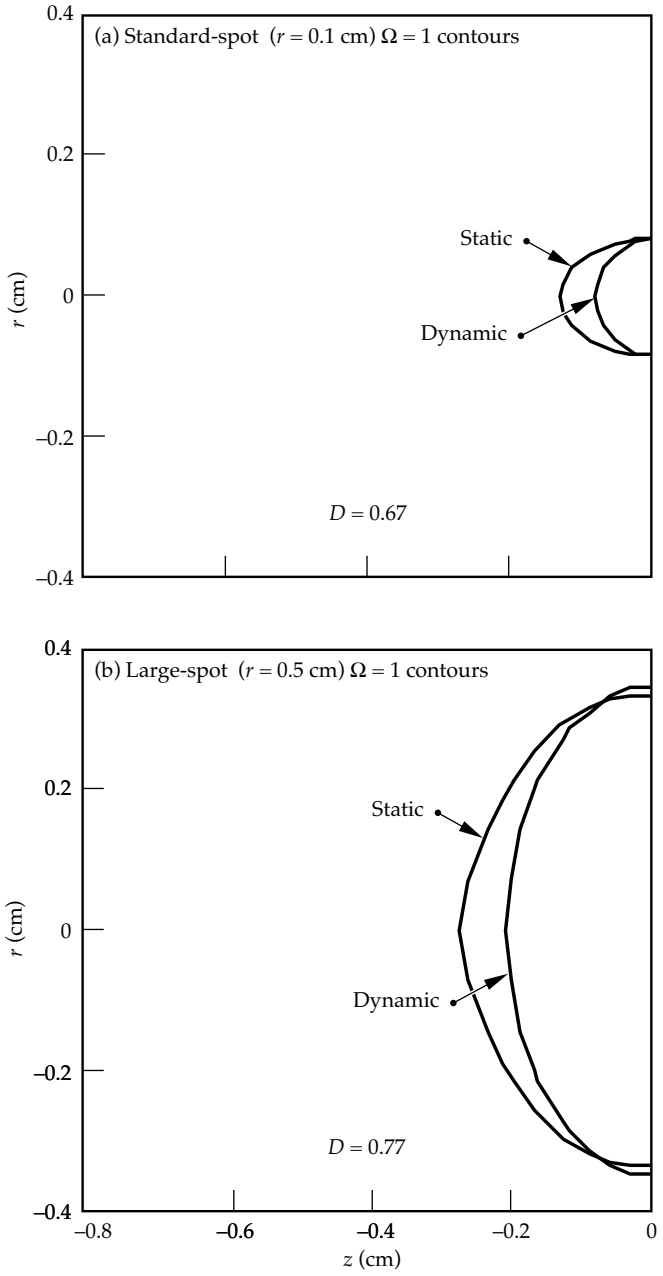

FIGURE 5. The size of the damage regions is reduced by dynamic optics, as shown for the standard case in (a) and for a case with a large spot in (b). The effect of dynamic optics is greater for the standard spot than for the large spot. All curves are for the end of the pulse (at 60 s). (50-03-0796-1588pb01)

The variation with spot size is the greatest. It can be understood by comparing the spot size to the diffusive optical penetration depth $\delta = [3\mu_a(\mu_s + \mu_a)]^{-1/2}$ (see Ref. 1, Chap. 6). For the undamaged tissue, $\delta = 0.46$ cm; for the damaged tissue, $\delta = 0.18$ cm. For spot sizes larger than δ (the case of 0.5 cm spot size), the deposition region is properly given by δ, which scales as $\mu_s^{-1/2}$ for $\mu_s >> \mu_a$ as is the case. For small spot sizes, the laser light scatters out of the beam, leading to smaller deposition region, scaling approximately as μ_s^{-1}. This higher dependence on μ_s leads to the relatively larger effect of dynamic optics for the smaller spots. The variation with pulse length stems from the relationship to the typical damage time scale. We controlled the surface temperature to an average value of 72.5°C, which gave a characteristic damage time scale of 20 s. Thus pulses of about 20 s or less do not have enough time to produce a large damage zone and therefore show less difference between the dynamic optics and the static optics cases as indicated in Table 1. We also explored variations in the isotropy of scattering and the blood perfusion rate. The isotropic scattering case assumed smaller scattering coefficients, so that the "reduced scattering coefficient" $\mu_s' = \mu_s(1 - g)$ was the same as for the standard case with $g = 0.9$. This was found to have very little effect on the simulation results. The case with no blood perfusion showed 10% larger damage depth in both dynamic and static cases, but very little differential effect, as seen in Table 1.

TABLE 1. Parameter variations and corresponding damage ratios.

Parameter variation	Damage ratio
Standard case	0.67
Short pulse (20 s)	0.76
Long pulse (180 s)	0.63
Small spot (0.01 cm)	0.39
Large spot (0.5 cm)	0.77
Isotropic scattering	0.67
No blood perfusion	0.66

In summary we see that dynamic optics reduces the depth of damage by about 33% in most cases, with the greatest sensitivity to the irradiation spot size and pulse length. This study illustrates the importance of including such nonlinear effects in designing protocols for laser thermotherapies. Projects on thermotherapy for benign prostate hyperplasia and laser–tissue welding are currently in progress in which similar modeling is being used to design experiments and to compare directly with measured data.

Summary

The LATIS computer program is being developed to treat all of the important aspects of laser–tissue interaction including laser propagation, thermal effects, material effects, and hydrodynamics, in a fully coupled manner. In LATIS, we now have a powerful tool for designing new medical devices and procedures through computational simulation. LATIS is being applied to areas of photothermal therapy, tissue welding, hard-tissue ablation, and thrombolysis.

Notes and References

1. A. J. Welch and M. J. C. Van Gemert, *Optical-Thermal Response of Laser-Irradiated Tissue* (Plenum Press, New York, 1995).
2. G. B. Zimmerman and W. L. Kruer, *Commun. Plasma Phys. Controlled Fusion* **11**, 82 (1975).
3. P. F. DuBois, *Computers in Physics* **8**, 70 (1994).
4. L. G. Henyey and J. L. Greenstein, *Astrophys. J.* **93**, 70 (1941).
5. S. L. Jacques, C. A. Alter, and S. A. Prahl, *Lasers Life Sci.* **1**, 309 (1987).
6. W. E. Alley, *A Maxwell equation solver for the simulation of moderately intense ultra-short pulse laser experiments,* p. 160, UCRL-LR-105820-92, Lawrence Livermore National Laboratory, Livermore, CA (1992).
7. Y. I. Cho, ed., "Bioengineering Heat Transfer," *Advances in Heat Transfer*, vol. 22 (Academic, San Diego, 1992).
8. C.-S. Orr and R. C. Eberhart, *Optical-Thermal Response of Laser-Irradiated Tissue,* p. 367, A. J. Welch and M. J. C. Van Gemert, Eds., Plenum Press, New York, 1995.
9. R. M. More, K. H. Warren, D. A. Young, and G. B. Zimmerman, *Phys. Fluids* **31**, 3059 (1988).
10. D. A. Young and E. M. Corey, *J. Appl. Phys.* **78**, 3748 (1995).
11. J. Pearce and S. Thomsen, *Optical-Thermal Response of Laser-Irradiated Tissue,* p. 561, A. J. Welch and M. J. C. Van Gemert, Eds., Plenum Press, New York, 1995.
12. R. A. London, M. E. Glinsky, G. B. Zimmerman, D. C. Eder, and S. L. Jacques, *Laser-Tissue Interaction VI* (SPIE—The International Society for Optical Engineering, Bellingham, WA, 1995; *Proc. SPIE* **2391**), p. 431.
13. M. E. Glinsky, R. A. London, G. B. Zimmerman, and S. L. Jacques, *Laser-Tissue Interaction VI* (SPIE—The International Society for Optical Engineering, Bellingham, WA, 1995; *Proc. SPIE* **2391**), p. 262.
14. M. E. Glinsky, R. A. London, G. B. Zimmerman, and S. L. Jacques, *Medical Applications of Lasers III* (SPIE—The International Society for Optical Engineering, Bellingham, WA, 1996; *Proc. SPIE* **2623**), p. 349.
15. D. J. Maitland, D. C. Eder, R. A. London, M. E. Glinsky, and B. A. Soltz, *Lasers in Surgery: Advanced Characterization, Therapeutics, and Systems VI* (SPIE—The International Society for Optical Engineering, Bellingham, WA, 1996; *Proc. SPIE* **2671**), p. 234.
16. R. A. London et al., *Laser–Tissue Interaction VII,* Ed. S. L. Jacques, *Proc. SPIE* **2681**, Bellingham WA, 1996, p. 233.
17. M. Strauss et al., *Lasers in Surgery: Advanced Characterization, Therapeutics, and Systems VI,* (SPIE—The International Society for Optical Engineering, Bellingham, WA, 1996; *Proc. SPIE* **2671**), p. 11.
18. G. Muller and A. Roggan, *Laser-Induced Interstitial Thermotherapy* (SPIE—The International Society for Optical Engineering, Bellingham, WA, 1995; *Proc. SPIE*).
19. J. W. Valvano, *Optical-Thermal Response of Laser-Irradiated Tissue,* p. 445, A. J. Welch and M. J. C. Van Gemert, Eds., Plenum Press, New York, 1995.
20. B.-M. Kim, S. L. Jacques, S. Rastegar, S. L. Thomsen, and M. Motamedi, *Laser-Tissue Interaction VI* (SPIE—The International Society for Optical Engineering, Bellingham, WA, 1995; *Proc. SPIE* **2391**), p. 443.
21. B. Lobel et al., *Lasers in Surgery: Advanced Characterization, Therapeutics, and Systems V* (SPIE—The International Society for Optical Engineering, Bellingham, WA, 1995; *Proc. SPIE* **2395**), p. 517.
22. I. Cilesiz, E. K. Chan, A. J. Welch, and S. L. Thomsen, *Lasers in Surgery: Advanced Characterization, Therapeutics, and Systems V* (SPIE—The International Society for Optical Engineering, Bellingham, WA, 1995; *Proc. SPIE* **2395**), p. 523.

THE ENERGETICS OF GAS-FILLED HOHLRAUMS

T. J. Orzechowski *D. E. Desenne*[*] *A. G. Dulieu*[*]
D. Juraszek[*] *R. L. Kauffman* *R. K. Kirkwood*
H. N. Kornblum *B. J. MacGowan* *D. S. Montgomery*
L. V. Powers *A. L. Richard*[*] *G. F. Stone*
L. J. Suter *R. J. Wallace*

Introduction

The x-ray drive generated in a laser-driven hohlraum ablates the high-*Z* wall material[1–3] that can then fill the hohlraum with a high-density plasma during the laser pulse. This high-*Z* plasma absorbs the laser energy in regions well removed from the original location of the hohlraum wall. Because this plasma is high-*Z*, the conversion from laser energy to x rays can occur in a volume of the hohlraum that is not as well localized as the original hohlraum wall location, and this in turn can effect the drive symmetry in an unwanted way.[4] To mitigate the problems associated with this high-*Z* filling of the hohlraum, a low-*Z* material is introduced to tamp the high-*Z* wall.[5] This tamper is typically less than one-tenth of the critical density n_c for the laser light used to illuminate the hohlraum. However, the pressure associated with the tamper is sufficient to keep the hohlraum wall material from moving significant distances into the hohlraum interior, thus preventing the laser deposition region from moving large distances during the laser pulse.

In the experiments we discuss here, the tamper is generated from a gas that is confined in the hohlraum. These gas-filled hohlraums must be designed with low-mass windows over the laser entrance holes (LEHs) and diagnostic holes to confine the gas. Thin (3500-Å) polyimide ($C_{22}H_{10}N_2O_5$) windows cover all of the apertures to provide a gas-tight seal. The laser light rapidly burns through the windows and gas, heating and ionizing the low-*Z* material as it propagates to the hohlraum wall. In the standard scale-1 Nova hohlraums, this occurs in about 200 ps. We have studied the effect of methane (CH_4), propane (C_3H_8), and neopentane (C_5H_{12}) on the hohlraum performance. When fully ionized, these gases at 1 atm generate plasmas with 0.025, 0.04, and 0.1 n_c, respectively. As the hohlraum wall moves inward, this low-*Z* plasma is compressed and the density is slightly higher than the "atmospheric" densities.

The laser beam interacting with the low-density plasma can generate parametric instabilities that can scatter the laser light.[6] If this scattered laser light leaves the hohlraum, this reduces the energy available to produce the x-ray drive. This article presents the results of hohlraum energetics measurements that are designed to quantify the energy losses in gas-tamped hohlraums. The hohlraum drive is characterized by a Planckian distribution of x rays that defines the hohlraum temperature. We determine this hohlraum temperature by measuring the radiation associated with the interior hohlraum wall, which differs slightly from the actual hohlraum temperature. In addition, we measure the time-dependent losses associated with the stimulated processes: stimulated Brillouin scattering (SBS) and stimulated Raman scattering (SRS).[6]

Measurements of Hohlraum Energy Balance

Hohlraum Temperature Measurements

The gas-tamped hohlraums (shown in Fig. 1) are required to hold 1 atm of the desired tamping gas (CH_4, C_3H_8, or C_5H_{12}). This conventional scale-1 Nova hohlraum (2700 μm long and 1600 μm diam) has 75% LEHs (1200 μm diam) and a nominal 500-μm-diam Dante hole, which is lined with Be to reduce the closure of this aperture during the drive pulse. The Dante hole is positioned 20° down from horizontal in the hohlraum's midplane. All of the apertures are covered

*Centre D'Etudes de Limeil–Valenton, France

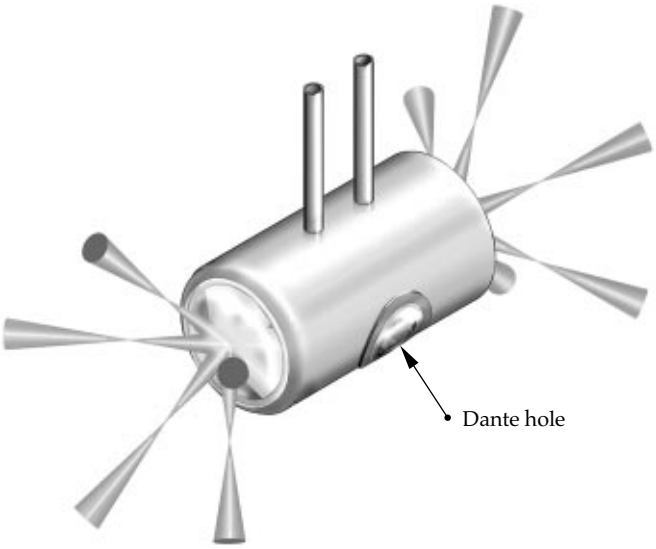

FIGURE 1. Schematic of a gas-filled hohlraum, showing five laser beams entering from each end. The fill gas is admitted through small tubes in the top of the hohlraum. The hohlraum temperature is monitored with an absolutely calibrated time-dependent soft x-ray spectrometer (Dante) that monitors the x-ray emission from the hohlraum wall through a small aperture. All of the apertures are covered with a 3500-Å polyimide membrane to provide a gas-tight seal. (08-00-0596-1242pb01)

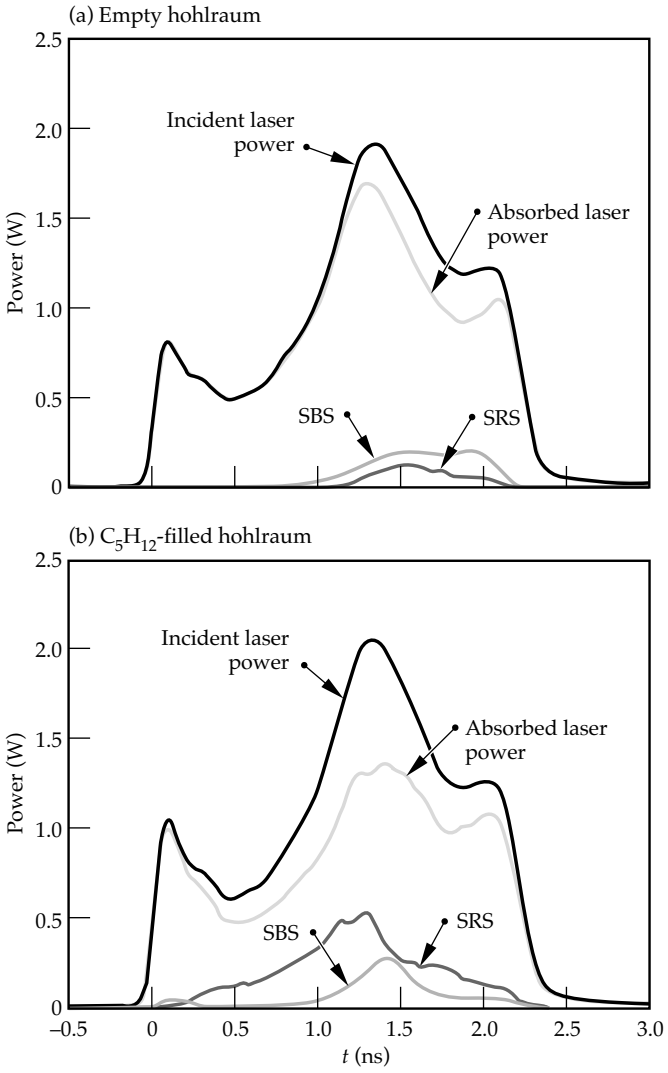

FIGURE 2. Measured incident laser pulse and the measured SRS and SBS for (a) an empty hohlraum and (b) a C_5H_{12}-filled hohlraum. The absorbed laser power is the difference between the incident power and the backscattered optical signal. (20-05-0796-1549pb01)

with a 3500-Å-thick polyimide membrane to provide a gas-tight seal. The gas enters the side of the hohlraum through two stainless-steel tubes (260 μm o.d. and 80-μm wall thickness). The total area occupied by these tubes is insignificant to the total interior area of the hohlraum.

Nova drives the hohlraum with five beams on each end, and the laser pulse is shaped in time with a foot and a peak. Figure 2 shows examples of the incident laser pulse shape, illustrating the laser power as a function of time and the SBS and SRS time histories, for an empty and a C_5H_{12}-filled hohlraum.† The laser beams are aimed at the center of the LEHs and defocused 1000 μm to give a laser spot size of 400 × 600 μm at the hohlraum wall. The spatially averaged laser intensity at the hohlraum wall (without subtracting the SBS and SRS losses) is then ~3×10^{14} W/cm^2 in the foot and rises to ~10^{15} W/cm^2 in the peak of the pulse.

The hohlraum temperature is measured with Dante,[7] which is an absolutely calibrated 10-channel, time-resolved soft-x-ray spectrometer. This diagnostic is located on the target chamber wall and views the hohlraum midplane along a line-of-sight 72° from vertical. The Dante views a section of the hohlraum wall that is not illuminated by the laser beams.

†The absorbed laser power is the difference between the incident and scattered laser power.

Dante measures the hohlraum wall temperature, which differs from the actual hohlraum temperature by a factor of the albedo (x-ray re-emission coefficient) to the 0.25 power. This corresponds to about a 5% correction to the hohlraum temperature, or ~10 eV at the peak of the drive. All of the measurements shown here correspond to the Dante (or wall) temperature.

Figure 3 shows the Dante measurements for various gas-filled hohlraums (the temperature histories for empty hohlraums with no windows; empty hohlraums with windows on the LEHs but no gas fill; and hohlraums filled with CH_4, C_3H_8, or C_5H_{12}). Each curve corresponds to two or three measurements with the same configuration (windows and/or gas fill), and the error bars correspond to the minimum and maximum measurement at each configuration. These data

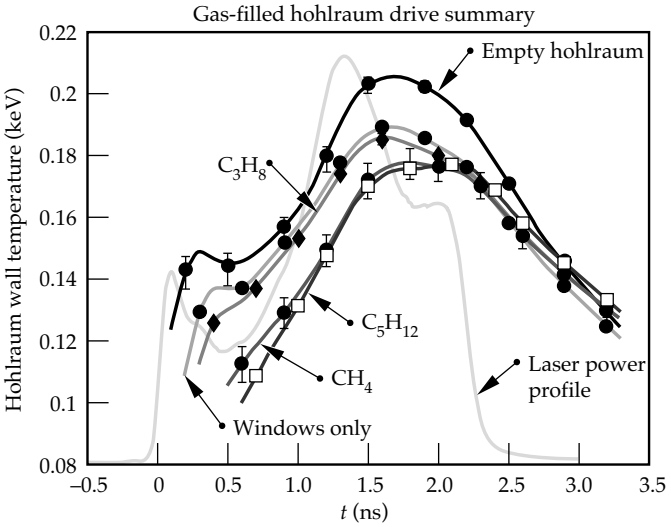

FIGURE 3. Hohlraum wall temperature as a function of time for empty hohlraums (with and without windows) and hohlraums with different gas fills (CH_4, C_3H_8, and C_5H_{12}). (20-05-0796-1548pb01)

show the drive to be quite reproducible. As expected, the addition of the gas causes an overall drop in the hohlraum temperature. However, the magnitude of the temperature drop cannot be attributed solely to the heat capacity of the gas and window material.

Two features are immediately apparent. First, the foot of the x-ray drive is significantly degraded in the hohlraum with windows only and the gas-filled hohlraum. This is due to the laser energy expended burning through the windows and then propagating through the gas. The small peak at the beginning of the laser pulse has completely disappeared, and the foot of the x-ray drive pulse rises more slowly. Second, the peak temperature decreases as the plasma density increases. Only a small part of this temperature decrease is attributable to the heat capacity of the gas; the major reduction in hohlraum drive can be attributed to backscattering (SRS and SBS) in the gas (discussed in the following section). Another interesting observation is the drop in temperature when the hohlraum has windows only and no gas. As can be seen from the data, the largest single temperature drop occurs when windows are added to the hohlraum.

Backscattered Energy Measurements

Nova's beamline 7 (BL7) is equipped with diagnostics[8] to monitor the laser energy that is reflected from the hohlraum via SBS and SRS. The diagnostics include calorimeters to monitor the total backscattered optical light energy (via each of the two processes) and streaked spectrometers to give the time-dependent optical spectra associated with each of the scattering mechanisms. The full aperture backscatter station (FABS) measures the radiation reflected back into the $f/4.3$ lens while the near beam imager (NBI)[9] monitors the optical light scattered at angles up to 20°. The temporal evolution of the backscattered radiation is inferred from normalizing the frequency- and time-integrated spectrum to the total backscattered energy.

Figure 4 shows the total reflected energy for the various gases and for the empty and windows-only hohlraums. In the empty hohlraum, most of the energy is reflected via SBS (6%) while an additional 3% is lost via SRS. When gas is introduced, the SRS becomes the dominant backscatter mechanism. The SRS level increases with the electron density n_e. While the time-integrated fraction of energy that is backscattered via stimulated processes can reach significant levels (~25% SRS + SBS in the C_5H_{12}-filled hohlraums), the time-dependent backscatter shows that during the laser pulse, the levels of backscatter can be even higher (see Fig. 2). Most of the scattered energy is associated with the main peak of the laser pulse, which starts about 1 ns into the pulse. This corresponds to the time at which the SRS and SBS gains are the largest due to the higher laser intensities (in the latter part of the pulse).

The laser beams used in these experiments are the standard, unsmoothed Nova laser beams. These beams include hot spots that can achieve intensities in excess of the average intensities quoted above. These higher intensities can exacerbate the growth of instabilities. To mitigate the problem of energy lost through backscattering, we intend to smooth the laser beams with random

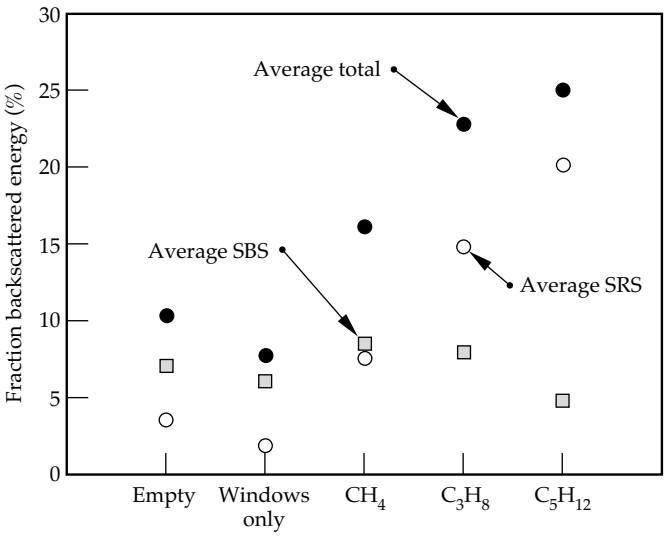

FIGURE 4. Fraction of backscattered laser energy (SRS, SBS, and their sum) for various hohlraum configurations (empty or windows only) and from hohlraums with various gas fills (CH_4, C_3H_8, and C_5H_{12}). (20-05-0796-1551pb01)

phase plates (RPPs) or kinoform phase plates (KPPs).[8] Figure 5 shows the effect of beam smoothing on the backscattered laser signal. We show the total backscatter levels for CH_4- and C_3H_8-filled hohlraums, using the standard Nova beam and a beam (BL7) smoothed with either a RPP or a KPP. The backscattered signal from the smoothed beam is a factor of 4 to 6 less than that for the unsmoothed beam.

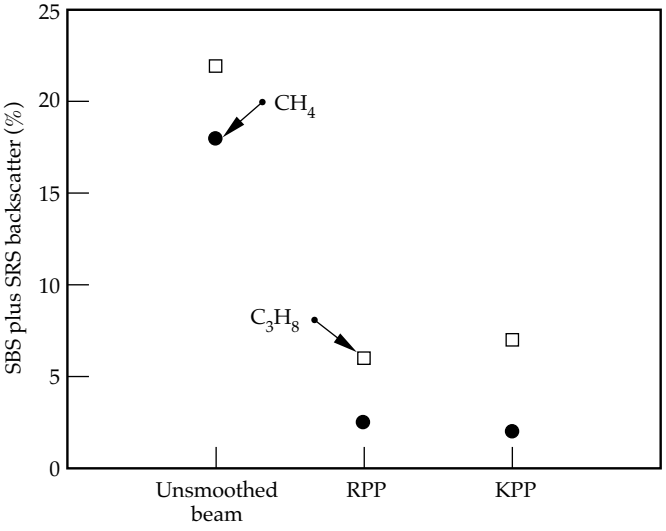

FIGURE 5. Fraction of backscatter laser energy (SRS plus SBS) in CH_4 or C_3H_8 gas corresponding to an unsmoothed laser beam and a laser beam smoothed with a random phase plate (RPP) or a kinoform phase plate (KPP). (20-05-0796-1550pb01)

An anomaly in these data is the energetics of the hohlraum with windows only. Note that the total backscatter fraction is slightly less than that for the standard, empty hohlraum. However, the temperature drop shown in Fig. 3 indicates a significant difference in absorbed energy. Comparing the integral over time of the radiated power (T_r^4) shows a difference of approximately 30% in total radiated energy while the backscatter energy shows virtually no difference. Looking again at Fig. 3, we see that the largest single energy difference is associated with attaching the windows to the hohlraum. We can speculate that the hohlraum is somehow contaminated in the process of installing the windows and that this contamination carries over to the remainder of the hohlraums with gas. On another series of measurements (less complete and with a slightly different temporal profile to the laser pulse), we saw a much smaller temperature drop associated with the hohlraum with windows only and no gas fill. There was no corresponding change in the relative levels of SRS and SBS. The contamination, if it is the problem, then, is associated with the fabrication technique and can vary from one set of hohlraums to another.

Modeling the Hohlraum Energetics

We use LASNEX[10] to simulate the time-dependent drive in the gas-tamped hohlraums. This code does not calculate the SBS and SRS losses; these losses are incorporated by using the net absorbed laser energy (i.e., measured incident minus SRS and SBS losses) in the calculation. We find that the code does not quite predict the level of temperature reduction that is observed in the experiment. The observed temperature drop in the CH_4-filled hohlraum is 20 eV, while the calculated temperature drop is 12 to 17 eV. This corresponds to a measured reduction in flux of 32% and a calculated reduction in flux of 21 to 28%. Similarly for C_3H_8, the measured reduction in temperature (flux) is 26 eV (40%), while the calculated drop in temperature (flux) is 18 to 21 eV (30 to 34%). This range in calculated temperature drop arises from a difference in calculated vs measured temperature as a function of time. The calculated temperature reaches a peak later in time. Simply comparing the peak calculated vs peak measured temperature results in a smaller difference. Looking at the calculated temperature at the time the measured temperature reaches a peak results in the larger difference.

In the modeling, there are two reasons for the reduction in drive in the gas-filled hohlraums. First, the radiation production is reduced because of the tamper. In the untamped hohlraum, the axial stagnation of the high-Z plasma is itself a source of radiation production. In the simulation, this reduced radiation production results in a temperature drop of 4 to 6 eV. Second, the drive is reduced due to decreased laser absorption (SRS and SBS). As mentioned, this part of the physics is added through the measured input power minus the measured SRS and SBS. In the simulation, this results in a 10- to 15-eV temperature drop.

Summary

We measured the time-dependent drive in gas-tamped hohlraums and compared the measurements with simulations. The addition of the gas tamper can result in as much as a 25-eV reduction in peak drive temperature. The overall drop in flux is as much as 40%, which is about 15% more than predicted by LASNEX simulations. Future experiments will use smoothed laser beams that will significantly reduce the levels of backscatter losses. Since these losses are not calculated by LASNEX, the new measurements will lend themselves to more accurate simulation.

Notes and References

1. R. E. Marshak, *Phys. Fluids* **1**, 24 (1958).
2. R. Pakula and R. Sigel, *Phys. Fluids* **28**, 232 (1985); **29**, 1340(E) (1986).
3. M. D. Rosen, *The Physics of Radiation Driven ICF Hohlraums*, Lawrence Livermore National Laboratory, Livermore, CA, UCRL-ID-121585 (1995); to be published in the *Proceedings of the 1995 Plasma–Physics Summer School of the La Jolla Institute for Advanced Physics*, V. Stefan, Ed. (1995).
4. J. D. Lindl, *Phys. Plasmas* **2**, 3933 (1995).
5. J. D. Lindl, *Laser Program Annual Report 1978*, Lawrence Livermore National Laboratory, Livermore, CA, UCRL-50055-78, 2–77 (1978).
6. W. L. Kruer, *The Physics of Laser Plasma Interactions* (Addison–Wesley Publishing Company, Redwood City, CA, 1988).
7. H. N. Kornblum, R. L. Kauffman, and J. A. Smith, *Rev. Sci Instrum*. **57**, 2179 (1986).
8. B. J. MacGowan, B. B. Afeyan, C. A. Back, R. L. Berger et al., *Phys. Plasmas* **3**(5), 2029 (1996).
9. R. K. Kirkwood, C. A. Back, M. A. Blain, D. E. Desenne et al., "Imaging Backscattered and Near to Backscattered Light in Ignition Scale Plasmas," Lawrence Livermore National Laboratory, Livermore, CA, UCRL-JC-124041 (1996); submitted to *Rev. Sci. Instrum*.
10. G. B. Zimmerman and W. L. Kruer, *Comments on Plasma Physics and Controlled Fusion* **2**, 51 (1975).

Fusion Reaction-Rate Measurements—Nova and NIF

R. A. Lerche

M. D. Cable

Introduction

Thermonuclear fusion can occur when laser energy compresses and heats a spherical capsule filled with deuterium (DD) or a deuterium–tritium (DT) mixture. A goal of the Inertial Confinement Fusion (ICF) Program is to achieve a compression of 1000 times liquid density at a temperature of ~10 keV for a plasma confined for ~100 ps.[1] During confinement, fuel atoms undergo fusion and release energy in the form of energetic charged particles, neutrons, and photons. We want to measure the fusion reaction rate as a function of time relative to the incident laser radiation because it is valuable information for researchers studying laser–target interactions. These measurements characterize the coupling of the drive energy to the target, the hydrodynamics of the capsule implosion, and the plasma conditions during peak emission. The fusion reaction rate, often referred to as "burn rate" or "burn history," is a sensitive indicator of our ability to accurately model energy transport between the laser and target.

The burn history for a target can be measured by monitoring the production rate of the fusion reaction products. At Nova, most measurements are made by recording the arrival time of 14-MeV neutrons produced in $T(d,n)^4He$ fusion reactions using a fast (30-ps resolution) detector several centimeters from the target.[2] Since fusion products are nearly monoenergetic and the target's emission region is submillimeter in size, the recorded signal is the target burn history with a time-of-flight delay dependent on the target-to-detector distance.

At the future National Ignition Facility (NIF), it is unlikely that the target burn history can be measured with the direct neutron technique used at Nova. This is because the thermal motion of the reacting plasma ions causes a broadening of the neutron energy spectrum, which in turn causes a temporal spread in neutron flight time to a detector. The time spread increases with target-to-detector distance. At NIF, there will be an exclusion zone around the target to minimize damage to blast shields and optics caused by ablated material. At anticipated detector distances of 1 to 5 m, the resulting spread in the neutron arrival times will mask burn-history information. Gamma rays, however, are virtually unaffected by plasma temperature and have negligible temporal dispersion at a distant detector. For these reasons, we are investigating techniques that use fusion gamma rays to measure burn history.

This article begins with a review of detector system characteristics required for making reaction-rate measurements. A description of the neutron-based measurement system implemented at Nova is followed with examples of reaction-rate measurements made for a variety of Nova targets. Finally, we discuss the challenge of measuring burn history at NIF and summarize current experiments associated with developing a gamma-ray-based technique to measure burn history.

Measurement Concept

One method for measuring the fusion reaction rate of an ICF target is to monitor the production rate of a fusion reaction product. Reactions available for DD- and DT-filled targets are

$$D + D \rightarrow {}^3He\,(0.82\ \text{MeV}) + n\,(2.54\ \text{MeV})$$

$$D + D \rightarrow {}^4T\,(1.01\ \text{MeV}) + p\,(3.02\ \text{MeV})$$

$$D + T \rightarrow {}^4He\,(3.56\ \text{MeV}) + n\,(14.03\ \text{MeV})$$

$$D + T \rightarrow {}^5He + \gamma\,(16.7\ \text{MeV}) \quad ,$$

where the particle energy is indicated in parentheses. The spectrum for each fusion product is nearly monoenergetic. The charged particles are slowed by Coulomb interactions with plasma ions and electrons before leaving the target. Most neutrons and gamma rays, however, escape from the target without collision. Since the reaction region is submillimeter in size, both neutron and gamma-ray temporal distributions at points outside the target preserve burn history. For this

reason, burn history may be measured with either a fast neutron or gamma-ray detector placed some distance away from the target. Since confinement times can be <100 ps, detectors with time resolutions of ~20 ps are desirable.

Temporal resolution for a neutron-based measurement is limited by the plasma ion temperature, the target-to-detector distance, and the detector thickness. Thermal motion of the reacting plasma ions causes a broadening of the neutron energy spectrum.[3] For neutrons leaving a target at the same instant, the energy spread causes a time spread in their arrival at a detector. The time spread Δt_e, which is proportional to distance, is given by $\Delta t_e = 1.22\sqrt{T} \times d$ for DT neutrons and $\Delta t_e = 7.88\sqrt{T} \times d$ for DD neutrons, where Δt_e is in ps, ion temperature T is in keV, and target-to-detector distance d is in cm. The detector must be placed close to the target to keep the time spread small. For example, to keep Δt_e below 20 ps for a 1-keV plasma requires d <16.4 cm for DT neutrons and <2.6 cm for DD neutrons.

A neutron detector must also be thin to achieve 20-ps response. In a detector, there is an uncertainty about the exact point of neutron interaction, and a corresponding uncertainty in the instant of the interaction. The uncertainty Δt_x is proportional to the detector thickness Δx and is given by $\Delta t_x = \Delta x / v_n$, where v_n is the speed of the neutron. Thus, to achieve a 20-ps response requires Δx <1 mm for DT neutrons and <0.4 mm for DD neutrons.

The less restrictive requirements of DT neutrons on target-to-detector distance and detector thickness are advantages for selecting DT fuel over DD fuel for making burn-history measurements. Furthermore, the larger fusion cross section for DT reactions results in a neutron yield nearly 100 times greater than for a hydrodynamically equivalent DD-filled target, an important consideration when working with low-yield targets. The 16.7-MeV fusion gamma rays were never seriously considered for Nova reaction-rate measurements because of the low branching ratio (5×10^{-5}) for the reaction.[4,5] There simply were not enough gamma rays to make burn-history measurements at Nova.

30-ps Neutron Detector

A critical step in our effort to record reaction rates with 30-ps resolution was the development of a sensitive, high-speed neutron detector. RIC (radiation-induced conductivity) detectors,[6] the fastest available before we developed a streak-camera-based instrument, were not sensitive and fast enough. Coupled to a 7-GHz transient recorder, RIC detectors had an impulse response of 125 ps full-width half-maximum (FWHM) and required yields of $>5 \times 10^{10}$ DT neutrons for a reaction-rate measurement.

Our detector is based on the fast rise time of a commercially available plastic scintillator. A thin piece of BC-422[7] converts neutron kinetic energy into light. As neutrons pass through the scintillator, some of them have elastic collisions with hydrogen nuclei. The recoil protons quickly transfer their kinetic energy to luminescent sites in the scintillator. For BC-422 the light output has a rise time <20 ps and a decay time of ~1.2 ns. The temporal distribution of the emitted light is the convolution of the neutron temporal distribution with the scintillator response. Burn-history information is encoded in the leading edge of the light pulse. A fast optical streak camera (<15 ps FWHM) records the signal.

The detector is the result of three technology advances. First we developed a detector concept based on the fast rise time of a plastic scintillator. At that time, the fastest plastic scintillators had nanosecond decay times and were believed to have rise times >100 ps, hardly fast enough for 30-ps measurements. Second, an experimental search for a fast-rise-time scintillator using a pulsed electron beam at the LLNL linac identified NE-111 (BC-422) as a potential candidate.[8] Later experiments at Nova with short bursts of x rays generated by irradiating gold disk targets with 20-ps-wide laser pulses demonstrated the scintillator rise time to be <20 ps.[9] Third, we discovered that our streak camera could be operated with a wide input slit without losing temporal resolution.[10] Wide slit operation allowed us a tenfold increase in system sensitivity by using a 1-mm-wide slit rather than the more typical 100-μm-wide slit used with other streak cameras.

Figure 1 shows the scintillator configuration. A 6-mm-diam, 1-mm-thick piece of BC-422 is housed in a Hevimet

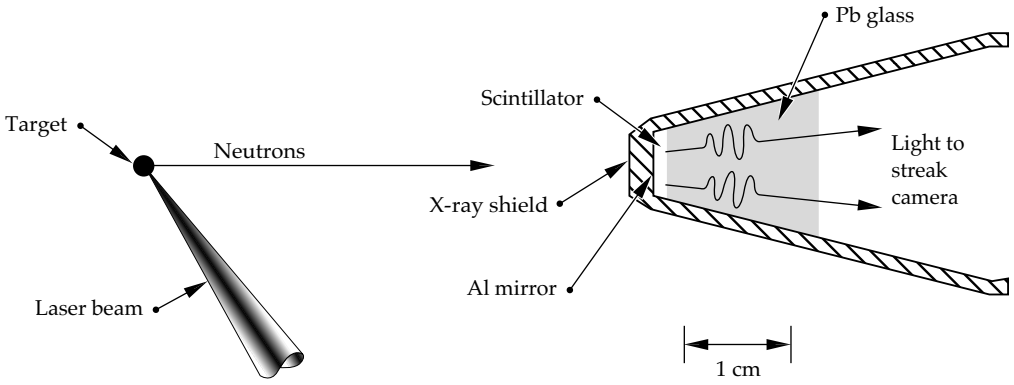

FIGURE 1. Detector nose cone configuration. Scintillator must be thin and close to the target to control temporal dispersion. (08-00-0896-1852pb01)

(90% tungsten) nose cone. The front of the nose cone, which is 3 mm thick, shields the scintillator from target x rays, scattered laser light, and target debris. A thin Al layer deposited on one surface of the scintillator acts as a mirror to double the light output directed towards the streak camera. A piece of Pb glass shields the back side of the scintillator from scattered x rays.

The detector system, which is called the NTD (for neutron timing diagnostic), features a nose cone assembly that can be positioned between 2 and 50 cm from the target. An achromatic $f/2$ zoom lens relays the scintillator image along a 4-m optical path to the S-20 photocathode of the streak camera located outside the vacuum chamber. Lens coupling produces minimal temporal dispersion. In contrast, using 4 m of graded-index optical fibers would produce ~80 ps of dispersion for the 350- to 450-nm scintillator light. Baffling and a light shield prevent scattered laser light from entering the lens system. Scintillator light passes through a glass window at the vacuum chamber wall. Components inside the chamber can operate at either vacuum or atmospheric pressure. The streak camera image is recorded with a charge-coupled device (CCD) camera. The relatively long distance between target and streak camera is an advantage of this configuration. Background caused by target x rays and neutrons interacting with the streak camera and the CCD decreases inversely with the square of the distance from the target.

Besides recording a neutron-induced signal, the streak camera also records an optical fiducial signal to provide an absolute time base. The Nova facility generates a 100-ps, 0.53-μm, optical timing pulse that is split and distributed to various diagnostic instruments via optical fibers. We insert a 527-ps etalon into its path to form a series of evenly spaced pulses. The first pulse provides an absolute timing reference required to temporally relate the neutron signal to the laser power recorded with other streak cameras with ±10-ps precision.[11] The pulse train provides a calibration check for the streak camera time base. The optical fiducial amplitude, timing, and pulse shape are easily controlled because they are independent of target type, incident laser energy, and target-to-detector distance. This is not the case when target-generated x rays are used as the fiducial.

Excellent data have been recorded with the NTD. Figure 2(a) shows an image recorded with the scintillator 2 cm from a low-yield target producing 6.7×10^8 DT neutrons. Figure 2(b) shows image exposure versus time averaged across the spatial extent of the neutron signal. Streak camera flat-field and time-base corrections are included in the signal processing. Information about the target burn history is encoded in the leading edge of the pulse.

We obtain the shape of the neutron temporal distribution by deconvolving the effect of the scintillator decay rate from the recorded neutron signal. The result, which is approximately the derivative of the recorded signal, actually represents the convolution of the target burn history with the streak camera response and the derivative of the scintillator rise time. Since the rise time and camera response are both <20 ps, the deconvolved signals are a good representation of the fusion reaction rate. The quality of each deconvolution is checked by comparing the recorded signal with the convolution of the burn history and the exponential decay of the scintillator.

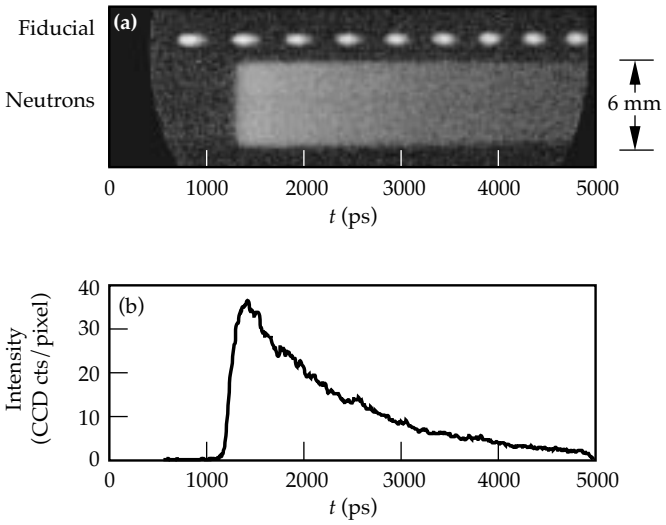

FIGURE 2. Neutron signal. (a) Streak camera image for a target producing 6.7×10^8 DT neutrons. (b) Average neutron signal intensity vs time. Burn history is encoded in the leading edge of the pulse. Pulse tail shows the characteristic decay of the scintillator. The complete burn history for this data is shown in Fig. 3(b). (08-00-0896-1853pb01)

Nova Reaction-Rate Measurements

Reaction-rate measurements with 30-ps resolution have been made for a variety of Nova targets whose DT yields ranged from 10^8 to 3.6×10^{13} neutrons. Measurements have also been made for targets with DD neutron yields between 10^9 and 10^{11}, but with temporal resolutions of ~50 ps. In this section, examples of burn histories for several different target types are presented. The intent of this section is to demonstrate the variety in burn-history signatures, and not to present a detailed examination of the performance of any particular target.

Direct-drive glass-microballoon targets are used for instrument development and calibration at Nova. Burn history is affected by target diameter, fill pressure, and wall thickness along with laser power and beam focusing. Diameters for microballoon targets range from 360 to 1500 μm, fill pressures from 10 to 100 atm, and wall thicknesses from 2 to 8 μm. High-yield targets (>10^{12} DT neutrons) typically have diameters >900 μm and are irradiated with temporally flat laser pulses 1 or 1.5 ns long. These targets typically have a burn duration between 175 and 250 ps (FWHM) and an emission time between 700 and 1500 ps after the leading edge of the laser pulse.

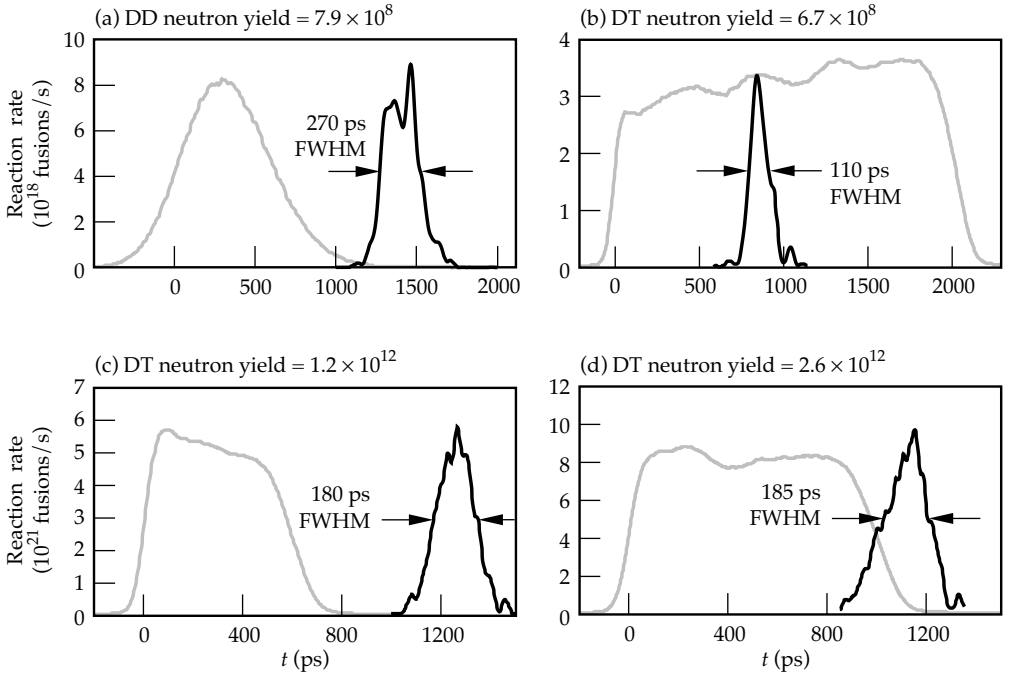

FIGURE 3. Reaction rates for four glass microballoon targets irradiated directly with 0.351-μm light. The black curves represent the reaction-rate history; the gray curves show the shape of the laser-power history. The target diameter/wall thickness, fill pressure, and incident laser energy for each experiment are (a) 360 μm/6 μm, 25 atm DD fuel, 15 kJ; (b) 360 μm/6 μm, 25 atm DT fuel, 20 kJ; (c) 800 μm/3 μm, 50 atm DT fuel, 11 kJ; and (d) 1000 μm/3 μm, 50 atm DT fuel, 22 kJ. (08-00-0896-1854pb01)

A small (360-μm) microballoon can have a burn duration as short as ~100 ps and an emission time as early as 500 ps after the leading edge of the laser pulse. Reaction history for microballoons is usually smooth but often shows an asymmetry of either a slow rise time or a slow fall time. Generally, larger, higher-pressure targets tend to burn later.

In July 1995, burn-history measurements provided the information needed to increase Nova's maximum yield from 2.1×10^{13} to 3.6×10^{13} neutrons. It was observed that neutron emission for large diameter (>1300 μm), thin-walled targets irradiated with 1-ns square pulses was occurring around 1400 ps, well after the laser pulse turned off. By changing to a 1.5-ns pulse with the same power, yield was immediately increased nearly twofold. Figure 3 shows the burn history for several microballoon targets along with the power history of the laser drive.

Our program has devoted significant effort to developing, designing, characterizing, and understanding indirect-drive targets. Fuel capsules for these targets are typically smaller diameter (360 μm) than direct-drive capsules, and are compressed to a higher convergence ratio at a lower temperature. Most indirect-drive capsules use deuterium fuel in a plastic capsule and produce yields between 10^7 and a few 10^9 DD neutrons. Reasonable burn-history measurements can only be made when DD yields are above 10^9, and signal quality for these low-yield targets depends very strongly on the background signal induced by x-ray emission from the target. Capsules in indirect-drive targets filled with DT fuel produce yields from 10^9 to over 10^{11}. Burn duration for these targets range from 50 to 125 ps. Two examples are shown in Fig. 4. Figure 4(a) is for a high-convergence implosion of a DT-filled glass capsule (from the HEP1 series of

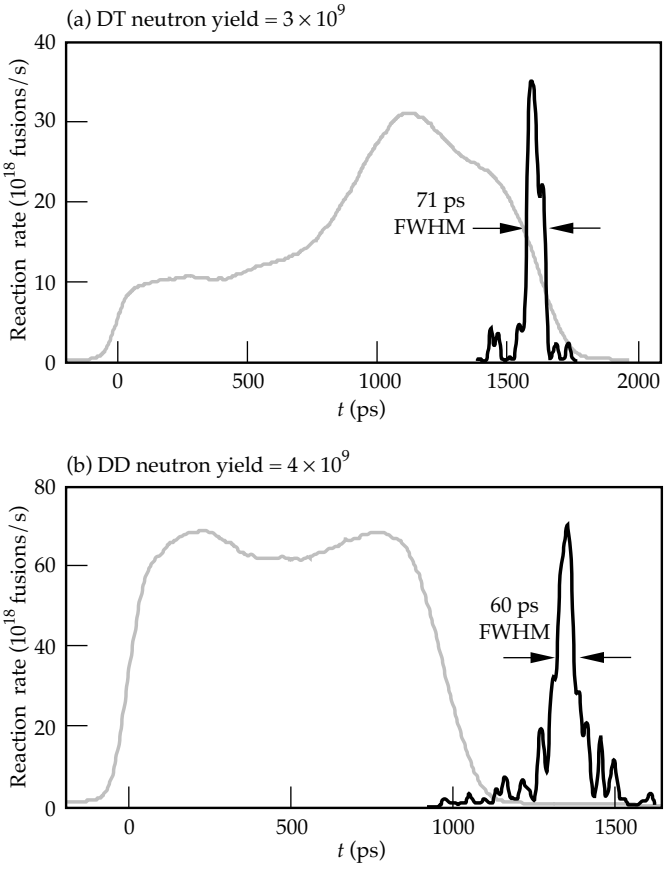

FIGURE 4. Reaction rates for two indirectly driven targets irradiated with 0.351-μm light. The black curves represent the reaction-rate history, the gray curves show the shape of the laser-power history. The type of target and its inner/outer diameters, fill pressure, and incident laser energy for each experiment are (a) glass capsule with CH layer, 180 μm/240 μm, 100 atm DT fuel, 25 kJ, and (b) plastic ball with CH layer, 430 μm/520 μm, 50 atm DD fuel, 27 kJ. (08-00-0896-1855pb02)

experiments)[12,13]; Fig. 4(b) is for an implosion of a DD-filled, Br-doped plastic capsule (from the HEP4 series of experiments)[14]. The reaction rate for the HEP4 capsule approaches the 50-ps resolution limit for DD neutrons in a 1-mm-thick detector.

Figure 5 shows the burn history for a special target used to resolve a "bang time" calibration issue with another detector used at Nova. The burn-history details differ significantly from the previous examples. The most important target characteristic is the very short time delay between laser irradiation and the start of neutron emission. Targets were 1-mm-by-2-mm, 320-μm-thick pieces of deuterated polystyrene (C_8D_8), each with a 400-μm hole drilled through it. Tritium was added to the targets by placing them in a tritium gas where tritium atoms replaced deuterium atoms. Targets were irradiated with 2.7 kJ of 0.351-μm laser light delivered in simultaneous 90-ps pulses from each of the ten Nova laser beams. Beams were set at best focus halfway down the inner wall of the hole and evenly spaced at five points around the circumference, one beam from each side of the target focused to each point. DT yields of 5×10^9 neutrons were high enough to produce good burn-history measurements. Low-level neutron emission was observed when the laser pulse reached 50% of its peak power. Significant neutron emission began 70 ps later and lasted ~300 ps. The other detector showed neutron emission starting ~250 ps earlier, before the start of the laser pulse.

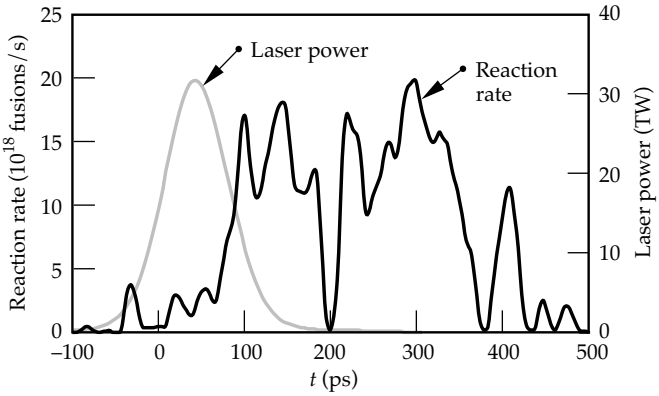

FIGURE 5. Reaction rate for a polystyrene target with a 400-μm-diam hole. There is almost no delay between laser irradiation and the start of neutron emission. (08-00-0896-1856pb01)

A serious concern for direct-drive ICF implosions is the early time "imprint" of laser-beam nonuniformity that can seed Rayleigh–Taylor instability growth. Los Alamos National Laboratory personnel recently conducted Nova experiments in their investigation of foam buffering as a way to reduce the effect of imprinting.[15] Figure 6 shows burn histories recorded for the three different target configurations irradiated in this study:

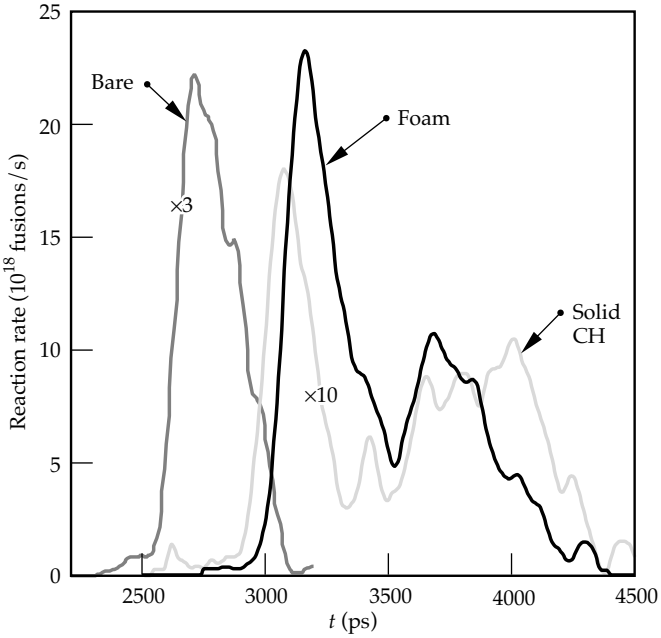

FIGURE 6. Reaction rates for three target types: a "bare" glass microballoon, a CH-foam-coated target, and a solid-CH-covered target. Laser power was delivered at a wavelength of 0.527-μm in 1.5-ns flat-topped pulses. Laser irradiation ends ~1.5 ns before fusion begins. The time base is relative to the beginning of the 1.5-ns wide laser pulse. The "bare" and "solid CH" curves have been scaled by factors of three and ten, respectively. (08-00-0896-1857pb01)

- A 1300-μm-diam, "bare" glass microballoon with a 4-μm-thick wall filled with 20 atm of DT fuel.
- Targets coated with a 200-μm-thick layer of 45-mg/cm^3 polystyrene (CH) foam.
- Targets covered with a 10-μm-thick layer of solid density CH.

Foam-coated targets were irradiated with 0.527-μm light at full Nova energy (34 kJ) delivered in a 1-ns flat-topped pulse. The bare microballoon and solid-CH-covered targets were irradiated at reduced energies of 9 kJ and 21 kJ, respectively, to better match implosion parameters with the foam-coated targets irradiated at 34 kJ. The bare microballoon had a single burn peak 290 ps FWHM. The peak is significantly delayed (~1.5 ns) from the peaks of bare microballoons irradiated under standard conditions. This delay is due to the large target diameter and low drive energy. Both the foam and solid-CH-covered targets show a narrow first peak followed by a broader second peak. Calculations suggest the first peak is caused by heating and compression of the first shock reaching target center and the second peak is from DT burn at the time of peak shell compression.

NIF Reaction-Rate Measurements

At the future NIF, fusion reaction rates cannot be measured with 30-ps resolution using the direct neutron-based technique employed at Nova. The target-to-detector spacing required by the NIF exclusion zone will cause

an excessive spreading in the neutron arrival times at the detector. Consider a very conservative example of a detector 1 m from a 4-keV plasma. The detector will see a temperature induced time spread of ~240 ps for DT neutrons. Since the plasma temperature and distance will likely be larger than these nominal values, this 240-ps time spread is a lower limit for neutron-based measurements at NIF. It is for this reason that we are investigating the use of gamma rays for making burn-history measurements.[16,17]

The increased neutron and gamma-ray yields expected for NIF targets should make a gamma-ray-based burn-history measurement possible. Measurements with gamma-rays are attractive because the gamma rays are virtually unaffected by the plasma temperature, have a large interaction cross section in many materials, and have no time dispersion at a distant detector. There are two possible sources of useful gamma rays in ICF experiments. The T(d,γ)^{5}He fusion reaction produces gamma rays with energies up to 16.7 MeV. The major disadvantage of this reaction is its low branching ratio of 5×10^{-5}. Another possible source of gamma rays is a small converter placed near the target, possibly built as a part of the target, that would convert neutrons to gamma rays through (n,γ) reactions. In this section, one detector concept and the first experimental observation of fusion gamma rays in an ICF experiment are described.[16] Much work remains to develop the sensitive, high-speed gamma-ray detector needed for NIF burn-history measurements.

Gamma-Ray Detector Concept

Figure 7 shows one concept for a gamma-ray-based burn-history measurement. Burning fuel isotropically emits fusion gamma rays, which travel radially outward from the compressed core of an ICF target. Some of the gamma rays interact with a two-stage converter to produce Cerenkov light. In the first converter stage, gamma rays produce forward-directed, relativistic electrons and positrons by Compton scattering and pair production. The charged particles move into a second converter stage, where they produce Cerenkov light. An optical system collects the Cerenkov light and relays it to a fast optical detector for recording.

Detector design will focus on providing an instrument with good time resolution ($\Delta t < 30$ ps) and sensitivity. The choice of low-Z or high-Z material for the first-stage gamma-ray converter determines whether the primary interaction is Compton scattering or pair production. For 16.7-MeV gamma rays, the interaction cross section for high-Z materials is ~100 times greater than it is for low-Z materials. Electron range, however, is much greater in low-Z materials. We estimate that about 15% of 16.7-MeV gamma rays incident on a high-Z converter several millimeters thick will produce electron-positron pairs that enter an adjacent Cerenkov converter.

The second converter stage determines the characteristics of the Cerenkov light. The threshold energy for production of Cerenkov radiation, the cone angle for its emission, and the number of photons emitted per centimeter of track length all depend on the index of refraction n of the converter material. Cerenkov light is produced in a material only when the speed of a charged particle exceeds the speed of light in that media. Thus, Cerenkov light is produced only when a particle's velocity relative to that of light in a vacuum β and n are such that $n\beta > 1$. Cerenkov radiation is emitted into a cone whose half angle θ relative to the direction of charged particle motion is given by $\cos\theta = (1/n\beta)$. The photon production rate in the visible spectrum (400 to 700 nm) is given by

$$\frac{dN}{dx} = 490\left(1 - \frac{1}{n^2\beta^2}\right) \text{photons/cm} \quad .$$

In Ref. 17, the secondary converter also forms part of the collection optics.

First Observation of Fusion Gamma Rays

We have conducted a set of direct-drive target experiments at Nova to assess our ability to detect fusion gamma rays. Yields from nominally 1-mm-diam DT-filled microballoons irradiated with 1-ns square

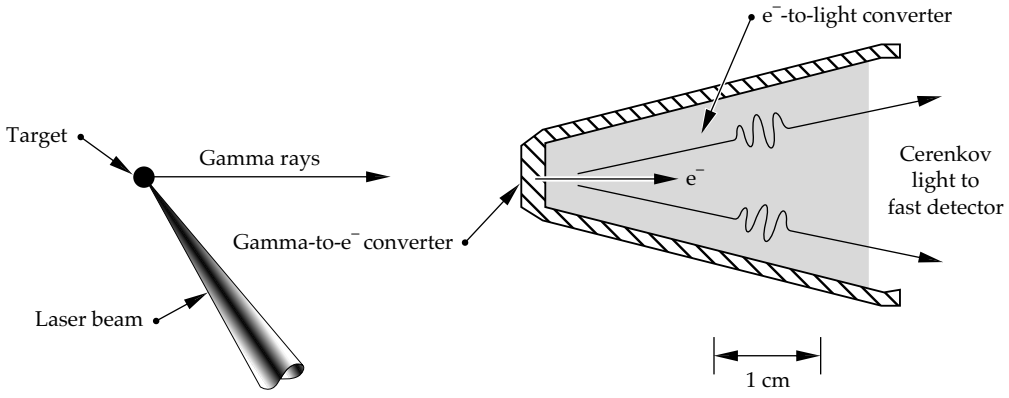

FIGURE 7. Cerenkov detector concept. A high-Z material converts target gamma rays to relativistic electrons and positrons that pass into a second converter stage. Since the charged particles are traveling faster than the speed of light in the second converter, Cerenkov light is produced. (08-00-0896-1858pb01)

pulses ranged from 10^{12} to 2×10^{13} neutrons. For these experiments, we adapted equipment normally used for our neutron burn-history measurements. The Hevimet (90% tungsten) nose cone (Fig. 1) acted as the first converter stage in which gamma rays interact primarily by pair production to produce electron-positron pairs. A 0.241-g/cm^3 silica aerogel filled the interior of the nose cone replacing the 1-mm-thick plastic scintillator and Pb glass. The aerogel acted as the second converter stage, converting relativistic electron energy into Cerenkov light. The aerogel, with $n = 1.06$, requires an electron energy >1.03 MeV to produce Cerenkov light. In our experiments, the high threshold level makes the detector relatively insensitive to target x rays and gamma rays from (n,γ) reactions near the target. A shallow cone angle of 19° allows some of the Cerenkov light to be collected by the $f/2$ optic and relayed to the streak camera. We estimate photon production at the rate of 53 photons per centimeter of track length. No modifications were made to the NTD optics to optimize collection of the Cerenkov light. Indeed, the optics, which were designed to pass scintillator light between 350 and 450 nm, have very poor transmission for Cerenkov light below 350 nm.

We observed weak gamma-ray signals in a set of target experiments with target-to-aerogel distances of 2, 3, and 4 cm (see Fig. 8). The signal for each experiment has a low-level gamma-ray pulse followed by a large 550-ps-wide pulse produced by 14-MeV target neutrons interacting with the 75-mm-diam $f/2$ optic of the telescope. The burn duration for these targets is nominally 200 ps FWHM. The neutron pulse width corresponds to the neutron transit time across the four-element optic ~2.5 cm behind the aerogel converter. The neutron signal amplitudes are normalized, temporally aligned, and overlaid. This allows us to easily observe the evolution of a small pulse to the left of the neutron peak. Its time relative to the neutron pulse changes with target-to-aerogel distance in a manner consistent with fusion gamma rays. Because the optic moves with the aerogel, a 1-cm increase in target-to-aerogel distance produces a 162-ps increase in the time separation between gamma-ray- and neutron-induced signals.

The streak camera simultaneously recorded a fiducial signal along with the aerogel signal. This allows us to determine the time of a gamma-ray signal relative to the laser power incident on a target. The time of the gamma-ray signal corresponds to the neutron emission time that we measure with a separate bang-time detector. For these targets, the nominal neutron emission time is at ~1 ns.

An additional experiment was performed with an aluminum nose cone replacing the Hevimet nose cone. In this configuration, the pair production cross section for 16.7-MeV gamma rays is reduced by a factor of 25 and the primary interaction mechanism changes to Compton scattering. The result (see Figure 9) is consistent with the small peak being caused by pair production in the high-Z nose cone. The gamma-ray signal observed with the Hevimet nose cone is not observed with the aerogel inside an aluminum nose cone. Also, with the substantially reduced shielding of the aluminum nose cone, there is no x-ray signal observed between the start of target irradiation and bang time, indicating a very low sensitivity to target x rays.

We believe these experiments are the first to detect fusion gamma rays emitted by T(d,γ)^{5}He reactions in ICF targets. The experimental evidence is consistent with this conclusion. First the change in time-of-flight

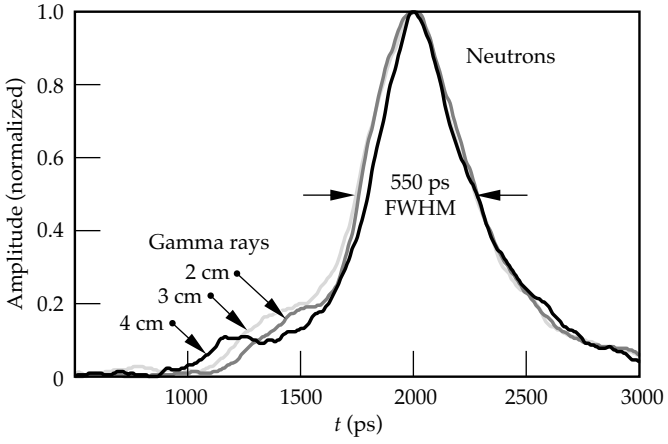

FIGURE 8. Aerogel signal intensity vs time for target-to-aerogel distances of 2, 3, and 4 cm. Neutron-induced signals from the first elements of the imaging optics are normalized, temporally aligned, and overlaid. Presented in this fashion, changes in the timing of the smaller gamma-ray signal relative to the neutron signal are easily observed. Time base is relative to incident laser power for the 4-cm gamma-ray data. (08-00-0896-1859pb01)

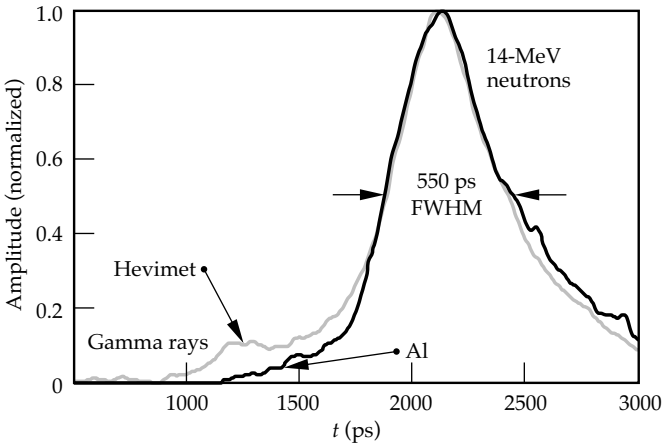

FIGURE 9. Aerogel signal intensity vs time for Hevimet and Al nose cones. The gamma-ray signal depends on high-Z converter material. (08-00-0896-1860pb01)

separation between gamma-ray and neutron pulses is consistent with the target-to-aerogel distances used. Second, the gamma-ray signals occur at the bang time of the target as determined with a separate neutron detector. Finally, the gamma-ray signal depends on the material used for the first converter stage in a manner consistent with pair production. The reduced shielding of the aluminum nose cone resulted in a decrease rather than an increase in the gamma-ray signal, indicating that the aerogel is a good threshold detector and that we are not detecting lower energy target x rays and gamma rays.

Conclusion

A neutron-based technique and a fast, sensitive neutron detector have been developed for measuring the fusion reaction rate of ICF targets. An absolute timing of ±20 ps and a temporal resolution of 30 ps have been achieved. Fusion reaction rates have been recorded for a variety of targets irradiated at the Nova Laser Facility. Target yields have ranged from 10^8 to 3.6×10^{13} DT neutrons.

Effort is now being directed towards developing a fast, sensitive burn-history detector based on fusion gamma rays. With a modification to our neutron detector, we have observed fusion gamma rays emitted from Nova high-yield targets, a significant first step in the development of a gamma-ray-based measurement. To obtain a temporal response <30 ps, we imagine the recording device of our final detector will remain a streak camera. Improved optical transmission of the second converter stage and imaging optics should enhance the signal by about a hundredfold. Based on the initial aerogel experiments, we predict a gamma-ray-based burn history can be made with a 25-cm-diam detector at the wall of the NIF chamber (5 m) when DT neutron yields are above ~10^{13}.

Acknowledgments

The following people contributed to the successful development of the fast neutron detector system: D. Phillion, G. Tietbohl, R. Ellis, J. Waldrep, J. Wass, G. Mant, R. Griffith, J. Hatch, J. Prior, N. Selchow, and D. Kumpf. The bang-time experiment with the deuterated polystyrene targets was designed and executed by T. Murphy. The initial gamma-ray experiments were done in collaboration with P. Dendooven. We also want to acknowledge S. Thomas for the development of the LLNL optical streak camera that made this work possible.

Notes and References

1. J. D. Lindl, R. L. McCrory, and E. M. Campbell, *Phys. Today* **45**, pp. 32–40 (1992); J. D. Lindl, *Phys. Plasmas* **2** (11), (1995).
2. R. A. Lerche, D. W. Phillion, and G. L. Tietbohl, *Rev. Sci. Instrum.* **66**(1), pp. 933–935 (1995).
3. H. Brysk, *Plasma Phys.* **15**, pp. 611–617 (1973).
4. F. E. Cecil and F. J. Wilkinson, III, *Phys. Rev. Lett.* **53**, pp. 767–770 (1984).
5. J. Kammeraad, J. Hall, K. E. Sale, C. A. Barnes, S. E. Kellogg, and T. R. Wang, *Phys. Rev. C* **47**(1), pp. 29–35, (1993).
6. D. R. Kania, S. M. Lane, and S. G. Prussin, *Appl. Phys. Lett.* **53** (20), pp. 1988–1989 (1988).
7. Bicorn Corp., Newbury, OH.
8. W. R. Graves, D. R. Slaughter, and R. A. Lerche, *Laser Program Annual Report 84,* pp. 5-64–5-65, Lawrence Livermore National Laboratory, Livermore, CA, UCRL-50021-84 (1985).
9. R. A. Lerche and D. W. Phillion, *Conference Record of the 1991 IEEE Nuclear Science Symposium and Medical Imaging Conference,* Vol. I, pp. 167–170, (IEEE, Piscataway, NJ, 91CH3100-5 1991).
10. R. A. Lerche and R. L. Griffith, "Resolution Limitations and Optimization of LLNL Streak Camera Focus," in *High-Speed Photography, Videography, and Photonics V*, H. C. Johnson, Ed., (SPIE —International Society for Optical Engineering, Bellingham, WA, 1988; *Proc. SPIE* **832**), pp. 266–274.
11. R. A. Lerche, "Timing Between Streak Cameras with a Precision of 10 ps," in *Ultrahigh- and High-Speed Photography, Videography, Photonics, and Velocimetry '90: Eighth in a Series,* L. L. Shaw, P. A. Jaanimagi, B. T. Neyer, Eds. (SPIE—International Society for Optical Engineering, Bellingham, WA, 1990; *Proc. SPIE*, **1346**) pp. 376–383.
12. M. D. Cable et al., *Phys. Rev. Lett.* **73**, pp. 2316–2319, (1994).
13. S. P. Hatchet et al., *ICF Quarterly Report* **5**(4), pp. 226–231, Lawrence Livermore National Laboratory, Livermore, CA, UCRL-LR-105821-95-4.
14. O. L. Landen et al., *ICF Quarterly Report* **5**(4), pp. 271–280, Lawrence Livermore National Laboratory, Livermore, CA, UCRL-LR-105821-95-4.
15. R. G. Watt et al., "Foam-Buffered Spherical Implosions at 527 nm," submitted for publication in *Phys. Plasmas.*
16. R. A. Lerche, "ICF Burn-History Measurements Using 17-MeV Fusion Gamma Rays," *12th International Conference on Laser Interaction and Related Plasma Phenomena, AIP Conference Proceedings* **369** Part 1, pp. 527–532 (1995).
17. K. P. Lewis, M. J. Moran, J. Hall, and M. Graser, *Rev. Sci. Instrum.* **63**(3), pp. 1988–1990 (1992).

Measurements of Laser-Speckle–Induced Perturbations in Laser-Driven Foils

S. G. Glendinning *M. H. Key*[*] *B. A. Remington*

S. N. Dixit *J. D. Kilkenny* *R. J. Wallace*

B. A. Hammel *J. P. Knauer*[**] *S. V. Weber*

D. H. Kalantar *D. M. Pennington*

Introduction

Growth of modulations in an inertial confinement fusion (ICF) capsule, whether initially due to capsule surface finish or drive nonuniformity, may fatally disrupt an ICF implosion by causing cold shell material to mix into the fuel.[1,2] When a capsule is driven by x rays produced inside a hohlraum, the dominant modulations are seeded by the capsule surface finish. When laser light directly drives the capsule, the modulations in the driver may be significant. Recent experiments[3,4] have reported reductions in imprint using smoothed laser beams, i.e., laser beams that have a reduced level of spatial nonuniformities. Another technique for reducing imprint has been the use of foams and gold layers.[5,6] In this article, we report measurements that quantified the equivalence between laser-imprinted modulations and surface perturbation.

Experimental Description

In our experiment, we used laser ablation to accelerate 20-μm-thick CH_2 foils with one arm of the Nova laser at 0.53-μm wavelength. This arm was smoothed with a random phase plate (RPP)[7] and spectral dispersion[8] (SSD), for three different bandwidths in separate experiments: 0.003 THz (the intrinsic bandwidth, introduced by the pulse-shaping system), 0.6 THz, and 0.9 THz. A diffraction grating gave 0.086-μrad/THz dispersion and a temporal skew of 110 ps to the pulse front (that is, one side arrived earlier than the other). The beam was split into nine segments, each independently steered in space with a glass wedge to form a flat-topped intensity distribution. We measured the time-integrated laser modulation level from an equivalent target-plane image of the beam. The drive pulse was a linear 1-ns ramp to about 10^{14} W/cm^2, held constant at this level for 2 ns.

The shock reached the back surface of the 20-μm-thick foil at about 0.7 ns after the start of the laser pulse. The foil then accelerated at about 50 μm/ns^2, allowing for 2 ns of constant acceleration to study Rayleigh–Taylor (RT) growth. We measured the areal-density modulations on the foils by conventional x-ray backlighting. We used a gated pinhole camera with 8-μm and 100-ps resolution,[9] which provided up to 12 frames per shot with arbitrary time spacing. The x-ray backlighter[10] was a uranium disk illuminated by a second 0.53-μm-wavelength Nova beam (smoothed with an RPP) at about 10^{15} W/cm^2, giving a broad spectrum peaked at ~1 keV.

Simulations

To examine the predicted evolution of imprinted modes compared to surface modes, we used the two-dimensional code LASNEX[11] to separately predict the evolution of a surface single mode and of an imprinted single mode (produced by modulating the incident laser intensity) under the same drive conditions. The LASNEX results showed that the evolution of a laser-imprinted single mode parallels that of a surface single mode after the shock reaches the back surface t_s (see Fig. 1). This suggested that, for our conditions, the laser imprint could be calibrated to an equivalent surface finish. We also used the simulations to estimate the correspondence of a spatial amplitude η with a measured modulation in optical depth $\Delta\tau$, finding that $\eta/\Delta\tau = 10\ \mu\text{m}/\tau$ after t_s. This allowed us to make use of the Haan criterion[12] to establish the onset of multimode nonlinear saturation. We restricted our analysis to data that were estimated to be in the linear regime.

[*] Rutherford Appleton Laboratory and University of Oxford, United Kingdom.
[**] Laboratory for Laser Energetics, Rochester, New York.

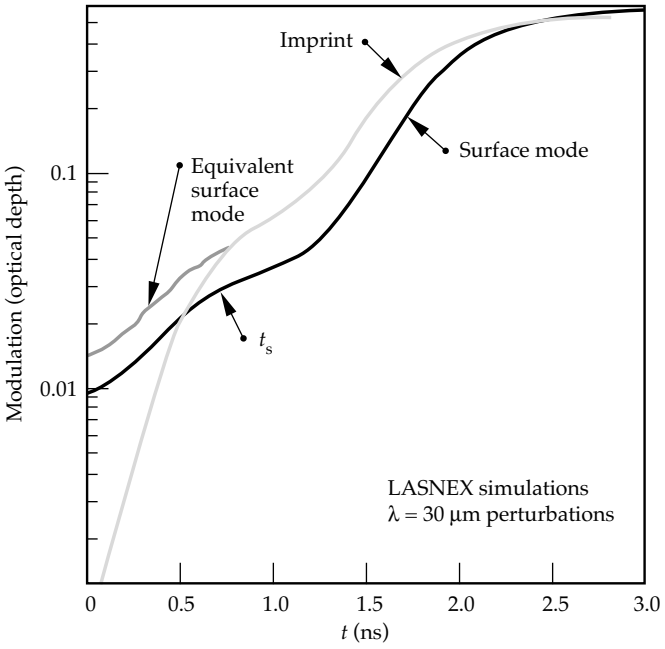

FIGURE 1. LASNEX simulation of optical-depth modulation vs time for a single surface mode and a single imprinted mode of the same wavelength (30 μm). The growth rate between t_s (0.7 ns) and the onset of saturation at $\Delta\tau = 0.3$ is 2.2 ns^{-1} for the imprinted mode and 2.5 ns^{-1} for the surface mode. While the imprint begins at zero modulation, an equivalent surface mode would begin at 0.02. (20-03-0796-1564pb01)

We analyzed each frame by converting the film density to exposure; removing the long-scale-length backlighter shape; filtering out noise with a parametric Wiener filter; converting to the natural logarithm of exposure; and taking the two-dimensional power spectrum of the result. A typical image of ln(exposure) is shown in Fig. 2(a). A vertical profile, which is the horizontal average of the image, is shown in Fig. 2(b). The surface mode in this case was $\lambda = 30$ μm (mode 10, initial amplitude $\eta_0 = 0.25$ μm) with the modulation vector **k** vertical in the image, and the bandwidth was 0.9 THz. We removed the contribution of the surface mode by using a notch filter at the point in Fourier space where the surface mode appears. The same image with the surface mode removed is shown in Fig. 2(c) and its corresponding horizontal average is the dark gray line in Fig. 2(b). Figures 3(a) and 3(b) show the radial power spectra (azimuthal integrals of the two-dimensional power spectra) for this shot at three different times, the noise power spectrum (measured on a separate shot with an undriven foil), and the instrument modulation transfer function (MTF). The laser imprint was almost indistinguishable from the noise for the higher bandwidths at t_s (not shown), but subsequent growth gave clearly measurable modulations at later times. Figures 4(a) and 4(b) show the time-integrated power spectra of the laser speckle and the imprinted spectra at $t = 1.5$ ns as measured for the different bandwidths. As is characteristic with SSD, while there was smoothing at all modes, the higher modes were smoothed preferentially.

To test the LASNEX prediction that the evolution of a laser-imprinted mode parallels the surface mode after t_s, we examined the growth for several shots. Figure 5 shows the results for the shot of Figs. 2 and 3. The modulation amplitudes for the surface mode ($\lambda = 30$ μm), for the imprinted spectrum at mode 10, and for the root-mean-square (rms) of the ln(exposure) are shown as a function of time after the start of the laser pulse. We subtracted in quadrature the noise component due to the instrument and backlighter from the values for the imprint modes. The

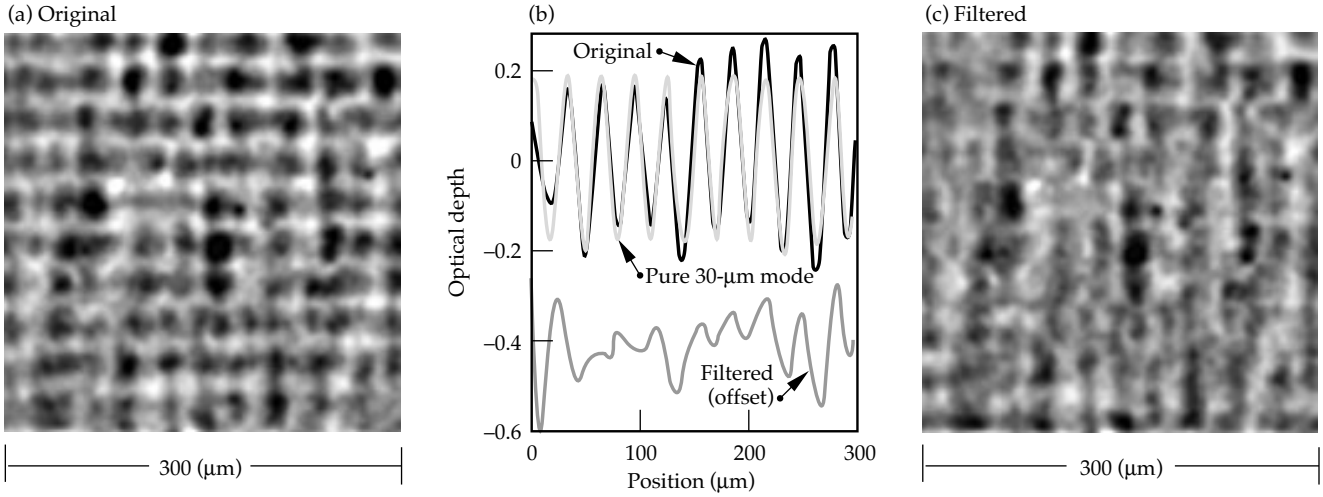

FIGURE 2. A single image from a framing camera radiograph at $t = 1.9$ ns (1.2 ns after t_s), shown in ln(exposure). (a) is the original image, with a $\lambda = 30$ μm, $\eta_0 = 0.25$ μm surface mode. The vertical profiles in (b) are made by horizontally averaging the images. In (b), the black curve is from (a) and the light gray curve is a pure 30-μm mode with $\Delta\tau = 0.2$ (optical depth), while the dark gray curve corresponds to (c). (c) has been digitally filtered to remove the $\lambda = 30$ μm mode in the vertical direction only. (20-03-0796-1565pb01)

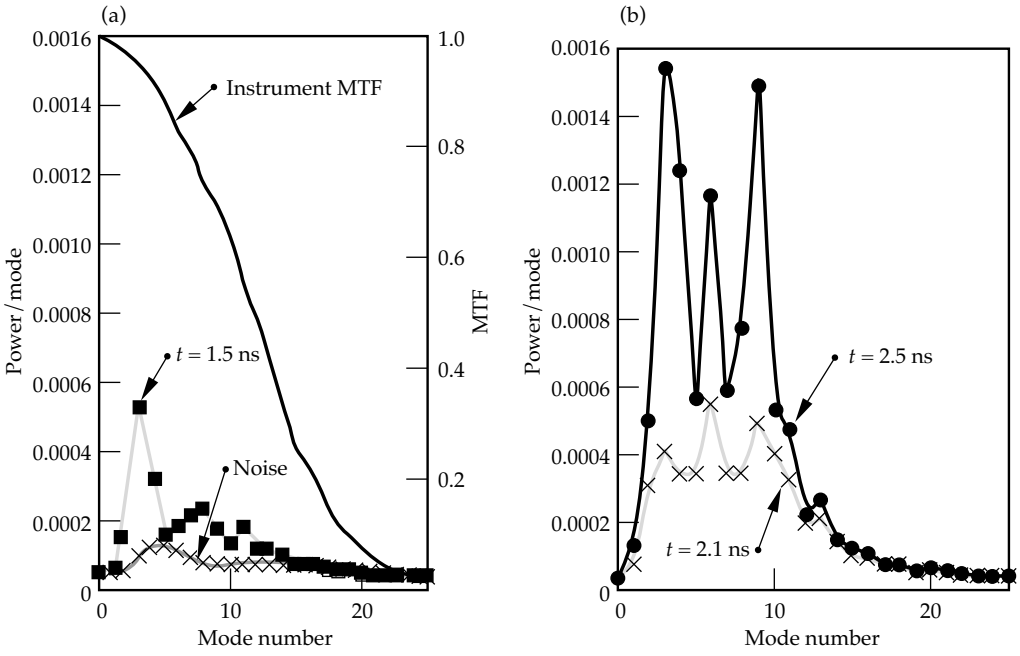

FIGURE 3. Azimuthally integrated radial profiles at three different times of the two-dimensional Fourier power spectra for the shot shown in Fig. 2. Also shown are the instrument noise (measured on a shot with an undriven foil) and the modulation transfer function (MTF) of the measurement system. The MTF uses the right axis. (20-03-0796-1566pb01)

two $\lambda = 30\ \mu$m modes from surface and imprint modulations grew at the same rate ($0.9 \pm 0.2\ \text{ns}^{-1}$). The rms grew at nearly the same rate ($0.8 \pm 0.2\ \text{ns}^{-1}$), suggesting that the growth rates for the dominant modes were similar.

At a given time in the linear regime, the ratio of the rms to the surface mode times the initial surface-mode amplitude gave the equivalent surface finish in microns at $t = 0$. The inferred rms surface finish was insensitive to the calibration wavelength we used, suggesting little variation in growth rate for the dominant wavelengths. We calculated the equivalent surface finish to be $0.26 \pm 0.07\ \mu$m with 0.9 THz of bandwidth on the drive laser, $0.51 \pm 0.24\ \mu$m with 0.6 THz bandwidth, and $1.24 \pm 0.27\ \mu$m with minimum bandwidth. Figure 6 shows these results vs bandwidth, along with the time-integrated rms modulation in the laser speckle. The imprinted-modulation rms appeared to decrease only about half as fast as the laser modulation as a function of bandwidth.

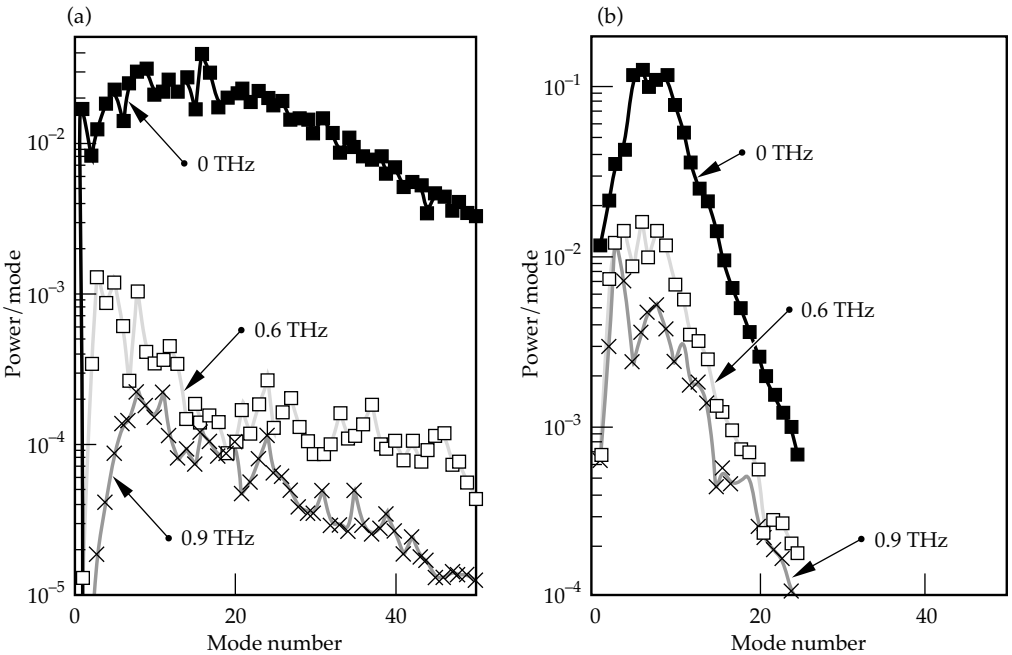

FIGURE 4. Power spectra of (a) the laser spots and (b) the imprinted modulation, converted to initial surface amplitudes, for the three bandwidths. (20-03-0796-1567pb01)

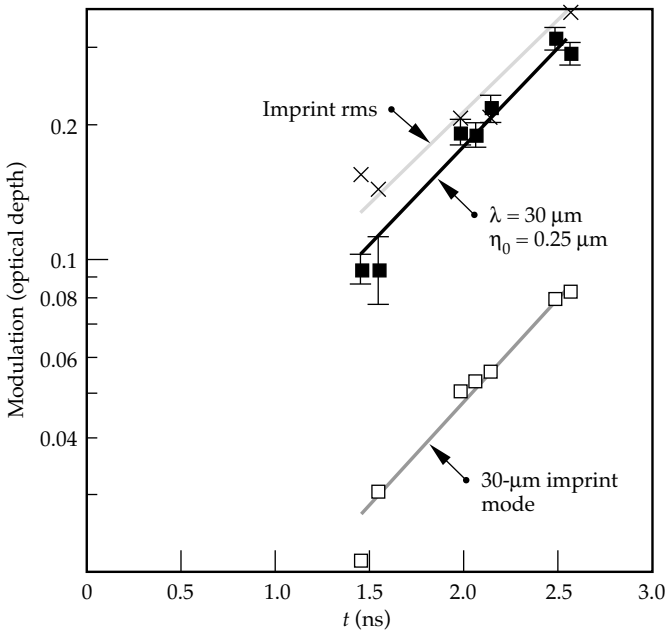

FIGURE 5. Modulation amplitudes for the shot shown in Figs. 2 and 3 vs *t*. The surface mode (shown with characteristic error bars), the imprinted mode at the same wavelength, and the rms grow at the same rate. (20-03-0796-1568pb01)

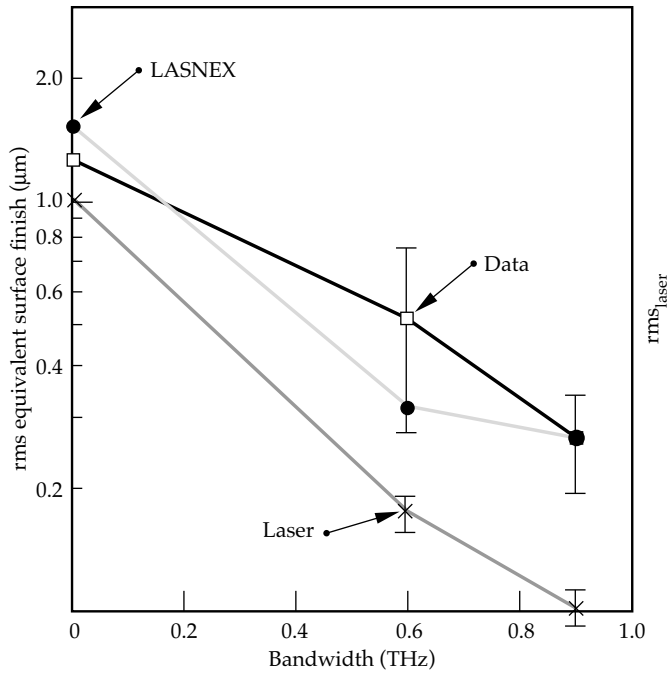

FIGURE 6. Equivalent surface finish for three bandwidths, as measured and simulated. The measured time-integrated laser-rms modulation vs bandwidth is also shown. The lines are a guide to the eye. (20-03-0796-1569pb01)

We used LASNEX to simulate the equivalent surface finish due to the laser imprinted modulations. The single-surface-mode simulation was done separately from the laser-imprint simulation. Since LASNEX is a two-dimensional code, the laser speckle is represented by a one-dimensional slice of the predicted laser-modulation pattern. With minimum bandwidth, the speckle is isotropic and the direction of the slice is not important. When SSD was added to the simulation, we used two directions—parallel and perpendicular to the direction of dispersion—and averaged the resulting predictions. The simulations propagated the measured backlighter spectrum through the simulated package and convolved the result with the instrument response function. The results are also shown on Fig. 6.

Conclusions

The predictions agreed with the experimental results. In particular, the predicted imprinted modulations did not decrease as rapidly with bandwidth as the time-integrated laser modulation. This effect has also been observed in experiments using a different measurement technique.[13,14] One possible explanation is the thermal smoothing of the drive modulations in the region between the laser light deposition and the ablation surface. In this region, the energy is propagated by electron thermal conduction and nonuniformities are smoothed inversely with the spatial scale of the nonuniformity. Thus, the minimum-bandwidth case showed more thermal smoothing because more of the laser modulation is at smaller spatial scales. If we calculate the laser time-integrated smoothing level including only lower modes (spatial structure > 30 μm), the rate of decrease of target imprint and the laser time-integrated smoothing level with increased bandwidth is the same. This suggests that the thermal smoothing for this experiment is most effective for modes with $\lambda < \sim 30\ \mu$m. Unfortunately, the instrument response greatly affects our ability to measure spatial structures less than 30 μm. While the LASNEX simulations predict that such structures are not present in the imprinted modulations, we cannot confirm this with the available data.

Summary

In summary, we have observed modulations due to laser speckle and we have shown that for a modest (less than a factor of three) amount of Rayleigh–Taylor growth, the speckle-imprinted modes grow at the same rate as a pre-imposed single-mode surface perturbation. We used this relationship to characterize the observed imprinted-rms modulation in optical depth as an equivalent surface finish for different bandwidths. The imprinted-foil modulations decreased with increasing bandwidth but not as rapidly as the time-integrated laser modulations, which is in agreement with numerical simulations. We suggest that this decrease is due to the additional smoothing of high spatial frequencies between the laser deposition region and the ablation surface.

Notes and References

1. J. Nuckolls, L. Wood, A. Thiessen, and G. Zimmerman, *Nature* **239**(5368), pp. 139–142 (1972).
2. M. M. Marinak, R. E. Tipton, O. L. Landen, T. J. Murphy et al., *Phys. Plasmas* **3** (5), pp. 2070–2075, (1996).
3. D. K. Bradley, J. A. Dellettrez, and C. P. Verdon, *Phys. Rev. Lett*. **68** (18), pp. 2774–1777 (1992).
4. J. D. Kilkenny, S. G. Glendinning, S. W. Haan, B. A. Hammel et al., *Phys. Plasmas* **1** (5), pp. 1379–1389 (1994).
5. M. Desselberger, T. Afshar-rad, F. Khattak, S. Viana et al., *Phys. Rev. Lett*. **68** (10), pp. 1539–1542 (1992).
6. R. J. Taylor, J. P. Dahlburg, A. Iwase, J. H. Gardner et al., *Phys. Rev. Lett*. **76** (10), pp. 1643–1646 (1996).
7. S. N. Dixit, I. M. Thomas, B. W. Woods, A. J. Morgan et al., *Appl. Optics* **32** (14), pp. 2543–2554 (1993).
8. S. Skupsky, R. W. Short, T. Kessler, R. S. Craxton, S. Letzring, and J. M. Soures, *J. Appl. Phys.* **66** (8), pp. 3456–3462 (1989).
9. O. L. Landen, P. M. Bell, J. A. Oertel, J. J. Satariano, and D. K. Bradley, *Ultrahigh- and High-Speed Photography, Videography, and Photonics '93* (SPIE—The International Society for Optical Engineering, Bellingham, WA, 1993; *Proc. SPIE* **2002)**, pp. 2–13.
10. S. G. Glendinning, P. Amendt, K. S. Budil, B. A. Hammel et al., *Applications of Laser Plasma Radiation II* (SPIE—The International Society for Optical Engineering, Bellingham, WA, 1995; *Proc. SPIE* **2523)**, pp. 29–39.
11. G. B. Zimmerman and W. L. Kruer, *Comments Plasma Phys. Controlled Fusion* **2** (2), pp. 51–61 (1975).
12. S. W. Haan, *Phys. Rev. A* **39** (11), pp. 5812–5825 (1989).
13. D. H. Kalantar, M. H. Key, L. B. Da Silva, S. G. Glendinning et al., *Phys. Rev. Lett*. **76** (19), pp. 3574–3577 (1996).
14. M. H. Key, *XUV Lasers and Applications* (SPIE—The International Society for Optical Engineering, Bellingham, WA, 1995; *Proc. SPIE* **2520)**, pp. 279–86.

WARP3d, a Three-Dimensional PIC Code for High-Current Ion-Beam Propagation Developed for Heavy-Ion Fusion

D. P. Grote *I. Haber*
A. Friedman *S. M. Lund*

Introduction

Heavy-ion induction accelerators are being developed in the United States as the principal candidate "drivers" for inertial confinement fusion (ICF) power production. They also represent an attractive option for a high-yield microfusion research facility. Heavy-ion drivers are attractive in both cases because they promise high reliability, high repetition rate (several pulses per second are required), greater efficiency (up to 30%), lifetime capacity (a power plant would need to last 30 years, or 10^{10} pulses), and sufficient cost savings. With indirectly driven targets, heavy-ion drivers allow a favorable fusion chamber geometry; furthermore, the final focus is accomplished with magnetic fields that are immune to damage by target debris, in contrast to the final optics for a laser.[1]

The requirements for high-gain ignition of the fusion targets control the design of the accelerator. A major constraint on the beam is the requirement of a small focal spot size on the target with a large distance between the final focus lens and the target, putting a tight limit on the temperature of the beam. A thorough understanding of the beam behavior as it propagates through the accelerator is necessary to maintain the required low temperatures.

Since the space-charge–dominated beams in an induction accelerator are effectively non-neutral plasmas, analysis of the beams can be performed with computational modeling techniques related to those used in both the accelerator and plasma physics fields. Because the beam resides in the accelerator for relatively few plasma oscillation periods, particle-in-cell (PIC) simulation techniques are especially effective and have proved valuable in the design and analysis of both ongoing experiments and future machines and in the study of basic physics issues. The three-dimensional (3-D) electrostatic PIC simulation code WARP3d[2,3] was developed to study beam behavior from first principles in realistic geometries. This article presents an overview of the WARP3d code, describing in detail some of its major features and present applications in a number of areas, and highlighting the important results.

Overview of WARP3d

WARP3d was designed and optimized for heavy-ion fusion (HIF) accelerator physics studies. It combines the PIC technique commonly used for plasma modeling with a description of the "lattice" of accelerator elements. In addition to its 3-D model, a simple beam envelope, or transverse root-mean-square (rms) size, analytic equation solver was included, primarily to obtain an initial beam well matched to the accelerator lattice. The code uses the BASIS development and run-time system, which affords a flexible and powerful interpretive user interface.

The ion beam is represented by a small number (relative to the number of beam ions in the physical system) of interacting particles whose motion is controlled by the Newton–Lorentz equations of motion. The fields affecting the particles include both the self-fields of the beam and the external fields from the lattice. The self-fields are assumed to be electrostatic and are calculated in the beam frame via Poisson's equation on a Cartesian grid that moves with the beam. The electrostatic assumption is valid since, with the high mass of the beam ions, the beam is nonrelativistic throughout the accelerator, its velocity only reaching roughly 10% of the speed of light at the end of the accelerator.

There are two "field solvers" to calculate the self-fields: (1) The fastest field solver, which is generally used for long-time simulations, uses Fourier decomposition with fast Fourier transforms (FFTs). (2) An iterative solver uses successive overrelaxation (SOR) with even-odd ordering[4] and allows inclusion of complex electrode geometry. For the FFT field solver, the 3-D transform is sine-sine-periodic, the transverse boundary is a rectangular

metal pipe, and the longitudinal boundary is periodic. Capacity matrices[5] can be used to include simple electrodes in the FFT field solver to handle round pipes, structures independent of the axial coordinate, and isolated internal structures. Another variant uses a tridiagonal matrix solver along the axial direction. This method is slightly faster, but at present is restricted to conducting boundaries on the longitudinal ends of the grid.

The SOR field solver, although significantly slower than the FFT field solver, allows simulation of a much broader class of problems with a more realistic model of the conductors. This field solver was implemented using a technique, described below, to obtain subgrid-scale resolution of the conductor boundaries. With both field solvers, transverse symmetry can be exploited, simulating only half or one quarter of the system.

The external fields are applied via a lattice, which is a general set of finite-length accelerator elements, including quadrupoles for focusing, dipoles for bending, induction gaps for accelerating, elements with arbitrary transverse multipole components, and curved accelerator sections (see Ref. 2). The transverse multipole components specify the applied fields, in one form, as an electrostatic or magnetostatic potential represented by an infinite sum of terms expressed in cylindrical coordinates with the direction of beam propagation along the longitudinal axis, z.

$$\phi = \sum_{n,\nu\geq 0} V_{n,\nu}(z) r^{n+2\nu} \cos(n\theta + \nu) \qquad (1)$$

The $V_{n,\nu}(z)$ determine the contribution of each term. The electric or magnetic fields are calculated by taking the appropriate derivatives. As an example, a quadrupole field is given by the term with $n = 2$, and $\nu = 0$. Terms with $n > 2$ or $\nu > 0$ are referred to as high-order terms.

The field from the lattice elements can be specified at one of several levels of detail—from hard-edged, axially uniform fields at the lowest level, to self-consistent inclusion of the conducting electrodes of electric elements in the field solution at the highest level.

Aspects of WARP

A number of features and capabilities have been implemented in WARP3d to enable simulation of a broader class of accelerators, both by way of inclusion of the relevant physics and by optimization of the code to allow simulation of larger-scale problems. This article describes the most important and novel of these in detail.

Lattice and Fields

A hard-edged field is the lowest level of description of lattice element fields—one that is uniform axially within the extent of the element and that has a sharp cutoff at the ends of the element. As the particles enter and exit hard-edged, axially uniform elements, the force applied on the particles is scaled by the fraction of the timestep spent inside the element. These "residence corrections" are used so that the particles receive the correct impulse from the element and allow larger timesteps to be used. Without the residence corrections, the forces applied to the particles would depend on the number of timesteps they spend inside the element; keeping the resulting error small would require a small timestep.

At a higher level of detail, fields that vary axially can be applied. This allows application of realistic fields, including fringe fields and the higher-order multipole moments of a magnetic quadrupole element, for example. In both the axially uniform and nonuniform descriptions, the applied field can be an arbitrary sum of multipole components, as given by Eq. (1).

The highest level of detail is specification of the field via a 3-D grid to allow application of fields that are not amenable to a multipole description, e.g., a field with many nonlinear components. The field can be calculated outside of WARP3d; for example, the magnetic field from a complex magnet design can be obtained from TOSCA[6] and input into WARP3d. With electric elements, the field can be calculated self-consistently with WARP3d by inclusion of the electrodes in the field solution, thereby obtaining the realistic fields and image effects from the electrode on the beam. This highest level of description allows modeling of complex electrode geometry and electrodes with time-varying voltages.

When electrodes are included in the field solution, to avoid the problems with the jaggedness of representing tilted or curved electrodes on a Cartesian grid, the SOR field solver allows subgrid-scale resolution of the conducting boundary locations as shown in Fig. 1. For grid points just outside the surface of a conductor, the form of Poisson's equation is changed to explicitly include the location of the surface. Normally, the evaluation of Poisson's equation at these points would require the potential at grid points that are just inside the surface of the electrode. The values inside are replaced by a value that is extrapolated from the potential at the surface and at the grid point just outside the surface. The method is similar to the method used in EGUN,[7] extended to three dimensions and time dependence.

Subgrid-scale resolution of the conducting boundaries allows more accurate modeling of electrodes for a given grid cell size, especially ones with curved surfaces, and it does so while allowing larger grid cell sizes. As an example, the fields from an electric quadrupole are produced from four parallel cylinders with appropriate voltages. Without the subgrid-scale resolution of the cylinder surfaces, the quadrupole focusing strength is reduced significantly since the jagged surface, produced by representing the cylinder by grid points only within

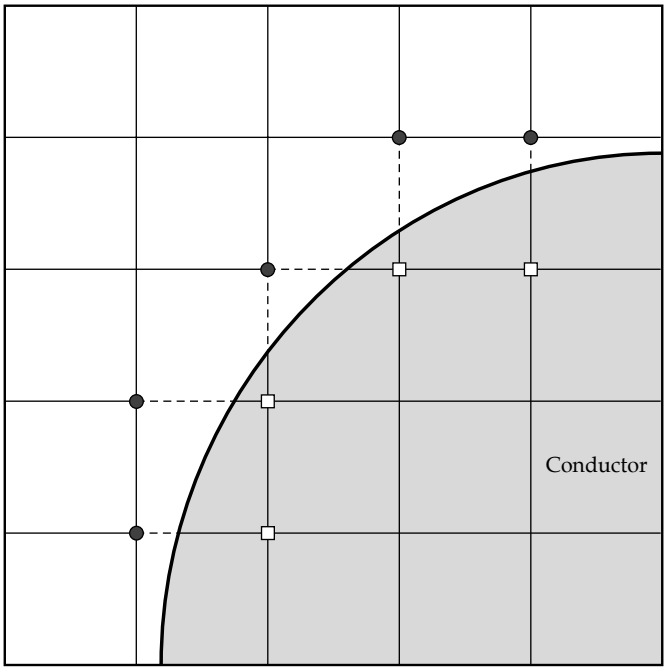

FIGURE 1. An example conductor on a grid. The numeric form of Poisson's equation is altered for the grid points at the dark circles. The equation would normally require the potentials at the nearby grid points, which are inside the conductor, marked by squares. The potential inside is replaced by a value extrapolated from the potential at the point outside and at the surface. (08-10-0896-1906pb01)

the cylinder, is effectively farther from the axis than that of the true surface. The reduced focusing changes the beam envelope on the order of 10%. A much finer grid would be needed to produce the same accurate focusing strength as that produced with the subgrid-scale resolution.

Beam Injection

Several models of particle beam injection are used, all of which can model emission from planar or curved surfaces. The first model injects particles from a surface at a constant current with a specified energy, modeling a beam emerging from a wire mesh or from a plane of uniform potential. It can be used to model injection from an emitting surface if the specified energy is low compared with the diode energy.

Two self-consistent models use space-charge–limited injection and are intended only for injection directly from emission surfaces. The beam current that is injected is not predetermined, but is calculated self-consistently from the conditions near the emitting surface to give space-charge–limited injection. The first model uses the Child–Langmuir[8] relation in a region in front of the emitting surface to calculate the emitted current. The length of the region is small compared with the length of the diode. The Child–Langmuir relation gives the space-charge–limited current in a 1-D diode. In the second model, the surface charge required to produce the desired zero-normal electric field on the surface is calculated assuming an infinite conducting plane. The amount of charge injected into a grid cell is then the surface charge integrated over the grid cell minus the charge already in the grid cell from earlier times.

With space-charge–limited injection, WARP3d can be run in an efficient iterative manner that captures only the steady-state behavior. The algorithm is similar to that used in the 2-D electron gun design code EGUN.[7] At each iteration, a group of particles is tracked through the diode. Along the paths of the particles, charge is deposited on a grid to build up a representation of the charge density of a full beam. The fields are recalculated, including the new charge density, giving the new fields through which the next group of particles is tracked on the next iteration. On the initial iteration, the particles are tracked through the fields given by the solution of Laplace's equation in the diode geometry. The process converges to the correct steady-state flow in typically 10 to 20 iterations. This capability was added to the code entirely through the BASIS interpreter and required no modification of the existing code.

Large Time-Step Algorithms

Under conditions that arise commonly in WARP3d applications, the applied focusing, bending, and accelerating fields vary rapidly with axial position, while the beam's self-fields (which are comparable in strength to the applied fields) vary smoothly. In such cases, it is desirable to employ timesteps that advance the particles over distances greater than the characteristic scales over which the applied fields vary. An example technique, used in WARP3d since the code's inception, is the residence correction described earlier. Research at Lawrence Livermore National Laboratory (LLNL) is extending this concept to cases where the effects of extended fringe fields and other smooth but rapid variations must be accurately captured, necessitating very small timesteps when a conventional "leapfrog" advance is used.[9]

Several related techniques are being evaluated: subcycling of the particle advance relative to the field solution (i.e., taking N substeps between each major timestep on which the self-consistent field is computed and applied, where N is a small integer); use of a higher-order time-advance algorithm; and force-averaging over the velocity-advance step by integration along approximate orbits (a generalization of the residence correction technique). The most straightforward of these techniques is particle subcycling. We are encouraged by subcycling tests that advance a particle through the extended field's quadrupole component of a pair of permanent-magnet quadrupole lenses, and we are in the process of implementing this technique in WARP3d.

Since the field solution and particle advance often use comparable amounts of computer time, subcycling with $N = 4$ will result in roughly a twofold speedup of the code. For some problems, the field solution dominates the run time and larger speedups can be expected.

Thick-Slice Model

Several simulations have identified the existence of short longitudinal-wavelength oscillations that can occur on a long beam. These short-length phenomena have been found to be particularly significant when the beam transverse temperature is somewhat greater than the longitudinal temperature.[10–13] In this case, the temperature anisotropy is a source of free energy that can drive the short wavelength modes unstable, leading to an "equilibration" of the temperatures. Short longitudinal-wavelength oscillations have also been seen (in simulations) in a recirculator with external nonlinearities (see the section entitled "Recirculating Induction Accelerator"). To investigate these phenomena numerically, therefore, it is important to examine the physics of a space-charge–dominated beam with numerical resolution in the longitudinal direction sufficiently fine to resolve phenomena that occur on the scale of the beam diameter. This requirement can be computationally expensive to satisfy if the beam is to be tracked through a realistic length of accelerator structure.

A new numerical technique currently being developed facilitates the investigation of such short longitudinal-scale phenomena. This approximation, which we call the "thick-slice" model, exploits the separation of scales that occur because of the locality of the phenomena being studied relative to the global beam variation along the accelerator structure. We assume that all the particles across a finite slice of the beam simultaneously experience the same external forces, in a manner similar to what is assumed in a single-slice (or 2-D transverse) model. However, the self-consistent beam dynamics within the slice are followed, including the longitudinal variation of the fields. The longitudinal particle and field boundaries at the ends of the slice are further assumed to be periodic.

Parallel Processing

WARP3d was originally designed to run on vector supercomputers and on workstations. With the present trend toward using massively parallel processing, WARP3d was ported to a parallel environment. Currently, WARP3d can run on the CRAY T3D, using both the PVM[14] message passing library and the native shared memory library, and on multi-workstation clusters. In the conversion, the interactive nature of the code (through the BASIS interpreter) was maintained. The user runs the code on a local serial workstation and interacts with it through the interpreter. That code then creates processes on the parallel machine to do the computational work. Via message passing, the user controls the progress of the simulation on the parallel machine and inquires or sets any of the code variables in a manner similar to that used when the code runs on a serial machine.

Using a model problem with up to 32 processors, timings were made by following a beam through five hard-edged lattice periods. The speedup of the code with an increasing number of processors was nearly linear. Figure 2 shows timings of the field solver and particle mover. The field solver has a slightly superlinear speedup, which is likely due to better cache memory use with the data spread out in smaller pieces on more processors.

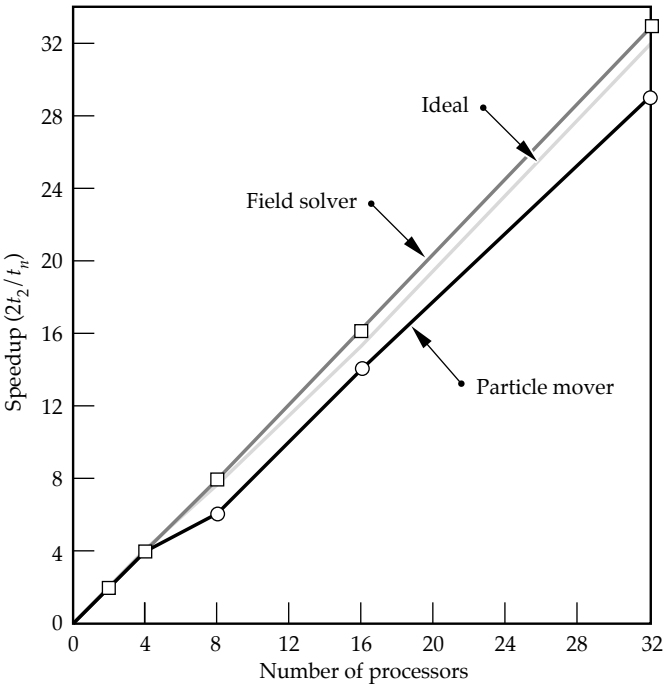

FIGURE 2. Plot showing the speedup of the code with an increasing number of processors. The speedup is twice the ratio of the time with two processors to the time with n processors, two being the fewest number of processors that the parallel code will run on. The light gray line shows the ideal linear speedup. The dark gray line with squares shows the speedup for the field solver. The black line with circles shows the speedup for the particle mover. Note that the speedup for the field solver is superlinear at first due to better use of cache memory with less data per processor. (08-10-0896-1907pb01)

Applications of WARP3d

WARP3d has been used extensively in the design and analysis of a number of experiments within the HIF program and in the study of the basic physics of the creation and transport of space-charge–dominated beams. In the following sections, we describe several of its most recent applications within HIF and an application outside of HIF.

Electrostatic Quadrupole Injector

A driver-scale injector and matching section is being built at Lawrence Berkeley Laboratory, in collaboration with LLNL, to address beam physics and technology issues.[15] The injector uses a sequence of electrostatic quadrupole (ESQ) lenses with a superposed voltage gradient along the axis. The net effect is to confine the beam transversely and to accelerate it. The beam is emitted from a hot-plate source and accelerated through a diode section into the quadrupole lenses. Figure 3 is an image of the injector when it is filled with the beam. Following the injector is a "matching section," a series of electric quadrupoles with decreasing aperture that reduce the transverse size of the beam down to "match" it into the following section of the accelerator.

WARP3d was used to understand a major issue in the injector design—the degradation of beam quality (brightness) by the nonlinear multipole components of the focusing fields and the so-called "energy effect." The energy effect arises from the spread transversely in the axial velocity of particles in the ESQ, which is due to the transverse variation of the electrostatic potential. Proper treatment of the beam dynamics requires detailed 3-D simulation with a realistic lattice model.

For design of the injector optics, the steady-state beam behavior was of primary interest. For efficiency, runs were made in a quasi-steady-state mode, taking several particle timesteps between each field solution and continuing until the system converged to a time-independent state. These 3-D simulations of the injector required less than 3 min on a single processor of the National Energy Research Scientific Computing Center's CRAY Y-MP C90 (at LLNL). This was fast enough to allow simulation of a large number of designs to optimize the injector, minimizing the beam degradation. Taking advantage of the ESQ's two-plane symmetry, the dimensions of the field grid were typically $40 \times 40 \times 348$. Typically, 100,000 particles and 500 timesteps were used. Fully time-dependent simulations of the transient behavior require several hours of C90 CPU time.

The simulations were used as a guide in the development of a scaled, proof-of-principle experiment and then a full-scale experiment. In both cases, excellent agreement was found between the experiment and simulation results. Figure 4 shows the simulated injected beam in the full-scale diode. Figure 5 shows a comparison of the phase space representations of the simulated and the full-scale experimental beams.

For the matching section, the envelope equation solver in WARP3d is used to calculate the beam transverse rms size in the presence of quadrupole and uniform focusing multipole components extracted from the field solution, including the full geometry of the electric quadrupole conductors. Good agreement between the analytic envelope solution and the results of full PIC simulation implies that the envelope solver can be used for rapid iteration of the applied voltages to achieve the desired beam state. The full simulations are conducted to evaluate possible degradations in beam quality that cannot be evaluated in the analytic envelope model.

In a full-scale driver, multiple injectors will be used and their beams will be channeled into a multiple beam transport line by the matching section, resulting in a curved matching section. This system was simulated with WARP3d, combining three of its major capabilities: injection, a bent accelerator lattice, and field solution with complex conductor geometry. The simulations found no significant degradation of beam quality, thereby validating the design concept.

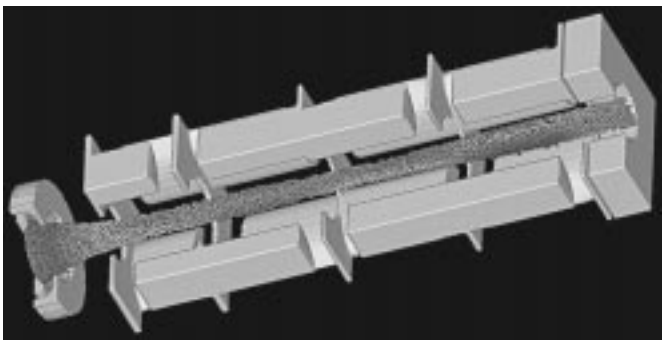

FIGURE 3. The 3-D image of the ESQ injector when filled with the beam. The shading of the beam particles is proportional to the particle energy relative to the energy at the beam center; the energy effect is evident in the darker shading of particles farther from the axis. (08-10-0896-1908pb01)

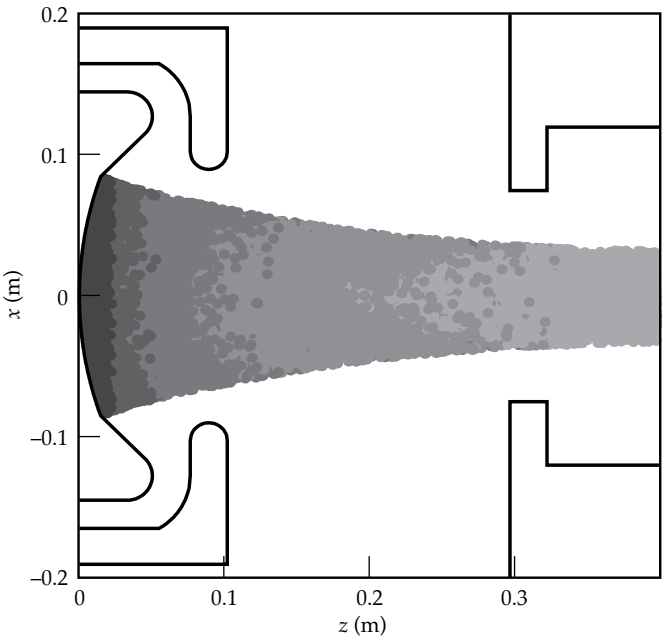

FIGURE 4. The diode of the ESQ injector filled with the beam. The outline is of the diode geometry. The shading of the beam particles is proportional to the time of injection of the particles, showing the darkest area injected last. (08-10-0896-1909pb01)

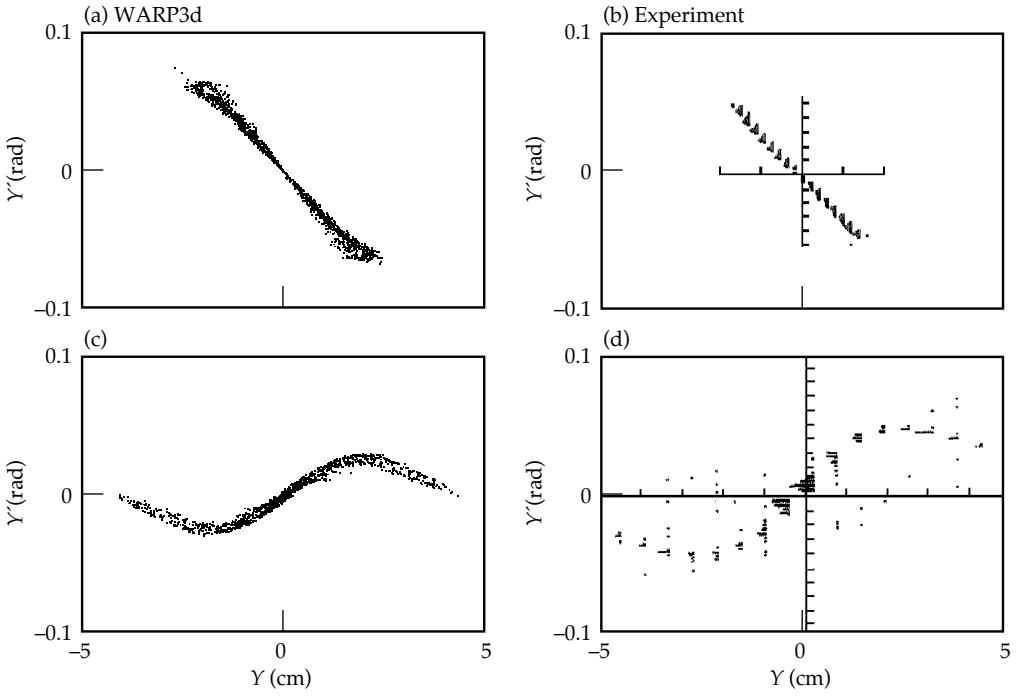

FIGURE 5. Comparison of experimental and simulation transverse phase space representations at the end of the ESQ injector. (a) and (b) compare the results at the design parameters. (c) and (d) compare the results with an increased diode voltage; in this nonoptimal case, the representations are significantly distorted from a straight line. (08-10-0896-1910pb01)

Recirculating Induction Accelerator

A recirculating induction accelerator, or "recirculator," offers the prospect of reduced cost relative to a conventional linear accelerator because the accelerating and focusing elements are reused many times per shot.[16] A small recirculator is being developed at LLNL to explore the beam dynamics of a full-sized fusion driver in a scaled manner; the key dimensionless parameters that characterize the beam are similar to those of a driver-scale ring, but the physical scale is much smaller.[17]

Although a full-scale driver will use magnetic dipole elements to bend the beam, electric dipole plates were chosen for the prototype to minimize costs. The size of the plates is constrained by space considerations and voltage-holding requirements, resulting in significant high-order fields. Using WARP3d, the plate shape was adjusted to minimize 3-D field nonlinearities and their influence on beam quality. Figure 6 compares the cross section of the beam after several laps with flat dipole plates and with shaped dipole plates.

WARP3d simulations were used to follow the beam for all 15 laps. Typically, the 2-μs-long beam is made up of 100,000 simulation particles. The field grid is a moving window covering four half-lattice periods. The grid measures 32×16 cells transversely (exploiting vertical symmetry) and 128 cells axially.

Figure 7 shows the time history of the normalized emittance at the midpulse for an acceleration schedule that does not compress the beam axially. The normalized emittance is a measure related to the transverse beam temperature and is given approximately by $\varepsilon_x \approx \tilde{x} v_x$

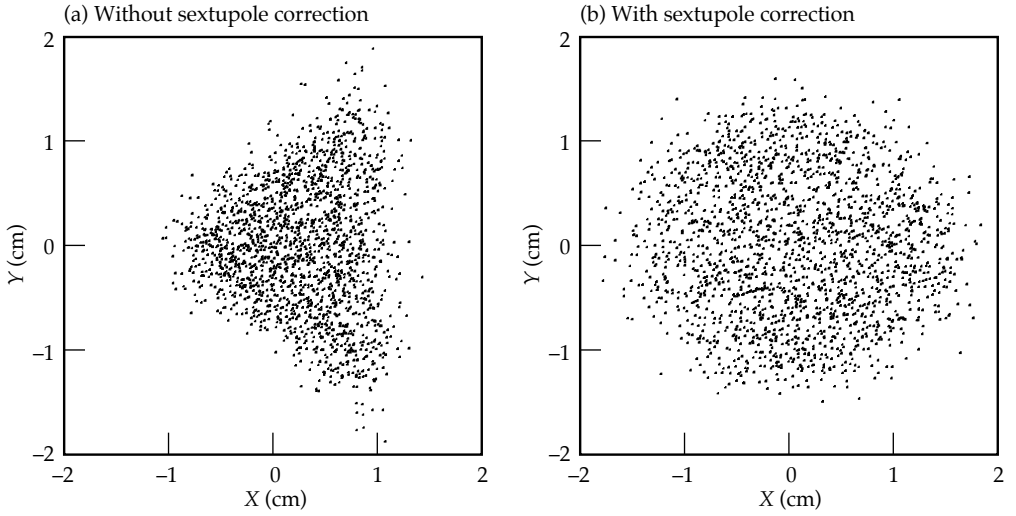

FIGURE 6. The beam cross section after several laps (a) with flat dipole plates and (b) with shaped dipole plates. The triangular shape in (a) is a result of the sextupole component from the flat dipole plates. (08-10-0896-1911pb01)

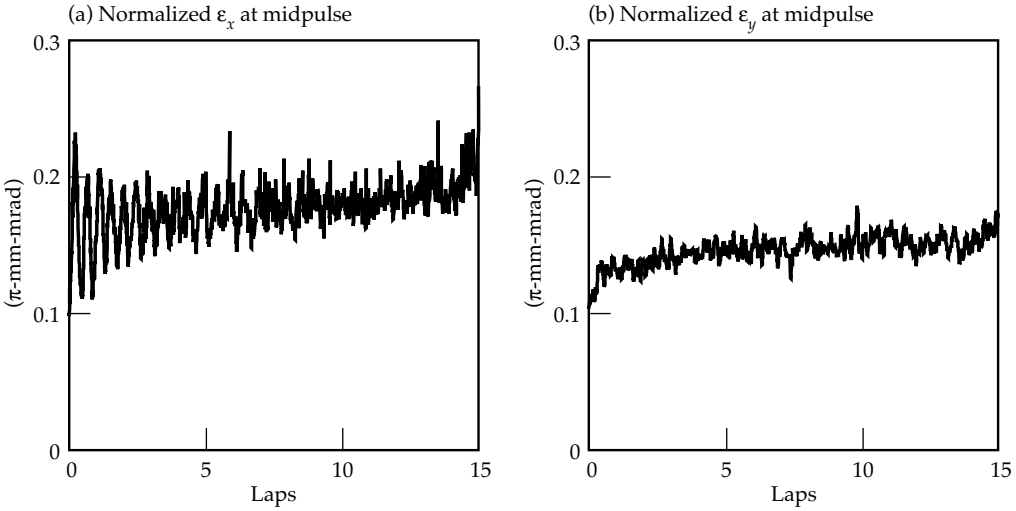

FIGURE 7. The time history of the normalized emittance and the beam midpulse show an acceptable increase. The initial oscillation and increase are due to axial thermal spread and the change from a straight to a bent lattice. (08-10-0896-1912pb01)

where x is a transverse dimension and σ_x is the rms of x. The simulations show an initial transverse heating of the beam on the order of 50% as the beam "matches" itself from the straight insertion line to the bent recirculator lattice. This heating is due to radial separation of particles with differing axial velocities in the bends, which leads to nonlinearities in the space-charge forces that thermalize to produce an increase in temperature. The observed growth agrees well with theoretical analysis.[18] After the initial heating, little further degradation in beam quality is seen over the 15 laps. The overall degradation is acceptable.

Near the end of the simulation, the emittance begins to rise due to the appearance of an instability that presents itself as a sinusoidal variation of the beam axial velocity along the beam. The variation begins to grow from the noise during laps 11 and 12 and becomes significant enough to affect the emittance during lap 15. The wavelength of the variation is on the order of the pipe radius. Numerous simulations seem to indicate that the instability is not numerical in origin; the wavelength and growth rate varied little with a wide range of numerical parameters, including timestep size and grid size. The instability requires all of the following: high space charge, bending, acceleration, and a uniform focusing force. The uniform focusing force results from the electric dipole plates. It is believed that the instability will not occur with magnetic dipoles, which will be used in a driver; the simulations made so far with magnetic dipoles have not shown the instability. The authors await the experimental results from the recirculator to see whether or not the instability indeed does occur as predicted.

Straight and Bending Experiment

As a precursor to the full recirculator experiment just described, the beam is being examined in a straight lattice and in a lattice with an 18° bend (using WARP3d). The straight experiment is being conducted to fully characterize the beam. The bent experiment will be the first detailed examination of a space-charge–dominated beam in a bent, alternating-gradient lattice.

The straight experiment consists of a series of electric quadrupoles and then magnetic quadrupoles. The field from the electric quadrupoles was calculated with WARP3d using the electrode geometry, and the field from the magnetic quadrupoles was calculated analytically. The quadrupole component was extracted from the fields and is used in the calculation of the envelope of the beam. Figure 8 shows a comparison of the

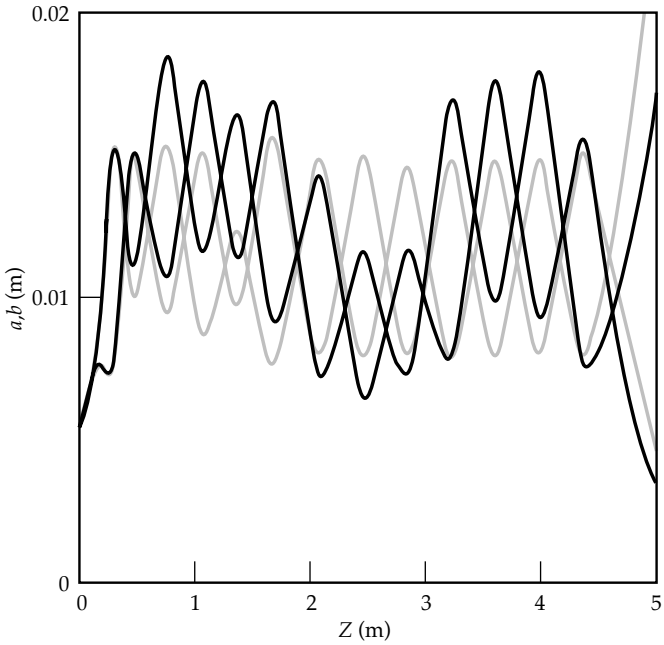

FIGURE 8. Comparison of the beam envelope as calculated with quadrupoles with hard-edged fields (gray) and with quadrupoles with calculated field profiles (black). The horizontal and vertical envelopes (a,b) for each case are shown in the same colors. The envelope was matched to the quadrupoles with hard-edged fields; this is seen in the nearly equal heights of the peaks in the gray curves. The significant difference shows the importance of including the correct quadrupole field profile. (08-10-0896-1913pb01)

envelope solution with hard-edge quadrupoles and with the calculated quadrupole data. Of course, given the detailed solution, it would be possible to construct a better hard-edged model.

The "simultaneous perturbation stochastic approximation"[19] optimization algorithm was implemented with the analytic envelope solver to find a matched envelope. The algorithm varies the voltages on the electric quadrupoles to find a matched beam in the first bent-lattice period. The envelope solver is being used by the experimentalists for the determination of the voltages for the experiment.

The bent beam experiment has been simulated with WARP3d to predict the amount of emittance growth from the bend correlated with the longitudinal thermal spread. Figure 9 shows the emittance growth for up to a 45° bend with a straight lattice afterward. Figure 10 shows the difference in the phase space before and after 18° using grayscales to show the relative longitudinal velocities of the particles. The simulations show that there should be an experimentally detectable amount of emittance growth in an 18° bend, assuming a longitudinal thermal spread of 0.05% of the axial velocity.

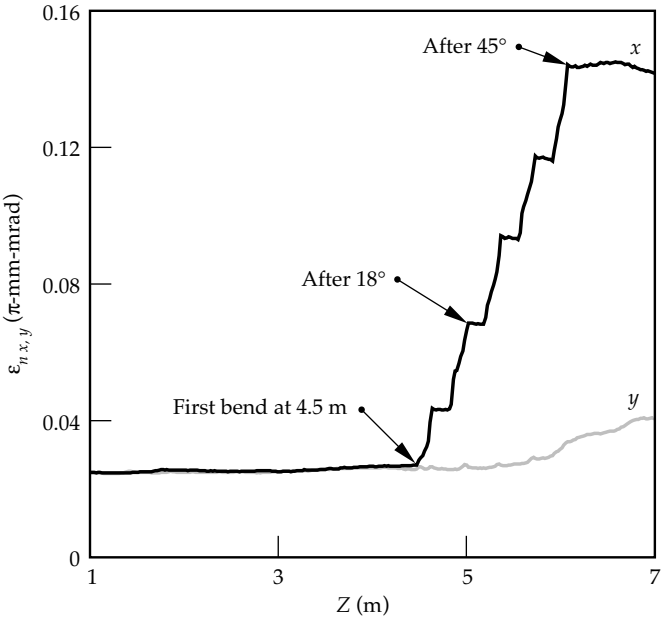

FIGURE 9. The WARP3d simulations show an emittance growth after 18° that should be experimentally detectable. (08-10-0896-1914pb01)

Sheet Beams

At the University of Wisconsin, WARP3d is being used in the examination of sheet electron beams formed by magnetic quadrupoles for use in high-power microwave sources.[20,21] The rapid axial variation of the beam profiles limits the use of the paraxial model and makes necessary the use of 3-D models. The 3-D envelope code TRACE-3D[22] is used for rapid iteration to design the system, but it does not model increases in emittance due to beam quality degradation. WARP3d simulations are used as a check of the envelope code design, to validate the envelope, and to examine the degradation of beam quality. An experiment is under construction and comparisons with simulation will be made.

Conclusions and Future Work

WARP3d was developed to examine high-current, space-charge–dominated beams for heavy-ion fusion and has proven its value in a broad range of applications, playing a critical role in the design and analysis of a number of experiments. Many features and capabilities have been implemented to allow inclusion of much of the relevant physics and simulation of large-scale problems.

Considerable further code development is planned, taking advantage of modern programming techniques such as object-oriented programming, and making more use of tools such as computer-aided design systems for geometry input, mesh generators, and massively parallel processing machines. These developments are geared to allow quicker and more complete analysis of ongoing experiments, leading to complete simulation of full-scale drivers.

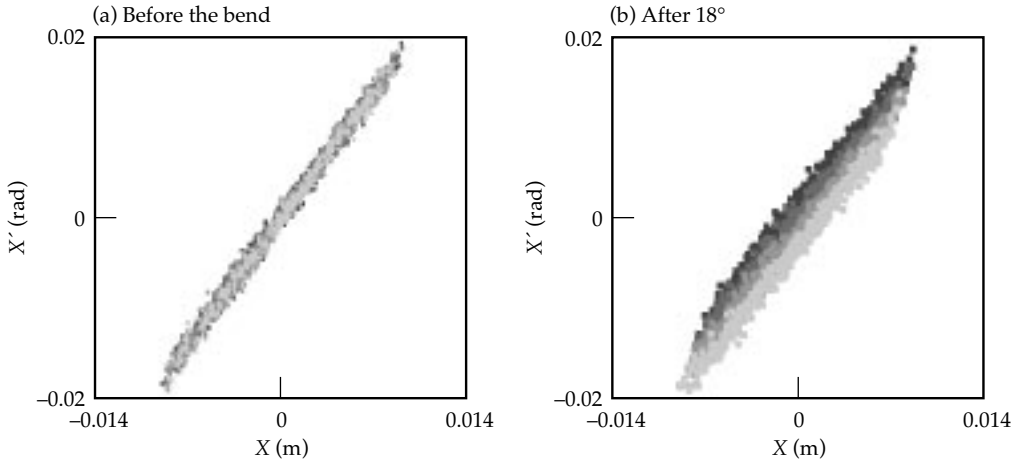

FIGURE 10. In the phase space, the transverse spreading of the beam due to axial thermal spread and a bend can be seen. The shading of the particles is proportional to axial velocity (lighter is faster). (08-10-0896-1915pb01)

Notes and References

1. R. O. Bangerter, *Il Nuovo Cimento* **106 A**(11), 1445 (1993).
2. A. Friedman, D. P. Grote, I. Haber, *ICF Quarterly Report* **1**(4), 115, Lawrence Livermore National Laboratory, Livermore, CA, UCRL-LR-105821-91-4 (1991).
3. A. Friedman, D. P. Grote, and I. Haber, *Physics of Fluids B* **4**(7), 2203 (July 1992).
4. William H. Press et al., *Numerical Recipes: The Art of Scientific Computing* (Cambridge University Press, 1986) pp. 652–659.
5. R. W. Hockney and J. W. Eastwood, *Computer Simulations Using Particles* (Adam–Hilger, Bristol, 1988) p. 215.
6. *TOSCA Reference Manual*, Technical Paper VF-11-92-14, Vector Fields Limited, 24 Bankside, Kidlington, Oxford OX5 1JE, England.
7. W. B. Herrmannsfeldt, *EGUN—An Electron Optics and Gun Design Program*, Technical Report 331, SLAC, 1988.
8. K. R. Spangenburg, *Fundamentals of Electron Devices* (McGraw–Hill, New York, 1957).
9. A. Friedman and D. P. Grote, "Large-Timestep Techniques for Particle-in-Cell Simulation of Systems wth Applied Fields that Vary Rapidly in Space," *Proc. 1996 Comput. Accel. Phys. Conf.*, Williamsburg, VA, Sept 24–Oct 7, 1996.
10. A. Friedman, R. O. Bangerter, D. A. Callahan, D. P. Grote, et al., "A 3D Particle Simulation Code for Heavy Ion Fusion Accelerator Studies," in *Proc. of the 2nd European Particle Accelerator Conf.*, Nice, France (Editions Frontiers, Gif–sur–Yvette, France, 1990), p. 1699.
11. I. Haber, D. A. Callahan, A. Friedman, D. P. Grote, and A. B. Langdon, "Transverse-Longitudinal Energy Equilibration in a Long Uniform Beam," *Proc. of the 1995 Particle Accelerator Conf.*, Dallas, TX, pp. 3283–4 (IEEE, 1996).
12. I. Haber, D. A. Callahan, A. Friedman, D. P. Grote, and A. B. Langdon, "Transverse-Longitudinal Temperature Equilibration in a Long Uniform Beam," to be published in *Proc. of the International Symposium on Heavy Ion Fusion*, Princeton, NJ, Sept 6–8, 1995, and in *Journal of Fusion Engineering Design*, 1996.
13. I. Haber, D. A. Callahan, C. M. Celata, W. M. Fawley et al., "PIC Simulation of Short Scale-Length Phenomena," *Space Charge Dominated Beams and Applications to High Brightness Beams*, S. Y. Lee, Ed., AIP Conf. Proc. No. 377 (AIP, New York, 1996) p. 244.
14. A. Giest et al., *PVM3 User's Guide and Reference Manual*, Technical Report ORNL/TM-12187.
15. S. Yu, "Heavy Ion Fusion Injector Program," *Proc. of the 1993 Particle Accelerator Conf.*, Washington, D.C., p. 703–705 (IEEE, 1993).
16. J. J Barnard, F. Deadrick, A. Friedman, D. P. Grote et al., *Physics of Fluids B*, **5**(7), 2698 (July 1993).
17. A. Friedman et al., "Progress Toward a Prototype Recirculating Induction Accelerator for Heavy-Ion Fusion," *Proc. of the 1995 Particle Accelerator Conf.*, Dallas, TX, pp. 828–830 (IEEE, 1996).
18. J. J. Barnard, H. D. Shay, S. S. Yu, A. Friedman, and D. P. Grote, "Emittance Growth in Heavy Ion Recirculators," *1992 Linear Accelerator Conf. Proc.* (Ottawa, Canada, AECL-10728, 1992) p. 229.
19. J. C. Spall, "Multivariate Stochastic Approximation Using a Simultaneous Perturbation Gradient Approximation," *IEEE Transactions of Automatic Control*, **37**, 332–341 (1992).
20. M. A. Basten, J. H. Booske, and J. Anderson, *IEEE Trans. Plasma Science* **22**(5), 960–966 (1994).
21. M. A. Basten, J. H. Booske, and S. M. Lund, "Three Dimensional Analysis of Electron Sheet Beam Formation Using Magnetic Quadrupoles," Lawrence Livermore National Laboratory, Livermore, CA; submitted to *Nucl. Instr. and Methods*.
22. *TRACE-3D Documentation*, Los Alamos Code Group, Los Alamos National Laboratory, Los Alamos, NM, Report LA-UR-90-4146 (1990).

Three-Dimensional Nonlinear Hydrodynamics Code to Study Laser–Plasma Interactions

C. H. Still *R. L. Berger*

A. B. Langdon *E. A. Williams*

Introduction

The development of a fully nonlinear, time-dependent hydrodynamic and heat transport code has allowed us to pursue several very interesting problems in laser beam self-focusing and filamentation for which the plasma density and flow velocities are strongly perturbed. Many treatments have used time-dependent linearized hydrodynamics in two and three dimensions (3-D) where the plasma motion is limited to directions transverse to the laser propagation direction.[1,2] A truly nonlinear treatment uses particle-in-cell codes.[3] Other nonlinear treatments have used a steady-state hydrodynamics response where the electron density is determined by equating the electron thermal and ponderomotive forces transverse to the laser propagation direction.[4]

These approaches ignore some important physical processes. For example, time-dependent, nonlinear hydrodynamics is needed to address steepening of wave fronts, harmonic generation and decay instabilities, all of which play an important role in saturation of filamentation, stimulated Brillouin scattering (SBS), and stimulated Raman scattering (SRS). Filamentation has been studied using 1-D and 2-D nonlinear hydrodynamics codes in planar or cylindrical geometry.[5] To our knowledge, the code we now describe is the only code with fully 3-D nonlinear hydrodynamics coupled to light wave propagation.

The Hydrodynamics Equations

The hydrodynamic, heat transport equations in conservative form are the mass conservation equation

$$\frac{\partial}{\partial t}\rho + \nabla\cdot(\mathbf{v}\rho) = 0 \quad , \tag{1}$$

the momentum conservation equation for the j^{th} component of the momentum $\mathbf{S}$

$$\frac{\partial}{\partial t}S_j + \nabla\cdot(\mathbf{v}S_j) + \nabla\cdot\mathbf{Q}_j + \frac{\partial}{\partial x_j}P + \frac{\partial}{\partial x_j}P_{\text{e}} + \rho\frac{\partial}{\partial x_j}\phi = 0 \, , \tag{2}$$

the ion energy conservation equation

$$\frac{3}{2}\left[\frac{\partial}{\partial t}P + \nabla\cdot(\mathbf{v}P)\right] + P\nabla\cdot\mathbf{v} + \mathbf{Q}:\nabla\mathbf{v} = 0 \quad , \tag{3}$$

and the electron energy conservation equation

$$\frac{3}{2}\left[\frac{\partial}{\partial t}P_{\text{e}} + \nabla\cdot(\mathbf{v}P_{\text{e}})\right] + P_{\text{e}}\nabla\cdot\mathbf{v} = -\nabla\cdot\mathbf{q}_{\text{e}} + H_{\text{e}} \quad . \tag{4}$$

In these equations, P is the ion pressure, P_{e} is the electron pressure, $\mathbf{Q}$ is the viscosity tensor (with j^{th} component $\mathbf{Q}_j$), $\mathbf{v}$ is the flow velocity, H_{e} is a source or sink, and $\mathbf{q}_{\text{e}}$ is the heat flow. The momentum is related to the flow velocity by

$$\mathbf{S} = \rho\mathbf{v} \quad , \tag{5}$$

and the electron and ion temperature are related to the corresponding pressures by a perfect gas equation of state

$$P_{\text{e}} = n_{\text{e}}T_{\text{e}} \tag{6}$$

$$P = n_{\text{i}}T_{\text{i}} \tag{7}$$

with $\rho = m_{\text{i}}n_{\text{i}}$. The ionization state is constant and, at present, quasi-neutrality is assumed, namely $n_{\text{e}} = Zn_{\text{i}}$. This last assumption will be relaxed in the near future.

The last term in the momentum equation [Eq. (2)] represents either a gravitation force, as used for

Rayleigh–Taylor instability calculations,[6] or a ponderomotive force, in which case

$$\phi = \frac{1}{2}\frac{m_i}{Zm_e}\left|\mathbf{v}_0\right|^2 \quad . \tag{8}$$

Here, $\mathbf{v}_0$ is the jitter velocity of the electron in the laser field $\mathbf{E}_0$,

$$\mathbf{v}_0 = \frac{e\mathbf{E}_0}{m_e\omega_0} \quad . \tag{9}$$

In Eq. (3), we neglect the ion heat flow and real viscosity, which are usually very small. The artificial viscosity **Q** is used to handle shocks in the standard way as will be described shortly.

In Eq. (4), H_e includes collisional heating (inverse bremsstrahlung). For problems of interest to date, the standard flux-limited heat flow

$$\mathbf{q}_e = -\kappa(T_e)\nabla T_e \tag{10}$$

where

$$\kappa(T_e) = \min\left(\kappa_{SH}, fn_e v_e T_e \frac{|\nabla T_e|}{T_e}\right) \tag{11}$$

is ineffective in limiting the heat flow because the gradients in T_e are small over the scales of interest to filamentation. On the other hand, nonlocal transport[7] can be quite important. Unfortunately, a nonlinear, nonlocal 3-D treatment of electron transport is a research project in itself. Thus, we have taken the approach of linearizing Eq. (4) about a uniform T_{e0} to obtain $\delta T_e = T_e - T_{e0}$, which is calculated from nonlocal electron transport. The choice for T_{e0} has come either from experimental data or from LASNEX simulations. In most cases of interest, this approximation has been satisfactory. It becomes questionable when there are large excursions in density because of the concomitant large excursions in electron–ion and electron–electron scattering mean-free-paths. Fortunately, in most applications with such large excursions, self-focusing is ponderomotively driven rather than thermally driven. Electron–ion energy exchange terms have been dropped in Eqs. (3) and (4) because they are of interest only for nanosecond time scales; in general, filamentation time scales are much shorter.

For completeness, we include the equation for the light wave propagation given by the modified paraxial equation

$$\left(\frac{\partial}{\partial t} + v_g\frac{\partial}{\partial z} - \frac{ic^2}{2\omega_0}D_\perp^2 + \nu\right)E = -\frac{4\pi e^2 i}{2\omega_0 m_e}\delta n_e E \tag{12}$$

for the complex light-wave envelope amplitude E oscillating at frequency ω_0 and wave vector

$$c^2k_z^2 = \frac{4\pi e^2}{m_e}\bar{n}_e - \omega_0^2 \quad . \tag{13}$$

Here, we define

$$\bar{n}_e(z) = \left\langle n_e(x,y,z)\right\rangle_{xy} \quad , \tag{14}$$

$$\delta n_e = n_e(x,y,z) - \bar{n}_e(z) \quad , \tag{15}$$

the light wave group velocity

$$v_g(z) = \frac{c^2k_0(z)}{\omega_0} \quad , \tag{16}$$

the inverse bremsstrahlung absorption rate ν and the generalized diffraction operator[8]

$$D_\perp^2 = \frac{2k_0\nabla_\perp^2}{k_0 + \sqrt{k_0^2 - \nabla_\perp^2}} \quad , \tag{17}$$

which extends validity of the paraxial equation to higher order in $k_\perp$. The numerical solution of Eq. (12) is described by Berger et al.[2]

Numerical Solution of the Hydrodynamical Equations

We followed the procedure outlined by Bowers and Wilson[9] and implemented by Miller in 2-D for spherical or cylindrical geometry.[10] Our code, called NH3 if uncoupled to laser light, or F3D when coupled to laser light, is 3-D Cartesian to match the fast Fourier transform (FFT) solution techniques used for the light equation solver.

The advection steps in the continuity and energy equations [Eqs. (1) and (3)] are done similarly. The equation is split into three 1-D equations, which are solved successively,

$$\frac{\partial}{\partial t}\rho^{(+1/3)} = -\frac{\partial}{\partial x}\left(\rho^{(+0)}v_x\right) \tag{18}$$

$$\frac{\partial}{\partial t}\rho^{(+2/3)} = -\frac{\partial}{\partial y}\left(\rho^{(+1/3)}v_y\right) \tag{19}$$

$$\frac{\partial}{\partial t}\rho^{(+1)} = -\frac{\partial}{\partial z}\left(\rho^{(+2/3)}v_z\right) \tag{20}$$

where $\rho^{(+0)}$ and $\rho^{(+1)}$ denote the actual time-iterates, and the other two quantities are intermediate results. The advection is done by a 1-D scheme,

$$\rho_{i-1/2}^{(t+1)} = \rho_{i-1/2}^{(t)} + \left(F_i^{M_x} - F_{i+1}^{M_x}\right)/\Delta x \tag{21}$$

$$F_i^{M_x} = \hat{\rho}_i \bar{v}_i \Delta t \tag{22}$$

$$\bar{v}_i = \frac{1}{4}\left(v_{i,j,k} + v_{i,j+1,k} + v_{i,j,k+1} + v_{i,j+1,k+1}\right) \quad , \tag{23}$$

where the subscripts denote spatial position, using Van Leer's second-order upwind monotonic approximation for $\hat{\rho}$.[9,11] The Van Leer method defines

$$\rho_{\max} = \max\left(\rho_{i-3/2}, \rho_{i-1/2}, \rho_{i+1/2}\right) \tag{24}$$

$$\rho_{\min} = \min\left(\rho_{i-3/2}, \rho_{i-1/2}, \rho_{i+1/2}\right) \tag{25}$$

$$\Delta\rho_1 = 2\min\left(\rho_{\max} - \rho_{i-1/2}, \rho_{i-1/2} - \rho_{\min}\right) \tag{26}$$

$$\Delta\rho_2 = \frac{1}{2}\left(\rho_{i+1/2} - \rho_{i-3/2}\right) \tag{27}$$

$$\Delta\rho_3 = \max\left(\rho_{\max} - \rho_{i-1/2}, -\rho_{i-1/2} - \rho_{\min}, |\Delta\rho_2|\right) \tag{28}$$

$$\delta_{i+1/2} = \text{sign}\left(\Delta\rho_2\right)\min\left(\Delta\rho_1, \Delta\rho_3\right)/\Delta x \tag{29}$$

$$\hat{\rho}_i = \begin{cases} \rho_{i-1/2} + \frac{1}{2}\delta_{i-1/2}\left(\Delta x - v_i \Delta t\right), & \text{if } v_i > 0 \\ \rho_{i+1/2} - \frac{1}{2}\delta_{i+1/2}\left(\Delta x + v_i \Delta t\right), & \text{otherwise} \end{cases} \quad . \tag{30}$$

This scheme guarantees a non-negative density.

Pressure changes due to mechanical work on a cell and artificial viscosity are handled separately. As with mass continuity, the energy equation is split into three 1-D equations to be solved successively, similar to Eqs. (17)–(20):

$$\frac{\partial}{\partial t} P^{(+1/3)} = -\frac{\partial}{\partial x}\left(P_{\mathbf{v}_x}^{(+0)}\right) \quad \text{, etc.} \tag{31}$$

Transport is done by a 1-D scheme similar to the mass equation:

$$P_i^{(t+1)} = P_i^{(t)} + \left(F_i^P - F_{i+1}^P\right)/\Delta x \tag{32}$$

$$F_i^P = \hat{P}_i \bar{v}_i \Delta t \tag{33}$$

$$\bar{v}_i = \frac{1}{4}\left(v_{i,j,k} + v_{i,j+1,k} + v_{i,j,k+1} + v_{i,j+1,k+1}\right) \tag{34}$$

where $\hat{P}$ is computed exactly the same way as $\hat{\rho}$. The $P\nabla\cdot\mathbf{v}$ (PdV work) and artificial viscosity at $t + \Delta t$ are done given the momentum equation solution, which is at time level $t + \frac{\Delta t}{2}$.

Again, each component of momentum is advected separately, e.g.,

$$\frac{\partial}{\partial t} S_x + \frac{\partial}{\partial x}\left(v_x S_x\right) + \frac{\partial}{\partial y}\left(v_y S_x\right) + \frac{\partial}{\partial z}\left(v_z S_x\right) = 0 \quad . \tag{35}$$

Artificial viscosity, pressure gradients, and ponderomotive force are each treated separately, and transport is done by an advection scheme:

$$\begin{aligned} \left(S_x^{t+1}\right)_{i,j,k} = &\left[S_x^{(t)}\right]_{i,j,k} \\ &+\left[\left(F_x^{S_x}\right)_{i-1/2,j,k} - \left(F_x^{S_x}\right)_{i+1/2,j,k}\right]/\Delta x \\ &+\left[\left(F_x^{S_y}\right)_{i,j-1/2,k} - \left(F_x^{S_y}\right)_{i,j+1/2,k}\right]/\Delta y \\ &+\left[\left(F_x^{S_z}\right)_{i,j,k-1/2} - \left(F_x^{S_z}\right)_{i,j,k+1/2}\right]/\Delta z \,, \end{aligned} \tag{36}$$

where

$$\left(F_x^{S_x}\right)_{i-1/2,j,k} = \left(\hat{v}_x\right)_{i-1/2,j,k} \bar{F}^{M_x}_{i+1/2,j-1/2,k-1/2} \tag{37}$$

$$\left(F_x^{S_y}\right)_{i-1/2,j,k} = \left(\hat{v}_y\right)_{i-1/2,j,k} \bar{F}^{M_x}_{i+1/2,j-1/2,k-1/2} \tag{38}$$

$$\left(F_x^{S_z}\right)_{i-1/2,j,k} = \left(\hat{v}_z\right)_{i-1/2,j,k} \bar{F}^{M_x}_{i+1/2,j-1/2,k-1/2} \quad . \tag{39}$$

$\bar{F}^{M_x}$ denotes the average mass-flux in the x-direction over the cell, and $\hat{v}_x$, $\hat{v}_y$, and $\hat{v}_z$ are computed using a slight modification of the Van Leer method defined in Eqs. (24)–(30) [the slope $\Delta\rho_3$ is excluded from Eq. (29)]:

$$\delta_i = \text{sign}\left(\Delta v_2\right)\min\left(\Delta v_1, |\Delta v_2|\right)/\Delta x \quad . \tag{40}$$

After the transport step is complete, the change in momentum from thermal pressure gradients

$$\frac{\partial}{\partial t} S_x = -\frac{\partial}{\partial x} P \tag{41}$$

$$\left(S_x\right)_{i,j,k}^{(t+1)} = \left(S_x\right)_{i,j,k}^{(t)} - \frac{\Delta t}{\Delta x}\left(\bar{P}_{i+1/2,j,k} - \bar{P}_{i-1/2,j,k}\right) \tag{42}$$

$$\begin{aligned} \bar{P}_{i+1/2,j,k} = (&P_{i+1/2,j-1/2,k-1/2} + P_{i+1/2,j+1/2,k-1/2} \\ &+P_{i+1/2,j-1/2,k+1/2} \\ &+P_{i+1/2,j+1/2,k+1/2})/4 \end{aligned} \tag{43}$$

and ponderomotive forces

$$\frac{\partial}{\partial t} S_x = -\rho \frac{\partial}{\partial x} \phi \tag{44}$$

$$\left(S_x\right)_{i,j,k}^{(t+1)} = \left(S_x\right)_{i,j,k}^{(t)} - \frac{\Delta t}{\Delta x} \bar{\rho}_{i,j,k} \left(\bar{\phi}_{i+1/2,j,k} - \bar{\phi}_{i-1/2,j,k}\right) \tag{45}$$

$$\begin{aligned} \bar{\phi}_{i+1/2,j,k} = (&\phi_{i+1/2,j-1/2,k-1/2} + \phi_{i+1/2,j+1/2,k-1/2} \\ &+ \phi_{i+1/2,j-1/2,k+1/2} \\ &+ \phi_{i+1/2,j+1/2,k+1/2}) / 4 \end{aligned} \tag{46}$$

is calculated, where $\bar{\rho}$ is the average over the cell.

The artificial viscosity is handled similarly and has the form

$$\left(Q_{xx}\right)_{i+1/2} = \begin{cases} C_Q \rho_{i+1/2} \left[\left(\Delta v_x\right)_{i+1/2}\right]^2, & \text{if } \left(\Delta v_x\right)_{i+1/2} < 0 \\ 0, & \text{otherwise} \end{cases} \tag{47}$$

where

$$\left(\Delta v_x\right)_{i+1/2} = \left(\bar{v}_x\right)_{i+1} - \left(\bar{v}_x\right)_i \tag{48}$$

and $\bar{v}_x$ is the average over the face

$$\left(\bar{v}_x\right)_i = \left[\left(v_x\right)_{i,j,k} + \left(v_x\right)_{i,j+1,k} + \left(v_x\right)_{i,j,k+1} + \left(v_x\right)_{i,j+1,k+1}\right] / 4 . \tag{49}$$

Note that we only keep the diagonal elements from the artificial viscosity term in Eq. (2). Through numerical experimentation, we have determined that $C_Q = 1$ is a reasonable choice, even in the presence of fairly steep shocks.

We have also included a time-step controller to allow a larger Δt when possible, but to ensure that the Courant condition is satisfied. In cases where plasma velocities grow an order of magnitude or more from their initial size, the time step is decreased so that the numerical scheme is stable. When coupled to F3D, the time step is never increased beyond the limit specified by the light propagation.

We have tested this hydrodynamics scheme on several different kinds of problems ranging from deflection of a laser beam in a flowing plasma[12] to plasma expansion into a vacuum.[13–14]

Simulation of the Self-Focusing of a High-Intensity Laser Beam

As an example of an interaction in which nonlinear hydrodynamics is important, we show the results of propagating a 1.06-μm laser beam with initial intensity of 10^{16} W/cm^2 through a CH plasma whose initial electron density and temperature are uniform with values of $n_e = 0.1 n_c$ and $T_e = 1$ keV and thus $v_0 / v_e = 2$. (These conditions are similar to those reported by Young et al.[15]) The laser electric field amplitude at $z = 0$ is taken to be

$$E(x,y)_{z=0} = \begin{cases} E_0(t) \cos^2\left(\frac{\pi x}{L_x}\right) \cos^2\left(\frac{\pi y}{L_y}\right), & \text{if } |x| \le \frac{L_x}{2}, |y| \le \frac{L_y}{2} \\ 0, & \text{otherwise,} \end{cases} \tag{50}$$

where $L_x = L_y = 40$ μm, $L_z = 100$ μm, $-L_x \le x \le L_x$, $-L_y \le y \le L_y$, and $0 \le z \le L_z$. The amplitude $E_0(t)$ rises from 0 to a constant peak value over 100 ps. The field is periodic in the transverse directions, and outgoing at $z = z_{max}$.

In Fig. 1(a), isocontours of the laser intensity at 252 ps are shown. The contours are 2.5, 4.5, 7.5×10^{16} W/cm^2, with the darkest contour being least intense. After propagating about 50 μm, the laser intensity reaches a strong focus with peak intensity $I = 5 \times 10^{17}$ W/cm^2, after which it breaks apart into about four filaments. The initial laser power at $z = 0$ is 100 times the critical power for self-focusing.[16] $P_{crit} = 9 \times 10^8$ W for these conditions, so we might expect the number of filaments $N \approx P / P_{crit} = 100$. The evolution to this highly filamented state requires simulation of a much longer plasma because the distance to focus of a filament varies inversely with power. The distance to the first focus in steady state can be estimated from the steady-state spatial growth rate κ as $L_f = \kappa^{-1} \cong 23\ \lambda_0$ for this case.[17] The steady-state focus actually is achieved at ~50 λ_0.

Isocontours of the electron density associated with this laser intensity distribution are shown in Fig. 1(b).

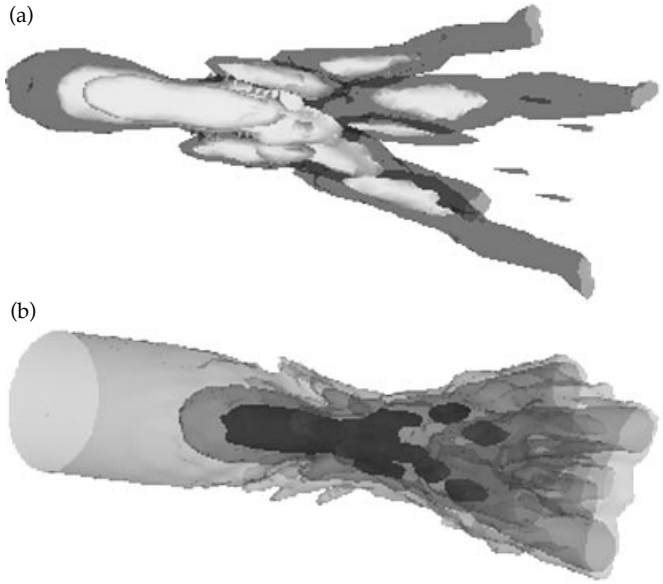

FIGURE 1. (a) Energy intensity contours; (b) density contours. Darkest contours are least intense (a) and least dense (b). (10-00-0896-1932pb01)

The density at the first focus, i.e. peak intensity, is essentially zero: $5 \times 10^{-8}\ n_c$. The contours in Fig. 1(b) are $10^{-2}\ n_c$, $10^{-4} n_c$, and $10^{-5} n_c$, lightest to darkest.

This configuration appears to be near the final state after a very dynamic epoch. The first focus of the laser moves backward at high velocity from $z = 100\ \mu$m at 47 ps to $z = 60\ \mu$m at 55 ps or a velocity of 5×10^8 cm/s. $E_0(t)$ is still increasing during this period. The first focus stays around 55 μm after 60 ps until the end of the simulation at 252 ps.

A number of filamentation codes, including the linearized hydrodynamic version of F3D, neglect the plasma motion along the laser propagation direction because the transverse scale length of the laser hot spot or speckle is much smaller than the axial scale; the ratio of lengths is $8f$ where f is the f-number of the focusing optic. In this simulation the axial flow is important. During the time the focus is moving from $z = 100\ \mu$m to $z = 60\ \mu$m at supersonic velocity, it accelerates the axial flow velocity of the fluid in front of best focus from near 0 to about -3×10^8 cm/s. The ponderomotive force also accelerates plasma supersonically in the positive axial direction at speeds up to 3×10^8 cm/s and transversely at velocities ~6×10^7 cm/s. At the sides of the filaments, the plasma is compressed and heated. The energy in the supersonically moving plasma, when dissipated, results in local ion temperatures in excess of 10 keV. The initial ion temperature was 500 eV.

Summary

As the self-focusing example of Fig. 1 illustrates, filamentation of intense laser beams produces a very nonlinear response in the plasma. The assumptions of a linearized treatment quickly break down. The nonlinear hydrocode described in this article has proven to be very robust and extends our ability to model experiments far beyond the limits of our earlier linear hydrodynamics treatment. Yet further improvements to the physical description are contemplated. The peak intensity achieved at best focus—5×10^{17} W/cm^2 at $\lambda_0 = 1.06\ \mu$m—is weakly relativistic, $v_0^2 / c^2 \approx 0.5$, and suggests that relativistically correct expressions for the ponderomotive force be used.[18] The ions are accelerated to such a high velocity, ~5×10^8 cm/s, that interpenetration[19] rather than stagnation is anticipated at the edges of the evacuated regions associated with filaments. This happens because the ion–ion mean-free-path is estimated in some cases to be larger than the distance over which the flow decelerates. For similar reasons, ion heat conduction should be included in some cases. Inclusion of Poisson's equation might also prove necessary to model the ion–wave dynamics correctly.[20]

Notes and References

1. In addition, the density perturbation is limited in magnitude by replacing the linear response $\delta N = (n - n_0)/n_0$ by $\ln(1 + \delta N)$ so the total density is never negative.
2. R. L. Berger, B. F. Lasinski, T. B. Kaiser, E. A. Williams, et al., *Phys. Fluids B* **5** (7), 2243–2258 (1993); R. L. Berger, B. F. Lasinski, A. B. Langdon, T. B. Kaiser, et al., *Phys. Rev. Lett.* **75** (6), 1078–1081 (1995); S. Hüller et al., "Numerical Simulation of Filamentation and its Interplay with SBS in Underdense Plasmas," submitted to *Physica Scripta* (1996); A. J. Schmitt, *Phys. Fluids* **31** (10), 3079–3101 (1988); A. J. Schmitt, *Phys. Fluids B* **3** (1), 186–194 (1991).
3. A. B. Langdon and B. F. Lasinski, *Phys. Rev. Lett.* **34** (15), 934–937 (1975).
4. M. A. Blain, G. Bonnaud, A. Chiron, and G. Riaguelo, *Autofocalisation de Filamentation d'un Faisceau Laser dans le Cadre de l'Approximation Paraxiale et Stationnaire*, CEA-R-5716; B. I. Cohen et al., *Phys. Fluids B* **3** (3), 766–775 (1991); V. E. Zakharov et al., *Sov. Phys. JEPT* **33** (1), 77–81 (1971).
5. D. Havazelet et al., *Phys. Fluids B* **1** (4), 893–900 (1989); R. Rankin et al., *Phys. Rev. Lett.* **63** (15), 1597–1600 (1989); H. A. Rose, *Phys. Plasmas* **3** (5), 1709–1727 (1996).
6. S. H. Langer, Rayleigh–Taylor calculations.
7. E. M. Epperlein, *Phys. Fluids B* **1** (11), 3082–3086 (1991); T. B. Kaiser, B. I. Cohen, R. L. Berger, B. F. Lasinski et al., *Phys. Plasmas* **1**, 1287 (1994); J. R. Albritton, E. A. Williams, I. B. Bernstein, and K. P. Swartz, *Phys. Rev. Lett.* **57**, 1887 (1986).
8. M. D. Feit and J. A. Fleck, Jr., *J. Opt. Soc. Am. B* **5** (3), 633–640 (1988).
9. R. L. Bowers and J. R. Wilson, *Numerical Modeling in Applied Physics and Astrophysics* (Jones and Bartlett, Boston, MA, 1991), 199–347.
10. D. S. Miller, *Convection in Type II Supernovae*, Ph. D. Thesis (1993).
11. B. Van Leer, *J. Comp. Phys.* **23** (3), 276–299 (1977); B. Van Leer, *J. Comp Phys.* **32** (1), 101–136 (1979).
12. D. Hinkel, E. A. Williams, and C. H. Still, *Phys. Rev. Lett.* **77** (7), 1298–1301 (1996).
13. C. H. Still, R. L. Berger, A. B. Langdon, and D. S. Miller, "Nonlinear Eulerian Hydrodynamics in Three Dimensions," Anomalous Absorption Conference, Aspen, CO (1995).
14. C. H. Still, R. L. Berger, A. B. Langdon, D. S. Miller, and E. A. Williams, "Nonlinear Eulerian Hydrodynamics in 3D," *Bull. APS* **40** (11), (1995).
15. P. E. Young, G. Guethlein, S. C. Wilks, J. H. Hammer, et al., *Phys. Rev. Lett.* **76** (17), 3128–3131 (1996).
16. C. E. Max, *Phys. Fluids* **19** (1), 74–77 (1976).
17. B. I. Cohen et al., *Phys. Fluids B* **3** (3), 766–775 (1991).
18. D. Bauer, P. Mulser, and W. H. Steeb, *Phys. Rev. Lett.* **75** (25), 4622–4625 (1996); G. Bonnaud, H. S. Brandi, C. Manus, G. Mainfray, et al., *Phys. Plasmas* **1** (4), 968–989 (1994); G. Sun et al., *Phys. Fluids* **30** (2), 526–532 (1987).
19. R. L. Berger et al., *Phys. Fluids B* **3** (1), 3–12 (1991).
20. B. I. Cohen et al., "Resonantly Excited Nonlinear Ion Waves," submitted to *Phys. Plasmas* (1996).

Three-Dimensional Simulations of National Ignition Facility Capsule Implosions with HYDRA

M. M. Marinak

S. W. Haan

R. E. Tipton

Introduction

Hydrodynamic instabilities are of critical importance in inertial confinement fusion (ICF) since they place fundamental limits on the design parameters required for capsule ignition. In capsule implosions in the National Ignition Facility (NIF), hydrodynamic instabilities are expected to evolve into the weakly nonlinear regime, so that nonlinear saturation of instability growth will control the amplitudes attained by perturbations in the shell. For perturbations with the same wave number, growth in the linear regime is the same in two and three dimensions. However, simulations of the Rayleigh–Taylor (RT) instability on classical interfaces[1–5]—as well as on foils driven by laser light[6,7] and x rays[8]—predict that symmetric three-dimensional (3-D) perturbations should grow largest in the nonlinear regime. An earlier potential flow model by Layzer[9] showed that round 3-D bubbles achieve the largest rise velocities. An increase in saturation amplitude with symmetry of the mode shape was seen in an extension of the potential flow model[10] and also with third-order perturbation theory.[11] Nova experiments done with planar foils driven by x rays exhibited this shape dependence, in quantitative agreement with simulations done with the HYDRA 3-D radiation hydrodynamics code. The larger, nonlinear saturation amplitudes attained by 3-D perturbations are a principal reason that simulations of surfaces with realistic 3-D perturbations are important to ICF research.

This article presents results from the first direct 3-D simulations of the NIF point-design (PT) capsule, which were performed with HYDRA. The effect of saturated hydrodynamic instability growth on NIF capsule implosions had been modeled previously using weakly nonlinear saturation analysis[12] and 2-D multimode simulations with LASNEX.[13–15] Direct 3-D numerical simulations most accurately treat saturation effects and multimode coupling for capsules with realistic surface perturbations in the presence of multiple shocks, ablation, convergence, and finite shell thickness.

In this article, we begin by describing the HYDRA radiation hydrodynamics code, which performed these simulations. Descriptions of the NIF PT capsule and of the scope of these simulations follow. Finally, we discuss results from a number of multimode simulations of hydrodynamic instabilities.

HYDRA

HYDRA is a 3-D radiation hydrodynamics code based upon a block structured mesh, which has Arbitrary Lagrange Eulerian (ALE) capability. An operator splitting technique is used to treat each of the physical processes in HYDRA separately and to combine the results. The Lagrangian phase solves the compressible hydrodynamic equations using a monotonic form of artificial viscosity,[16] with predictor-corrector time stepping. A control volume technique is used to calculate surface areas and volumes of the hexahedral elements. This technique results in a consistent set of surfaces and volumes on distorted meshes while conserving momentum. The ALE capability allows the mesh to be remapped according to a specified grid motion algorithm, using Van Leer advection in these simulations.[17] Material interfaces are maintained with an Eulerian interface tracker, which is based upon the volume fraction method,[18] generalized to run on arbitrary hexahedrons. "Mixed" zones, which contain one or more material interfaces, are subdivided into separate components for each material.

Radiation transport is treated in a multigroup diffusion routine using tabular opacities. A thermonuclear burn package was installed that treats fusion reactions, including the production and depletion of isotope concentrations, with reaction cross sections obtained from

the Thermonuclear Data File (TDF) library.[19] Energetic charged particles are transported using an efficient multigroup algorithm.[20] It is an extension of diffusion, which retains the straight-line motion of particles undergoing collisions with electrons. Charged particles deposit momentum and energy into the fluid as they slow down, with the energy deposition divided among separate electron and ion channels. The user can specify independently the isotopes for which concentrations are to be followed and the energetic particle species which are to be transported. Since ICF capsules are thin to neutrons, an accurate treatment of neutron energy deposition is obtained with a model based upon an analytic solution to the neutron transport equations in the free-streaming limit. In the calculations presented here, the neutrons that interact with the capsule locally deposit the energy exchanged. Electron and ion conduction are treated, as well as electron–ion energy exchange, using coefficients from the model of Lee and More.[21]

By coupling several adjacent zones together, the user obtains greater freedom in zoning without the additional computational overhead and increased memory requirements associated with an unstructured mesh. Coupling the zones is essential to avoid the small Courant time step limits that would occur, for example, in narrow zones near the center or the pole of a mesh used in a 3-D capsule implosion simulation. This capability can be applied in the presence of mixed zones.

Several forms of the equations of state (EOS) are available, including the EOS4 tabular database and the inline quotidian EOS (QEOS). HYDRA runs on workstations and on vector supercomputers, and currently runs in parallel on the shared memory Cray J-90 SMP using multitasking.

Besides the planar foil simulations mentioned earlier,[5] HYDRA has been applied extensively to model Nova capsule implosions.[22]

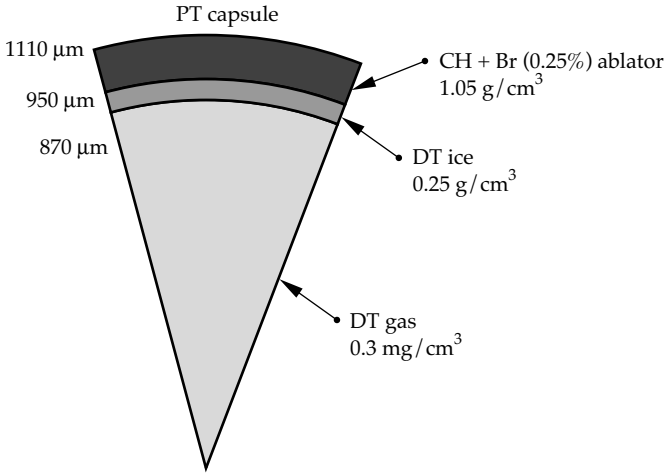

FIGURE 1. Schematic of the "point design" PT capsule shell. (50-05-0896-2031pb01)

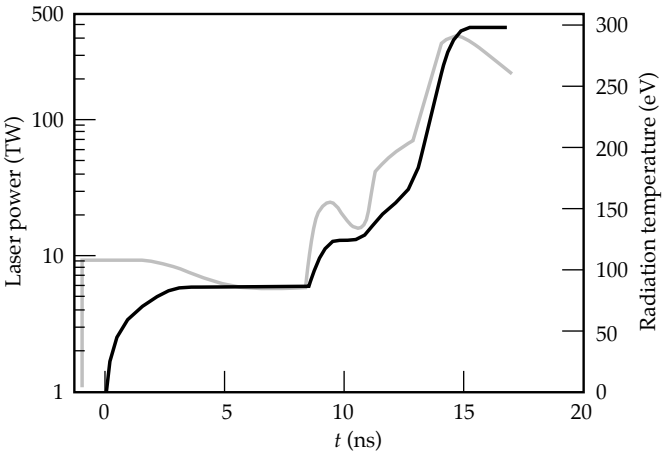

FIGURE 2. Laser power vs time to drive the PT target (gray curve, left scale), and temperature vs time optimal for the PT capsule (solid curve, right scale). (50-05-0896-2032pb01)

Point Design (PT) Capsule

The baseline capsule for the NIF, called the PT for "point design," has a 160-μm-thick polystyrene ablator doped with bromine (Fig. 1). The ablator encloses an 80-μm-thick layer of cryogenic DT ice. DT gas in equilibrium with the ice fills the capsule center at a density of 0.3 mg/cm^3. The capsule is mounted in a gold cylindrical hohlraum 9.5 to 10.0 mm long by 5.5 mm in diameter.

The laser pulse is staged in order to implode the capsule on a low-entropy adiabat (Fig. 2). This pulse delivers 1.35 MJ of laser light, 150 kJ of which is absorbed by the capsule. This 1.35-MJ pulse, which is somewhat less than NIF's maximum (1.8 MJ), was chosen to leave an extra margin for errors in modeling. The light comes into each laser entrance hole in two cones. The relative power in these cones is dynamically varied to minimize the time-varying pole-to-waist asymmetry, which is described as a P_2 Legendre polynomial. Since the NIF has 192 beams clustered in groups of four, there are effectively eight spots in each of the inner cones and 16 in the outer cones. In the absence of significant pointing and power balance errors, the intrinsic azimuthal variation in the hohlraum flux is small. With the standard cylindrical hohlraum, the drive asymmetries are designed to be nearly 2-D. The capsule surface roughness should be the primary source of 3-D asymmetries in the implosion.

The capsule-only simulations presented here model the hydrodynamic instabilities seeded by surface roughness. The average hohlraum flux obtained from an integrated LASNEX simulation[3] is imposed on the capsule. Hydrodynamic instabilities are simulated over a portion of the capsule solid angle, which extends equal amounts in the polar and azimuthal angles ($\Delta\theta$, $\Delta\phi$), with one of the boundaries coincident with the capsule equator. Multimode perturbations imposed are of the form $G(\theta,\phi) = \sum_m \sum_n a_{mn} \cos\left(\frac{m\pi\theta}{\Delta\theta}\right)\cos\left(\frac{n\pi\phi}{\Delta\phi}\right)$ where a_{mn}

is the mode coefficient. Symmetry conditions exist at the transverse boundaries. These modes are the 3-D analog to the modes used in 2-D axisymmetric simulations performed over a portion of a quadrant.

Perturbations initialized on the outer ablator surface are based on traces from Nova capsules, while those on the inner DT surface are based on measurements of cryogenic ice. The data are Fourier analyzed to obtain a 1-D power spectrum. This spectrum may be shifted in mode number when applying the information to the PT capsule, which has a larger radius. The 1-D spectrum is converted to an estimated 3-D power spectrum[23] and the power is distributed isotropically among the 3-D modes with equivalent wave number. Equivalent mode amplitudes from the spectra used in the simulations are shown in Fig. 3 as a function of the l mode number. Random phase factors are assigned to a_{mn} so that the topology of the surface does not have unusually large peaks and valleys due to excessive phase coherence.

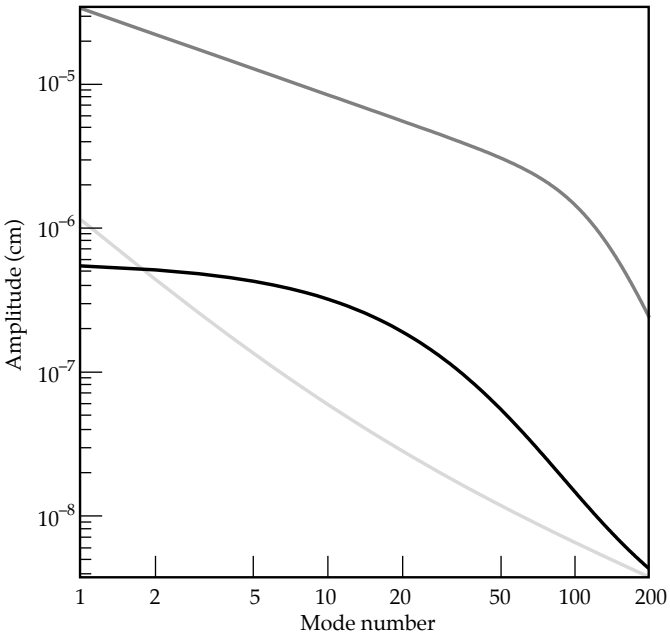

FIGURE 3. Surface perturbation spectra used in simulations of NIF PT capsules. The black curve is the early spectrum for the ablator surface obtained from measurements of a Nova capsule. The light gray curve is the spectrum from a more recent measurement of an optimized Nova capsule. The dark gray curve shows the spectrum of the ice surface. (50-05-0996-2212pb01)

Multimode Simulation Results

We consider first a capsule with perturbation amplitudes, in the range of modes l = 10–1000, equal to 24 nm rms on the outer surface and 1 μm rms on the inner cryogenic DT surface. A domain extending 18° in each angle is used to simulate modes in the range l = 10–40. The grid used here measured $32 \times 32 \times 169$ zones in the polar, azimuthal, and radial directions respectively, so that there are at least 16 transverse zones per wavelength for the least well resolved modes. As the laser pulse rises to peak power, it generates four staged shocks that compress the capsule shell, reducing the shell thickness to 20 μm early in the implosion phase. The grid motion algorithm employed follows this large change in shell aspect ratio and ensures that perturbation growth in the shell is resolved by zones with a fine spacing of 0.75 μm in the radial direction.

Perturbations that grow on the simulated ablator are seeded by initial ablator surface roughness and by the perturbed rarefaction wave that returns from the inner ice surface after the first inward-going shock arrives. During the implosion phase, the shell areal density $A(\theta, \phi) = \int \rho(r, \theta, \phi)\, dr$ strongly resembles the initial outer surface perturbation, indicating that modes growing in the ablator are seeded predominantly by ablator surface perturbations. Valleys initially on the ablator surface develop into bubbles on the ablator, surrounded by interconnecting spike sheets and larger individual spikes, as shown by the iso-density contour plot Fig. 4(a).

Figure 4(b) shows bubble and spike ridge structures that are growing on the pusher–hot spot interface after

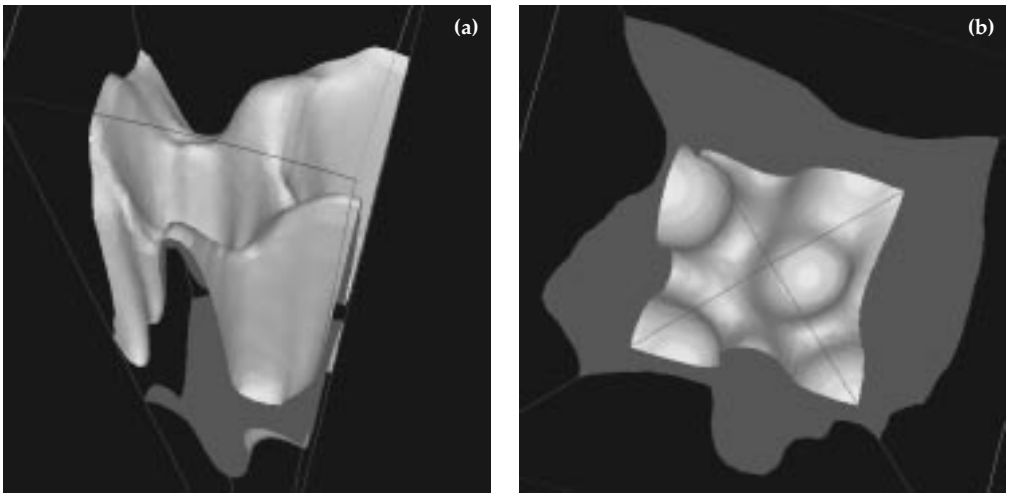

FIGURE 4. Two perspectives of the iso-density contours of 60 g/cm^3 at 17.0 ns from a PT capsule simulation having 24-nm– and 1-μm–rms perturbations initially on the outer ablator and inner ice surfaces, respectively. Multimode perturbations with l = 10–40 were initialized. (a) View of region just inside of the DT–ablator interface. (b) View of pusher–hot spot interface. (50-05-0896-2033pb01)

the rebounding shock has reached it. The locations of these bubbles correspond to the locations of equivalent structures in the ablator, which have fed through the shell. The resemblance to the imposed surface perturbation is characteristic of weakly nonlinear behavior. Some degree of roll-up is apparent, due to a Kelvin Helmholtz instability,[7,9,10] but it is much less than was observed on the classical fuel–pusher interface in Nova capsule simulations.[20,22] The structure of these perturbations has much power in modes $l \lesssim 40$. These growing structures remain visible until the capsule reaches peak compression and the hot spot achieves ignition conditions, with a column density of $\rho r \sim 0.3$ g/cm^3 and ion temperature of ~10 keV. As the capsule reaches peak compression and begins to ignite, the inner surface structure evolves toward lower mode numbers characterized by $l = 10$–15. This behavior appears to be strongly influenced by ablation driven by conduction from the hot spot and the effect of convergence, rather than by mode coupling, as was seen in planar geometry.[7,24–27] Since the shell has a peak convergence ratio of 37, there is a large decrease in the wavelength associated with a particular mode number during the implosion. At ignition the deposition of alpha particles is mostly responsible for "bootstrapping" the central temperature to over 60 keV. This burn propagates into the fuel layer, which has a peak density of > 1000 g/cm^3 at this time. Simulations are carried into the expansion phase for as long as the capsule continues to burn at a significant rate.

Figure 5 shows yields from simulations of several PT capsules that have different multimode surface perturbations with modes $l = 10$–40. The capsule with the largest perturbation amplitudes failed to ignite because, at the time of stagnation, spikes had penetrated 10 μm into the 30-μm-radius hot spot, and bubbles were burning through the shell. Quench of ignition in the DT capsule by 10-μm spikes is consistent with results obtained with other modeling techniques.[3] The location of the yield cliff in Fig. 5 corresponds to a roughness on the outer surface which is ~40% smaller than that obtained with 2-D multimode simulations over this range of modes.[3,4] Higher nonlinear saturation amplitudes and nonlinear growth rates occur for the round, 3-D-bubble-spike features than for the 2-D bubble ridges, and these are responsible for the smaller allowable surface roughness. Differences in instability growth are illustrated by comparing results from one of these 3-D multimode simulations with an axisymmetric 2-D HYDRA simulation that also has surface perturbations consisting of modes $l = 10$–40. The initial rms value for roughness on the capsule surfaces is identical for these 2-D and 3-D simulations. The roughnesses correspond to surfaces with overall perturbations of 19.4 nm and 1.0 μm rms on the ablator and ice surfaces respectively. These amplitudes were chosen so that perturbations would evolve into the weakly nonlinear regime. Figure 6 compares filled contour plots of density on the domain boundaries at 17.0 ns for the 2-D and 3-D simulations with equivalent surface roughnesses. The larger saturated amplitudes attained by the 3-D perturbations are clearly apparent. Since the larger 3-D ablator bubbles are close to penetrating the shell, the bubble tips accelerate,[22] thereby increasing the apparent difference between the growth of 2-D and 3-D bubbles.

The nonlinear growth of the 3-D multimode perturbations is affected by mode coupling and perturbation shape effects. Broad bubbles and narrow

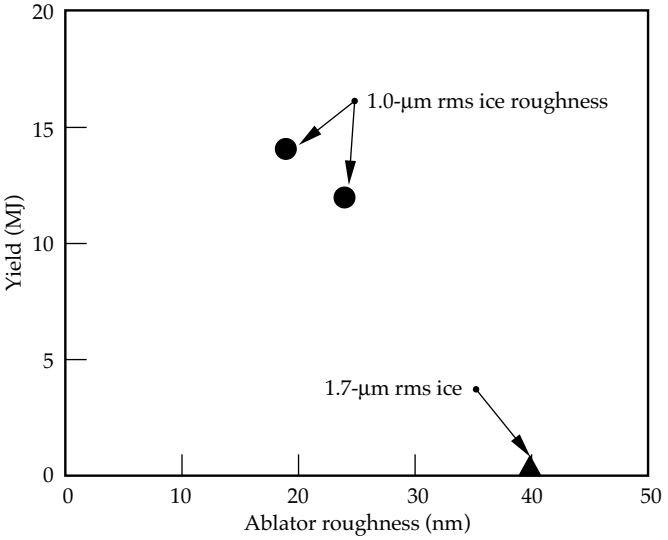

FIGURE 5. Yields for several PT capsule simulations having multimode perturbations with $l = 10$–40 at both the ablator and inner DT-ice surfaces. Ice surface roughness was varied while the ablator roughness was fixed at 24 nm. (50-05-0896-2034pb01)

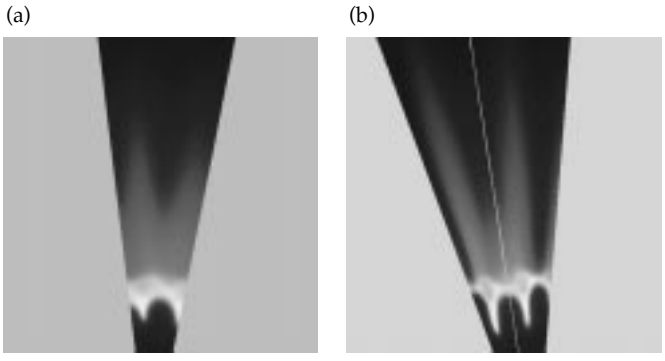

FIGURE 6. Filled contour plots of density at 17.0 ns for two capsules each having initial roughnesses equivalent to 19 nm rms and 1.0 μm rms on the ablator and DT-ice surfaces, respectively. Contours are shown along the planar boundaries of the domains simulated with the radial direction extending upward. Both perturbations contain modes with $l = 10$–40. Perturbation in (a) is 2-D axisymmetric while perturbation in (b) is 3-D, shown along two orthogonal boundary planes. The lightest color corresponds to peak density. (50-05-0896-2035pb01)

spike sheets begin to form early in the nonlinear regime, and for a time it can be described by second-order mode coupling theory.[24,28] Nearby structures strongly influence the evolution of individual bubbles and spikes in the nonlinear phase. Previous attempts to estimate the effect of the higher 3-D saturation amplitudes within direct 2-D axisymmetric capsule simulations involved placing a single bubble or spike on the pole. This treatment is limited because it cannot reproduce the complex multimode coupling and interference effects that occur on a realistic 3-D surface.

The simulations we have discussed so far contain initial perturbations with modes l = 10–40. Modes 40 < l < 120, which are also RT unstable on the ablator, are much less capable of feeding through the shell and producing spikes during deceleration. The shorter length scales of their mode structures reduce their ability to feed through. But the shorter-wavelength modes can threaten the shell integrity during implosion, when the shell is thinnest. We now consider a simulation that includes modes spanning both of these ranges. Perturbations with modes l = 15–120 were simulated on both the inner ice and outer ablator surfaces on a 12° wedge. The grid measured 64 × 64 × 169 zones in the polar, azimuthal, and radial directions respectively. The outer surface perturbation corresponded to the best surface finish measured on a Nova capsule. Similar traces from Russian capsule shells, which have larger radii than Nova capsules, suggest that the long-wavelength surface roughness will not scale strongly to our disadvantage as we go to larger capsules.[29] Figure 7 shows contour plots of the initial perturbations simulated, which have amplitudes of 21 nm and 1.3 μm peak-to-valley on the outer ablator and inner DT ice surfaces, respectively.

Late in the implosion phase, the structure of the growing multimode perturbation has its peak amplitude at the classical interface between the polystyrene ablator and the DT fuel. Centered at this location, the perturbation will penetrate the shell when the amplitude is only a fraction of the shell thickness. The higher modes, which grow fastest on the classical ablator–DT interface, are of concern for the period before the peak implosion velocity is reached. After the implosion velocity peaks, convergence causes the capsule shell to thicken and the classical interface becomes RT stable. Although these perturbations continue to grow inertially, the rapid thickening of the shell separates the classical interface from the shell's inner surface fast enough that further growth of short wavelength modes is unimportant. The longer wavelength modes that feed through the shell, combined with perturbations on the inner capsule surface, assume principal importance once the rebounding shock begins to traverse the shell.

In the present simulation, the shell integrity was never threatened. Figure 8 shows the iso-density contours at 17.1 ns, when the capsule is close to igniting. The contour surface shown in Fig. 8(a) is located in the DT-fuel region of the shell, somewhat inside the polystyrene–DT interface, while the contour surface in Fig. 8(b) corresponds to the pusher–hot spot interface. The high modes apparent near the classical interface, typically near l = 90, have not fed through appreciably to the inner interface, which has features typically in the range l = 15–20. The yield (15.5 MJ) approaches that for an unperturbed capsule. Thus a PT capsule, with a surface finish equal to the best measured on a Nova capsule, easily ignites in the simulation. The margin of ignition in this simulation implies that substantially larger perturbation amplitudes can be tolerated on the outer surface, even with high-l modes present.

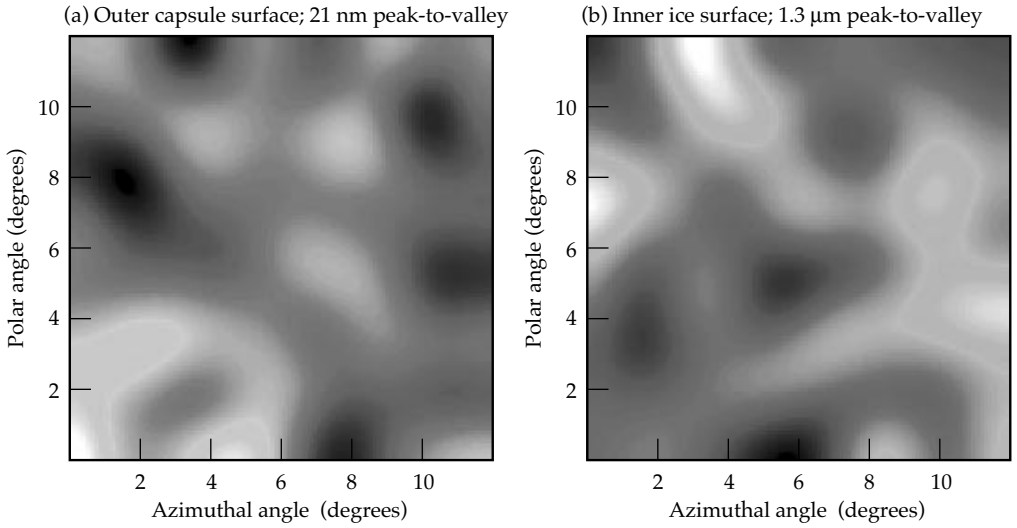

FIGURE 7. Contour plots of multimode perturbations initialized in simulation containing modes l = 15–120. (a) Ablator surface perturbation with peak-to-valley amplitude 21 nm. (b) Inner ice surface perturbation with peak-to-valley amplitude 1.3 μm. (50-05-0896-2036pb01)

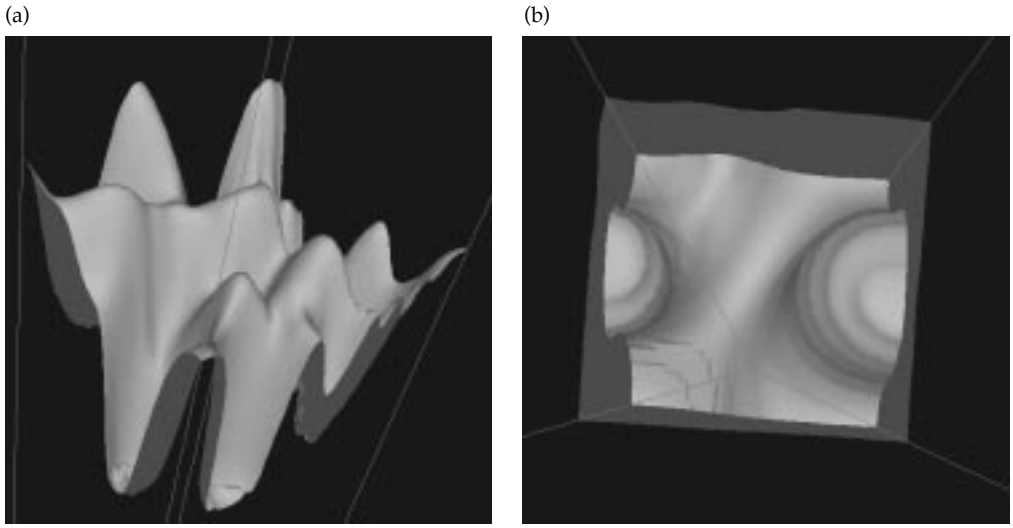

FIGURE 8. Iso-density contour surfaces near ignition time for a PT capsule simulation containing modes l = 15–120. (a) 130 g/cm^3 surface just inside the DT–ablator interface. (b) 650 g/cm^3 surface at pusher–hot spot interface. (50-05-0896-2037pb01)

Conclusions

We presented results from the first 3-D simulations of the NIF PT capsule design. Realistic multimode perturbations seeded hydrodynamic instabilities that evolved into the weakly nonlinear regime. These perturbations were characterized by broad round bubbles surrounded by interconnecting spike sheets and larger individual spikes. Simulations showed that modes with $l < 40$ could threaten ignition by feeding through the shell and developing into spikes when the shell decelerates. Higher modes are much less capable of generating spikes that quench ignition, but they can threaten shell integrity during the implosion phase. The simulations showed that the PT capsule can tolerate spikes with amplitudes up to 10 μm before ignition is quenched.

Three-dimensional multimode perturbations attained larger nonlinear amplitudes than 2-D multimode perturbations having the same initial rms roughness. This results in a constraint on the roughness of the ablator surface that is ~40% smaller than was obtained from 2-D multimode simulations over a similar range of modes. Even when modes spanning the range l = 15–120 were included, however, a PT capsule with surface finishes equal to the best currently attainable easily ignited in the simulation. Future simulations of the PT will quantify the sensitivity of the capsule to surface roughnesses contained in different ranges of modes.

Notes and References

1. G. Tryggvason and S. O. Unverdi, *Phys. Fluids A* **2** (5), 656–659 (1990).
2. T. Yabe, H. Hoshino, and T. Tsuchiya, *Phys. Rev. A* **44** (4), 2756–2758 (1991).
3. J. Hecht, D. Ofer, U. Alon, D. Shvarts, S. A. Orszag, and R. L. McCrory, *Laser Part. Beams* **13** (3), 423–440 (1995); D. Ofer, J. Hecht, D. Shvarts, Z. Zinamon, S. A. Orszag, and R. L. McCrory, *Proceedings of the 4th International Workshop on the Physics of Compressible Turbulent Mixing*, edited by P. F. Linden, D. L. Youngs, and S. B. Dalziel (Cambridge University Press, Cambridge, 1993), pp. 119–128.
4. H. Sakagami and K. Nishihara, *Phys. Rev. Lett.* **65** (4), 432–435 (1990).
5. R. P. J. Town and A. R. Bell, *Phys. Rev. Lett.* **67** (14), 1863–1866 (1991).
6. J. P. Dahlburg, J. H. Gardner, G. D. Doolen, and S. W. Haan, *Phys. Fluids B* **5** (2), 571–584 (1993).
7. J. P. Dahlburg, D. E. Fyfe, J. H. Gardner, S. W. Haan, S. E. Bodner, and G. D. Doolen, *Phys. Plasmas* **2** (6) 2453–2459 (1995).
8. M. M. Marinak, B. A. Remington, S. V. Weber, R. E. Tipton, S. W. Haan, K. S. Budil, O. L. Landen, J. D. Kilkenny, and R. Wallace, *Phys. Rev. Lett.* **75** (20), 3677–3680 (1995).
9. D. Layzer, *Astrophys. J.* **122** (1), 1–12 (1955).
10. J. Hecht, U. Alon, D. Shvarts, *Phys. Fluids* **6** (12), 4019–30 (1994).
11. J. W. Jacobs and I Catton, *J. Fluid Mech.* **187**, 329–352 (1988).
12. S. W. Haan, *Phys. Rev. A* **39** (11), 5812–5825 (1989).
13. G. B. Zimmerman and R. M. More, *J. Quant. Spectrosc. Radiat. Transfer* **23** (5), 517–522 (1980); R. M. More, *ibid*. **27** (3), 345–357 (1982).
14. S. W. Haan, S. M. Pollaine, J. D. Lindl, J. J. Suter, et al., *Phys. Plasmas* **2** (6), 2480–2487 (1995).

15. W. J. Krauser, N. M. Hoffman, D. C. Wilson, B. H. Wilde, W. S. Varnum, D. B. Harris, F. J. Swenson, P. A. Bradley, S. W. Haan, S. M. Pollaine, A. S. Wan, J. C. Moreno, and P. A. Amendt, *Phys. Plasmas* **3** (5), 2084–2093 (1996).
16. D. J. Benson, *Comp. Methods Appl. Mech. Eng.* **93**, 39–95 (1991).
17. B. Van Leer, *J. Comput. Phys.* **23** (3), 276–299 (1977).
18. D. L. Youngs, in *Numerical Methods for Fluid Dynamics,* edited by K. W. Morton and M. J. Baines (Academic Press, New York, 1982) pp. 273–285.
19. R. M. White, D. A. Resler, and S. I. Warshaw, in *Proceedings of the International Conference on Nuclear Data for Science and Technology,* 13–17 May 1991, *Jülich,* edited by S. M. Qaim (Springer–Verlag, Berlin, 1992) p. 834.
20. G. Zimmerman, private communication.
21. Y. T. Lee and R. M. More, *Phys. Fluids* **27** (5), 1273–1286 (1984).
22. M. M. Marinak, R. E. Tipton, O. L. Landen, T. J. Murphy, P. Amendt, S. W. Haan, S. P. Hatchett, C. J. Keane, R. McEachern, and R. Wallace, *Phys. Plasmas* **3** (65), 2070–2076 (1996).
23. S. M. Pollaine, S. P. Hatchett, and S. H. Langer, *ICF Quarterly Report*, **4** (3), 87–89, Lawrence Livermore National Laboratory, Livermore, CA, UCRL LR105821-94-3 (1994).
24. M. M. Marinak, R. E. Tipton, B. A. Remington, S. W. Haan, S. V. Weber, *ICF Quarterly Report*, **5** (3), 168–178, Lawrence Livermore National Laboratory, Livermore, CA, UCRL LR105821-95-3 (1995).
25. D. H. Sharp, *Physica D* **12** (1–3), 3–18 (1984).
26. U. Alon, D. Shvarts, and D. Mukamel, *Phys. Rev. E* **48** (2), 1008–1014 (1993); *Phys. Rev. Lett.* **72** (18), 2867–2870 (1994).
27. D. Shvarts, U. Alon, D. Ofer, R. L. McCrory, and C. P. Verdon, *Phys. Plasmas* **2** (6), 2465–2472 (1995).
28. S. W. Haan, *Phys. Fluids B* **3** (8), 2349–2355 (1991).
29. R. Cook, private communication.

LASNEX—A 2-D Physics Code for Modeling ICF

J. A. Harte

W. E. Alley

D. S. Bailey

J. L. Eddleman

G. B. Zimmerman

Introduction

The LASNEX computer code was developed to study inertial confinement fusion (ICF), to design ICF experiments, and to analyze the results. The code has evolved over time and been greatly enhanced with improved physics and modern computer science tools. LASNEX was first referred to in the literature in 1972[1] and first documented in 1975.[2]

This article presents an overview of the code, describing the physics models, the code structure, the methods used to solve the equations, and the user interface, providing supplemental information and updates to the previous review article published in 1980.[3] Although the general structure of the physics in the code is very much the same, many improvements have been added since 1980. For instance, the user interface has been greatly enhanced by the addition of the Basis code development system.[4] In addition, the code has been improved in response to requests, suggestions, and feedback from its users, who often challenge its capabilities to a far greater degree than the code developers do. The success of LASNEX as an important scientific tool is due to the team effort of the code developers and its users.

LASNEX models in two dimensions by assuming axial symmetry. It represents the spatial variation of its many physical quantities, such as temperature, density or pressure, on a two-dimensional (2-D), axially symmetric mesh composed of arbitrarily shaped quadrilaterals. LASNEX evolves the hydrodynamics and follows the electron, ion, and radiation heat conduction, and the coupling among these energy fields. There are many possible sources and boundary conditions that can be imposed on a LASNEX simulation, which can vary both in time and space. The possible sources include fully three-dimensional (3-D) lasers or ion beams using a ray tracing algorithm, temperature sources, frequency-dependent radiation sources, velocity sources, external electric circuits, and pressure sources. Thermonuclear reactions can be modeled by LASNEX, including the energy produced as well as the reaction products and their transport through the problem. We have several different atomic physics packages available which supply the coupling and transport coefficients and self-consistent thermodynamic quantities. LASNEX combines all these physical processes and evolves the system forward in time, rather than just solving for an equilibrium or steady-state configuration. This complexity and the large number of physical processes modeled present a challenge to us (as we try to describe the code) and to those using the code and interpreting the results. A computer simulation of an experiment calculates all the independent physical quantities at each time step to enable the system to evolve forward. Any quantity can be "measured" or monitored. Huge amounts of data are often the problem for computational physicists, rather than a lack of data (which can be a problem for experimentalists).

With LASNEX, a "typical" problem does not exist—its calculations can take many different forms. Because of this, in this paper we describe the code by presenting all its different parts and how they fit together, organized around the "circles and arrows" diagram shown in Fig. 1. Following the descriptions of the physics packages, we outline the computer science enhancements that have been added to increase LASNEX's power, versatility, and convenience. Finally, we present several LASNEX calculations that accurately model laboratory experiments. Ultimately, it is the agreement between the code calculation and experimental data that validates the code and gives us confidence that LASNEX can be used to predict and design future experiments (the National Ignition Facility, for example).

Circles and Arrows Diagram

Figure 1 is a "circles and arrows" diagram that represents the LASNEX computer code: *circles* represent the fields in which energy resides and *arrows* represent the interactions among the various fields. There is also a circle labeled atomic physics that is connected to the arrows. This process supplies the physical data necessary for many of the other packages.

LASNEX solves a large set of coupled, nonlinear, partial differential equations that determine the temporal evolution of the many spatially dependent quantities as they are influenced by different physical processes. The solution of the equations for the different physical processes is "split," so that the code evolves one process after another forward in time by one timestep until they have all been done, feeding the results from one into the next. For each package, a maximum allowable or reasonable timestep is calculated for the next cycle. When all the processes have been solved for one step, the next step is taken using a value for the timestep that is the smallest of all the possible time steps.

One of the basic design philosophies of LASNEX is to allow the different physics packages to be turned on or off by the users based on their particular application. The actual processes that are used in any calculation are determined by the user, usually when the calculation is initialized. Also, in a circle there can be several models for a given physical process. Once again, the physicists will choose which models to use based upon the problem parameters and the computer resources available. This choice of models can also affect the interactions among the different parts of the calculation represented by the arrows. The ability to choose at execute time between alternative modules for the same physical process has allowed us to develop and debug new physics packages while simultaneously maintaining a stable code for production use. Redundant physics models also allow a user to validate the correctness of each model and to trade computer time and problem size for accuracy, according to the needs of the particular situation.

Hydrodynamics

The spatial variation of the physical quantities are described on a 2-D, axially symmetric mesh composed of arbitrarily shaped quadrilaterals. Typically, the hydrodynamics is Lagrangian[5] in which the mesh moves along with the material. LASNEX uses a staggered grid hydro algorithm adapted from the HEMP code of Wilkins.[6] On a regular mesh, it is second-order accurate in time and space. Several artificial viscosities are provided to treat shock waves of arbitrary strength, one of which approximates the dissipation given by a

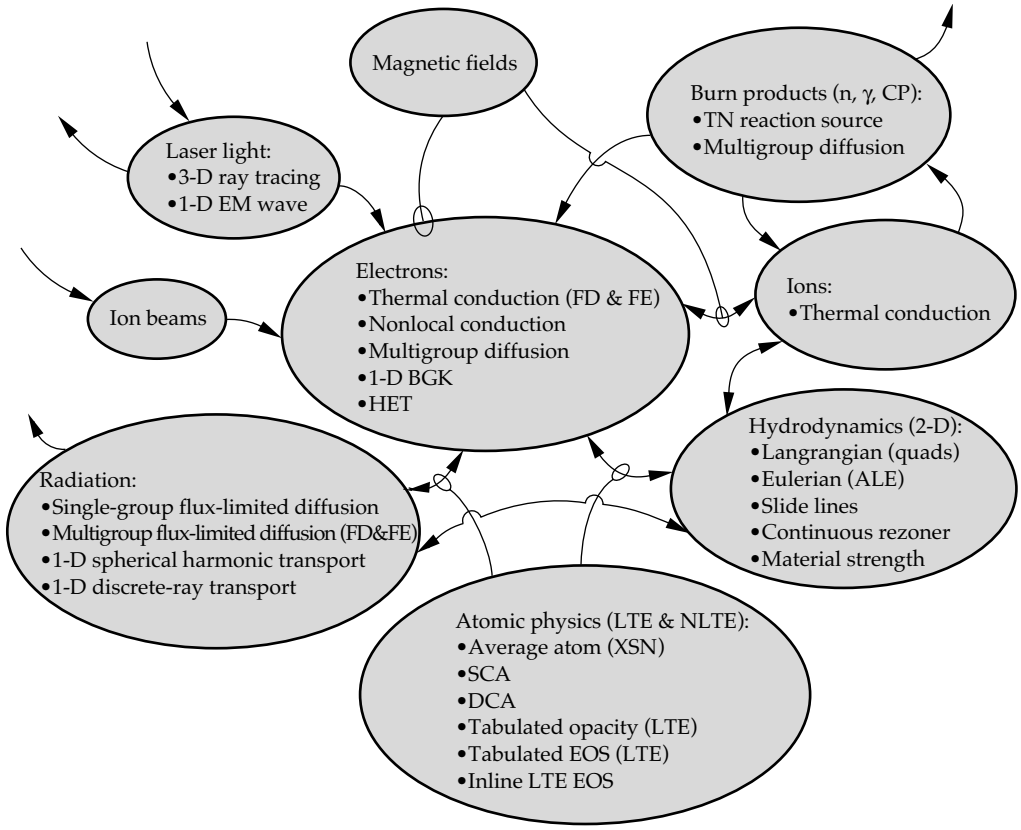

FIGURE 1. A schematic overview of LASNEX. The *circles* represent the fields in which energy resides; the *arrows* represent interactions among the different fields.
(02-08-1292-3795pb02)

Riemann solution of the flow. There are also velocity filters used to damp spurious mesh oscillations, including anti-hourglass filters and artificial shear viscosities.

A material strength capability is available that generalizes the scalar pressure to a stress tensor appropriate for isotropic materials. It includes elastic and plastic flow regimes and a Von Mises yield criterion for the transition to plastic flow. There are provisions for user specification of the elastic constants and yield stress limits to allow very general constitutive models. There is a history-dependent fracture model that includes both compression and tensile failure modes, based on computing a strain damage integral from the plastic flow and using this damage to lower the yield strength in a prescribed way. The model allows effects such as spallation of brittle material to be treated. Its parameters are designed for great flexibility in treating material failure.

The hydrodynamics calculation usually takes a small fraction of the computer time required for a complete physics cycle, and often the Courant timestep (set by the requirement that a signal can travel only one zone width in one timestep) can be much smaller than all the other timesteps. In this case, LASNEX can "subcycle" the hydrodynamics, taking many hydrodynamics cycles per major physics cycle to speed up the calculation.

When the LASNEX hydrodynamics method leads to severe mesh distortions or suboptimal resolution of the important physics, the user can request that the mesh be moved. There are two rezoners used in LASNEX—one for rezones at discrete times and another which operates continuously. The discrete time rezoner takes explicit user input to generate the new mesh coordinates. Discrete rezoning can be done interactively with graphical feedback or can be preprogrammed using Basis[4] interpreted user-defined functions to determine when and how to rezone the problem. (See the "User Interface" section for an example.) The continuous rezoner accepts user commands to define the desired mesh configuration and tries to satisfy these requirements through a relaxation process (one of which tends toward a mesh of equipotential lines). Rezoning every timestep can be equivalent to performing Eulerian or Arbitrary Lagrange Eulerian (ALE)[7] hydrodynamics. It requires that the remapping of all variables to the new mesh be done with high accuracy.

Both of the rezoners use a Van Leer slope limiting method in which spatial quantities are represented as

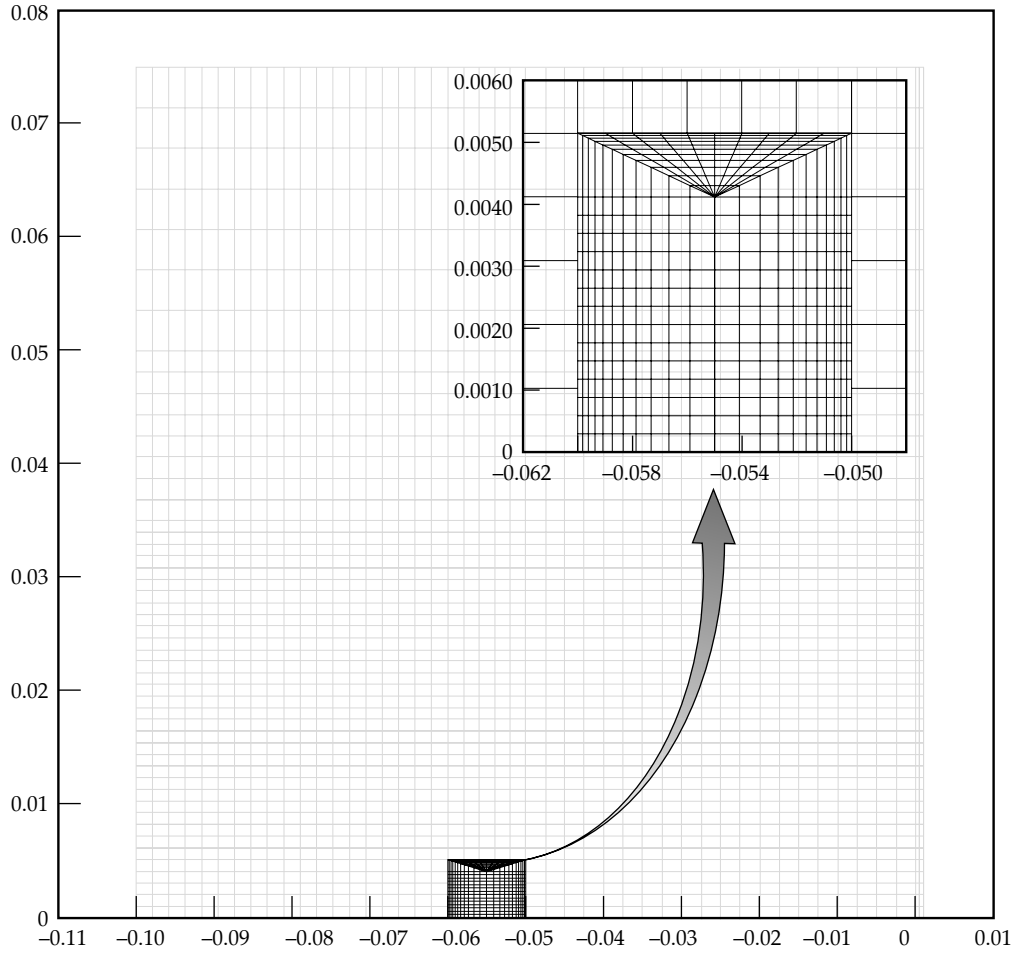

FIGURE 2. This mesh models a small, dense impurity in an otherwise homogeneous, lower density region. It is composed of two simply connected parts that are joined by slide lines. The slide lines allow part of the mesh to be much more finely resolved than the rest of the problem. Without slide lines, the fine zones would have extended all the way in both directions, increasing the problem size by over 50% and creating many small low-density zones with a much more restrictive Courant condition. (40-00-1196-2729pb01)

linear functions within each zone. This allows for second-order remap accuracy in smooth regions, while not generating extraneous maxima/minima at discontinuities. This is adequate for most quantities, but the material composition suffers some numerical diffusion. The addition of a material interface tracking algorithm would substantially reduce these errors.

The discrete rezoner allows an arbitrary overlap between the old and new mesh, but the continuous rezoner demands local overlap of the two meshes. The locality assumption permits an accurate momentum remap that also conserves kinetic energy,[8] while the more general case is treated by a less accurate interpolation method.

Ordinarily, the LASNEX mesh has a simple logical structure in which each interior quadrilateral zone has four nearest neighbors, a relationship that remains constant throughout the calculation. Optionally, one can specify slide lines,[9] logical line segments along which zones on one side are free to slide relative to the other side. This allows simulations with discontinuous velocities and also provides a means of zoning complicated initial geometries, such as shine shields or connecting regions of differing resolution. Figure 2 shows a LASNEX mesh with slide lines to connect regions of differing resolution. Every physics model that involves neighbor zones (hydrodynamics, diffusion, transport, laser ray trace, etc.) has had to be modified to include the special (time-dependent) slide line connectivities. These slide line modifications which connect logically disjoint zones have also been used to establish the periodic boundary conditions needed for multimode *z*-pinch calculations.

Electrons

To model the electrons, the user can choose thermal conduction, multigroup diffusion, one-dimensional (1-D) or 2-D nonlocal conduction, 1-D Bhatnagar, Gross, Krook (BGK) conduction, or a hybrid electron transport (HET) model that is currently under development. All the 1-D models allow either planar or spherical configurations.

Thermal electrons are assumed to be in a Maxwellian distribution. The electron thermal energy is transported using tensorial plasma conductivities in a magnetic field modified by applying a flux limiter (described later). The electrical conductivities in LASNEX go beyond the low-density, high-temperature formulae of Spitzer/Braginskii[10] by including dense plasma effects.[11] They include the effects of electron degeneracy, Debye–Hückel screening, ion–ion coupling, and electron-neutral scattering (see refs. in Ref. 11). The treatment is based on a relaxation time (Krook[12]) model of the Boltzmann equation ignoring e–e collisions. LASNEX approximately includes e–e collisional effects by making Braginskii's correction to the Lee/More coefficients. The cross sections used are analytic fits of a Coulomb cross-section form to numerical partial-wave expansions, with cut-off parameters to avoid unphysical answers. The effects of ion correlations in the liquid/solid regimes are treated by a modified Bloch–Grüneisen[13] formula. Finally, the various magnetic coefficients (which do satisfy the Onsager symmetry relations) are fits to the numerical integrals in the weak-field case and tabulated for the intermediate and strong-field case. Overall, the conductivities are believed accurate to a factor of 2 over a very wide range of densities (to 100× solid) and temperatures (eVs to 100 keV) and expressed in a computationally simple form.

Thermal electron conduction involves the solution of the diffusion equation on the arbitrary quadrilateral mesh. Since the mesh lines are not necessarily orthogonal, this requires a nine-point diffusion operator. The resulting matrix is solved by the Incomplete Cholesky–Conjugate Gradient (ICCG) method.[14] Both a finite difference and a finite element scheme are available to calculate the electron conduction. Finite difference schemes[15] are employed throughout the code to diffuse the zonal quantities, which are the basic unknowns. The finite element method[16] gives better solutions on nonorthogonal meshes. However, the finite element energy densities are point centered and must be integrated into the LASNEX architecture of zonally averaged quantities.

The diffusion equation is derived in the limit of near isotropy. Thus the mean free path should be considerably shorter than the characteristic length scale of the problem. Nevertheless, the diffusion equation can give meaningful results in other regimes if modified to insure that physical expectations will not be violated. The flux of energy should be bounded by the limit of all the energy flowing in one direction at the average velocity of the Maxwellian distribution. This is referred to as "flux limiting" and is achieved by modifying the diffusion coefficient so that when the gradients are very large the energy flux will be bounded by this criterion.

The thermal electron energy is coupled with the other fields in LASNEX as indicated by the arrows in Fig. 1. The energy of the electrons is shared with the ions through Coulomb collisions.[17] The electrons affect the material hydrodynamic motion by contributing to the plasma pressure.

Nonthermal, actually suprathermal, electron distributions can also be treated in LASNEX. This method was developed to study the hot electrons that are found in ICF applications.[18] In the code hot electrons are created by either a laser source or an ad hoc source defined by the user. They are transported and thermalized by a multigroup, flux limited diffusion method that is relativistically correct and allows for arbitrary isotropic distributions.[19] When suprathermal electrons

are being modeled, the thermal electrons are also present. Suprathermal electron transport is iterated, along with the determination of a self-consistent electrostatic potential, in a way that assures zero net current. Suprathermal electrons lose energy to the thermal electrons by Coulomb collisions, including the effect of the degree of ionization[20] and by doing Ohmic work through the electric field. The suprathermal electron bins can have arbitrary bin structure.[21] Suprathermal electron bremsstrahlung is modeled by a parametrized fit to the bremsstrahlung spectrum,[22] which accounts for partial ionization. The suprathermal electrons produce frequency-dependent bremsstrahlung photons that are transported in LASNEX's radiation package. The suprathermals also contribute to the plasma pressure.

The nonlocal electron conduction package in LASNEX solves the electron conduction equation with a nonlocal heat flux that vanishes at the boundaries. This nonlocal package models the features of fully kinetic Fokker–Planck calculations. These features are a reduced heat flux in the hotter region of the heat front, a preheat foot, and nonisothermal, low-density corona.[23] The nonlocal electron transport option is available in both one and two dimensions. The 1-D model solves finite difference equations. (For all 1-D models, LASNEX allows either spherical or planar configurations.) The 2-D nonlocal conduction uses the finite element machinery.

Often in laser-produced plasmas, the range of the hot electrons is much larger than the temperature or density scale lengths, which give rise to free streaming and nonlinearities in the heat conduction. The 1-D BGK[24] electron thermal conduction model accounts for free streaming effects in steep temperature gradients by evaluating the electron distribution within the plasma via the BGK approximation to the Fokker–Planck equation. The resulting distribution is then used to evaluate the heat flux in the plasma.[25] A distribution function approach was developed because other models were unable to account reliably for the nonlocal electron heat transport.[26] The BGK approximation is used to improve the speed of the algorithm over a direct solve of the Fokker–Planck equation. Nevertheless, iteration of the algorithm is necessary to calculate the electric field, insuring charge neutrality and particle and energy conservation, neither of which is explicitly guaranteed by a blind application of the BGK approximation.

A package for hybrid electron transport (HET) is being developed to incorporate 2-D electromagnetic effects into electron transport. The model draws heavily on the ideas of Rodney Mason, associated with 2-D implicit plasma simulations.[27] The algorithm is designed to incorporate particle and/or fluid electrons—the particles would represent hot electrons generated by plasma processes, and the fluid electrons would represent the background thermal electrons. Currently, only the field solver and the thermal electron parts of the package are implemented. The package accounts for electron transport via a generalized Ohm's law[28] which includes all of the Braginskii coefficients,[29] including the Hall and Nernst terms. For heat transport, the package also includes all of the Braginskii coefficients, including the Righi–Leduc term. Because the electric field is also important in transport, a field solver for Maxwell's equations, including the displacement current, was written that goes beyond the MHD approximation used in the present magnetic field package in LASNEX.[30] The MHD approximation assumes charge neutrality in the plasma which results in the displacement current being ignored. The HET package does not ignore the displacement current and therefore is not charge neutral. HET also does not ignore $\partial j/\partial t$. The fields are represented by continuous finite elements; the electric current is represented by discontinuous finite elements. The effects on transport using this model are already dramatic. In some situations the spontaneously generated magnetic field magnetizes the electrons with the result that thermal transport is inhibited. Improved results for laser-heated foil experiments have been noted.[31]

Ions

Thermal ions are assumed to be in a Maxwellian distribution. Flux limited diffusion methods are used to mix spatially different types of ions and to transport the ion thermal energy. Ion conduction uses the same ICCG method to solve the diffusion matrix as the electron conduction package. Real ion viscosity (momentum diffusion) is optionally included in the hydrodynamics equations, although it is typically small by comparison with the usual artificial viscosity.

The ions affect the material hydrodynamic motion by contributing to the pressure. Hydrodynamic work, including that done by the artificial viscosity, and the thermonuclear reactions heat the ions. The heat exchange with the electrons limits the ion temperature. The ion temperature is important for three practical reasons: (1) the thermonuclear fusion reaction rate is very sensitive to T_i; (2) T_i controls the Coulomb logarithm used to calculate laser absorption by inverse bremsstrahlung and electron thermal and electrical conduction; and (3) T_i determines the Doppler contributions to the width of spectral lines, which can be important for x-ray laser designs.

Radiation

Radiative energy flow is one of the principal means of coupling laser energy into a target. Because of its importance in ICF, LASNEX has several methods

for calculating radiation transport: single group flux limited diffusion, multigroup flux limited diffusion using either finite difference or finite element solution scheme, 1-D spherical harmonic expansion of the transport equation, 1-D discrete-ray transport, and detailed radiation transport.

Single group flux limited diffusion assumes that the photons are in a Planck distribution characterized by a local radiation temperature. This method uses only Rosseland mean opacities and is valid if the system is thick to radiation.

Multigroup flux limited radiation diffusion assumes nearly isotropic photon distributions and allows for arbitrary frequency dependence. Frequency-dependent opacity data is required. The diffusion algorithm to model multigroup radiation diffusion can be treated by either the finite difference approximation or the finite element method,[32] similar to the electron diffusion. The ICCG linear system solver is employed in both schemes. By default, the finite difference and finite element models use an iterative scheme to couple the radiation energy to the matter.[33] A "partial temperature" coupling scheme which is often much faster (see Ref. 42) is also available for use, but it can give large swings of the intermediate values of the electron temperature during a single timestep, decreasing accuracy. Accuracy is controlled by reducing the timestep until the swings in the partial temperature are acceptable. However, this can result in very small timesteps. The recommended radiation electron coupling scheme is differenced implicitly in time; in steady state, it will relax to the correct answer in one step. This method, related to a scheme of Axelrod and Dubois,[34] may be thought of as a form of alternating-direction implicit iteration, in which one direction corresponds to photon energy and the other to spatial location. In certain circumstances, particularly when the timestep is large and the rates associated with transport and radiation-matter coupling are similar, the convergence can be quite slow. We have a convergence-acceleration scheme for use in these unusually stiff cases.[35] Shestakov et al.[36] describe test problems in radiative transfer and compare finite difference and finite element solutions to the radiation diffusion equations, illustrating the use of analytic solutions to validate the results of computer simulations.

Photon Compton scattering and its resulting energy exchange with electrons is also treated in LASNEX. To model relativistic Compton scattering, we evaluate the Compton scattering kernel by averaging the Klein–Nishina cross section over a relativistic Maxwellian distribution.[37] This scattering kernel is then integrated over all directions to obtain the transfer matrix used to solve the Boltzmann equation for isotropic photon distributions.[38] Finally, one can make the Fokker–Planck approximation which assumes that the photon frequency shift is small compared with the photon frequency.[39] LASNEX can do Compton energy exchange by either the Boltzmann or Fokker–Planck methods. The Fokker–Planck method is finite differenced in a way that obtains exact steady-state results.[40] Since x-ray mean free paths are often comparable to the size of ICF targets, the diffusion approximation is not appropiate and we must solve the transport equation.

LASNEX has a 1-D (either spherical or slab) P_n radiation transport package in which the photon angular distribution is expanded in spherical harmonics where P_l is the coefficient of the lth Legendre polynomial.[41] The radiation transport equation is written as an infinite set of coupled equations for the P_l's. Rather than terminating this infinite set at the lth moment by zeroing out P_{l+1}, Kershaw improved the results of the P_n calculation by setting P_{l+1} to a value within its bounds. Probability theory is used to calculate the upper and lower bounds. The 1-D P_n package uses the same relativistic Compton methods described earlier to evolve the 0th (isotropic) moment. Other moments only undergo Thompson scattering with no frequency shift. The P_n package couples the photon energy to matter using the "partial temperature scheme."[42] The 1-D P_n radiation transport has been useful both in actual design calculations and in testing the accuracy of various extensions to the diffusion theory.

Radiation transport in LASNEX is also modeled by a 1-D discrete-ray method.[43] It consists of solving the finite difference equations for the radiation intensity for a few selected directions. The total intensity at any point in space is the sum over the intensities of each of the discrete directions weighted in some consistent way, for example, by the fraction of the solid angle that each ray represents. We difference the radiation transport equation using upstream, implicit differencing, and we couple the radiation energy with matter by iteration using the multifrequency gray approximation.[44] A persistent problem with the Lund–Wilson scheme has been the accuracy in the thermal wave limit, when the zones are many mean free paths thick. LASNEX also has a 1-D, discontinuous finite element radiation transport package, bilinear in space and photon direction, which behaves correctly in the thermal wave limit.[45] The radiation transport equation has upwinded, discontinuous elements; the electron temperature equation has continuous elements. The resulting linear equations are solved by a modified splitting of the intensity and temperature parts. There is an optional Newton iteration for problems where the nonlinearity of the Planckian function is significant over a single timestep. In this, the Compton scattering is treated nonrelativistically, including scattering only in angle (Thomson scattering).

All radiation transport models deposit momentum when a photon is absorbed or scattered. In the Atomic Physics section, we describe the derivation of the

frequency-dependent radiative opacities used in the photon transport packages. Basically, we include bound-bound, bound-free, and free-free processes in either local thermodynamic equilibrium (LTE) or non-LTE. The frequency-dependent radiation intensity that escapes from a LASNEX mesh is often a very valuable problem diagnostic to compare with corresponding experimental spectra.

Lasers, Ion Beams, and Other Sources

A LASNEX calculation can be driven by several different types of sources and/or boundary conditions. Some sources, such as temperature, pressure, frequency-dependent radiation intensity, and velocity are imposed arbitrarily, while the beam deposition sources interact with the plasma in a more complete and physically consistent manner. Lasers and ion beams are calculated by tracking a number of rays through the spatial mesh. Power on the ray is decremented as deposition occurs. The temporal and spatial variations of all the possible sources can be specified by the users.

In 1983, a 3-D laser ray tracing package was added to LASNEX.[46] Prior to this, all light rays were forced to travel in the *(r,z)* plane, which often created anomalously high intensities near the symmetry axis. The 3-D laser package computes the trajectories of an arbitrary set of laser rays through the mesh. The rays are bent according to the laws of refraction. Ray trajectories are computed using the gradient-index geometrical-optics equations. On the basis of computed ray path lengths, energy is deposited in each zone by inverse bremsstrahlung, including nonlinear corrections.[47] The laser energy is also absorbed by a photoionization model based on the Saha equation.[48]

Noncollisional processes—plasma instabilities and resonance absorption—are modeled by angle-dependent absorption[49] or more simply by absorbing a given fraction of the energy that is left in each ray at its turning point. The ray intensity is correspondingly attenuated. When suprathermal electrons are present, absorption by the noncollisional process creates an electron distribution with a "hot" temperature derived from fits to plasma simulations.[50]

Typically, the LASNEX computational mesh is too course to resolve steep, inhomogeneous plasma-density structures that might arise from uneven illumination or hydrodynamic instabilities. Therefore, the code has a statistical model of the refractive scattering of laser light by random density fluctuations in the subcritical plasma.[51] The scattering can occur along the entire ray path or only at the turning point. The hydrodynamic effect of the laser light is included with a ponderomotive force algorithm which has both scalar and tensor terms.[52]

Since LASNEX tracks a finite number of rays through the mesh, we often see "ray effects," causing the laser intensity to vary unphysically. A "fatray" package smoothes the laser energy deposition, using a finite element diffusion equation.[53] This will not cause energy to be deposited past the critical surface because the smoothing takes place only for regions where the electron density is less than or equal to the critical electron density. Another option to decrease the ray effects (which we call "smearing") is to average the deposition over two zones each time it is applied, and it can be applied any number of times. The user has some directional control by choosing to apply the smearing along particular logical mesh lines.

Charged-particle beam deposition is calculated from stopping-power formulas that account for straggling and partial ionization.[54] We have made calculations from first principles of the dynamic charge state of a fast, heavy ion as it experiences various ionization and recombination processes while slowing down in a heated target material.[55] The important processes are collisional ionization balanced at equilibrium by radiative recombination.

Ion beams do not refract as light does. Therefore, we have a separate, simpler and faster ray trace package for ions. It assumes only straight ray paths in 3-D, which become hyperbolae when projected onto the (r, z) plane.[56] Momentum deposition from ion beams is implemented consistently.

For moderately intense, ultrashort pulse lasers, we have a subroutine which actually solves Maxwell's equations in 1-D, rather than using a ray trace approximation.[57] The algorithm takes advantage of the rapid oscillation and propagation of light waves compared with hydrodynamic motion. Thus, the steady-state 1-D solution to Maxwell's equations results in the Helmholtz equations. Both *s*- and *p*-polarized cases are accounted for by the package. Plasma waves are generated at the critical surface in the case of *p*-polarized light. To account for losses due to plasma waves without explicitly following the waves in the plasma, the total collision rate is modified in the resonance region to be the sum of: the electron–ion collision rate + the Landau damping rate at the critical point + the rate at which plasma waves leave the resonance region + the loss rate due to the wavebreaking of the plasma waves.[57] To maintain consistency, the algorithm automatically incorporates a WKB approximation in the low-density blow-off region when the low-density zone sizes approach the laser wavelength. The frequency-dependent conductivity has been improved to go beyond the Drude approximation and results in improved modeling of absorption in solids.

Burn Products

LASNEX calculates all significant thermonuclear reactions among isotopes of H, He, Li, Be, and B.[58]

Charged particles and neutrons produced are transported by multigroup diffusion methods that take into account nuclear scattering, in-flight reactions, and momentum deposition.[59] Gamma rays produced by inelastic nuclear interactions are also transported by multigroup diffusion, accounting for Compton scattering, photoionization, and pair production.[60] The neutron and gamma diffusion both use a multigroup extension of Levermore's diffusion method.[61] The charged particle transport is an extension of diffusion that retains particle inertia as it undergoes straight-line energy loss to electrons.[62] Charged particle energy loss rates include the effects of an arbitrary ratio of particle to electron thermal velocity, Fermi degenerate electrons, and bound electrons.[63] All burn products either escape from the problem, providing numerous diagnostic opportunities, or deposit their energy back into the thermal electron and ion fields.

Magnetic Fields

Magnetic fields are generated automatically in 2-D problems or can be imposed by user-specified sources. The magnetic field package[64] in LASNEX includes J × B forces and the full Braginskii cross-field transport model. The Braginskii model has been extended with the Lee and More conductivities and includes the magnetic diffusion, Nernst, grad P, grad T, and Hall terms in Ohm's law, as well as the perpendicular and Righi–Leduc heat flows, j•E, and other terms in the heat equation. The user may optionally specify source terms that self-consistently couple the plasma to an external LRC circuit.

If requested, the magnetic package modifies the electrical conductivity to account for the anomalous resistivity due to lower-hybrid waves. Periodic boundary conditions are available for the study of multimode Rayleigh–Taylor (RT) perturbations. The energy conservation has been improved (order-of-magnitude improvement for 1-D, purely-Lagrangian calculations) and the magnetic flux is conserved during mesh rezoning. These enhancements, together with new, high-resolution rezoning schemes, programmed by the users with the Basis interface, have allowed the successful modeling of high-energy, radiating *z*-pinches. Features typically exhibited in these simulations are the strong nonlinear growth of magnetic RT modes,[65] and the formation of hot spots[66] near the axis due to unstable ($m = 0$) sausage modes.

Also, magnetic fields can be spontaneously generated in the presence of nonparallel temperature and density gradients which may occur in laser-produced plasmas. The resulting changes in the magnetic-field-dependent transport coefficients for all charged particles may significantly alter the plasma temperature and pressure profiles. This may be an important effect in the design of some hohlraums or direct-drive targets which require a high degree of symmetry and efficient utilization of laser power.

Atomic Physics

The atomic physics models in LASNEX supply the equation-of-state (EOS) variables (e.g., pressure and energy as a function of temperature and density) used in the hydrodynamics, the degree of ionization used to establish various electron collisional rates, and the frequency-dependent opacities used by the radiation transport routines. In LTE, these quantities are functions only of the density and electron temperature and can be conveniently tabulated or evaluated by analytic expressions. LASNEX can access the internal Lawrence Livermore National Laboratory (LLNL) EOS data and the Los Alamos National Laboratory (LANL) Sesame data,[67] and it can use its own quotidian EOS (QEOS) package.

The QEOS[68] is an in-line EOS routine that is based on the Thomas–Fermi electron-gas approximation. The QEOS total energy is split up into three parts:

$$E_{\mathrm{tot}}(\rho, T) = E_{\mathrm{e}}(\rho, T) + E_{\mathrm{b}}(\rho) + E_{\mathrm{n}}(\rho, T) \qquad (1)$$

where E_{e} is the Thomas–Fermi (TF) energy, E_{b} is an analytic (Cowan) bonding correction used to fit the experimentally known solid density and bulk modulus at standard temperature and pressure, and E_{n} is the nuclear motion energy. It provides separate EOSs for electrons and ions. Since QEOS is based on a free energy, thermodynamic consistency is guaranteed, and the smooth TF term together with the analytic ion part generate continuous results from cold solid conditions through the liquid, vapor, and plasma states. The *Z*-scaling property of the TF model allows a single table to generate data for any element as well as provide the speed necessary for an in-line calculation.

LASNEX can also access LTE frequency-dependent opacity data in three different formats: it reads Cray binary files of opacity information in a format unique to LASNEX designed 20 years ago; it reads the LANL Paradise[69] opacity files; and it reads the LLNL machine independent opacity files,[70] using the portable data file (PDB) library of Stewart Brown.[71]

In non-LTE, the EOS, degree of ionization, and the opacity must be determined from the atomic populations which are found by solving rate equations and, in general, depend on the photon and suprathermal electron distribution functions. LASNEX has incorporated three major atomic physics packages, XSN, SCA, and DCA, which can be run in either LTE or non-LTE modes. All three provide LASNEX with pressure, energy, and frequency-dependent opacity and emissivity due to bound-bound, bound-free, and free-free processes.

XSN[72] is an average atom, atomic physics code that uses a simple *Z*-scaled, screened hydrogenic model to perform in-line calculations of arbitrary mixtures at all temperatures and densities. It is used to obtain material opacities for LTE and non-LTE, as well as EOS values under non-LTE conditions. It includes the effects of Fermi degeneracy, continuum lowering, and pressure ionization,[73] which are required to correctly model cold solids at high densities and is designed to closely match the Thomas–Fermi ionization values along the cold curve. The lack of *l*-splitting and the simple line-width formulae limit the accuracy of the opacities to average values. However, XSN's simplicity does provide the required speed and allows any mixture to be treated. Since the EOS is based on a free energy, it is automatically thermodynamically consistent. The lack of a bonding correction means that XSN's pressures at low temperature are too high, but in most cases, non-LTE effects are small under those conditions, and this package would rarely be run.

The average-atom atomic physics package Statistical Configuration Accounting (SCA)[74] produces more accurate opacity information than the default XSN package because its underlying atomic physics data is evaluated off line by a self-consistent, relativistic, Hartree–Slater program, called LIMBO.[75] Because the database which LIMBO produces is based on relativistic physics, the resulting opacity which SCA produces shows fine-structure splitting. Whereas, fine-structure splitting can be included into an XSN opacity only in an ad hoc fashion. As in XSN, the atomic physics is simplified by using the hydrogenic approximation, where the states of an ion are described by the quantum numbers of a single electron which is immersed in a spherically symmetric screened Coulomb potential.

The Detailed Configuration Accounting (DCA) atomic physics package[76] solves rate equations for the number of ions in each important excited state in each ionization state. This package is more expensive than XSN or SCA. It is used when accurate atomic physics is needed for line diagnostics or x-ray laser modeling. DCA can handle any number of states connected by radiative and collisional bound-bound, bound-free, and auto-ionization and dielectronic recombination processes. The states and transition rates are specified in data files generated by other codes. Optionally, a simple screened hydrogenic model can be produced at problem initialization. In addition, the DCA package calculates Voigt line shapes due to Doppler, Lorentz, and Stark broadening and, if requested, handles line transfer by a general purpose escape probability method that reduces to 1-D, static or Sobolev limits in planar or cylindrical geometry.[77] It includes effects of Fermi degeneracy and handles pressure ionization and continuum lowering in the Stuart/Pyatt approximation[78] by reducing the statistical weight smoothly to zero as continuum lowering ionizes the weakest bound electron. To save computer time, the levels which are eliminated by continuum lowering or which are ionization states of low probability are removed from rate calculations and from the system of rate equations. The resulting reduced linearized system is then solved by banded or iterative matrix methods.

Another relatively new feature of the LASNEX atomic physics package is a multiphoton, dielectric breakdown package which models multiphoton–ionization seeding of avalanche breakdown. The model is based on the work of Feit et al.[79] in which a simple seeded exponential model was inferred from their Fokker–Planck studies. The seed rate is proportional to an integral power of the energy density of the laser light in the material. In this process, the electron density will build until a threshold level is reached. Above the threshold, the material breaks down by electron avalanche, which is modeled by an electron distribution that exponentially increases in time. The avalanche is quenched when a maximum of one electron per ion is reached, justified by assuming that the ionization potential for the next electron to be removed increases substantially.

User Interface

LASNEX has been a pioneer in interactive and steered computations. Even in its early days (more than twenty years ago), the users were able to investigate and modify their simulations while they were running. Graphical displays and numerical edits of the problem could be produced at any time, allowing the users to ascertain quickly whether the problem was running correctly and efficiently. With the inclusion of the Basis code development system,[80] a huge leap in interactivity was achieved at once. The programmable interface provided by Basis transformed LASNEX into "a whole new generation of design code."[81] It gives LASNEX a complete, up-to-date, well maintained, and well documented computer science interface, allowing users to innovate without the intervention of the code developers. The code developers no longer have to get involved with specific user requests for diagnostics or special purpose models, freeing them from straightforward but time-consuming tasks.

Basis has a fully featured, FORTRAN-like interactive programming language interpreter which can access the variables and functions in the LASNEX compiled code. Basis supplies an interface to a complete graphics package that includes curves, markers, contours, text, frame control, and viewport control, as well as LASNEX-specific plotting commands, such as mesh plots and mesh-based contour commands. Basis also offers many mathematical packages, such as Bessel functions, fast-Fourier transforms, random-number generators, and polynomial fitting.

One of the most important components of Basis is a history package that allows the user periodically to execute specified commands and/or to collect any number of sets of values of arbitrary expressions. A variety of mechanisms can be used to select the frequency at which these generations are collected. Users may also specify logical conditions under which actions will occur, such as the occurrence of bowties, a zone reaching a certain temperature, etc. The history package employs the portable database system (PDB)[71] to store the collected data. The Portable-Files-from-Basis (PFB) package of Basis gives the users a convenient interface to the data files.

LASNEX users now accomplish many tasks using the tools of the Basis system. They have automated the tedious chore of generating sets of similar problems by writing Basis functions to do the work. Instead of a user issuing instructions from the terminal for a discrete problem rezone, they now can use the Basis interpreter and history functionality to sense when the mesh is in trouble, decide what should be done, and execute the rezone. In this way, LASNEX provides user-controlled, automatic mesh refinement facilities.

In many processes the users can add their own models to work with or to replace those of LASNEX. To accommodate the users' new programming power, we have introduced many "user defined arrays," in which they calculate their own values for various LASNEX quantities. For example, a user can supply the material EOS by calculating, at each timestep, the electron pressure and its derivatives with respect to density and temperature, the electron energy and its derivatives, and the corresponding ion components. Similarly, a user can define the thermal conductivities, zonal energy sources, zonal energy leak rates, or zonal electron thermal flux limit multipliers. We continue to add more user-defined variables to the code to take advantage of this capability.

Another application of the Basis interpreter is to create self-tuning simulations or a self-optimizing series of simulations. As a calculation is running, the Basis interpreter can decide how well the design is working based on certain criteria. Then, for example, the laser pulse shape or spatial profile can be changed to satisfy the criteria better.

Table 1 provides an automatic rezoning example to illustrate how Basis works within LASNEX to save the designers' time and to allow many jobs to run to completion without user intervention.

TABLE 1. Example of automatic rezoning.

Problem Description:

Whenever any zone becomes folded over on itself ("bowtied"), return the mesh to a given "good" configuration, perform the rezone (mesh overlay and remapping of all the LASNEX variables), and proceed.

The user must define the function that tests the LASNEX mesh for troubles (here bowties) and corrects it, if necessary. In this example the mesh is simply set back to the original configuration defined when r_good and z_good were declared. The "h" card tells when (i.e., at every cycle from 1 to 10000) the function, "test_n_rezone," should be invoked.

Note: the "#" symbol indicates that the following text is a comment.

The Basis Coding:

```
real8 r_good = rt, z_good = zt   # Declare "good" coordinates and
                                 # equate to LASNEX's rt and zt.
h 1:10000:1 test_n_rezone        # At every cycle call the function
                                 # test_n_rezone.
function test_n_rezone           # Function definition.
  if(nbowt(rt,zt,ireg).ne.0) then # Test for bowties.
    prezone                      # Execute LASNEX command to
                                 # prepare for rezoning.
    rt=r_good                    # Reset the LASNEX mesh to the
    zt=z_good                    #"good" ones.
    rezone                       # Mesh overlay and remap physical
                                 # quantities.
  endif
endf
```

Example Calculations

This section describes three ICF experiments simulated with LASNEX: a planar hydrodynamic instability experiment, a spherical hydrodynamic instability experiment, and a capsule implosion mix experiment. These examples illustrate that LASNEX can accurately model actual laboratory experiments.

Planar Hydrodynamic Instability Experiment

A series of experiments was conducted with the Nova laser to measure hydrodynamic instabilities in planar foils accelerated by x-ray ablation.[82] We show results of a single-mode experiment and the corresponding LASNEX calculation. A low-density fluid pushing on a high-density fluid is RT[83] unstable, and perturbations on the surface between the fluids grow and take on a characteristic bubble and spike appearance. In these experiments, surface perturbations were imposed on one side of a foil that was mounted across a diagnostic hole in the wall of a cylindrical Au hohlraum. The foil was accelerated by the indirect x-ray drive generated by focusing eight pulse-shaped Nova beams into the hohlraum and was backlit with a large area spot of x-rays created by shining another Nova beam on discs of Mo, Rh, Sc, or Fe. Figure 3(a) shows the experimental image of a foil with 100-μm sinusoidal perturbations viewed side-on with a 2-D grated x-ray imager at 4.4 ns into the pulse. The foil has evolved into the classic bubble and spike shape characteristic of nonlinear RT instability. The LASNEX calculation Fig. 3(b) at 4.4 ns agrees with the experimental image. In fact, they are almost identical.

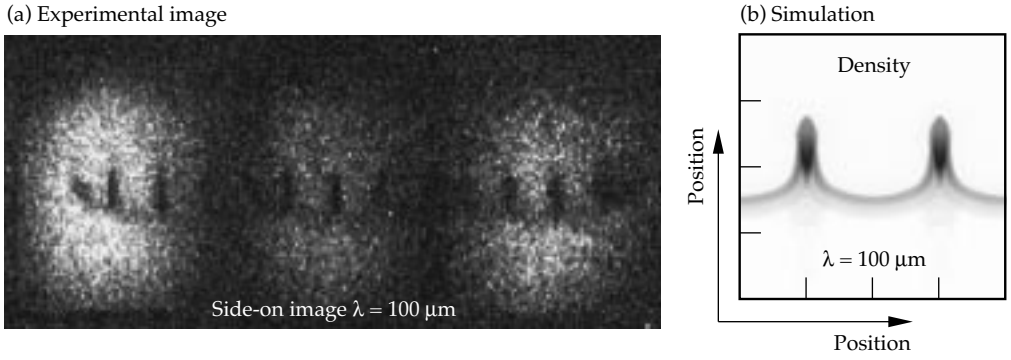

FIGURE 3. (a) Results of perturbation growth experiment viewed side-on at a time of 4.4 ns. (b) Shaded density plot of the transmitted backlighter x-rays at 4.4 ns in the corresponding 2-D LASNEX simulation.
(20-03-1293-4393pb02)

The 2-D LASNEX simulation used the time-dependent laser power that was measured in the experiment, tabular opacities created by a "first principles opacity" code, and tabular EOS data. The transmitted backlighter x-rays included the instrumental response.

Spherical Hydrodynamic Instability Experiment

The next experiment was designed to study the physics of implosions with high RT growth factors. Using indirect drive, we imploded capsules with Germanium-doped ablators to minimize x-ray preheat and shell decompression and hence increased the in-flight aspect ratios. X-ray backlit images of the capsule implosion were recorded at 4.7 keV with 55 ps and 15-μm resolution. Three parallel 3-μm-deep grooves were machined in the ablator to seed the instability. One groove encircled the center of the target; the other two were parallel and on opposite sides. Figure 4 shows the backlit image of the capsule from the experiment and the LASNEX calculation at 2.22 ns to be virtually identical.[84] The grooves machined into the ablator for this experiment were not uniformly spaced—the one on the right was closer to the center; the effect of this is seen in both the experiment and code results. The groove on the left being farther from the center allowed a double ridge to be created as the perturbation amplitude grew from each groove. This did not occur on the right side, where the grooves were closer and the RT growth from the central and right-hand grooves merged into just one modulation. The LASNEX simulation was a standard 2-D calculation. It was able to accommodate many zones while still properly modeling the radiation by using a special method of weighting opacities that allows a faster convergence with a much smaller number (typically 5 or 6 compared with 50 to 100) of photon groups compared with the standard Rosseland weighted mean.[85]

Capsule Implosion Mix Experiment

This experiment addressed the issue of the hydrodynamic stability of the imploding fuel capsule. Experiments on Nova were performed to study how imperfections on the capsule surface grow by RT instability into large perturbations that cause pusher–fuel mix and degrade the capsule performance.[86] To diagnose

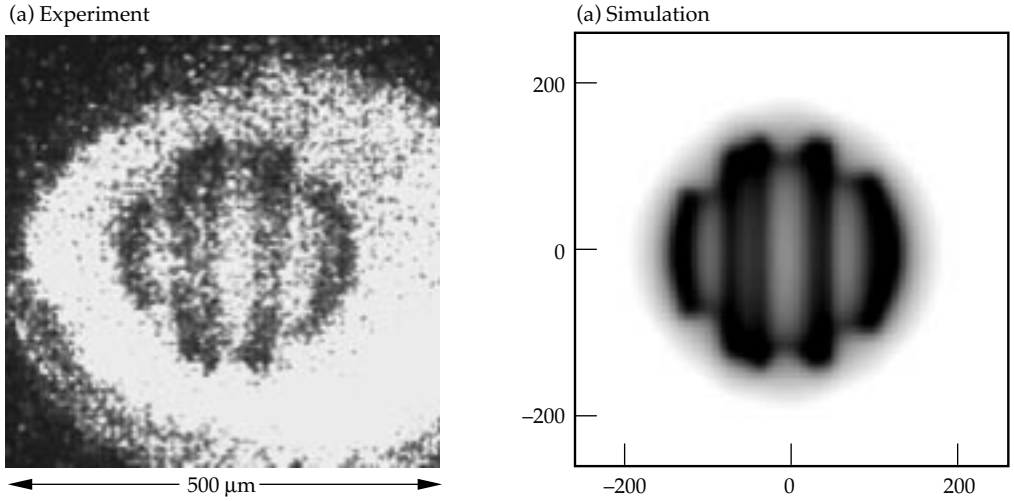

FIGURE 4. Backlit image of grooved Ge-doped imploded capsule at 2.2 ns into the pulse. Both the experimental data on the left and the LASNEX results on the right show the growth of the modulation.
(40-00-1196-2730pb01)

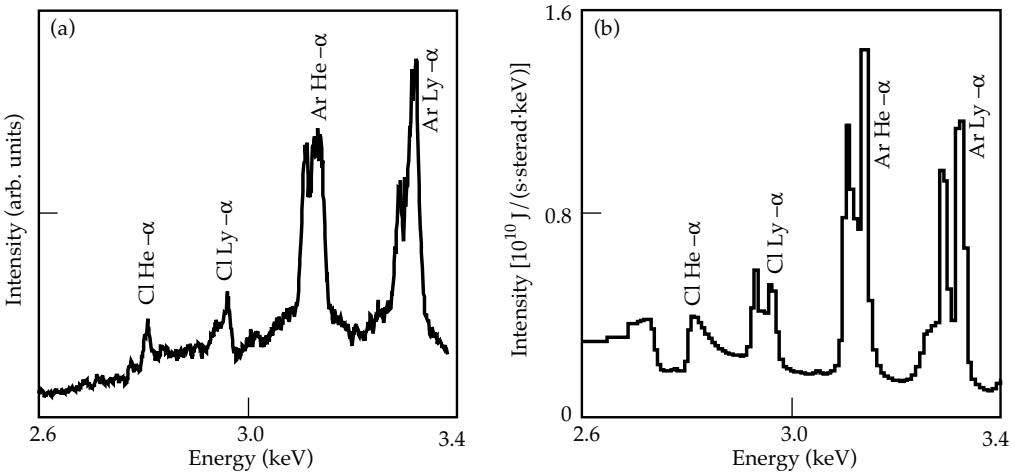

FIGURE 5. Spectra at peak x-ray emission in units of 10^{10} J/s/sterad/keV from the implosion of a smooth surface capsule. (a) The experimental streaked crystal spectrometer data. (b) The 1-D DCA LASNEX simulation result. Relevant emission lines of Cl (the pusher dopant) and Ar (the fuel dopant) are labeled. (20-03-0795-1850pb02)

the enhanced mix, x-ray emission spectra of trace elements in the pusher (Cl) and fuel (Ar) were measured as the surface roughness increased. (Figure 5 shows example spectra.) The emission of the pusher dopant relative to the fuel dopant did increase with surface roughness as the cold pusher mixed more thoroughly with the hot fuel, due presumably to RT instabilities (see Fig. 6). Simulating the implosion of these capsules was a multistep process, employing both 1- and 2-D LASNEX calculations. The 2-D calculations were used to estimate linear growth for single-perturbation modes. The surface roughness and the linear perturbation growth factors combined with Haan's[87] nonlinear saturation prescription were used to calculate the time-dependent width of the mix region. In 1-D implosion simulations with LASNEX, material was atomically mixed and thermal transport enhanced over a distance about the fuel–pusher interface, according to the width of the mix region.

Emission spectra were generated with the DCA atomic physics package. As seen in Fig. 6, the LASNEX results for the ratio of time-integrated Cl to Ar Lyman–alpha emission agrees well with the experimental results. The trend of increased mix for rougher surfaces is very apparent. The experimental spectra and the spectra calculated by LASNEX also match as seen in Fig. 5.

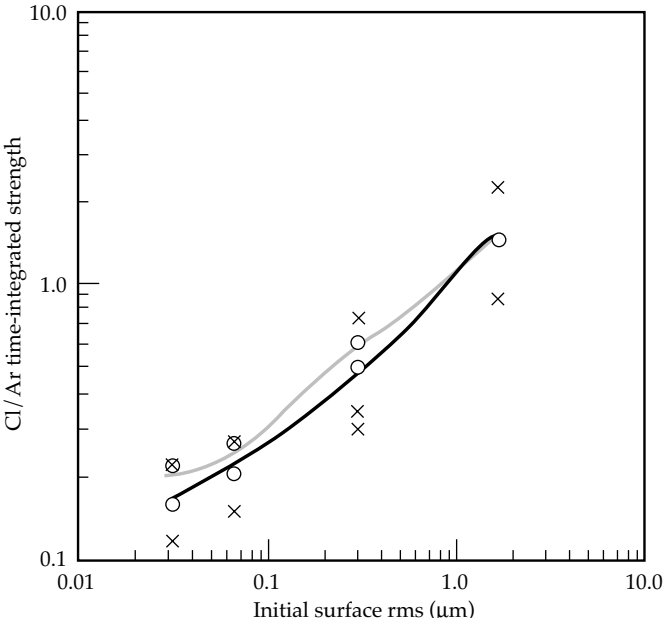

FIGURE 6. The ratio of the time-integrated Cl and Ar Lyman–alpha emission lines is plotted vs the initial surface roughness. An X (O) marks each experimental (simulation) point. The black (gray) lines connect the average values of the experimental (simulated) data at each distinct initial surface rms. (08-00-0996-2154pb01)

Acknowledgments

The extensive references in this article illustrate the number of scientists that have worked on LASNEX. In addition to George Zimmerman who originated LASNEX, we would like to acknowledge all those who have also contributed to it: Roberta Allsman, Harry Bruestle, Lee Busby, Paul Dubois, Art Edwards, Alex Friedman, Fred Fristch, David Kershaw, Jim Kohn, Zane Motteler, Dale Nielsen, Paul Nielsen, Jeff Painter, Manoj Prasad, Rich Sacks, Alek Shestakov, Al Springer, Lynd Stringer, Janet Takemoto, Susan Taylor, Sharon Wilson, and Brian Yang. The support and encouragement of John Nuckolls and Lowell Wood were instrumental in its early development and application. We also acknowledge the continuing support by division leaders from A, CP, and X-Divisions—from Peter Moulthrop and Bill Lokke through Dave Nowak, Dan Patterson, and Mordy Rosen. Feedback from the LASNEX users has also been invaluable, ranging from their encouragement and clever ideas to bug reports and complaints.

Notes and References

1. J. Nuckolls, L. Wood, A. Thiessen, and G. B. Zimmerman, *Nature*, **239**, 5368, pp. 139–142 (1972).
2. G. B. Zimmerman and W. L. Kruer, comments in *Plasma Physics and Controlled Fusion* **2**, 51 (1975).
3. G. B. Zimmerman, *Laser Programs Annual Report*, 3–71, Lawrence Livermore National Laboratory, Livermore, CA, UCRL-50021-80 (1980).
4. P. F. Dubois, "Making Applications Programmable," *Computers in Physics* **8**(1), Jan–Feb 1994.
5. W. Schultz, *Methods in Computational Physics* (Academic Press New York, 1970), vol. 3, p. 1.
6. M. L. Wilkins, *Meth. Comp. Physics* **3**, 211 (1964).
7. F. W. Harlow and A. A. Amsden, *J. Comp. Phys.* **16**, 1 (1974).
8. D. S. Bailey, *Laser Programs Annual Report*, 3–57, Lawrence Livermore National Laboratory, Livermore, CA, UCRL-50021-84 (1984).
9. M. L. Wilkins, "Calculation of Elastic–Plastic Flow" in *Methods in Computational Physics*, Bernie Alder, Sidney Fernbach, and Manuel Rotenberg, Eds. (Academic Press, New York, NY, 1964).
10. S. I. Braginskii, "Transport Processes in a Plasma," in *Reviews of Plasma Physics*, M. A. Leontovich, Ed. (Consultants Bureau, N.Y. 1965), vol. 1, p. 205.
11. Y. T. Lee and R. M. More, *Phys. Fluids* **27**, 1273 (1984); Y. T. Lee, R. M. More, and G. B. Zimmerman, "A New Electron Transport Model for LASNEX," *Laser Programs Annual Report*, 3–61, Lawrence Livermore National Laboratory, Livermore, CA, UCRL-50021-81 (1981).
12. N. A. Krall and A. W. Trivelpiece, *Principles of Plasma Physics* (McGraw–Hill, New York, 1973) p. 317.
13. J. M. Ziman, *Principle of Theory of Solids* (Cambridge University Press, Cambridge, England, 1964).
14. D. S. Kershaw, *J. Comp. Phys.* **26**, (1978); *Ibid*., **38**, 114 (1978); *Idem*, "Solution of Single Tridiagonal Linear Systems and Vectorization of the ICCG Algorithm on the Cray-1," in *Parallel Computations*, (Academic Press, New York, NY, 1982; *Idem*, *Laser Programs Annual Report*, 3–77, 3-79, Lawrence Livermore National Laboratory, Livermore, CA, UCRL-50021-79 (1979); *Ibid*., 3–67, UCRL-50021-81 (1981).
15. G. J. Pert, *J. Comp. Phys.* **42**, 20 (1981); D. S. Kershaw, *Laser Programs Annual Report*, 4–52, Lawrence Livermore National Laboratory, Livermore, CA, UCRL-50021-76 (1976); *Idem*, "Differencing of the Diffusion Equation in LASNEX," Lawrence Livermore National Laboratory, Livermore, CA, UCRL-82747 (1980); *Idem*, *J. Comp. Phys.* **39**, 2, 375 (1981).
16. A. I. Shestakov, J. A. Harte, and D. S. Kershaw, *J. Comp. Phys.* **76**(2), 385 (1988).
17. This document describes the electron–ion coupling model in LASNEX: D. C. Eder, "Electron–Ion Coupling in LASNEX," Lawrence Livermore National Laboratory, Livermore, CA, UCID-21544 (1988).
18. D. W. Forslund, J. M. Kindel, and K. Lee, *Phys. Rev. Lett.* **39**, 284 (1977); K. Estabrook and W. L. Kruer, *Phys. Rev. Lett.* **40**, 42 (1978) .
19. D. S. Kershaw, "Interaction of Relativistic Electron Beams with High-Z Plasmas," UCRL-77047 (1975); *Idem*, *Laser Programs Annual Report*, 3–69, Lawrence Livermore National Laboratory, Livermore, CA, UCRL-50021-78 (1978); *Idem*, Lawrence Livermore National Laboratory, Livermore, CA, UCRL-83494 (1979); *Idem*, "Computer Simulation of Suprathermal Transport for Laser Fusion," *Laser Programs Annual Report*, 3–78, Lawrence Livermore National Laboratory, Livermore, CA, UCRL-50021-80 (1980).
20. J. A. Harte and R. M. More, *Laser Programs Annual Report*, 3–66, Lawrence Livermore National Laboratory, Livermore, CA, UCRL-50021-82 (1982).
21. J. A. Harte and D. S. Kershaw, *Laser Programs Annual Report*, 3–63, Lawrence Livermore National Laboratory, Livermore, CA, UCRL-50021-81 (1981).
22. I. J. Feng and R. H. Pratt, "Parameterization of the Bremsstrahlung Spectrum," University of Pittsburgh, Internal Report, PITT–266 (1981); J. A. Harte and Y. T. Lee, *Laser Programs Annual Report*, 3–64, Lawrence Livermore National Laboratory, Livermore, CA, UCRL-50021-82 (1982).
23. M. K. Prasad and D. S. Kershaw, *Phys. Fluids B* **1**, 2430 (1989); *Ibid.*, **3**, 3087 (1991).
24. P. L. Bhatnagar, E. P. Gross, and M. Krook, *Phys. Rev.* **94**, 511 (1954); M. Krook, *J. Fluid Mech.* **6**, 523 (1959).
25. G. Ecker, *Theory of Fully Ionized Plasmas* (Academic Press, New York, NY, 1972); I. P. Shkarofsky, T. W. Johnston, and M. P. Bachynski, *The Particle Kinetic of Plasmas*, (Addison–Wesley, Reading, Massachusettes, 1966).
26. J. F. Luciani, P. Mora, and R. Pellat, *Phys. Fluids* **28**, 835 (1985); J. R. Albritton, E. A. Williams, I. B. Bernstein, and K. P. Swartz, *Phys. Rev. Lett.* **57**, 1887 (1986); M. Prasad, and D. Kershaw, *Phys. Fluids B* **1**, 2430 (1989).
27. R. J. Mason, *J. Comp. Phys.* **71**, 429 (1987); R. J. Mason, "Hybrid and Collisional Implicit Plasma Simulation Models," in *Multiple Time Scales*, J. U. Brackbill and B. I. Cohen, Eds. (Academic Press, Reading, MA, 1985).
28. T. J. M. Boyd and J. J. Sanderson, *Plasma Dynamics* (Barnes & Noble, Inc., New York, NY, 1969).
29. S. I. Braginskii, "Transport Processes in a Plasma," in *Reviews of Plasma Physics*, M. A. Leontovich, Ed. (Consultants Bureau, New York, NY, 1965), vol. 1, p. 205.
30. P. D. Nielsen and G. B. Zimmerman, "Treatment of Theta–Directed Magnetic Fields in LASNEX," Lawrence Livermore National Laboratory, Livermore, CA, UCRL-53123 (1981).
31. J. H. Hammer, Lawrence Livermore National Laboratory, Livermore, CA, private communication (1996).
32. A. I. Shestakov, J. A. Harte, D. S. Kershaw, *J. Comp. Phys.*, **76**, 2, 385 (1988); A. I. Shestakov, "Radiation Diffusion with the Finite-Element Method," *Laser Programs Annual Report*, Lawrence Livermore National Laboratory, Livermore, Ca, UCRL-50021-85 (1985); *Idem*, *Laser Programs Annual Report*, 2–94, Lawrence Livermore National Laboratory, Livermore, CA, UCRL-50021-86 (1986).
33. A. Friedman and D. S. Kershaw, *Laser Programs Annual Report*, 3–68, Lawrence Livermore National Laboratory, Livermore, CA, UCRL-50021-82 (1982).
34. T. S. Axelrod, P. F. Dubois, and C. E. Rhoades, Jr., *J. Comp. Phys.* **54**, 204 (1984).
35. A. Friedman, *Laser Programs Annual Report*, 3–62, Lawrence Livermore National Laboratory, Livermore, CA, UCRL-50021-83 (1983).
36. A. I. Shestakov, D. S. Kershaw, and G. B. Zimmerman, *Nuclear Science and Engineering* **105**, 88 (1990).
37. D. S. Kershaw and M. K. Prasad, *Laser Programs Annual Report*, 2–73, Lawrence Livermore National Laboratory, Livermore, Ca, UCRL-50021-85 (1985).
38. D. S. Kershaw, *Laser Programs Annual Report*, 2–96, Lawrence Livermore National Laboratory, Livermore, CA, UCRL-50021-86 (1986); A. I. Shestakov, D. S. Kershaw, M. K. Prasad, and G. B. Zimmerman, *Ibid.*, 2–89 (1987); A. I. Shestakov, D. S. Kershaw, and M. K. Prasad, *J. Quant. Spectrosc. Radiat. Transfer* **40**(5), 577 (1988).
39. M. K. Prasad, A. I. Shestakov, D. S. Kershaw, and G. B. Zimmerman, *J. Quant, Spectrosc. Radiat. Transfer* **40**(1), 29 (1988).
40. C. D. Levermore, *Discretization Methods for Fokker–Planck Operators*, UCRL-91396 (August 1984).

41. D. S. Kershaw, "Flux Limiting on Nature's Own Way," Lawrence Livermore National Laboratory, Livermore, CA, UCRL-78378 (1976); *Idem*, *Laser Programs Annual Report*, 4–56, Lawrence Livermore National Laboratory, Livermore, CA, UCRL-50021-76 (1976).
42. A. I. Shestakov, J. A. Harte, and D. S. Kershaw, "Solution of the Diffusion Equation by Finite Elements in Lagrangian Hydrodynamic Codes," 2, Lawrence Livermore National Laboratory, Livermore, CA, UCRL-95066 (1986).
43. B. G. Carlson, "The Numerical Theory of Neutron Transport," in *Methods in Computational Physics* (Academic Press, New York, 1963) vol. 1.
44. C. M. Lund and J. R. Wilson, "Some Numerical Methods for Time-Dependent Multifrequency Radiation Transport Calculations in One Dimension," Lawrence Livermore National Laboratory, Livermore, CA, UCRL-84678 (1980).
45. D. S. Kershaw, *Laser Programs Annual Report*, 2–78, Lawrence Livermore National Laboratory, Livermore, CA, UCRL-50021-85 (1985); J. F. Painter, "Finite Element Radiation Transport in One Dimension," Lawrence Livermore National Laboratory, Livermore, CA, UCRL-MI-119254 (1994).
46. A. Friedman, *Laser Programs Annual Report*, 3–51, Lawrence Livermore National Laboratory, Livermore, CA, UCRL-50021-83 (1983); *Idem*, "Calculation of Laser Light Transport on a Lagrangian *R–Z* Mesh," Lawrence Livermore National Laboratory, Livermore, CA, UCRL-93644 (1985).
47. A. B. Langdon, *Phys. Rev. Lett.* **44**, 575 (1980); V. P. Silin, *Sov. Phys.–ETP* **20**, 1510 (1965).
48. Ya. B. Zel'dovich and Yu. P. Raizer, *Physics of Shock Waves and High Temperature Hydrodynamic Phenomena* (Academic Press, New York, NY, 1966) vol. I, chp. V, p. 265; D. Eder, Lawrence Livermore National Laboratory, private communication (1995).
49. D. S. Bailey, *Laser Programs Annual Report*, 2–91, Lawrence Livermore National Laboratory, Livermore, CA, UCRL-50021-75 (1975).
50. K. Estabrook, J. Harte, and D. Bailey, *Laser Programs Annual Report*, 3–31, Lawrence Livermore National Laboratory, Livermore, CA, UCRL-50021-78 (1978).
51. A. Friedman and E. A. Williams, *Laser Programs Annual Report*, 3–61, Lawrence Livermore National Laboratory, Livermore, CA, UCRL-50021-84 (1984).
52. J. Harte, *Laser Programs Annual Report*, 4–31, Lawrence Livermore National Laboratory, Livermore, CA, UCRL-50021-77 (1977); J. Harte and G. Zimmerman, "Ponderomotive Force in a Hydrodynamic Simulation Code," Lawrence Livermore National Laboratory, Livermore, CA, UCRL-79860 (1977).
53. M. K. Prasad, Lawrence Livermore National Laboratory, Livermore, CA, private communication.
54. R. M. More and D. S. Bailey, *Laser Programs Annual Report*, 2–72, Lawrence Livermore National Laboratory, Livermore, CA, UCRL-50021-79 (1979).
55. D. S. Bailey, Y. T. Lee, and R. M. More, *Laser Programs Annual Report*, 3–64, Lawrence Livermore National Laboratory, Livermore, CA, UCRL-50021-81 (1981).
56. A. I. Shestakov, Lawrence Livermore National Laboratory, Livermore, CA, private communication.
57. W. E. Alley, *ICF Quarterly Report* **2**(4), 160–165**,** Lawrence Livermore National Laboratory, Livermore, CA, UCRL-LR-105821-92-4 (1993).
58. R. M. White, D. A. Resler, and S. I. Warshaw, "Evaluation of Charged–Particle Reactions for Fusion Applications," *Proc. of the Int'l. Conf. Nuclear Data for Science and Technology*, S. M. Qaim, Ed. (Julich, Germany, 1991) p. 834; M. J. Harris, W. A. Fowler, G. R. Caughlan, and B. A. Zimmerman, *Ann. Rev. Astron. Astrophys.* **21**, 165 (1983); G. B. Zimmerman, *Laser Programs Annual Report*, 3–64, Lawrence Livermore National Laboratory, Livermore, CA, UCRL-50021-83 (1983).
59. R. J. Howerton, R. E. Dye, and S. T. Perkins, "Evaluated Nuclear Data Library," Lawrence Livermore National Laboratory, Livermore, CA, UCRL-50400, vol. 4, Rev. 1 (1981) .
60. D. E. Cullen, M. H. Chen, J. H. Hubbell, S. T. Perkins, E. F. Plechaty, J. A. Rathkopf, and J. H. Scofield, "Tables and Graphs of Photon-Interaction Cross Sections from 10 eV to 100 GeV Derived from the LLNL Evaluated Photon Data Library (EPDL)," Lawrence Livermore National Laboratory, Livermore, CA, UCRL-50400, vol. 6, Rev. 4 (1989).
61. C. D. Levermore and G. C. Pomraning, *The Astrophysical Journal* **248**, 321 (1981).
62. G. B. Zimmerman, *Laser Programs Annual Report*, 3–76, Lawrence Livermore National Laboratory, Livermore, CA, UCRL-50021-79 (1979); E. G. Corman, W. E. Loewe, G. E. Cooper, and A. M. M. Winslow, *Nuclear Fusion* **15**, 377 (1975).
63. G. B. Zimmerman, "Recent Developments in Monte Carlo Techniques," 6–7, Lawrence Livermore National Laboratory, Livermore, CA, UCRL-JC-105616 (1990).
64. P. D. Nielsen and G. B. Zimmerman, "Treatment of Theta-Directed Magnetic Fields in LASNEX," Lawrence Livermore National Laboratory, Livermore, CA, UCRL-53123 (1981); P. D. Nielsen, "A Computational Investigation of the Limits to Pease–Braginskii Collapse of a Z-Pinch," Lawrence Livermore National Laboratory, Livermore, CA, UCRL-53166 ((Ph.D. Thesis, 1981).
65. J. H. Hammer, J. L. Eddleman, P. T. Springer, M. Tabak, A. Toor, K. L. Wong, G. B. Zimmerman, C. Deeney, R. Humphreys, T. J. Nash, T. W. L. Sanford, R. B. Spielman, and J. S. De Groot, *Phys. Plasmas* **3**, 2063 (1996).
66. S. Maxon, J. H. Hammer, J. L. Eddleman, M. Tabak, G. B. Zimmerman, W. E. Alley, K. G. Estabrook, J. A. Harte, T. J. Nash, T. W. L. Sanford, and J. S. De Groot, *Phys. Plasmas* **3**, 1737 (1996).
67. "Sesame: The LANL EOS Database," S. P. Lyon and J. D. Johnson, Eds., LANL, Los Alamos, NM, LA-UR-92-3407 (1992).
68. R. M. More and G. B. Zimmerman, *Laser Programs Annual Report*, 3–55, Lawrence Livermore National Laboratory, Livermore, CA, UCRL-50021-83 (1983); R. M. More, K. H. Warren, D. A. Young, and G. B. Zimmerman, *Phys. Fluids* **31**, 3059 (1988); D. A. Young and E. Corey, *J. Appl. Physics* **78**, 3748 (1995).
69. J. Abdallah and B. E. H. Clark, Los Alamos National Laboratory, Los Alamos, NM, private communication (1994).
70. C. Iglesias, B. Wilson, and J. Harte, Lawrence Livermore National Laboratory, Livermore, CA, private communication (1996)
71. S. A. Brown and D. Braddy, "PACT Users' Guide," Lawrence Livermore National Laboratory, Livermore, CA, UCRL-MA-112087 (1995).
72. W. A. Lokke and W. Grasberger, "XSNQ-U: A Non-LTE Emission and Absorption Coefficient Subroutine," Lawrence Livermore National Laboratory, Livermore, CA, UCRL-52276 (1977); G. Pollak, "Detailed Physics of XSN-U Opacity Package," LANL, Los Alamos, NM, LA-UR-90-2423 (1990).
73. G. B. Zimmerman and R. M. More, *J. Quant. Spectrosc. Radiat. Transfer* **23**, 517 (1979).
74. W. E. Alley, Lawrence Livermore National Laboratory, Livermore, CA, private communication (1995).
75. D. A. Liberman, J. R. Albritton, B. G. Wilson, and W. E. Alley, *Phys. Rev. A* **50**, 171 (1994).
76. Y. T. Lee, G. B. Zimmerman, D. S. Bailey, D. Dickson, and D. Kim, "A Time-Dependent Ionization Balance Model for Non-LTE Plasma," Lawrence Livermore National Laboratory, Livermore, CA, UCRL-95149; Y. T. Lee, *J. Quant. Spectrosc. Radiat. Transfer* **38**, 131 (1987).
77. Y. T. Lee, R. A. London, and G. B. Zimmerman, *Phys. Fluids B* **2**, 2731 (1990); A. I. Shestakov and D. C. Eder, *J. Quant. Spectrosc. Radiat. Transfer* **42**, 483 (1989).

78. J. C. Stewart and K. D. Pyatt, *Ap. J.* **144**, 1204 (1966).
79. B. C. Stuart, M. D. Feit, A. M. Rubenchik, B. W. Shore, and M. D. Perry, *Phys. Rev. Lett.* **74**, 2248 (1995).
80. P. F. Dubois, *Computers in Physics* **8** (1), Jan./Feb. 1994; L. Busby, P. F. Dubois, S. Wilson, *ICF Quarterly Report* **3**(1), 50 Lawrence Livermore National Laboratory, Livermore, CA, UCRL-LR-105521-93-1(1993).
81. L. Suter, Lawrence Livermore National Laboratory, Livermore, CA, veteran LASNEX user, private communication (1996).
82. B. A. Remington, S. V. Weber, S. W. Haan, J. D. Kilkenny, S. G. Glendinning, R. J. Wallace, W. H. Goldstein, B. G. Wilson, and J. K. Nash, *Phys. Fluids B* **5**, 2589 (1993) .
83. S. Chandarsekhar, *Hydrodynamic and Hydromagnetic Stability* (Oxford University Press, London, 1968), Ch. 10.
84. S. W. Haan, Lawrence Livermore National Laboratory, Livermore, CA, private communication (1996).
85. M. M. Marinak, Lawrence Livermore National Laboratory, Livermore, CA, private communication (1996).
86. T. R. Dittrich, B. A. Hammel, C. J. Keane, R. McEachern, R. E. Turner, S. W. Haan, and L. J. Suter, *Phy. Rev. Lett.* **74**, 2324 (1994).
87. S. W. Haan, *Phys. Rev. A* **39**, 5812 (1989).

The ICF3D Code

A. I. Shestakov *M. K. Prasad* *J. L. Milovich*

N. A. Gentile *J. F. Painter* *G. Furnish*

Z. Motteler *T.-Y. B. Yang* *P. F. Dubois*

Introduction

ICF3D is a three-dimensional radiation hydrodynamics simulation computer code being developed for ICF applications. It has a number of distinguishing features:

- Portable; works on uniprocessors and massively parallel processors (MPP).
- Written in the object-oriented programming (OOP) language C++.
- Based on unstructured grids.
- Discretized using finite elements; the hydrodynamics is modeled using discontinuous functions.

We believe these features are important for a variety of reasons.

These design codes must be portable, if they are to run on future computers. Computers are evolving at such a rapid pace that today's supercomputer will be obsolete in two to three years. However, software development is a painfully slow and labor-intensive task.[1] Thus, it is important that codes developed now can run efficiently on tomorrow's computers. Today's supercomputer is a parallel machine, a collection of individual "boxes" each with its own memory and with one or more processing elements (PEs). ICF3D is written to take advantage of this architecture. It parallelizes by decomposing physical space into nearly disjoint subdomains and relies on explicit calls to system message-passing routines. This approach allows us to scale the computation. If more boxes are available, bigger problems can be run.

In order to have reusable code, software should be robust and modular. This is facilitated by an OOP approach. In a modular code, if something needs to be rewritten or modified, one can retain the trusted components. Functions or modules often need to protect their internal variables from inadvertent corruption by other routines; such protection leads to "data hiding." For better organization, one may wish to use "classes," or to define new entities, each with their individual methods, e.g., a cell and a means of calculating its volume. These requirements are easily accommodated by OOP languages such as C++. Traditionally, scientific software has used FORTRAN. ICF3D is embracing C++. This approach is not without risks. Although OOP in general, and C++ in particular, is now widely used, it rarely appears in computational physics. In the past, C++ compilers were notoriously slow in optimizing code, and for scientists, speed is nearly as important as accuracy. This state of affairs is changing, and the pessimistic results previously reported by Haney[2] are no longer true.[3]

Codes based on unstructured grids can easily model real experiments with complicated geometries. For example, in an indirectly driven ICF experiment, a spherical capsule is embedded in a nearly vacuous cylindrical hohlraum with partially opened ends. Some experiments may have additional shields inside the hohlraum to protect the capsule. During the experiment, the walls and capsule undergo significant displacement. In modeling, a traditional, fully structured mesh will have difficulty simulating and resolving the initial configuration and its subsequent motion. An unstructured grid is useful as it allows different cell types to be connected. The extra overhead in allowing complicated cells is offset by the flexibility afforded when the original domain is discretized and/or the problem regridded.

Simulation codes of this type benefit by being discretized using finite elements. Unstructured grids and complicated geometries naturally lead to finite element (FE) methods. ICF3D's grid consists of a collection of hexahedra, prisms, pyramids, and/or tetrahedra. Processes such as diffusion are modeled by nodal FE methods in which the variables are given a continuous representation throughout the domain. The hydrodynamics is simulated by a novel scheme[4] based on the discontinuous FE method. This allows a natural representation of inherently discontinuous phenomena, such as shocks.

In this article, the first section provides an overview of ICF3D's modules, discusses how the physics packages are coupled, and describes the individual packages in more detail. The next section presents some results. In the conclusion, we describe our future plans.

We have a couple of clarifications to make about our word usage. In internal discussions, the name "ICF3D" sometimes denotes both the "stand-alone" physics code as well as the environment used to initialize problems, execute them, control the execution, and analyze the results. To avoid confusion, in this article ICF3D refers only to the stand-alone code. In addition, throughout the article, we use "module" and "package" interchangeably to denote a set of routines that perform a specific task.

ICF3D Modules

ICF3D runs on a variety of machines. Its I/O is in a special format, which is described in this article in "ICF3D Initialization"(see p. 168). Once the input files are prepared, ICF3D may be run like any other C++ program. ICF3D also has an interactive controlling environment. The interpretive language Python[5] controls the execution.

In the following subsections, we discuss the ICF3D modules. The modules consist of one or more C++ functions. When properly designed, modules should be easy to check, and if the need arises, easy to replace with better modules. The modules' execution is controlled by user-set parameters. Most modules can be run separately. This code has separate modules for Initialization, Hydrodynamics, Heat Conduction, Radiation Diffusion, Equation of State (EOS), and Parallel Processing.

One important issue is how to couple the physics packages. The problem is complicated since the packages may have different representations of the variables, e.g., cell or node centered. This difference is exemplified by the hydro and radiation diffusion packages. The former evolves equations for the density ρ, the momentum density $\rho\mathbf{v}$, and the total energy density ρE. The radiation diffusion package couples the temperature T to the spectral radiation energy density u_ν where ν is the photon frequency. The coupling difficulty arises because hydro variables have a discontinuous FE representation, whereas any quantity undergoing diffusion (a second-order differential operator) must have a continuous representation, if the diffusion is modeled by FE. A straightforward coupling of a nodal u_ν to a zonal T may create anomalous diffusion.[6] Hence, the radiation-to-matter coupling should be done with functions having similar (nodal and continuous) representations.

The equations of interest are the conservation laws for mass, momentum, and total matter energy, respectively:

$$\partial_t \rho + \nabla \cdot \mathbf{F}_\rho = 0 \quad , \tag{1}$$

$$\partial_t (\rho \mathbf{v}) + \nabla \cdot \mathbf{F}_{\rho\mathbf{v}} = \rho \mathbf{g} \quad , \tag{2}$$

and

$$\partial_t (\rho E) + \nabla \cdot \mathbf{F}_{\rho E} = \rho \mathbf{g} \cdot \mathbf{v} + H_\varepsilon + S_\varepsilon + \int K_{\nu\varepsilon} d\nu \quad . \tag{3}$$

Equation (3) is coupled to the transport (diffusion) equation of the radiation field

$$du_\nu / dt = \nabla \cdot (D_\nu \nabla u_\nu) - K_{\nu\varepsilon} \quad . \tag{4}$$

In Eqs. (1) to (3), $\mathbf{F}_i$ denotes the flux of i, i.e., $\mathbf{F}_\rho v_x = \rho v_x \mathbf{v} + p$, and $\mathbf{F}_{\rho E} = (\rho E + p)\mathbf{v}$, where v_x is the x velocity component and p is the pressure. In Eqs. (2) to (4), $\rho\mathbf{g}$ is an external force density, ε is the internal energy, H_ε is the heat conduction term, S_ε is a source of energy (e.g., due to laser deposition), $K_{\nu\varepsilon}$ describes the radiation-to-matter coupling, d/dt is the Lagrangian derivative, and D_ν is the diffusion coefficient of the radiation field. In the future, when ε is split into separate electron and ion components, $K_{\nu\varepsilon}$ will denote the radiation-to-electron coupling, and S_ε, if due to a laser, will be an electron source.

Equation (3) is solved by operator splitting. At the start of the time cycle, we compute all the coefficients we need, such as conductivity. Then, we do a hydro step; Eqs. (1) to (3) are advanced together except that in Eq. (3) the H, S, and K terms are ignored.

The hydro module allows for the passive advection of an arbitrary number of other variables. Presently, this feature is only used for the "mass fractions." In the future, Eq. (4) would also be solved by operator splitting. The convective part would be done by the hydro, while the transport and radiation-to-matter coupling would be done at the end of the cycle.

The hydro module produces an intermediate total energy $E^{(1)}$. We now introduce the subscript d to denote variables whose numerical representation is discontinuous. If the grid consists of only regular hexahedra, there are eight cells adjacent to each node. Hence, f_d denotes a function with eight values per node. At the conclusion of the hydro step, we compute an intermediate internal energy

$$\varepsilon_d^{(1)} = E_d^{(1)} - \upsilon_d^2 / 2 \quad . \tag{5}$$

This step is potentially dangerous since Eq. (5) implicitly assumes that $\upsilon_d^2 / 2$ is a valid representation for the kinetic energy e_k. Unfortunately, e_k is not computed directly but is only derived by squaring the velocity. The difficulty is illustrated by considering an ideal gas for which we require $\varepsilon \geq 0$. Since the code evolves ρ, $\rho\mathbf{v}$, and ρE, there are no explicit assurances that $E \geq \upsilon_d^2 / 2$.

The variables ρ_d and $\varepsilon_d^{(1)}$, and the EOS yield the pressure $p_d^{(1)}$ and the temperature $T_d^{(1)}$. The other physics packages compute changes to the internal energy $\Delta\varepsilon_d$. The cycle concludes by computing the final energies

$$\varepsilon_d = \varepsilon_d^{(1)} + \Delta\varepsilon_d \quad \text{and} \quad E_d = E_d^{(1)} + \Delta\varepsilon_d \quad . \tag{6}$$

The change $\Delta\varepsilon_d$ consists of the H, S, and K terms that were ignored by the hydro step. At the end of the time cycle, we have both a continuous nodal T and a discontinuous ε_d. The two variables may not be consistent. If necessary, we use the EOS to get a self-consistent pressure p_d and a temperature T_d from ρ_d and ε_d. Since T_d has a discontinuous FE representation, it may not agree with the continuous FE (nodal) value obtained by coupling to the radiation. To be more precise, after multiplying through by the time step, we write

$$\rho\Delta\varepsilon = H_\varepsilon + S_\varepsilon + \int K_{\nu\varepsilon} d\nu \quad . \tag{7}$$

The energy difference is expressed as a temperature difference

$$\Delta\varepsilon = c_v\left(T - T^{(1)}\right) \quad , \tag{8}$$

where

$$c_v = \frac{\partial\varepsilon}{\partial T}\Big|_{\rho^{(0)},T^{(0)}} \tag{9}$$

is the specific heat computed at the start of the time cycle.

We now specify how the variables of Eqs. (7) to (9) are defined. The continuous FE representation of the temperature at the end of the hydro at the j^{th} grid point is

$$T_j^{(1)} = \frac{\int_\Omega dV\ \phi_j\ \rho_d\ c_{v,d}\ T_d^{(1)}}{\int_\Omega dV\ \phi_j\ \rho_d\ c_{v,d}} \quad , \tag{10}$$

where Ω denotes the entire domain and ϕ_j is the FE basis function centered at the j^{th} grid point. The integrals in Eq. (10) are sums over all the cells that support ϕ_j. Furthermore, the integrals are lumped, i.e., for any

$$\int_\Omega dV\,\phi_j\, f = \sum_{cell}\left(\int_{\Omega\cap cell_j} dV\,\phi_j\right) f_{d,j} \quad , \tag{11}$$

where $cell_j$ is a cell with x_j as one of its vertices and $f_{d,j}$ is the discontinuous value in $cell_j$ at $x = x_j$. In the FE discretization of the heat conduction and radiation-to-matter coupling equations, we lump all but the transport term. Each equation is discretized by multiplying by $\Delta t\ \phi_j$ and integrating over Ω.

Once $T^{(1)}$ is known, we use operator splitting and FE to first do the heat conduction and the energy deposition

$$\rho c_v\left(T^{(2)} - T^{(1)}\right) = \nabla\cdot\kappa^{(0)}\nabla T^{(2)} + S\left(\rho, T^{(1)}\right) \quad . \tag{12}$$

In Eq. (12), the heat transport is implicit in $\Delta T^{(2)}$, but the conductivity is computed using values at the start of the cycle. The source S is explicit. If it is due to a laser, and its deposition depends on both ρ and T, we use the latest values, the ones obtained after the hydro step. For laser deposition, we need continuous representations of ρ and T in order to compute their gradients. A continuous (nodal) density is given by its nodal values

$$\rho_j = \frac{\int_\Omega dV\ \phi_j\ \rho_d}{\int_\Omega dV\ \phi_j} \quad , \tag{13}$$

where the integral in the numerator is lumped, as in Eq. (11). Using the nodal values, $\nabla\rho$ is easily obtained from the analytic, continuous representation

$$\rho(x,y,z) = \sum_j \phi_j(x,y,z)\,\rho_j \quad . \tag{14}$$

The gradient is continuous within cells and discontinuous across cell faces.

Equation (12) is followed by the radiation-to-matter coupling. Equation (4) is coupled to

$$\rho c_v\left(T^{(3)} - T^{(2)}\right) = \int K_{\nu\varepsilon}^{(3)} d\nu \quad , \tag{15}$$

where K is implicit in the final, continuous temperature. Equations (4) and (15) are solved by standard FE techniques; everything except the transport term in Eq. (4) is lumped. The result is a continuous representation for both the final radiation energy density u_ν and matter temperature $T^{(3)}$.

To summarize, T is a derived quantity and ε is fundamental. During the heat conduction and radiation-to-matter coupling, we keep track of the energy changes in each cell. If the changes are small, then the ε after the hydro is not modified much. Hence, any sharp features are not smeared out. In particular, if there are no matter energy sources, very small heat-transport coefficients, and insignificant radiation-to-matter coupling, then the hydro should work as if it is the only package running. Similarly, if we have only hydro and a zonal matter energy source running, and the source is distributed according to Eq. (11), then the results should still stay sharp.

ICF3D Initialization

The grid consists of three types of objects: cells, faces, and nodes. A node is characterized by its sequence number and its coordinates. Cells and faces use the object-oriented concept of inheritance. Faces may be quadrilateral or triangular, whereas four types of cells are allowed: tetrahedra, pyramids, prisms, and/or hexahedra. The cell, face, and node objects are related. For example, a hexahedron has 6 faces and 8 nodes. Each interior face has two cells on either side. The cells need not be regular; the quadrilateral faces need not be coplanar. However, the cells cannot be so distorted to preclude an isoparametric mapping to regular elements, e.g., quadrilaterals to a unit cube. For Lagrangian node motion, this implies that if the grid becomes sufficiently distorted, the problem must be regridded. We do not yet have a means of regridding.

We have not yet written a general, unstructured mesh generator. In order to run test problems, we have instead written a simple, separate mesh generator that outputs mesh description files for subsequent reading by ICF3D. However, we stress that ICF3D is written to run on completely unstructured meshes. Our generator is described in "Problem Generation" (see p. 172); it writes ICF3D input files that describe the mesh in the Advanced Visual Systems (AVS) Unstructured Cell Data (UCD) format. (AVS is a commercial software visualization product.) This format, which consists of two lists, is a terse description of the grid. The first is a node list; each node is described by its unique sequence number (an integer) and by the values of its coordinates (three real numbers). The second is a cell list; each cell is described by its type—e.g., a pyramid—and by a list of integer sequence numbers that comprise the cell's vertices. The cell's vertices must be given in a prescribed way, e.g., a pyramid's apex is listed first.

We have used the UCD because it is commercially available, but it is not adequate for use in generating an unstructured mesh. For example, the format does not explicitly list which cells share given a node. Also the format never mentions faces. To define the mesh, ICF3D requires that the different objects (cells, faces, and nodes) have a set of interconnecting pointers to describe which cells lie on either side of a face, which nodes make up the face, etc.

The discontinuous hydrodynamic scheme imposes even more requirements on the mesh description. The dependent variables are cell–node based. For example, each cell's density is described by its value on the vertices. Since the hydrodynamic variables are allowed to be discontinuous, a neighboring cell has different nodal values. Thus, such variables are considered "doubly indexed": once over cells, then again over the cell's nodes. When the hydrodynamic face fluxes are computed, the routine loops over each face, follows the pointer to each of the adjoining cells, and goes to the appropriate node to pick up the value. This requires the mesh to provide an additional set of pointers: face→cell→node.

Some physics packages are more efficient if additional connectivity information is supplied. For the hydrodynamics, the limiting routine, which deletes unphysical extrema, requires that each cell point to all other cells that share its nodes. The continuous, piecewise-linear, nodal FE scheme that discretizes the second-order elliptic operator imposes a similar requirement. Each node, which by construction is a vertex of one or more cells, needs a list of the other vertices. On a regular hexahedral grid, the nodal neighbor list gives rise to a 27-point stencil.

All this information is computed at the start of the run and saved. Presently, since we do not have a regridding routine, the topological description of the grid does not change during the course of a run—even in a Lagrangian calculation.

EOS Package

In the discontinuous finite element method, density, pressure, and velocity are linear functions. These variables are used to calculate the hydrodynamic fluxes. The Roe solver (which computes the fluxes) needs various derivatives of thermodynamic quantities. This requires that the EOS module compute some variables as functions of different combinations of other quantities. In particular, we need

$$\varepsilon(\rho, p),\ p(\rho, \varepsilon),\ \frac{\partial \varepsilon(\rho, p)}{\partial p},\ \frac{\partial \varepsilon(\rho, p)}{\partial \rho},\ \text{and}\ \frac{\partial \varepsilon(\rho, T)}{\partial T}\quad .$$

Such functions are part of our C++ EOS class. Compartmentalizing these functions into a class allows for better management of data common to all functions for a specific material. For example, in the case of tabulated equations of state, the functions are calculated from the same database. The ICF3D EOS class uses the C++ concepts of inheritance and virtual function overloading to allow new equations of state to be easily implemented.

Currently, three different types of equations of state are supported by the EOS class: ideal gases, ASCII versions of EOS tables for various materials, and a version of the SESAME equation-of-state tables from the Los Alamos National Laboratory.[7] Tabular data are fitted by bicubic splines. The EOS class "constructor," called after the problem initializes, computes spline coefficients. The coefficients are saved and used to evaluate the functions. This makes for faster calls, at the cost of storing a larger amount of data. We intend to add a class that uses the TABLib library.[8] This will

allow ICF3D to use tabular equations of state stored as PDB files.

If a cell has more than one material, ICF3D calculates and advects mass fractions. In this case, the cell's thermodynamic quantities are specified by a total ρ, total energy density (or total p, or total T), and a set of mass fractions for the different materials.

Hydrodynamics

The ICF3D hydrodynamic scheme is described in Ref. 4. The algorithm advances two scalar hyperbolic equations for the density ρ and the total energy density ρE, and the vector equation for the momentum density ρ**v**. The scheme is compact and is easily parallelized since it gets all of its accuracy locally; it does not reach out to more than one neighboring cell to approximate the dependent variables.

The two essential features of the hydro scheme are its ability to do fully Arbitrary Lagrangian Eulerian (ALE) calculations and its ability to run in different coordinate systems. ALE combines the best features of Eulerian and Lagrangian codes. The "arbitrary" aspect allows the user to specify the mesh's motion to resolve a feature that would not be possible to resolve with either a purely Eulerian or a purely Lagrangian code. The hydro module is implemented in 3-D Cartesian, cylindrical, and spherical geometries. We are continuing to develop the ALE features to ensure code robustness. In particular, we have focused attention on two areas. The first involves the Lagrangian limit of the ALE code where the mesh follows the fluid motion. This is a nontrivial problem since discontinuous functions represent the velocity fields, whereas the mesh is required to be continuous. We have developed a scheme to move the grid points that ensures a vanishing average mass flux across a face.

Secondly, the shock stabilization algorithm has been adapted to combine the pure Runge-Kutta solution, the 3-D generalized Van Leer stabilized solution (the limiting procedure), and the first-order Godunov limit solution. This "adaptive" combination assures the greatest possible accuracy as we go from very smooth regions to extremely strong shocks. However, in 2- and 3-D problems, this stabilization is insufficient to stabilize extremely strong shocks. We have implemented a Lapidus-type artificial viscosity[9] to stabilize the remaining "transverse" oscillations near such shocks.

We have successfully run the code on two test problems of particular interest to ICF: the 3-D Rayleigh–Taylor (RT) instability growth problem and the 2-D Richtmyer–Meshkov (RM) shocked perturbation problem. The ressults are described in the "Hydrodynamic Problems" section of this article (see p. 175).

Heat Conduction

Currently, ICF3D uses only a single matter temperature T. The change of the internal energy ε due to temperature is expressed as

$$\rho c_v \partial_t T = \nabla \cdot \kappa \ \nabla T + S_\varepsilon \quad , \tag{16}$$

where S_ε is an external source term, κ is the conductivity, and $c_v = \partial_\varepsilon / \partial T$ is the specific heat. In the future, sources such as laser energy deposition will be incorporated into S_ε.[10]

Equation (16) is discretized by a standard nodal FE scheme in which T is given a continuous "piecewise linear" representation. The dependent variable is the nodal temperature value. For testing purposes, we provide three conductivity models: κ = constant, a power law, and one given by the Spitzer–Härm formula.[11]

The heat conduction package gathers the various coefficients (c_v, κ, etc.) of Eq. (16) and calls the mathematical diffusion solver package described in "FE Diffusion Package" (see p. 170).

Radiation Transport

Radiation transport is modeled with the diffusion approximation. The coupling to matter is governed by the opacity κ_ν. The relevant equations are

$$\partial_t u_\nu = \nabla \cdot D_\nu \nabla u_\nu + c\rho\kappa_\nu \left[B_\nu(T) - u_\nu \right] \tag{17}$$

and

$$\rho c_v \partial_t T = -\int d\nu c\rho\kappa_\nu \left[B_\nu(T) - u_\nu \right] \quad , \tag{18}$$

where $B_\nu(T)$ is the Planck function. In the above equations the unknowns are the radiation energy densities u_ν and the matter temperature T.

The same FE scheme used for heat conduction discretizes Eq. (17). In addition, u_ν is discretized with respect to frequency: for each range, or frequency "group," u_ν is its average radiation energy density.

To solve the two equations, we use the "fully implicit" scheme described in Ref. 12. First, the source term is linearized about the temperature at the start of the time cycle

$$B_\nu(T) = B_\nu\Big|_{T_o} + dB_\nu / dT\Big|_{T_o} \left(T - T_o \right) \quad . \tag{19}$$

The discretization leads to a large system of linear equations, which is solved by a matrix-splitting iteration. We write the system as $A\mathbf{x} = S$, where $\mathbf{x} = (u_\nu, T)$ denotes the vector of unknown energy densities and temperature. As described below, we split A in two

ways: first, as $A = A_d + A_c$, then, as $A = A_l + A_{nl}$. For the first splitting, we solve

$$A_d \mathbf{x}_1 = S - A_c \mathbf{x}_0 \quad .$$

For the second, we solve

$$A_1 \mathbf{x}_2 = S - A_{nl} \mathbf{x}_1 \quad .$$

The two splittings constitute one iteration. The iterations are repeated until u_ν and T converge.

In the first splitting, A_d is the part of the matrix that arises from the diffusion operator in Eq. (17). A_c is the remaining part of A and includes the radiation–matter coupling. The first splitting is equivalent to solving for u_ν while keeping T fixed. Since the groups are only coupled through T, the individual group densities may be solved independently of each other. This results in repeated calls to the diffusion solver.

In the second splitting, A_l is the "local" part of the matrix, formed from A by ignoring all spatial coupling. A_l is a block diagonal matrix, with each block corresponding to a single mesh point. The blocks are of order $N_\nu + 1$. By ordering u_ν first, it follows that each block consists of an order N_ν diagonal matrix in the upper left corner and completely filled last row and column. Hence, the blocks are quickly solved with Gaussian elimination.

We plan to experiment with other linear solution methods and to choose the ones that offer the best combinations of speed and accuracy. One such method is the "partial temperature" scheme.[6] This method has the advantage of not requiring any iterations. For the price of advancing a single diffusion equation once, one gets u_ν and T implicitly coupled.

We also plan to add the advection of u_ν. The above method is physically correct only when the code runs in the Lagrangian mode. For Eulerian or other modes in which the mesh does not move with the fluid, we need to consider that the radiation is also carried by the fluid.

Lastly, we need to incorporate a routine to calculate realistic opacities κ_ν. Presently, ICF3D has only three types of opacities: a user-specified constant, a simple formula $\kappa_\nu = (T/\nu^3)(1 - \alpha e^{-\nu/T})$, and tabulated "cold" opacities.

FE Diffusion Package

The heat conduction and radiation diffusion modules both call the diffusion package, a routine that solves the generic equation

$$g\partial_t f = \nabla \cdot D\nabla f + S - \alpha f \quad . \tag{20}$$

The diffusion package transforms Eq. (20) into a linear system and calls the solver. Equation (20) is discretized by FE methods. The unknown function f is represented in terms of basis functions

$$f = \sum \phi_j(x) f_j \quad ,$$

where ϕ_j is the usual piecewise linear function $\phi_j(x_i) = \delta_{ij}$. The main difference between the diffusion basis functions and those used for the hydrodynamic module is that for diffusion, support (ϕ_j) extends over all cells with x_j as a vertex.

The time derivative in Eq. (20) is discretized using fully implicit differencing. With one exception, all coefficients are assumed to be known and constant within a cell. The exception is the radiative source, Eq. (19), in which T and T_0 have nodal representations.

After discretizing the temporal derivative, Eq. (20) is multiplied by $\phi_i \Delta t$ and integrated over the entire domain. This leads to a sparse linear system for the coefficients f_j,

$$\left(g + \alpha - \nabla \cdot D\nabla\right) f = g \;\; f_0 + S \quad . \tag{21}$$

Integration by parts turns the transport term into a surface integral and a volume integral of the type

$$\int_\Omega dV \;\; D \;\; \nabla\phi_i \cdot \nabla\phi_j \quad . \tag{22}$$

If x_i is not a boundary node, or if one prescribes a boundary symmetry condition for the flux ($-D\partial f/\partial n = 0$), then the surface integral does not appear. All terms except the transport term are lumped. This implies that only the flux contributes to the off-diagonal coefficients of the matrix. Because of the symmetry in Eq. (22), the matrix is symmetric. It is easy to show that the matrix is also positive definite.

Unfortunately, we may not get an M matrix since some off-diagonal coefficients may be positive. The M-matrix property—only non-negative coefficients for the matrix inverse—is desirable since the diffusion module advances positive quantities such as T. The right-hand side of Eq. (21) is itself positive since it is a sum of the source and the old energy. To show the loss of the M-matrix property, recall that the transport term is discretized by Eq. (22). The diagonal contribution with $i = j$ is clearly positive. For the off-diagonal terms, consider the contribution to Eq. (22) from just one element, K. By construction, D is constant and positive over the element. Hence, let $D = 1$. In 2-D triangles, it is easy to show that $\nabla\phi_i \cdot \nabla\phi_j \le 0$, if none of the interior angles are obtuse. In 2-D quadrilaterals, the result is more restrictive, since the sign depends on the aspect ratio of the sides. The issue is exacerbated in 3-D. Consider the hexagon

$$K = \left\{(x, y, z) : |x| \le 1, \;\; |y| \le Y, \;\; |z| \le Z\right\}$$

and the functions

$$\phi\pm = (1 \pm x)(Y + y)(Z + z) / 8YZ \quad .$$

A direct integration yields

$$\int_\kappa dV \, \nabla\phi_+ \cdot \nabla\phi_- = \left(Y^2 + Z^2 - 2Y^2Z^2\right) / 9YZ \quad . \qquad (23)$$

Again, the sign depends on the aspect ratio. If $Y = Z$ and $Y < 1$, we get the undesired positive sign.

It remains to be seen whether the lack of the M-matrix property proves harmful. It does make the system harder to solve (see the section below, "Solution of Linear Systems.") We are aware that for the case: $S = \alpha = 0$ and $g = 1$, the linear system of Eq. (21) has the form

$$(M + \Delta t S) f = M f_0 \quad , \qquad (24)$$

where M is the lumped (diagonal) mass matrix and S, the stress matrix, is the discretization of the diffusion operator. For negligibly small Δt, $(M + \Delta t\, S)^{-1} \approx M - \Delta t S$. Hence, if S has positive off-diagonal terms, then for a properly chosen and still positive f_0, we may obtain an f with some components negative.

Once the diffusion module has initialized the linear system, it calls the linear solver.

Solution of Linear Systems

ICF3D generates two types of linear systems. One kind arises when the hydrodynamic module inverts mass matrices to compute the fundamental variables. The order of those systems equals the number of degrees of freedom in a cell, e.g., eight in a hexahedron. To solve these systems, we have written a set of general routines that perform Gaussian elimination with partial pivoting.[13]

The second type of systems is created by the diffusion module. For such problems, the matrix A is large, sparse, symmetric, and positive definite (SPD). Because of the unstructured grid, the matrix sparsity pattern is random. SPD systems are best solved by the preconditioned conjugate gradient (PCG) method. Three preconditioners are available: Incomplete Cholesky (IC), one-step Jacobi (diagonal scaling), and multistep Jacobi. In this section, we only discuss the uniprocessor version of the solver. "Parallel Solution of Linear Systems" (see p. 175) describes the MPP modifications.

The PCG algorithm is well documented in the literature.[13] We shall not rederive it here, but instead describe our implementation. Unless the grid topology is changed, the sparsity pattern remains the same. Hence, if the discretization couples node x_i to node x_j, then the i^{th} row of the matrix has a nonzero entry in the j^{th} column. Since the matrix is symmetric, row j has the same entry in the i^{th} column. Thus, the following data structure suffices to describe the sparsity pattern. For each row i, we define an integer array C_i of dimension $C_{i,\,dim}$ where the integer $C_{i,\,dim}$ is the number of nonzero entries in row i to the left of the diagonal. For some rows, for example the first, $C_{i,\,dim} = 0$. The array C_i contains the column numbers of the nonzero matrix entries. For example, if the seventh unknown is only coupled to the third and fifth, $C_{7,\,dim} = 2$ and $C_7 = (3, 5)$.

This description is computed only once, at the start of the run. The pattern is computed from the nodal neighbor construct described in "ICF3D Initialization" (see p. 168). Of course, if the problem were to be regridded (and the mesh topology changed), the sparsity pattern would be recomputed. Although the above discussion focuses on a sparsity pattern due to an FE discretization of a nodal quantity, the procedure can be generalized. For example, if we need to discretize a zonal quantity, we first determine the zone's neighbors for this application and then follow the same procedure. The linear solver need not distinguish how the linear system was derived. All we supply is a description of the system, i.e., the matrix order and sparsity pattern, the matrix elements, the maximum number of iterations allowed, the preconditioner desired, etc.

To use the IC preconditioner, we do more preliminary work. For uniprocessors, the IC variant factors the matrix into the product

$$A = LDL^T \quad ,$$

where D is diagonal, L is lower triangular with unit diagonal and a sparsity pattern that matches that of A, i.e., no fill-in. It can be shown[14] that computing an entry in the lower triangle of L, e.g., row i and column j, involves a dot product of the previously computed entries of row i and row j. For efficiency, we do not compute products of a nonzero entry in one row by a zero entry in another. Avoiding such unnecessary multiplications requires extra preliminary work and additional storage in order to describe which entries contribute to the product. As a result, the evaluation of L proceeds faster, but with the penalty of indirect addressing of the necessary elements.

We have only tested our solver on small problems. First of all, we have confirmed that for sparsity patterns in which all nonzero matrix entries are bunched about the diagonal, IC returns the exact decomposition and PCG converges in one step. Secondly, we obtain the results in Table 1 for Laplace's equation on the unit cube with Dirichlet boundary conditions. Using a uniform grid with $L = 1/(n + 1)$ and $n = 15$, we obtain a system of order n^3.

Note that even though two-step Jacobi took nearly 50% more iterations than IC, the time spent was almost

TABLE 1. Results for Laplace's equation on the unit cube with Dirichlet boundary conditions $L = 1/(n+1)$ and $n = 15$. Time is in arbitrary units.

Preconditioner	Iterations	Time
One-step Jacobi	30	—
Two-step Jacobi	18	56.15
Incomplete Cholesky	13	56.13

identical. The nearly twofold decrease in the iteration count between one- and two-step Jacobi agrees with the results of Ref. 15. However, this problem is characterized by uniform and equal Δ_x, Δ_y, and Δ_z, which implies that we obtain an M matrix. Hence, the first-order Jacobi iterative method converges,[16] and one can apply the results of Ref. 15 to make the two-step Jacobi method an efficient preconditioner.

However, for nonuniform meshes, Eq. (23) implies a loss of the M-matrix property. Furthermore, it is easily shown that the matrix need not be strictly diagonally dominant. Hence, the Jacobi method need not converge and the two-step preconditioner may even delay convergence. To illustrate, we consider the same problem as above except we set $X_{max} = 1$ and $Y_{max} = Z_{max} = 0.1$. We again use $n + 1$ uniformly spaced points in each direction. The results appear in Table 2.

TABLE 2. Same problem as for Table 1, with $X_{max} = 1$, and $Y_{max} = Z_{max} = 0.1$.

n	Preconditioner	Iterations
11	None	40
11	One-step Jacobi	37
11	Two-step Jacobi	40
11	Incomplete Cholesky	10
21	None	58
21	One-step Jacobi	56
21	Two-step Jacobi	441

For $n = 11$, two-step Jacobi is slightly worse than one-step and no better than the conjugate gradient method without a preconditioner, while IC took four times fewer iterations. However, for $n = 21$, two-step Jacobi actually did considerably more harm than good.

Lastly, in the above problem, we confirmed that the numerical solution equals the exact solution, $(1 - x)(1 - y)(1 - z)$. On a hexagonal mesh, the exact solution belongs to the domain spanned by the test functions.

Problem Generation

The task of generating truly unstructured meshes, even those limited to hexagonal, prismatic, pyramidal, and/or tetrahedral cells, is a formidable job and is, in itself, the subject of ongoing research of other groups and companies. For our test problems, we improvised by writing a separate code, the generator, that creates only logically hexagonal grids.

To each point, the generator assigns an integer three-tuple (k, l, m), where the indices are positive and bounded by $(k_{max}, l_{max}, m_{max})$. The generator also specifies the initial and (currently, time independent) boundary conditions, the material(s) of choice via EOS tables, and discretizes the frequency spectrum. To facilitate the generation, we have enveloped this process under a controller or script language parser. The system was originally developed under Basis,[17] but we have adopted Python,[5] a new, portable language that is easily extended. Using a technique similar to that for LASNEX, a set of generator functions describe the problem in an ASCII file written in Python. After the generator reads the file, it writes the ICF3D input files in the UCD format.

The generator has been extended to specify meshes that are not logically hexagonal. We allow for voids within the domain, e.g., to represent solid bodies. The generator also allows the user to describe the grid in one coordinate system and write the input file in another. Thus, we may discretize the sphere in (r, θ, ϕ) and compute in Cartesian coordinates. This presents a special challenge, because the individual elements are not symmetric in the expected directions. The generator also decomposes the domain for MPPs. The user chooses along which of the k, l, and/or m directions to parallelize. For example, one could divide a k_{max}, l_{max}, $m_{max} = (31, 51, 81)$ domain amongst $2 \times 2 \times 4 = 16$ PEs, where each PE owns $15 \times 25 \times 20$ cells.

Python can interact with and "steer" the execution. Steering permits the user to directly interact with the various code modules, thereby allowing real-time analysis of the computed results. Unfortunately, this mode of operation requires that the controller/interpreter be portable to the machine of choice. This requirement may not be simple to fulfill, particularly on MPPs. Consequently, we provide two modes of operation. In one, which is still under development, the computing core (ICF3D) and the controller (Python) are tightly coupled. We use this mode on uniprocessors. The second mode gives us the flexibility of running ICF3D on a variety of platforms with no concern of the steering engine's portability. This mode evokes the distributed computing model; the stand-alone ICF3D is controlled by a Python session executing at a local workstation.

ICF3D is run in this second, distributed mode, on a variety of computers, uniprocessors and MPPs. This

allows us to use the parallel machines exclusively for computations and relegates the generation and post-processing chores to the desktop. The user directs where to execute ICF3D, and the generator takes care of the details: reading the user's deck, preparing the input files, shipping them to the computer of choice, initializing the run, etc. While this is not as flexible as a truly steerable code where parser and code are intimately connected in a single executable, it has given us an invaluable means to develop and debug ICF3D and has provided an easy interface to the MPP of choice. The system supports continuation runs via restart files as well as a link to the debugger on the remote machine. Our only requirements on the remote machine are a correct C++ environment with standard remote-shell execution capabilities. Since the interface is the same regardless of the computing engine—MPP or uniprocessor—the parallelization is completely transparent to the user. The decomposition of the domain and subsequent recombination of the results from the individual PEs are done by the generator. In a typical run, after ICF3D finishes, the data is automatically transmitted to the workstation to be saved for later postprocessing or examined immediately. For subsequent processing with the AVS visualization software, ICF3D also writes files in the AVS UCD data format.

Parallel Processing

We target distributed memory processors (DMPs) and rely on explicit calls to message passing functions. This is the optimal strategy for computers such as the CRAY T3D and the IBM SP2, as well as networks of workstations (if the network is provided with the appropriate message-passing library). The strategy also works on shared memory computers (SMPs). ICF3D has successfully run on uniprocessor workstations and DMPs such as the T3D, as well as on SMPs like the 12-node SGI Power Challenge.

We divide the physical domain into nearly disjoint subdomains, one per PE, and "leave" the subdomains distributed on the PEs. Each PE receives a description of only its subdomain plus a layer of adjacent ghost cells. In Fig. 1, we display the entire subdomain (including ghost cells) sent to one PE. The subdomain consists of 96 owned cells and 236 ghosts. (This example has a bad surface-to-volume ratio.) There are 108 hexahedra, 96 prisms, 96 pyramids, and 32 tetrahedra. Only 48 hexahedra, 16 prisms, 24 pyramids, and 8 tetrahedra are owned cells. The peculiar cones and innermost sphere primarily consist of ghost cells. They appear since the domain decomposition requires that each owned cell know about all cells that share one of its vertices.

The subdomains are described in the input files, which are written in the modified AVS UCD format. The modification consists of assigning global as well as local sequence numbers to both cells and nodes, and tagging the cells with the number of the PE that owns it. The input files are written by the generator; and only it has access to the entire domain. The generator initializes the problem, decomposes the domain, and determines which PE owns which cell. The assignment of nodes to specific PEs is done by ICF3D itself. Thus, since cells do not migrate across the PEs, the task of load balancing the PEs is assigned to the generator.

We use a "coarse grained" parallelization strategy; the code is not replete with parallelization commands. Crucial code segments have been identified as requiring information that resides on another PE. At such segments we insert statements of the type

```
if (Number PEs >1) call fooMPP();
```

Such branching statements appear at a high level in the code.

For parallelization purposes, the physics modules may be roughly divided into three kinds: embarrassingly parallel, clearly parallelizable, and hard to parallelize efficiently. The first type consists of modules such as the EOS; nothing special is done since each PE works only on the cells it owns. Explicit time-differencing methods such as the hydrodynamic step are clearly parallelizable. Such methods have an easily identifiable, compact domain of dependence. For example, a cell's hydro variables at one time step depend on only

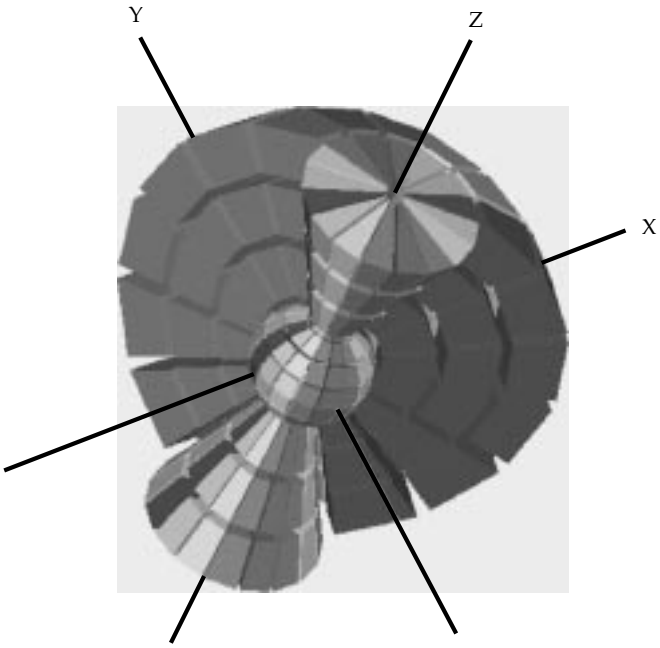

FIGURE 1. Entire subdomain given to a PE when decomposing a sphere and running in Cartesian coordinates. Figure includes both owned and ghost cells. (50-06-1296-2785pb01)

old values of that cell and its neighbors. If the neighbor cells are owned by the same PE, no extra work is required. If some of the surrounding cells belong to another PE, a copy of that cell is a ghost cell of this PE. It is the responsibility of the message-passing routines to get the required information. The third, hard-to-parallelize-efficiently are those modules that require global communication, e.g., the initialization and solution of linear systems. That subject is discussed in "Parallel Solution of Linear Systems" (see p. 175).

When running in parallel, we use one of two libraries in one of two modes. In one mode, for portability, we call routines from the industry standard MPI message-passing library. On the Cray T3D, we also provide the option of using the native SHMEM library, since efficient implementation of MPI is site-dependent. In the early stages of our parallelization work, the LLNL MPI library was extremely slow. Now, the SHMEM and MPI performances are nearly equivalent. Nevertheless, having a choice of libraries has proved invaluable; when one breaks, we switch to the other. In the other mode, we have an additional object-oriented layer, C4,[18] which is itself written in C++ and thus allows better use of that language. For example, MPI routines require that we explicitly state the data type of the arguments. In C++, such type-description is unnecessary since, unlike in FORTRAN, the argument carries information about its type. C4 has also been generalized so that it either calls SHMEM or MPI.

The interface to the MPI, SHMEM, or C4 functions is through special message-passing objects (MPOs), which are constructed at the start of the run. These objects store the information required to effect the message passing. For example, assume that at each time step, PE_0 sends to PE_9 nodal data corresponding to nodes with global sequence numbers 500 and 1,000,001. These nodes will have different local sequence numbers, e.g., 10, 11 on PE_0, and 50, 70 on PE_9. The MPO stores the number of the other PE, the length of the message, and the local sequence numbers on this PE. Thus, on PE_9 the MPO knows it is to receive two numbers from PE_0 which are to be stored in locations 50, 70.

Whenever we enter a module that requires communication, such as the hydro package, we allocate buffers of the proper size to store the messages. The buffers are deallocated when that module is exited. In the future, to avoid repeated calls to memory allocation routines, we will allocate a permanent block of memory during the initialization step and have the MPO reuse this block.

Parallel Hydrodynamics

The hydrodynamic module is fully parallelized. We use three kinds of MPOs. (Only two are needed for Eulerian calculations.) One communicates facial information, the other nodal. The former is used to compute fluxes (on cell faces) on inter-PE boundaries. The latter is used in the limiting process, which deletes unphysical extrema in the solution. For Lagrangian runs, additional MPOs pass the required information to compute the velocity of nodes lying on inter-PE boundaries. We have verified that, to round-off precision, the results are independent of the partitioning of the domain amongst the PEs.

The hydro scheme, being explicit, lends itself nicely to parallelization, with results scaling with the number of PEs used. In Table 3, we display timings from a test problem. The problem is run in Cartesian coordinates, but the mesh is generated with cylindrical coordinates. In the results, we fix the number of cells and increase the number of PEs. Let N_{PE} denote the total number of PEs, PE_{config} the PE configuration in the (R, θ, Z) directions, $cell_{config}$ the number of owned cells in (R, θ, Z), $cell_{ratio}$ the ratio of owned to ghost cells, Time the execution time, Speedup the ratio of Time to Time for the 32-PE run, and E = Speedup/(N_{PE}/32) the efficiency. The efficiency results reflect the fact that as N_{PE} increases, $cell_{ratio}$ degrades, which creates a greater message passing overhead.

TABLE 3. Timing results (in s) obtained from a test problem run in Cartesian coordinates and with mesh generated with cylindrical coordinates.

N_{PE}	PE_{config}	$Cell_{config}$	$Cell_{ratio}$	Time	Speedup	E
32	(8, 1, 4)	(8, 16, 8)	1.32	959.7	—	—
64	(8, 1, 8)	(8, 16, 4)	0.90	501.0	1.92	0.96
128	(16, 1, 8)	(4, 16, 4)	0.74	264.6	3.63	0.91
256	(16, 1, 16)	(4, 16, 2)	0.42	149.9	6.40	0.80

Parallel Solution of Linear Systems

At the time of writing this article, we are still developing parallel solutions to linear systems. What follows here is a general discussion of the topic; timings and scalings will be presented at a later date.

The linear systems generated by ICF3D are large, sparse, symmetric, and positive definite, and therefore ideally suited for PCG. For uniprocessors, we offer three kinds of preconditioners: IC, one-step, and multistep Jacobi. Their parallel implementation is described below.

The CG iterations consist of vector sums, inner products, matrix vector multiplications, and the solution of the preconditioning system. These operations are easy to implement if the nodes are assigned to the PEs. This is done in parallel at the start of the run. Nodes on or inside inter-PE boundaries are assigned without any

need for message passing. Ownership of nodes on the "outside" of the ghost cells requires point-to-point communication. After this initialization, every node on every PE has been tagged with the PE that "owns it."

Once the nodes have been assigned, the vector sums are trivial to implement. Each PE only updates the nodes it owns. For the inner products, each PE computes a preliminary accumulation of its owned nodes and then calls a global "reduction" routine provided by the message-passing library. These calls are potential bottlenecks since they require an all-to-all PE communication.

The matrix is distributed amongst the PEs as follows. We use a row-wise assignment of the matrix coefficients. Each PE eventually gets all the matrix coefficients for the rows corresponding to nodes that it owns. The coefficients come from integrations over cells, e.g., Eq. (22). If x_i is owned by the PE but lies on an inter-PE boundary, the contribution from a particular cell is done by the PE that owns the cell. With the FE scheme, each PE computes the matrix coefficients just as in the uniprocessor case, i.e., it integrates only over owned cells. Then, special MPOs determine which contributions need to be exchanged with other PEs. As for the hydro MPOs, the matrix MPOs are constructed during the initialization phase.

Once the matrix is distributed, the matrix vector multiplications are relatively straightforward. If

$$y_i = \sum_j A_{i,j} x_j \tag{25}$$

is one of the owned elements of the PE, the product is easily done if the PE has the latest x_j values. For some y_i, the requisite x_j are owned by other PEs. Those values are delivered to the PE by other MPOs.

Lastly, we discuss the preconditioners. For one-step Jacobi, message passing is not required. Multistep Jacobi, which is one example of a polynomial preconditioner,[13] requires a matrix vector multiplication. Each step is preceded by a send/receive. For IC, our plan is to perform the usual ICCG(0) algorithm but ignore coupling across the PEs. In this way, we avoid the fundamental bottleneck of ICCG, namely, how to parallelize the solutions of the triangular systems. If the domain decomposition has a low surface-to-volume ratio, this approach is efficient. Effectively, the decomposition is even more incomplete than on a uniprocessor. At the very least, this parallelizes, does not require any message passing, and should outperform one-step Jacobi because the latter is the limiting case of a decomposition so incomplete that it ignores all coupling.

Numerical Results

In this section we present results of test problems in order to display some of ICF3D's capabilities and check the algorithms. The section is divided into three parts. "Hydrodynamic Problems" (see below) discusses two hydrodynamic problems—the Rayleigh–Taylor and Richtmyer–Meshkov instabilities—which use only the hydro physics module and ideal gases, i.e.,

$$(\gamma - 1)c_v T = (\gamma - 1)\varepsilon = p/\rho \quad ,$$

where γ and c_v are user-specified constants. In "Non-linear Diffusion Problem" (see p. 177), we turn our attention to the heat conduction module and simulate nonlinear diffusion. The calculation is done in 3-D Cartesian coordinates, but by construction, the problem should be spherically symmetric. Finally, in "Coupled Physics Problem" (see p. 178), we discuss a contrived test problem that exercises all of the available physics modules, a realistic material, hydro, heat conduction, and radiation, and compare our results to LASNEX.

Hydrodynamic Problems

We consider a class of instabilities where two fluids of different densities are subjected to an acceleration **g**. Theoretical work on the growth of a perturbed interface in which a light fluid supports a heavy fluid was originally presented by Taylor[19] who studied perturbations of the type

$$\delta z = a \cos kx \quad , \tag{26}$$

where z_0 = const., $ka << 1$, and the wave number $k = 2\pi/\lambda$. Taylor showed that the amplitude a satisfies

$$\frac{d^2 a}{dt^2} = kg(t)a(t)A \quad , \tag{27}$$

where $A = (\rho_2 - \rho_1)/(\rho_2 + \rho_1)$ is the Atwood number, defined in terms of the densities on either side of z_0, and where $\mathbf{g} = -g\,\hat{\mathbf{z}}$.

We simulate two cases: (1) the Rayleigh–Taylor instability in which g = const. and (2) the Richtmyer–Meshkov instability in the acceleration is impulsive, e.g., caused by a shock.

Rayleigh–Taylor Instability

We consider the nearly incompressible case suggested by Tabak,[20] we set $\gamma = 10$ in both gases. The computational domain consists of a box with axial extent, $0 \le z \le 2\lambda$. The initial equilibrium density distribution is

$$\rho = \begin{cases} 10(z/l)^{1/9} & 0 \le z \le \lambda \\ 100(z/l)^{1/9} & \lambda \le z \le 2\lambda \end{cases} \tag{28}$$

where $l = 1.1\lambda$. We run this problem in the Lagrangian mode. At $t = 0$, we initialize the grid with a sinusoidal

perturbation at $z = \lambda$ with amplitude $a = 2.25 \times 10^{-4}\ \Delta z$ where $\Delta z = 2\lambda / N_z$ is the unperturbed grid spacing. The perturbation is feathered into the z direction three zones deep on either side of the interface. We consider three problems. In each one, we initialize one-half wavelength in the transverse direction. In all cases we use 40 cells in the z direction. The problems are

- A 2-D case with 20 cells in the x direction. The perturbation is given by Eq. (26) with $z_0 = \lambda$.
- A 3-D case with 20 cells in both x and y directions. The perturbation is given by

$$\delta z = z_o = a\cos\left(k_x x\right)\cos\left(k_y y\right) \quad , \text{ and } k_x = k_y.$$

- A 3-D case with 20 cells in both x and y directions. The perturbation is as above except $k_x = 3k_y$.

The wavelengths are chosen so that all cases have the same total wave number $k = \sqrt{k_x^2 + k_y^2}$.

For constant g, Eq. (27) implies that the perturbation grows exponentially with growth rate $\Gamma = \sqrt{Agk}$. Hence, all three cases should grow at the same rate. With $k = 2\pi / 0.001$ and $g = 0.33671717$, we obtain $\Gamma = 41.6$. Figure 2 displays $\log_{10}(a)$ vs t for $t \le 0.25$ and $t \ge 0.05$, after the system has settled into an eigenmode. After 0.25, the mode reaches an amplitude of approximately 0.1 λ and saturates. The numerical Γ is within 1% of the theoretical value. This test problem shows the ability of ICF3D to model the linear regime thereby demonstrating the accuracy of the method. In Fig. 3, we display the interface at $t = 0.14$ for the $k_x = k_y$ case.

Richtmyer–Meshkov Instability

In this problem, analyzed by Richtmyer,[21] a perturbed interface interacts with an incident planar shock. Before the shock's arrival, the interface is in equilibrium since the two gases have equal pressures. From 1-D theory (no perturbation), a shock-on-contact interaction results in a displacement of the interface and two waves, one transmitted, another reflected. The transmitted wave is always a shock. The type of reflected wave depends on the unshocked density of the gas on the side from which the shock is traveling. If this side is of higher (lower) density than the other gas, the transmitted wave is a rarefaction (shock). If the "shock-incident" side is of higher density, the amplitude of the perturbation changes sign. In either case, after the interaction, the amplitude is abruptly diminished, but later grows linearly in time.

For the simulation, we run in the Eulerian mode to avoid tangling the mesh and to follow the growth into the nonlinear regime. In the results, z is the horizontal direction and x the vertical. We use the specifications relayed by Dimonte.[22] The domain consists of $(0, 0) \le (z, x) \le (0.04, 0.005)$. We simulate only half a wavelength along x and apply symmetry conditions at transverse boundaries. For z, we apply symmetry at $z = 0$, and inflow at $z = 0.04$. The initial perturbation is given by Eq. (26) with $a = 10^{-3}$, $k = 200\ \pi$, and $z_0 = 0.03$. The initial conditions are characterized by three regions: the left $z < z_0$, the right unshocked $z_0 \le z < z_s$, and the right shocked $z_s \le z$, where $z_s = 0.32$ is the position of the incident, planar shock. The conditions are described in cgs units in Table 4.

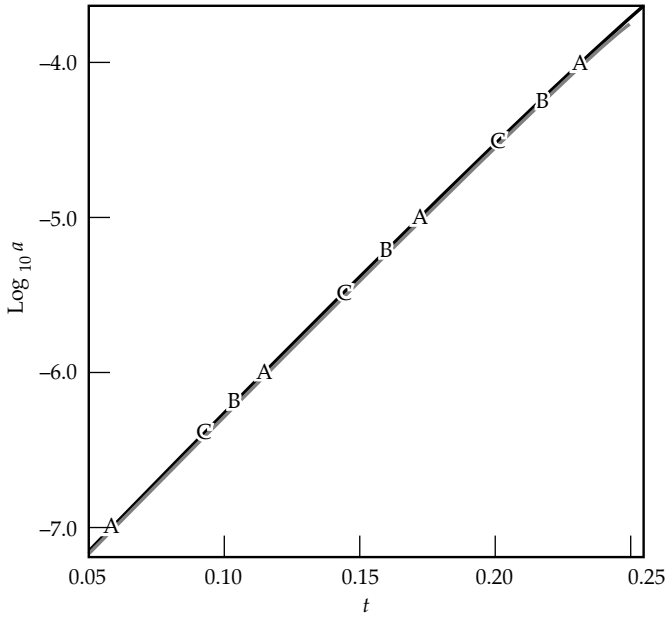

FIGURE 2. Rayleigh–Taylor problem showing common logarithm of mode amplitude vs time. Labels A, B, and C correspond to 2-D, 3-D square, and 3-D asymmetric cases, respectively. (50-06-1296-2786pb01)

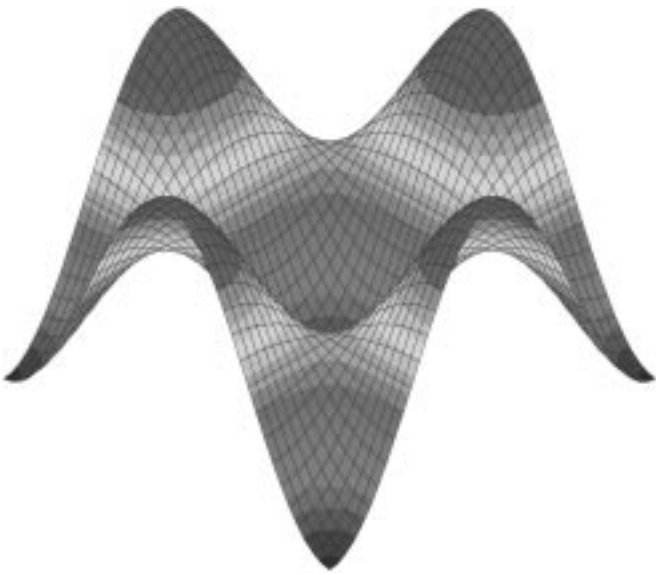

FIGURE 3. Rayleigh–Taylor problem showing perturbed interface at $t = 0.14$ ns. (50-06-1296-2787pb01)

TABLE 4. Conditions (cgs units) used in the Richtmyer–Meshkov instability problem.

Region	Density	Velocity	Pressure	γ
$z < z_0$	0.12	0	$4.92048\ 10^{10}$	1.45
$z_0 \le z < z_s$	1.7	0	$4.92048\ 10^{10}$	1.8
$z < z_0$	3.6617120	$-2.453647\ 10^5$	$2.4\ 10^{11}$	1.8

With these conditions, we expect a reversal of the interface, followed by a growth of the amplitude and an eventual nonlinear stage setting in. In Fig. 4, we present a time sequence of ρ. Fig. 4(a) shows the initial condition. In Fig. 4(b), $t = 7$ ns, the shock has already hit the interface, producing a transmitted shock and a reflected rarefaction. Note the reversal of the interface. The results in Figs. 4(c) and 4(d), at $t = 22$ ns and 37 ns respectively, show the onset of the nonlinear stage. In Fig. 4(e), $t = 53$ ns, the interface is beginning to form spikes. By this time, the shock has reflected off the left boundary but has not yet interacted with the interface. By the end of the simulation, $t = 77.5$ ns Fig. 4(f), the reflected shock has passed through the interface. The interface is now severely deformed. At this time the shock is at $z = 0.014$ and has itself developed a slight deformation. These results are in qualitative agreement with the ones published by Cloutman et al.[23]

Nonlinear Diffusion Problem

We now consider the spherically symmetric, nonlinear diffusion equation

$$\frac{\partial T}{\partial t} = \frac{a}{r^2}\frac{\partial}{\partial r}\left(r^2 T^n \frac{\partial T}{\partial r}\right) \quad , \tag{29}$$

where a and n are constants. If the initial condition is a delta function and the domain extends to infinity, the analytic solution is given in Ref. 24. By conservation of energy (heat), the solution satisfies

$$\int_0^\infty 4\pi r^2 T dr = Q \quad .$$

The analytic solution is given in terms of the radial position of the front r_f and the temperature at the center T_c in

$$T = T_c\left(1 - r^2 / r_f^2\right)^{1/n} , r \le r_f \quad , \tag{30}$$

$$r_f = \xi\left(aQ^n t\right)^{1/(3n+2)} \quad , \tag{31}$$

and

$$T_c = \left[\frac{n\xi^2}{2(3n+2)}\right]^{1/n}\left[\frac{Q^2}{(at)^3}\right]^{1(3n+2)} \quad . \tag{32}$$

The constant ξ depends only on the conductivity exponent n. For our test, we use $n = 3$ and obtain

$$\xi\big|_{n=3} = 0.8979 \ .$$

For the numerical test, we set $a = Q = 1$ and discretize 1/8 of a sphere: $0 \le r \le 1$ and $0 \le \theta, \phi \le \pi/2$,

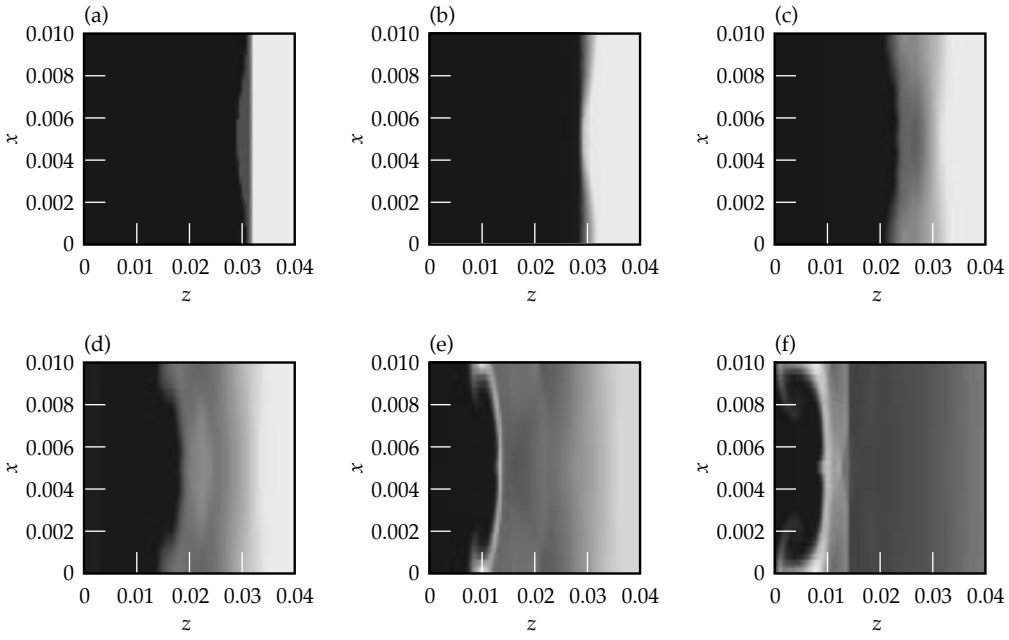

FIGURE 4. Richtmyer–Meshkov problem showing density (g/cm^3) at various times. (a) is at $t = 0$ ns; (b) at $t = 7.0$ ns, (c) at $t = 22.2$ ns, (d) at $t = 36.8$ ns, (e) at $t = 53.3$ ns, and (f) at $t = 77.5$ ns. (50-06-1296-2788pb01)

where θ denotes the polar angle. We impose symmetry conditions along $\phi = 0$ and $\theta = \phi = \pi/2$. Along $r = 1$ we also impose symmetry, but this condition is unnecessary since we halt the calculation when $r_f \approx 0.8$.

We generate the grid in spherical coordinates by constructing a logical (k, l, m) grid, where $(1, 1, 1) \le (k, l, m) \le (k_{max}, l_{max}, m_{max}\}$, set $(k_{max}, l_{max}, m_{max}) = (21, 9, 9)$, and use uniform grid spacing. There are $(k_{max} - 1)\ (l_{max} - 1)\ (m_{max} - 1) = 1280$ cells. Before running, we convert the grid into Cartesian coordinates. This creates cells of all admissible types since the spherical to Cartesian coordinate transformation results in degenerate nodes. There are $(m_{max} - 1)\ (k_{max} - 2)$ prisms along the z axis. At the origin there are $m_{max} - 1$ tetrahedra and $(m_{max} - 1)\ (l_{max} - 1)$ pyramids. The remaining cells are hexahedra.

In Fig. 5 we present the numerical solution at $t = 0.2821$ ns along each Cartesian coordinate axis. The analytic solution given by Eqs. (30) through (32) is also displayed as curve D. The numerical solutions on the three axes are nearly indistinguishable. Examination of the data shows that the central temperature, 0.0671, is within 1% of the analytic value, 0.0676.

Coupled Physics Problem

The final test problem was constructed to test the interaction of all the physics packages presently available in ICF3D: a real gas EOS, hydro motion, Spitzer-Härm heat conduction, and radiation diffusion. The problem models a shock tube filled with beryllium (SESAME table no. 2020); the numbers used in the simulation are not meant to model any experiment.

We run this in a 1-D mode, i.e., only one cell in each of the x and y directions. The initial conditions vary only with z. The initial density ρ is 1.0 gm/cc everywhere. We initialize with a higher (1 keV) temperature on the left, and on the right, we set $T = 0.1$ keV. The initial velocity is set to zero. For the radiation, we use only one group and set the opacity to a constant 1 cm^2/gm. We impose symmetry conditions on the left and right boundaries and run in the Lagrangian mode, using 203 zones in the calculation. Initially, the grid is uniform.

In Fig. 6 we display the pressure at $t = 0.1$ ns when ICF3D computes the joint effect of hydrodynamics, radiation transport, and heat conduction. Since there are no analytic solutions for this problem, we compare the ICF3D calculation to one done with LASNEX. The

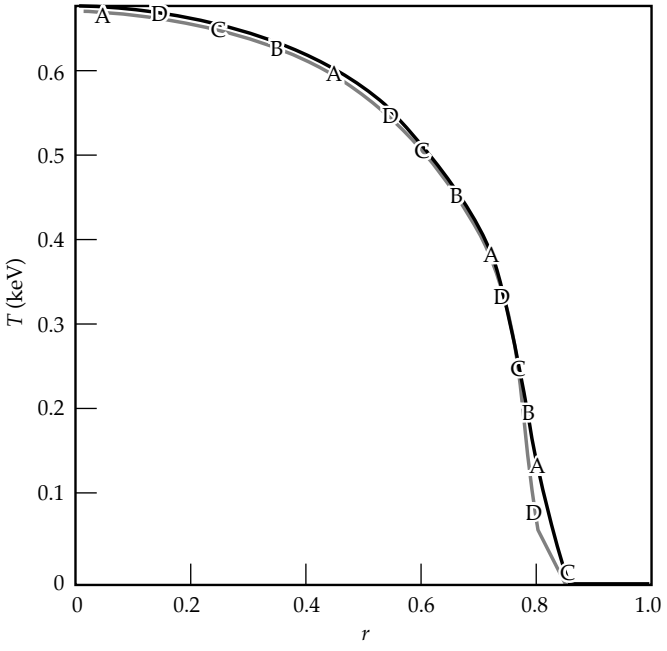

FIGURE 5. Diffusion problem showing temperature profile vs radius along coordinate axes x, y, and z (curves A, B, and C) at $t = 0.2821$ ns. Curve D is the analytic solution. (50-06-1296-2789pb01)

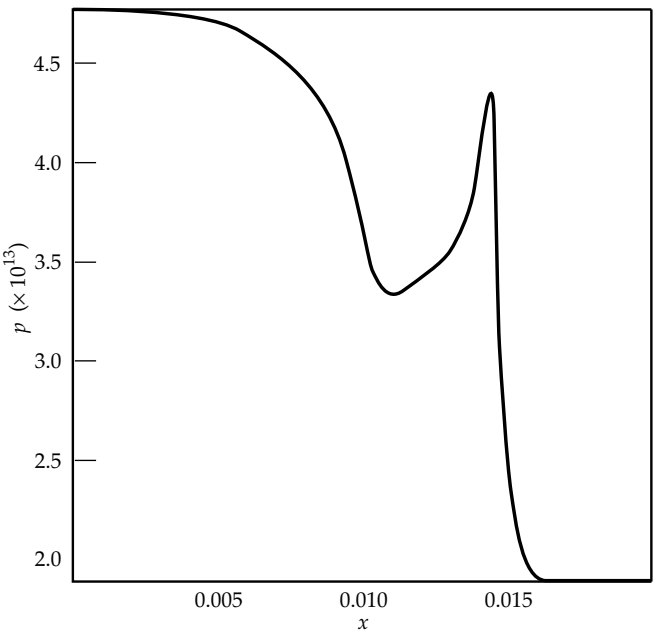

FIGURE 6. Shock tube problem results from ICF3D showing p vs z. All physics running. (50-06-1296-2790pb01)

LASNEX result (Fig. 7) agrees with ours: similarly shaped curves with the same pressures at the boundaries, the same shock location, and so forth. The main differences are that ICF3D gives a slightly sharper shock front and a sharper pressure peak behind the shock.

Conclusion

At the moment, ICF3D is an experimental code. We have made many advances, but much more needs to be done before ICF3D may be called a real design tool. Nevertheless, it is useful to list our accomplishments to date and our plans for the future.

After running numerous test problems, we are convinced of the viability of the hydrodynamic scheme. It may require some revision and modification, but it is fundamentally sound and is well suited for ICF design calculations. As opposed to higher order schemes like PPM,[25] ICF3D's scheme is very compact. Hence, it parallelizes easily.

The other physics modules are straightforward 3-D extensions of standard FE methods. Our previous experience with FE in LASNEX (see accompanying article on p. 150) shows that piecewise linear functions suffice for diffusive transport. Our other primary concern is whether or not the inherently nodal representation of diffusion type problems clashes with the fundamentally cellular representation of the hydro variables. Again, experience in LASNEX as well as the encouraging results from the "Coupled Physics Problem" section (see p. 178) alleviates this concern. Hence, we should be able to reap all of the benefits from FE methods.

So far, the parallelization efforts are a resounding success. In the past year, most of the hydro development effort has been done on the LLNL CRAY T3D because we obtain results that much faster when running on 32 PEs. We are now finishing parallelizing the linear solver and look forward to running coupled problems in parallel.

We have found the C++ programming language to be a helpful tool in organizing a physics code of the complexity of ICF3D. Our experience has given us new ideas on how to organize even larger codes for ease of maintenance and how to program them for maximum speed. We plan to implement these ideas so that ICF3D can grow into the best possible full-scale production code. The full-scale code will also benefit from our research in such areas as numerical hydrodynamics and the use of parallel processors to solve linear equations for diffusion problems.

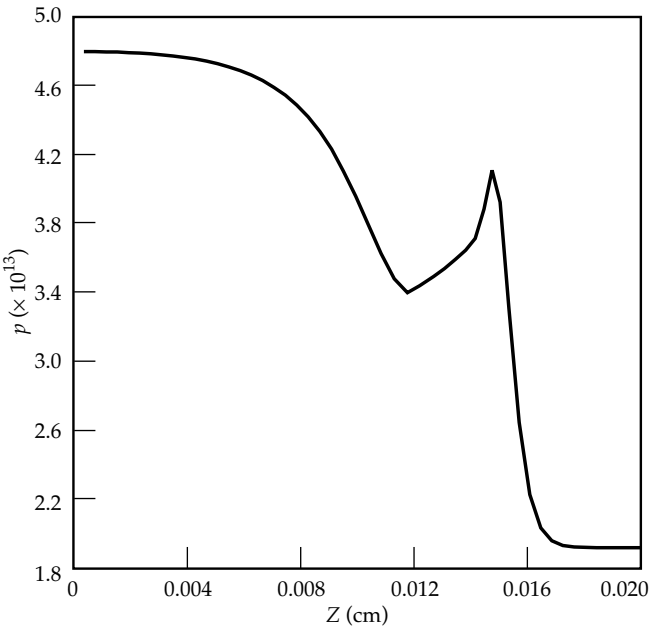

FIGURE 7. Shock tube problem results from LASNEX showing p vs z. (50-06-1296-2791pb01)

Notes and References

1. Furthermore, the time to develop codes does not scale linearly. For example, LASNEX represents a nearly 100 man-year effort; yet 200 developers would not be able to reproduce LASNEX from scratch in six months.
2. S. W. Haney, *Computers in Physics* **8** (6), 690–694 (1994).
3. S. W. Haney, Lawrence Livermore National Laboratory, CA, private lecture series (1996).
4. D. S. Kershaw, M. K. Prasad, and M. J. Shaw, "3D Unstructured Mesh ALE Hydrodynamics with the Upwind Discontinuous Finite Element Method," Lawrence Livermore National Laboratory, Livermore, CA, UCRL-JC-122104 Rev.1 (1996).
5. P. F. Dubois, K. Hinsen, and J. Hugunin, *Computers in Physics* **10** (3), 262-267 (1996). *Python Documentation* [online]. Available: www.python.org.
6. A. I. Shestakov, J. A. Harte, and D. S. Kershaw, *J. Comp. Physics*, **76** (2), 385–413 (1988).
7. "SESAME: The Los Alamos National Laboratory Equation of State Database," Eds. S. P. Lyon and J. D. Johnson, Los Alamos National Laboratory Report LA-UR-92-3407. Also: "T-1 Handbook of Material Properties Data Bases," K. S. Holian, Ed., Los Alamos National Laboratory Report LA-10160-MS November 1984.

8. S. A. Brown, "TABLib User's Manual," Lawrence Livermore National Laboratory internal report (1995).
9. A. Lapidus, *J. Comp. Phys*. **2**, 154–177 (1967).
10. T. B. Kaiser and J. A. Byers, *Bull. Am. Phys. Soc.* **41** (7), 1555 (1996).
11. L. Spitzer, Jr., and R. Härm, *Phys. Rev*. **89** (5), 977–981 (1953).
12. A. Friedman and D. S. Kershaw, *1982 Laser Program Annual Report* , pp. 3–68, Lawrence Livermore National Laboratory, Livermore, CA, UCRL-50021-82 (1982).
13. G. H. Golub and C. F. Van Loan, *Matrix Computations*, Second Edition (John Hopkins Univ. Press, Baltimore, 1989).
14. A. I. Shestakov and D. S. Kershaw, "ICCG on Unstructured Grids," Lawrence Livermore National Laboratory informal report, April 30, 1996. Contact by email: shestakov@llnl.gov.
15. P. F. Dubois, A. Greenbaum, and G. H. Rodrigue, *Computing* **22** (3) 257–268 (1979).
16. R. S. Varga, *Matrix Iterative Analysis* (Prentice Hall, Inc., Englewood Cliffs, N.J., 1962) p. 84.
17. P. F. Dubois, *Computers in Physics* **8** (1), 70–73 (1994).
18. G. Furnish, *Gyrokinetic Simulation of Tokamak Turbulence and Transport in Realistic Geometry*, Ph.D. thesis, Appendix C, Univ. of Texas, Austin, 1996, Institute of Fusion Studies doc. IFSR-740. [Also available online at http://dino.ph.utexas.edu/furnish/c4.]
19. G. Taylor, *Proc. R. Soc. London Ser. A.* **201** (1095), 192–196 (1950).
20. M. Tabak, D. H. Munro, and J. D. Lindl, *Phys. Fluids B* **2** (5), 1007–1014 (1990).
21. R. D. Richtmyer, *Commun. Pure Appl. Math.* **13** (2), 297–319 (1960).
22. G. Dimonte and B. Remington, *Phys. Rev. Lett.* **70** (12), 1806–1809 (1993).
23. L. D. Cloutman and M. F. Wehner, *Phys. Fluids A* **4** (8), 1821–1830 (1992).
24. Ya. B. Zel'dovich and Yu. P. Raizer, *Physics of Shock Waves and High-Temperature Hydrodynamic Phenomena*, Vol. II, Ch. X, Sec. 6 (Academic Press, New York and London, 1967) pp. 668–672.
25. P. Colella and P. W. Woodward, *J. Comp. Phys*. **54** (1), 174–201 (1984).

NIF Design Optimization

W. Williams
C. Orth
R. Sacks
J. Lawson
K. Jancaitis
J. Trenholme
S. Haney
J. Auerbach
M. Henesian
P. Renard

Introduction

There are many potential designs for the proposed National Ignition Facility (NIF) that would be expected to meet the machine's functional requirements, but at widely varying costs. Given the size of this project, an effort has been made to assure that we are, indeed, designing the least expensive option possible.

During the previous three years of NIF design, we have considerably refined computer codes used for such optimization analysis. During the conceptual design phase of NIF, we used a simplified code, culminating in the configuration presented in the *Conceptual Design Report* (CDR)[1] published in May 1994. For the NIF Advanced Conceptual Design (ACD), we used a grouping of several codes that allowed design optimization coupled with more sophisticated propagation models. In this article, we review some of the assumptions and modeling procedures used in both sets of computer codes. We also summarize our results from the ACD optimization activity that resulted in the current (Title I) NIF design.

Computer Codes Used in NIF Optimization

Two computer codes were primarily used in NIF optimization: CHAINOP and PROPSUITE. The multiplatform code CHAINOP is the original optimization tool used during the CDR design process for NIF. CHAINOP's goal is to combine models of laser chain layout, cost, and performance in a way amenable to speedy analysis of several thousand potential system designs, identifying those least expensive configurations that fulfill functional requirements. (A laser "chain" refers to the sequence and spacing of optical components in one beam of a large laser system; there are 192 laser chains in NIF.) CHAINOP permits certain kinds of constraints, such as damage fluence limits, B-integral limits, and irradiance modulation limits, that guide the optimization into safe laser designs via simple, often heuristic models. With a ray-trace model for tracking beam size changes and single-value loss and saturating gain models for energetics, CHAINOP reveals little specific detail of spatial and temporal characteristics of pulse propagation. These apparent simplifications are somewhat deceptive, however. Many of the heuristic models contained in CHAINOP are the result of detailed studies of physical processes, and allow the code to predict reliably laser designs that are consistent with the more robust modeling tools that were subsequently developed.

As our confidence grew in the modeling efforts for individual processes like diffraction propagation, frequency conversion, amplifier pumping, and optics damage, we were able to assemble individual computer codes into a more sophisticated optimization package called PROPSUITE. The backbone of PROPSUITE is a beam propagation code called PROP92 that uses Fourier methods to follow temporal and spatial details of a laser pulse as it traverses an optical chain. Among other things, this code includes effects of paraxial, nonlinear beam diffraction, beam movement for vignetting purposes, energy clipping at pinholes, and clipping of the beam on a hard aperture. It also allows for inclusion of detailed phase representations of optics surfaces. For a detailed discussion of PROP92, see p. 207 of this *Quarterly*. During optimizations, the laser was modeled along the direction of beam propagation, and in one transverse dimension—in this case, along the horizontal axis. The spatial resolution considered was up to ~32,000 points over a 50-cm aperture, sufficient to resolve the fine spatial features of the optics surfaces. Simulations involving both transverse dimensions are too slow to put in an optimization loop; however, designs from the one-dimensionsal (1-D) optimizations have been further analyzed and confirmed in two-dimensional (2-D) simulations.

The PROPSUITE collection also includes frequency-conversion computer codes with either plane-wave models or a 1-D spatio-temporal model of conversion (THGFT02 and THGXTZ002). Specifics of amplifier flashlamp pumping are modeled by a 2-D optical ray-trace computer code. The thermo-mechanical effects that cause pump-induced distortions are handled with public-domain software TOPAZ and NIKE3D. PROPSUITE also used the SUPERCODE shell, exercised extensively for tokamak systems studies, to perform multivariable optimizations. Additional codes were developed to do system layout calculations, based on rules in CHAINOP, and to tie the codes together. For optimizations, calculations of several thousand possible designs were done on a cluster of 28 workstations using parallel processing with the public domain software PVM.

In the following sections we discuss some of the basic modeling concepts contained in both CHAINOP and PROPSUITE.

Chain Layout

Both CHAINOP and PROPSUITE were designed around the NIF multipass architecture of a relayed, mirrored cavity containing one or two amplifiers, a spatial filter, and a Pockels cell switch/polarizer. The cavity is followed by a booster amplifier, transport spatial filter, transport mirrors, frequency converter, final focusing lens, kinoform diffractive optic plate, and debris shield. A schematic of the layout is shown in Fig. 1. Other architectures were considered for NIF over the years, including Nova-like Master Oscillator–Power Amplifiers (MOPAs), two-pass systems, and others. CHAINOP and PROPSUITE have also been employed to look at the French Reverser/U-turn architecture.

For most NIF optimizations, this basic architecture was fixed, with the thickness of laser slabs and the number of slabs in each amplifier being the only layout parameters varied.

Laser Beam Size

CHAINOP and PROPSUITE use the same approach for determining the size of the laser beam that can be fit within a chain, starting with the hard (metal) aperture of the laser. This aperture can be square or rectangular, the current NIF design being 40 cm square. Determination of the size of beam that can fit within this aperture is dependent on the component spacings in the layout and necessary alignment tolerances. Component spacings determine the slight angle of the beam with respect to the chain axis necessary to pass through different pinholes on each pass in the spatial filters. As this angle increases, the size of beam that can fit within the hard aperture is reduced. This reduction in fill factor is known as vignetting. Separate pinholes for each pass are necessary primarily because ablated plasma on the edge of a pinhole can potentially block that pinhole to any subsequent passes of the beam. Pinhole separations are set by the more restrictive of either machining constraints in pinhole fabrication or sizes of optics that sit near the pinhole plane. These pinhole-plane optics include a mirror to inject the beam on the first pass in the transport spatial filter and a beam dump to catch that small fraction of the beam in the cavity not ejected by the Pockels switch on switch-out. The cavity filter pinhole spacings in NIF are set by machining constraints.

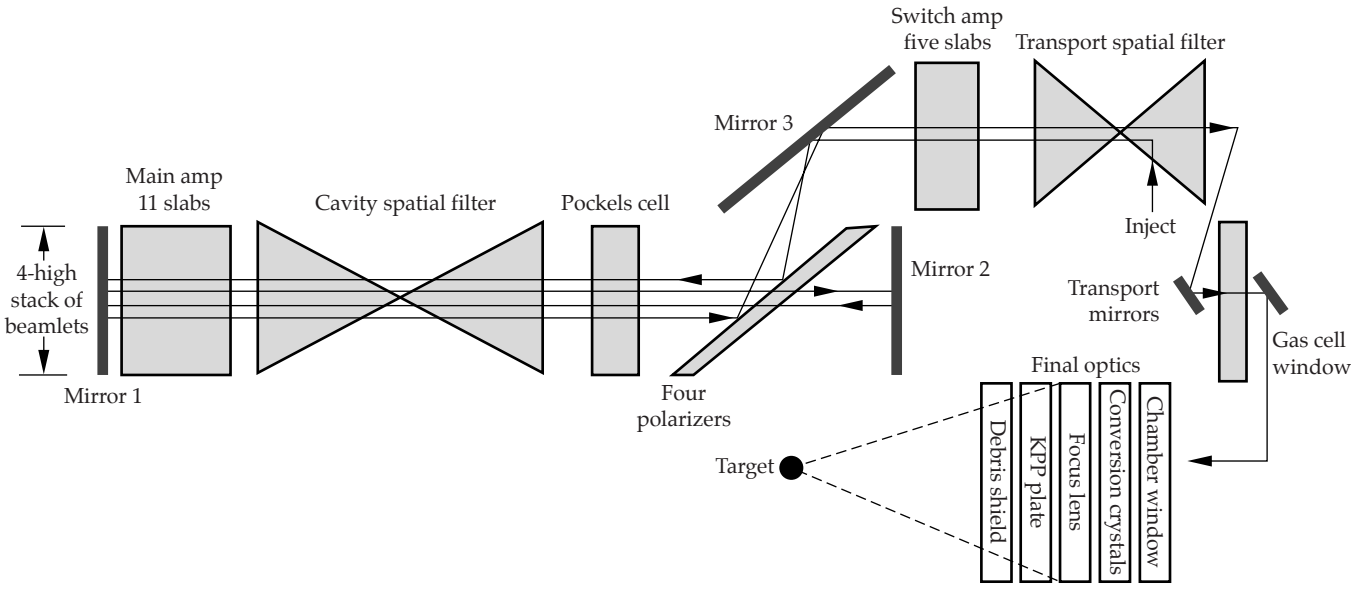

FIGURE 1. Schematic of NIF layout (not to scale). (70-00-1296-2745pb01)

An alignment tolerance of ~0.5 cm is included around the injected beam inside the hard aperture. This allows for beam or optics misalignment in the chain.

The beam intensity is nominally flat-topped, spatially, and tapers to zero at the edges. This taper is modeled with an error function, a shape somewhat more robust against diffraction ripples than some other shapes. Steeper edges increase the beam fill factor but simultaneously cause intensity spikes from edge diffraction and beam clipping at the pinholes. The taper distance of ~3 cm in the baseline design was determined as part of our optimization process.

The variables studied during NIF optimization affecting the beam size were hard aperture, number of laser slabs (which affects vignetting loss), and apodization tolerance.

Amplifier Gain and Pump-Induced Distortions

Gain of an amplifier slab depends on the stored energy density in the slab. This in turn depends on the pumping from flashlamps, Nd^{3+} concentration, slab thickness, and depumping due to Amplified Spontaneous Emission (ASE). The pumping term from flashlamps depends on the number of lamps per slab, their diameter, and electrical power pumped into the lamps. Both CHAINOP and PROPSUITE used a representation of the emission spectrum of flashlamps as a function of pumping power, absorption spectrum of laser glass, ASE depumping rate, and lamp-to-slab coupling efficiency. Coupling efficiency was based on 2-D ray-trace calculations, validated by measurements on Beamlet (a prototype of one NIF beamline in operation at LLNL), and is a function of reflector geometries, component spacings, slab thicknesses, and other parameters. Ray tracing was not included in the optimization directly. Rather, both codes used information from previous runs that covered the parameter space of interest.

Because PROPSUITE considers propagation effects on the beam spatial profile, we included pump-induced distortions in modeling. This distortion is the local steering imposed on the beam caused by the nonuniform heating of laser slabs and their subsequent deformation. Predicting this distortion requires three-dimensional (3-D) thermo-mechanical modeling of laser slabs under pumping conditions, giving time-dependent slab motion. These are lengthy computations, so prior to doing optimizations, a large number of cases were run covering ranges of the variables of interest. These results were stored in a database in which the code could interpolate to find distortions for any given combination of variable values.

Laser slab gain in both CHAINOP and PROPSUITE was modeled using the Frantz–Nodvick equations, which describe both the exponential growth of the beam fluence and the decay of the population inversion.[2] These equations are based on assumptions that (1) pumping to the upper laser level is negligible during the time the laser pulse extracts energy; (2) gain reduction due to spontaneous emission is negligible compared to stimulated emission during extraction; and (3) the cavity geometry is such that the laser pulse does not overlap on itself in space at any given time. With these approximations, extraction is only a function of fluence, and information regarding the detailed temporal shape of the pulse is not necessary. This allows us to reduce calculation time significantly by approximating a temporally shaped pulse with a temporally square pulse, while still accurately calculating the energetics of extraction and saturation. This is described in more detail below in the section entitled Temporal Pulse Shape.

The variables studied during NIF optimization affecting the gain and pump-induced distortion were thickness of the laser slabs, Nd^{3+} concentration in the laser glass, duration of the flashlamp pumping pulse, and number-per-slab and diameter of flashlamps.

Optics Losses and Aberrations

Optics losses in CHAINOP are simply subunity multipliers on beam energy and power. They include representations of laser glass surface scatter and bulk transmission, transmission of antireflection (AR) coated optics at 1ω and 3ω, bulk absorption of KDP/KD*P at 1ω and 3ω, and reflectivity of high-reflectivity (HR) coated mirrors. Bulk absorption of the fused silica is negligible for thicknesses of optics considered in NIF. Transmissivity and reflectivity of the polarizer were used to represent several effects, including coating reflectivity, BK7 substrate absorption, switching efficiency of the Pockels cell, and depolarization fraction of the beam due to stressed optics. Losses were not temporally dependent.

Losses were similarly included in PROPSUITE. In addition, by using a propagation code, it became possible to include spatially dependent representations of the surface finishes and bulk homogeneity properties of optics in the chain. This information was taken from a variety of measured parts chosen to reflect projected NIF manufacturing and finishing techniques. Because considerably fewer parts had been measured than were needed to represent an entire laser chain, it became necessary to synthesize the 100-plus necessary files. We did this by assuming that, for example, amplifier slabs will have the same finish as the measured parts, as quantified by the Power Spectral Density (PSD) curve.[3] We assumed, however, that phases of the Fourier components of the surface representations are randomized from one slab to another, resulting in less constructive addition of phase noise from slab to

slab. These aberration files are the dominant source for beam intensity and phase modulation in simulations.

During NIF optimization, losses and aberration files were not varied from a baseline set of assumptions.

Temporal Pulse Shape

NIF will use temporally shaped pulses for many experiments, including ICF ignition. To reduce calculational requirements, these pulses were represented in CHAINOP by an equivalent square pulse, having a power the same as the required peak power for a shaped pulse, and having the same total energy. This is a reasonable approximation because the Frantz–Nodvick equations depend only on beam energy (fluence), not the time history of power over the nanosecond durations of interest for NIF. Consequently, temporally square pulses of a given energy see the same overall gain as temporally shaped pulses of the same energy.

In CHAINOP, a square pulse is divided into two pieces: the main body and the tail end. Because gain in a laser slab is dependent on fluence history through the slab previous to that point in time, as the amplifier saturates, the tail end of the pulse sees a significantly lower gain than the front. A pulse that will be temporally flat at the end of the chain must, therefore, be temporally increasing at injection. Beam filamentation —catastrophic self-focusing due to the effects of a nonlinear refractive index—depends on the instantaneous beam irradiance. Consequently, monitoring the power of the pulse's tail in CHAINOP allows us to track and limit the tendency of the beam to filament.

In contrast, PROPSUITE is capable of tracking the beam shape at an arbitrary number of times. We used eight time steps to represent the temporally shaped indirect-drive ICF ignition pulse (See Fig. 2). For this pulse, the maximum effect from the nonlinear index of refraction of the optics occurs somewhat before the end of the pulse and at a time that varies with position in the chain, justifying this more detailed modeling.

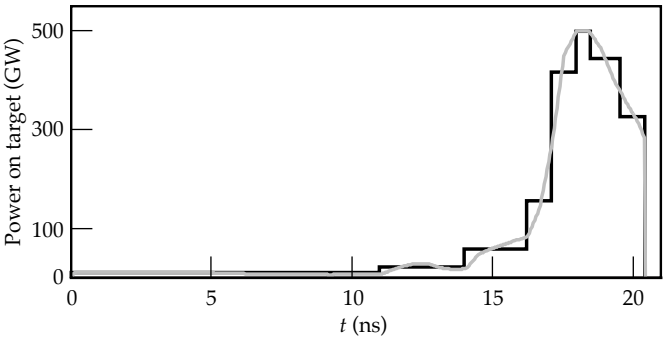

FIGURE 2. Temporally shaped pulse used for optimizations. The gray line is the actual pulse shape needed on target. The black line is the eight-step approximation to this shape used in modeling. (70-00-1296-2748pb01)

Frequency Conversion

The frequency conversion efficiency (3ω irradiance/1ω irradiance) can be a function of space and time given temporal or spatial variations of the beam. Since neither temporal nor spatial modulation is calculated in CHAINOP, both peak-power conversion efficiency (averaged across the beam aperture) and energy conversion efficiency for temporally shaped pulses needed for NIF are code inputs. Power conversion efficiency is used to determine the filamentation threat to the 3ω optics and peak power on target. Energy conversion efficiency is used to determine energy on target and damage threat calculations.

In PROPSUITE both temporal and spatial intensity information are available. Consequently, we use three codes to calculate conversion efficiency directly. A plane-wave/temporally varying field code is used to predict the 1ω temporal shape that would give the required 3ω pulse on target for any given converter design. The spatially and temporally resolved 1ω pulse at the converter with this temporal shape is then generated with PROP92. The conversion of this beam is then calculated with a full spatio-temporal code that includes the capability of having converter-crystal surface-finish noise added to the beam phase. See the article "Frequency-Conversion Modeling" on p. 199 of this *Quarterly* for a discussion of these frequency conversion codes.

For NIF optimizations, thicknesses of the type I doubler (KDP) and type II tripler (KD*P) and the detuning angle of the doubler crystal were varied independently. To allow for difficulties in aligning crystals with respect to the beam, and for other problems, conversion calculations for the 1ω beam were actually done at three detuning angles of the doubler, a variable center angle and ±30 μrad around that. A weighted average of the three was then used to determine energy on target.

Beam Modulation

Since CHAINOP is zero-dimensional, the spatial intensity/fluence modulation of the beam cannot be directly calculated. This information, however, is necessary for evaluating damage to optics from high fluences. Accordingly, a semi-empirical rule was implemented that the peak-to-mean modulation in fluence (ϕ) is given by

$$\phi_{peak} = \phi_{avg}(1.3 + 0.1e^{\Delta B}) \quad . \tag{1}$$

ΔB is the B integral accumulated by the beam between pinhole passes (using approximately the mean spatial intensity). The B integral, in general, is defined as

$$B(z) = \frac{2\pi}{\lambda}\gamma_{nl}\int_0^z I(z')dz' = \frac{80\pi^2 n_2}{\lambda cn}\int_0^z I(z')dz' \quad , \tag{2}$$

and is the nonlinear phase retardation (in radians) experienced by a beam of intensity I (W/m²) and wavelength λ (m) in traversing a medium of thickness z (m) with refractive index n_0 and nonlinear index n_2 (from $n = n_0 + n_2|E|^2$). (The nonlinear index may also be a function of z in nonisotropic materials.) Bespalov–Talanov theory predicts[4] that small-scale spatial ripples in the beam will grow nonlinearly, with the most unstable perturbations growing as $e^{\Delta B}$. This, combined with the fact that beam modulation past a scatterer in the absence of nonlinear effects is no more than 1.4:1, and that in large laser systems it has been experimentally observed that beam modulation is ~2:1 after a ΔB of 2 radians, leads to Eq. (1).

In PROPSUITE, beam modulation is calculated directly, including diffraction and nonlinear effects.

Optics Damage Thresholds from High Fluence

High laser fluences on optics over nanosecond-pulse durations of interest for NIF can cause surface or bulk damage sites. This damage is seen as pits in the surface or coating of an optic, or damage spots in bulk. The fluence threshold when this damage occurs is experimentally found to be a function of the pulse duration. For temporally Gaussian pulses, the experimental database is well matched by the functional form fluence damage threshold (J/cm²) = $a\tau^b$, where a and b are experimentally determined and material-dependent constants and τ (ns) is the full-width-half-maximum of the pulse.

NIF pulses will typically range in temporal shape, and may be significantly non-Gaussian. To account for the effect of arbitrarily shaped pulses on damage threshold, we used a damage diffusion model[5] to determine the damage thresholds. Because the ICF indirect-drive ignition pulse shape used for optimizations is more square than Gaussian, the result is a 5 to 20% reduction in damage thresholds from those for a Gaussian pulse for various materials and coatings. This diffusion model adjustment of damage threshold has not yet been experimentally tested.

The 3ω optics (tripler, final focus lens, kinoform phase plate, and debris shield) are exposed to 1, 2, and 3ω light simultaneously. In general, damage fluence limits at the longer wavelengths are significantly higher than at shorter wavelengths, but we have found no additional information regarding multiwavelength interactions. Accordingly, we have based our damage limits on the 3ω fluence only, with a damage threshold decreased by 10% from its value under monochromatic illumination. This assumption remains an area of uncertainty in our modeling, since we predict system performance to be limited by 3ω damage in the tripler.

Both CHAINOP and PROPSUITE used the same damage thresholds.

Filamentation Risk

Filamentation damage (or "angel hair" damage) is seen when the nonlinear index of refraction of an optical material causes self-focusing of small sections of a high-intensity beam. These sections may start out as small-intensity (a few percent above average) ripples or bumps of a few millimeters in size on the beam. As they self-focus, they decrease in size to hundreds of micrometers in diameter or smaller, and increase to very high irradiances (>100 GW/cm²). At some point the irradiance is high enough to damage the material and leave a visible track.

This filamentation growth is a complex function of the beam irradiance, nonlinear index of the material, and size and shape of the irradiance perturbation that self-focuses. It is also an inherently three-dimensional problem, making modeling calculationally intensive, although possible with present tools.[6] However, it is in fact not necessary to model growth of a filamenting bump to the point of damage in order to design NIF because we desire to be far from this limit. Consequently, a more heuristic approach was used in the optimizations, based on the experimental observation that *if small-scale beam noise is present*, large lasers tend to begin to break up into filaments after the beam has experienced a B integral of ~2 radians. This deserves a little more explanation.

The presence of small-scale beam noise is important because bumps of small size (a few millimeters) grow significantly faster than large-scale modulations. This difference in growth rate has been understood for many years.[4]

Elimination of these small-scale noise ripples is one of the purposes of spatial filters in large laser systems. Each laser chain in NIF will have two such spatial filters, one in the cavity, and one for transport to the target, as shown in Fig. 1. At the focal plane of each filter there is a pinhole through which the beam passes. The pinhole size, however, is such that only spatial frequencies present in the beam (in either phase or intensity) of less than a certain value can pass through the pinhole. Power at frequencies higher than this cut-off value is dumped on the surface around the hole. For NIF this cut-off half-angle is 100 μrad, corresponding to spatial ripple wavelengths of 1 cm. The net effect of this spatial filtering is that perturbations with transverse wavelengths less than 1 cm are clipped off at the pinholes. Consequently they cannot grow for more than the B integral they experience between pinhole passes.

In the chain design, then, we can limit B integral seen by the laser between pinholes to a certain value as a surrogate for calculating the beginnings of filament growth. For NIF optimizations, the between-pinhole B integral limit (also known as ΔB) was set to 2.2 rad. This constraint was used in both CHAINOP and PROPSUITE.

Optimization Variables and Constraints

Techniques used in laser system optimizations are discussed in the article "Laser Optimization Techniques" on p. 192 of this *Quarterly*. Our codes were implemented with simplex, parabolic interpolation, and gradient-search routines. The figure of merit that the optimizer attempted to minimize by changing variables, and, at the same time, honoring several constraints, was system cost divided by energy on target. These variables included hard aperture, injection fluence, number of laser slabs in each amplifier, laser slab thickness, Nd^{3+} concentration in laser slabs, flashlamp packing fraction, and apodization edge width. In using a gradient-search optimization technique, we took care in code development that there were no discontinuities in value or 1st derivative of figure of merit or constraints, as a function of these variables. Constraints that the optimizer used included energy on target, fluence damage to components, and ΔB limits.

Cost Algorithms

We have used different levels of cost modeling during development of the NIF design. Those used in later calculations included cost scaling rules, as a function of the optimization variables, for ~30 nonoptical subsystems of NIF, and ~140 optical cost categories. These rules were built on a cost database in the NIF *Conceptual Design Report*, and were provided by the NIF engineering team.

NIF Optimizations

Optimization studies with CHAINOP resulted in the CDR design. Similar studies with PROPSUITE resulted in the Advanced Conceptual Design (ACD) layout. The current NIF design (Title I, or preliminary design) has changed little overall since the ACD, so, for purposes of this discussion, the two will be considered equivalent. In this section, we describe the ACD optimization process and compare those results to the conceptual design.

During the ACD, we used three optimization approaches. In two approaches, optimization routines were used to find the least expensive design that meets functional requirements. These methods yielded a high-quality answer, but gave limited insight into tradeoffs in design options. The third method was to evaluate a large number of separate configurations manually, covering some range of parameter space on a uniform grid, and to graphically sort data according to design criteria. This approach enables greater understanding of the design space, but does not offer assurance that the best possible design has been included on the grid. The combination of this and the optimization approaches gives confidence that available design space has been explored thoroughly. Results from these methods are discussed below.

Studies Using Optimizing Software

By decision of the NIF project, some parameters were not varied during the final ACD optimization. Specifically, after some preliminary results, the optical clear aperture of the laser was fixed at 40 cm, laser slab thickness at 4.1 cm, and transport spatial filter length at ≥60 m. The optical clear aperture and slab thickness values were both larger than those found by the unbiased application of our optimization process. They were chosen to increase the 1ω performance margin (larger stored energy) and to decrease the risk of beam filamentation (lower between-pinhole B integral). The minimum transport spatial filter length was set primarily from concerns about pinhole blowoff in the last beam pass through the filter. (A shorter filter would proportionately decrease the pinhole size necessary to filter features of given scale. This would both increase the irradiance on the pinhole edge and decrease the closure distance.) The detailed physics of pinhole closure is currently poorly understood, making a more conservative choice advisable. Other values for these parameters would have saved additional money, but at the cost of decreased experimental flexibility and increased technical risk.

Given these constraints, we performed an optimization to determine the least expensive design overall, and also the least expensive design with no amplifier adjacent to the Pockels cell switch (the current design). These results are shown in Table 1. They are compared to the design arrived at during the CDR using CHAINOP (with small changes to allow better comparison between cases). The expected reduction in NIF cost by moving from the CDR design to the other two designs, as determined from the cost algorithms, is also included.

It can be seen in this table that the least expensive design (with the above constraints) is a 9/5/3 layout (the layouts are referred to by the number of slabs in each of the three amplifiers); the 9/5/3 layout is approximately $10M less expensive than the CDR design, but has a somewhat higher peak ΔB. The optimal design without a switch amp is the 11/0/7 design, with a cost approximately $4M less than that in the CDR. The $4M difference between the CDR and Title I designs is a small fraction of the total cost (~0.5%). The fact that CHAINOP, used for the CDR optimization, would suggest a design so close in cost (fractionally) to the Title I design, developed by PROPSUITE, gives confidence that CHAINOP provides accurate answers in spite of its relative simplicity.

Although we predict that both the 9/5/3 and 11/0/7 designs will meet the performance criteria that were set, there are a number of operational reasons to

TABLE 1. Comparison of the CDR design (9/5/5) and ACD optimized cases (9/5/3 and 11/0/7).

Parameter	Modified* CDR with new converter	Least expensive, constrained,** optimized	11/0/7, constrained,** optimized
Hard aperture (cm)	40	40	40
Main amp # slabs	9	9	11
Switch amp # slabs	5	5	0
Boost amp # slabs	5	3	7
Slab thickness (cm)	3.36	4.1	4.1
Injection energy (J) ***	3.2	1.2	2.2
Doubler thickness (cm)	1.35	1.36	1.36
Tripler thickness (cm)	1	1	1
Doubler detuning angle (μrad)	200	200	200
Flashlamp pump pulse length (μsec)	360	390	360
Nd^{3+} concentration ($10^{20}/cm^3$)	4.18	3.87	3.59
Transport spatial filter length (m)	65	60	60
Last two ΔB's (radian) (at beam center)	1.3/2.05	1.7/2.2	1.7/1.8
Conversion efficiency (energy/peak power) (%)****	60/80	60/79	60/79
Capacitor bank (MJ)	373	347	353
Total length (M1 to L4) (m)	135	128	123
Energy (MJ)/peak power (TW) in 600 μm LEH ***	2.2/612	2.2/608	2.2/607
Cost relative to CDR (M$)	0	–10	–4

* Changes from CDR: 1 × 1-cm pinhole spacing in cavity, new gain/loss assumptions, 4 × 2 amplifiers, 3.5-cm spatial filter lenses, and addition of target chamber window. These assumptions were common to the other two designs.

** Constraints: 192 beamlets, 40-cm hard aperture, 60-m transport spatial filter, 4.1-cm thick slabs.

*** Before spatial preshaping for gain roll-off across the aperture.

**** Averaged over ±30-μrad doubler detuning angle.

prefer the 11/0/7 layout. Most apparently, from Table 1, it has a noticeably lower maximum ΔB, yielding some additional safety against nonlinear effects. Equally compelling, the similarity to the 11/0/5 design for Beamlet (the operational prototype NIF beamline) makes operational experience gained on that machine more relevant and will likely decrease prototyping costs and/or risks. The absence of a switch amplifier also both obviates concerns about the effects of magnetic fields on the operation of the plasma electrode Pockels cell and greatly simplifies the alignment procedure. There are also some design cost savings in not having a switch amplifier included in the analysis. For all of these reasons, the NIF project chose the 11/0/7 design as its baseline for the ACD.

The shift to the current NIF 11/0/5 design was done as part of the Title I preliminary design activities. It entailed slightly different assumptions than used here, with somewhat increased risk, in order to realize a lower cost.

Studies Using Parameter Scan Optimization

In addition to optimizations, we used PROPSUITE to perform parameter scans of the cost and performance of a large number of designs (~50,000) in the vicinity of the optimized NIF design. Parameters varied for this study were slab thickness, number of slabs in each amplifier, Nd^{3+} concentration, and flashlamp pump pulse length. This was done for 26 different combinations of the slab counts in the three amplifiers ($X/Y/Z$).

Figure 3 shows the results for cases with no switch amp ($Y = 0$). Cost is plotted vs output energy, with the several points for each slab combination being different combinations of Nd^{3+} concentration, slab thickness, and pump pulse length. The temporally shaped ICF indirect-drive pulse from Fig. 2 was used in each case. All other parameters were the same between designs (including a 40-cm hard aperture). It can be seen that there is some grouping of the various designs, with the least expensive designs being 11/0/7, 11/0/5, and 13/0/5. Some designs with tighter grouping show a greater robustness to parameter changes than others (e.g., 11/0/7 vs 9/0/7). This is desirable in a system. The designs at higher cost are typically characterized by thin slabs and large injection energies. For instance, the large number of thin slabs incurs a higher slab finishing cost and larger capacitor bank. Too few slabs in the boost amplifier, which is only double-passed, requires a larger injection energy and a more expensive front end.

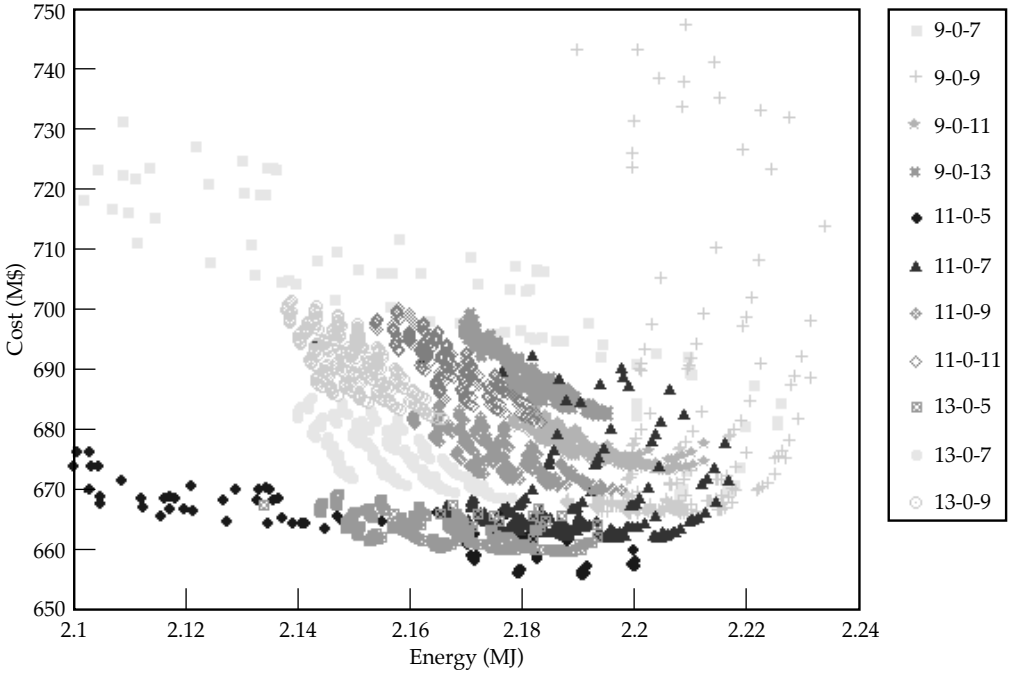

FIGURE 3. Full parameter scan results for cases with no switch amp (*X*-0-*Z*).
(70-00-1296-2779pb01)

All the designs in Fig. 3 produce slightly different energies and peak powers on target. In order to simplify comparisons, it is possible to normalize all the designs to have 2.2 MJ/600 TW on target by projecting small changes in hard aperture and by scaling cost accordingly. This scaling of the aperture leaves the B integral unchanged for each design by increasing/decreasing the beam area. For example, if a design produced 2.15 MJ and 580 TW, it would be scaled to a 40.7-cm hard aperture, giving 600 TW and 2.22 MJ. The cost was scaled as (hard aperture)$^{0.8046}$, based on studies done previously with CHAINOP.

With this normalization, we plotted the various cases against maximum ΔB in the system (Fig. 4). In this display it can be seen that the 11/0/7, 11/0/5, and 13/0/5 designs are still least expensive, but that they have substantial differences in maximum ΔB, with the 11/0/7 design displaying the lowest ΔB.

In Figs. 5 through 7, successive filters are applied to the data in Fig. 4. A large injection energy requirement typically indicates a design where the modeled pulse is close to the extraction limit of the system. This leaves system performance very vulnerable to small uncertainties in losses or gains. Designs with injection energies of a few joules or less are safer; Fig. 5 shows cases that have injection energies ≤5 J. The most attractive designs are still the 11/0/7, 11/0/5, and 13/0/5, although many of the 11/0/5 designs with thinner slabs were eliminated.

Designs with overly large capacitor banks (and correspondingly small injection energies) are simply uneconomical, as more energy is stored than necessary. These can also be thought of as designs with too many slabs. Figure 6 shows cases filtered for capacitor bank size ≤400 MJ. The 11/0/7, 11/0/5, and 13/0/5 designs are still most attractive. Note that the optimum number of slabs is 16 to 18.

Results of a final filtering requiring laser slab thicknesses ≤4.2 cm are shown in Fig. 7, reflecting fabrication uncertainties with thick slabs. This filter removes all the remaining 11/0/5 designs, leaving the 11/0/7 and the 13/0/5 designs as having comparable minimum costs. The 11/0/7 designs, however, have lower B integral. Clearly, given these criteria, the best design with no switch amplifier is the 11/0/7.

We can compare these results to cases with a switch amplifier. In Fig. 8, a subset of cases is shown having slab counts of *X*/0/*Z*, *X*/3/*Z*, and *X*/5/*Z*, with all the aforementioned filters applied. It is first useful to note that there are a large number of cases with approximately the same cost ($660–$670M), but some difference in B integral. Given that, however, it can be seen that the 9/5/3 design is the least expensive design, with the 9/3/5 and 11/0/7 close behind. These results agree with those cases found by the optimizer, and shown in Table 1: the 9/5/3 design is the least expensive, but has a somewhat higher B integral than the 11/0/7 (2.1 to 2.2 vs 1.7 to 1.8 rad). The design chosen by the project is circled on Figs. 7 and 8. The 11/0/7 designs that have slightly lower cost and B integral than the one selected have thinner slabs than the prescribed 4.1 cm.

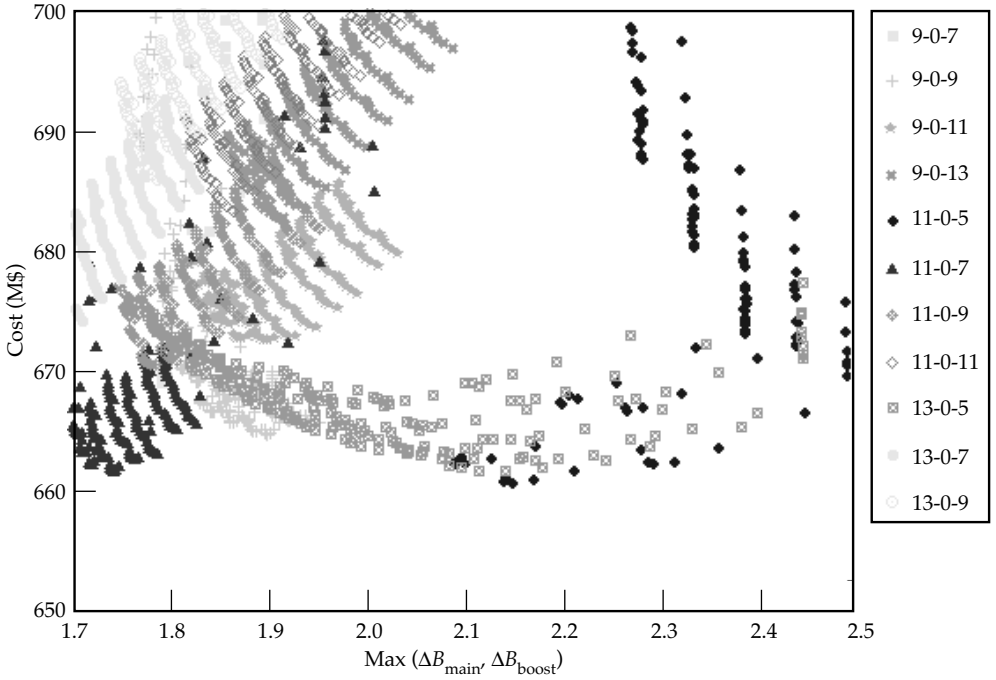

FIGURE 4. Data from Fig. 3 (*X*-0-*Z* parameter scan), aperture-scaled to 2.2 MJ, and compared on the basis of maximum B integral.
(70-00-1296-2780pb01)

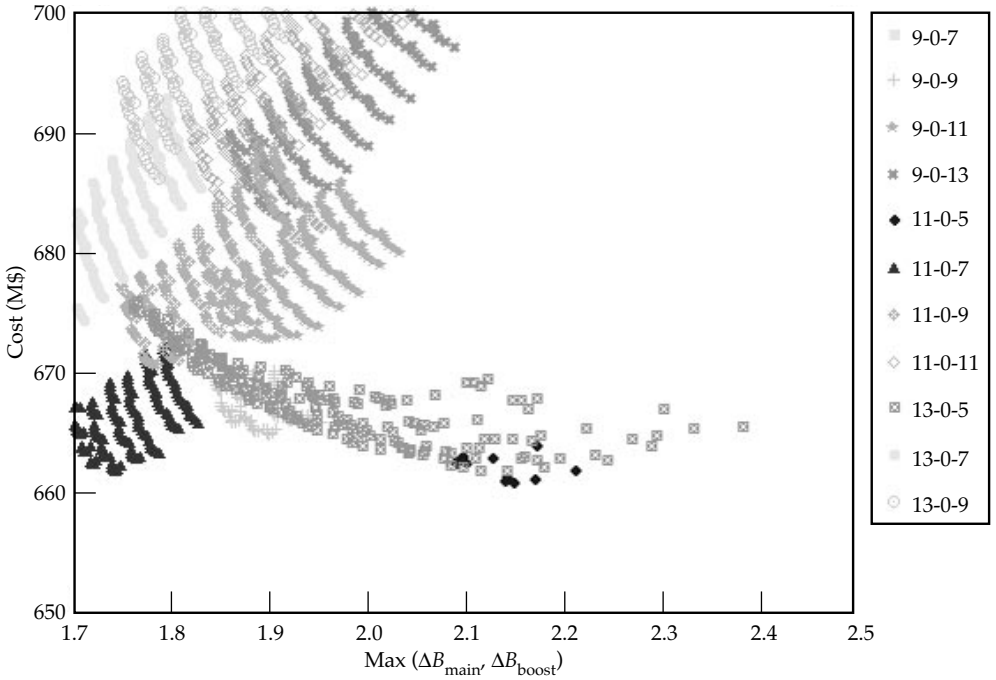

FIGURE 5. Data from Fig. 4 (*X*-0-*Z* parameter scan), clipped at injection energy ≤5 J.
(70-00-1296-2781pb01)

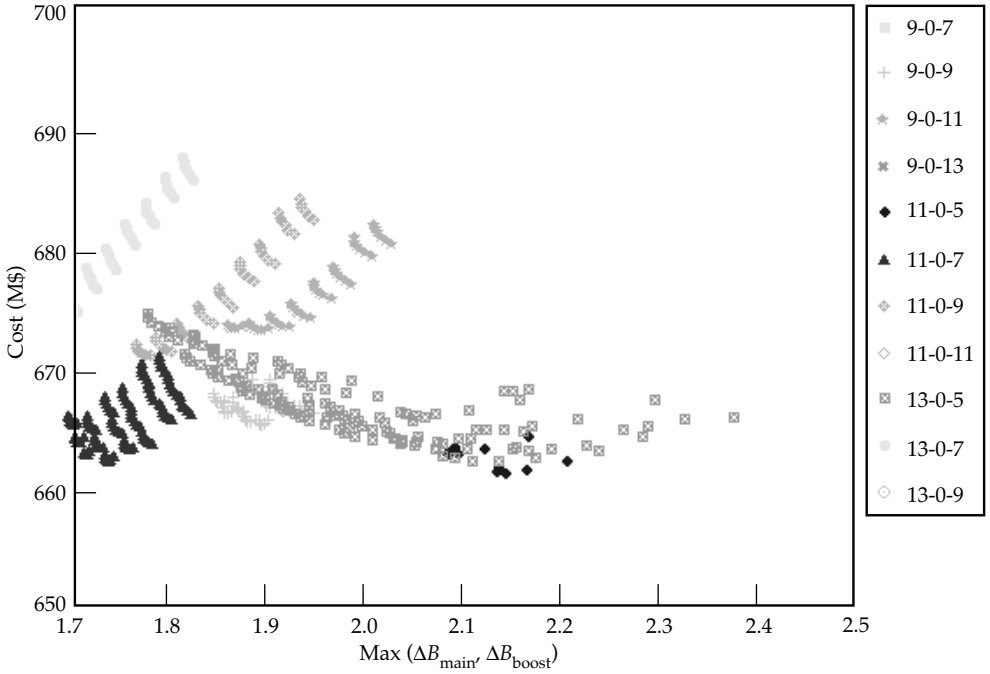

FIGURE 6. Data from Fig. 5 (*X*-0-*Z* parameter scan), clipped at injection energy ≤5 J and capacitor bank size ≤400 MJ. (70-00-1296-2782pb01)

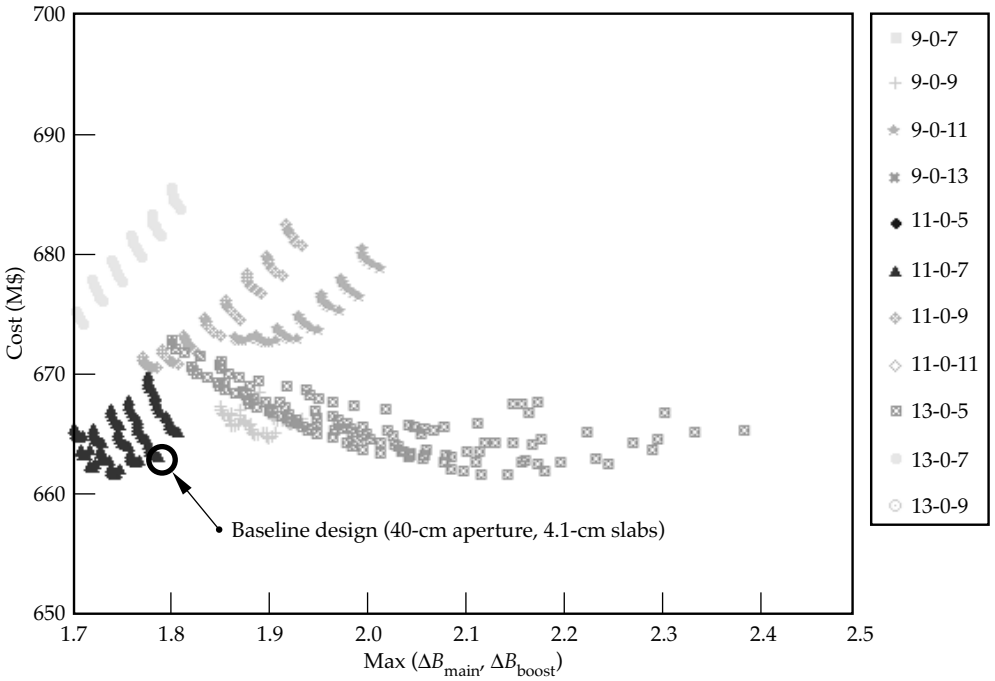

FIGURE 7. Data from Fig. 6 (*X*-0-*Z* parameter scan), clipped at injection energy ≤5 J, capacitor bank size ≤400 MJ, and laser slab thickness ≤4.2 cm. (70-00-1296-2783pb01)

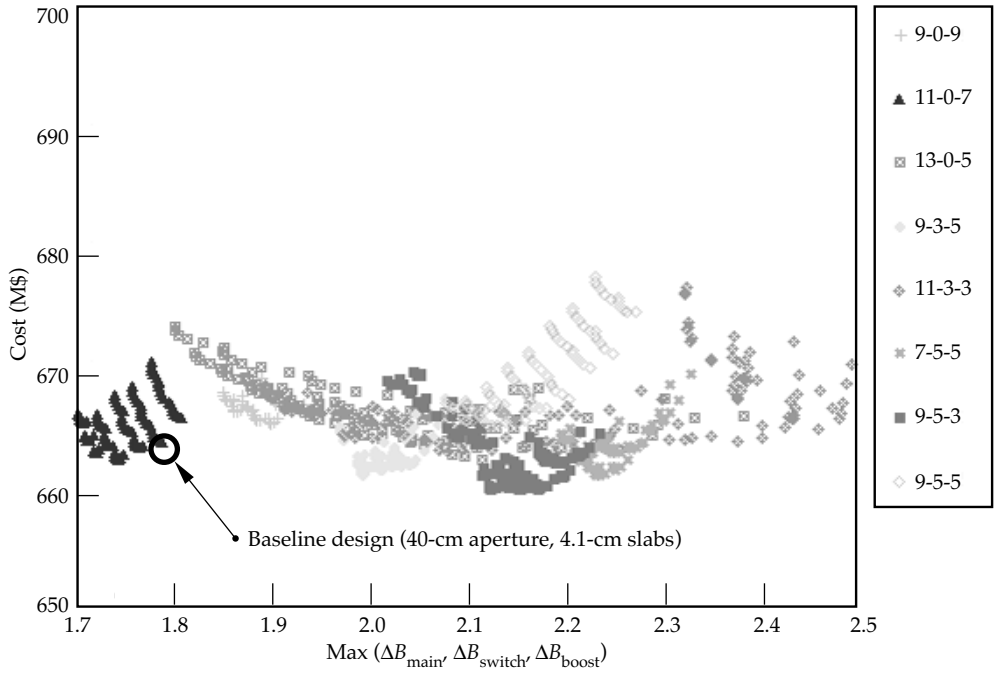

FIGURE 8. Comparison of subset of parameter scans for *X*-0-*Z* and *X*-*Y*-*Z* with injection energy ≤5 J, capacitor bank size ≤400 MJ, and laser slab thickness ≤4.2 cm.
(70-00-1296-2784pb01)

Summary

The NIF design is based on cost/performance optimization studies. These studies were done in two phases, and with two codes: a zero-dimensional performance model (CHAINOP) for the *Conceptual Design Report*, and a one-dimensional propagation model (PROPSUITE) for the Advanced Conceptual Design (ACD). These ACD results using PROPSUITE led to 11/0/7 design of Table I. The current Title I 11/0/5 design activity was a result of further cost and risk studies. These efforts give us confidence that we are designing the (approximately) least expensive system meeting the functional requirements.

Acknowledgments

The authors would like to thank Mark Rotter (LLNL) for assistance in setting up and running the NIKE3D and TOPAZ codes used in thermo-mechanical modeling of laser slabs.

Notes and References

1. *National Ignition Facility Conceptual Design Report*, UCRL-PROP-117093, Lawrence Livermore National Laboratory, Livermore, CA, 94550 (1994).
2. L. M. Frantz and J. S. Nodvik, *J. Appl. Phys.*, **34**(8), 2346 (1963).
3. J. Lawson, *Proc. Conf. on Optical Manufacturing and Testing*, SPIE Vol. 2536, pg. 38 (July 1995).
4. J. Trenholme, *LLNL Laser Program Annual Report*, UCRL-50021-74, pg. 179 (1974).
5. J. Trenholme, personal communication.
6. W. Williams, K. Manes, J. Hunt, P. Renard, et al., *ICF Quarterly Report*, **6**(1), 7, Lawrence Livermore National Laboratory, Livermore, CA UCRL-LR-105821-96-1 (1995).

Laser Optimization Techniques

C. D. Orth

S. W. Haney

W. H. Williams

Introduction

One of the challenges in designing a large laser system like the proposed National Ignition Facility (NIF) is determining which configuration of components meets the mission needs at the lowest construction cost with the largest margin in performance without any optical damage. Such an endeavor could credibly require evaluation of a million different designs because we must consider a range of values for each of many parameters: different numbers of beamlets, different aperture sizes, different numbers of laser slabs, different thicknesses of slabs, etc. The evaluation of so many designs with even a minimum of detail is impractical with current computing ability. There is hence a premium on the development of techniques to determine the best design without evaluating all of the practical configurations.

What Is an Optimization?

Optimization is the process of finding the best set of values for a system's identified design parameters. There are three steps to optimization. First, we identify exactly what aspects or measures of the system would define a better system if they were enhanced, such as improved output, lowered cost, improved reliability, or a combination of measures with appropriate weighting factors. This is often the most difficult step, because it requires that we truly understand what constitutes a better system. Second, we define a mathematical function known as a figure of merit (FOM) that incorporates these measures and has both of the following characteristics: (1) the value of the FOM increases or decreases according to our selected measure of goodness, and (2) the FOM is dependent on all of the design parameters under study, such that the value of the FOM varies if the value of any parameter is varied. Third, we search the parameter space to find the design that maximizes or minimizes the FOM, depending on how the FOM is defined.

To optimize a large laser system, we must consider more than just an FOM. Much of the physics of light propagation is nonlinear, in the sense that a change in each of the many parameters does not produce a proportional change in the laser output. This means that we cannot use any of the linear optimization methods that are known. There are also many equality and inequality constraints to consider, such as not exceeding a certain construction cost, not exceeding a certain input energy, not damaging any of the optical elements, and outputting at least a certain 3ω laser energy. Optimization of a laser system is thus not only nonlinear, but also constrained, and is hence called nonlinear constrained optimization. In addition, because a graph of the FOM plotted as a function of all of the variable parameters is often a multiple-peaked surface, with several peaks of different heights, there are local maxima (peaks) in the FOM that can easily fool a computer into incorrectly "thinking" it has found the optimum. What we need, therefore, is a method that can quickly and correctly find the highest peak in the FOM space, the so-called global optimum. Moreover, the FOM space is sometimes noisy in one or more of the parameters, with additional peaks and valleys superimposed on top of the otherwise smooth topology. We thus need a technique that can smooth out the noise. A mathematical statement of such a nonlinear constrained optimization problem is to maximize (or minimize) a suitably smoothed (or averaged) FOM function $f(\mathbf{x})$ subject to equality constraints $c_i(\mathbf{x}) = 0$, $i = 1, ..., k$, and inequality constraints $c_i(\mathbf{x}) \geq 0$, $i = k+1, ..., m$, where parameter vector $\mathbf{x} = (x_1, x_2, ..., x_n)$ represents n variables.

Selecting an Optimization Technique

Many different techniques exist for nonlinear constrained optimization. These techniques differ in the way in which the computer navigates the FOM space in search of the tallest peak or deepest valley. The most common methods sample the topology in some region to determine the slope of the terrain in various directions, and hence the direction that leads to the optimum. These methods, which are all iterative, differ in the following ways in which the local terrain is sampled:

1. The downhill simplex method[1] uses only function evaluations (i.e., evaluations of the FOM), not derivatives, to move in the direction of the optimum using manipulations of the geometrical figure (simplex) formed by the original point and n somewhat arbitrary displacements in the n directions corresponding to the n parameters considered. This method is robust, but typically slow to converge.
2. Simple derivative (gradient) methods sample the space for two (or more) values of each parameter to determine a local slope in the FOM, and then step off a fixed step in the direction of maximum slope. One serious problem with this method is that, once the best direction in which to go for the next calculation is identified, we don't really know how far to go in that direction. Consequently, this method can be slow to converge.
3. Quadratic methods, in essence, calculate the FOM for three values of each parameter, fit the resulting FOM values to a quadratic function such as a parabola, and calculate exactly how far to go for the next estimate of where the FOM peak might lie. This method is much "smarter" than the above methods because it knows how far to step out for the next iteration. Two common methods of this type are Brent's method and Powell's method. Brent's method uses parabolic interpolation. Powell's method finds the solution that zeros the gradient of a Lagrange function formed as a sum of the FOM function and a linear combination of the constraint functions. It approximates the full nonlinear problem by a quadratic problem to find the direction to go in the FOM space, then determines how far to go in that direction by doing a one-dimensional optimization in that direction. While Brent's method uses only three function evaluations for each parameter, Powell's method uses one function evaluation, one derivative evaluation, one estimate for the second derivative, plus other function evaluations for each subsequent line search. These methods are powerful and fast, and are the methods used in the codes that we employ.
4. Simulated annealing methods[2] randomly sample points over a large portion of the parameter space and then slowly decrease the size of the sampling space around any optimum so found, according to mathematics analogous to Boltzmann thermodynamic cooling. This method is good for selecting the best global ordering of a large combination of discrete elements of some kind when many local optima exist, but it converges too slowly and is thus not practical for our problem.
5. Genetic methods[3] form a pool of design candidates, "mate" the ones having the highest FOMs (the parents) by combining attributes in some way to produce other candidates (the offspring), and then remove the unlikely candidates (extinction). This method can also be effective in finding a global optimum among many local optima, but it also converges too slowly.

The first three methods listed above can be confused if the FOM (or constraint) surface is noisy, unless additional smoothing algorithms are included. Simulated annealing and genetic methods are inherently more able to navigate successfully along noisy surfaces, but are expected to converge too slowly to be effective for the optimization of a large laser system. We therefore chose to use quadratic optimization methods to speed up the computational time. As a result, however, we had to deal with discontinuities in the FOM as one form of noise.

Dealing with Discontinuities in the FOM

There are several sources of fluctuations in the FOM that affect an optimizer evaluating various designs of a large laser system. Although stochastic (statistical) noise can sometimes be a problem when methods employ random numbers, a more typical problem arises from the discontinuous FOM jumps that correspond to integer steps. Integers are encountered in such parameters as the numbers of laser slabs in the amplifiers, the number of flashlamps for each slab, and the number of beamlets in the laser. If the FOM (or a constraint) moves abruptly as the optimizer searches from one integer to the next, as it usually does, the optimizer can be confused by the local optima thereby introduced. This is especially true for gradient-search techniques, which are based on real numbers. We can overcome such fluctuations by incorporating either some type of smoothing technique or by substituting real numbers for the integer quantities so that the optimizer can consider noninteger (i.e., nonphysical) values of the parameters.

A second source of discontinuities arises in optimizations involving spatial-filter pinholes because

of the integer-like effect of the transverse spatial representation of the beam by a fixed number of grid points (e.g., 512 points over a horizontal width of 50 cm). To explain these discontinuities, we must first explain the purpose and function of pinholes.

All of the large laser chains at LLNL involve the use of spatial filters that focus the beam and force it to go through a 100- to 200-μm-diam pinhole in a metal plate. The purpose of such a pinhole is to cut off the high-angle noise present in the beam, thereby smoothing the transverse spatial intensity profile. Such smoothing occurs because, in the focal plane of a lens, the spatial intensity profile corresponds to the power in the various angular components in the beam. Thus, if the intensity profile is decomposed into its Fourier components, the relative powers in the low-frequency components correspond to the intensities seen near the centerline of the focal plane. Higher-frequency components focus at increasingly farther distances from the centerline because they are propagating at larger angles. These various frequency components grow in magnitude at different rates due to, among other things, the nonlinear indices of refraction of the optical materials in the laser, as described by the Bespalov–Talanov theory.[4] The high-frequency components tend to grow faster, so it becomes desirable to clip off the power in these frequencies periodically in the laser chain to keep the beam as spatially flat as possible. For a beam with a reasonably smooth spatial profile, the power in the high-frequency components is low enough to permit a pinhole to do this clipping without ablating away too much of the pinhole structure and thereby disrupting the last temporal portions of the laser pulse.

In propagation simulations employing a finite number of grid points, the power in the Fourier components is summed into the same number of bins as there are grid points. Consequently, as the diameter of the pinhole changes with changing pinhole acceptance angle, there are discrete jumps in clipped-beam power as the edge of the pinhole moves from one frequency bin (grid point) to the next. These jumps result in abrupt changes in the spatial intensity profile of the beam after it leaves the filter. If the optimizer is monitoring, for example, the peak fluence as a constraint against optical damage, it can be confused by the local optima that such discontinuities generate. The solution we have used to overcome this confusion is to average the FOM over several adjacent function evaluations.

Optimizing the NIF Design

Optimization of the NIF design is one example of how we can use our optimization techniques. As described in more detail in the article "NIF Design Optimization" on p. 181 of this *Quarterly*, the conceptual design[5] for the NIF configuration arose through use of a code called CHAINOP,[6] which was capable of using either a simplex optimization routine or a gradient-search routine. We accessed this gradient-search routine as part of a large systems analysis programming shell called SUPERCODE.[7] SUPERCODE uses the quadratic version of Powell's method, as written in an Argonne National Laboratory implementation of a variable metric method labeled VMCON.[8] Because VMCON evaluates gradients, care was taken to minimize discontinuities in the FOM and constraints by using noninteger laser slab and flashlamp counts, as well as smoothed cost functions.

In the second optimization effort, for the Advanced Conceptual Design (ACD) phase of the NIF, we implemented three separate approaches. In one approach, we used SUPERCODE to evaluate ~100,000 specific designs distributed around the conceptual design point in the major parameters, and we applied various cuts to constrain dynamical and engineering quantities such as cost and nonlinear growth of spatial noise. For a second approach, we used SUPERCODE to do an optimization. As with CHAINOP, we used fractional slabs and noninteger flashlamp counts, but optimization over pinhole acceptance angle could not be performed. A third approach, coded as OPTIMA1, is based on a modified version of Brent's method (parabolic interpolation). A similar approach had been used in the diode-pumped solid-state laser (DPSSL) design studies for inertial fusion energy.[9] OPTIMA1 can use either of two different methods to smooth the FOM space and can treat integer parameters directly. This code therefore allowed the consideration of noisy parameters, including integer slab and flashlamp counts, and pinhole acceptance angles.

There were several reasons we chose multiple approaches in optimizing the NIF laser for the ACD. First, when we started, we knew that there were complexities such as noisy parameters, and we were not sure that any one approach would prove successful in the end. Second, the performance of optimizers is usually dependent on the problem considered, so the length of time needed for any one optimizer to converge to a solution was unknown for the NIF problem. In general, performance is better if the optimization algorithm is tailored to the problem in some way. On the other hand, the use of a well tested fast algorithm like VMCON can often prove very effective. Third, we wanted multiple opinions from independent approaches to improve the reliability of the results.

All three approaches used parallel processing through Parallel Virtual Machine (PVM) software. This software allows one master computer to send tasks to many different slave computers and retrieve the results. In our case, we had one HP 715/80 UNIX master workstation tasking 28 similar slave workstations that each evaluated the performance of one NIF design (SUPERCODE) or performed the suboptimization for one

parameter (OPTIMA1). The total computing power was 20–30 megaflops for each of 28 computers, or about 0.75 gigaflops. The use of this workstation cluster enabled the codes to search through a space representing a million candidate designs at a rate over 20 times faster than it would have taken with only one computer. This facility proved valuable because it reduced the total calculation time from the 46 days it would have taken for 10^6 assessments at about two minutes per assessment of each candidate design on one computer to about one or two days using the workstation cluster.

Features of SUPERCODE

SUPERCODE[7] couples a toolbox of systems analysis tools to a powerful user interface. The systems analysis tools currently consist of the following:

- A constrained nonlinear optimization package based on VMCON.[8]
- A nonlinear optimization package based on a genetic algorithm.[3]
- A nonlinear equation solver.
- A Monte Carlo sampling package for performing uncertainty analyses.
- Parameter scans.
- Uncertainty analyses.
- Facilities for exploiting PVM software to speed up optimizations.

These tools are controlled by a programmable shell that understands a large subset of the C++ computer language, including arithmetic expressions, loops, decision structures, functions, classes, and objects. Users can interactively manipulate the set of equations to be passed to the systems analysis tools, monitor progress of a calculation, postprocess results, and plot them using an interactive graphics package. SUPERCODE was the main code used in setting the NIF baseline design, and has been used to design tokamak reactors and experiments, hybrid electric vehicles, rail guns, and neutron sources. SUPERCODE is available on UNIX, MacOS, and Windows platforms.

The OPTIMA1 Code

OPTIMA1 is based on the particular parabolic-interpolation method that proved successful for the DPSSL inertial fusion energy study.[9] This method increases the independence of the parameters, often permitting the full optimization to be accomplished by independent one-parameter optimizations. The key to this method is to incorporate an inner loop that maximizes the laser's injection energy subject to all constraints. An outer loop then deals with all of the other parameters designated as active optimization variables. Both loops advance by making one function evaluation and using that together with the last two calculations nearest the current best value to determine a next guess. Penalty functions reduce the value of the FOM by exponentially degrading the FOM as any active variable violates a constraint. The current list of features includes the following:

- Easy addition of parameters.
- Treatment of both discrete (integer, even-integer, or odd-integer) and analog (real) parameters.
- Two types of smoothing for noisy parameters (random-number smoothing and perturbation smoothing).
- Ability to restart runs from a dump file.
- Operation on either a single or multiple (parallel-processing) platforms (using PVM software).
- Table-like scans over a single parameter.
- Input-file selection of the optimization FOM from among any product or quotient of the parameters or calculated quantities.
- Performance of a sensitivity study around the final parameter vector.

OPTIMA1 is very flexible and robust. It usually takes more time to converge to a solution for small ($<10^{-3}$) precisions, however, because the penalty functions create a "cliff" in the FOM space that requires special treatment in the parabolic interpolator. In addition to helping choose the NIF design parameters, OPTIMA1 has been useful in performing sensitivity studies on the parameters (e.g., the maximum allowable doubler detuning angle) and in determining optical specifications through studies varying the aberrations placed on the optical components. OPTIMA1 is written in UNIX HP FORTRAN.

Overcoming Specific Modeling Difficulties

After selecting a set of optimization techniques, we had to deal with many problems that were specific to the optimization of a large laser. First, we found many designs having the same value of energy delivered to the laser entrance hole (LEH) of the target, but with differing construction costs, so we had to include cost in the FOM or cost as a constraint. Two solutions that proved effective were (1) minimizing cost subject to performance constraints and (2) maximizing the ratio of energy delivered to the LEH and total cost, subject to the other constraints.

The second problem was finding a way to include realistic aberration sources for every optic that would account for surface roughness and bulk phase retardations. The challenge was to develop techniques to use measurements taken over varying aperture sizes and on a limited number of parts while preserving the spatial distributions of wavefront roughness in such a form that realistic aberration sources could be simulated for every optic. This was done by devising a technique using a

power spectral density (PSD) function defined as the square of the discrete Fourier transform of the measured phase retardations, multiplied by the length of the 1–D measurement (or multiplied by the length and width in 2D).[10] We combined the measurements from three spatial-frequency ranges (0 to 0.1 mm^{-1}, 0.1 to 1 mm^{-1}, and 1 to 10 mm^{-1}) while mitigating the effects of finite sampling apertures by using a windowing filter function (a Hanning filter). This filter broadened (or blurred) the resulting width of the spatial frequency structures and eliminated frequencies generated by the discontinuities at the edges of the samples. The PSDs thereby obtained did not possess any relative phase information in the Fourier domain, but were merely the spectral distributions of the wavefront errors. We then used the PSD for a given type of optic to determine the magnitude of the Fourier coefficient and added a random phase in the Fourier domain. Using inverse Fourier transformation, we obtained a unique wavefront distortion for every optic needing a simulated phase-front aberration.

The third modeling difficulty was that laser gain and pump-induced distortions depend on the choice of pumping parameters (pump pulse duration, Nd doping concentration, flashlamp explosion fraction, flashlamp diameter, and flashlamp packing fraction). Pump-induced distortion is phase noise added to the beam because the nonuniform distribution of flashlamp light absorbed by the laser slabs causes nonuniform heating, which distorts the slabs. Because determining the proper pump-induced distortions is calculationally intensive (involving ray tracing and 3-D thermomechanical modeling), we ran the 3-D codes for a range of each of the pumping parameters and incorporated the results in the optimizations using a table look-up procedure.

The fourth problem was that the use of spatial-filter pinholes with abrupt edges in calculations with a finite number of transverse spatial grid points causes ringing (aliasing), which introduces artificial modulation of the downstream beam intensity profile. We therefore used high-resolution runs with many points to define problem areas and incorporated smoothing algorithms developed at LLNL.

The fifth problem was damage to the optical components that can arise from either high fluence or filamentation, which both depend on the noise on the beam. (Filamentation is the process by which the intensity of a narrow beamlet increases as the beamlet is focused by nonlinear propagation through solid materials.) A proper treatment of these effects therefore requires very high spatial resolution to define the peaks in the transverse intensity profiles. Such resolution would make the iteration cycle time prohibitively slow if many points had to be used in two transverse dimensions. Consequently, we performed most of our calculations using 1-D codes with 512 spatial points, which is insufficient to determine filamentation, and evaluated the likelihood of filament formation and the resultant optical damage using a phenomenological model[11] developed at LLNL based on measured Beamlet data. For ordinary (nonfilamentation) optical damage assessment, we used measured peak fluence limits as constraints for every component.

The sixth modeling difficulty was that the desired NIF laser pulse at the LEH is a 3ω pulse consisting of a long low-power foot followed by a main pulse roughly 3.5 ns wide. Because the laser input is at 1ω, and because the harmonic conversion from 1ω to 3ω is intensity-dependent, we had to incorporate precise algorithms for this conversion process (see the article entitled "Frequency Conversion Modeling" on p. 199 of this *Quarterly*); we also had to iterate to make sure that the 1ω pulse shape produced the desired output 3ω pulse shape.

Optimization Flow

Each optimization iteration included a number of steps involving other codes, as outlined in Fig. 1 for the particular case of OPTIMA1 using the Ethernet connections to the cluster of 28 workstations. As directed by the master, a slave machine would suboptimize one parameter by first running two codes to help establish the temporal shape of the input beam: a plane-wave frequency conversion code (thgft02) to assess the converter performance with the given parameter values and an inverse harmonic-conversion code (invconv3) to calculate the 1ω input temporal shape that would give the desired 3ω output temporal shape with that converter. Following the formation of the apodized transverse spatial shape of the input beam, the optimizer would generate the input file for PROP92 and run PROP92 to propagate the input signal down the chain of optical components from the input of the laser to the harmonic converter. This step included phase aberration sources to simulate the experimental surface finishes and bulk properties for each optic, as well as the amplifier gain files generated from 2.5-D amplifier modeling and the pump-induced distortion files generated from 3-D thermomechanical modeling (see the companion article entitled "The PROP92 Fourier Beam Propagation Code" for a complete description of the physics in PROP92). After running a code to analyze the PROP92 output file, the optimizer would run a frequency conversion code (thgxtz001) to convert the 1ω light to 3ω light. Thereafter, the optimizer would formulate an input file for PROP92, this time for the 3ω light, and run PROP92 to propagate the beam down the rest of the laser chain to obtain the laser pulse entering the target LEH. After

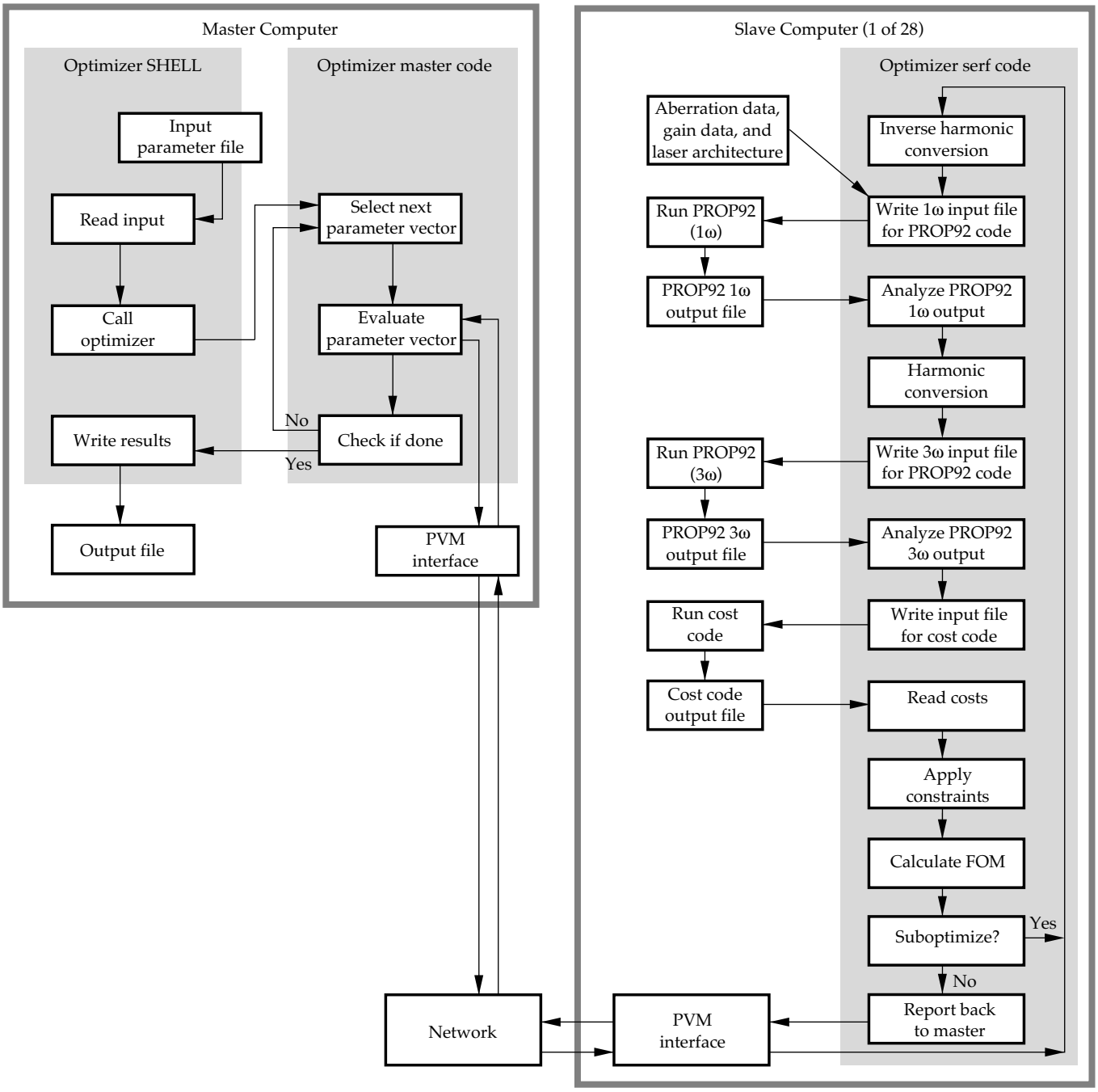

FIGURE 1. NIF optimization flow chart for OPTIMA1. (40-00-1296-2752pb01)

running a code to analyze the PROP92 3ω output file, the optimizer would run a routine to generate an input file for the cost code, run the cost code to calculate the resulting cost of the NIF facility, and run a routine to apply the constraints.The optimizer would then calculate the FOM as the LEH energy, or the ratio of that energy to the cost, or simply as the cost constrained to obtain the desired energy and power at the LEH—all as penalized by the constraints that failed. After several suboptimizations, the slave reports the results for that parameter back to the master, which decides how to form the full parameter vector for the next set of suboptimizations. When the changes in all parameters are less than specified precisions, the process stops.

Summary

Nonlinear constrained optimization of the design of a large laser such as the NIF is the process of finding the set of values for the laser's identified design parameters that optimizes the figure of merit (FOM). Among the different optimization techniques available, we selected quadratic methods based on Brent's method and Powell's method, as modified to treat the discontinuities imposed by integer parameter values. An established code (SUPERCODE) and a new code (OPTIMA1) were configured with realistic aberration sources for every optic, a cost model of the whole laser system, methods to incorporate the effects of different values of the pumping parameters, models for optical damage as well as filamentation, and full harmonic conversion of the desired 3ω pulse shape. We also incorporated parallel processing through use of Parallel Virtual Machine (PVM) software operating on a group of 28 workstations. The resulting techniques allow optimization of the NIF laser and other laser systems based on realistic components and realistic laser light propagation.

Notes and References

1. J. A. Nelder and R. Mead, *Computer Journal* **7**, 308–313 (1965).
2. S. Kirkpatrick, C. D. Gelatt, and M. P. Vecchi, *Science* **220**, 671–680 (1983); S. Kirkpatrick, *Journal of Statistical Physics* **34**, 975–986 (1984).
3. E.g., E. Betensky, *Opt. Eng*. **32,** 1750 (1993).
4. J. Trenholme, *Laser Program Annual Report*, Lawrence Livermore National Laboratory, Livermore, CA, UCRL-50021-74, p. 177 (1975).
5. *National Ignition Facility Conceptual Design Report*, Lawrence Livermore National Laboratory, Livermore, CA, UCRL-PROP-117093 Vol. 2, NIF-LLNL-94-113 (1994).
6. J. Trenholme, "CHAINOP: Laser Chain Optimization Code," Lawrence Livermore National Laboratory, Livermore, CA, internal report (Oct. 1992); also see accompanying article on p. 181 in this *Quarterly*.
7. S. W. Haney, W. L. Barr, J. A. Crotinger, L. J. Perkins, et al., *Fusion Technology* **21**, 1749 (1992).
8. R. L. Crane, K. E. Hillstrom, and M. Minkoff, "Solution of the General Nonlinear Programming Problem with Subroutine VMCON," Report ANL-80-64, Argonne National Laboratory (1980).
9. C. D. Orth, S. A. Payne, and W. F. Krupke, *Nuclear Fusion* **36**(1), 75 (1996).
10. J. K. Lawson, D. M. Aikens, R. E. English, Jr., C. R. Wolfe, "Specification, Production, and Testing of Optical Components and Systems," SPEIE Proceedings, 13–16 May 1996, Glasgow, Scotland, UK, vol. 2775, p. 345 (1996).
11. Mark A. Henesian, "Simulations of 3ω Beam Filamentation in the Beamlet Focus Lens and General Comments on Filamentation Theory," Lawrence Livermore National Laboratory, Livermore, CA, internal memo LS&T-LMO 96-001 (May 1996); and "Simulations of 1ω Beam Filamentation in the Beamlet Laser, Filamentation Theory in Glass Slabs, and PROP92's Filamentation Code," Lawrence Livermore National Laboratory, Livermore, CA, internal memo, LS&T-LMO 96-003 (May 1996).

FREQUENCY-CONVERSION MODELING

J. M. Auerbach
C. E. Barker
D. Eimerl
K. R. Manes
D. Milam
*P. W. Milonni**
J. B. Trenholme
B. Van Wonterghem

Introduction

With respect to the rest of the Nd:glass laser system, the frequency converter is quite small in terms of weight and size. However, it is a critical component because laser fusion targets require irradiation by ultraviolet laser light to operate successfully. The frequency converter produces ultraviolet light ($\lambda = 0.351$ μm) from the infrared light ($\lambda = 1.053$ μm) generated in the neodymium-doped glass section of the laser.

As shown in Fig. 1, the basic frequency converter for tripling consists of two crystals (advanced designs have more than two crystals). The first crystal, known as the second harmonic generator (SHG), frequency doubles a predetermined amount of incident infrared (1ω) light. The frequency-doubled (2ω) light has a wavelength of 0.526 μm. The 2ω and 1ω light are then mixed in the second crystal, known as the third harmonic generator (THG) or mixer, to form ultraviolet (3ω) light at a wavelength of 0.351 μm. The output of the THG is 1ω, 2ω, and 3ω light. The proportions of light at the three wavelengths depend on the operating configuration and the intensity and phase of the input laser pulse to the converter.

The goal of frequency-conversion modeling is to produce a converter design that results in the best performance for a required output laser pulse and that is the least sensitive to operational tolerances (such as alignment) and crystal manufacturing faults (such as surface roughness).

A frequency converter requires precise tolerances. Crystals must be tilted to an accuracy of microradians, and crystal thicknesses must be accurate to millimeters to achieve desired performance. Crystal surfaces must also be finished to a smoothness of hundredths of a micron so that the energy of a 3ω laser pulse will almost completely pass through the laser entrance hole of the hohlraum.

Frequency conversion is one example of the process of three-wave mixing. The crystals used in frequency converters are anisotropic, thus, frequency-conversion modeling must take account of the directions of the principal axes of the crystals with respect to the polarizations of electric fields in three-wave mixing. Frequency conversion is optimal at a phase-matched condition. Phase matching involves placing the principal axis of each crystal of the converter at a certain angular separation from the propagation direction. This angular separation, which must be accurate to within microradians, is called the phase-matching angle. The codes used for frequency-conversion modeling calculate phase-matching angles and the variation of converter performance for departures from the phase-matched condition. In mathematical terms, phase matching means that the difference between the wave number of the output harmonic field and the wave numbers of the input harmonic fields equals zero.

We can define the phase mismatch factor Δk as follows:

$$\Delta k = 2\pi/\lambda_h - 2\pi/\lambda_f - 2\pi/\lambda_g \ , \qquad (1)$$

where λ is the wavelength in the media, h denotes the output harmonic field, and f and g denote the input harmonic fields. Here, $\lambda = \lambda_0/n$, where n is the index of refraction, and λ_0 is the wavelength in vacuum. The value of n depends on the type of crystal material, the polarization of the field, crystal orientation, the local propagation angle of the electric field, the instantaneous wavelength if it is time-varying due to phase modulation, and temperature. Modeling codes must

*Los Alamos National Laboratory, Los Alamos, New Mexico.

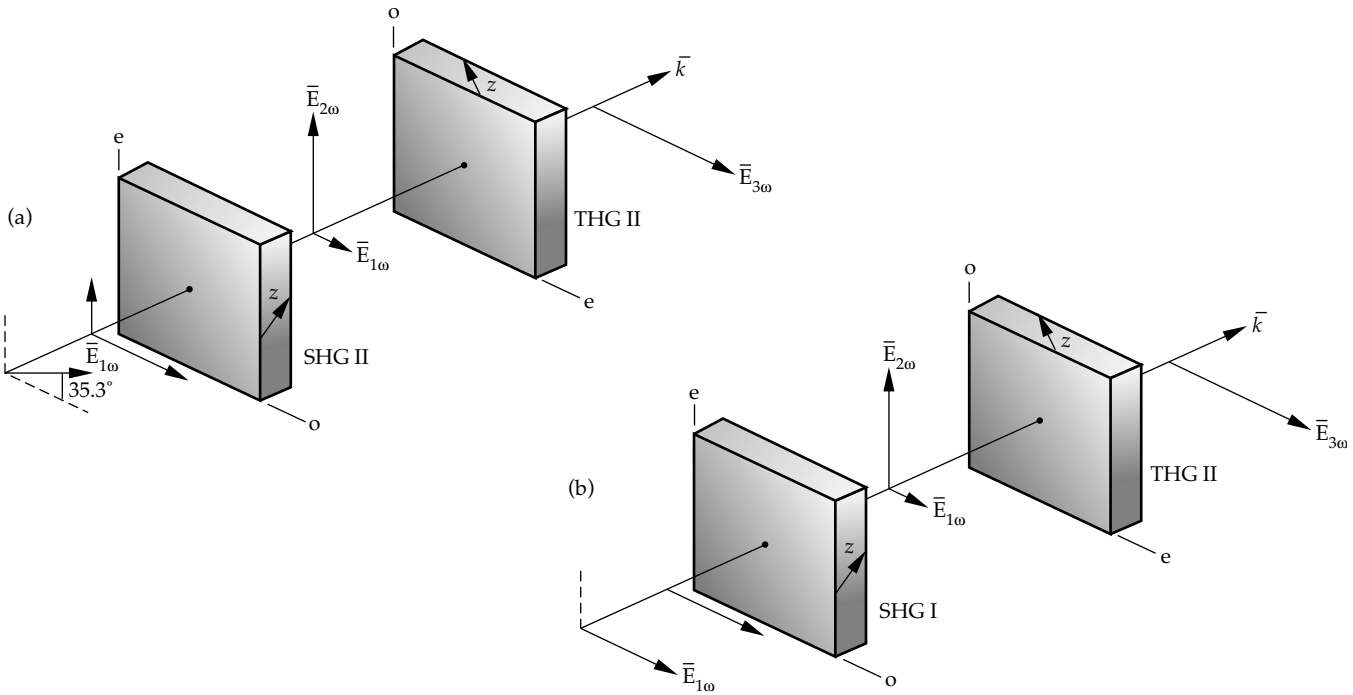

FIGURE 1. Schematic of two-crystal frequency triplers. (a) Type II/Type II crystal scheme and polarization directions for tripling. (b) Type I/Type II crystal scheme and polarization directions for tripling. 40-00-1296-2736pb01

take into account all these dependencies. Whereas $\Delta k = 0$ for phase matching, as we will show later, Δk is sometimes deliberately made nonzero in the SHG to obtain a certain amount of red and green light for the THG.

We have developed a class of frequency-conversion codes such that each code is differentiated from the others by the level of detail in the specification of the input electric field **E** to the converter. In the most general case:

$$\mathbf{E} = \mathbf{E}(x,y,z,t,\lambda_c) \ , \tag{2}$$

where, x and y are the transverse spatial coordinates, z is the coordinate in the direction of propagation, t is time, and λ_c is the center wavelength.

The different codes and electric field specifications are as follows:

1. For plane-wave steady-state fields:

$$\mathbf{E} = \mathbf{E}(z,\lambda_c) \ . \tag{3}$$

2. For plane-wave time-varying fields:

$$\mathbf{E} = \mathbf{E}(z,t,\lambda_c) \ . \tag{4}$$

3. For spatially varying steady-state fields (in three dimensions):

$$\mathbf{E} = \mathbf{E}(x,y,z,\lambda_c) \ . \tag{5}$$

4. For spatially varying and time-varying fields:

$$\mathbf{E} = \mathbf{E}(x,z,t,\lambda_c) \tag{6a}$$

for one transverse spatial dimension, and

$$\mathbf{E} = \mathbf{E}(x,y,z,t,\lambda_c) \tag{6b}$$

for two transverse spatial dimensions.

Types of Frequency Converters

The two types of crystal material used in the frequency converters for Nova, Beamlet, and the National Ignition Facility (NIF) are potassium dihydrogen phosphate (KDP) and deuterated potassium dihydrogen phosphate (KD*P). The crystals are of the negative uniaxial type.[1]

As shown in Fig. 1, each crystal can be operated in a Type I or Type II configuration. In a Type I configuration, incoming electric fields are all in one polarization direction, and the output harmonic field polarization is orthogonal to the input field's polarization. In a Type II configuration, incoming electric fields are orthogonal. The crystal axes along which the incoming electric fields are aligned are called the ordinary (o) and the extraordinary (e) axis. In the plane defined by the propagation direction and ordinary axis, there is no dependence of the index of refraction on crystal tilt angle θ. In the plane defined by the propagation direction and the extraordinary axis, the index of refraction varies with crystal tilt angle. This feature is used to adjust the phase mismatch Δk by a process called angular detuning.

In the following discussion, we denote the electric fields involved in the three-wave mixing process by f, g, and h. A scalar representation can be used because each field is in one polarization, which is parallel to either the ordinary or extraordinary axis of each crystal. In a SHG crystal, f and g represent the 1ω fields, and h represents the 2ω field. In a THG crystal, f represents the 1ω field, g represents the 2ω field, and h represents the 3ω field. In a Type I SHG, f and g are parallel to the ordinary axis, and h is parallel to the extraordinary axis. In a Type II THG, f and h are parallel to the extraordinary axis, and g is parallel to the ordinary axis. From these configurations and field conventions, we can formulate equations governing the evolution of fields in the converter crystals.

Equations of Frequency Conversion

The evolution of the f, g, and h fields in a crystal for the most general case, with $f = f(x,y,z,t)$, $g = g(x,y,z,t)$, and $h = h(x,y,z,t)$, is determined by solving the following set of coupled, nonlinear differential equations:

$$\partial f/\partial z + 1/v_{g1}\partial f/\partial t = iC(\theta)hg^*e^{i\Delta kz} - 0.5\alpha_1 f + k_0[\gamma_{11}|f|^2 + 2\gamma_{12}|g|^2 + 2\gamma_{13}|h|^2]f - i/2k_f(\nabla^2 f) - \rho f\partial_f/\partial r_e \ , \quad (7)$$

$$\partial g/\partial z + 1/v_{g2}\partial g/\partial t = iC(\theta)fh^*e^{i\Delta kz} - 0.5\alpha_2 g + i\lambda_1/\lambda_2 k_0[2\gamma_{21}|f|^2 + \gamma_{22}|g|^2 + 2\gamma_{23}|h|^2]g - i/2k_g(\nabla^2 g) - \rho_g\partial g/\partial r_e \ , \quad (8)$$

and

$$\partial h/\partial z + 1/v_{g3}\partial h/\partial t = iC(\theta)fge^{-i\Delta kz} - 0.5\alpha_3 h + i\lambda_1/\lambda_3 k_0[2\gamma_{31}|f|^2 + 2\gamma_{32}|g|^2 + \gamma_{33}|h|^2]h - i/2k_h(\nabla^2 h) - \rho_h\partial h/\partial r_e \ , \quad (9)$$

where ∇^2 is the Laplacian operator, which for Cartesian coordinates is:

$$\nabla^2 = \partial^2/\partial x^2 + \partial^2/\partial y^2 \ . \quad (10)$$

We derived Eqs. (7–9) by starting with Maxwell's equations for a nonlinear medium. The first term on the left side of Eqs. (7–9) is the derivative in the propagation direction to be integrated. We want to calculate the evolution of the three fields as a function of z, the propagation direction.

The second term on the left side of Eqs. (7–9) is used only in the conversion codes that model time-varying electric fields. Here, v_{gn} is the group velocity, where n = 1, 2, 3. The group velocity is defined by the equation

$$v_g = \partial\omega/\partial k \ , \quad (11)$$

where $\omega = \omega(k)$ is the dispersion relationship for a converter crystal material. The use of only v_g indicates that we are using only a first-order approximation to the dispersion relation. For the bandwidths in our modeling, this is an excellent approximation.

The first term on the right side of Eqs. (7–9) is the three-wave mixing or frequency-conversion term. (This term is included in all the types of our conversion codes.) Here, C is the coupling coefficient, which is a function of angle θ between the z axis and the principal axis of the converter crystal. The phase mismatch factor Δk is in the complex exponential. A nonzero value of Δk degrades the conversion.

The second term on the right side of Eqs. (7–9) corresponds to bulk absorption, where α_n denotes the absorption coefficients.

The third term on the right side corresponds to phase retardation arising from the nonlinear index of refraction. Note that the phase retardation for each field not only depends on its own intensity but also on the intensities of the other two fields. The quantities γ_{mn} are the nonlinear index coefficients. This term is included in all codes with temporal-field variations and/or spatial-field variations in at least one transverse dimension. It is not needed in plane-wave, steady-state codes because the uniform phase produced would have no effect.

The fourth term on the right side corresponds to paraxial diffraction. This term is included in codes where the fields vary in one or two transverse dimensions.

The fifth term on the right side is the "walk-off" factor, which is nonzero only if the field vector is in the extraordinary direction. Thus, we use the notation r_e for the coordinate in the extraordinary direction, which can be x or y, depending on the crystal configuration. The term ρ is the walk-off factor, which gives the variation of refractive index with angle θ. Walk-off accounts for the fact that, as a field propagates in a direction different from the phase-matching direction, it will no longer move with the other fields but will "walk off" from them because the index of refraction varies with direction.

Method of Solution

Equations (7–9) are solved by a split-step method to give the fields as a function of x, y, z, and t (or a subset of these variables, depending on the type of code). In this method, the derivative of each field with respect to z is split into two components with

different terms from the right hand sides of Eqs. (7–9). The integration for one component is carried out in the space–time domain, and the integration for the other component is carried out in the frequency/spatial-frequency domain. The terms in the equations are divided in the space–time domain according to:

- Frequency conversion (three-wave mixing).
- Passive loss.
- Nonlinear index phase retardation.

This part of the derivative of each field with respect to z is integrated using a fourth-order Runge–Kutta method.

The second component, which includes the time derivative of each field and the diffraction and walk-off terms, is integrated by first Fourier transforming the terms into the frequency/spatial-frequency (for x, y) domain. After the equations are transformed, they become ordinary differential equations in z instead of partial differential equations in x, y, z, t. The equations are then integrated with respect to z and inverse Fourier transformed to give the second component of the updated fields.

Thus, in Eqs. (12–14) below, we denote the angular frequency as ω and the wave numbers in the x, y , and extraordinary axes directions with κ_x, κ_y, and κ_e, respectively. After Fourier transforming the time-derivative, diffraction, and walk-off terms, the second part of the split-step solution involves integrating:

$$dF/dz = -i\omega/v_{g1}F + i(\kappa_x^2 + \kappa_y^2)/2k_f F + i\rho_f\kappa_e F \ , \qquad (12)$$

$$dG/dz = -i\omega/v_{g2}G + i(\kappa_x^2 + \kappa_y^2)/2k_2 G + i\rho_g\kappa_e G \ , \qquad (13)$$

and

$$dH/dz = -i\omega/v_{g3}H + i(\kappa_x^2 + \kappa_y^2)/2k_3 H + i\rho_h\kappa_e H \ , \qquad (14)$$

where F, G, and H denote the Fourier transforms of the second part of the split-step solution of f, g, and h. Here, κ_e can be either κ_x or κ_y depending on the orientation (x or y) of the crystal extraordinary axis. After Eqs. (12–14) are integrated with respect to z, the results are inverse Fourier transformed to give the second component of the updated fields. The two components of the fields are then added to give the total updated field after a z increment, Δz.

Outputs of the Codes

Our codes have various tabular and graphics outputs, which are illustrated below. In addition, the spatial and space–time codes can produce a file containing output harmonic and residual harmonic field distributions, which are compatible with the PROP92 propagation code. With this capability, we can propagate a converted beam through a set of optics using PROP92, as well as a 1ω beam created by PROP92 as the input 1ω field distribution for a conversion calculation.

Applications of the Frequency-Conversion Codes

Sensitivity Study of Doubler Detuning Angle by Plane-Wave Codes

As previously mentioned, the frequency-conversion crystals must be tilted with an accuracy of microradians for proper operation. This is especially true for a Type I SHG, where angular detuning is used to control the mix of 1ω and 2ω light into the THG. For design of the converter mounting and alignment equipment, it is important to know the alignment accuracy required for conversion efficiency within specifications. The variation of conversion efficiency with doubler detuning angle can be easily determined for a wide set of converter designs using the plane-wave frequency-conversion codes.

Figure 2 shows the output from a plane-wave frequency-conversion code. The plot shows 3ω conversion efficiency vs initial 1ω intensity for several values of SHG detuning angle. The latter quantity is the identifying parameter for each curve. The modeled converter configuration consisted of a 13-mm-thick KDP Type I SHG and a 11-mm-thick KD*P THG with a fixed detuning angle of 30 μrad. Notice that the sensitivity of

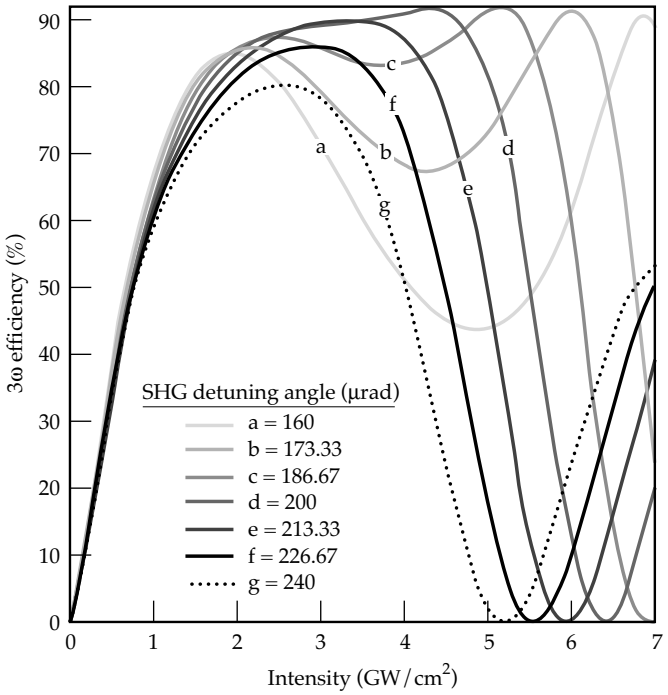

FIGURE 2. Output of plane-wave, steady, frequency-conversion code showing 3ω conversion efficiency as a function of input 1ω intensity for various doubler crystal detuning angles. 40-00-1296-2737pb01

converter performance increases with initial 1ω intensity. Thus, in considering the effect of SHG detuning angle alignment on converter performance for temporally shaped pulses, one must analyze the converter performance at the peak intensity of the shaped pulse. It is also important to note that conversion efficiency can drop off drastically as 1ω intensity increases. Decreased efficiency results from the incorrect ratio of 1ω and 2ω light into the THG. This behavior is important in the design of the dynamic range of the converter.

Effects of Applied Temporal Phase Modulation on Conversion

When phase modulation is applied to a field, $\mathbf{E}_0(z,t)$, the resulting field for a single modulation frequency f and depth of modulation σ is given by:

$$\mathbf{E}_{pm}(z,t) = \mathbf{E}_0(z,t)e^{i\sigma\sin 2\pi ft} \quad . \tag{15}$$

The bandwidth bw over which the phase modulation sweeps is given by:

$$bw = 2\sigma f \quad . \tag{16}$$

As the frequency sweeps from one limit to the other, the effective wavelength of each field also changes, which affects, in turn, the phase mismatch factor [Eq. (1)]. As the phase mismatch Δk varies, the conversion efficiency varies. It is this process that turns a periodic phase modulation into an amplitude modulation.

There are two current uses for applied phase modulation on laser pulses. First, bandwidth is used to suppress Stimulated Brillouin Scattering (SBS) in large optics. The bandwidth used in this application is 30 GHz. Our conversion codes show that this bandwidth causes a small degradation in conversion efficiency, which needs to be considered along with other degrading factors.

The second application is for beam smoothing by spectral dispersion. Plans are for 1ω bandwidths in the range of 90 to 150 GHz. Our frequency-conversion codes have shown that planned converter designs suffer significant degradation in performance at such large bandwidths.

In the following examples, we show how the temporal codes model conversion of laser pulses having complex time dependencies. We show the effects of applying a 150-GHz-bandwidth phase modulation on a laser pulse having a temporal shape like that proposed for NIF indirect drive. The converter design we used consists of a 12.7-mm-thick KDP Type I SHG and a 9-mm-thick KD*P Type II THG.

Figure 3(a) shows the 3ω intensity temporal pulse shape, and Figure 3(b) shows the 1ω intensity pulse used to generate the 3ω pulse for the case with no bandwidth. The two graphs were produced by one of the temporal frequency-conversion codes. The peak 1ω intensity is 2.75 GW/cm^2. The energy conversion efficiency was calculated to be 56.5%.

The code was then run a second time starting with the 1ω pulse of Fig. 3(b); however, a phase modulation with a bandwidth of 150 GHz was impressed on the 1ω pulse. Figure 4 shows the temporal profile of intensity of the resulting 3ω pulse. The calculated energy conversion efficiency is 43.4%. Thus, the energy conversion efficiency relative to that of the pulse of Fig. 3(a) decreases by about 13%. In addition, the pulse has severe intensity modulation at twice the phase modulation frequency. The lowest intensity values correspond to times when Δk is largest in magnitude, and the peak values correspond to the times when $\Delta k = 0$. These simulations show the need for alternate converter designs for large-bandwidth operation of NIF.

One of the alternate designs is a converter with one SHG and two THG crystals. The temporal frequency-conversion code shows that this design produces a

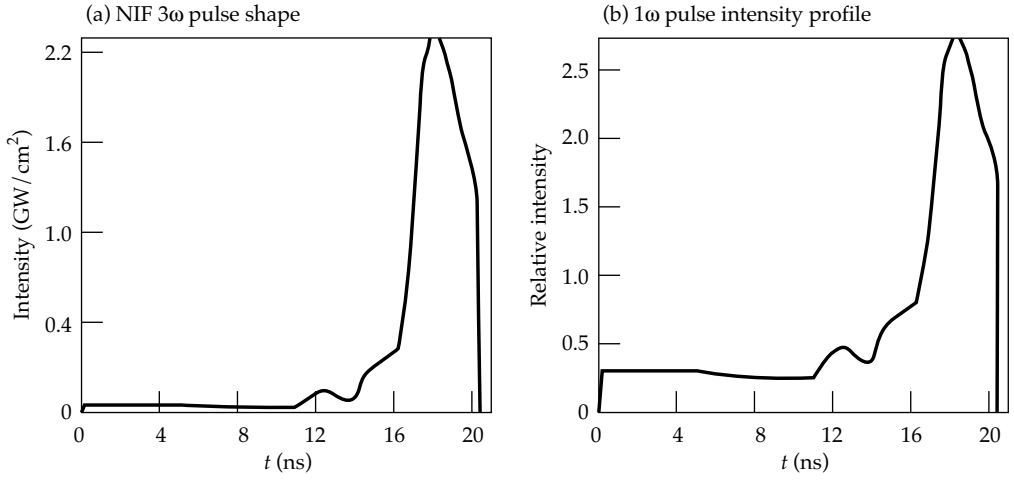

FIGURE 3. Sample output from the temporal frequency-conversion codes. (a) Temporal profile of intensity of a 3ω laser pulse with a NIF-like shape. (b) Temporal profile of intensity of the 1ω pulse derived from the pulse shape of (a) for a converter consisting of a 1.27-cm-thick KDP doubling crystal and a 0.9-cm-thick KD*P tripling crystal. 40-00-1296-2738pb01

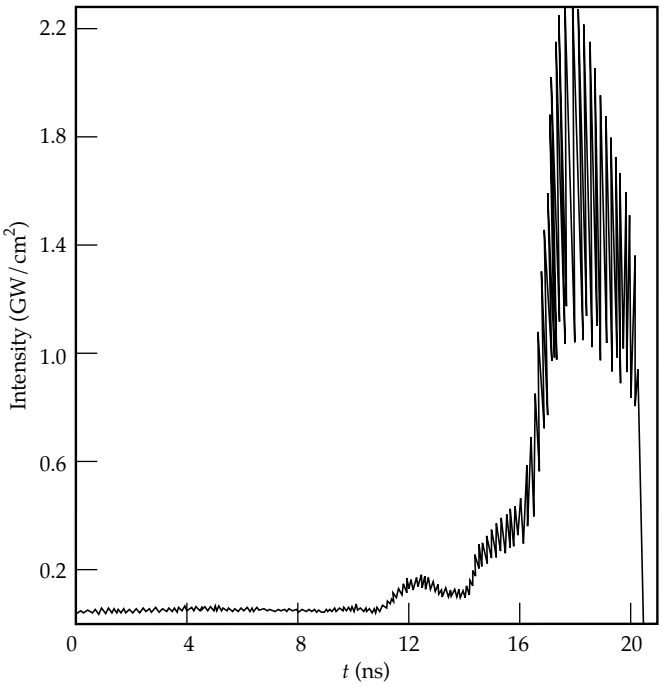

FIGURE 4. Temporal profile of intensity of the 3ω pulse produced when the 1ω pulse of Fig. 3(b) with 150 GHz of applied phase modulation is propagated through the two-crystal 1.27/0.9 converter. 40-00-1296-2740pb01

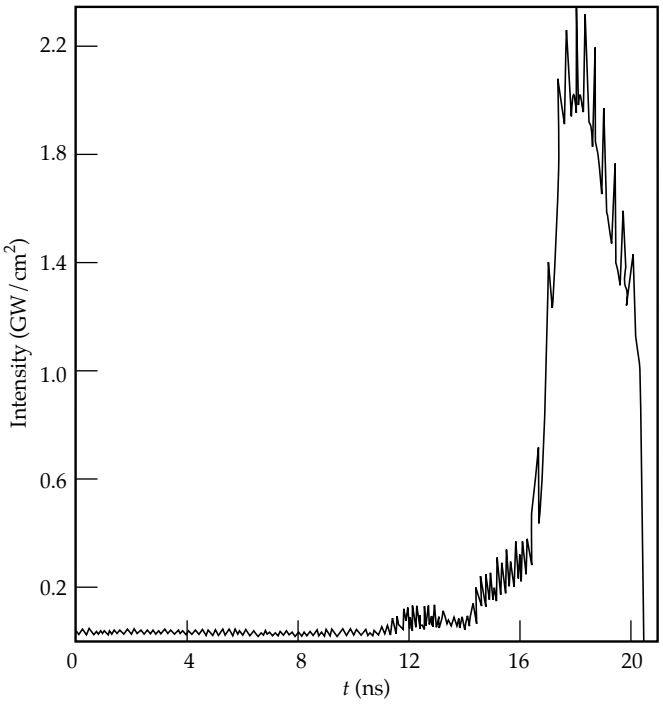

FIGURE 5. Temporal profile of intensity of the 3ω pulse produced when the 1ω pulse of Fig. 3(b) with 150 GHz of applied phase modulation is propagated through a three-crystal converter. The KDP doubler is 1.2 cm thick with a detuning angle of 210 μrad. The first KD*P tripler crystal is 0.7 cm thick with a detuning angle of 950 μrad. The second KD*P tripler crystal is 0.9 cm thick with a detuning angle of –350 μrad. 40-00-1296-2741pb01

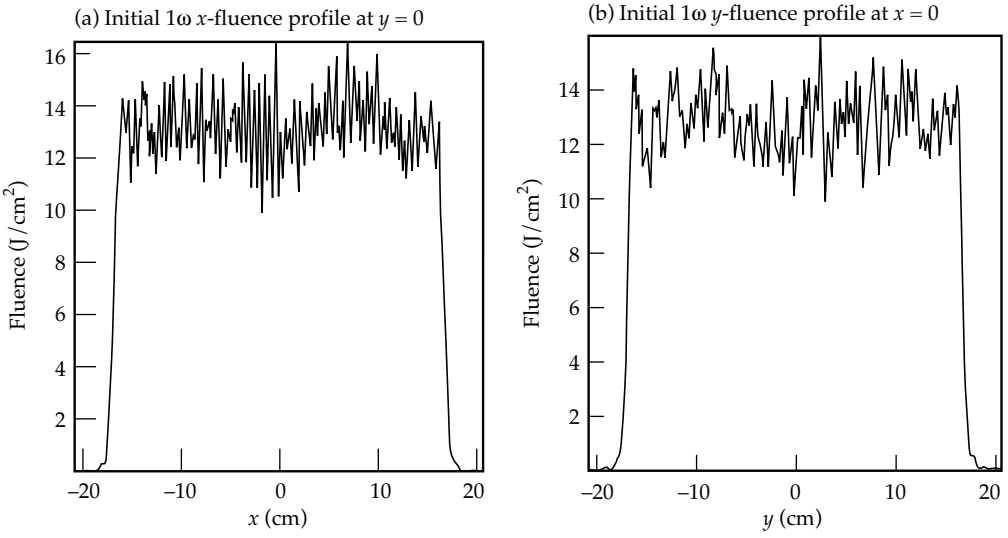

FIGURE 6. Profiles of fluence of the initial 1ω field distribution. (a) Center ($y = 0$) x profile of fluence. (b) Center ($x = 0$) y profile of fluence. 40-00-1296-2742pb01

much smoother 3ω pulse, as shown in Fig. 5. In addition, the calculated conversion efficiency is 53.3%, which corresponds to a drop of only 3% relative to that of the pulse of Fig. 3(a). For higher peak intensities in the NIF-like pulse, the difference in conversion efficiency between the two-crystal design and the three-crystal design will increase.

Simulations of Field Distributions with Temporal and Transverse Spatial Variations (x, y, z, t) Using PROP92

The PROP92 code models the propagation of laser beams with spatial variations in one or two transverse dimensions and a temporal variation represented in a

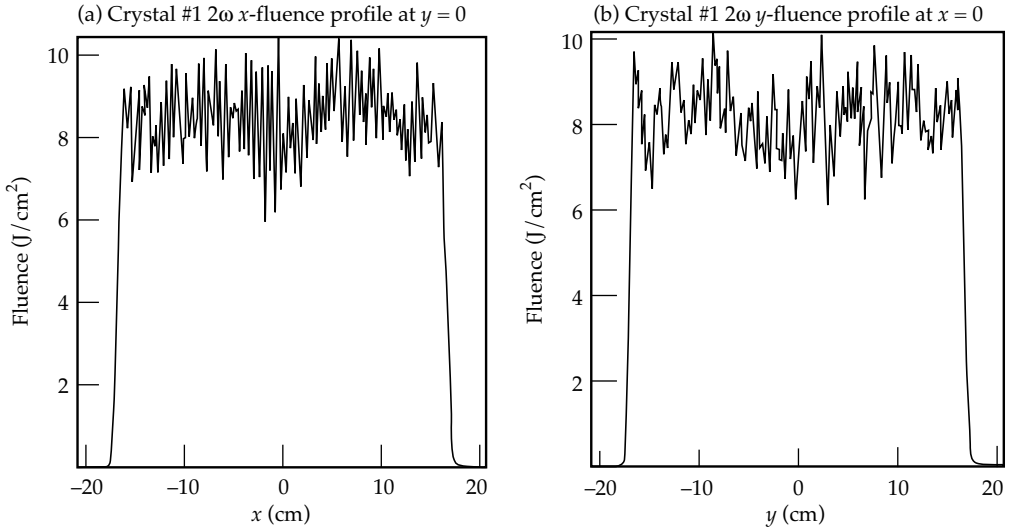

FIGURE 7. Profiles of fluence of the 2ω field distribution at the output of the doubler crystal. (a) Center ($y = 0$) x profile of fluence. (b) Center ($x = 0$) y profile of fluence. 40-00-1296-2744pb01

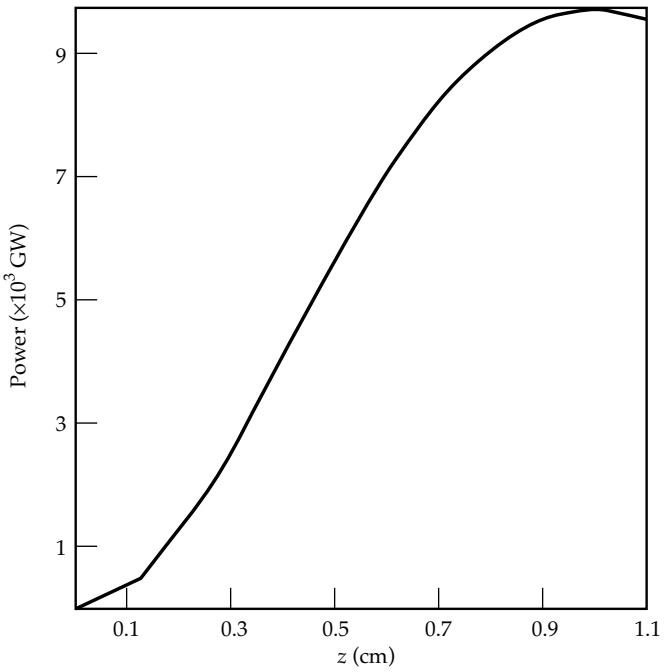

FIGURE 8. 2ω energy as a function of distance into the doubler crystal. 40-00-1296-2746pb01

discrete set of time slices. With this temporal representation, it is difficult to model conversion of fields with applied bandwidth, but it is easy to model beams with intensity envelopes of arbitrary temporal shape and no bandwidth. However, for small bandwidths and the converter designs of interest for NIF, the effects of bandwidth are small, and results from PROP92 are quite accurate. Following is an example of the use of the frequency-conversion code for which the fields are functions of x, y, z, and Δt_n, where Δt_n denotes the time slice array.

The 1ω field distribution used in this example corresponds to simulation of a shot on the Beamlet laser system in which the 1ω output fluence is 13 J/cm^2 in a 3-ns temporally flat pulse. The pulse is represented by three time slices. The first slice corresponds to the first 0.01 ns of the pulse; the second slice to the next 2.98 ns of the pulse; and the last slice to the last 0.01 ns of the pulse. Each slice is a field distribution defined on an x–y grid. Figures 6(a) and 6(b) show the center x and y profiles, respectively, of the initial 1ω fluence. The converter used in this example consists of an 11-mm-thick KDP SHG detuned at 240 μrad and a 9-mm-thick KD*P THG. The 1ω field distributions are propagated through the SHG. Modeled physical processes include frequency conversion, nonlinear index phase retardation, paraxial diffraction, and walk-off.

Figures 7(a) and 7(b) show the center x and y profiles, respectively, of the 2ω fluence distribution. The SHG energy conversion efficiency was calculated to 63.37%. This value is determined by the internal detuning angle, which is set as close as possible to produce equal intensities of 1ω and 2ω light into the SHG. Because the fields are spatially varying, only a few grid points of the beams will meet the equal-intensity condition for a specified detuning angle. Note that the 2ω fluence modulation is almost identical in shape to the 1ω fluence modulation, indicating that intensity dominates the conversion process. This result is expected because the phase profiles from the PROP92 calculation indicate only small transverse gradients. However, with large, local transverse phase gradients (which do not apply in the present example), the walk-off term can become large and affect frequency conversion.

Figure 8 shows the 2ω energy in the doubler crystal as a function of distance z into the crystal. Note the slight rollover in the curve at the end of the crystal, which indicates that the detuning angle was not quite at the value for optimum conversion.

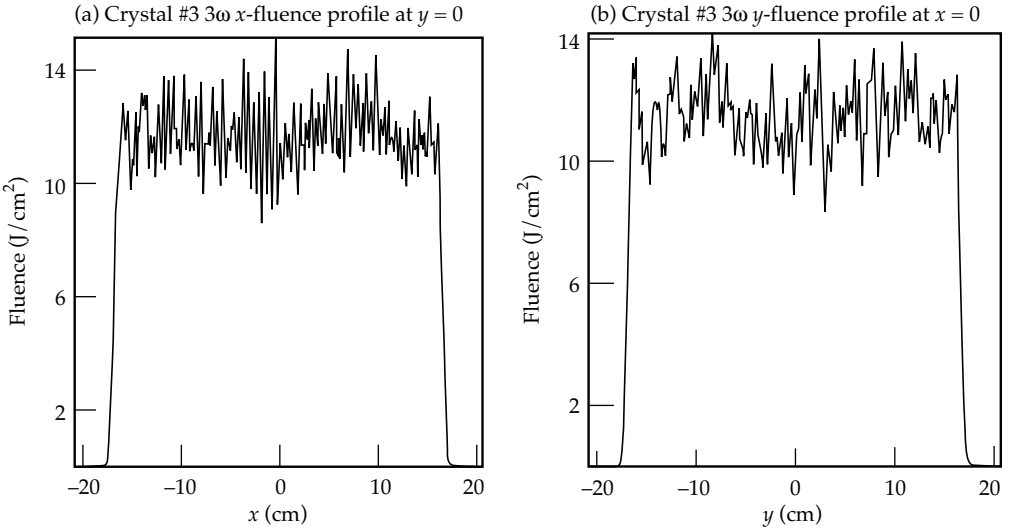

FIGURE 9. Profiles of fluence of the 3ω field distribution at the output of the tripler crystal. (a) Center ($y = 0$) x profile of fluence. (b) Center ($x = 0$) y profile of fluence. 40-00-1296-2747pb01

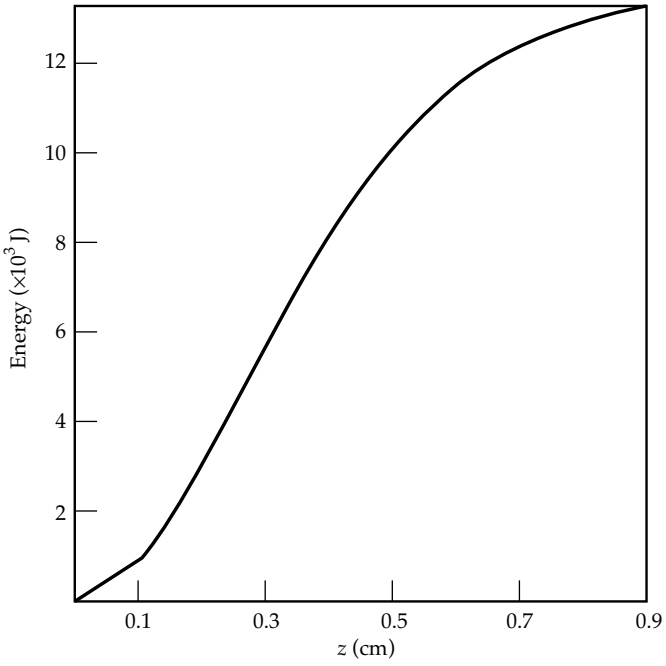

FIGURE 10. 3ω energy as a function of distance into the tripler crystal. 40-00-1296-2749pb01

Figures 9(a) and 9(b) show the center x and y profiles, respectively, of 3ω fluence. Once again, the modulation is almost identical to that of the 1ω fluence profiles, indicating that conversion is determined mainly by the intensity distributions of the fields and not by their phase distributions. Calculated 3ω energy conversion efficiency is 88.38%. Figure 10 shows the 3ω energy as a function of distance into the tripler crystal. The 3ω field distributions calculated by this code can be used as input to PROP92 to model propagation of the 3ω beam in the output section of Beamlet and NIF. The output section extends from the output of the frequency converter to the output of the final focusing lens.

Summary

Frequency conversion is a complex nonlinear process requiring precise tolerances for optimum results. The newly developed frequency-conversion codes have aided the designers of Beamlet and NIF in specifying the correct converter designs needed for a variety of operating scenarios.

References

1. J. F. Nye, *Physical Properties of Crystals* (Oxford University Press, 1986) pp. 237–238.

THE PROP92 FOURIER BEAM PROPAGATION CODE

R. A. Sacks

M. A. Henesian

S. W. Haney

J. B. Trenholme

Introduction

Numerical simulations of the laser beam propagation[1] have been used in designing and optimizing all of LLNL's high-power lasers for inertial confinement fusion (ICF). The architecture and design of the laser for the National Ignition Facility (NIF) were determined and optimized using a suite of new codes including CHAINOP, BTGAIN, and PROP92.

CHAINOP[2] is a very fast lumped-element energetics code with an extensive cost database, a choice of optimization algorithms, and a set of heuristic rules for diffraction and nonlinear effects and for operational constraints.

BTGAIN[3] is a far-field model based on the Bespalov–Talanov theory[4] for the linearized growth of decoupled single-mode beam perturbations in a nonlinear medium. It includes Frantz–Nodvik saturated gain, the facility to input beam perturbations of arbitrary spectral content at each component, and a postprocessor that can construct near-field beam statistics.

PROP92 was originally written and released by R. G. Nelson[5] in 1992, with advice and assistance from J. B. Trenholme. It is a full-featured optics propagation and laser simulation code. Internal models are included for most of the components in the optical amplifier and transport system. A Fourier technique is used to solve the nonlinear Schrödinger (NLS) equation, yielding a representation of the (single-polarization) complex electric field in two transverse directions plus time (2D) as the beam transports through and is affected by the optical elements. Alternatively, PROP92 can also operate in 1-D planar or 1-D circularly symmetric modes. In the latter case, Hankel/Bessel transforms are used instead of Fourier transforms. Average wavefront curvature is explicitly removed in the Talanov transformation. Both gain and nonlinear index effects are calculated in the near field with a split-step approach. Propagation is done in the far field.

In this article, we describe the algorithms and structure of the PROP92 code. We discuss 2-D operation, since the restriction to either 1-D planar or 1-D circular is straightforward.

Vacuum Propagation Algorithm

PROP92 describes the laser beam in terms of a complex electric field, $\mathbf{E}(x,y,z,t)$. The dominant plane-wave portion of the beam and its center-point position, tilt, and curvature are all explicitly removed to define a wave function u for numerical evaluation

$$\begin{aligned}&\mathbf{E}(x,y,z,t)\\&= \mathbf{e}e^{i(k_0 z-\omega_0 t)}e^{i[\bar{\kappa}_x(x-x_0)+\bar{\kappa}_y(y-y_0)]}e^{-ik_0(x-x_0)^2/2R(z)}\\&\times e^{-ik_0(y-y_0)^2/2R(z)}u(x,y,z,t)\ .\end{aligned} \tag{1}$$

In Eq. (1), the laser's optical frequency is ω_0, and the wave number is $k_0 = n_0\omega_0/c$, where n_0 is the index of refraction of the medium through which the beam is propagating, and c is the vacuum speed of light. The average tilt on the wavefront is described by the quantities $\bar{\kappa}_x$ and $\bar{\kappa}_y$, and the central position (x_0,y_0) satisfies

$$\begin{aligned}x_0(z+\delta z) &= x_0(z)+\bar{\kappa}_x\,\delta z/k_0\\ y_0(z+\delta z) &= y_0(z)+\bar{\kappa}_y\,\delta z/k_0\ .\end{aligned} \tag{2}$$

R is the average wavefront curvature, with the convention that positive R corresponds to a focusing wave. It satisfies

$$R(z+\delta z) = R(z)-\delta z\ . \tag{3}$$

The complex wave function u is represented on a regular rectangular grid

$$u_{j,k} = u(x_j + x_0, y_k + y_0, z, t) \ , \tag{4}$$

where j and k are integers in the range $-N_x/2 \le j < N_x/2$, $-N_y/2 \le k < N_y/2$, $x_j = jL_x \ / \ N_x$, $y_k = kL_y \ / \ N_y$, L_x and L_y are the physical dimensions of the calculational grid, and N_x and N_y are the number of grid points.

In a linear medium (no gain, no nonlinear index effects), the electric field obeys the wave equation

$$\nabla^2 \mathbf{E} - \frac{n_0^2}{c^2}\frac{\partial^2}{\partial t^2}\mathbf{E} = 0 \ . \tag{5}$$

Using Eq. (1) and applying the slowly varying ($\partial u/\partial t << \omega_0 u$) and paraxial ($\partial^2 u/\partial z^2 << k_0 \partial u/\partial z$) approximations, we find that u translates as

$$u(\mathbf{r}, z+\delta z) = \frac{R_0}{R}\int \frac{d^2\kappa}{(2\pi)^2} e^{i\frac{R_0}{R}\kappa\cdot\mathbf{r}} e^{-\frac{iR_0}{2k_0 R}\kappa^2 \delta z} \times \int d^2\mathbf{r}' \, e^{-i\kappa\cdot\mathbf{r}'} u(\mathbf{r}', z, t) \tag{6}$$

where $R_0 = R(z)$, and $R = R(z+\delta z)$. In Eq. (6), we can see the familiar Fourier propagation algorithm: (a) Fourier transform, (b) multiply each Fourier mode by a phase that is linear in propagation distance and quadratic in angle, and (c) inverse transform. Because u is represented on a discrete mesh, the continuous transform in Eq. (6) is replaced by a discrete fast Fourier transform (FFT). This means that the field is actually represented by a function that is periodic in both near-field and far-field coordinates. The effective grid dilatation apparent in the inverse transform is actually carried out in PROP92 by changing the values of L_x and L_y at the new observation point $z + \delta z$. Scaling the computational grid tends to maintain resolution for focusing beams (which would otherwise occupy progressively less of the grid) and avoids aliasing of defocusing beams (which would otherwise try to outgrow the grid and thus "wrap" information around the edges). The prefactor, R_0/R, may be thought of as scaling the intensity to conserve energy as the transverse extent of the beam changes.

Nonlinear Self-Focusing

In centro-symmetric (invariant under inversion through the origin) and isotropic materials, the single-frequency wave equation may generally be written as

$$\left(\nabla^2 + \frac{n^2(E)\omega^2}{c^2}\right)\mathbf{E} = 0 \ , \tag{7}$$

where the field-dependent refractive index is

$$n(E) = n_0 + \frac{1}{2}n_2 E^2 + \ldots \ . \tag{8}$$

Applying the slowly varying wave and paraxial approximations yields the NLS equation

$$\left[\frac{\partial}{\partial z} - \frac{i}{2k_0}\nabla_T^2 - \frac{2\pi i}{\lambda_{\text{vac}}}\gamma I\right]u = 0 \ , \tag{9}$$

where $\gamma = n_2/(n_0 c\varepsilon_0)$, λ_{vac} is the vacuum wavelength, and $I = n_0 c\varepsilon_0 |u|^2/2$ is the local irradiance. The parameter γ is a material property that measures the field phase advance per unit of intensity and per unit of length. Because n_2 and γ are positive for materials of interest, local high-intensity perturbations create their own focusing phase perturbations, thereby amplifying the perturbation, and ultimately leading to catastrophic filament collapse. Equation (9) is written with the intensity explicitly introduced because in PROP92, the electric field is normalized such that $|u|^2 = I$. As presented, Eqs. (5), (6), and (9) are not affected by this normalization choice.

In PROP92, nonlinear propagation effects are computed by a split-step algorithm. The propagation through the nonlinear medium is divided into a number of steps of length δz. Vacuum propagation steps [Eq. (6)] are alternated by thin-optic transformations,

$$u(x,y,z) \leftarrow u(x,y,z)e^{i\Delta B(x,y,z)} \ ,$$

where

$$\Delta B(x,y,z) = \frac{2\pi\gamma}{\lambda_{\text{vac}}}|u(x,y,z)|^2 \delta z \ . \tag{10}$$

For higher-order accuracy, the process is "leapfrogged," with a diffraction step of length $\delta z/2$ at the beginning and end of the nonlinear optic.

Research shows that PROP92's split-step algorithm agrees with experimental results both at 1ω and at 3ω[6,7] when sufficient resolution is included in the calculation. There are, however, two difficulties with simply relying on the propagation algorithm for computing all self-focusing threats:

1. Catastrophic self-focusing cannot occur in 1D,[8] but time and resource constraints require that we use PROP92's 1-D planar mode for much of our design optimization.[9,10]
2. Even in 2D, it is often not feasible to adequately resolve beam features at the sizes that are most prone to self-focusing amplification.

Given these difficulties, we have recently added[11] a number of features to the code to warn users about filamentation danger.

Sulem et al. have shown[12] that intensity perturbations of the most unstable size and shape will collapse, during propagation through a uniform nonlinear medium, in a distance such that $\Delta B_0 = \gamma I_0 \Delta z = 2.3$, where I_0 is the maximum intensity at the peak of the initial perturbation. By detecting and reporting the maximum over the transverse position of the ΔB through the thickness of any given optic, PROP92 tracks the safety margin with respect to collapse in that optic. To allow for optical gain (also calculated by a split-step algorithm), the maximum $\Delta B(x,y)$ is recalculated from the current z-position to the exit face of the optic at each z-step.

Before the NLS becomes singular, the collapse process is limited by nonlinear processes, such as optical breakdown (not included in the model). These breakdown processes led to the "angel hair" tracks in the Nova and Beamlet high-power optics. PROP92 has a test for breakdown-induced tracking, based on an extrapolation of the peak irradiance in the beam. Trenholme[13] has numerically verified that during the filamentation process, all perturbations evolve to a shape resembling the "ground state" (which collapses most rapidly) and that late in the collapse the intensity scales as $(z_c - z)^{-4/3}$, where z_c is the position of the singular collapse point. At each z-step through the slab, the maximum calculated intensity is scaled by $[z_c/(z_c - z_{exit})]^{4/3}$ to project a maximum anticipated self-focused intensity in the slab. A warning message is printed if this projected intensity exceeds a user-entered breakdown intensity.

Finally, PROP92 includes a check on the adequacy of the grid spacing to resolve the most important structure. This check is based on the Bespalov–Talanov (BT) theory of the linearized growth of independent Fourier modes.[3,4] If we expand u as

$$u(x,y,z) = u_0\left[1 + \sum_{\kappa} \alpha_\kappa(z) e^{i\kappa\cdot\mathbf{r}}\right] , \tag{11}$$

substitute u into Eq. (9), and drop terms of order α^2, we find that α_κ and $\alpha^*_{-\kappa}$ are coupled, and they grow such that

$$\begin{pmatrix} \alpha_\kappa(z) \\ \alpha^*_{-\kappa}(z) \end{pmatrix} = \begin{bmatrix} \cosh S\Theta - i\dfrac{\Theta - B}{S\Theta}\sinh S\Theta & i\dfrac{B}{S\Theta}\sinh S\Theta \\ -i\dfrac{B}{S\Theta}\sinh S\Theta & \cosh S\Theta + i\dfrac{\Theta - B}{S\Theta}\sinh S\Theta \end{bmatrix} \begin{pmatrix} \alpha_\kappa(0) \\ \alpha^*_{-\kappa}(0) \end{pmatrix} , \tag{12}$$

where

$$\Theta = \kappa^2 z/2k_0$$

$$B = \gamma u_0{}^2 z$$

$$S = \sqrt{1 - 2B/\Theta} \ . \tag{13}$$

Defining the mode amplitude as $|\alpha_\kappa|^2 + |\alpha_{-\kappa}|^2$, maximum gain at given κ occurs when

$$\alpha^*_{-\kappa} = e^{-i\phi}\alpha_\kappa$$

$$\phi = \frac{\pi}{2} + \tan^{-1}\left[\frac{\Theta - B}{S\Theta}\tanh S\Theta\right] . \tag{14}$$

This maximum modal gain is

$$G = 1 + \frac{2B^2}{(S\Theta)^2}\sinh^2 S\Theta$$

$$+ \frac{2B}{S\Theta}\sinh S\Theta\sqrt{1 + \frac{B^2}{(S\Theta)^2}\sinh^2 S\Theta} \ . \tag{15}$$

Maximizing G with respect to Θ, we find that the mode with maximum growth according to BT is

$$\Theta_{max} = B \tag{16}$$

PROP92 issues a warning if the spatial frequency of this mode is greater than the Nyquist frequency $\kappa_{Ny} = 2\pi \min(N_x/L_x, N_y/L_y)$.

Optical Damage

Besides tracking caused by nonlinear self-focusing, which leads to superhigh intensity and plasma formation, large optical *fluence* can lead to optical damage ranging from color-center formation to material fracture. So far, there is no adequate explanation of what causes the formation of these damage sites. However, Campbell et al. have compiled[14] an extensive experimental database of damage fluences for various materials during their exposure to nearly Gaussian pulses of various pulse lengths. When the pulse length is between about 10 ps and about 100 ns, the data are consistent with the scaling

$$\Phi_D = C\tau^{\beta} \quad , \tag{17}$$

where Φ_D is the fluence at which damage sites first appear, τ is the Gaussian pulse width, and C and β are material-dependent constants. In particular, β ranges between about 0.3 and 0.5 for the various materials of interest and is independent of τ, for a given material, over 4 to 5 decades of pulse duration.

For many applications, such as driving ICF targets on NIF, it is necessary to subject optical materials to high fluence with a temporal pulse history that does not resemble Gaussian. To assess the danger of optical damage from such pulses, we have implemented a phenomenological diffusion-like model,[15] for damage from arbitrarily shaped pulses.

The model assumes that damage is related to the accumulation of some quantity D whose source is proportional to the local laser irradiance, and which accumulates with a diffusive kernel. Damage is presumed to occur instantly if D exceeds some material-dependent critical value D_D. Trenholme demonstrated that no true diffusion model in 1, 2, or 3 dimensions can match the observed data. Rather, he was led to posit a form,

$$D(t) = A\int_0^{\infty} \frac{I(t-s)}{s^{d/2}}\, ds \quad , \tag{18}$$

where d is an effective dimensionality, I is the local irradiance, and A is a constant. Although Eq. (18) is formally singular when $d \geq 2$, this is not important because all existing damage data correspond to $d \leq 1$. Equation (18) is related to the measured data by substituting for I, a Gaussian with peak value I_D and full width at half maximum τ. Evaluating the maximum over t of the resulting damage integral gives

$$D_D = I_D A \tau^{1-d/2} \max_{\xi} \int_0^{\infty} \frac{\exp\left[-4\ln 2(\xi - s)^2\right]}{s^{d/2}}\, ds \quad , \tag{19}$$

where, for given d, the maximum of the integral is simply a number that can be evaluated once numerically, and the scaling with τ is explicit. Evaluating the fluence, Φ_D, for the same Gaussian pulse and setting it equal to $C\tau^{\beta}$ identifies d as 2β and yields

$$D_D = \frac{AC}{\sqrt{\pi}}(4\ln 2)^{\beta/2} \max_{\xi} \int_0^{\infty} \frac{e^{-(\xi-s)^2}}{s^{\beta}}\, ds \quad . \tag{20}$$

For each optic for which damage calculations are desired, the experimental scaling values C and β are input to PROP92. Equation (20) is then evaluated, and the limit value of the damage integral is stored. Each time that the beam passes that point in the laser chain, the damage integral [Eq. (18)] is evaluated for each spatial grid point on the calculational mesh. The maximum of the ratio D/D_D is reported. If that maximum is greater than one, a warning is issued and the damaged area fraction is reported. Note that the constant A drops out of this calculation.

Laser Component Models

PROP92 is a general-purpose computational tool for simulating the operation of laser chains and for optimizing their performance. To enable this process, it contains a library of models of the components that make up the chain and a sequencer that controls the order in which the beam encounters each of these modules. In 2D, the beam is stored as an $N_x \times N_y \times N_t$ array of complex numbers. We have already described how the propagation between components is modeled as an inverse FFT of a phase times an FFT of this array. We have also described how the array is diagnosed to assess the danger of filamentation or optical damage. In this section, we describe the transformations we use to model some of the more important optical components that comprise typical laser chains.

Slabs

In PROP92, a slab is a region of space, of length Δz, filled with a uniform medium of given n_0 and γ, with given small-signal gain G (at small input fluence, Φ_{in}, the output fluence is $G\,\Phi_{in}$), saturation fluence Φ_{sat}, and transmissivity T. If the gain is not unity, then gain typically depends on the transverse coordinates and evolves as part of the propagation algorithm.

Propagation through slabs is modeled by a split-step process, with the step size δz ($\Delta z/\delta z$ = integer) specified by the user. A propagation step with length $\delta z/2$ is followed by the application of nonlinear phase $B(x,y,\delta z)$ and a gain calculation (described below) that also correspond to length δz. After that, propagation steps of length δz are alternated with near-field effects corresponding to δz. A final propagation of length $\delta z/2$ completes the slab. Transmissivity is applied as a field multiplier at the slab entrance and exit.

The gain calculation is a simple Frantz–Nodvik[16] transformation. The initial slab gain $G(x,y)$ is divided equally among the z-slices—each has gain $g(x,y,z) = G(x,y)\,\delta z/\Delta z$. This array of real numbers is stored on disk and read into memory successively as needed. At each spatial point, the temporal dependence of the field is thought of as a sequence of piecewise-constant values, so a fluence $\Phi_j = |E(x,y,t_j)|^2\,\delta t_j$ can be associated with each time slice. As the j^{th} time slice at x,y passes

through the gain slice at x,y,z, the Frantz–Nodvick model for a two-level, homogeneously broadened laser line is

$$\Phi_{\text{out}} = \Phi_{\text{sat}} \ln\left[1 + g\left(e^{\Phi_{\text{in}}/\Phi_{\text{sat}}} - 1\right)\right]$$

$$g_{\text{out}} = \frac{g_{\text{in}}}{g_{\text{in}} - e^{-\Phi_{\text{in}}/\Phi_{\text{sat}}}(g_{\text{in}} - 1)} \quad . \tag{21}$$

The field for this time slice is scaled to the new fluence, and the gain distribution for this z-slice is overwritten by the new values so that the slab is cumulatively saturated.

Aberrations

PROP92 is capable of imposing a variety of phase aberrations on the field. Included are the low-order Seidel aberrations tilt, focus, astigmatism, spherical, and coma. Also, phase ripples,

$$E \leftarrow E e^{2\pi i a \cos(\mathbf{q}\cdot\mathbf{r} + \chi)} \quad , \tag{22}$$

can be applied at arbitrary amplitude, scale length, transverse direction, and phase. Another possibility is random phase noise with specified peak-to-valley amplitude and correlation length. Finally, an arbitrary phase-shift distribution can be specified numerically.

Lenses

A lens is treated as a combination of a slab (with unity gain but with some thickness and given linear and nonlinear indices) and a thin lens transformation,

$$R \leftarrow \frac{Rf}{R + f} \quad . \tag{23}$$

Lens aberrations must be specified as separate "aberration" components.

Spatial Filters

A spatial filter consists of two focusing lenses of focal lengths f_1 and f_2, separated by a distance $f_1 + f_2$, and a pinhole at the common focal plane. In a laser chain, spatial filters fulfill three important functions. First, since the field at the lens focal plane is a dimensional-scale and an intensity-scale of the incoming field's Fourier transform, the pinhole strips off the high-spatial-frequency portions of the beam. Otherwise the beam would be more prone to self-focusing. Second, in passing through the filter, the beam's transverse dimensions are magnified by the factor $m = f_2 / f_1$, with a corresponding change in irradiance. Third, since an object at distance d before the filter is imaged at a distance $m(f_1 + f_2 - md)$ after the filter, the evolution of long-scale-length phase noise into amplitude modulation is inhibited by proper placement of filters in the system.

Spatial filters can be treated as a sum of their constituent parts: a lens transformation, followed by a propagation of length f_1, clipping at the pinhole, propagation by f_2, and another lens. As long as the beam entering the filter is not focusing or defocusing, it is rigorously correct to use the lumped-element transformation implemented in PROP92 instead. The lumped-element transformation consists of clipping the Fourier transform of the field array, propagating through a negative distance $-(f_1 + f_2)/m$, magnifying the beam by m, and spatially inverting the beam in the transverse plane $E(x,y) \leftarrow E(-x,-y)$. PROP92 offers a variety of options for pinhole sizes, shapes, orientations, and transverse offsets (including the option to describe the filter function numerically). The pinhole edge is smoothed over several transverse grid steps to avoid aphysical numerical ringing.

Mirrors

Mirror components reverse the logical direction that the beam sequencer traverses chain components, enabling us to model multipass architectures. Tilts on the mirrors are permitted, affecting $\bar{\kappa}_x$ and $\bar{\kappa}_y$ in Eq. (1), and thereby affecting the beam's average transverse position as it samples aberration and gain fields. Recently, Henesian has added a model for phase-conjugating mirrors, including an intensity-thresholding effect.

Masks and Obscurations

Both masks and obscurations modify the beam by applying a near-field intensity filter that varies with transverse position. Both offer a number of built-in shapes and orientations. They offer control over the degree of edge smoothing, and both offer the option for numerical description of the filter function. A mask represents a filter that passes the center of the beam and removes the edge (such as would occur because of the finite physical aperture of chain components). An obscuration removes some small portion of the center of the beam (such as would occur if the beam struck a small obscuration). Obscurations also offer the option of applying a specified phase to a portion of the beam, to represent, for example, regions of surface irregularity or of bulk index variation.

Adaptive Optics

Adaptive optics are used in laser systems to correct for long-scale-length aberrations induced on the beam. At some point in the chain, the beam reflects from a deformable mirror. The mirror's surface can be distorted by as much as several wavelengths by displacing an array of mechanical actuators. At another point, a phase sensor is located. Operation of the adaptive optic consists of adjusting the displacement of the mirror actuators to minimize the transverse variation of the phase at the sensor.

On NIF, the deformable mirror is one of the end mirrors in the multipass cavity. Phase is detected by a Hartmann sensor, which consists of a lenslet array (on NIF it will be triangular) and a light sensor capable of detecting the centroid of the focal spot from each lenslet. The operational algorithm attempts to minimize the sum of the squares of the focal spot displacements. A transfer matrix is measured by observing the spot movements resulting from small travel of each of the actuators. A matrix inversion then predicts the actuator displacements necessary to best cancel a measured set of spot displacements. By placing this correction procedure into a feedback loop, continuous correction for time-varying effects (such as air-path turbulence and decaying thermal sources) has been accomplished.[17]

Modeling the correction procedure has two parts: (1) determining the beam phase modification accompanying a given set of actuator displacements and (2) finding the best set of displacements to use. For the first part, we have implemented a model where the mirror surface (hence the applied phase field) is assumed to be a sum of Gaussians,

$$\phi(x,y) = \sum_j a_j e^{-\left|\mathbf{r}-\mathbf{r}_j\right|^2/\sigma^2} \quad . \tag{24}$$

In Eq. (24), the sum is over the set of actuators, $\mathbf{r}_j$ are the set of centers of influence (nearly the same as the physical actuator positions), σ is the influence width, and the source strengths a_j are related to the actual actuator displacements. Typically, the $\mathbf{r}_j$ are located on a regular triangular or rectangular array with some outward displacement for the sources on the array boundary caused by their nonhomogenous environment. The values of $\mathbf{r}_j$ and σ are inputs to PROP92's adaptive-optic model. In one of its modes of operation, the a_j are also input parameters, in which case the component is modeled as a determined phase modification. This form of operation allows optimization of the best set of source strengths to meet some external objective, for example maximizing the energy into a hohlraum laser entrance hole.

In another mode of operation, PROP92 can adjust the a_j to apply a best local phase correction in minimizing the fluence-weighted mean square deviation from flat phase. "Adapt" components that are multipassed retain the shape that is determined the first time they are encountered. This method, since the phase correction is local and simply determined, is useful for obtaining a quick and reasonably accurate approximation of the performance enhancement that might be expected.

Although it is not strictly part of PROP92, Henesian has built up a realistic model of the adaptive optic operation as it will be implemented on Beamlet and NIF.[18] At the end of a PROP92 simulation of a chain, the field array is dumped to disk. This file is read by a postprocessor routine that simulates the action of the Hartmann sensor. Portions of the array are masked off and brought to focus, and the centroid of each focal spot is calculated. If there are N_a actuators, then N_a separate PROP92 runs are required to determine the transfer matrix, which is easily inverted (or SV decomposed if, as typically, it is nonsquare). For a given set of component aberrations, two more PROP92 runs suffice to measure the corrections required and to predict the performance with those corrections.

Plots

Considerable attention has been given to the graphical presentation of PROP92 results. At any point in the chain simulation, the user can display plots of near-field intensity, fluence, or phase—or of intensity or fluence either in the far field or in a partial focus region. These can be displayed as surface plots, contour plots, or cuts, either through specified position or through the maximum intensity point. The vertical scale can be linear or logarithmic. PROP92 has the capability to window the plots, which add resolution to a region of interest. As mentioned, PROP92 is capable of dumping the field array to disk, which enables us to use the graphical power of packages such as IDL for postprocessing.

Summary

PROP92 is a full-featured Fourier optics laser modeling, design, and optimization tool. It includes integrated models for a comprehensive set of optical elements and effects, as well as sophisticated algorithms for assessing the risk of optical damage and filamentation. As detailed elsewhere in this *Quarterly*, PROP92 predictions have been validated by comparison with Nova, OSL, and Beamlet experiments. Given reliable data on material properties and optical quality, we have confidence in PROP92's predictions of NIF performance.

Notes and References

1. W. W. Simmons, J. T. Hunt, and W. E. Warren, *IEEE J. Quantum Electron.*, **QE-17**, 1727–1743 (1981).
2. W. Williams, J. Trenholme, C. Orth, S. Haney, R. Sacks, et al., *ICF Quarterly Report* **6**(4), Lawrence Livermore National Laboratory, Livermore, CA, UCRL-LR-105821-96-4 (1996).
3. J. B. Trenholme, *1975 Laser Program Annual Report*, Lawrence Livermore National Laboratory, Livermore, CA, UCRL-50021-75 (1975), pp. 236–245.
4. V. I. Bespalov and V. I. Talanov, *JETP Letters* **3**, 307–312 (1966).
5. R. G. Nelson, "PROP92, A Family of Laser Beam Propagation Codes," Lawrence Livermore National Laboratory, Livermore, CA, internal memo (unnumbered), August 1992.
6. W. H. Williams, K. R. Manes, J. T. Hunt, P. A. Renard et al., *ICF Quarterly Report* **6**(1), 7–14, Lawrence Livermore National Laboratory, Livermore, CA, UCRL-LR-105821-96-1 (1996).
7. D. Milam et al., "Beam Breakup and Filamentation at the Third Harmonic Wavelength," Proceedings of the Second Annual International Conference on Solid State Lasers for Application to Inertial Confinement Fusion, Paris, France, October 20–25, 1996.
8. H. C. Yuen and W. E. Ferguson, Jr., *Phys. Fluids* **21**(8), 1275–1278 (1978); E. Fermi, J. Pasta, and S. Ulam, *Collected Papers of Enrico Fermi*, edited by E. Segré (University of Chicago, Chicago, 1965), vol. 2, p. 978.
9. W. Williams, S. Haney, R. Sacks, C. Orth, et al., "The 11-0-7 NIF Laser Design: Description and Background," Lawrence Livermore National Laboratory, Livermore, CA, memo NIF-LLNL-96-283 (1996).
10. S. W. Haney, W. H. Williams, R. A. Sacks, J. M. Auerbach, and C. C. Widemeyer, "Report on Work Package #1: NIF Energetics Under Reduced Slab Count/Reduced PAM Size Operation," Lawrence Livermore National Laboratory, Livermore, CA, memo NIF-0000582 (1996).
11. M. A. Henesian, "Simulations of 3ω Beam Filamentation in the Beamlet Focus Lens and General Comments on Filamentation Theory," Lawrence Livermore National Laboratory, Livermore, CA, memo LS&T-LMO-96-001 (1996).
12. P. L. Sulem, C. Sulem, and A. Patera, "Numerical Simulations of Singular Solutions to the Two-Dimensional Cubic Schrödinger Equation," *Communications on Pure and Applied Mathematics*, (John Wiley and Sons, New York), vol. XXXVII, pp. 755–778.
13. J. B. Trenholme, "Overview of Basic Filamentation Concepts," Laser Modeling and Optimization talk, August 17, 1995; see also J. T. Hunt, "A Comparison of Nova and Beamlet's Design Margin Against Filamentation," Lawrence Livermore National Laboratory, Livermore, CA, memo NIF-LLNL-95-498, L-20374-01 (1995).
14. J. H. Campbell and F. Rainer, "Optical Glasses for High-Peak-Power Laser Applications," Lawrence Livermore National Laboratory, Livermore, CA, UCRL-JC-109255 (1992); Proceedings of the 1992 SPIE Conference, San Diego, CA, July 19–24, 1992.
15. J. B. Trenholme, "Damage from Pulses with Arbitrary Temporal Shapes," Lawrence Livermore National Laboratory, Livermore, CA, memo LST-LMO-94-001 (Ver. 2) L-18179-2 (1995).
16. L. M. Frantz and J. N. Nodvik, *J. Appl. Phys.* **34(8)**, 2346–2349 (1963).
17. M. W. Kartz, W. C. Behrendt, R. G. Hartley, A. F. Hinz, et al., "Wavefront Correction for Static and Dynamic Aberrations to Within 1 Second of the System Shot in the NIF Demonstration Facility," Second Annual International Conference on Solid State Lasers for Application to Inertial Confinement Fusion, Paris, France, October 22–25, 1996.
18. M. A. Henesian, S. W. Haney, M. Thomas, and J. B. Trenholme, "Modeling for Deformable Mirrors and the Adaptive Optics Optimization Program," Second Annual International Conference on Solid State Lasers for Application to Inertial Confinement Fusion, Paris, France, October 22–25, 1996.

NOVA/BEAMLET/NIF UPDATES OCTOBER–DECEMBER 1995

G. Hermes/R. Speck/S. Kumpan

Nova Operations

During this quarter, Nova Operations fired a total of 294 system shots, resulting in 324 experiments. These experiments were distributed among inertial confinement fusion (ICF) experiments, Defense Sciences experiments, X-Ray Laser experiments, Laser Sciences, and facility maintenance shots.

A second, 8× magnification, x-ray charge-coupled device (CCD) camera was installed and activated on the 10-beam chamber. The east and west 8× CCD cameras will replace the film based pinhole cameras currently being used to acquire x-ray images from precision pointing shots. We are currently characterizing these cameras and doing a direct comparison of the data with the existing pinhole cameras. Using the CCD cameras will greatly reduce the time required to analyze data from the pointing shots.

A complete design review is planned for the second quarter to examine the design requirements and cost of upgrading Nova to have spatial beam smoothing capabilities on all 10 beamlines. Currently, only beamlines 6 and 7 (BL–6 and –7) have the capability of smoothing by spectral dispersion (SSD). Adding SSD to all beamlines will require modification to the pre-amplifier beamline and the addition of 10 phase plates on the target chamber.

We are also reviewing the design requirements that would provide beam phasing capability to the Nova system. Beam phasing would allow us to divide each Nova beamline spatially into two halves and then to propagate two different pulse shapes through each half. At the target chamber, we would use phase plates to separate and position the beams, as required, to provide two uniform rings of illumination at each end of a hohlraum target. Each of the two rings could have a different pulse duration and shape and could be separated temporally to provide the desired laser irradiation. We are also looking into combing the capability of beam phasing with SSD.

In support of the ongoing Petawatt project, the compressor vacuum chamber was installed in the 10-beam target bay. This vacuum chamber (9 ft i.d. and 43 ft long) contains an input and output turning mirror, the diffraction gratings used for pulse re-compression, a diagnostic beam-reducing telescope, and other optics to direct the diagnostic beam outside of the chamber. An initial set of large aperture (ϕ75 cm) gratings are being fabricated for installation into the compressor, planned for the second quarter. A preliminary set of laser output diagnostics was designed and component orders have been placed. This system will also be installed and activated next quarter.

Also for the Petawatt project, a new beamline was designed for injecting the pulse from the Petawatt Master Oscillator Room into the Nova laser. The optics, mounts, and associated equipment for this beamline should be available for installation and activation during the third quarter. We are planning for a series of test shots late second quarter that demonstrate pulse compression with this system at low energy. The compressor chamber will not require vacuum for this series and the pulses will not be propagated to the target chamber.

We continued the activation and characterization of the 100 TW system. The focal spot size at the center of the 2-beam target chamber was measured to be approximately 16 μm × 22 μm using an attenuated 10 Hz (short pulse) beam. This results in about 10^{20} W/cm^2 at 40 J in 400 fs.

Beamlet Operations

During this quarter, we completed the installation, alignment, and activation of a major addition to Beamlet—a large vacuum tank equipped with optics to focus and characterize the third-harmonic beam (3ω) generated at the output of Beamlet. We also installed and activated a number of diagnostics associated with

this system that will measure the properties of the beam at the plane of an inertial confinement fusion (ICF) target. We plan to use these systems to evaluate the effectiveness of focal-spot beam-smoothing schemes proposed for the National Ignition Facility (NIF), including phase plates and smoothing by spectral dispersion (SSD). The system will also provide the opportunity to test the focusing optics to be used on the NIF at operating fluences. In initial experiments done during this quarter, we measured the prime focus of the 3ω beam both with and without a phase plate. The diagnostics ready for these initial experiments included:

- Energy diagnostics consisting of a whole-beam calorimeter that measures the sum of all wavelengths, and a set of small calorimeters and diodes that measures individually the 1ω, 2ω, and 3ω energy and power.
- 1ω pointing and centering diagnostics to establish and maintain beam alignment to the focusing optics.
- Medium and narrow field-of-view imaging diagnostics to record the focal spot.
- A temporary imaging diagnostic to record the 3ω near-field beam.

At the end of the quarter, we performed several shots at 200-ps pulse duration to extend our study of 1ω near-field beam modulation at the Beamlet output. By analyzing these shots, we can determine the power threshold for severe beam breakup and filamentation that could damage Beamlet optics and can aid in determining the performance limits of the NIF laser design. In this series, we propagated a short (200 ps FWHM) high-power pulse from the cavity amplifier through the unpumped booster amplifier to simulate the conditions at the end of a long, highly saturating pulse and examined the near-field output beam carefully for evidence of breakup and filamention. We obtained higher resolution images, using an improved near-field imaging system. The system consists of a CCD camera with 1024×1024 pixels to record a 25 cm square portion of the beam and optics with a wider angular acceptance. In the December series of shots, we obtained data from several image planes between the frequency converters and 11.5 m beyond the converter location. These data will be helpful in determining the optimum location of the frequency converters, and the length of the NIF transport spatial filter. An analysis of the data is being performed.

We finished the design and initiated procurements for diagnostics to do central dark-field imaging of the 1ω focal spot at the Beamlet output. The purpose of these measurements is to determine the distribution of scattered light at small off-axis angles. We plan to install and activate this diagnostic during the second quarter.

NIF Design

This quarter, the Department of Energy (DOE) authorized funding to begin the Advanced Conceptual Design (ACD) for the NIF Project. Due to the delays in the FY 1996 congressional budget process, the Title I Design work was postponed until late December, at which time the full $61M for the fiscal year was received.

The ACD prepares the Project for the engineering design activity to be conducted during Title I. By the end of the quarter, the Project organization was in place and the NIF staff exceeded 75 people. Major contractors were chosen for the building architectural design and for engineering support. The Ralph M. Parsons Company was chosen for design of the Laser and Target Area Building (LTAB) and A.C. Martin for the design of the Optics Assembly Building. Master Task Agreements for engineering support were placed with TRW, SAIC, Westinghouse, and Physics International. Engineering tasks were assigned to the participating ICF laboratories (Los Alamos National Laboratory; Sandia National Laboratory, Albuquerque; and the Laboratory for Laser Energetics at the University of Rochester.

The ACD engineering activity centered around several major tasks, all leading to the general arrangement of the special equipment and the overall size of the LTAB. These tasks include: the design impact of incorporating capability for direct-drive physics experiments, determination of the need for beam expansion at the end of the laser, the length of the spatial filters, and the accommodation of requirements for the radiation effects users. Another important activity was the preparation of requirements and design concepts for assembly and maintenance of the laser system optical components and for the Optics Assembly Building. A review will be held in February to discuss the design work conducted during the ACD. Concurrent with ACD activity the NIF Project's *Primary Criteria and Functional Requirements* top-level document, which provides a hierarchy of all design requirements, was reviewed and revised. During the second quarter, the DOE will review proposed changes to this document.

NOVA/BEAMLET/NIF UPDATES JANUARY–MARCH 1996

G. Hermes/R. Speck/A. Clobes

Nova Operations

During this quarter, Nova Operations fired a total of 309 system shots resulting in 319 experiments. These experiments were distributed among inertial confinement fusion (ICF) experiments, Defense Sciences experiments, X-Ray Laser experiments, Laser Sciences, and facility maintenance shots.

As planned, we held a design review to discuss upgrading Nova to include spatial beam smoothing capability on all 10 beamlines. In support of this upgrade, a prototype phase plate and debris shield holder was fabricated, installed, and tested on the 10-beam target chamber. A prototype of the kinoform phase plate (KPP) was also fabricated and used on several target experiments. The KPP produces a smoother focus spot on target than the present phase plate and is planned to be used on the National Ignition Facility (NIF). Design modifications to the optical system for the preamplifier beamline modifications were completed, and the orders were placed. The substrates and finishing required for the KPPs were also ordered. Experiments using beam smoothing on all 10 beamlines are planned for the fourth quarter.

In support of the ongoing Petawatt project, we achieved the following tasks:

- Completed the vacuum compressor chamber and vacuum leak tested the system.
- Installed and aligned primary optical components required to demonstrate pulse compression (mirrors, gratings, and diagnostic telescope).
- Activated the basic diagnostics required to measure pulse width and bandwidth.
- Installed and aligned the new injection beamline from the Petawatt Master Oscillator Room to the Nova laser.
- Took several shots at low energy and with the compressor at atmospheric pressure to check the initial system performance.
- Obtained a low-energy compressed pulse of ~650 ps.
- Scheduled full-power shots to demonstrate Petawatt performance to be done during the third quarter .

We also developed a design for a small target chamber to be installed between the compressor and 10-beam target chamber to allow using the Petawatt beam for simple target experiments that do not require the full diagnostic capability of the 10-beam chamber. This configuration would provide more flexibility and would allow the Nova system to support Petawatt target shots without impacting the 10-beam target chamber. A final design review for the mini-chamber is scheduled for the third quarter.

Several modifications were made to the 100-TW system to improve system reliability and performance:

- Reviewed the design and purchased the hardware for a closed loop alignment system to improve system shot-to-shot stability and repeatability. Installation is planned for the third quarter.
- Installed a graphical user interface to the control system to allow the operators to configure the system more efficiently.
- Relocated the power conditioning hardware outside the oscillator room, due to excessive electrical noise problems.
- Ordered several spare parts to reduce system downtime during maintenance and repair.

To reduce film handling, processing, and digitizing, we use charge-coupled-device (CCD) cameras. We modified one of the six-inch-manipulator (SIM) based diagnostics used on the 10-beam target chamber to replace its film back with a CCD camera. We plan to modify an additional SIM diagnostic with a CCD camera by the end of FY 1996.

Beamlet

During the quarter, experiments continued on Beamlet to validate the laser physics foundations for the NIF design and addressed the following issues:

- Controlling the growth of near-field amplitude modulation in the 1.06-μm laser amplifier.
- Determining the source terms for scattered light, and its nonlinear amplification at high power in the 1.06-μm laser.
- Performing large-area damage tests and online damage conditioning of KDP.
- Performing online conditioning tests of high-fluence 1ω reflective coatings.

All of these experiments are part of long-term continuing campaigns that will include two or more experimental series.

The shots to study near-field beam modulation were in support of a working group studying the power and energy limits imposed on the output of the 1.06-μm laser by the nonlinear growth of optical noise that originates from imperfections in the beam optics. In this series, we studied the increase in near-field modulation at several planes beyond the booster amplifier output as the B-integral increased and as a function of pinhole size in the cavity and transport spatial filters. With 200-ps pulses, we used pinholes as small as 130 μrad in the cavity spatial filter and 100 μrad in the transport filter. As expected, and in contradiction to the observation made on Nova, the smaller pinholes produced smoother beams. We produced pulses with B-integrals up to, and exceeding, the NIF requirement with well controlled modulation and no evidence of filamentation. We have not yet tested small pinholes with long, high-energy pulses required for NIF; this will be an issue in future experiments.

We activated a new dark-field imaging output diagnostic to provide sensitive measurements of small-angle scattered light at the Beamlet 1ω output. This diagnostic improves our ability to accurately measure optical noise within the band between 33 and 800 μrad half angle and will allow us to quantify noise amplification that results from nonlinear phase retardation effects. We fired low- and high-power shots with various cavity pinhole sizes and dark field image blocks in the initial series to measure the noise power.

In support of the NIF materials development group, we performed large-area damage tests on KDP samples. The tests determined an unconditioned damage threshold of 8 J/cm^2 and demonstrated that large area online conditioning of KDP in a vacuum environment is effective.

We installed a set of four high-damage-threshold 1ω mirrors between the output transport spatial filter and the frequency converter, simulating the NIF transport mirror system, to investigate the feasibility of online conditioning. The alternative offline raster scan conditioning is time consuming and costly; if online conditioning can be demonstrated, it provides a more cost-effective and efficient substitute. Two of the four mirrors were offline conditioned and the other two were to be online conditioned. Anomalously high amplitude modulation (3 to 1, peak/average) at the output of Beamlet occurred on two shots early in this series. In each case, both of the unconditioned mirrors were damaged and the tests had to be terminated. The offline conditioned mirrors were more robust—only one damaged on one of the shots. We will renew our attempt to demonstrate online conditioning later in the year when additional mirrors become available.

We also removed two cavity amplifier slabs and replaced them with recently refinished slabs. During the disassembly, we noticed some degradation of amplifier components and are investigating the cause. The slabs removed had been finished using unoptimized small-tool polishing techniques. We will use high-resolution interferometry to characterize these slabs to determine if refinishing is necessary, and the laser modeling group will use the data in propagation modeling.

National Ignition Facility

During the quarter, we began Title I design, which was initially affected by delays in the Project FY 1996 total estimated cost funding. To support Title I design efforts, we updated the technical basis of the design, increased Project staff to the planned levels, developed key Project controls and documentation, and developed support infrastructure required to support the design support. The NIF Project activities are now proceeding as planned.

The technical basis of the design was updated through a formal technical review process that included the following:

- Completing an Advanced Conceptual Design (ACD) review in February, including technical and financial impacts of user requirements.
- Updating the Primary Criteria/Functional Requirements.
- Updating and improving the System Design Requirements.
- Developing optics assembly capability requirements.
- Updating the laser system design/performance baseline.

Key Project controls and reporting procedures were put in place, including the following:

- Implementing the *NIF Project Control Manual*, the *Configuration Management Plan*, and the DOE-approved *Quality Assurance Program Plan*, and providing training on key procedures and configuration management.
- Installing the commercial NIF Sherpa Product Data Management system that provides a project-wide centralized document engineering drawing, and configuration-control capability.

- Establishing cost account plans and authorizations for each work breakdown structure element.
- Developing a detailed Title I design schedule.
- Establishing regular Title I baseline costs and schedule reviews to track progress.
- Preparing and distributing monthly and quarterly progress reports.

To reflect the national scope of the NIF Project, the NIF participating Laboratories agreed to, and implemented, the following expanded workscopes:

- Sandia National Laboratories (SNL) expanded the workscope includes conventional facilities management, construction management, mechanical systems integration, target area structure analysis, the target experimental data acquisition system, and diagnostic system integration. The SNL team includes engineering design staff at Sandia—Livermore, California.
- The expanded Los Alamos National Laboratory workscope includes structural support for key optomechanical assemblies (cavity mirror, Pockels cell polarizer, and extra-cavity turning mirror) and target area robotics.
- The Laboratory for Laser Energetics at the University of Rochester expanded workscope includes large-aperture polarizer coatings and exploration of production capabilities for high-performance, large-aperture optics coatings.

All major contracts for the Title I design have been decided including the architecture/engineering contract for the Laser and Target Area Building (LTAB), contracted to Parsons; the Optics Assembly Building (OAB), contracted to A. C. Martin; the Construction Manager, contracted to Sverdrup; Engineering Design Services contracted to Northrup/Grumman, TRW, Physics International, and SAIC; and Management Services, contracted to XEC and LRL.

The laser system design was updated through an optimization analysis performed by a NIF Project and ICF Core Science and Technology team. This update resulted in a NIF laser configuration that is improved from the Conceptual Design Review (CDR) version. The design (the 11-0-7 configuration) has an 11-slab main amplifier, no switch amplifier, and a 7-slab boost amplifier that meets the NIF 1.8-MJ and 500-TW on-target technical requirements. This design is comparable in cost to the CDR design within the available resolution, and it meets the NIF functional requirements at lower risk. Design improvements include:

- A lower filamentation risk due to lower B-integral (1.8 vs 2.1).
- Greater similarity to the Beamlet 11-0-5 configuration, thereby reducing development costs and risks.
- Elimination of switch amplifier magnetic field interactions with the adjacent plasma electrode Pockels cell.
- Fewer laser support structures, and a shorter LTAB length.

Significant design progress has been made in all areas. Following extensive functionality and cost analysis of various building layouts and configurations, Title I design of the LTAB building began. A general arrangement of the facility was developed and is now in configuration control, and laser layouts have been incorporated into the overall facility layout (Fig. 1). Locating the LTAB and OAB at the preferred Livermore site has also been completed, which minimizes site development costs.

(a) LTAB ground level view

(b) LTAB composite view

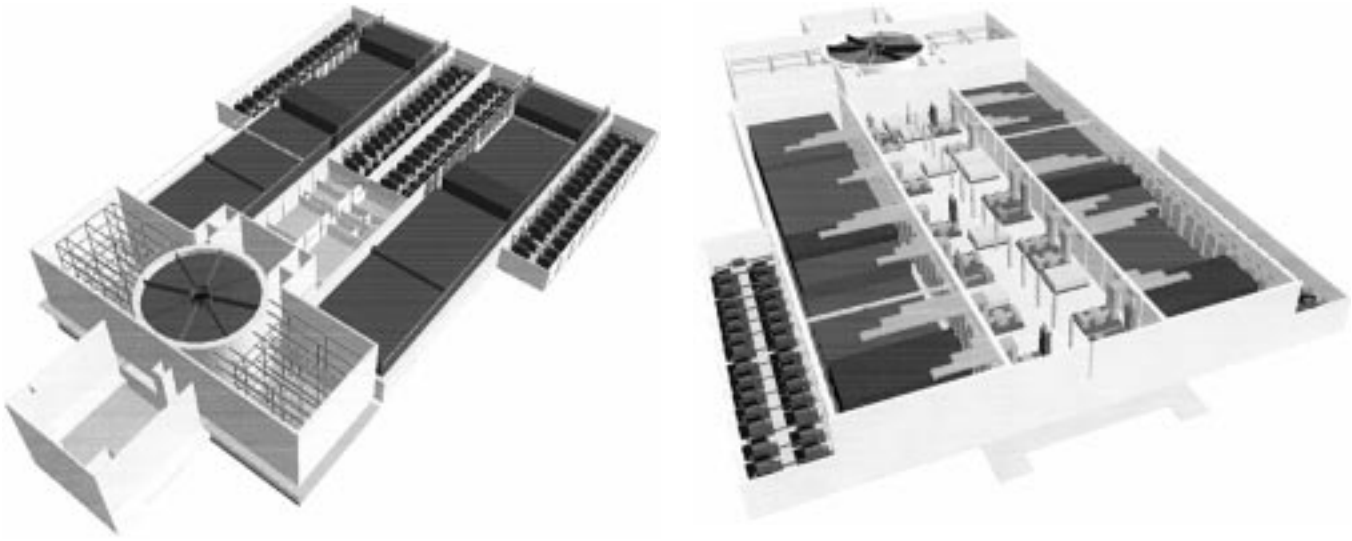

FIGURE 1. 3-D CAD models for the NIF Laser and Target Area Building (LTAB). (40-00-0496-0847pb01)

In the laser area, we completed the design analysis to determine pumping uniformity of the end slabs in the amplifier. The analysis shows that the required uniformity is met without the addition of end lamps. Design iterations, based on finite-element analysis on all the laser bay support structures, have been completed. These structures were re-engineered from the CDR to minimize construction costs and to improve their performance in terms of increasing the first resonant frequency a significant 20%. Designs for bottom loading line replaceable units (such as amplifier cassettes) into the beamline have been developed.

We completed the beamline optical component layouts within the LTAB. The design includes first-order raytrace to establish the approximate spacing between the optical components followed by the Code V layouts that provide detailed locations of the optical components. The optical sizes of the main laser components have been determined and clear aperture analysis is under way.

The NIF is a part of the Stockpile Stewardship and Management (SSM) Programmatic Environmental Inpact Statement (PEIS). The SSM PEIS reaffirms the Secretary of Energy's statement during Key Decision One that LLNL is the preferred site for the NIF. In support of the PEIS, writeups, supporting analysis, and reviews have been provided to the DOE, as well as a Preliminary Safety Analysis statement draft document. A final site selection will occur after public review of the SSM PEIS and a formal Record of Decision by the Secretary in September 1996.

During the third quarter, the mid-Title I design review will be conducted, and we will continue toward completion of the conventional facilities Title I design in September and special equipment design in October, as scheduled.

NOVA/BEAMLET/NIF UPDATES APRIL–JUNE 1996

G. Hermes/R. Speck/A. Clobes

Nova Operations

During this quarter, Nova Operations fired a total of 274 system shots resulting in 288 experiments. These experiments were distributed among ICF experiments, Defense Sciences experiments, X-Ray Laser experiments, Laser Sciences, and facility maintenance shots.

As a result of gradual budget reductions over the past several years, the number of Nova Operations staff has been slowly reduced to the point that a standard double-shift operation is no longer able to be supported. In an attempt to improve facility performance, the Nova Operations group formed a team to evaluate the use of an alternate work schedule for system operations. The previous schedule consisted of two standard eight-hour shifts overlapping by one hour, five days per week. The team reviewed a variety of work schedules to determine which schedule would best meet criteria provided by the Program. As a result of their study, the team recommended four ten-hour days per week of two shifts overlapping by three hours. This alternate schedule provides slightly more time for experiments, while leaving adequate maintenance time and without requiring the use of regularly scheduled overtime. As of June 10, the operations personnel have been working this new shift. Preliminary evaluation of this work schedule indicates that the system shot rate is very near that of the standard two-shift operation and that system maintenance has improved.

A final design review was presented by Los Alamos National Laboratory for phase 2 of the Full Aperture Backscatter Station (FABS II). This diagnostic incorporates a reflecting telescope to produce a high-resolution image of the target plane. Subsequent to the review, LANL determined that the primary turning mirror produced a second surface reflection that resulted in unacceptable interference with the signal from the first surface. An alternate mirror will be coated with a wide-band, high-reflective coating on the first surface to eliminate this issue. The installation schedule for FABS II will be reevaluated after the coating of this mirror.

The Gated X-Ray Imager #5 (GXI 5), modified last quarter to use a charge-coupled-device (CCD) camera readout, is still undergoing development. During initial activation, several problems were noted and repaired. We are continuing to use this camera as opportunities arise to complete testing and work out any additional issues. The use of a CCD camera allows immediate viewing of data following a system shot.

In ongoing support of the Petawatt Project, we completed the following:

- Installation and activation of the compressor vacuum system.
- Installation and alignment of a subaperture beam-diagnostic station to support the May shot series.
- Demonstration of subaperture pulse compression in a vacuum by achieving 1.25 PW during the May shots.
- Continued system installation and activation in preparation for the full-aperture Petawatt demonstration.

We are developing a plan to install a minichamber between the Petawatt compressor and the ten-beam target chamber. This minichamber will be used during the initial Petawatt demonstration to measure system performance and beam spot at focus. The detailed engineering continues for the parabolic mirror mount, target alignment viewer, and miscellaneous diagnostic hardware required to support target experiments with the Petawatt system.

We are removing the one-beam chamber located in the west end of the two-beam area to provide a lab area for the testing of the NIF final optics assembly. Other assembly processes and hardware stored in this area are also being relocated.

Beamlet

Beamlet continues to provide the testbed to validate the laser physics foundations of the National Ignition Facility (NIF) and to check laser engineering concepts and components proposed for the NIF. During the quarter, activities on Beamlet included the following:

- We quantified the limits on power output of the NIF 1.06-μm laser design that are safe from beam filamentation in the system's 1ω optics.
- We obtained far-field images in the new dark-field-imaging diagnostic that quantified the fraction of the 1ω power scattered at small angle as a function of laser output power.
- We installed reworked 37-cm aperture frequency-conversion crystals.
- We upgraded the 3ω focal-plane diagnostic system.
- We began a series of shots to characterize the 3ω focal spot and assess the damage threat to the final optics components.
- We activated an improved control system for the deformable mirror that will allow correction for gas turbulence.

The shots to study beam filamentation propagated 200-ps-duration pulses through the unpumped booster amplifier to simulate the conditions at the end of long, high-energy, saturating pulses. The short pulses provided a "snapshot" of the most stressful part of the saturating pulse and greatly reduced the irradiance averaging that takes place when a near-field image of the entire pulse is taken. The most important diagnostic in this series was a high-magnification near-field camera recorded by a 1024 × 1024-pixel CCD camera. The results confirmed that the NIF can operate safe from filamentation with delta-B values of up to 1.8 and can have adequate margin for beam-to-beam and shot-to-shot fluctuations in output. Smaller pinholes (130 μrad in the cavity spatial filter and 100 μrad in the transport filter) provide added margin over the standard 200-μrad pinholes and are preferable.

Dark-field image data of the 1ω output were also gathered from 200-ps pulses and an unpumped booster amplifier. Much of the data came from the same shots as the 1ω near-field modulation data. The diagnostic system measured the fraction of the power scattered outside far-field beam blocks of ±33, ±66, and ±100 μrad. The data provides a measurement of (1) power scattered from imperfections and finishing errors on the optics at low laser output power and (2) the growth in this scattered power with increasing laser power. This information is useful in determining noise source values for use in laser propagation modeling.

Beginning in mid-May, we installed refinished 37-cm-aperture frequency-conversion crystals on Beamlet following their characterization on the high-resolution phase matching interferometer. At this time we also aligned and calibrated the Phase II diagnostics for the 3ω focal-plane diagnostics system. New diagnostics include a very-high-resolution near-field camera that records on photographic film, a medium-resolution near-field camera that records on a CCD array, a wide-field-of-view calorimeter, a 3ω streak camera, a multiple-plane 3ω far-field camera, and a number of new and upgraded energy sensors.

Experiments to investigate 3ω beam quality and focusability began in early June following the calibration of the new diagnostics and the angle tuning of the conversion crystals. We fired a total of 19 shots in this campaign; 14 to measure the 3ω beam quality and focal spot and 5 to characterize the focal spot obtained with a kinoform phase plate (KPP). Ten of the 14 shots without the KPP were with 200-ps-duration pulses and with the booster amplifiers unpumped to achieve delta-Bs of up to 1.8 rad at power levels up to 2 TW. We investigated both small pinholes (130-μrad cavity/100-μrad booster) and large pinholes (200-μrad/200-μrad). The focal spot data at 2.8 TW power with and without a KPP yielded 80% power half angles of 33 μrad and 20 μrad respectively and 95% power half angles of 53 μrad and 32 μrad. Preliminary analysis indicates that the spot size is strongly influenced by thermal effects in the amplifiers, as well as by output power.

At the end of June, we completed the activation of the T_0-1 second wavefront correction system. This system allows the deformable mirror to run in closed loop up to one second before shot time and thus provides the capability for wavefront correction up to the last second before shot time. On a limited number of shots during its activation, the system corrected wavefront error caused by turbulence on shots taken early in the day but was increasingly unable to make the correction as the heat accumulation in the amplifiers and the corresponding turbulence increased after repeated shots, indicating that turbulence cell sizes become smaller than the deformable mirror could correct due to its finite actuator separation.

National Ignition Facility

We made significant progress in Title I design this quarter; based on current accomplishments, the Project is expected to meet all FY 1996 critical-path milestones and complete the design as planned in September (Laser and Target Area Building conventional facility) and October (special equipment and Optical Assembly Building). The Mid-Title I Design Review, completed at the end of May, served as an interim checkpoint in the design process. The status of the mid-Title I design was presented to a review committee consisting of individuals from all the participating Laboratories as well as outside reviewers. The recommendations and comments were documented and assembled into a package and distributed to Project personnel for use in updating the design.

While the three-month total estimated cost (TEC) funding delay slowed NIF staffing and delayed the start of design, a catch-up plan was developed and implemented and is working well. This catch-up is based on a well integrated NIF/ICF team, augmented by effective use of Master Task Agreements (MTAs) with commercial companies, coupled with rapid narrowing of design options.

Engineering documentation and infrastructure are developed to the degree necessary for the current design effort. The Computer Aided Design and Drafting (CADD) systems are fully operational, the Product Data Management (Sherpa) hardware and software are implemented, and the required subsystem design requirements and interface control documents are in place.

In addition and in parallel with the intensive design effort, Title I cost and schedule estimates are being developed in all areas. The system and database are operational, with inputs generated by the responsible engineers and the system and rates controlled by the NIF Project Office. Initial inputs are essentially complete, and verification is under way.

Specific progress in the various areas is outlined below.

- The contract for construction management services was awarded to Sverdrup, and personnel were onboard for the Mid-Title I Design Review. Fast tracking is being considered to meet the construction schedule milestones, and special construction methods are being evaluated.
- The NIF general arrangement drawings for the NIF Laser and Target Area Building (LTAB) have been completed and are under configuration control. Design iterations continue for cost containment and reduction to assure that the design results in the minimum platform to achieve the requirements.
- An embedded laser-amplifier structure that offers important installation and operational advantages over the original conceptual design was developed and is the basis of the Title I design. This approach also simplifies utility interfaces above the amplifiers, which are now an integral part of the structure.
- Following an extensive technical and cost tradeoff evaluation, we selected flexible transmission lines for power conditioning over rigid lines and established a routing layout. Flexible lines result in easier installation and improved accessibility.
- We optimized the preamplifier module/preamplifier beam transport system layout to permit the output sensor packages to be located underneath the transport spatial filter for reduced cost and improved stability and operational accessibility. We completed the preamplifier module maintenance area layout and utility requirements.
- We have successfully resolved numerous conflicting requirements in the beam transport system and have established an end-to-end comprehensive design solution (see Fig. 1). Space allocations have been frozen for all laser bay and switchyard subsystems. Baseline switchyard and laser bay structures, which meet all stability, access and safety requirements, have been established and integrated with the other systems.
- We selected a hybrid concrete-steel construction early in the quarter for use on all the laser bay support structures. Detailed analysis confirmed the performance advantage of the hybrid structure over all-steel or all-concrete structures. The laser support structures have been integrated with all other subsystems.

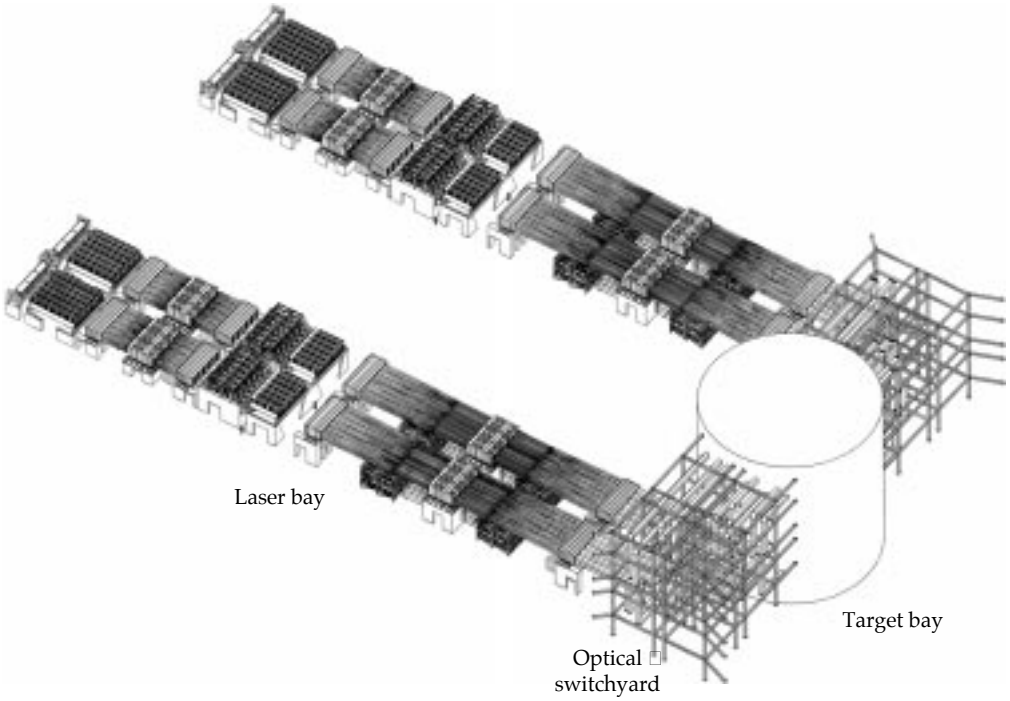

FIGURE 1. A comprehensive "end-to-end" integrated design has been developed. (40-00-0796-1771pb01)

- In collaboration with the ICF Core Science and Technology Program, a NIF prototype automatic-alignment loop, based on analysis of the beam profile and commercial Datacube processing system, was activated and is undergoing tests. CORBA and Ada95 software, which are planned for NIF use, are currently being tested in the front-end processors.
- We established the optical component layout for the main laser system. Title I optics sizes and thickness have been established, component spacing issues resolved, and configuration drawings generated for the laser optical train. We have completed individual system elements of the clear-aperture budget analysis, and integration and consistency checks are in progress.
- We resolved complicated design issues in the transport spatial filter, including optics locations, and paths for injection, alignment, diagnostics, wavefront control, and main beams. The optical stability has been improved by use of top-loading towers separate from the vacuum chamber.
- Major revisions to the target area design were carried out to incorporate the color separation filter in the final optics assembly. The beam transport codes were revised, the building configuration modified, new analytic models of the building developed, and the mirror supports redesigned and presented at the Mid-Title I Design Review.
- The finite-element integrated target-building/switchyard-structures model was refined to reflect the most recent design details (see Fig. 2). We continue to analyze structural/damping supports between the chamber/pedestal and target building floors. We delivered structural drawings of the target room floors, ribs, columns, and associated equipment loads to the LTAB Architecture/Engineering firm, Parsons, for their civil and structural analysis. Layouts of the target room floors and special equipment lasers were also delivered so that Parsons could model the area for the thermal analysis.
- Material flow studies have been effective in resolving LTAB corridor, doorway, and elevator size requirements. Development continued on requirements for optics transport and handling, and requirements for top-loading line replacable units were evaluated.
- The *Final Programmatic Environmental Impact Statement* is complete except for DOE comment resolution. The *Preliminary Safety Analysis Report* was completed as scheduled and submitted to DOE for concurrence review.

Twelve students from colleges and universities throughout the country, representing a number of technical disciplines, are employed by the NIF Project for the summer supporting the above activities.

Planning for the Title I Design Review is well under way. The Title I Design Review Plan was completed and released to Project personnel for their use in detailed planning of the remaining Title I work. The plan includes the overall objectives, organization, and schedules, as well as the agenda for the review meetings and contents of the Design Basis Books. The overall chairman of the review committee was selected and considerable progress made in identifying review committee members that will include DOE and external reviewers.

During the coming quarter, Title I documentation packages including design, cost, and schedule will be prepared, and the Title I Design Reviews will begin.

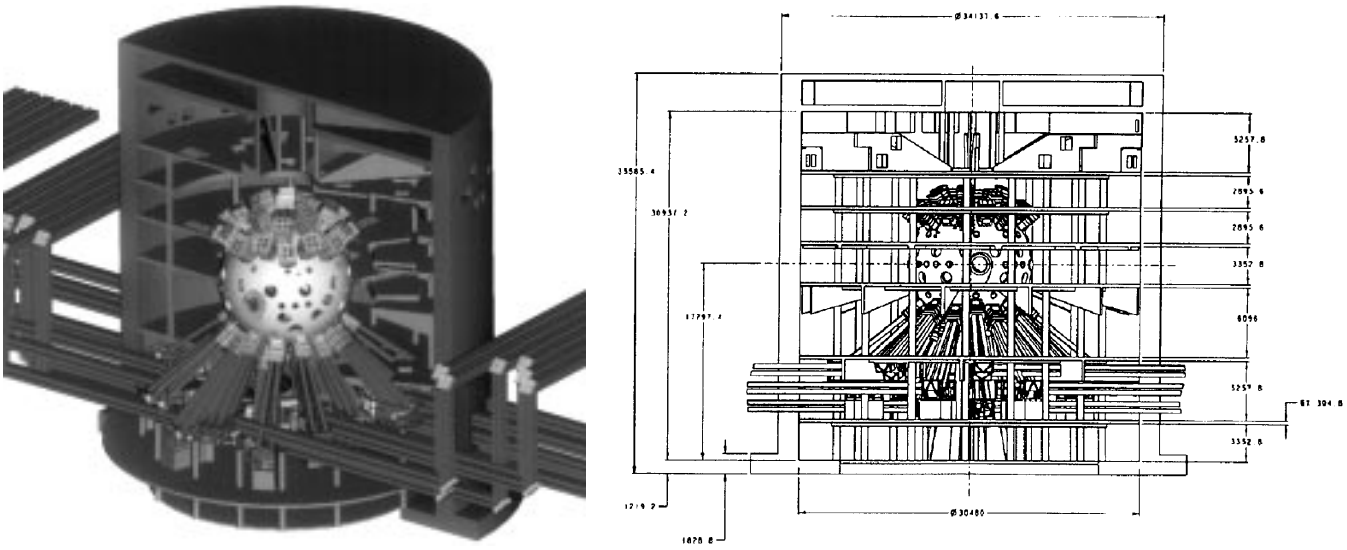

3-D CADD model NIF drawing no. NM96-1.8.1-0000044-A

FIGURE 2. Engineering drawings are rapidly emerging from a comprehensive 3-D solid CADD model. (40-00-0796-1633pb01)

NOVA/BEAMLET/NIF UPDATES JULY–SEPTEMBER 1996

G. Hermes

R. Speck

A. Clobes

Nova Operations

During this quarter, Nova Operations fired a total of 314 system shots resulting in 320 experiments. These experiments were distributed among ICF experiments, Defense Sciences experiments, X-Ray Laser experiments, Laser Sciences, and facility maintenance shots.

This is the final report for FY 1996. During the past year, Nova fired a total of 1192 system shots resulting in a total of 1263 experiments. There were 981 target experiments done in the 10-beam chamber and 86 experiments done in the 2-beam chamber. There were 110 experiments conducted in support of laser science work, including precision pointing, Petawatt system activation, and miscellaneous beam propagation experiments. We fired 85 calibration shots in support of routine and precision operations.

We have started implementing smoothing by spectral dispersion (SSD) on all 10 beamlines of Nova. Hardware for the preamplifier grading table and relay lens assemblies was installed this quarter. Experiments using 10-beam SSD are planned for FY 1997.

A conceptual design for a 4ω probe beam for the 10-beam chamber has been completed. This beamline will be created by a "pick-off" mirror installed into the center obscuration of beamline 8 in the switchyard. This subaperture, 1ω beam will be propagated to the 10-beam chamber, where it will be converted to 4ω and used as a target diagnostic probe beam. Actual installation of hardware will begin next quarter.

In continuing support of the Petawatt Project, the design of the Petawatt minichamber was completed and fabrication has started. This minichamber will be used during the initial Petawatt demonstration to measure system performance and beam focusability. Installation of the minichamber is planned for January 1997. The design of the parabolic mirror system that will be used for the Petawatt beam on the 10-beam chamber has been completed. The vacuum housing and mirror gimbals for the parabola are being fabricated. The vacuum system for the Petawatt compressor chamber was also installed and activated.

The Gated X-Ray Imager #5 (GXI 5), modified to use a charge-coupled device (CCD) readout, is continuing to be used as a secondary diagnostic to provide opportunities for shakedown and activation. The GXI is also being characterized off-line to evaluate its performance using the CCD readout as compared to film. The use of a CCD camera allows immediate viewing of data following a system shot.

Beamlet

During the fourth quarter of FY 1996, experiments done on Beamlet addressed the following issues:

- Correcting the wavefront for thermally driven gas turbulence in the amplifiers and the beam tubes.
- Measuring the 3ω conversion efficiency of the 34-cm output beam, the modulation of the 3ω near-field beam at the focus lens, and the 3ω focal-spot energy distribution.
- Conducting large-area damage tests of KDP at 3ω.
- Determining the performance of Beamlet with 20-ns pulses shaped like those required for indirect-drive ignition on NIF.
- Measuring the contrast ratio and beam modulation of the near-field beam input into the main amplifier.

The Beamlet control system was modified to allow the adaptive optics system to correct the beam wavefront up to one second before shot time (T-1s) to provide a capability to correct for gas turbulence effects in the beam path. To test this system, we fired shots to compare the 1ω spot size and beam brightness with and without the T-1s system. We observed that beam quality was improved with the T-1s system but that the improvement was smaller than expected. Because Beamlet has no active cooling system, we saw a more

dominant effect from the accumulation of thermal distortion with repeated shots. Spot size and small-angle scatter increased substantially when repeated shots separated by 2-h intervals were fired. After the fourth shot, up to 15% of the energy was scattered outside of 33 μrad. The T-1s system has been used continuously since it was installed in early July.

We fired 53 shots in the 3ω campaign, 13 to activate and calibrate new diagnostics and 40 to obtain data on 3ω conversion efficiency, near-field beam modulation at the focus lens, and the 3ω focal-spot energy distribution. The new diagnostics included a 3ω dark-field imaging capability that allowed direct comparison of the scattered power fraction outside 33 μrad with corresponding 1ω measurements. The data shots were with short pulses of nominally 200-ps duration. In one series, the booster amplifier was unpumped to simulate the end of a NIF ignition pulse. In this series, we obtained 3ω power up to 2.3 TW with delta B in the booster amplifier up to 1.7 and with 200-μrad pinholes in both the cavity and transport spatial filters. We obtained up to 3.1 TW (delta B up to 2.0) with smaller 130-μrad cavity and 100-μrad transport filter pinholes. In a second series to reach powers similar to NIF SBSS performance requirements (3.5 TW of 3ω power in 1-ns pulses), we pumped the full 11-5 amplifier set. We achieved 3ω power up to 3.65 TW (corresponding to 4.6 TW for a NIF-sized beam) with 200-μrad pinholes in both the cavity and transport spatial filters at a 1ω drive power of 5.7 TW. Attempts to use smaller pinholes (130/100 μrad) with the pumped booster resulted in back reflections from the transport spatial filter that damaged the injection optics. This problem was not observed with the larger pinholes.

The large-aperture damage tests of KDP were the second series to test KDP. The samples were tested with 3-ns FWHM Gaussian pulses. During the series, Beamlet provided 3ω energies very close to those requested by the experimenters. Three samples were tested: a previously conditioned crystal, a new crystal, and a fast-growth crystal. All three samples were damaged below the expected fluence. In previous Beamlet campaigns, however, our 32-cm and 37-cm KDP/KD*P frequency-conversion crystals generated NIF output fluences on several shots without damage.

In the long-pulse campaign, we evaluated Beamlet's performance with typical pulse shapes proposed for indirect-drive ignition on NIF. The shots did not include frequency conversion but used absorbing glass as a beam dump in the frequency-conversion enclosure. We modified the pulse generation system to generate 20-ns shaped pulses. The modification in the master oscillator room (MOR) used a slow pulser to generate a long foot and used the prototype Arbitrary Wavefront Generator to provide a shaped main pulse. A cavity extension in the regenerative amplifier extended the gain window to 23 ns without affecting the stability and performance. We began the series with standard 200-μrad carbon pinholes in the transport spatial filter. We started at low energy and slowly increased the output energy up to slightly in excess of 13 kJ when evidence of pinhole closure was apparent. We changed the transport filter pinhole to a 200-μrad stainless steel conical pinhole designed to alleviate closure problems and repeated the energy ramp-up. With this design we reached in excess of 15 kJ, with no evidence of closure. Unfortunately, because of a failure in the bandwidth generation system, stimulated Brillouin scattering (SBS) generated in lens L3 caused the lens to fail and implode into the transport spatial filter, and the series had to be terminated. Rebuilding the spatial filter with new square lenses is expected to take 3 to 4 weeks.

In an attempt to resolve a discrepancy between the measured and calculated near-field profiles of the Beamlet output beam, we recorded near-field images at various planes in the preamplifier and injection optics. From these data we determined the spatial modulation at the input to the main amplifier (the calculations had assumed zero modulation at the input). Preliminary analysis now indicates that nearly all of the spatial intensity modulation is already present on the beam before input to the main amplifiers. When this is taken into account, the discrepancy between measured and calculated profiles at the output should be resolved.

NIF

This quarter, the engineering effort focused on narrowing the design options, further developing the specific designs, and updating the *Conceptual Design Report* (CDR) cost estimate based on extensive vendor quotations. The Conventional Facilities Title I Design, including the cost estimate, is now complete, and the Special Equipment Design and cost estimate 95% complete. The comprehensive Title I Design Review will begin early next quarter (October 8).

The Title I Design Reviews were delayed from the Title I Plan by one month following delay in the release of the *Programmatic Environmental Impact Statement for Stockpile Stewardship and Management* (PEIS) beyond the planned mid-September date. This time was used for value engineering of the designs and cost optimization to ensure that NIF is consistent with the minimum platform to achieve the Primary Criteria and Functional Requirements and the DOE Baseline Change Control Board Level 1 directions. The revised schedule completes the Title I Design in ten months, which is two months faster than the CDR schedule.

Planning for the Title I Design Review was completed, including completing the *Title I Design Review Plan,* which was released to Project personnel and used in detailed planning of the remaining Title I work. The

plan includes the overall objectives, organization, and schedule, as well as an outline of the agenda for the review meetings and the contents of the Design Basis books. The overall Chairman of the Review Committee was selected, as well as committee members consisting of external and internal reviewers with significant expertise in their areas of review.

In parallel with the design effort, Title I cost and schedule estimates were developed. The cost estimate establishes the project cost baseline, is used as the basis for final design and construction estimation, and provides a high degree of confidence that the Project can be completed within the established baseline. The estimate provides budget outlay (BO) and budget authority (BA) profiles, a time-phased resource requirements plan, and a commitment profile. "Bottoms-up" estimates were generated by the lead/responsible engineers based on extensive vendor quotations. These estimates will be inputted to the NIF Planning system, which is an extension of the Business Planning system developed by LLNL and has been in use for over 10 years.

Following data input and verification, a Title I cost estimate contingency analysis based on a Monte Carlo simulation built from individual system risk assessment was developed. This analysis resulted in an overall contingency allocation for the Project. Planning for the DOE Independent Cost Estimate (ICE) Review has been completed and a kickoff meeting scheduled for the first week in October; ICE Review team members have been invited to the Title I Design Review.

In Manufacturing Engineering, manufacturing assessments were provided to the Special Equipment and lead engineers in support of the Title I design and costing effort. Over 270 detailed cost estimate validations were generated. A manufacturability report was drafted for the Title I Design Reviews.

In support of completion of Title I Design, and in preparation of Title II Design, upgrade and modification of the engineering support systems, including computer-aided design and drafting (CADD) and the Sherpa Product Data Management (PDM) systems, continued. An updated version of the PDM software was implemented and tested on a selected basis. This version, which is user-friendly and contains expanded help functions, reduces or eliminates the need for training. Conversion of the entire system to the updated version was delayed to ensure noninterference with completion of Title I Design. Classes on use of the NIF PDM system continue, and administrative support personnel are providing assistance to new and less experienced users.

PDM release procedures have been updated, and training on use of the PDM system continue to reflect the modifications to documents and design drawings control. The number of documents in the PDM system increases by about 50 per week, and by the end of the quarter there were over 600 documents in the system. Also, configuration management implementation continues. Training and implementation continue on drawing release, drawing revisions, and Engineering Change Request preparation.

The engineering effort focused this quarter on continuing design iterations to simplify the systems, reduce cost, and ensure a minimum platform system that meets the Primary Criteria and Functional Requirements and the Level 1 DOE Baseline Change Control Board actions. Extensive vendor quotes and refined cost estimates were collected, reviewed, and incorporated into the Title I cost estimate.

Specific Title I Design and supporting activities this past quarter include the following:

- Value Engineering of the LTAB and OAB was completed by Sverdrup to augment the continuing value engineering efforts. The study was completed and the results reviewed and incorporated into the design.
- Parsons was awarded the Project Labor Agreement Development and Oversight contract. The process for negotiating a Conventional Facilities Project Labor Agreement has been defined to reduce the schedule risks and cost impacts due to labor disputes during the Conventional Facilities construction.
- In cooperation with Conventional Facilities, issues associated with co-occupancy of special equipment installers and building constructors in the laser bay to expedite the schedule were resolved. An integrated plan for installing switchyard structures into the building erection sequence was established. Safety planning with the NIF Construction Manager for job site operations was begun.
- A combined target chamber/building construction schedule has been finalized. The schedule interfaces suggest that the chamber be built on the pedestal rather than constructed outside the target building and moved onto the pedestal.
- The Statement of Work for the target chamber fabrication was completed. Comments have been received and incorporated by NIF procurement, selection criteria were refined, and a Request for Proposal is scheduled for release early in FY 1997. Meetings with two potential target chamber fabricators were held, and both vendors confirmed the estimated fabrication time as well as choice of material.
- Changes to the target chamber diagnostic port locations were made based on input received from the Joint Committee for Target Diagnostics, consisting of members from the participating Laboratories. A port location interface control document (ICD) was completed and approved to document the information and assure that future changes are adequately reviewed and approved.

- Design iterations in the Final Optics Assembly continue. Individual 1 × 1 Integrated Optics Modules (IOMs) were selected to simplify the system and for ease of maintenance. Work was performed on a plan for the manufacturing of final optics cells by various methods, and visits to selected vendors for building a prototype final optics cell were prepared.
- Potential effects of distributed heat sources on the thermal stability of the optical systems were addressed by the NIF Thermal Working Group. This effort is closely coupled with the Parsons team performing the computational fluid dynamics analyses and members of the LLNL Thermal/Fluids Group.
- The Optical Configuration Layout drawing set, describing optical component position, orientation, and sizes, was completed. These drawings are an important source of interface information to the Special Equipment areas.
- To enable the initiation of long-lead optics procurement, several key drawings relating to fused silica material, lens finishing, and flat finishing have progressed to a near-final design state. Several significant analyses were documented. Among these were the clear-aperture budget and component damage-threshold requirements.
- All vendor optical cost studies were received, and NIF costs updated with the most current information available. Procurement strategy for optics has been completely defined, and the final version will be released with the Title I Design Basis Book.
- Significant cost savings were realized by production engineering of the amplifier demonstration AMPLAB components for use in NIF under a TRW Master Task Agreement work order. Concepts for amplifier cooling, support, and assembly hardware that meet NIF clean assembly requirements were completed.
- Several key amplifier power conditioning drawings were completed as part of Title I design, including the modified module layout and updated capacitor bay general arrangement. Life testing began at LLNL, in collaboration with the ICF Core Science and Technology Program, on prototype capacitors from two vendors and on the prototype module at Sandia National Laboratories-Albuquerque as part of the development program. Cost estimates were completed for key components, such as capacitors, and incorporated into the Title I cost rollup.
- The Software Requirement Specifications are essentially complete. Quality Level assessments for the Integrated Computer Control System were completed and approved. Remaining ICDs were completed, except for some minor revisions.
- Precision optical diagnostics design was improved with a simplified trombone and provisions for transport mirror maintenance. The midchain sensor design was completed, and requirements were completed for the target chamber diagnostic instrument manipulator.
- In Beam Transport, numerous design improvements that simplified the system and reduced costs were incorporated. They include simplified spatial filter beam tubes and reduced thickness of switchyard structure floor gratings, saving dead weight and increasing optical stability. Additional design optimization on the periscope structure reduced its weight, and use of component commonality reduced the part count in the switchyard and target bay mirror mounts.
- Utility layouts in the target bay and diagnostic building were completed. Revised cost estimates were generated and incorporated into the Title I estimate.
- Samples are arriving to validate parts of the NIF finishing process from Zygo and Tinsley. The first Phase 1 lens was received from Tinsley and is currently under evaluation.
- The draft *Startup Plan* and a preliminary startup schedule were completed. The second draft of the operations engineering schedule was completed for project inclusion and integration. The Title I Operations modeling effort has been completed and a report drafted.
- The NIF *Preliminary Safety Analysis Report* has been completed, and related DOE and institutional comments have been resolved. Institutional approval of the report by the Associate Directors for Laser Programs and Plant Operations has been received. DOE has concurred and will provide the *Safety Evaluation Report*, which gives final concurrence in early October.
- The PEIS has delayed the Notice of Availability to late October 1996 at the earliest. An analysis of delay impacts was prepared for DOE. The NIF *Technical Analysis* document, which includes justification and site comparisons, has been completed and is ready for publication.
- The environmental permit strategy was reviewed with DOE/OAK and DOE/HQ. All DOE comments to support the *Safety Evaluation Report* have been resolved.
- The *Quality Assurance Program Plan* (QAPP) was revised for Title II design, equipment procurement, and construction. Laboratory Project and DOE approval have been received. Eight Project procedures to implement the QAPP update were revised or prepared.

The Title I Design Reviews will be done time-phased, starting with the schedule critical path Conventional Facilities (including the Laser and Target Area Building, Optics Assembly Building, and site preparation) followed by three Special Equipment review segments. DOE actions, including determination by DP-1, with EH-1 concurrence, to proceed with limited Title II design concurrent with completion of the final PEIS and Record of Decision (ROD), will minimize the near-term adverse impact to the Project.

To maintain progress and keep the Project on schedule requires an ROD by mid-December 1996. Other activities that will be completed next quarter, leading to beginning of site preparation in mid-March 1997, include completing the ICE Review and preparing packages for the DOE Level 1 Baseline Change Control Board meeting in mid-December.

PUBLICATIONS

A

Afeyan, B. B., Chou, A. E., and Luhmann, N. C., *Studies of the Localization Paradox of Fluctuation Reflectometry via Multidimensional SOFTSTEP Simulations,* Lawrence Livermore National Laboratory, Livermore, CA, UCRL-JC-123320 ABS. Prepared for the *11th Topical Conf on High Temperature Plasma Diagnostics,* Monterey, CA, May 12–16, 1996.

Afeyan, B. B., and Williams, E. A., *Unified Theory of Stimulated Raman Scattering and Two Plasmon Decay in Inhomogeneous Plasmas: The High Frequency Hybrid Instability,* Lawrence Livermore National Laboratory, Livermore, CA, UCRL-JC-121846; *Phys. Rev. Lett.* **75**(23), 4218–4221 (1995).

Afeyan, B. B., and Chou, A. E., *SOFTSTEP Simulations of Stimulated Raman Scattering in Multidimensional Inhomogeneous Plasmas Driven by Structured Laser Beams,* Lawrence Livermore National Laboratory, Livermore, CA, UCRL-JC-124458 ABS. Prepared for the *26th Annual Anomalous Absorption Conf,* Fairbanks, AK, Aug 26–30, 1996.

Afeyan, B. B., Kruer, W. L., and Chou, A. E., *Electron Plasma and Ion Acoustic Waves in Flat Top Electron Velocity Distributions,* Lawrence Livermore National Laboratory, Livermore, CA, UCRL-JC-124459 ABS. Prepared for the *26th Annual Anomalous Absorption Conf,* Fairbanks, AK, Aug 26–30, 1996.

Afeyan, B. B., and Chou, A. E., *Theory and Simulation of Parametric Instabilities in Turbulent Plasmas Illuminated by Lasers with Spatial Structure,* Lawrence Livermore National Laboratory, Livermore, CA, UCRL-JC-124670 ABS. Prepared for *38th Annual Mtg of the American Physical Society Div of Plasma Physics,* Denver, CO, Nov 11–15, 1996.

Afeyan, B. B., Chou, A. E., and Luhmann, N. C., *Externally Launched Narrow-Wavepacket Approach to Fluctuation Reflectometry,* Lawrence Livermore National Laboratory, Livermore, CA, UCRL-JC-124668 ABS. Prepared for *38th Annual Mtg of the American Physical Society Div of Plasma Physics,* Denver, CO, Nov 11–15, 1996.

Aikens, D., Lawson, J., Baumler, M., Rich, L., Donovan, P., Schmitt, G., Lewis, T., and Wilson, T., *Ripple Free Finishing Process,* Lawrence Livermore National Laboratory, Livermore, CA, UCRL-JC-122731. Submitted to *1996 R&D 100 Award.*

Akunets, A. A., Dorogotovtsev, V. M., Merkuliev, Y. A., Startsev, S. A., and Cook, R., *Production of Hollow Microspheres from Plastic Solid Granules,* Lawrence Livermore National Laboratory, Livermore, CA, UCRL-JC-120206; *Fus. Tech.* **28**(12), 1781–1786 (1995).

Alexeev, I. V., De Yoreo, J. J., and Rashkovich, L. N., *Fast Growth from Solutions: Mechanisms and Defects,* Lawrence Livermore National Laboratory, Livermore, CA, UCRL-JC-123595 ABS. Prepared for the *XVII Congress and General Assembly of the Intl Union of Crystallography,* Seattle, WA, Aug 8–17, 1996.

Amendt, P., Glendinning, S. G., Hammel, B., Landen, O., and Suter, L. J., *Shocked Witness Foam-Ball Drive Diagnostic at Target Center,* Lawrence Livermore National Laboratory, Livermore, CA, UCRL-JC-124462 ABS. Prepared for the *26th Annual Anomalous Absorption Conf,* Fairbanks, AK, Aug 26–30, 1996.

Amendt, P., Glendinning, S. G., Hammel, B., Landen, O., and Suter, L. J., *Evidence of Drive Enhancement in Modified Nova Hohlraums from Backlit Ablatively-Shocked Surrogate Targets,* Lawrence Livermore National Laboratory, Livermore, CA, UCRL-JC-124464; *Phys. Rev. Lett.* **77**(18), 3815–3818 (1996).

Amendt, P., Murphy, T. J., and Hatchett, S. P., *Novel Symmetry Tuning in Nova Hohlraums Using Axial Gold Discs,* Lawrence Livermore National Laboratory, Livermore, CA, UCRL-JC-124292; *Phys. of Plasmas* **3**(11), 4166–4171 (1996).

Amendt, P., Glendinning, S. G., Hammel, B. A., Hatchett, S., Landen, O., Murphy, T. J., Rosen, M. D., Suter, L. J., Desenne, D., Jadaud, J. P., and Lafitte, S., *New Methods for Controlling and Diagnosing Hohlraum Drive Symmetry,* Lawrence Livermore National Laboratory, Livermore, CA, UCRL-JC-124658 ABS. Prepared for *38th Annual Mtg of the American Physical Society Div of Plasma Physics,* Denver, CO, Nov 11–15, 1996.

Anderson, A. T., *X-Ray Ablation Measurements and Modeling for ICF Applications,* Lawrence Livermore National Laboratory, Livermore, CA, UCRL-LR-125352. Submitted to *Experimental Heat Transfer.*

Anderson, A. T., Burnham, A. K., Tobin, M. T., and Peterson, P. F., *Modeling and Experiments of X-Ray Ablation of National Ignition Facility First Wall Materials,* Lawrence Livermore National Laboratory, Livermore, CA, UCRL-JC-123553. Prepared for the *American Nuclear Society 12th Topical Mtg on the Technology of Fusion Energy,* Reno, NV, Jun 16–20, 1996.

Anderson, A. T., Managan, R. A., Tobin, M. T., Peterson, P. F., *X-Ray Emission from National Ignition Facility Indirect Drive Targets,* Lawrence Livermore National Laboratory, Livermore, CA, UCRL-JC-123557. Prepared for the *American Nuclear Society 12th Topical Mtg on the Technology of Fusion Energy,* Reno, NV, Jun 16–20, 1996.

Auerbach, J. M., Eimerl, D., Milam, D., and Milonni, P. W., *A Perturbation Theory for Electric Field Amplitude and Phase Ripple Transfer in Frequency Doubling and Tripling,* Lawrence Livermore National Laboratory, Livermore, CA, UCRL-JC-124005; *Applied Optics: Lasers, Photonics, & Environ. Optics* **36**(3), 606–612 (1997).

B

Back, C. A., Glenzer, S. H., Estabrook, K., Kauffman, R. L., Landen, O. L., MacGowan, B. J., Powers, L. V., Shepard, T. D., and Stone, G. F., *Localized Measurements of Electron Temperature in Hohlraum Targets by X-Ray Spectroscopy,* Lawrence Livermore National Laboratory, Livermore, CA, UCRL-JC-121290 ABS Rev 1. Prepared for the *24th European Conf on Laser Interaction with Matter,* Madrid, Spain, Jun 3–7, 1996.

Back, C. A., Kalantar, D. H., Kauffman, R. L., Lee, R. W., MacGowan, B. J., Montgomery, D. S., Powers, L. V., Shepard, T. D., Stone, G. F., and Suter L. J., *Measurements of Electron Temperature by Spectroscopy in mm-Size Hohlraum Targets,* Lawrence Livermore National Laboratory, Livermore, CA, UCRL-JC-122046; *Phys. Rev. Lett.* **77**(21), 4350–4353 (1996).

Back, C. A., Glenzer, S. H., Lee, R. W., MacGowan, B. J., Moreno, J. C., Nash, J. K., Powers, L. V., and Shepard, T. D., *Spectroscopic Temperature Measurements of Non-Equilibrium Plasmas,* Lawrence Livermore National Laboratory, Livermore, CA, UCRL-JC-123074. Prepared for the *10th American Physical Society Topical Conf on Atomic Processes in Plasmas,* San Francisco, CA, Jan 14–18, 1996.

Back, C. A., Glenzer, S. H., Landen, O. L., MacGowan, B. J., and Shepard, T. D., *X-Ray Diagnostics of Hohlraum Plasma Flow,* Lawrence Livermore National Laboratory, Livermore, CA, UCRL-JC-123283. Prepared for the *11th Topical Conf on High Temperature Plasma Diagnostics,* Monterey, CA, May 12–16, 1996.

Back, C. A., Glenzer, S. H., Estabrook, K., Kauffman, R. L., Landen, O. L., MacGowan, B. J., Powers, L. V., Shepard, T. D., and Stone, G. F., *Characterization of Electron Temperature in Hohlraum Targets by X-Ray Spectroscopy,* Lawrence Livermore National Laboratory, Livermore, CA, UCRL-JC-124655 ABS. Prepared for *38th Annual Mtg of the American Physical Society Div of Plasma Physics,* Denver, CO, Nov 11–15, 1996.

Back, C. A., Woolsey, N. C., Asfaw, A., Glenzer, S. H., Hammel, B. A., Keane, C. J., Lee, R. W., Liedahl, D., Moreno, J. C., Nash, J. K., Osterheld, A. L., Calisti, A., Stamm, R., Talin, B., Godbert, L., Mosse, C., Ferri, S., and Klein, L., *Experiments on Hot and Dense Laser-Produced Plasmas,* Lawrence Livermore National Laboratory, Livermore, CA, UCRL-JC-123592. Prepared for *13th Intl Conf on Spectral Line Shapes,* Florence, Italy, Jun 17–21, 1996.

Barker, C. E., Sacks, R. A., Van Wonterghem, B. M., Caird, J. A., Murray, J. R., Campbell, J. H., Kyle, K., Ehrlich, R. B., and Nielsen, N. D., *Transverse Stimulated Raman Scattering in KDP,* Lawrence Livermore National Laboratory, Livermore, CA, UCRL-JC-118106. Prepared for the *1st Annual Int'l Conf on Solid-State Lasers for Application to Inertial Confinement Fusion,* Monterey, CA, May 30–Jun 2, 1995. Submitted to the *Society of Photo-Optical Instrumentation Engineers.*

Barker, C. E., Van Wonterghem, B. M., Auerbach, J. M., Foley, R. J., Murray, J. R., Campbell, J. H., Caird, J. A., Speck, D. R., and Woods, B., *Design and Performance of the Beamlet Laser Third Harmonic Frequency Converter,* Lawrence Livermore National Laboratory, Livermore, CA, UCRL-JC-118105. Prepared for the *1st Annual Int'l Conf on Solid-State Lasers for Application to Inertial Confinement Fusion,* Monterey, CA, May 30–Jun 2, 1995. Submitted to the *Society of Photo-Optical Instrumentation Engineers.*

Barker, C. E., Auerbach, J. M., Adams, C. H., Bumpas, S. E., Hibbard, R. L., Lee, C. L., Roberts, D. H., Campbell, J. H., Wegner, P. J., Van Wonterghem, B. M., and Caird, J. A., *National Ignition Facility Frequency Converter Development,* Lawrence Livermore National Laboratory, Livermore, CA, UCRL-JC-124856 ABS. Prepared for *2nd Annual Intl Conf on Solid-State Lasers for Application to Inertial Confinement Fusion,* Paris, France, Oct 22–25, 1996.

Barnard, J. J., and Lund, S. M., *Theory of Longitudinal Beam Halo in High Current Ion RF Linacs,* Lawrence Livermore National Laboratory, Livermore, CA, UCRL-JC-124883 ABS. Prepared for *38th Annual Mtg of the American Physical Society Div of Plasma Physics,* Denver, CO, Nov 11–15, 1996.

Bayramian, A. J., Marshall, C. D., Payne, S. A., and Quarles, G. J., *Efficient Ultraviolet Ce:LiSAF Laser Using Anti-Solarant Pump Beam,* Lawrence Livermore National Laboratory, Livermore, CA, UCRL-JC-122123 EXT ABS. Prepared for the *Advanced Solid State Lasers 11th Topical Mtg,* San Francisco, CA, Jan 31–Feb 3, 1996. Submitted to the *Optical Society of America.*

Beach, R., Bibeau, C., and Honea, E., *Scaling Diode End-Pumped Solid-State Lasers to High Average Power,* Lawrence Livermore National Laboratory, Livermore, CA, UCRL-JC-124929 ABS. Prepared for *High-Power Lasers and Applications,* San Jose, CA, Feb 8–14, 1997.

Beach, R. J., *Medical Applications of High Power Laser Diode Arrays,* Lawrence Livermore National Laboratory, Livermore, CA, UCRL-JC-124018 ABS. Prepared for the *Optical Society of America Annual Mtg & Exhibit,* Rochester, NY, Oct 20–25, 1996.

Beach, R. J., Sutton, S. B., Honea, E. C., Skidmore, J. A., and Emanuel, M. A., *High Power 2 Micron Diode-Pumped Tm:YAG Laser,* Lawrence Livermore National Laboratory, Livermore, CA, UCRL-JC-121647. Prepared for the *Society of Photo-Optical Instrumentation Engineers Photonics West '96 Symp,* San Jose, CA, Jan 27–Feb 2, 1996.

Beach, R. J., Sutton, S. B., Honea, E. C., Skidmore, J. A., and Emanuel, M. A., *High Power 2 Micron Wing-Pumped Tm^{3+}:YAG Laser,* Lawrence Livermore National Laboratory, Livermore, CA, UCRL-JC-122121. Prepared for the *Advanced Solid-State Lasers 11th Topical Mtg,* San Francisco, CA, Jan 31-Feb 3, 1996.

Beach, R. J., Sutton, S. B., Skidmore, J. A., and Emanuel, M. A., *High Power 2-μm Wing-Pumped Tm:YAG Laser,* Lawrence Livermore National Laboratory, Livermore, CA, UCRL-JC-122121 SUM. Prepared for the *Conf on Lasers and Electro-Optics (CLEO '96),* Anaheim, CA, Jun 2–7, 1996.

Bel'kov, S. A., Dolgopolov, Yu. V., Kochemasov, G. G., Kulikov, S. M., Solov'eva, M. N., Sukharev, S. A., and Voronich, I. N., *Measurement of SBS Physics Parameters,* Lawrence Livermore National Laboratory, Livermore, CA, UCRL-CR-122700.

Bell, P. M., Lee, F. D., and Conder, A. D., *Development and Characterization of a CCD Camera System for Use on Six Inch Manipulator Systems,* Lawrence Livermore National Laboratory, Livermore, CA, UCRL-JC-123281 ABS. Prepared for the *11th Topical Conf on High Temperature Plasma Diagnostics,* Monterey, CA, May 12–16, 1996.

Berger, R. L., Still, C. H., Hinkel, D. E., Langdon, A. B., Williams, E. A., Kirkwood, R. K., MacGowan, B. J., Montgomery, D. S., and Moody, J. D., *Multi-Dimensional Evolution of Stimulated Scattering and Filamentation,* Lawrence Livermore National Laboratory, Livermore, CA, UCRL-JC-124465 ABS. Prepared for the *26th Annual Anomalous Absorption Conf,* Fairbanks, AK, Aug 26–30, 1996.

Berger, R. L., Still, C. H., Hinkel, D. E., Langdon, A. B., Munro, D. H., Williams, E. A., Kirkwood, R. K., MacGowan, B. J., Montgomery, D. S., and Moody, J. D., *Multi-Dimensional Evolution of Stimulated Scattering and Filamentation,* Lawrence Livermore National Laboratory, Livermore, CA, UCRL-JC-124465 ABS Rev. 1. Prepared for *38th Annual Mtg of the American Physical Society Div of Plasma Physics,* Denver, CO, Nov 11–15, 1996.

Bernat, T., *Limits to the Smoothness of Solid Hydrogen-Isotope Surfaces,* Lawrence Livermore National Laboratory, Livermore, CA, UCRL-JC-125138 ABS. Prepared for *11th Target Fabrication Specialists' Mtg,* Orcas Island, WA, Sept 8–12, 1996.

Bernat, T. P., *Technologies and Prospects for Fabricating NIF Targets,* Lawrence Livermore National Laboratory, Livermore, CA, UCRL-JC-124238 SUM. Prepared for the *16th Intl Atomic Energy Agency Fusion Energy Conf on Plasma Physics and Controlled Nuclear Fusion Research,* Montreal, Canada, Oct 7–11, 1996.

Bernat, T. P., *Design and Reality for NIF Ignition Targets,* Lawrence Livermore National Laboratory, Livermore, CA, UCRL-JC-124276. Prepared for the *24th European Conf on Laser Interaction with Matter,* Madrid, Spain, Jun 3–7, 1996.

Berning, M., Budil, K. S., Glendinning, S. G., Kane, J., Remington, B. A., and Rubenchik, A., *Dynamic Rayleigh–Taylor Instability,* Lawrence Livermore National Laboratory, Livermore, CA, UCRL-JC-123280 ABS. Prepared for the *Intl Seminar on Physics of High Energy Density Matter,* Vancouver, B.C., Canada, May 26–29, 1996.

Berning, M., Rubenchi, A., and Wood-Vasey, M., *Weakly Nonlinear Evolution of Interface Instabilities,* Lawrence Livermore National Laboratory, Livermore, CA, UCRL-JC-124673 ABS. Prepared for *38th Annual Mtg of the American Physical Society Div of Plasma Physics,* Denver, CO, Nov 11–15, 1996.

Bibeau, C., *Diode End-Pumped Geometry with "Light Funnel" Produces High Power Nd:YAG Laser,* Lawrence Livermore National Laboratory, Livermore, CA, UCRL-JC-122309 ABS. Submitted to *Laser Focus World.*

Bibeau, C., Beach, R. J., and Payne, S. A., *Performance of a Q-Switched Yb:Sr_5 (PO_4)$_3$F Laser,* Lawrence Livermore National Laboratory, Livermore, CA, UCRL-JC-122128 EXT ABS. Prepared for the *Advanced Solid State Lasers 11th Topical Mtg,* San Francisco, CA, Jan 31–Feb 3, 1996.

Bibeau, C., Payne, S. A., and Powell, H. T., *Direct Measurements of the Terminal Laser Level Lifetime in Neodymium-Doped Crystals and Glasses,* Lawrence Livermore National Laboratory, Livermore, CA, UCRL-JC-117099; *J. Opt. Soc. Am. B* **12**(10), 1981-1992 (1995).

Bibeau, C., and Beach, R., *CW and Q-Switched Performance of a Diode End-Pumped Yb:YAG Laser,* Lawrence Livermore National Laboratory, Livermore, CA, UCRL-JC-124042 ABS & SUM. Prepared for the *1996 Conf on Lasers and Electro-Optics/Quantum Electronics and Laser Science Conf,* Anaheim, CA, Jun 2–7, 1996.

Bibeau, C., Beach, R., Honea, E., Page, R., Sutton, S., Emanuel, M., Skidmore, J., and Payne, S., *High Power Diode End-Pumped Yb:YAG and Tm:YAG Laser Systems,* Lawrence Livermore National Laboratory, Livermore, CA, UCRL-JC-123789 ABS. Prepared for the *9th Annual Diode Laser Technology Review,* Albuquerque, NM, Apr 15–18, 1996.

Boley, C. D., and Rhodes, M. A., *Model of the Influence of Magnetic Fields on a Plasma Electrode Pockels Cell,* Lawrence Livermore National Laboratory, Livermore, CA, UCRL-JC-124539 ABS. Prepared for *2nd Annual Intl Conf on Solid-State Lasers for Application to Inertial Confinement Fusion,* Paris, France, Oct 22–25, 1996.

Boyd, R. D., Britten, J. A., Decker, D. E., Shore, B. W., Stuart, B. C., Perry, M. D., and Li, L., *High-Efficiency Metallic Diffraction Gratings for Laser Applications,* Lawrence Livermore National Laboratory, Livermore, CA, UCRL-JC-115589; *Appl. Opt*. **34**(10), 1697–1706 (1995).

Brown, N. J., and Taylor, J. S., *Calculations of Relative Velocity in Abrasive Wear Systems Employing Laps of Constant Radius of Curvature,* Lawrence Livermore National Laboratory, Livermore, CA, UCRL-JC-122833 ABS. Prepared for the *Optical Society of America, Optical Fabrication and Testing,* Boston, MA, Apr 29–May 3, 1996.

Brusasco, R., Cook, R., Wilemski, G., Saculla, M., and Gaines, D., *Beryllium Doped Plasma Polymer Coatings Using Cyclopentadienyl Beryllium Methyl as a Precursor,* Lawrence Livermore National Laboratory, Livermore, CA, UCRL-JC-125143 ABS. Prepared for *11th Target Fabrication Specialists' Mtg,* Orcas Island, WA, Sept 8–12, 1996.

Brusasco, R. M., Dittrich, T., and Cook, R. C., *Feasibility of Organo-Beryllium Target Mandrels Using Organo-Germanium PECVD as a Surrogate,* Lawrence Livermore National Laboratory, Livermore, CA, UCRL-JC-119533 Rev 1; *Fusion Technol.* **28**(12), 1854–1858 (1995).

Buckley, S., Letts, S. A., Wilemski, G. J., Fearon, E., Vu, D., Cook, R. C., and Schroen-Carey, D., *Processing and Properties of NIF Scale Targets Using Interfacial Polycondensation,* Lawrence Livermore National Laboratory, Livermore, CA, UCRL-JC-125123 ABS. Prepared for *11th Target Fabrication Specialists' Mtg,* Orcas Island, WA, Sept 8–12, 1996.

Budil, K. S., Cauble, R. C., Celliers, P. M., Collins, G. W., Da Silva, L. B., Hammel, B. A., Chiu, G., and Ng, A., *Characterization of Preheat in Laser-Driven Target Using Interferometry,* Lawrence Livermore National Laboratory, Livermore, CA, UCRL-JC-124880 ABS. Prepared for *38th Annual Mtg of the American Physical Society Div of Plasma Physics,* Denver, CO, Nov 11–15, 1996.

Budil, K. S., Remington, B. A., Rubenchik, A. M., Berning, M., Wood-Vasey, W. M., Peyser, T. A., Mikaelian, K. O., and Perry, T. S., *Investigation of the Multimode Classical Rayleigh–Taylor Instability,* Lawrence Livermore National Laboratory, Livermore, CA, UCRL-JC-124548 ABS. Prepared for *38th Annual Mtg of the American Physical Society Div of Plasma Physics,* Denver, CO, Nov 11–15, 1996.

Budil, K. S., Remington, B. A., Peyser, T. A., Mikaelian, K. O., Miller, P. L., Woolsey, N. C., Wood-Vasey, W. M., and Rubenchik, A. M., *Experimental Comparison of Classical versus Ablative Rayleigh–Taylor Instability,* Lawrence Livermore National Laboratory, Livermore, CA, UCRL-JC-123293; *Phys. Rev. Lett.* **76**(24), 4536–4539 (1996).

Budil, K., Perry, T. S., Alvarez, S. A., Hargrove, D., Mazuch, J. R., Nikitin, A., and Bell, P. M., *Point Projection Radiography with the FXI,* Lawrence Livermore National Laboratory, Livermore, CA, UCRL-JC-123135. Prepared for the *11th Topical Conf on High Temperature Plasma Diagnostics,* Monterey, CA, May 12–16, 1996.

Budil, K. S., Remington, B. A., Peyser, T. A., Mikaelian, K. O., Rubenchik, A. M., Berning, M., and Wood-Vasey, M. W., *Experimental Investigation of the Classical Rayleigh-Taylor Instability,* Lawrence Livermore National Laboratory, Livermore, CA, UCRL-JC-123293. Prepared for the *24th European Conf on Laser Interaction with Matter,* Madrid, Spain, Jun 3–7, 1996.

Budil, K. S., Remington, B. A., Perry, T. S., Rubenchik, A. M., Berning, M., Peyser, T. A., Louis, H., Demiris, T., and Wallace, R., *A Novel Method for Diagnosing the Growth of Subresolution-Scale Perturbations,* Lawrence Livermore National Laboratory, Livermore, CA, UCRL-JC-124033. Prepared for the *11th Topical Conf on High-Temperature Plasma Diagnostics,* Monterey, CA, May 12–14, 1996.

Budil, K. S., Remington, B. A., Rubenchik, A. M., Berning, M., Wood-Vasey, W. M., Miller, P. L., Perry, T. S., Peyser, T. A., and Mikaelian, K. O., *Multimode Classical Rayleigh-Taylor Experiments at Nova,* Lawrence Livermore National Laboratory, Livermore, CA, UCRL-JC-124278 ABS. Prepared for the *26th Anomalous Absorption Conf,* Fairbanks, AK, Aug 26–30, 1996.

Burkhart, S. C., and Penko, F. A., *Ultra-High Bandwidth Arbitrary Waveform Generator,* Lawrence Livermore National Laboratory, Livermore, CA, UCRL-JC-123657. Submitted to the *1996 R&D 100 Award.*

Burkhart, S. C., Wilcox, R., Penko, F., and Browning, D., *Amplitude and Phase Modulation with Waveguide Optics,* Lawrence Livermore National Laboratory, Livermore, CA, UCRL-JC-124531 ABS. Prepared for *2nd Annual Intl Conf on Solid-State Lasers for Application to Inertial Confinement Fusion,* Paris, France, Oct 22–25, 1996.

Burnham, A. K., Tobin, M. T., and Anderson, A. T., *Evaluation of First Wall Materials for the National Ignition Facility Target Chamber,* Lawrence Livermore National Laboratory, Livermore, CA, UCRL-JC-124510 ABS. Prepared for *2nd Annual Intl Conf on Solid-State Lasers for Application to Inertial Confinement Fusion,* Paris, France, Oct 22–25, 1996.

Burnham, A., Alford, C., Dittrich, T., Makowiecki, D., Wallace, R., Honea, E., King, C., and Steinman, D., *Evaluation of B_4C as an Ablator Material for NIF Capsules,* Lawrence Livermore National Laboratory, Livermore, CA, UCRL-JC-125144 ABS. Prepared for *11th Target Fabrication Specialists' Mtg,* Orcas Island, WA, Sept 8–12, 1996.

Burnham, A. K., Tobin, M. T., Anderson, A. T., Honea, E. C., Skulina, K. M., Milam, D., Evans, M., Rainer, F., and Gerassimenko, M., *Development and Evaluation of First Wall Materials for the National Ignition Facility,* Lawrence Livermore National Laboratory, Livermore, CA, UCRL-JC-123561. Prepared for the *American Nuclear Society 12th Topical Mtg on the Technology of Fusion Energy,* Reno, NV, Jun 16–20, 1996.

Busby, L. E., *Gist: a Scientific Graphics Package for Python,* Lawrence Livermore National Laboratory, Livermore, CA, UCRL-JC-124008 ABS. Prepared for the *4th Intl Python Workshop,* Livermore, CA, Jun 3–6, 1996.

Busby, L. E., *Gist: a Scientific Graphics Package for Python,* Lawrence Livermore National Laboratory, Livermore, CA, UCRL-JC-124228. Prepared for the *4th Intl Python Workshop,* Livermore, CA, Jun 3–6, 1996.

C

Cable, M. D., Barbee, T. W., Lerche, R. A., Nelson, M. B., Moran, M. J., Ress, D. B., Sangster, T. C., Trebes, J. E., Turner, R. E., Phillips, T. W., Hicks, D., Li, C. K., Petrasso, R. D., and Seguin, F., *Diagnostics for High Density Implosions at the National Ignition Facility,* Lawrence Livermore National Laboratory, Livermore, CA, UCRL-JC-124239 SUM. Prepared for the *16th Intl Atomic Energy Agency Fusion Energy Conf on Plasma Physics and Controlled Nuclear Fusion Research,* Montreal, Canada, Oct 7–11, 1996.

Cable, M. D., Barbee, T. W., Lerche, R. A., Nelson, M. B., Moran, M. J., Ress, D. B., Sangster, T. C., Trebes, J. E., Turner, R. E., Phillips, T. W., Hicks, D., Li, C. K., Petrasso, R. D., and Seguin, F., *Diagnostics for High Density Implosions at the National Ignition Facility,* Lawrence Livermore National Laboratory, Livermore, CA, UCRL-JC-124239. Prepared for *Intl Atomic Energy Agency (IAEA) 16th Fusion Energy Conf,* Montreal, Canada, Oct 7–11, 1996.

Caird, J. A., Patton, H. G., Seppala, L. G., Thompson, C. E., and Wegner, P. J., *Beamlet Focal Plane Diagnostic,* Lawrence Livermore National Laboratory, Livermore, CA, UCRL-JC-124872 ABS. Prepared for *2nd Annual Intl Conf on Solid-State Lasers for Application to Inertial Confinement Fusion,* Paris, France, Oct 22–25, 1996.

Caird, J. A., Auerbach, J. M., Behrendt, W. C., Bliss, E. S., Barker, C., Campbell, J. H., Hackel, R. P., Hartley, R. G., Henesian, M. A., Hinz, A. F., Hunt, J. T., Kartz, M. W., Lawson, J. K., Mathieu, F., Murray, J. E., Pollock, G. G., Powell, H. T., Salmon, J. T., Smith, I. C., and Speck, D. R., *The Beamlet Laser System as a Prototype for the National Ignition Facility (NIF),* Lawrence Livermore National Laboratory, Livermore, CA, UCRL-JC-124500 ABS & SUM. Prepared for the *9th Annual Mtg of the IEEE Lasers and Electro-Optics Society*, Boston, MA, Nov 18–21, 1996.

Callahan, D. A., *Chamber Propagation Physics for Heavy Ion Fusion,* Lawrence Livermore National Laboratory, Livermore, CA, UCRL-JC-121279. Prepared for the *Int'l Symp on Heavy Ion Fusion,* Princeton, NJ, Sept 6–9, 1995.

Callahan, D. A., *Interactions Between Neighboring Beams in a Heavy Ion Fusion Reactor Chamber,* Lawrence Livermore National Laboratory, Livermore, CA, UCRL-JC-121132; *Appl. Phys. Lett.* **67**(11), 3254–3256 (1995).

Campbell, E. M., *Experimental Astrophysics Using Intense Lasers,* Lawrence Livermore National Laboratory, Livermore, CA, UCRL-JC-123036 ABS. Prepared for the *1996 Joint American Physical Society and American Association of Physics Teachers Mtg,* Indianapolis, IN, May 2–5, 1996.

Campbell, E. M., Holmes, N. C., Libby, S. B., Remington, B. A., and Teller, E., *High Energy-Density Physics: from Nuclear Testing to the Superlasers,* Lawrence Livermore National Laboratory, Livermore, CA, UCRL-JC-121636 Rev 1. Prepared for the *American Physical Society Topical Conf on Shock Compression of Condensed Matter,* Seattle, WA, Aug 13–18, 1995.

Campbell, E. M., Eimerl, D., Kruer, W. L., Weber, S., and Verdon, C. P., *The 0.53-μm Laser Option for Inertial Fusion,* Lawrence Livermore National Laboratory, Livermore, CA, UCRL-JC-125112. Submitted to *Comments on Plasma Physics and Controlled Fusion.*

Campbell, E. M., Holmes, N. C., Libby, S. B., Remington, B. A., and Teller, E., *The Evolution of High Energy-Density Physics: from Nuclear Testing to the Superlasers,* Lawrence Livermore National Laboratory, Livermore, CA, UCRL-JC-124258 Rev. 1. Submitted to *Laser and Particle Beams.*

Campbell, J. H., Hurst, P., Heggins, D., Steele, W., and Bumpas, S., *Laser Induced Damage and Fracture in Fused Silica Vacuum Windows,* Lawrence Livermore National Laboratory, Livermore, CA, UCRL-JC-124876 ABS. Prepared for *28th Annual Symp on Optical Materials for High Power Lasers,* Boulder, CO, Oct 7–9, 1996.

Campbell, J. H., *Recent Advances in Phosphate Laser Glasses for High Power Applications,* Lawrence Livermore National Laboratory, Livermore, CA, UCRL-JC-124244. Prepared for the *Society of Photo-Optical Instrumentation Engineers 1996 Intl Symp on Optical Science, Engineering and Instrumentation,* Denver, CO, Aug 4–9, 1996.

Celliers, P., Da Silva, L. B., Dane, C. B., Norton, M., Mrowka, S., Harder, J., Hackel, L., Matthews, D., Abate, J., and Maldonado, J., *X-Ray Conversion Efficiency Using a High Average Power Nd:Glass Laser System,* Lawrence Livermore National Laboratory, Livermore, CA, UCRL-JC-122656 ABS & VG. Prepared for the *37th Annual Mtg of the American Physical Society Div of Plasma Physics,* Louisville, KY, Nov 6–10, 1995.

Celliers, P. M., Da Silva, L. B., Dane, C. B., Mrowka, S., Norton, M., Harder, J., Hackel, L., Matthews, D. L., Fiedorowicz, H., Bartnik, A., Maldonado, J. R., and Abate, J. A., *Optimization of X-Ray Sources for Proximity Lithography Produced by a High Average Power Nd:Glass Laser,* Lawrence Livermore National Laboratory, Livermore, CA, UCRL-CR-121294 Rev 1.

Celliers, P., Da Silva, L. B., Heredia, N. J., Mammini, B. M., London, R. A., and Strauss, M., *Dynamics of Laser-Induced Transients Produced by Nanosecond Duration Pulses,* Lawrence Livermore National Laboratory, Livermore, CA, UCRL-JC-124047. Prepared for the *Society of Photo-Optical Instrumentation Engineers '96 Conf,* San Jose, CA, Jan 28–Feb 2, 1996.

Celliers, P. M., Da Silva, L. B., Hammel, B. A., Cauble, R., Ng, A., Chiu, G., Forsman, A., and Chandler, G., *Interferometric Techniques for Probing Laser-Generated Shocks in Transparent Solids,* Lawrence Livermore National Laboratory, Livermore, CA, UCRL-JC-124030 ABS. Prepared for the *24th European Conf on Laser Interaction with Matter,* Madrid, Spain, Jun 3–7, 1996.

Celliers, P. M., Da Silva, L., Dane, C. B., Norton, M., Mrowka, S., Harder, J., Hackel, L., Matthews, D., Abate, J., and Moldonado, J., *X-Ray Conversion Efficiency Using a High Average Power Nd:glass Laser System,* Lawrence Livermore National Laboratory, Livermore, CA, UCRL-JC-122656 ABS Rev. 1. Prepared for the *23rd IEEE Intl Conf on Plasma Science,* Boston, MA, Jun 3–5, 1996.

Celliers, P. M., Estabrook, K., Wallace, R. J., Murray, J. E., Da Silva, L. B., MacGowan, B. J., Van Wonterghem, B. M., and Hunt, J. T., *Novel Spatial Filter Pinhole for High Energy Pulsed Lasers,* Lawrence Livermore National Laboratory, Livermore, CA, UCRL-JC-124029 ABS. Prepared for *24th European Conf on Laser Interaction with Matter,* Madrid, Spain, Jun 3–7, 1996.

Chang, J. J., Arnold, P. A., and Warner, B. E., *Improvement of High-Current Large-Volume Discharge with Profiled Hollow-Cathode Electrodes,* Lawrence Livermore National Laboratory, Livermore, CA, UCRL-JC-125247. Submitted to *IEEE Transaction of Plasma Science.*

Chang, J. J., and Warner, B. E., *Laser-Plasma Interaction During Visible Laser Ablation of Metals,* Lawrence Livermore National Laboratory, Livermore, CA, UCRL-JC-123313; *Appl. Phys. Lett.* **69**(4), 473–475 (1996).

Chou, A. E., Afeyan, B. B., and Luhmann, N. C., *Two Dimensional Simulations of Fluctuation Reflectometry,* Lawrence Livermore National Laboratory, Livermore, CA, UCRL-JC-124669 ABS. Prepared for *38th Annual Mtg of the American Physical Society Div of Plasma Physics,* Denver, CO, Nov 11–15, 1996.

Chou, A. E., Afeyan, B. B., and Luhmann, N. C., *A Comparison of the Oscillating Mirror and Bragg Resonance Pictures of Fluctuation Reflectometry in 1D Plasmas,* Lawrence Livermore National Laboratory, Livermore, CA, UCRL-JC-123319 ABS. Prepared for the *11th Topical Conf on High Temperature Plasma Diagnostics,* Monterey, CA, May 12–16, 1996.

Chow, R., Loomis, G. E., Bibeau, C., Molau, N. E., Kanz, V. K., and Beach, R. J., *Optical Tuning a Dichroic Multilayer for a High Fluence Laser Application,* Lawrence Livermore National Laboratory, Livermore, CA, UCRL-JC-121678**.** Prepared for the *Annual Symp on Optical Materials for High Power Lasers,* Boulder, CO, Oct 30–Nov 1, 1995.

Clark, G. A., Glinsky, M. E., Sandhya Devi, K. R., Robinson, J. H., Cheng, P. K. Z., and Ford, G. E., *Automatic Event Picking in Pre-Stack Migrated Gathers Using a Probabilistic Neural Network,* Lawrence Livermore National Laboratory, Livermore, CA, UCRL-JC-124022. Prepared for the *1996 Society of Exploration Geophysicists,* Denver, CO, Nov 10–15, 1996.

Cohen, B. I., Lasinski, B. F., Langdon, A. B., and Williams, E. A., *Resonantly Excited Nonlinear Ion Waves,* Lawrence Livermore National Laboratory, Livermore, CA, UCRL-JC-124922; *Physics of Plasmas* **4**(4), 956–977 (1997).

Collins, G. W., Bittner, D., Monsler, E., Letts, S., Tiszauer, D., Feit, M., Mapoles, E., and Bernat, T., *Forming and Smoothing D_2 and HD Layers for ICF by Infrared Heating,* Lawrence Livermore National Laboratory, Livermore, CA, UCRL-JC-124255 ABS. Prepared for *11th Target Fabrication Specialists' Mtg,* Orcas Island, WA, Sept 8–12, 1996.

Collins, G. W., Budil, K. S., Cauble, R., Celliers, P., Da Silva, L. B., Holmes, N., Wallace, R., Dixit, S., Hammel, B. A., Kilkenny, J. D., and Ng, A., *Temperature Measurements of Shock Compressed Liquid D_2,* Lawrence Livermore National Laboratory, Livermore, CA, UCRL-JC-124885 ABS. Prepared for *38th Annual Mtg of the American Physical Society Div of Plasma Physics,* Denver, CO, Nov 11–15, 1996.

Collins, G. W., Kozioziemski, B. J., Bernat, T. P., Mapoles, E. R., and Unites, W., *Crystal Growth and Roughening of Solid D_2,* Lawrence Livermore National Laboratory, Livermore, CA, UCRL-JC-125121 ABS. Prepared for *11th Target Fabrication Specialists' Mtg,* Orcas Island, WA, Sept 8–12, 1996.

Collins, G. W., Mapoles, E. R., Sanchez, J. J., Bernat, T., Sater, J. D., Bittner, D., Sheliak, J. D., and Hoffer, J. K., *Reducing DT Surface Roughness for Cryogenic Ignition Targets,* Lawrence Livermore National Laboratory, Livermore, CA, UCRL-JC-124884 ABS. Prepared for *38th Annual Mtg of the American Physical Society Div of Plasma Physics,* Denver, CO, Nov 11–15, 1996.

Collins, G. W., Bernat, T. P., Mapoles, E. R., and Duriez, C., *Heat-Flux Induced Changes to Multicrystalline D_2 Surfaces,* Lawrence Livermore National Laboratory, Livermore, CA, UCRL-JC-124261. Submitted to *Phys. Rev. Lett.*

Collins, G. W., Bittner, D. N., Monsler, E., Tiszauer, D., Feit, M., Mapoles, E., and Bernat, T. P., *Forming and Smoothing D_2 and HD Layers for ICF by Infra-Red Heating,* Lawrence Livermore National Laboratory, Livermore, CA, UCRL-JC-124255. Prepared for the *24th European Conf on Laser Interaction with Matter,* Madrid, Spain, Jun 3–7, 1996.

Collins, G. W., Bittner, D. N., Monsler, E., Letts, S., Tiszauer, D., Feit, M., Mapoles, E. R., and Bernat, T. P., *Forming and Smoothing D2 and HD Layers for ICF,* Lawrence Livermore National Laboratory, Livermore, CA, UCRL-JC-123596 ABS. Prepared for the *24th European Conf on Laser Interaction with Matter,* Madrid, Spain, Jun 3–7, 1996.

Collins, G. W., Letts, S. A., Mapoles, E. R., Bernat, T. P., Bittner, D. N., and Monsler, E., *Infra-Red Redistribution of D_2 and HD Layers for ICF,* Lawrence Livermore National Laboratory, Livermore, CA, UCRL-JC-122449; *J. Vac. Sci. Technol. A* **14**(5), 2897–2900 (1996).

Collins, G., and Shevtsov, V., *Ortho-Para Conversion in Solid Hydrogen Isotopes, Catalyzed by Paramagnetic Impurities,* Lawrence Livermore National Laboratory, Livermore, CA, UCRL-PROP-123760.

Collins, G. W., Tiszauer, D., Feit, M., Unites, W. G., Mapoles, E. R., Bernat, T. P., Bittner, D. N., and Monsler, E., *Smoothing Thick Hydrogen Films by Laser Heating,* Lawrence Livermore National Laboratory, Livermore, CA, UCRL-JC-122690 ABS. Prepared for the *1996 March Mtg of the American Physical Society,* St Louis, MO, Mar 18–22, 1996.

Colston Jr., B., Everett, M., Nathel, H., and Otis, L., *Optical Coherence Tomography for Dental Applications,* Lawrence Livermore National Laboratory, Livermore, CA, UCRL-JC-125241-ABS. Prepared for *Optical Society of America,* Rochester, NY, Oct 20, 1996.

Colvin, J., Hogan, W., Perry, M., and Tabak, M., *Inertial Fusion Energy Development at LLNL: the National Ignition Facility, 100-1000 TW Lasers, and Fast Ignitor Physics,* Lawrence Livermore National Laboratory, Livermore, CA, UCRL-JC-124285 ABS. Prepared for the *8th Intl Conf on Emerging Nuclear Energy Systems,* Obninsk, Russia, Jun 24–28, 1996.

Correll, D., *1995 ICF Annual Report,* Lawrence Livermore National Laboratory, Livermore, CA, UCRL-LR-105820-95.

Correll, D. L., and Vergino, E., *NIFTY,* Lawrence Livermore National Laboratory, Livermore, CA, UCRL-JC-124868 ABS. Prepared for *38th Annual Mtg of the American Physical Society Div of Plasma Physics,* Denver, CO, Nov 11–15, 1996.

Crane, J., Martinez, M., Moran, B., Laumann, C., Davin, J., Beach, R., Golick, B., Jones, R., Wing, R., Braucht, J., Perry, M., and Mitchell, S., *Description and Performance of the Preamplifier for the National Ignition Facility (NIF) Laser System,* Lawrence Livermore National Laboratory, Livermore, CA, UCRL-JC-124517 ABS. Prepared for *2nd Annual Intl Conf on Solid-State Lasers for Application to Inertial Confinement Fusion,* Paris, France, Oct 22–25, 1996.

Crane, J., Martinez, M., Moran, B., Laumann, C., Davin, J., Rothenberg, J., Beach, R., Golick, B., Jones, R., Wing, R., Braucht, J., Skulina, K., and Mitchell, S., *High-Gain, Nd-Doped-Glass Preamplifier for the National Ignition Facility (NIF) Laser System,* Lawrence Livermore National Laboratory, Livermore, CA, UCRL-JC-124483 ABS & SUM. Prepared for the *Lasers and Electro-Optics Society '96,* Boston, MA, Nov 18–21, 1996.

Crane, J. K., Martinez, M., Beach, R. J., Mitchell, S., Pratt, G., and Christensen, J. J., *Ultra-Stable, Diode-Pumped Nd-Doped Glass Regenerative Amplifier for the National Ignition Facility (NIF),* Lawrence Livermore National Laboratory, Livermore, CA, UCRL-JC-122738. Prepared for the *Conf on Lasers and Electro-Optics (CLEO '96),* Anaheim, CA, Jun 2–7, 1996.

D

Darinskii, A., Lyulin, A., Torchinskii, F., Neelov, I., and Cook, R., *Conformational Properties and Spectrum of Relaxation Times for Polymer Chain in Quadrupole Field Computer Simulation,* Lawrence Livermore National Laboratory, Livermore, CA, UCRL-JC-123512 ABS. Prepared for the *Intl Symp on Molecular Order and Mobility in Polymer Chemistry,* St. Petersburg, Russia, May 21–24, 1996.

Da Silva, L. B., Barbee Jr., T. W., Cauble, R., Celliers, P., Ciarlo, D., Libby, S., London, R. A., Matthews, D., Mrowka, S., Moreno, J. C., Ress, D., Trebes, J. E., Wan, A. S., and Weber, F., *Electron Density Measurements of High Density Plasmas Using Soft X-Ray Laser Interferometry,* Lawrence Livermore National Laboratory, Livermore, CA, UCRL-JC-120243; *Phys. Rev. Lett.* **20**(5), 3991–3994 (1995).

Da Silva, L. B., Barbee Jr., T. W., Cauble, R., Celliers, P., Harder, J., Lee, H. R., London, R. A., Matthews, D. L., Mrowka, S., Moreno, J. C., Ress, D., Trebes, J. E., Wan, A., and Weber, F., *X-Ray Lasers for High Density Plasma Diagnostics,* Lawrence Livermore National Laboratory, Livermore, CA, UCRL-JC-116411; *Rev. Sci. Inst.* **66**(1), 574–578 (1995).

Da Silva, L. B., MacGowan, B. J., Mrowka, S., Koch, J. A., London, R. A., Matthews, D. L., and Underwood, J. H., *Power Measurements of a Saturated Yttrium X-Ray Laser,* Lawrence Livermore National Laboratory, Livermore, CA, UCRL-JC-113178 (1995). Submitted to *Opt. Lett.*

Da Silva, L. B., Barbee, T. W., Cauble, R., Celliers, P., Decker, C. D., London, R. A., Moreno, J. C., Trebes, J. E., Wan, A. S., and Weber, F., *Applications of Soft X-Ray Lasers for Probing High Density Plasmas,* Lawrence Livermore National Laboratory, Livermore, CA, UCRL-JC-124006 ABS. Prepared for the *5th Intl Conf on X-Ray Lasers,* Lund, Sweden, Jun 10–14, 1996.

Da Silva, L. B., Barbee, T. W., Cauble, R., Celliers, P., Decker, C. D., London, R. A., Moreno, J. C., Trebes, J. E., Wan, A. S., and Weber, F., *Electron Density Measurements Using Soft X-Ray Lasers,* Lawrence Livermore National Laboratory, Livermore, CA, UCRL-JC-124028 ABS. Prepared for the *24th European Conf on Laser Interaction with Matter,* Madrid, Spain, Jun 3–7, 1996.

Da Silva, L. B., Barbee, T. W., Cauble, R., Celliers, P., Kalantar, D. H., Key, M. H., Libby, S., Matthews, D. L., Moreno, J. C., Trebes, J. E., Wan, A. S., and Weber, F., *Application of X-Ray Laser to Probe High Density Plasmas,* Lawrence Livermore National Laboratory, Livermore, CA, UCRL-JC-124048 ABS. Prepared for the *23rd IEEE Intl Conf on Plasma Science,* Boston, MA, Jun 3–5, 1996.

Da Silva, L. B., Stuart, B. C., Celliers, P. M., Chang, T. D., Feit, M. D., Glinsky, M. E., Heredia, N. J., Herman, S., Lane, S. M., London, R. A., Matthews, D. L., Neev, J., Perry, M. D., and Rubenchik, A. M., *Comparison of Soft and Hard Tissue Ablation with Sub-ps and ns Pulse Lasers,* Lawrence Livermore National Laboratory, Livermore, CA, UCRL-JC-124044. Prepared for the *Society of Photo-Optical Instrumentation Engineers '96 Conf,* San Jose, CA, Jan 28–Feb 2 , 1996.

Da Silva, L. B., Barbee Jr., T. W., Cauble, R., Celliers, P., Decker, C. D., Kalantar, D. H., Key, M. H., London, R. A., Moreno, J. C., Trebes, J. E., Wan, A. S., and Weber, F., *Application of Soft X-Ray Lasers for Probing High Density Plasmas,* Lawrence Livermore National Laboratory, Livermore, CA, UCRL-JC-125218. Prepared for *5th Intl Conf on X-ray Lasers,* Lund, Sweden, Jun 10–14, 1996.

Da Silva, L. B., Budil, K. S., Cauble, R. C., Celliers, P. M., Collins, G. W., Hammel, B. A., Holmes, N. C., Wallace, R. J., Dixit, S. N., Kilkenny, J. D., and Ng, A., *Density Measurements of Shock Compressed Liquid D_2,* Lawrence Livermore National Laboratory, Livermore, CA, UCRL-JC-124921 ABS. Prepared for *38th Annual Mtg of the American Physical Society Div of Plasma Physics,* Denver, CO, Nov 11–15, 1996.

Davin, J., Braucht, J., Skulina, K., Deadrick, F., Laumann, C., Martinez, M., Bartlow, M., and Hawkins, S., *Design of the Preamplifier Integration Testbed for the National Ignition Facility (NIF),* Lawrence Livermore National Laboratory, Livermore, CA, UCRL-JC-124382 ABS. Prepared for *2nd Annual Intl Conf on Solid-State Lasers for Application to Inertial Confinement Fusion (ICF),* Paris, France, Oct 22–25, 1996.

Davis, J. F., *Final Report Facilitization of the National Ignition Facility (NIF) for Radiation Sciences Experiments,* Lawrence Livermore National Laboratory, Livermore, CA, UCRL-CR-123781.

Decker, C. D., and London, R. A., *Design Calculations of a Compact Ni-Like Tungsten Soft X-Ray Laser,* Lawrence Livermore National Laboratory, Livermore, CA, UCRL-JC-124489 ABS. Prepared for the *26th Annual Anomalous Absorption Conf,* Fairbanks, AK, Aug 26–30, 1996.

Decker, C. D., Mori, W. B., Tzeng, K. C., and Katsouleas, T., *Modeling Single-Frequency Laser-Plasma Acceleration Using Particle-in-Cell Simulations: the Physics of Beam Breakup,* Lawrence Livermore National Laboratory, Livermore, CA, UCRL-JC-124016; *Transactions on Plasma Science* **24**(2), 379–392 (1996).

Decker, C., *Evolution of Ultra-Intense, Short-Pulse Lasers in Underdense Plasmas,* Lawrence Livermore National Laboratory, Livermore, CA, UCRL-JC-122408 ABS. Prepared for the *37th Annual Mtg of the American Physical Society Div of Plasma Physics,* Louisville, KY, Nov 6–10, 1995.

Decker, C. D., Mori, W. B., Katsouleas, T., and Hinkel, D. E., *Spatial Temporal Theory of Raman Forward Scattering,* Lawrence Livermore National Laboratory, Livermore, CA, UCRL-JC-123023; *Phys. of Plasmas* **3**(4), 1360–1372 (1996).

Decker, C., Mori, W. B., Tzeng, K.-C., and Katsouleas, T., *The Evolution of Ultra-Intense, Short-Pulse Lasers in Underdense Plasmas,* Lawrence Livermore National Laboratory, Livermore, CA, UCRL-JC-122408. Prepared for the *37th Annual Mtg of the American Physical Society Div of Plasma Physics,* Louisville, KY, Nov 6–10, 1995.

Decker, C. D., Turner, R. E., Landen, O. L., Kornblum H. N., Amendt, P., Suter, L. J., Murphy, T. J., Wallace, J., Hauer, A. A., Knauer, J., Marshall, F. J., Bradley, D., McCrory, R. L., Seka, W., and Soures, J. M., *Modeling Radiation Drive in Recent Hohlraum Experiments on Omega,* Lawrence Livermore National Laboratory, Livermore, CA, UCRL-JC-124671 ABS. Prepared for *38th Annual Mtg of the American Physical Society Div of Plasma Physics,* Denver, CO, Nov 11–15, 1996.

De Groot, J. S., Denney, C., Eddleman, J. L., Estabrook, K. G., Hammer, J. H., Sanford, T. W. L., Speilman, R. B., and Toor, A., *Non-LTE Effects in Imploding Z-Pinches,* Lawrence Livermore National Laboratory, Livermore, CA, UCRL-JC-124687 ABS. Prepared for *38th Annual Mtg of the American Physical Society Div of Plasma Physics,* Denver, CO, Nov 11–15, 1996.

De Groot, J. S., Matte, J. P., Estabrook, K., and Kruer, W. L., *Heat Transport in High Temperature Hohlraums,* Lawrence Livermore National Laboratory, Livermore, CA, UCRL-JC-125108 ABS. Prepared for *26th Anomalous Absorption Conf,* Fairbanks, AK, Aug 26–30, 1996.

Demiris, A., *Metal-Plastic Composite Targets for Instability Studies on Nova,* Lawrence Livermore National Laboratory, Livermore, CA, UCRL-JC-125129 ABS. Prepared for *11th Target Fabrication Specialists' Mtg,* Orcas Island, WA, Sept 8–12, 1996.

De Yoreo, J. J., Land, T. A., Rashkovich, L. N., Onishchenko, T. A., and Monovskii, O. V., *An AFM Investigation of Growth Hillock Morphology and Surface Smoothening on KH_2PO_4 (101),* Lawrence Livermore National Laboratory, Livermore, CA, UCRL-JC-123599 ABS. Prepared for the *10th American Conf on Crystal Growth and the 9th Intl Conf on Vapor Growth & Epitaxy,* Vail, CO, Aug 4–9, 1996.

Ditmire, T., Donnelly, T., Falcone, R. W., and Perry, M. D., *Strong X-Ray Emission from High-Temperature Plasmas Produced by Intense Irradiation of Clusters,* Lawrence Livermore National Laboratory, Livermore, CA, UCRL-JC-121304; *Phys. Rev. Lett.* **75**(17), 3122–3125 (1995).

Ditmire, T., Nguyen, H., and Perry, M. D., *Amplification of Femtosecond Pulses to 1 J in Cr:$LiSrAlF_6$,* Lawrence Livermore National Laboratory, Livermore, CA, UCRL-JC-118531 Rev. 1; *Opt. Lett.* **20**(10), 1142–1144 (1995).

Dittrich, T. R., Haan, S. W., and Strobel, G. L., *NIF Capsule Design Candidates,* Lawrence Livermore National Laboratory, Livermore, CA, UCRL-JC-124667 ABS. Prepared for *38th Annual Mtg of the American Physical Society Div of Plasma Physics,* Denver, CO, Nov 11–15, 1996.

Dittrich, T., Haan, S., Pollaine, S., Burnham, A., and Strobel, G., *NIF Capsule Design Update,* Lawrence Livermore National Laboratory, Livermore, CA, UCRL-JC-124913 ABS Rev. 1. Prepared for *11th Target Fabrication Specialists' Mtg,* Orcas Island, WA, Sept 8–12, 1996.

Dixit, S. N., Rushford, M. R., Thomas, I. M., Herman, S. M., Britten, J. A., Shore, B. W., and Perry, M. D., *Color Separation Gratings for Diverting the Unconverted Light Away from the NIF Target,* Lawrence Livermore National Laboratory, Livermore, CA, UCRL-JC-124512 ABS. Prepared for *2nd Annual Intl Conf on Solid-State Lasers for Application to Inertial Confinement Fusion,* Paris, France, Oct 22–25, 1996.

Dixit, S., and Feit, M., *Synthesis of Fully Continuous Phase Screens for Tailoring the Focal Plane Irradiance Profiles,* Lawrence Livermore National Laboratory, Livermore, CA, UCRL-JC-124012. Prepared for the *1996 Diffractive Optics and Micro Optics Topical Mtg,* Boston, MA, Apr 29–May 2, 1996.

Dixit, S. N., Feit, M. D., Perry, M. D., and Powell, H. T., *Designing Fully Continuous Phase Screens for Tailoring Focal Plane Irradiance Profiles,* Lawrence Livermore National Laboratory, Livermore, CA, UCRL-JC-123842. Submitted to *Opt Lett.*

Dixit, S. N., Feit, M. D., Perry, M. D., and Powell, H. T., *Designing Fully Continuous Phase Screens for Tailoring Focal Plane Irradiance Profiles,* Lawrence Livermore National Laboratory, Livermore, CA, UCRL-JC-123842 Rev. 1; *Opt Lett.* **21**(21), 1715–1717 (1996).

Dubois, P. F., *Introduction to Python,* Lawrence Livermore National Laboratory, Livermore, CA, UCRL-JC-124262. Prepared for the *4th Intl Python Workshop,* Livermore, CA, Jun 3–6, 1996.

Dubois, P. F., *Object Technology for Scientific Computing,* Lawrence Livermore National Laboratory, Livermore, CA, UCRL-JC-124451. Prepared for the *Tools USA '96,* Santa Barbara, CA, Jul 28–Aug 2, 1996.

Dubois, P. F., and Yang, T.-Y. B., *Extending Python,* Lawrence Livermore National Laboratory, Livermore, CA, UCRL-JC-123346. Submitted to *Comput. Phys.*

E

Eder, D. C., Bardsley, J. N., Boley, C. D., Feit, M. D., Koniges, A. E., Kozlowski, M. R., London, R. A., Penetrante, B. M., Rubenchik, S., Wurz, H., and Kappler, F., *Low Temperature Plasma Ablation,* Lawrence Livermore National Laboratory, Livermore, CA, UCRL-JC-124666 ABS. Prepared for *38th Annual Mtg of the American Physical Society Div of Plasma Physics,* Denver, CO, Nov 11–15, 1996.

Eder, D. C., Maitland, D. J., London, R. A., Small, W., Heredia, N. J., and Soltz, B. A., *2D Simulations of Laser Assisted Tissue Welding,* Lawrence Livermore National Laboratory, Livermore, CA, UCRL-JC-124936 ABS. Prepared for *Society of Photo-Optical Instrumentation Engineers BiOS '97 Mtg,* San Jose, CA, Feb 8–14, 1997.

Ehrlich, R. B., Amendt, P. A., Dixit, S. N., Hammel, B. A., Kalantar, D. H., Pennington, D. M., and Weiland, T. L., *Developing Beam Phasing on the Nova Laser,* Lawrence Livermore National Laboratory, Livermore, CA, UCRL-JC-124513 ABS. Prepared for *2nd Annual Intl Conf on Solid-State Lasers for Application to Inertial Confinement Fusion,* Paris, France, Oct 22–25, 1996.

Emanuel, M. A., Skidmore, J. A., and Carlson, N. W., *High-Power Laser Diodes at 808, 941 and 1800 nm,* Lawrence Livermore National Laboratory, Livermore, CA, UCRL-JC-124909 ABS. Prepared for *Society of Photo-Optical Instrumentation Engineers Optoelectronics '97,* San Jose, CA, Feb 8–19, 1997.

Emanuel, M. A., Carlson, N. W., and Skidmore, J. A., *High Efficiency AlGaAs-Based Laser Diode at 808 nm with Large Transverse Spot Size,* Lawrence Livermore National Laboratory, Livermore, CA, UCRL-JC-124003; *IEEE Photonics Technology Letters* **8**(10), 1291–1293 (1996).

English, R. E., Seppala, L. G., Vann, C. S., and Bliss, E. S., *Use of an Intermediate Wavelength Laser for Alignment to Inertial Confinement Fusion Targets,* Lawrence Livermore National Laboratory, Livermore, CA, UCRL-JC-120509. Prepared for the *1st Annual Int'l Conf on Solid-State Lasers for Application to Inertial Confinement Fusion,* Monterey, CA, May 30–Jun 2, 1995.

Erlandson, A. C., Rotter, M. D., Horvath, J., Frank, D. N., McCracken, R. W., Jancaitis, K. S., Seznec, S. E., LeTouze, G., Cabourdin, O., Fornerod, C., and Bosch, P., *Multisegment Nd:Glass Amplifiers for the U.S. National Ignition Facility and the French Laser Megajoule,* Lawrence Livermore National Laboratory, Livermore, CA, UCRL-JC-122542 ABS & SUM. Prepared for the *Conf on Lasers and Electro-Optics (CLEO '96),* Anaheim Conf Center, Anaheim, CA, Jun 2–7, 1995. Submitted to the *Optical Society of America.*

Erlandson, A. C., Zapata, L. E., Pedrotti, L., Jancaitis, K. S., Saks, R. W., Rotter, M. D., Seznec, S. E., LeTouze, G., Carbourdin, O., and Fornerod, J. C., *The Effect of Amplifier Component Maintenance on Laser System Availability and Operating Costs for the U.S. National Ignition Facility and the French Laser Megajoule,* Lawrence Livermore National Laboratory, Livermore, CA, UCRL-JC-124911 ABS. Prepared for 2*nd Annual Intl Conf on Solid-State Lasers for Application to Inertial Confinement Fusion,* Paris, France, Oct 22–25, 1996.

Eroshenko, V. A., Bondarenko, S. V., and Kochemasov, G. G., *Multidimensional Theoretical/Computational Modeling of Non-Coaxial SBS,* Lawrence Livermore National Laboratory, Livermore, CA, UCRL-CR-122699.

Estabrook, K. G., De Groot, J. S., Kruer, W. L., and Matte, J. P., *Heat Transport in High Z Plasmas at High Laser Powers,* Lawrence Livermore National Laboratory, Livermore, CA, UCRL-JC-124689 ABS. Prepared for *38th Annual Mtg of the American Physical Society Div of Plasma Physics,* Denver, CO, Nov 11–15, 1996.

Estabrook, K. G., De Groot, J. S., Kruer, W. L., and Matte, J. P., *Heat Transport in High Z Plasmas at High Laser Powers,* Lawrence Livermore National Laboratory, Livermore, CA, UCRL-JC-124852 ABS. Prepared for *38th Annual Mtg of the American Physical Society Div of Plasma Physics,* Denver, CO, Nov 11–15, 1996.

Estabrook, K. G., Celliers, P., Murray, J., Wallace, R., Stone, G., Van Wonterghem, B., MacGowan, B., Hunt, J., and Manes, K., *An Improved Pinhole Spatial Filter,* Lawrence Livermore National Laboratory, Livermore, CA, UCRL-JC-124475 ABS. Prepared for the *26th Annual Anomalous Absorption Conf,* Fairbanks, AK, Aug 26–30, 1996.

Estabrook, K. G., Glenzer, S. H., Back, C. A., MacGowan, B. J., Montgomery, D. S., Stone, G. F., Moody, J. D., and Kirkwood, R. K., *Electron Temperature and Density Measurements in Large Scale-Length Gasbag Plasmas by K-Shell Spectroscopy,* Lawrence Livermore National Laboratory, Livermore, CA, UCRL-JC-124474 ABS. Prepared for the *26th Annual Anomalous Absorption Conf,* Fairbanks, AK, Aug 26–30, 1996.

Everett, M. J., Lal, A., Clayton, C. E., Mori, W. B., Joshi, C., and Johnston, T. W., *Coupling Between Electron Plasma Waves in Laser-Plasma Interactions,* Lawrence Livermore National Laboratory, Livermore, CA, UCRL-JC-122651 ABS (1995); *Phys. Plasmas* **3**(5), 2041–2046 (1996).

F

Fearon, E., Letts, S., Allison, L., and Cook, R., *Attempts to Fabricate Special ICF Targets Using the Decomposable Mandrel Technique,* Lawrence Livermore National Laboratory, Livermore, CA, UCRL-JC-125130 ABS. Prepared for *11th Target Fabrication Specialists' Mtg,* Orcas Island, WA, Sept 8–12, 1996.

Feit, M. D., and Rubenchik, A. M., *Laser Intensity Modulation by Nonabsorbing Defects,* Lawrence Livermore National Laboratory, Livermore, CA, UCRL-JC-124536 ABS Rev. 1. Prepared for *28th Annual Symp on Optical Materials for High Power Lasers,* Boulder, CO, Oct 7–9, 1996.

Feit, M. D., and Rubenchik, A. M., *Laser Intensity Modulation by Nonabsorbing Defects,* Lawrence Livermore National Laboratory, Livermore, CA, UCRL-JC-124536 ABS. Prepared for 2*nd Annual Intl Conf on Solid-State Lasers for Application to Inertial Confinement Fusion,* Paris, France, Oct 22–25, 1996.

Feit, M. D., Rubenchik, A. M., Faux, D. R., Riddle, R. A., Eder, D. C., Penetrante, B. M., Milam, D., Genin, F. Y., and Kozlowski, M. R., *Modeling of Laser Damage Initiated by Surface Contamination,* Lawrence Livermore National Laboratory, Livermore, CA, UCRL-JC-124538 ABS Rev. 1. Prepared for *28th Annual Symp on Optical Materials for High Power Lasers,* Boulder, CO, Oct 7–9, 1996.

Feit, M. D., Rubenchik, A. M., Faux, D. R., Riddle, R. A., Eder, D. C., Penetrante, B. M., Milam, D., Genin, F. Y., and Kozlowski, M. R., *Modeling of Laser Damage Initiated by Surface Contamination,* Lawrence Livermore National Laboratory, Livermore, CA, UCRL-JC-124538 ABS. Prepared for *2nd Annual Intl Conf on Solid-State Lasers for Application to Inertial Confinement Fusion,* Paris, France, Oct 22–25, 1996.

Ficini, G., and Campbell, J. H., *Development of Large Scale Production of Nd-Doped Phosphate Glasses for Megajoule-Scale Laser Systems,* Lawrence Livermore National Laboratory, Livermore, CA, UCRL-JC-124027. Prepared for the *EUROPTO Conf,* Berlin, Germany, May 13–17, 1996. Submitted to *European Optical Society and The Intl Society for Optical Engineering.*

Fochs, S. N., Garcia, M., Rhodes, M., and Boley, C., *B-Field Interactions and Electrode Optimization in the Plasma Electrode Pockels Cell,* Lawrence Livermore National Laboratory, Livermore, CA, UCRL-JC-124532 ABS. Prepared for *2nd Annual Intl Conf on Solid-State Lasers for Application to Inertial Confinement Fusion,* Paris, France, Oct 22–25, 1996.

Franco, E. D., Ryon, R. W., Janssens, L. V., and Janssens, K., *Capillary Optics for Microanalysis Applications,* Lawrence Livermore National Laboratory, Livermore, CA, UCRL-JC-124358 ABS. Prepared for the *European Conf on X-Ray Spectrometry,* Universidade de Lisboa, Portugal, Jun 23–29, 1996.

Friedman, H., Erbert, G., Kuklo, T., Salmon, T., Smauley, D., Thompson, G., Malik, J., Wong, N., Kanz, K., and Neeb, K., *Sodium Laser Guide Star Results at the Lick Observatory,* Lawrence Livermore National Laboratory, Livermore, CA, UCRL-JC-121903. Prepared for the *Proceedings of the 1995 Adaptive Optics (AO'95) Topical Mtg,* Technical University of Munich, Garching, Germany, Oct 2–6, 1995.

Furnish, G. M., Miller, D. S., Painter, J. F., Gentile, N. A., and Eme, W. G., *HED: an Inertial Confinement Fusion Modelling Code for High Energy Density Simulations,* Lawrence Livermore National Laboratory, Livermore, CA, UCRL-JC-124685 ABS. Prepared for *38th Annual Mtg of the American Physical Society Div of Plasma Physics,* Denver, CO, Nov 11–15, 1996.

Furnish, G. M., Nystrom, W. D., and Lebrun, M. J., *Continuing Development of the Generalized Tokamak Simulator,* Lawrence Livermore National Laboratory, Livermore, CA, UCRL-JC-124678 ABS. Prepared for *38th Annual Mtg of the American Physical Society Div of Plasma Physics,* Denver, CO, Nov 11–15, 1996.

G

Garcia, M., *2D Fluid Model of the DC Planar Magnetron Cathode,* Lawrence Livermore National Laboratory, Livermore, CA, UCRL-JC-122494. Submitted to the *J. Vac. Sci. Technol.*

Genin, F. Y., and Stolz, C. J., *Morphologies of Laser-Induced Damage in Hafnia-Silica Multilayer Mirror and Polarizer Coatings,* Lawrence Livermore National Laboratory, Livermore, CA, UCRL-JC-124879 ABS & VG. Prepared for *Society of Photo-Optical Instrumentation Engineers 3rd Intl Workshop on Laser Beam and Optics Characterization,* Quebec, Canada, Jul 8–10, 1996.

Genin, F. Y., and Stolz, C. J., *Morphologies of Laser-Induced Damage in Hafnia-Silica Multilayer Mirror and Polarizer Coatings,* Lawrence Livermore National Laboratory, Livermore, CA, UCRL-JC-124879 VG. Prepared for *Society of Photo-Optical Instrumentation Engineers 3rd Intl Workshop on Laser Beam and Optics Characterization,* Quebec, Canada, Jul 8–10, 1996.

Genin, F. Y., and Stolz, C. J., *Morphologies of Laser-Induced Damage in Hafnia-Silica Multilayer Mirror and Polarizer Coatings,* Lawrence Livermore National Laboratory, Livermore, CA, UCRL-JC-124879. Prepared for *Society of Photo-Optical Instrumentation Engineers 3rd Intl Workshop on Laser Beam and Optics Characterization,* Quebec, Canada, Jul 8–10, 1996.

Genin, F. Y., Furr, J., Kozlowski, M. R., and Brusasco, R. M., *Massive Laser Damage of Fused Silica at 355 and 1064 nm Initiated by Surface Contamination,* Lawrence Livermore National Laboratory, Livermore, CA, UCRL-JC-124537 ABS. Prepared for *2nd Annual Intl Conf on Solid-State Lasers for Application to Inertial Confinement Fusion,* Paris, France, Oct 22–25, 1996.

Genin, F. Y., Furr, J., Michlitsch, K., Kozlowski, M. R., and Krulevitch, P., *Laser-Induced Damage of Fused Silica at 355 and 1064 nm Initiated at Aluminum Contamination Particles on the Surface,* Lawrence Livermore National Laboratory, Livermore, CA, UCRL-JC-124878 ABS. Prepared for *28th Annual Symp on Optical Materials for High Power Lasers,* Boulder, CO, Oct 7–9, 1996.

Genin, F. Y., Stolz, C. J., and Kozlowski, M. R., *Growth of Laser-Induced Damage During Repetitive Illumination of HfO_2-SiO_2 Multilayer Mirror and Polarizer Coatings,* Lawrence Livermore National Laboratory, Livermore, CA, UCRL-JC-124877 ABS. Prepared for *28th Annual Symp on Optical Materials for High Power Lasers,* Boulder, CO, Oct 7–9, 1996.

Genin, F. Y., Stolz, C. J., Kozlowski, M. R., Atherton, L. J., and Hue, J., *Functional Damage Threshold of NIF and LMJ Mirrors and Polarizers at 1064 nm,* Lawrence Livermore National Laboratory, Livermore, CA, UCRL-JC-124533 ABS. Prepared for *2nd Annual Intl Conf on Solid-State Lasers for Application to Inertial Confinement Fusion,* Paris, France, Oct 22–25, 1996.

Genin, F. Y., Stolz, C. J., Reitter, T., Bevis, R., and Von Gunten, M., *Effect of Electric Field Distribution on the Morphologies of Laser-Induced Damage in Hafnia-Silica Multilayer Polarizers,* Lawrence Livermore National Laboratory, Livermore, CA, UCRL-JC-124873 ABS. Prepared for *28th Annual Symp on Optical Materials for High Power Lasers,* Boulder, CO, Oct 7–9, 1996.

Glendinning, S. G., Dixit, S. N., Hammel, B. A., Kalantar, D. H., Key, M. H., Kilkenny, J. D., Knauer, J. P., Pennington, D. M., Remington, B. A., Wallace, R. J., and Weber, S. V., *Measurements of Linear Regime Rayleigh–Taylor Growth Rates in Laser-Driven Planar Targets,* Lawrence Livermore National Laboratory, Livermore, CA, UCRL-JC-124653 ABS. Prepared for *38th Annual Mtg of the American Physical Society Div of Plasma Physics,* Denver, CO, Nov 11–15, 1996.

Glendinning, S. G., Dixit, S. N., Hammel, B. A., Kalantar, D. H., Key, M. H., Kilkenny, J. D., Knauer, J. P., Pennington, D. M., Remington, B. A., Wallace, R. J., and Weber, S. V., *Measurements of Linear Regime Rayleigh–Taylor Growth Rates in Laser-Driven Planar Targets,* Lawrence Livermore National Laboratory, Livermore, CA, UCRL-JC-124653 Rev. 1. Submitted to *Phys. Rev. Lett.*

Glendinning, S. G., and Correll, D., *Inertial Confinement Fusion Quarterly Report,* Volume 5, Number 3, Lawrence Livermore National Laboratory, Livermore, CA, UCRL-LR-105821-95-3.

Glendinning, S. G., Dixit, S. N., Hammel, B. A., Kalantar, D. H., Key, M. H., Kilkenny, J. D., Knauer, J. P., Pennington, D. M., Remington, B. A., Wallace, R. J., and Weber, S. V., *Equivalent Surface Finish of Laser Speckle Induced Perturbations in Laser Driven Foils,* Lawrence Livermore National Laboratory, Livermore, CA, UCRL-JC-123286 ABS. Prepared for the *11th Topical Conf on High Temperature Plasma Diagnostics,* Monterey, CA, May 12–16, 1996.

Glendinning, S. G., Dixit, S. N., Hammel, B. A., Kalantar, D. H., Key, M. H., Kilkenny, J. D., Knauer, J. P., Pennington, D. M., Remington, B. A., Wallace, R. J., and Weber, S. V., *Measurements of Laser Speckle Induced Perturbations in Laser Driven Foils,* Lawrence Livermore National Laboratory, Livermore, CA, UCRL-JC-123082; *Phys. Rev. E* **54**(4), 4473–4475 (1996).

Glendinning, S. G., Dixit, S. N., Hammel, B. A., Kalantar, D. H., Key, M. H., Kilkenny, J. D., Knauer, J. P., Pennington, D. M., Remington, B. A., Wallace, R. J., and Weber, S. V., *Measurements of Laser Speckle Induced Perturbations in Laser Driven Foils,* Lawrence Livermore National Laboratory, Livermore, CA, UCRL-JC-123292 ABS. Prepared for the *24th European Conf on Laser Interaction with Matter,* Madrid, Spain, Jun 3–7, 1996.

Glendinning, S. G., Powers, L. V., Kauffman, R. L., Landen, O. L., Ress, D. B., Stone, G. F., Suter, L. J., and Richard, A. L., *Measurements of Wall X-Ray Emission Patterns in Gas-Filled Hohlraums,* Lawrence Livermore National Laboratory, Livermore, CA, UCRL-JC-123021. Submitted to *Phys. Rev. Lett.*

Glendinning, S. G., Dixit, S. N., Hammel, B. A., Kalantar, D. H., Key, M. H., Kilkenny, J. D., Knauer, J. P., Pennington, D. M., Remington, B. A., Wallace, R. J., and Weber, S. V., *Measurement of a Dispersion Curve for Linear-Regime Rayleigh–Taylor Growth Rates in Laser-Driven Planar Targets,* Lawrence Livermore National Laboratory, Livermore, CA, UCRL-JC-124653; *Phys. Rev. Lett.* **78**(17), 3318–3321 (1997).

Glendinning, S. G., Hsing, W., Galmiche, D., Remington, B. A., Kalantar, D. H., Haan, S. W., Wallace, R. J., and Marinak, M. M., *Measurements of Rayleigh–Taylor Growth in Ablatively Driven Converging Hemispherical Targets at Nova,* Lawrence Livermore National Laboratory, Livermore, CA, UCRL-JC-124674 ABS. Prepared for *38th Annual Mtg of the American Physical Society Div of Plasma Physics,* Denver, CO, Nov 11–15, 1996.

Glenzer, S. H., Back, C. A., Estabrook, K. G., Kirkwood, R. K., Wallace, R., MacGowan, B. J., Hammel, B. A., Cid, R. E., and De Groot, J. S., *Thomson Scattering from Two-Species Laser-Produced Plasmas,* Lawrence Livermore National Laboratory, Livermore, CA, UCRL-JC-123752. Submitted to *Rev. Sci. Instrum.*

Glenzer, S. H., Back, C. A., Estabrook, K. G., MacGowan, B. J., Montgomery, D. S., Kirkwood, R. K., Moody, J. D., Munro, D. H., and Stone, G. F., *Electron Temperature and Density Measurements in Laser-Produced Large Scale-Length Gasbag Plasmas by X-Ray Spectroscopy,* Lawrence Livermore National Laboratory, Livermore, CA, UCRL-JC-124948; *Phys. Rev. Lett. E* **55**(1), 927–938 (1997).

Glenzer, S. H., Wrubel, Th., and Kunze, H.-J., *Investigation of a Short-Wavelength Laser Plasma of a Gas-Liner Pinch Discharge,* Lawrence Livermore National Laboratory, Livermore, CA, UCRL-JC-124886; *Phys. Rev. Lett. E* **55**(1), 939–946 (1997).

Glenzer, S. H., Back, C. A., Estabrook, K. G., and MacGowan, B. J., *The Effect of Laser Beam Smoothing on the Electron Temperature of a Laser-Produced Gold Plasma,* Lawrence Livermore National Laboratory, Livermore, CA, UCRL-JC-123282 ABS. Prepared for the *11th Topical Conf on High Temperature Plasma Diagnostics,* Monterey, CA, May 12–16, 1996.

Glenzer, S. H., Back, C. A., Estabrook, K. G., MacGowan, B. J., Montgomery, D. S., Stone, G. F., Moody, J. D., and Kirkwood, R. K., *Electron Temperature Measurements in Gasbag Plasmas by X-Ray Spectroscopy,* Lawrence Livermore National Laboratory, Livermore, CA, UCRL-JC-123546 ABS. Prepared for the *24th European Conf on Laser Interaction with Matter,* Madrid, Spain, Jun 3–7, 1996.

Glenzer, S. H., Back, C. A., Estabrook, K. G., Wallace, R. J., Baker, K., Hammel, B. A., Cid, R. E., and DeGroot, J. S., *Thomson Scattering from Two Species Laser-Produced Plasmas,* Lawrence Livermore National Laboratory, Livermore, CA, UCRL-JC-123752 ABS. Prepared for the *11th Topical Conf on High-Temperature Plasma Diagnostics,* Monterey, CA, May 12–16, 1996.

Glenzer, S. H., *Critical Tests of Line Broadening Theories by Precision Measurements,* Lawrence Livermore National Laboratory, Livermore, CA, UCRL-JC-123573. Prepared for the *37th Annual Mtg of the American Physical Society Div of Plasma Physics,* Louisville, KY, Nov 6–10, 1996.

Glenzer, S., and Kunze, H.-J., *Stark Broadening of Resonance Transitions in B III,* Lawrence Livermore National Laboratory, Livermore, CA, UCRL-JC-123045 Submitted to *Phys. Rev. Lett.*

Glenzer, S. H., Back, C. A., Estabrook, K. G., and MacGowan, B. J., *Thomson Scattering in the Corona of Laser-Produced Gold Plasmas,* Lawrence Livermore National Laboratory, Livermore, CA, UCRL-JC-123282. Prepared for the *11th Topical Conf on High Temperature Plasma Diagnostics,* Monterey, CA, May 12–16, 1996.

Glenzer, S. H., Back, C. A., Estabrook, K. G., Wallace, R., Baker, K., MacGowan, B. J., Hammel, B. A., Cid, R. E., and DeGroot, J. S., *Thomson Scattering from Two Species Laser-Produced Plasmas,* Lawrence Livermore National Laboratory, Livermore, CA, UCRL-JC-123752 ABS Rev. 1. Prepared for the *26th Annual Anomalous Absorption Conf,* Fairbanks, AK, Aug 26–30, 1996.

Glenzer, S. H., Back, C. A., Estabrook, K. G., Wallace, R., Baker, K., MacGowan, B. J., Hammel, B. A., Cid, R. E., and DeGroot, J. S., *Observation of Two Ion Acoustic Waves in a Two-Species Laser-Produced Plasma with Thomson Scattering,* Lawrence Livermore National Laboratory, Livermore, CA, UCRL-JC-124283; *Phys. Rev. Lett.* **77**(8), 1496–1499 (1996).

Grote, D. P., Friedman, A., Haber, I., and Yu, S., *Three-Dimensional Simulations of High-Current Beams in Induction Accelerators with WARP3D,* Lawrence Livermore National Laboratory, Livermore, CA, UCRL-JC-121280. Prepared for the *Int'l Symp on Heavy Ion Fusion,* Princeton, NJ, Sept 6–9, 1995.

H

Haan, W. S., Dittrich, T. R., and Strobel, G., *Modeling of Hydrodynamic Instabilities on Indirect Drive Ignition Targets,* Lawrence Livermore National Laboratory, Livermore, CA, UCRL-JC-124545 ABS. Prepared for *38th Annual Mtg of the American Physical Society Div of Plasma Physics,* Denver, CO, Nov 11–15, 1996.

Hamilton, R., and Tietbohl, G. L., *Design of a 0.94-cm Mirror Mount for the Petawatt Project on Nova,* Lawrence Livermore National Laboratory, Livermore, CA, UCRL-ID-122342.

Hammel, B. A., Amendt, P., Glendinning, S. G., Landen, O. L., and Suter, L. J., *Measurements of Time-Dependent Asymmetry in Nova Hohlraums by Witness Foam Balls,* Lawrence Livermore National Laboratory, Livermore, CA, UCRL-JC-123295 ABS. Prepared for the *24th European Conf on Laser Interaction with Matter,* Madrid, Spain, Jun 3–7, 1996.

Hammel, B. A., Cauble, R., Celliers, P., Da Silva, L., Dittrich, T. R., Griswold, D., Haan, S. W., Holmes, N., Landen, O. L., Orzechowski, T., and Perry, T. S., *Shock Physics with the Nova Laser for ICF Applications,* Lawrence Livermore National Laboratory, Livermore, CA, UCRL-JC-121637 Rev 1. Prepared for the *1995 American Physical Society Topical Conf on Shock Compression of Condensed Matter,* Seattle, WA, Aug 13–18, 1995. Submitted to the *American Physical Society.*

Hammel, B. A., *High Energy Density Physics with the Nova Laser,* Lawrence Livermore National Laboratory, Livermore, CA, UCRL-JC-123578 ABS. Prepared for the *Intl Seminar on Physics on High Energy Density Matter,* Vancouver, Canada, May 26–29, 1996.

Hammer, J. H., Eddleman, J. L., Tabak, M., Toor, A., Zimmerman, G. B., and DeGroot, J. S., *Sheath Broadening in Imploding Z-Pinches due to Large-Bandwidth Rayleigh-Taylor Instability,* Lawrence Livermore National Laboratory, Livermore, CA, UCRL-JC-123519. Prepared for the *Institute of Plasma Physics,* Czech, Republic, Jun 10–14, 1996.

Hammer, J. H., Eddleman, J. L., Estabrook, K. G., Foord, M., Maxon, S., Springer, P., Tabak, M., Toor, A., Wong, K., Zimmerman, G. B., and De Groot, J. S., *2D Radiation MHD Simulations of Neon-Argon SATURN Z-Pinches,* Lawrence Livermore National Laboratory, Livermore, CA, UCRL-JC-124855 ABS. Prepared for *38th Annual Mtg of the American Physical Society Div of Plasma Physics,* Denver, CO, Nov 11–15, 1996.

Haney, S. W., *Beating the Abstraction Penalty in C++ Using Expression Templates,* Lawrence Livermore National Laboratory, Livermore, CA, UCRL-JC-125237. Submitted to *Comput. & Phys.*

Hatchett, S. P., Moody, J. D., Hammer, J. H., and Tabak, M., *Designs for Hole-Boring and Integrated Fast Ignitor Experiments,* Lawrence Livermore National Laboratory, Livermore, CA, UCRL-JC-124485 ABS. Prepared for the *26th Annual Anomalous Absorption Conf,* Fairbanks, AK, Aug 26–30, 1996.

Hayden, J. S., Thorne, A. J., Sapak, D. L., Grilz, D. A., Finnerty, P. J., and Heusing, E., *Cost Analysis and Conceptual Design of an Advanced Discontinuous Melter,* Lawrence Livermore National Laboratory, Livermore, CA, UCRL-CR-123005.

Havstad, M. A., McLean II, W., and Lewis, R. C., *Miniature Kinematic Mirror Mount for UHV Service,* Lawrence Livermore National Laboratory, Livermore, CA, UCRL-JC-118118; *Appl. Opt.* **34**(34), 8078 (1995).

Hayden, J. S., *Report Characterization of FOM-148 Composition,* Lawrence Livermore National Laboratory, Livermore, CA, UCRL-CR-122048.

Heestand, G. M., Anklam, T. M., and Shepp, T. A., *Use of Electron Beam Physical Vapor Deposition (EBPVD) for Rapid Tooling and Net Shape Forming,* Lawrence Livermore National Laboratory, Livermore, CA, UCRL-JC-123586 ABS. Prepared for *1996 The Mineral, Metal and Material Society/The Metallurgical Society Fall Mtg/Materials Week,* Cincinnati, OH, Oct 6–10, 1996.

Herman, S. M., Britten, J. A., Body, R. D., Shore, B. W., Agayan, R. R., and Perry, M. D., *Further Development of Shallow-Relief Gratings for Beam Diagnostics Applications on NIF,* Lawrence Livermore National Laboratory, Livermore, CA, UCRL-JC-124505 ABS. Prepared for *2nd Annual Intl Conf on Solid-State Lasers for Application to Inertial Confinement Fusion,* Paris, France, Oct 22–25, 1996.

Hermes, G., *Facility Safety Procedure Building 391 Complex Nova Facility,* Lawrence Livermore National Laboratory, Livermore, CA, UCRL-FSP-391-95.

Hinkel, D. A., Williams, E. A., and Still, C. H., *Laser Beam Deflection Induced by Transverse Plasma Flow,* Lawrence Livermore National Laboratory, Livermore, CA, UCRL-JC-121493. Submitted to *Phys. Rev. Lett.*

Hinkel, D. E., Still, C. H., Afeyan, B. B., Berger, R. L., Langdon, A. B., and Williams, E. A., *Simulation of Filamentation in Plasmas with Transverse and Axial Flows,* Lawrence Livermore National Laboratory, Livermore, CA, UCRL-JC-124473 ABS. Prepared for the *26th Annual Anomalous Absorption Conf,* Fairbanks, AK, Aug 26–30, 1996.

Hinkel, D. E., Still, C. H., Berger, R. L., Langdon, A. B., and Williams, E. A., *Backscatter, Filamentation and Laser Light Smoothing in Flowing Plasmas,* Lawrence Livermore National Laboratory, Livermore, CA, UCRL-JC-124684 ABS. Prepared for *38th Annual Mtg of the American Physical Society Div of Plasma Physics,* Denver, CO, Nov 11–15, 1996.

Hinkel, D. E., Williams, E. A., Berger, R. L., and Langdon, A. B., *Filamentation and Beam Deflection in Flowing Plasmas: Latest Results,* Lawrence Livermore National Laboratory, Livermore, CA, UCRL-JC-124466 ABS. Prepared for the *26th Annual Anomalous Absorption Conf,* Fairbanks, AK, Aug 26–30, 1996.

Ho, D. D.-M., "Laser Cooling for Heavy-Ion Fusion," Lawrence Livermore National Laboratory, Livermore, CA, UCRL-JC-124289 ABS. Prepared for *26th Annual Absorption Conf,* Fairbanks, AK, Aug 26–30, 1996.

Ho, D. D.-M., and Brandon, S. T., "Autoneutralization of Space-Charge-Dominated Beams for Heavy-Ion Fusion," Lawrence Livermore National Laboratory, Livermore, CA, UCRL-JC-120830; *Nuclear Fusion* **36**(6), 769–781 (1996).

Hogan, W. J., Atherton, L. J., and Paisner, J. A., *National Ignition Facility Design Focuses on Optics, Laser Fusion World* **32**(11), 107–114 (1996).

Horvath, J., Rodriguez, S., Fornerod, J., Bosch, P., Alger, T., Lee, T., Swort, D., Seznec, S., and Erlandson, A., *NIF/LMJ Prototype Amplifier Mechanical Design,* Lawrence Livermore National Laboratory, Livermore, CA, UCRL-JC-124520 ABS. Prepared for *2nd Annual Intl Conf on Solid-State Lasers for Application to Inertial Confinement Fusion,* Paris, France, Oct 22–25, 1996.

Hsieh, E. J., Greenfield, B. J., Behymer, R. D., Lindsey, E. F., and King, C. M., *The Coating Structure and H_2 Fill Characteristics of Be Micro Shells Produced by Sputter Coating with Gas Pulsing,* Lawrence Livermore National Laboratory, Livermore, CA, UCRL-JC-124227 ABS. Prepared for the *American Vacuum Society 43rd Natl Symp*, Philadelphia, PA, Oct 14–18, 1996.

Hsieh, E. J., Landen, O. L., and Wallace, R. J., *Be Tamping of Diagnostic Holes for NIF Scaled Experiments,* Lawrence Livermore National Laboratory, Livermore, CA, UCRL-JC-124893 ABS. Prepared for *11th Target Fabrication Specialists' Meeting,* Orcas Island, WA, Sept 8–12, 1996.

Hue, J., Genin, F., Maricle, S., and Kozlowski, M., *Towards Predicting the Threshold of the Large Area: Threshold Mapping,* Lawrence Livermore National Laboratory, Livermore, CA, UCRL-JC-124874 ABS. Prepared for *28th Annual Symp on Optical Materials for High Power Lasers,* Boulder, CO, Oct 7–9, 1996.

J

Jin, H., Peterson, P. F., Turner, R. E., and Anderson, A. T., *Experiment and Analysis of Ablation and Condensation in NIF First Wall Materials,* Lawrence Livermore National Laboratory, Livermore, CA, UCRL-JC-124540. Prepared for *American Nuclear Society 12th Topical Mtg on the Technology of Fusion Energy,* Reno, NV, Jun 16–20, 1996.

Johnson, R. R., and Correll, D. L., *Progress in ICF Research in Support of the National Ignition Facility,* Lawrence Livermore National Laboratory, Livermore, CA, UCRL-JC-123026 ABS. Prepared for the *American Physical Society/American Association of Physics Teachers Joint Mtg,* Indianapolis, IN, May 2–5, 1996.

K

Kalantar, D. H., Barbee, T. W., Da Silva, L. B., Glendinning, S. G., Key, M. H., Knauer, J. P., Weber, F., and Weber, S. V., *X-Ray Laser Radiography of Perturbations Due to Imprint of Laser Speckle in 0.35-μm Laser Irradiation of a Thin Si Foil,* Lawrence Livermore National Laboratory, Livermore, CA, UCRL-JC-121625 Rev 1. Submitted to the *Rev. Sci. Instrum.*

Kalantar, D. H., Budil, K. S., Hammel, B. A., Landen, O. L., and Keane, C. J., *X-Ray Backlit Imaging to Measure the In-Flight Pusher Density of an Indirect Drive Capsule Implosion Core,* Lawrence Livermore National Laboratory, Livermore, CA, UCRL-JC-123285 ABS. Prepared for the *11th Topical Conf on High Temperature Plasma Diagnostics,* Monterey, CA, May 12–16, 1996.

Kalantar, D., Da Silva, L. B., Glendinning, S. G., Weber, F., Remington, B. A., Weber, S. V., Key, M. H., Neely, D., Wolfrum, E., Demir, A., Lin, J., Smith, R., Kim, N., Zhang, J., McPhee, A., Warwick, J., and Knauer, J. P., *Measurements of Laser Imprint by XUV Radiography Using an X-Ray Laser,* Lawrence Livermore National Laboratory, Livermore, CA, UCRL-JC-123289 ABS. Prepared for the *24th European Conf on Laser Interaction with Matter,* Madrid, Spain, Jun 3–7, 1996.

Kalantar, D. H., Da Silva, L. B., Glendinning, S. G., Weber, F., Remington, B. A., Weber, S. V., Key, M. H., Neely, D., Wolfrum, E., Demir, A., Lin, J., Smith, R., Kim, N., Zhang, J., McPhee, A., Warwick, J., and Knauer, J. P., *XUV Probing of Laser Imprint in a Thin Foil Using an X-Ray Laser Backlighter,* Lawrence Livermore National Laboratory, Livermore, CA, UCRL-JC-123284 ABS. Prepared for the *11th Topical Conf on High Temperature Plasma Diagnostics,* Monterey, CA, May 12–16, 1996.

Kalantar, D. H., Hammel, B. A., Landen, O. L., Keane, C. J., and Munro, D. H., *Measurement of the In-Flight Pusher Density of an Indirect Drive Capsule Implosion Core Using X-Ray Backlighting,* Lawrence Livermore National Laboratory, Livermore, CA, UCRL-JC-123294 ABS. Prepared for the *24th European Conf on Laser Interaction with Matter,* Madrid, Spain, Jun 3–7, 1996.

Kalantar, D. H., Key, M. H., Da Silva, L. B., Glendinning, S. G., Knauer, J. P., Remington, B. A., Weber, F., and Weber, S. V., *Measurement of 0.35-μm Laser Imprint in a Thin Si Foil Using an X-Ray Laser Backlighter,* Lawrence Livermore National Laboratory, Livermore, CA, UCRL-JC-122446. Submitted to *Phys. Rev. Lett.*

Kalantar, D. H., Bell, P. M., Costa, R., Landen, O. L., and Orzechowski, T. J., *Characterization of X-Ray Streak Cameras for Use on Nova*, Lawrence Livermore National Laboratory, Livermore, CA, UCRL-JC-123776 ABS. Prepared for the *22nd Intl Congress on High Speed Photography and Photonics,* Santa Fe, NM, Oct 27–Nov 1, 1996.

Kalantar, D. H., Da Silva, L. B., Glendinning, S. G., Weber, F., Remington, B. A., Weber, S. V., Key, M. H., Neely, D., Wolfrum, E., Demir, A., Lin, J., Smith, R., Tallents, G. J., Kim, N., Zhang, J., Wark, J. S., McPhee, A., Warwich, J., Lewis, C. L. S., and Knauer, J. P., *XUV Probing of Laser Imprint in a Thin Foil Using an X-Ray Laser Backlighter,* Lawrence Livermore National Laboratory, Livermore, CA, UCRL-JC-123284. Prepared for the *11th Topical Conf on High Temperature Plasma Diagnostics,* Monterey, CA, May 12–16, 1996.

Kalantar, D. H., Da Silva, L. B., Glendinning, S. G., Weber, F., Remington, B. A., Weber, S. V., Wolfrum, E., Key, M. H., Neely, D., Kim, N. S., Wark, J. S., Zhang, J., Lewis, C. L. S., McPhee, A., Warwich, J., Demir, A., Lin, J., Smith, R., Tallents, G. J., and Knauer, J. P., *Measurements on Laser Imprint by XUV Radiography Using an X-Ray Laser,* Lawrence Livermore National Laboratory, Livermore, CA, UCRL-JC-123289. Prepared for the *24th European Conf on Laser Interaction with Matter,* Madrid, Spain, Jun 3–7, 1996.

Kalantar, D. H., Da Silva, L. B., Glendinning, S. G., Weber, F., Remington, B. A., Weber, S. V., Key, M. H., Neely, D., Wolfrum, E., Demir, A., Lin, J., Smith, R., Tallents, G. J., Kim, N. S., Wark, J. S., Zhang, J., Lewis, C. L. S., McPhee, A., Warwick, J., and Knauer, J. P., *Measurements of Laser Imprint in a Thin Foil Using an X-Ray Laser for XUV Radiography,* Lawrence Livermore National Laboratory, Livermore, CA, UCRL-JC-124288 ABS. Prepared for the *26th Annual Anomalous Absorption Conf,* Fairbanks, AK, Aug 26–30, 1996.

Kalantar, D. H., Demir, A., Key, M. H., Kim, N. S., Lewis, C. L. S., Lin, J., Neely, D., McPhess, A., Remington, B. A., Smith, R., Talents, G. J., Wark, J. S., Warwick, J., Weber, S. V., Wolfrum, E., and Zhang, J., *XUV Radiography Measurements of Direct Drive Imprint in Thin Aluminum Foils Using a GE X-Ray Laser on Vulcan,* Lawrence Livermore National Laboratory, Livermore, CA, UCRL-ID-123779.

Kalantar, D. H., Haan, S. W., Hammel, B. A., Landen, O. L., Keane, C. J., and Munro, D. H., *X-Ray Backlit Imaging Measurement of In-Flight Pusher Density for an Indirect Drive Capsule Implosion,* Lawrence Livermore National Laboratory, Livermore, CA, UCRL-JC-123285. Prepared for the *11th Topical Conf on High Temperature Plasma Diagnostics,* Monterey, CA, May 12–16, 1996.

Kalantar, D. H., Haan, S. W., Hammel, B. A., Keane, C. J., Landen, O. L., and Munro, D. H., *Measurement of the In-Flight Pusher Density of an Indirect Drive Capsule Implosion Core Using X-Ray Backlighting,* Lawrence Livermore National Laboratory, Livermore, CA, UCRL-JC-123294. Prepared for the *24th European Conf on Laser Interaction with Matter,* Madrid, Spain, Jun 3–7, 1996.

Kalantar, D. H., *Measurements of Direct Drive Laser Imprint in Thin Foils by XUV Radiography Using an X-Ray Laser Backlighter,* Lawrence Livermore National Laboratory, Livermore, CA, UCRL-JC-124654 ABS. Prepared for *38th Annual Mtg of the American Physical Society Div of Plasma Physics,* Denver, CO, Nov 11–15, 1996.

Kalantar, D. H., Bell, P. M., Costa, R., Landen, O. L., and Orzechowski, T. J., *Characterization of X-Ray Streak Cameras for Use on Nova,* Lawrence Livermore National Laboratory, Livermore, CA, UCRL-JC-123776. Prepared for *22nd Intl Congress on High Speed Photography and Photonics, Santa Fe,* NM, Oct 27–Nov 1, 1996.

Kalantar, D. H., Haan, S. W., Hammel, B. A., Landen, O. L., Keane, C. J., and Munro, D. H., *X-Ray Backlit Imaging of Indirect Drive Implosions to Measure In-Flight Capsule Aspect Ratio and Convergent Hydrodynamics,* Lawrence Livermore National Laboratory, Livermore, CA, UCRL-JC-124652 ABS. Prepared for *38th Annual Mtg of the American Physical Society Div of Plasma Physics,* Denver, CO, Nov 11–15, 1996.

Kalantar, D., Bell, P. M., Costa, R., Landen, O. L., and Orzechowski, T. J., *Characterization of X-Ray Streak Cameras for Use on Nova,* Lawrence Livermore National Laboratory, Livermore, CA, UCRL-JC-123776 ABS Rev. 1. Prepared for *22nd Intl Congress on High Speed Photography and Photonics, Santa Fe,* NM, Oct 27–Nov 1, 1996.

Kane, J., Glendinning, S. G., Wood-Vassey, M., Remington, B. A., Arnett, D., Rubenchik, A., Liang, E. P., London, R., and Castor, J., *Modeling of Supernova-Relevant Hydrodynamic Instability Experiments on the Nova Laser,* Lawrence Livermore National Laboratory, Livermore, CA, UCRL-JC-124550 ABS. Prepared for *38th Annual Mtg of the American Physical Society Div of Plasma Physics,* Denver, CO, Nov 11–15, 1996.

Kane, J., Arnett, D., Remington, B. A., Glendinning, S. G., Rubenchik, A., Castor, J., and Berning, M., *Supernova-Relevant Hydrodynamic Instability Experiment on Nova,* Lawrence Livermore National Laboratory, Livermore, CA, UCRL-JC-123291 ABS. Prepared for the *24th European Conf on Laser Interaction with Matter,* Madrid, Spain, Jun 3–7, 1996.

Kane, J., Arnett, D., Remington, B., Glendinning, S. G., Rubenchik, A., Castor, J., and Berning, M., *Supernova-Relevant Hydrodynamic Instability Experiment on the Nova Laser,* Lawrence Livermore National Laboratory, Livermore, CA, UCRL-JC-121488. Prepared for the *Workshop in Astrophysics Experiments with Large Lasers,* Pleasanton, CA, Feb 26–27, 1996.

Kauffman, R. L., Powers, L. V., Glendinning, S. G., Orzechowski, T., Suter, L. J., Berger, R. L., Dixit, S., Hammel, B. A., Hinkel, D. E., Kirkwood, R. K., Kornblum, H. N., Landen, O. L., MacGowan, B. J., Pennington, D., Shepard, T. D., Williams, E. A., Juraszek, D., Richard, A. L., and Blain, M. A., *Effects of Beam Conditioning on Gas-Filled Hohlraum Performance,* Lawrence Livermore National Laboratory, Livermore, CA, UCRL-JC-124682 ABS. Prepared for *38th Annual Mtg of the American Physical Society Div of Plasma Physics,* Denver, CO, Nov 11–15, 1996.

Kauffman, R. L., Glendinning, S. G., Powers, L. V., Berger, R. L., Hinkel, D. E., Landen, O. L., Ress, D., Suter, L. J., Shepard, T. D., Williams, E. A., Richard, A. L., and Blain, M. A., *Effects of Beam Conditioning on Wall Emission from Gas-Filled Hohlraums,* Lawrence Livermore National Laboratory, Livermore, CA, UCRL-JC-124468 ABS. Prepared for the *26th Annual Anomalous Absorption Conf,* Fairbanks, AK, Aug 26–30, 1996.

Keane, C. J., *Applications of Plasma Spectroscopy to the Study of High Energy Density Matter,* Lawrence Livermore National Laboratory, Livermore, CA, UCRL-JC-123782 ABS. Prepared for the *Intl Seminar on Physics of High Energy Density Matter,* Vancouver, Canada, May 26–29, 1996.

Keane, C. J., Landen, O. L., Cable, M. D., Hammel, B. A., Levedahl, W. K., Amendt, P., Cook, R. C., Haan, S. W., Hatchett, S. P., McEachern, R. C., Marinak, M., Murphy, T., Nelson, M., and Wallace, R., *Observation of Large-Growth Factor Behavior in Indirectly Driven Spherical Implosions,* Lawrence Livermore National Laboratory, Livermore, CA, UCRL-JC-123022. Submitted to *Phys. Rev. Lett.*

Kershaw, D. S., Prasad, M. K., and Shaw, M. J., *3D Unstructured Mesh ALE Hydrodynamics with the Upwind Discontinuous Finite Element Method,* Lawrence Livermore National Laboratory, Livermore, CA, UCRL-JC-122104. Submitted to the *J. Comput. Phys.*

Kershaw, D. S., Milovich, J. L., Prasad, M., Shaw, M. J., and Shestakov, A. I., *ICF3D-Hydro: 3D Parallel Unstructured Mesh Hydrodynamics Code,* Lawrence Livermore National Laboratory, Livermore, CA, UCRL-JC-124683 ABS. Prepared for *38th Annual Mtg of the American Physical Society Div of Plasma Physics,* Denver, CO, Nov 11–15, 1996.

Kilkenny, J. D., Bernat, T. P., Hammel, B. A., Lindl, J. D., and Rosen, M. R., *The Status of the ICF Target Physics Program at Lawrence Livermore National Laboratory,* Lawrence Livermore National Laboratory, Livermore, CA, UCRL-JC-123543 ABS. Prepared for the *24th European Conf on Laser Interaction with Matter,* Madrid, Spain, Jun 3–7, 1996.

Kilkenny, J. D., Bernat, T. P., Hammel, B. A., Kauffman, R. L., Landen, O. L., MacGowan, B. J., Orzechowski, T. J., Powers, L. V., Rosen, M. D., and Suter, L. J., *The Status of the ICF Target Physics Program at Lawrence Livermore National Laboratory,* Lawrence Livermore National Laboratory, Livermore, CA, UCRL-JC-123543. Prepared for the *24th European Conf on Laser Interaction with Matter,* Madrid, Spain, Jun 3–7, 1996.

Kirkwood, R. K., Afeyan, B. B., Back, C. A., Blain, M. A., Estabrook, K. G., Glenzer, S. H., Kruer, W. L., MacGowan, B. J., Montgomery, D. S., Moody, J. D., and Williams E. A., *The Effect of Ion Wave Damping on Stimulated Raman Scattering in High Z Laser Produced Plasmas,* Lawrence Livermore National Laboratory, Livermore, CA, UCRL-JC-124019; *Phys. Rev. Lett.* **77**(13) 2706–2709 (1996).

Kirkwood, R. K., Afeyan, B. B., Back, C. A., Blain, M. A., Berger, R. L., Estabrook, K. G., Glenzer, S. H., Kruer, W. L., Lasinski, B. F., MacGowan, B. J., Montgomery, D. S., Moody, J. D., Wallace, R., and Williams, E. A., *Saturation of SRS by the Stimulation of Ion Waves in Ignition Relevant Plasmas,* Lawrence Livermore National Laboratory, Livermore, CA, UCRL-JC-124297 ABS. Prepared for the *26th Annual Anomalous Absorption Conf,* Fairbanks, AK, Aug 26–30, 1996.

Kirkwood, R. K., Back, C. A., Glenzer, S. H., MacGowan, B. J., Montgomery, D. S., and Moody, J. D., *Imaging Back Scattered and Near Back Scattered Light in Ignition Scale Plasmas,* Lawrence Livermore National Laboratory, Livermore, CA, UCRL-JC-124041. Prepared for the *11th Topical Conf on High Temperature Plasma Diagnostics,* Monterey, CA, May 12–16, 1996.

Kirkwood, R. K., Afeyan, B. B., Kruer, W. L., MacGowan, B. J., Moody, J. D., Montgomery, D. S., Pennington, D. M., Weiland, T. L., and Wilks, S. C., *Observation of Energy Transfer between Frequency Mismatch Laser Beams in a Large Scale Plasma,* Lawrence Livermore National Laboratory, Livermore, CA, UCRL-JC-122102; *Phys. Rev. Lett.* **76**(12) 2065–2068 (1996).

Kirkwood, R. K., Back, C. A., Blain, M. A., Casanova, M., Desenne, D. E., Estabrook, K. G., Glenzer, S. H., MacGowan, B. J., Montgomery, D. S., Moody, J. D., Rousseaux, C., Wallace, R., and Williams, E. A., *The Effect of Secondary Decay Processes on Stimulated Raman Scattering in High Z Plasmas,* Lawrence Livermore National Laboratory, Livermore, CA, UCRL-JC-123547 ABS. Prepared for the *24th European Conf on Laser Interaction with Matter,* Madrid, Spain, Jun 3–7, 1996.

Kirkwood, R. K., Back, C. A., Glenzer, S. H., MacGowan, B. J., Montgomery, D. S., and Moody, J. D., *Imaging Back-Scattered and Near to Back-Scattered Light in Laser Produced Plasmas,* Lawrence Livermore National Laboratory, Livermore, CA, UCRL-JC-123296 ABS. Prepared for the *11th Topical Conf on High Temperature Plasma Diagnostics,* Monterey, CA, May 12–16, 1996.

Kirkwood, R. K., *Observation of Multiple Mechanisms for Stimulating Ion Waves in Ignition Scale Plasmas,* Lawrence Livermore National Laboratory, Livermore, CA, UCRL-JC-124651 ABS. Prepared for *38th Annual Mtg of the American Physical Society Div of Plasma Physics,* Denver, CO, Nov 11–15, 1996.

Kirkwood, R. K., MacGowan, B. J., Montgomery, D. S., Afeyan, B. B., Kruer, W. L., Moody, J. D., Estabrook, K. G., Back, C. A., Glenzer, S. H., Blain, M. A., Williams, E. A., Berger, R. L., and Lasinski, B. F., *Effect of Ion Wave Damping on Stimulated Raman Scattering in High-Z Laser Produced Plasmas,* Lawrence Livermore National Laboratory, Livermore, CA, UCRL-JC-124019 Rev. 1; *Phys. Rev. Lett.* **77**(13), 2706–2709 (1996).

Kirkwood, R. K., Wharton, K., Afeyan, B., Back, C., Berger, R., Blain, M., Estabrook, K., Glenzer, S., Kruer, W., MacGowan, B., and Moody, J., *Experimental Investigation of the Electromagnetic Decay Instability,* Lawrence Livermore National Laboratory, Livermore, CA, UCRL-JC-124854 ABS. Prepared for *38th Annual Mtg of the American Physical Society Div of Plasma Physics,* Denver, CO, Nov 11–15, 1996.

Koch, J. A., Estabrook, K. G., Bauer, J. D., Back, C. A., Klein, L., Rubenchik, A. M., Hsieh, E. J., Cook, R. C., MacGowan, B. J., Moody, J. D., Moreno, J. C., Kalantar, D., and Lee, R. W., *Time-Resolved X-Ray Imaging of High-Power Laser-Irradiated Underdense Silica Aerogels and Agar Foams,* Lawrence Livermore National Laboratory, Livermore, CA, UCRL-JC-117814; *Phys. Plasmas* **2**(10), 3820-3831 (1995).

Kolosov, V. V., Ratowsky, R. P., Zemlyanov, A. A., and London, R. A., *X-Ray Laser Coherence in the Presence of Density Fluctuations,* Lawrence Livermore National Laboratory, Livermore, CA, UCRL-JC-123027 ABS. Prepared for the *Society of Photo-Optical Instrumentation Engineers Annual Mtg,* Denver, CO, Aug 4–9, 1996.

Kopf, D., Keller, U., Emanuel, M. A., Beach, R. J., Skidmore, J. A., and Weingarten, K. J., *1-W Continuous-Wave Diode-Pumped Cr:LiSAF Laser,* Lawrence Livermore National Laboratory, Livermore, CA, UCRL-JC-124870 ABS & SUM. Prepared for *1996 Intl Quantum Electronics Conf,* Sydney, Australia, Jul 14–19, 1996.

Kozioziemski, B. J., Collins, G. W., Mapoles, E. R., and Bernat, T. P., *Rotational and Vibrational Spectroscopy of Solid D_2-DT-T_2,* Lawrence Livermore National Laboratory, Livermore, CA, UCRL-JC-122689 ABS. Prepared for the *1996 March Mtg of the American Physical Society,* St. Louis, MO, Mar 18–22, 1996.

Kruer, W. L., Afeyan, B. B., Wilks, S. C., and Chou, A., *Strongly-Driven Laser Plasmas with Self-Consistent Electron Distribution,* Lawrence Livermore National Laboratory, Livermore, CA, UCRL-JC-124491 ABS. Prepared for the *26th Annual Anomalous Absorption Conf,* Fairbanks, AK, Aug 26–30, 1996.

Kruer, W. L., Wilks, S. C., Afeyan, B. B., and Kirkwood, R. K., *Energy Transfer between Crossing Laser Beams,* Lawrence Livermore National Laboratory, Livermore, CA, UCRL-JC-120776 Rev 1; *Phys. Plasmas* **3**(1), 382–385 (1996).

Kruer, W. L., *Deflection, Spraying and Induced Scattering of Intense Laser Beams in Plasmas,* Lawrence Livermore National Laboratory, Livermore, CA, UCRL-JC-123551. Prepared for *1996 Intl Conf on Plasma Physics, Nagoya,* Japan, Sept 9–13, 1996.

Kruer, W. L., Afeyan, B. B., Wilks, S. C., and Chou, A. E., *Strongly-Driven Laser Plasmas with Self-Consistent Electron Distributions,* Lawrence Livermore National Laboratory, Livermore, CA, UCRL-JC-124491 ABS Rev. 1. Prepared for *38th Annual Mtg of the American Physical Society Div of Plasma Physics,* Denver, CO, Nov 11–15, 1996.

Kruer, W. L., and Hammer, J. H., *Laser Beam Deflection in Nonlinearly-Steepened Flow Profiles,* Lawrence Livermore National Laboratory, Livermore, CA, UCRL-JC-124447; *Comments on Plasma Phys. and Controlled Fusion* **18**(2), 85–93 (1997).

Kyker, R., *Local Positioning System,* Lawrence Livermore National Laboratory, Livermore, CA, UCRL-JC-121677. Prepared for Wescon, San Francisco, CA, Nov 7–9, 1995.

L

Labaune, C., Baldis, H. A., Schifano, E., Bauer, B. S., Michard, A., Renard, N., Seka, W., Moody, J. D., and Estabrook, K. G., *Location of Ion Acoustic Waves from Back and Side Brillouin Scattering,* Lawrence Livermore National Laboratory, Livermore, CA, UCRL-JC-123550; *Phys. Rev. Lett.* **76**(20), 3727–3730 (1996).

Lambert, S. M., Overturf, G. E., Wilemski, G., Letts, S. A., Cook, R. C., and Schroen-Carey, D., *Fabrication of Low-Density Foam Shells from Resorcinol-Formaldehyde Aerogel,* Lawrence Livermore National Laboratory, Livermore, CA, UCRL-JC-124663. Submitted to *J. of Applied Polymer Science.*

Land, T. A., De Yoreo, J. J., Malkin, A. J., Kutznesov, Yu. G., McPherson, A., and Lee, J. D., *An In-Situ AFM Study of Canavalin Protein Crystal Growth,* Lawrence Livermore National Laboratory, Livermore, CA, UCRL-JC-123600 ABS. Prepared for the *10th American Conf on Crystal Growth and the 9th Intl Conf on Vapor Growth & Epitaxy,* Vail, CO, Aug 4–9, 1996.

Land, T., Malkin, A., Kuznetsov, Y., McPherson, A., and De Yoreo, J., *Mechanisms of Protein and Virus Crystal Growth; an Atomic Force Microscopy Study of Canavalin and STMV Crystals,* Lawrence Livermore National Laboratory, Livermore, CA, UCRL-JC-124110. Prepared for the *11th Intl Conf on Crystal Growth,* The Hague, the Netherlands, Jun 1995; *J. of Crystal Growth* **166**(1–4), 893–899 (1996).

Land, T., Malkin, A. J., Kuznetsov, Y. G., McPherson, A., and De Yoreo, J. J., *Investigation of Virus Crystal Growth Mechanisms by In Situ Atomic Force Microscopy,* Lawrence Livermore National Laboratory, Livermore, CA, UCRL-JC-121141. Submitted to *Phys. Rev. Lett.*

Landen, O. L., Lobban, A., Bell, P., and Costa, R., *Simple Model for X-Ray Sensitivity of Microchannel Plate-Based X-Ray Framing Cameras,* Lawrence Livermore National Laboratory, Livermore, CA, UCRL-JC-123777 ABS. Prepared for the *22nd Intl Congress on High Speed Photography and Photonics*, Santa Fe, NM, Oct 27–Nov 1, 1996.

Landen, O. L., Back, C. A., Bernat, T. P., Cable, M. D., Chrien, R. E., Collins, G. W., Delamater, N. D., Failor, B., Glendinning, S. G., Glenzer, S. G., Hammel, B. A., Hay, R. G., Hsing, W. W., Kalantar, D. H., Kauffman, R. L., Kilkenny, J. D., Kirkwood, R. K., Kornblum, H. N., Lerche, R. L., and MacGowan, B. J., *Recent Progress in Indirect-Drive Implosions at the Nova Laser Facility,* Lawrence Livermore National Laboratory, Livermore, CA, UCRL-JC-123310 ABS. Prepared for the *12th Topical Mtg on the Technology of Fusion Energy,* Reno, NV, Jun 16–20, 1996.

Landen, O. L., Keane, C. J., Hammel, B. A., Levedahl, W. K., Amendt, P. A., Colvin, J. D., Cable, M. D., Cook, R., Dittrich, T. R., Haan, S. W., Hatchett, S. P., Hay, R. G., Lerche, R. A., McEachern, R., Murphy, T. J., Nelson, M. B., Suter, L., and Wallace, R. J., *Effects of Variable X-Ray Preheat Shielding in Indirectly-Driven Implosions,* Lawrence Livermore National Laboratory, Livermore, CA, UCRL-JC-122749 Rev 1; *Phys. of Plasmas* **3**(5), 2094–2097 (1996).

Landen, O. L., Keane, C. J., Hammel, B. A., Levedahl, W. K., Colvin, J. D., Amendt, P. A., Hatchett, S. P., Marinak, M. M., Cable, M. D., Cook, R., Dittrich, T. R., Haan, S. W., Hay, R. G., Kalantar, D. H., Kornblum, H. N., Lerche, R. A., McEachern, R. L., Murphy, T. J., Nelson, M. B., and Suter, L., *Indirectly-Driven, High Growth Factor ICF Implosions,* Lawrence Livermore National Laboratory, Livermore, CA, UCRL-JC-123316 ABS. Prepared for the *24th European Conf on Laser Interaction with Matter,* Madrid, Spain, Jun 3–7, 1996.

Landen, O. L., Hammer, J. A., Suter, L. J., Orzechowski, T. J., Weiland, T., Perry, T. S., Bauer, J., Bach, D., Ward, R., Hammel, B. A., Kilkenny, J. D., and Wallace, R. J., *Long Duration Indirect-Drive Experiments at Nova,* Lawrence Livermore National Laboratory, Livermore, CA, UCRL-JC-124675 ABS. Prepared for *38th Annual Mtg of the American Physical Society Div of Plasma Physics,* Denver, CO, Nov 11–15, 1996.

Langdon, A. B., and Williams, E. A., *Spot and Speckle Motion in SSD Illumination,* Lawrence Livermore National Laboratory, Livermore, CA, UCRL-JC-124453 ABS. Prepared for the *26th Annual Anomalous Absorption Conf,* Fairbanks, AK, Aug 26–30, 1996.

Langer, S. H., Keane, C. J., Scott, H. A., *Yield and Emission Line Ratios from ICF Target Implosions with Multi-Mode Raleigh-Taylor Perturbations,* Lawrence Livermore National Laboratory, Livermore, CA, UCRL-JC-124484 ABS. Prepared for the *26th Annual Anomalous Absorption Conf,* Fairbanks, AK, Aug 26–30, 1996.

Langer, S. H., Keane, C. J., and Scott, H. A., *Yield and Emission Line Ratios from ICF Target Implosions with Multi-Mode Rayleigh–Taylor Perturbations,* Lawrence Livermore National Laboratory, Livermore, CA, UCRL-JC-124484 ABS Rev. 1. Prepared for *38th Annual Mtg of the American Physical Society Div of Plasma Physics,* Denver, CO, Nov 11–15, 1996.

Lasinski, B. F., Cohen, B. I., Langdon, A. B., and Williams, E. A., *Stimulated Brillouin Scatter in PIC-Fluid Simulations,* Lawrence Livermore National Laboratory, Livermore, CA, UCRL-JC-124457 ABS Rev. 1. Prepared for *38th Annual Mtg of the American Physical Society Div of Plasma Physics,* Denver, CO, Nov 11–15, 1996.

Lasinski, B. F., Cohen, B. I., Langdon, A. B., and Williams, E. A., *Stimulated Brillouin Scatter in PIC-Fluid Simulations,* Lawrence Livermore National Laboratory, Livermore, CA, UCRL-JC-124457 ABS. Prepared for the *26th Annual Anomalous Absorption Conf,* Fairbanks, AK, Aug 26–30, 1996.

Latkowski, J. F., Sanz, J., Vujic, J. L., and Tobin, M. T., *Sequential Charged-Particle and Neutron Activation of Flibe in the HYLIFE-II Inertial Fusion Energy Power Plant Design,* Lawrence Livermore National Laboratory, Livermore, CA, UCRL-JC-123558. Prepared for the *American Nuclear Society 12th Topical Mtg on the Technology of Fusion Energy*, Reno, NV, Jun 16–20, 1996.

Latkowski, J. F., and Tobin, M. T., *Time and Motion Study for the National Ignition Facility Target Area,* Lawrence Livermore National Laboratory, Livermore, CA, UCRL-JC-123552. Prepared for the *American Nuclear Society Intl Topical Mtg on Probabilistic Safety Assessment '96,* Park City, UT, Sept 29–Oct 3, 1996.

Latkowski, J. F., *TARTREAD v1.0 User's Manual,* Lawrence Livermore National Laboratory, Livermore, CA, UCRL-MA-122003.

Latkowski, J. F., and Tobin, M. T., *The Selection of Concrete Compositions for Use in the National Ignition Facility Target Area,* Lawrence Livermore National Laboratory, Livermore, CA, UCRL-JC-123566 SUM. Prepared for the *American Nuclear Society 12th Topical Mtg on the Technology of Fusion Energy,* Reno, NV, Jun 16–20, 1996.

Latkowski, J. F., and Tobin, M. T., *Time and Motion Study for the National Ignition Facility Target Area,* Lawrence Livermore National Laboratory, Livermore, CA, UCRL-JC-123552 SUM. Prepared for the *Intl Topical Mtg on Probabilistic Safety Assessment,* Park City, UT, Sept 29–Oct 3, 1996.

Latkowski, J. F., Sanz, J., and Vujic, J. L., *The Impact of Pulsed Irradiation upon Neutron Activation Calculations for Inertial and Magnetic Fusion Energy Power Plants,* Lawrence Livermore National Laboratory, Livermore, CA, UCRL-JC-123559 SUM. Prepared for the *American Nuclear Society 12th Topical Mtg on the Technology of Fusion Energy,* Reno, NV, Jun 16–20, 1996.

Latkowski, J. F., Sanz, J., Vujic, J. L., and Tobin, M. T., *Sequential Charged Particle and Neutron Activation of Flibe in the HYLIFE-II Inertial Fusion Energy Power Plant Design,* Lawrence Livermore National Laboratory, Livermore, CA, UCRL-JC-123558 SUM. Prepared for the *American Nuclear Society 12th Topical Mtg on the Technology of Fusion Energy,* Reno, NV, Jun 16–20, 1996.

Latkowski, J. F., Sanz, J., and Vujic, J. L., *The Impact of Pulsed Irradiation upon Neutron Activation Calculations for Inertial and Magnetic Fusion Energy Power Plants,* Lawrence Livermore National Laboratory, Livermore, CA, UCRL-JC-123559. Prepared for *American Nuclear Society 12th Topical Mtg on the Technology of Fusion Energy,* Reno, NV, Jun 16–20, 1996.

Lawson, J. K., Seppala, L. G., Smith, I. C., and Thompson, C. E., *Beamlet Schlieren Diagnostic and Experiments,* Lawrence Livermore National Laboratory, Livermore, CA, UCRL-JC-124516 ABS. Prepared for *2nd Annual Intl Conf on Solid-State Lasers for Application to Inertial Confinement Fusion,* Paris, France, Oct 22–25, 1996.

Lawson, J. K., Aikens, D. M., English, R. E., and Wolfe, C. R., *Power Spectral Density Specifications for High-Power Laser Systems,* Lawrence Livermore National Laboratory, Livermore, CA, UCRL-JC-123105. Prepared for the *Intl Symp on Optical Systems Design and Production II,* Glasgow, Scotland, May 12–16, 1996.

Lee, H.-R., Da Silva, L., Haddad, L., Trebes, J., Yeh, Y., and Ford, G., *A Novel Iterative Optimizing Quantization Technique for Three Dimensional Reconstruction from a Limited Number of Views,* Lawrence Livermore National Laboratory, Livermore, CA, UCRL-JC-121137. Prepared for the *Society of Photo-Optical Instrumentation Engineers Intl Symp,* San Diego, CA, Jul 9–14, 1995.

Lerche, R A., *Neutron-Induced Noise in NIF-Class Diagnostic Instruments,* Lawrence Livermore National Laboratory, Livermore, CA, UCRL-JC-123556. Prepared for the *11th Topical Conf on High-Temperature Plasma Diagnostics,* Monterey, CA, May 12–16, 1996.

Lerche, R. A., Ehrlich, R. B., Laumann, C. W., and Miller, J. L., *Streak Camera Power Measurements for Large-Aperture, High-Power Laser Beams,* Lawrence Livermore National Laboratory, Livermore, CA, UCRL-JC-124240 ABS. Prepared for the *22nd Intl Conf on High-Speed Photography and Photonics,* Santa Fe, NM, Oct 27–Nov 1, 1996.

Lerche, R. A., Ress, D., and Fisher, R. K., *Efficient, High-Spatial Resolution Neutron Detector for Coded Aperture Imaging of ICF Targets,* Lawrence Livermore National Laboratory, Livermore, CA, UCRL-JC-124660 ABS. Prepared for *38th Annual Mtg of the American Physical Society Div of Plasma Physics,* Denver, CO, Nov 11–15, 1996.

Le Sage, G. P., Feng, H. X. C., Laurent, L., Hartemann, F. V., Luhman, N. C., Fochs, S. N., Perry, M. D., and Westenskow, G. A., *Theory and Design of a Photoinjector-Driven Chirped Pulse Free-Electron Maser,* Lawrence Livermore National Laboratory, Livermore, CA, UCRL-JC-123029 (1995). Submitted to *IEEE Trans. on Plasma Sci.*

Letts, S. A., Fearon, E. M., Allison, L. M., and Cook, R., *Fabrication of Special ICF Targets Using a Depolymerizable Mandrel Technique,* Lawrence Livermore National Laboratory, Livermore, CA, UCRL-JC-121115. Prepared for the *42nd Nat'l Symp of the American Vacuum Society,* Minneapolis, MN, Oct 16–20, 1995; *Fus. Tech.* **28**(12), 1797–1802 (1995).

Letts, S., Bittner, D., Collins, G. W., and Monsler, E., *Generation of Uniform Solid HD Layers inside Spherical Capsules Using Infra-Red Illumination,* Lawrence Livermore National Laboratory, Livermore, CA, UCRL-JC-125140 ABS. Prepared for *11th Target Fabrication Specialists' Mtg, Orcas Island,* WA, Sept 8–12, 1996.

Letts, S., Buckely, S., and Schroen-Carey, D., *Analysis of the Effect of pH on Poly(Vinyl Phenol),* Lawrence Livermore National Laboratory, Livermore, CA, UCRL-JC-125134 ABS. Prepared for *11th Target Fabrication Specialists' Mtg,* Orcas Island, WA, Sept 8–12, 1996.

Letts, S., Buckley, S. R., Fearon, E. M., Hamilton, K. E., Vu, D., Wilemski, G., Cook, R. C., and Schroen-Carey, D., *Role of Reactant Transport in Determining the Properties of NIF Shells Made by Interfacial,* Lawrence Livermore National Laboratory, Livermore, CA, UCRL-JC-125125 ABS. Prepared for *11th Target Fabrication Specialists' Mtg,* Orcas Island, WA, Sept 8–12, 1996.

Levedahl, W. K., and Lindl, J. D., *Energy Scaling of Inertial Confinement Fusion Targets for Ignition and High Gain,* Lawrence Livermore National Laboratory, Livermore, CA, UCRL-JC-120200 Rev. 1; *Nuclear Fusion* **37**(2), 165–173 (1997).

Liang, E. P., Wilks, S. C., and Tabak, M., *Pair Production by Ultra-Intense Lasers,* Lawrence Livermore National Laboratory, Livermore, CA, UCRL-JC-124499. Submitted to *Phys. Rev. Lett.*

Lindl, J. D., *Progress on the Physics of Ignition for Radiation Driven Inertial Confinement Fusion (ICF) Targets,* Lawrence Livermore National Laboratory, Livermore, CA, UCRL-JC-124004 ABS. Prepared for the *16th Intl Atomic Energy Agency Fusion Energy Conf on Plasma Physics and Controlled Nuclear Fusion Research,* Montreal, Canada, Oct 7–11, 1996.

Lindl, J. D., and Campbell, E. M., *Inertial Confinement Fusion with High Powered Lasers,* Lawrence Livermore National Laboratory, Livermore, CA, UCRL-JC-124461. Submitted to *Scientific American.*

Lindl, J., and Correll, D., *Inertial Confinement Fusion Quarterly Report,* Volume 5, Number 4, Lawrence Livermore National Laboratory, Livermore, CA, UCRL-LR-105821-95-4.

Lindl, J. D., *Development of the Indirect-Drive Approach to Inertial Confinement Fusion and the Target Physics Basis for Ignition and Gain,* Lawrence Livermore National Laboratory, Livermore, CA, UCRL-JC-119015; *Phys. Plasmas* **2**(11), 3933–4024 (1995).

Lindl, J. D., *Time-Dependent Asymmetries in Laser-Fusion Hohlraums: a Response,* Lawrence Livermore National Laboratory, Livermore, CA, UCRL-JC-122654 (1995). Submitted to *Plasma Phys. and Controlled Fusion*.

Lindl, J. D., and Marinak, M. M., *Progress on the Physics of Ignition for Radiation Driven Inertial Confinement Fusion (ICF) Targets,* Lawrence Livermore National Laboratory, Livermore, CA, UCRL-JC-124004. Prepared for *16th Intl Atomic Energy Agency Fusion Energy Conf,* Montreal, Canada, Oct 7–11, 1996.

Logan, B. G., Lindl, J. D., and Meier, W. R., *Inertial Fusion Energy Development Approaches for Direct and Indirect-Drive,* Lawrence Livermore National Laboratory, Livermore, CA, UCRL-JC-123788. Prepared for *16th Intl Atomic Energy Agency Fusion Energy Conf,* Montreal, Canada, Oct 7–11, 1996.

Logory, L. M., Bell, P. M., Conder, A. D., and Lee, F. D., *Development and Characterization of a CCD Camera System for Use on Six-Inch Manipulator Systems,* Lawrence Livermore National Laboratory, Livermore, CA, UCRL-JC-123281. Prepared for the *11th Topical Conf on High Temperature Plasma Diagnostics,* Monterey, CA, May 12–16, 1996.

M

MacGowan, B. J., Afeyan, B. B., Back, C. A., Berger, R. L., Bonnaud, G., Casanova, M., Cohen, B. I., Desenne, D. E., Dubois, D. F., Dulieu, A. G., Estabrook, K. G., Fernandez, J. C., Glenzer, S. H., Hinkel, D. E., Kalantar, D. H., Kauffman, R. L., Kirkwood, R. L., Kruer, W. L., Langdon, A. B., and Lasinski, B. F., *Laser Plasma Interactions in Ignition-Scale Hohlraum Plasmas,* Lawrence Livermore National Laboratory, Livermore, CA, UCRL-JC-121499. Submitted to *Phys. of Plasmas.*

MacGowan, B. J., Afeyan, B. B., Back, C. A., Berger, R. L., Bonnaud, G., Casanova, M., Cohen, B. I., Desenne, D. E., Dubois, D. F., Dulieu, A. G., Estabrook, K. G., Fernandez, J. C., Glenzer, S. H., Hinkel, D. E., Kaiser, T. B., Kalantar, D. H., Kauffman, R. L., Kirkwood, R. K., Kruer, W. L., and Langdon, A. B., *Laser Plasma Interactions in Ignition-Scale Hohlraum Plasmas,* Lawrence Livermore National Laboratory, Livermore, CA, UCRL-JC-121499 Rev 1; *Phys. of Plasmas* **3**(5), 2029–2040 (1996).

MacGowan, B. J., Back, C. A., Blain, M. A., Berger, R. L., Glenzer, S. H., Hinkel, D. E., Kirkwood, R. K., Kornblum, H. N., Lasinski, B. F., Montgomery, D. S., Moody, J. D., Munro, D. H., Powers, L. V., Rousseaux, C., Wallace, R. J., and Williams, E. A., *Laser Scattering in Large-Scale-Length Plasmas Relevant to National Ignition Facility Hohlraums,* Lawrence Livermore National Laboratory, Livermore, CA, UCRL-JC-123545 ABS. Prepared for the *24th European Conf on Laser Interaction with Matter,* Madrid, Spain, Jun 3–7, 1996.

MacGowan, B. J., *Laser Scattering in Large-Scale-Length Plasmas Relevant to National Ignition Facility Hohlraums,* Lawrence Livermore National Laboratory, Livermore, CA, UCRL-JC-123545 ABS Rev. 1. Prepared for the *16th Intl Atomic Energy Agency Fusion Energy Conf on Plasma Physics and Controlled Nuclear Fusion Research,* Montreal, Canada, Oct 7–11, 1996.

MacGowan, B. J., Afeyan, B. B., Back, C. A., Blain, M. A., Berger, R. L., Canaud, B., Glenzer, S. H., Hinkel, D. E., Kirkwood, R. K., Kornblum, H. N., Langdon, A. B., Lasinski, B. F., Montgomery, D. S., Moody, J. D., Munro, D. H., Powers, L. V., Rousseaux, C., Still, C. H., Wallace, R. J., and Williams, E. A., *The influence of smoothing by spectral dispersion on laser scattering and beam propagation in large-scale-length plasmas relevant to National Ignition Facility hohlraums,* Lawrence Livermore National Laboratory, Livermore, CA, UCRL-JC-124467 ABS. Prepared for the *26th Annual Anomalous Absorption Conf,* Fairbanks, AK, Aug 26–30, 1996.

MacGowan, B. J., Back, C. A., Blain, M. A., Berger, R. L., Canaud, B., Glenzer, S. H., Hinkel, D. E., Kirkwood, R. K., Lasinski, B. F., Montgomery, D. S., Moody, J. D., Munro, D. H., Powers, L. V., Rousseaux, C., and Williams, E. A., *The Effect of Smoothing by Spectral Dispersion on Laser Scattering and Beam Propagation in Large-Scale-Length Plasmas Relevant to National Ignition Facility Hohlraums,* Lawrence Livermore National Laboratory, Livermore, CA, UCRL-JC-124656 ABS. Prepared for *38th Annual Mtg of the American Physical Society Div of Plasma Physics,* Denver, CO, Nov 11–15, 1996.

Maitland, D. J., Eder, D. C., London, R. A., Glinsky, M. E., and Soltz, B. A., *Dynamic Simulations of Tissue Welding,* Lawrence Livermore National Laboratory, Livermore, CA, UCRL-JC-121630. Prepared for the *Society of Photo-Optical Instrumentation Engineers '96 Conf,* San Jose, CA, Jan 28–Feb 2, 1996.

Mapoles, E. R., Sater, J. D., Monsler, E., and Pipes, J., *Reducing Deuterium-Tritium ICF Roughness by Electrical Heating of the Saturated Vapor,* Lawrence Livermore National Laboratory, Livermore, CA, UCRL-JC-124253. Prepared for the *24th European Conf on Laser Interaction with Matter,* Madrid, Spain, Jun 3–7, 1996.

Mapoles, E. R., Sater, J., Pipes, J., and Monsler, E., *Smoothing of Deuterium-Tritium Ice by Electrical Heating of the Saturated Vapor,* Lawrence Livermore National Laboratory, Livermore, CA, UCRL-JC-124938. Submitted to *Physical Review B.*

Mapoles, E. R., Sater, J., Pipes, J., and Monsler, E., *Smoothing of Solid DT ICF Targets by Electrical Heating,* Lawrence Livermore National Laboratory, Livermore, CA, UCRL-JC-125122 ABS. Prepared for *11th Target Fabrication Specialists' Mtg,* Orcas Island, WA, Sept 8–12, 1996.

Mapoles, E., and Burmann, J., *Cryogenic Testing of Liquid and Solid Layering Cells,* Lawrence Livermore National Laboratory, Livermore, CA, UCRL-JC-125137 ABS. Prepared for *11th Target Fabrication Specialists' Mtg,* Orcas Island, WA, Sept 8–12, 1996.

Mapoles, E., and Pipes, J. W., *Conceptual Design of an In Situ System for Cryogenic Hohlraum Assembly,* Lawrence Livermore National Laboratory, Livermore, CA, UCRL-JC-125131 ABS. Prepared for *11th Target Fabrication Specialists' Mtg,* Orcas Island, WA, Sept 8–12, 1996.

Marcy, H. O., Rosker, M. J., Cunningham, P. H., DeLoach, L. A., Ebbers, C. A., Kanatzidis, M. G., Thomas, C. A., Warren L. F., Velsko, S. P., and Liao, J.-H., *L-Histidine Tetrafluoroborate: a Solution-Grown "Semiorganic" Crystal for Nonlinear Frequency Conversion,* Lawrence Livermore National Laboratory, Livermore, CA, UCRL-JC-116737. Submitted to *Appl. Phys. Lett.*

Marinak, M. M., Haan, S. W., Pollaine, S. M., Tipton, R. E., and Zimmerman, G. B., *Three-Dimensional Simulations of National Ignition Facility Capsule Implosions,* Lawrence Livermore National Laboratory, Livermore, CA, UCRL-JC-123783 ABS. Prepared for the *16th Intl Atomic Energy Agency Fusion Energy Conf on Plasma and Controlled Nuclear Fusion Research,* Montreal, Canada, Oct 7–11, 1996.

Marinak, M. M., Remington, B. A., Weber, S. V., Tipton, R. E., Haan, S. W., Budil, K. S., Landen, O. L., Kilkenny, J. D., and Wallace, R. J., *Three-Dimensional Single Mode Rayleigh–Taylor Experiments on Nova,* Lawrence Livermore National Laboratory, Livermore, CA, UCRL-JC-120191; *Phys. Rev. Lett.* **75**(20), 3677–3680 (1995).

Marinak, M. M., and Hatchett, S. P., *3-D Hydrodynamic Effects of Pointing and Power Balance Errors on Nova Capsule Implosions,* Lawrence Livermore National Laboratory, Livermore, CA, UCRL-JC-124672 ABS. Prepared for *38th Annual Mtg of the American Physical Society Div of Plasma Physics,* Denver, CO, Nov 11–15, 1996.

Marinak, M. M., Haan, S. W., Tipton, R. E., and Zimmerman, G. B., *Three-Dimensional Simulations of National Ignition Facility Capsule Implosions,* Lawrence Livermore National Laboratory, Livermore, CA, UCRL-JC-123783 ABS Rev. 2. Prepared for *38th Annual Mtg of the American Physical Society Div of Plasma Physics,* Denver, CO, Nov 11–15, 1996.

Marshall, C. D., Speth, J. A., and Payne, S. A., *Penetrating Radiation Impact on NIF Final Optic Components,* Lawrence Livermore National Laboratory, Livermore, CA, UCRL-JC-124523 ABS. Prepared for *2nd Annual Intl Conf on Solid-State Lasers for Application to Inertial Confinement Fusion,* Paris, France, Oct 22–25, 1996.

Marshall, C. D., Payne, S. A., Emanuel, M. A., Schaffers, K. I., Smith, L. K., Powell, H. T., and Krupke, W. F., *Diode-Pumped Solid-State Laser Based Inertial Fusion Energy,* Lawrence Livermore National Laboratory, Livermore, CA, UCRL-JC-123098 ABS. Prepared for the *12th Topical Mtg on the Technology of Fusion Energy,* Reno, NV, Jun 16–20, 1996.

Marshall, C. D., Quarles, G. J., Castillo, V. K., Bayramian, A. J., Speth, J. A., Tassano, J. B., Payne, S. A., and Krupke, W. F., *Ce:LiSAF, First Tunable Ultraviolet Solid-State Laser Product,* Lawrence Livermore National Laboratory, Livermore, CA, UCRL-JC-123653. Submitted to *R&D 100 Award*.

Marshall, C. D., Speth, J. A., Latkowski, J. F., Tobin, M. T., and Payne, S. A., *Radiation-Hardness of Optical Materials Subjected to Neutrons and Gamma Rays,* Lawrence Livermore National Laboratory, Livermore, CA, UCRL-JC-123097 ABS. Prepared for the *12th Topical Mtg on the Technology of Fusion Energy,* Reno, NV, Jun 16–20, 1996.

Marshall, C. D., *Diode-Pumped Gas-Cooled-Slab Laser Performance,* Lawrence Livermore National Laboratory, Livermore, CA, UCRL-JC-122023 ABS. Prepared for the *Int'l Conf on Lasers 1995,* Charleston, SC, Dec 4, 1995.

Marshall, C. D., Smith, L. K., Sutton, S., Emanuel, M. A., Schaffers, K. I., Mills, S., Payne, S. A., Krupke, W. F., and Chai, B. H. T., *Diode-Pumped Gas-Cooled-Slab Laser Performance,* Lawrence Livermore National Laboratory, Livermore, CA, UCRL-JC-122023. Prepared for *Conf on Lasers and Electro-Optics (CLEO '96),* Anaheim, CA, Jun 2, 1996.

Marshall, C. D., Smith, L. K., Sutton, S., Emanuel, M. A., Schaffers, K. I., Mills, S., Payne, S. A., Krupke, W. F., and Chai, B. H. T., *Diode-Pumped Gas-Cooled-Slab Laser Performance,* Lawrence Livermore National Laboratory, Livermore, CA, UCRL-JC-122023 ABS Rev 1 & SUM. Prepared for *Conf on Lasers and Electro-Optics (CLEO '96),* Anaheim, CA, Jun 2, 1996.

Marshall, C. D., Smith, L. K., Beach, R. J., Emanuel, M. A., Schaffers, K. I., Payne, S. A., and Chai, B. H. T., *Diode-Pumped Ytterbium-Doped $Sr_5(PO_4)_3F$ Laser Performance,* Lawrence Livermore National Laboratory, Livermore, CA, UCRL-JC-122010. Submitted to the *Institute of Electrical and Electronics Engineers.*

Marshall, C. D., Smith, L. K., Sutton, S., Emanuel, M. A., Schaffers, K. I., Mills, S., Payne, S. A., Krupke, W. F., and Chai, B. H. T., *Diode-Pumped Gas-Cooled-Slab Laser Performance,* Lawrence Livermore National Laboratory, Livermore, CA, UCRL-JC-122023 EXT ABS. Prepared for *Advanced Solid State Lasers 11th Topical Mtg,* San Francisco, CA, Jan 31–Feb 3, 1996.

Marshall, C. D., Speth, J. A., and Payne, S. A., *Radiation Effects Testing on the National Ignition Facility Final Optical Components,* Lawrence Livermore National Laboratory, Livermore, CA, UCRL-JC-122404 ABS. Prepared for the *5th Biannual DOD Fiber Optics and Photonics Mtg,* McLean, VA, Mar 25–28, 1996.

Marshall, C. D., Speth, J. A., and Payne, S. A., *Induced Optical Absorption in Gamma and Neutron Irradiated Fused Quartz and Silica,* Lawrence Livermore National Laboratory, Livermore, CA, UCRL-JC-122652. Submitted to the *J. of Non-Cryst. Solids*.

McEachern, R., and Correll, D., *Inertial Confinement Fusion Quarterly Report,* vol. 6, No. 1, Oct–Dec 1995, Lawrence Livermore National Laboratory, Livermore, CA, UCRL-LR-105821-96-1.

McEachern, R., Honea, E., and Collins, G., *Surface Roughness Scaling of Beryllium Thin Films,* Lawrence Livermore National Laboratory, Livermore, CA, UCRL-JC-125132 ABS. Prepared for *11th Target Fabrication Specialists' Mtg,* Orcas Island, WA, Sept 8–12, 1996.

Meier, W. R., *Developing Inertial Fusion Energy—Where Do We Go from Here?* Lawrence Livermore National Laboratory, Livermore, CA, UCRL-JC-123079 SUM. Prepared for *12th Topical Mtg on the Technology of Fusion Energy,* Reno, NV, Jun 16–20, 1996.

Meier, W. R., and Abdou, M. A., *Chamber Technology Concepts for Inertial Fusion Energy,* Lawrence Livermore National Laboratory, Livermore, CA, UCRL-JC-125147 ABS. Prepared for *4th Intl Symp on Fusion Nuclear Technology,* Tokyo, Japan, Apr 6–11, 1997.

Meier, W., Moir, R., Monsler, M., Petzoldt, R., and Unites, W., *Target Design, Fabrication and Injection Considerations for Inertial Fusion Energy,* Lawrence Livermore National Laboratory, Livermore, CA, UCRL-JC-125120 ABS. Prepared for *11th Target Fabrication Specialists' Mtg,* Orcas Island, WA, Sept 8–12, 1996.

Meier, W. R., and Logan, B. G., *Developing Inertial Fusion Energy—Where Do We Go From Here?,* Lawrence Livermore National Laboratory, Livermore, CA, UCRL-JC-123079. Prepared for the *American Nuclear Society 12th Topical Mtg on the Technology of Fusion Energy,* Reno, NV, Jun 16–20, 1996.

Merkuliefv, Y., Startsev, S., and Cook, R., *Simulation of High Temperature Formation of Large (2 mm) Polystyrene Shells from Solid Granules,* Lawrence Livermore National Laboratory, Livermore, CA, UCRL-JC-125126 ABS. Prepared for *11th Target Fabrication Specialists' Mtg,* Orcas Island, WA, Sept 8–12, 1996.

Milam, D., Hunt, J. T., Manes, K. R., Sell, W. D., and Williams, W. H., *Modeling of Filamentation Damage Induced in Silica by 351-nm Laser Pulses,* Lawrence Livermore National Laboratory, Livermore, CA, UCRL-JC-124925 ABS. Prepared for *Symp on Optical Materials for High Power Lasers '96,* Boulder, CO, Oct 7–9, 1996.

Moir, R. W., *IFE Power Plant Design Strategy,* Lawrence Livermore National Laboratory, Livermore, CA, UCRL-JC-123287; *Fusion Technology* **30**(3), 1613–1623 (1996).

Moir, R. W., *IFE Power Plant Design Strategy,* Lawrence Livermore National Laboratory, Livermore, CA, UCRL-JC-123287 SUM. Prepared for the *12th Topical Mtg on the Technology of Fusion Energy,* Reno, NV, Jun 16–20, 1996

Moir, R., *Letter to editor of the Economist,* Lawrence Livermore National Laboratory, Livermore, CA, UCRL-JC-122306 COM. Submitted to the *Economist.*

Moir, R. W., *Feasibility and Advantages of Liquid Walls for MFE Power Plants,* Lawrence Livermore National Laboratory, Livermore, CA, UCRL-JC-122007 ABS. Prepared for the *Advanced Approaches to Economical Fusion Power,* Monterey, CA, Sept 11–15, 1995.

Moir, R. W., *The Inertial Fusion Energy Approach to Economical Fusion Power: HYLIFE-II,* Lawrence Livermore National Laboratory, Livermore, CA, UCRL-JC-122008 ABS. Prepared for the *Advanced Approaches to Economical Fusion Power,* Monterey, CA, Sept 11–15, 1995.

Moir, R. W., *Letter dated Sept 26, 1995, addressed to The Editor, The Economist, 25 St. James's Street, London SW1A1Hg, and e-mail addressed to letters@economist.com,* Lawrence Livermore National Laboratory, Livermore, CA, UCRL-JC-122126 SUM.

Molau, N. E., Brand, H. R., Kozlowski, M. R., and Shang, C. C., *2-1/2-D Electromagnetic Modeling of Nodular Defects in High-Power Multilayer Optical Coatings,* Lawrence Livermore National Laboratory, Livermore, CA, UCRL-ID-124808.

Montgomery, D. S., MacGowan, B. J., Kirkwood, R. K., Moody, J. D., Stone, G. F., Afeyan, B. B., Berger, R. L., Kruer, W. L., Lasinski, B. F., Munro, D. H., Williams, E. A., Desenne, D., and Rousseaux, C., *Suppression of Stimulated Brillouin Scattering with Large Levels of Stimulated Raman Scattering in Laser Plasma Interactions,* Lawrence Livermore National Laboratory, Livermore, CA, UCRL-JC-123548 ABS. Prepared for the *24th European Conf on Laser Interaction with Matter,* Madrid, Spain, Jun 3–7, 1996.

Montgomery, D. S., Moody, J. D., Baldis, H. A., Afeyan, B. B., Berger, R. L., Estabrook, K. G., Lasinski, B. F., Williams, E. A., and Labaune, C., *Effects of Laser Beam Smoothing on Stimulated Raman Scattering in Exploding Foil Plasmas,* Lawrence Livermore National Laboratory, Livermore, CA, UCRL-JC-123014; *Physics of Plasmas* **3**(5), 1728–1736 (1996).

Moody, J. D., MacGowan, B. J., Hinkel, D. E., Kruer, W. L., Williams, E. A., Estabrook, K., Shepard, T. D., Kirkwood, R. K., Montgomery, D. S., and Berger, R. L., *First Observation of Intensity Dependent Laser Beam Deflection in a Flowing Plasma,* Lawrence Livermore National Laboratory, Livermore, CA, UCRL-JC-123081; *Phys. Rev. Lett.* **77**(7), 1294–1297 (1996).

Moody, J. D., MacGowan, B. J., Kirkwood, R. K., Montgomery, D. S., Munro, D. H., and Estabrook, K. E., *Direct Measurement of Laser Propagation through a High-Temperature Large Scalelength Plasma,* Lawrence Livermore National Laboratory, Livermore, CA, UCRL-JC-123321 ABS. Prepared for the *11th Topical Conf on High Temperature Plasma Diagnostics,* Monterey, CA, May 12–16, 1996.

Moody, J. D., Baldis, H. A., Montgomery, D. S., Berger, R. L., Estabrook, K., Kruer, W. L., Lasinski, B. F., Williams, E. A., Dixit, S., and Labaune, C., *Beam Smoothing Effects on the SBS Scattering Instability in Nova Exploding Foil Plasmas,* Lawrence Livermore National Laboratory, Livermore, CA, UCRL-JC-119892 Rev. 1; *Phys. Plasmas* **2**(11), 4285–4296 (1995).

Moody, J. D., MacGowan, B. J., Kirkwood, R. K., and Montgomery, D. S., *Measurements of High Intensity Laser Beam Transmission through Large Scalelength Plasmas,* Lawrence Livermore National Laboratory, Livermore, CA, UCRL-JC-123321. Submitted to *Rev. Sci. Instrum.*

Moody, J. D., MacGowan, B. J., Berger, R. L., and Munro, D. E., *Optical Spectral Characteristics of Light Transmitted through Nova Gasbag Plasmas,* Lawrence Livermore National Laboratory, Livermore, CA, UCRL-JC-124293 ABS. Prepared for the *26th Annual Anomalous Absorption Conf,* Fairbanks, AK, Aug 26–30, 1996.

Moody, J. D., MacGowan, B. J., Kirkwood, R. K., Back, C. A., Glenzer, S. H., Munro, D. E., and Berger, R. L., *Power Balance Studies of a Nova Gasbag Plasma,* Lawrence Livermore National Laboratory, Livermore, CA, UCRL-JC-124294 ABS. Prepared for the *26th Annual Anomalous Absorption Conf,* Fairbanks, AK, Aug 26–30, 1996.

Moody, J. D., MacGowan, B. J., Berger, R. L., and Munro, D. E., *Analysis of Transmitted Light Angular Divergence in Nova Gasbag Plasmas,* Lawrence Livermore National Laboratory, Livermore, CA, UCRL-JC-124296 ABS. Prepared for the *26th Annual Anomalous Absorption Conf,* Fairbanks, AK, Aug 26–30, 1996.

Moody, J. D., MacGowan, B. J., Kirkwood, R. K., Montgomery, D. S., Berger, R. L., Hinkel, D. E., Shepard, T. D., and Williams, E. A., *Experimental Studies of Beam Deflection through an Exploding Foil Plasma,* Lawrence Livermore National Laboratory, Livermore, CA, UCRL-JC-121486 ABS Rev. 1. Prepared for *38th Annual Mtg of the American Physical Society Div of Plasma Physics,* Denver, CO, Nov 11–15, 1996.

Moon, S. J., and Eder, D. C., *Target Considerations for Inner-Shell Photo-Ionized X-Ray Lasing,* Lawrence Livermore National Laboratory, Livermore, CA, UCRL-JC-123798. Prepared for *5th Intl Conf on X-Ray Lasers,* Lund, Sweden, Jun 10–14, 1996.

Moran, M. J., *Nuclear Diagnostics in Support of ICF Experiments,* Lawrence Livermore National Laboratory, Livermore, CA, UCRL-JC-124232 ABS & VG. Prepared for the *11th Topical Conf on High Temperature Plasma Diagnostics,* Monterey, CA, May 12–16, 1996.

Moran, M. J., *A Thresholded Cherenkov Detector for ICF Diagnostics,* Lawrence Livermore National Laboratory, Livermore, CA, UCRL-JC-124242 ABS. Prepared for the *11th Topical Conf on High Temperature Plasma Diagnostics,* Monterey, CA, May 12–16, 1996.

Moran, M. J., and Hall, J., *Nuclear Diagnostics in Support of ICF Experiments,* Lawrence Livermore National Laboratory, Livermore, CA, UCRL-JC-124232. Prepared for the *11th Topical Conf on High-Temperature Plasma Diagnostics,* Monterey, CA, May 12–16, 1996.

Motteler, Z. C., *A Python Interface with Narcisse Graphics,* Lawrence Livermore National Laboratory, Livermore, CA, UCRL-JC-124001. Prepared for the *4th Intl Python Workshop,* Livermore, CA, Jun 3–6, 1996.

Murray, J. E., Estabrook, K. G., Van Wonterghem, B. M., Milam, D., Sell, W. D., Boley, C., Feit, M. D., and Rubenchik, A. M., *Preventing Spatial Filter Pinhole Closure with the Pinholes Required to Control Beam Breakup for the NIF,* Lawrence Livermore National Laboratory, Livermore, CA, UCRL-JC-124524 ABS. Prepared for *2nd Annual Intl Conf on Solid-State Lasers for Application to Inertial Confinement Fusion,* Paris, France, Oct 22–25, 1996.

Murray, J. E., Milam, D., Sell, W. D., Estabrook, K. G., Feit, M. D., and Rubenchik, A. M., *Maximum Background Pressure in Spatial Filters for High Power Lasers,* Lawrence Livermore National Laboratory, Livermore, CA, UCRL-JC-124866 ABS. Prepared for *2nd Annual Intl Conf on Solid-State Lasers for Application to Inertial Confinement Fusion,* Paris, France, Oct 22–25, 1996.

N

Neev, J., Nelson, S., Critelli, M., Cheung, E., Carrasco, W. A., Rubenchik, A. M., Da Silva, L. B., Perry, M. D., and Stuart, B. C., *Ablation of Human Nail by Pulsed Lasers,* Lawrence Livermore National Laboratory, Livermore, CA, UCRL-JC-124251. Submitted to *Lasers in Surgery and Medicine.*

Newman, D. L., Goldman, M. V., Afeyan, B. B., and Fedutenko, E., *Effect of Density Gradient on Parametric Growth Rates in Ionospheric Modification Experiments,* Lawrence Livermore National Laboratory, Livermore, CA, UCRL-JC-122034 (1995) ABS. Prepared for the *American Geophysical Union*, Moscone Center, San Francisco, CA, Dec 4–8, 1995.

Newton, M. A., Deadrick, F. J., Hanks, R. L., Hawkins, S. A., Holm, K. A., Kirbie, H. C., Karpenko, V. P., Longinotti, D. B., and Nattrass, L. A., *Engineering Development for a Small-Scale Recirculator Experiment,* Lawrence Livermore National Laboratory, Livermore, CA, UCRL-JC-121456. Prepared for the *Int'l Symp on Heavy Ion Fusion*, Princeton, NJ, Sept 6–9, 1995.

Newton, M., Larson, D., Ullery, G., Hulsey, S., Test, P., Wilson, M., Harjes, C., and Anderson, B., *Component Development for the NIF Power Conditioning System,* Lawrence Livermore National Laboratory, Livermore, CA, UCRL-JC-124376 ABS. Prepared for *2nd Annual Intl Conf on Solid-State Lasers for Application to Inertial Confinement Fusion,* Paris, France, Oct 22–25, 1996.

Nguyen, H. T., Shore, B. W., Britten, J. A., Bryan, S. J., and Perry, M. D., *High-Efficiency Transmission Gratings Fabricated in Bulk Fused Silica,* Lawrence Livermore National Laboratory, Livermore, CA, UCRL-JC-123585 ABS Rev. 1. Prepared for *2nd Annual Intl Conf on Solid-State Lasers for Application to Inertial Confinement Fusion,* Paris, France, Oct 22–25, 1996.

Norton, M. A., Murray, J. E., Boley, C. D., Milam, D., Sell, W. D., Feit, M. D., and Rubenchik, A. M., *Development of Long-Lifetime, Low-Contamination Beam Dumps for NIF,* Lawrence Livermore National Laboratory, Livermore, CA, UCRL-JC-124863 ABS. Prepared for *2nd Annual Intl Conf on Solid-State Lasers for Application to Inertial Confinement Fusion,* Paris, France, Oct 22–25, 1996.

O

Orzechowski, T. J., Rosen, M. D., Kornblum, H. N., Porter, J. L., Suter, L. J., Thiessen, A. R., and Wallace, R., *The Rosseland Mean Opacity of a Composite Material at High Temperatures,* Lawrence Livermore National Laboratory, Livermore, CA, UCRL-JC-123579; *Phys. Rev. Lett.* **77**(17), 3545–3548 (1996).

Orzechowski, T. J., Afeyan, B., Berger, R. L., Blain, M. A., Kirkwood, R. K., Kruer, W. L., MacGowan, B. J., Powers, L. V., Springer, P. S., Rosen, M. D., Moody, J. D., and Suter, L. J., *Energetics of Small, High-Temperature Laser-Driven Hohlraums,* Lawrence Livermore National Laboratory, Livermore, CA, UCRL-JC-124279 ABS. Prepared for the *26th Annual Anomalous Absorption Conf,* Fairbanks, AK, Aug 26–30, 1996.

Orzechowski, T. J., Afeyan, B., Berger, R. L., Kirkwood, R. K., Kruer, W. L., Kornblum, H. N., MacGowan, B. J., Montgomery, D. S., Moody, J. D., Powers, L. V., Rosen, M. D., Springer, P. S., Suter, L. J., Wallace, R. J., and Blain, M. A., *Energetics of High-Temperature Laser Driven Hohlraums,* Lawrence Livermore National Laboratory, Livermore, CA, UCRL-JC-124657 ABS. Prepared for *38th Annual Mtg of the American Physical Society Div of Plasma Physics,* Denver, CO, Nov 11–15, 1996.

Overturf, G. E., Cook, R., Letts, S. A., Buckley, S. R., McClellan, M. R., and Schroen-Carey, D., *Resorcinol-Formaldehyde Foam Shell Targets for ICF,* Lawrence Livermore National Laboratory, Livermore, CA, UCRL-JC-120195; *Fus. Tech.* **28**(12), 1803–1808 (1995).

Overturf III, G., Lambert, S., Wilemski, G., Letts, S., Cook, R., and Schroen-Carey, D., *Fabrication of Low-Density Foam Shells from Resorcinol-Formaldehyde Aerogel,* Lawrence Livermore National Laboratory, Livermore, CA, UCRL-JC-124663 ABS. Prepared for *11th Target Fabrication Specialists' Mtg*, Orcas Island, WA, Sept 8–12, 1996.

P

Page, R. H., DeLoach, L. D., Schaffers, K. I., Patel, F. D., Payne, S. A., Krupke, W. F., and Burger, A., *Recent Developments in Cr^{2+}–Doped II-VI Compound Lasers,* Lawrence Livermore National Laboratory, Livermore, CA, UCRL-JC-122122 EXT ABS. Prepared for the *Advanced Solid State Lasers 11th Topical Mtg,* San Francisco, CA, Jan 31–Feb 3, 1996.

Page, R. H., Schaffers, K. I., Wilke, G. D., Waide, P. A., Tassano, J. A., Beach, R. J., Payne, S. A., and Krupke, W. F., *Observation of 1300 nm Gain in Dysprosium-Doped Chloride Crystals,* Lawrence Livermore National Laboratory, Livermore, CA, UCRL-JC-122030 ABS & SUM. Prepared for the *Conf on Optical Fiber Communication '96,* San Jose, CA, Feb 25–Mar 1, 1996.

Page, R. H., Schaffers, K. I., Payne, S. A., and Krupke, W. F., *Dy-Doped Chlorides as Gain Media for 1.3 μ Telecommunications Amplifiers,* Lawrence Livermore National Laboratory, Livermore, CA, UCRL-JC-123544. Submitted to the *J. Lightwave Technol.*

Page, R., Schaffers, K. I., Beach, R. J., Payne, S. A., and Krupke, W. F., *1300-nm Gain Obtained with Dysprosium-Doped Chloride Crystals,* Lawrence Livermore National Laboratory, Livermore, CA, UCRL-JC-123523. Prepared for the *Optical Amplifiers and Their Applications,* Monterey, CA, Jul 10–13, 1996.

Page, R., DeLoach, L., Schaffers, K., Patel, F., Beach, R., Payne, S., Krupke, W., and Burger, A., *Recent Developments in Cr^{2+}-Doped II-VI Compound Lasers,* Lawrence Livermore National Laboratory, Livermore, CA, UCRL-JC-122122. Prepared for *Advanced Solid State Lasers '96,* San Francisco, CA, Jan 31–Feb 2, 1996.

Page, R., Schaffers, K. I., Skidmore, J. A., Beach, R. J., Payne, S. A., and Krupke, W. F., *$ZnSe:Cr^{2+}$, the "Ti-Sapphire of the Mid-IR,"* Lawrence Livermore National Laboratory, Livermore, CA, UCRL-JC-124436. Submitted to *Optics & Photonics News special issue—Optics in 1996.*

Page, R. H., Schaffers, K. I., DeLoach, L. D., Wilke, G. D., Patel, F. D., Tassano, J. B., Payne, S. A., Krupke, W. F., Chen, K.-T., and Burger, A., *Cr^{2+}-Doped Zinc Chalcogenides as Efficient, Widely-Tunable Mid-Infrared Lasers,* Lawrence Livermore National Laboratory, Livermore, CA, UCRL-JC-123768. Submitted to *J. of Quantum Electronics.*

Paisner, J. A., and Powell, H. T., *The National Ignition Facility and Its Laser Technology,* Lawrence Livermore National Laboratory, Livermore, CA, UCRL-JC-123764 ABS Rev. 1. Prepared for the *16th Intl Atomic Energy Agency Conf on Plasma Physics and Controlled Nuclear Fusion Research,* Montreal, Canada, Oct 7–11, 1996.

Paisner, J., Lowdermilk, H., Hogan, W., Hunt, J., Murray, J., Karpenko, V., Sawicki, R., Kumpan, S., Boyes, J., Sorem, M., and Sources, R., *Progress in the Title I Design of the National Ignition Facility,* Lawrence Livermore National Laboratory, Livermore, CA, UCRL-JC-123560 SUM. Prepared for the *American Nuclear Society 12th Topical Mtg on the Technology of Fusion Energy,* Reno, NV, Jun 16–20, 1996.

Payne, S. A., *Conduction Band States and 5d-to-4f Laser Transition of Rare Earth Ion Dopants,* Lawrence Livermore National Laboratory, Livermore, CA, UCRL-JC-124497. Prepared for *2nd Intl Conf on Tunable Solid State Lasers,* Warsaw, Poland, Sept 1–4, 1996.

Payne, S. A., Page, R. H., Marshall, C. D., Schaffers, K. I., Bayramian, A. J., and Krupke, W. F., *New Tunable Lasers for Potential Use in LIDAR Systems,* Lawrence Livermore National Laboratory, Livermore, CA, UCRL-JC-124015. Prepared for *1996 Intl Symp on Optical Science, Engineering and Instrumentation,* Denver, CO, Aug 4–9, 1996.

Payne, S. A., *Materials and Techniques for Scaling Lasers to High Power,* Lawrence Livermore National Laboratory, Livermore, CA, UCRL-JC-124488 ABS. Prepared for the *Materials Research Society Fall Mtg,* Boston, MA, Dec 2–6, 1996.

Payne, S. A., *Conduction Band States and 5d-to-4f Laser Transition of Rare Earth Ion Dopants,* Lawrence Livermore National Laboratory, Livermore, CA, UCRL-JC-124497 ABS. Prepared for the *2nd Intl Conf on Tunable Solid State Lasers,* Warsaw, Poland, Sept 1–4, 1996.

Payne, S. A., and Krupke, W. F., *Beyond the Present: a Glimpse into the Laser-Crystal Ball,* Lawrence Livermore National Laboratory, Livermore, CA, UCRL-JC-124274; *Optics & Photonics News* [8/96].

Payne, S. A., Page, R. H., Marshall, C. D., Schaffers, K. I., and Krupke, W. F., *New Tunable Laser Materials for Potential Use in LIDAR Systems,* Lawrence Livermore National Laboratory, Livermore, CA, UCRL-JC-124015 ABS. Prepared for the *Society of Photo-Optical Instrumentation Engineers 1996 Intl Symp on Optical Science, Engineering and Instrumentation,* Denver, CO, Aug 4–9, 1996.

Pennington, D. M., Dixit, S. N., Weiland, T. L., Ehrlich, R., and Rothenberg, J. E., *Implementation and Performance of Beam Smoothing on 10 Beams of the Nova Laser,* Lawrence Livermore National Laboratory, Livermore, CA, UCRL-JC-124503 ABS. Prepared for *2nd Annual Intl Conf on Solid-State Lasers for Application to Inertial Confinement Fusion,* Paris, France, Oct 22–25, 1996.

Pennington, D. M., Milam, D., and Eimerl, D., *Gain Saturation Studies in LG-750 and LG-770 Amplifier Glass,* Lawrence Livermore National Laboratory, Livermore, CA, UCRL-JC-124504 ABS. Prepared for *2nd Annual Intl Conf on Solid-State Lasers for Application to Inertial Confinement Fusion,* Paris, France, Oct 22–25, 1996.

Pennington, D., *Inertial Confinement Fusion Quarterly Report,* Volume 6, Number 2, Lawrence Livermore National Laboratory, Livermore, CA, UCRL-LR-105821-96-2.

Pennington, D. M., Milam, D., and Eimerl, D., *Gain Saturation Studies in Phosphate Amplifier Glasses,* Lawrence Livermore National Laboratory, Livermore, CA, UCRL-JC-123588 ABS & SUM. Prepared for the *1996 Conf on Lasers and Electro-Optics, Anaheim,* CA, Jun 2–7, 1996.

Perkins, A. E., Milam, D., and Eimerl, D., *Terahertz Bandwidth Produced by Multi-Pass Phase Modulation at 3 GHz,* Lawrence Livermore National Laboratory, Livermore, CA, UCRL-JC-123307. Submitted to *Opt Lett.*

Peterson, A. B., Marshall, C. D., and Quarles, G. J., *High Repetition Rate Ce:LiCAF Tunable UV Laser,* Lawrence Livermore National Laboratory, Livermore, CA, UCRL-JC-122680 ABS & SUM. Prepared for *Conf on Lasers and Electro-Optics (CLEO '96),* Anaheim, CA, Jun 2–7, 1996.

Petrasso, R. D., Li, C. K., Cable, M. D., Kilkenny, J. D., Knauer, J. P., and Kremens, R. L., *Measuring Inertial Fusion Conditions That Rival the Sun's Core,* Lawrence Livermore National Laboratory, Livermore, CA, UCRL-JC-122672. Submitted to *Nature.*

Petrasso, R. D., Li, C. K., Cable, M. D., Pollaine, S. M., Haan, S. W., Kilkenny, J. D., Bernat, T., Knauer, J. P., Cremer, S., and Kremens, R. L., *Implosion Symmetry and ρ Measurements on the National Ignition Facility from Nascent 27→31 MeV Tertiary Protons,* Lawrence Livermore National Laboratory, Livermore, CA, UCRL-JC-123569; *Phys. Rev. Lett.* **77**(13), 2718–2721 (1996).

Phillips, T. W., Cable, M. D., Hicks, D. G., Li, C. K., Petrasso, R. D., and Seguin, F. H., *A Study of CR-39 Track Response to Charged Particles from Nova Implosions,* Lawrence Livermore National Laboratory, Livermore, CA, UCRL-JC-124231. Prepared for the *11th Topical Conf on High Temperature Plasma Diagnostics,* Monterey, CA, May 12–16, 1996.

Pollaine, S. M., and Haan, S. W., *Selection of Beam Angles for the National Ignition Facility (NIF),* Lawrence Livermore National Laboratory, Livermore, CA, UCRL-JC-124266 ABS. Prepared for the *26th Annual Anomalous Absorption Conf,* Fairbanks, AK, Aug 26–30, 1996.

Poole, B. R., Ng, W. C., Shang, C. C., and Caporaso, G. J., *Theory and Modeling of Wake Fields Generated by Relativistic Electron Beams in Long Accelerator Structures,* Lawrence Livermore National Laboratory, Livermore, CA, UCRL-JC-121313-ABS (1995). Prepared for the *1st Biennial Tri-Laboratory Engineering Conf on Computational Modeling,* Pleasanton, CA, Oct 31–Nov 2, 1995.

Powell, H. T., *The Challenge of Solid-State Lasers for Inertial Confinement Fusion,* Lawrence Livermore National Laboratory, Livermore, CA, UCRL-JC-122330 ABS & SUM. Prepared for the *1996 Advanced Solid State Lasers Topical Mtg,* San Francisco, CA, Jan 31–Feb 3, 1996.

Powers, L. V., Glendinning, S. G., Suter, L. J., Ress, D. B., Landen, O. L., and Shepard, T. D., *Simulation and Analysis of Wall Emission Patterns from Nova Hohlraum Targets,* Lawrence Livermore National Laboratory, Livermore, CA, UCRL-JC-122412 ABS. Prepared for the *37th Annual Mtg of the Div of Plasma Physics,* Louisville, KY, Nov 6–10, 1995.

Powers, L. V., Glendinning, S. G., Berger, R. L., Hinkel, D. E., Kauffman, R. L., Kruer, W. L., Pollaine, S. M., Shepard, T. D., Suter, L. J., Williams, E. A., Delamater, N. D., Hauer, A. A., Lindman, E. L., Magelssen, G. R., Murphy, T. J., Failor, B. F., and Richard, A. R., *Studies of Radiation Symmetry in Gas-Filled Hohlraums,* Lawrence Livermore National Laboratory, Livermore, CA, UCRL-JC-123571 ABS. Prepared for the *24th European Conf on Laser Interaction with Matter,* Madrid, Spain, Jun 3–7, 1996.

Powers, L. V., Orzechowski, T. J., Springer, P. T., Suter, L. J., MacGowan, B. J., Berger, R. L., Budil, K. S., Foord, M. E., Kruer, W. L., Langdon, A. B., Perry, T. S., Rosen, M. D., Shepard, T. D., Still, C. H., Williams, E. A., Desenne, D., Juraszek, D., Monteil, M.-C., and Richard, A. R., *Radiation Temperature Scaling in Hohlraums for Nova and NIF,* Lawrence Livermore National Laboratory, Livermore, CA, UCRL-JC-123572 ABS. Prepared for the *24th European Conf on Laser Interaction with Matter,* Madrid, Spain, Jun 3–7, 1996.

Powers, L. V., Back, C. A., Berger, R. L., Glendinning, S. G., Glenzer, S., Hinkel, D. E., Kauffman, R. L., Kruer, W. L., MacGowan, B. J., Orzechowski, T. J., Pollaine, S. M., Ress, D. B., Shepard, T. D., Suter, L. J., Williams, E. A., Delamater, N. D., Hauer, A. A., Lindman, E. L., Magelssen, G. R., and Murphy, T. J., *Studies of Energetics and Symmetry in Gas-Filled Hohlraums,* Lawrence Livermore National Laboratory, Livermore, CA, UCRL-JC-123784 ABS. Prepared for the *16th Intl Atomic Energy Agency Fusion Energy Conf on Plasma and Controlled Nuclear Fusion Research,* Montreal, Canada, Oct 7–11, 1996.

Powers, L. V., Berger, R. L., Kirkwood, R. K., Kruer, W. L., Langdon, A. B., MacGowan, B. J., Orzechowski, T. J., Rosen, M. D., Springer, P. T., Still, C. H., Suter, L. J., and Williams, E. A., *Radiation Temperature Scaling in Hohlraums for Nova and NIF,* Lawrence Livermore National Laboratory, Livermore, CA, UCRL-JC-123572 ABS Rev. 1. Prepared for the *26th Annual Anomalous Absorption Conf,* Fairbanks, AK, Aug 26–30, 1996.

Powers, L. V., Berger, R. L., Kirkwood R. K., Kruer, W. L., Langdon, A. B., MacGowan, B. J., Orzechowski, T. J., Rosen, M. D., Springer, P. T., Still, C. H., Suter, L. J., Williams, E. A., and Blain, M. A., *Analysis of Reduced-Scale Nova Hohlraum Experiments,* Lawrence Livermore National Laboratory, Livermore, CA, UCRL-JC-124680 ABS. Prepared for *38th Annual Mtg of the American Physical Society Div of Plasma Physics,* Denver, CO, Nov 11–15, 1996.

Prasad, M., Shaw, M. J., Milovich, J., and Kershaw, D. S., *3D Unstructured Mesh ALE Hydrodynamics with the Upwind, Discontinuous Finite Element Method,* Lawrence Livermore National Laboratory, Livermore, CA, UCRL-JC-122104 Rev. 1. Submitted to *J. of Computational Physics.*

R

Rainer, F., Anderson, A., Burnham, A., Milam, D., and Turner, R., *Lifetime Survivability of Contaminated Target-Chamber Optics,* Lawrence Livermore National Laboratory, Livermore, CA, UCRL-JC-124943 ABS. Prepared for *Symp on Optical Materials for High Power Lasers '96,* Boulder, CO, Oct 7–9, 1996.

Rashkovich, L. N., Lowdermilk, W. H., and De Yoreo, J. J., *Effect of pH on the Growth of KDP,* Lawrence Livermore National Laboratory, Livermore, CA, UCRL-CR-122742.

Rashkovich, L. N., Lowdermilk, W. H., and De Yoreo, J. J., *Effect of Impurities on Growth Rate and Stability of KDP Surfaces,* Lawrence Livermore National Laboratory, Livermore, CA, UCRL-CR-122743.

Reisman, D., Denney, C., De Groot, J. S., Estabrook, K. G., Hammer, L. H., Sanford, T. W. L., Speilman, R. B., and Toor, A., *Energetics in Imploding Z-Pinches,* Lawrence Livermore National Laboratory, Livermore, CA, UCRL-JC-124688 ABS. Prepared for *38th Annual Mtg of the American Physical Society Div of Plasma Physics,* Denver, CO, Nov 11–15, 1996.

Reitz, T., Drobnik, F., Evans, M., Tobin, M., and Karpenko, V., *Utilization of the CO_2 Pellet Blasting Process for the National Ignition Facility,* Lawrence Livermore National Laboratory, Livermore, CA, UCRL-JC-123565 SUM. Prepared for the *American Nuclear Society 12th Topical Mtg on the Technology of Fusion Energy,* Reno, NV, Jun 16–20, 1996.

Remington, B. A., Campbell, E. M., Holmes, N. C., Libby, S. B., and Teller, E., *Evolution of High Energy-Density Physics: from Nuclear Testing to the Superlasers,* Lawrence Livermore National Laboratory, Livermore, CA, UCRL-JC-124258 Rev. 2. Submitted to *Laser and Particle Beams.*

Remington, B. A., Glendinning, S. G., Kalantar, D. H., Budil, K. S., Landen, O. L., Hammel, B. A., Marinak, M. M., Weber, S. V., Keane, C. J., Haan, S. W., Rubenchik, A., Wallace, R., Key, M. H., Knauer, J. P., Ofer, D., Hsing, W. W., Galmiche, D., Blain, M. A., Wood-Vasey, W. M., and Shvarts, D., *Hydrodynamic Instability Experiments on the Nova Laser,* Lawrence Livermore National Laboratory, Livermore, CA, UCRL-JC-123775. Prepared for *16th IAEA Intl Conf on Plasma Physics and Controlled Nuclear Fusion Research,* Montreal, Canada, Oct 7–11, 1996.

Remington, B. A., Glendinning, S. G., Kalantar, D. H., Budil, K. S., Marinak, M. M., Weber, S. V., Colvin, J., Griswold, D., Knauer, J. P., Key, M., Hsing, W. W., Galmiche, D., Rubenchik, A., Kane, J., Arnett, W. D., and Wood-Vasey, W. M., *Laser-Driven Hydrodynamics Experiments at Nova,* Lawrence Livermore National Laboratory, Livermore, CA, UCRL-JC-124480. Prepared for *26th Anomalous Absorption Conf,* Fairbanks, AK, Aug. 26–30, 1996.

Remington, B. A., Glendinning, S. G., Kane, J., Castor, J., Rubenchik, A., Colvin, J., Drake, R. P., London, R., Liang, E., and McCray, R., *Hydrodynamics Experiments on Supernovae and on Nova—the Laser,* Lawrence Livermore National Laboratory, Livermore, CA, UCRL-JC-124949 ABS. Prepared for *38th Annual Mtg of the American Physical Society Div of Plasma Physics,* Denver, CO, Nov 11–15, 1996.

Remington, B. A., Kalantar, D. H., Woolsey, N., Colvin, J., Griswold, D., Cauble, R., Lee, R., Wark, J. S., Hauer, A., and Rubenchik, A., *Nova Experiments on Hydrodynamics and Instabilities in the Solid State,* Lawrence Livermore National Laboratory, Livermore, CA, UCRL-JC-124549 ABS. Prepared for *38th Annual Mtg of the American Physical Society Div of Plasma Physics,* Denver, CO, Nov 11–15, 1996.

Remington, B. A., Kane, J., Arnett, D., Glendinning, S. G., Rubenchik, A., Berning, M., and Castor, J., *An Investigation of Hydrodynamic Instabilities in Supernovae Using the Nova Laser,* Lawrence Livermore National Laboratory, Livermore, CA, UCRL-JC-123035 ABS. Prepared for the *1996 Joint American Physical Society and American Association of Physics Teachers Mtg,* Indianapolis, IN, May 2–5, 1996.

Remington, B. A., Glendinning, S. G., Kalantar, D. H., Budil, K. S., Landen, O. L., Hammel, B. A., Marinak, M. M., Weber, W. V., Keane, C. J., Haan, S. W., Rubenchik, A., Wallace, R. J., Key, M. H., Knauer, J. P., Hsing, W. W., Galmiche, D., Blain, M. A., Kane, J., Arnett, D., and Berning, M., *Hydrodynamic Instability Experiments on the Nova Laser,* Lawrence Livermore National Laboratory, Livermore, CA, UCRL-JC-123775 ABS. Prepared for the *16th Intl Atomic Energy Agency Fusion Energy Conf on Plasma Physics and Controlled Nuclear Fusion Research,* Montreal, Canada, Oct 7–11, 1996.

Remington, B. A., Glendinning, S. G., Kalantar, D. H., Budil, K. S., Marinak, M. M., Weber, S. V., Colvin, J., Griswold, D., Knauer, J. P., Key, M., Hsing, W. W., Galmiche, D., Rubenchik, A., Kane, J., Arnett, W. D., and Wood-Vasey, W. M., *Laser-Driven Hydrodynamics Experiments at Nova,* Lawrence Livermore National Laboratory, Livermore, CA, UCRL-JC-124480 ABS. Prepared for the *26th Annual Anomalous Absorption Conf,* Fairbanks, AK, Aug 26–30, 1996.

Remington, B. A., Marinak, M. M., Budil, K. S., Wallace, R. J., Weber, S. V., and Robey, H., *Ablation Front Rayleigh-Taylor Experiments in 2D and 3D,* Lawrence Livermore National Laboratory, Livermore, CA, UCRL-JC-124000. Submitted to *Phys. of Plasmas.*

Remington, B., Marinak, M. M., Budil, K. S., and Robey, H., *Ablation Front Rayleigh–Taylor Experiments in 3D,* Lawrence Livermore National Laboratory, Livermore, CA, UCRL-JC-123290 ABS. Prepared for the *24th European Conf on Laser Interaction with Matter,* Madrid, Spain, Jun 3–7, 1996.

Ress, D., and Lerche, R. A., *Recent Results from the Nova Neutron Microscope,* Lawrence Livermore National Laboratory, Livermore, CA, UCRL-JC-124542 ABS. Prepared for *38th Annual Mtg of the American Physical Society Div of Plasma Physics,* Denver, CO, Nov 11–15, 1996.

Ress, D., Lerche, R. A., Ellis, R. J., Heaton, G. W., and Lehr, D. E., *High-Sensitivity Scintillating-Fiber Imaging Detector for High-Energy Neutrons,* Lawrence Livermore National Laboratory, Livermore, CA, UCRL-JC-119904; *Rev. Sci. Inst.* **66**(10), 4943–4948 (1995).

Rhodes, M. A., Fochs, S. N., and Alger, T. W., *1×2 Prototype PEPC for the NIF,* Lawrence Livermore National Laboratory, Livermore, CA, UCRL-JC-124514 ABS. Prepared for *2nd Annual Intl Conf on Solid-State Lasers for Application to Inertial Confinement Fusion,* Paris, France, Oct 22–25, 1996.

Robey, H. F., Budil, K. S., and Remington, B. A., *Spatial Resolution of Gated X-Ray Pinhole Cameras,* Lawrence Livermore National Laboratory, Livermore, CA, UCRL-JC-123044 ABS. Prepared for the *11th Topical Conf on High-Temperature Plasma Diagnostics,* Monterey, CA, May 12–16, 1996.

Robey, H. F., Budil, K. S., and Remington, B. A., *Spatial Resolution of Gated X-Ray Pinhole Cameras,* Lawrence Livermore National Laboratory, Livermore, CA, UCRL-JC-123044. Prepared for the *11th Topical Conf on High Temperature Plasma Diagnostics,* Monterey, CA, May 12–16, 1996.

Rosen, M. D., *The Science Applications of the High Energy Density Plasmas Created on the Nova Laser,* Lawrence Livermore National Laboratory, Livermore, CA, UCRL-JC-121476. Submitted to *Phys. of Plasmas.*

Rothenberg, J. E., *Smoothing by Spectral Dispersion Using Random Phase Modulation for Inertial Confinement Fusion,* Lawrence Livermore National Laboratory, Livermore, CA, UCRL-JC-122668. Prepared for the *Conf on Lasers and Electro-Optics (CLEO '96),* Anaheim, CA, Jun 2, 1996.

Rothenberg, J. E., *Electro-Optic Deflectors as a Method of Beam Smoothing for Inertial Confinement Fusion,* Lawrence Livermore National Laboratory, Livermore, CA, UCRL-JC-124507 ABS. Prepared for *2nd Annual Intl Conf on Solid-State Lasers for Application to Inertial Confinement Fusion,* Paris, France, Oct 22–25, 1996.

Rothenberg, J. E., *Improved Beam Smoothing with SSD Using Generalized Phase Modulation,* Lawrence Livermore National Laboratory, Livermore, CA, UCRL-JC-124508 ABS. Prepared for *2nd Annual Intl Conf on Solid-State Lasers for Application to Inertial Confinement Fusion,* Paris, France, Oct 22–25, 1996.

Rothenberg, J. E., and Weber, S. V., *The Impact of Beam Smoothing Method on Direct Drive Target Performance for the National Ignition Facility,* Lawrence Livermore National Laboratory, Livermore, CA, UCRL-JC-124509 ABS. Prepared for *2nd Annual Intl Conf on Solid-State Lasers for Application to Inertial Confinement Fusion,* Paris, France, Oct 22–25, 1996.

Rothenberg, J. E., Moran, B. D., Wing, R. R., and Van Wonterghem, B. M., *Performance of Smoothing by Spectral Dispersion on Beamlet,* Lawrence Livermore National Laboratory, Livermore, CA, UCRL-JC-124506 ABS. Prepared for *2nd Annual Intl Conf on Solid-State Lasers for Application to Inertial Confinement Fusion,* Paris, France, Oct 22–25, 1996.

Rothenberg, J., *SSD with Generalized Phase Modulation,* Lawrence Livermore National Laboratory, Livermore, CA, UCRL-ID-123083.

Rothenberg, J. E., *A Comparison of Beam Smoothing Methods for Direct Drive Inertial Confinement Fusion,* Lawrence Livermore National Laboratory, Livermore, CA, UCRL-JC-124038. Submitted to *J. of the Optical Society of America B.*

Rothenberg, J. E., and Weber, S. V., *Effects of Beam Smoothing on the Hydrodynamics of Direct Drive Inertial Confinement Fusion,* Lawrence Livermore National Laboratory, Livermore, CA, UCRL-JC-124476 ABS. Prepared for the *26th Annual Anomalous Absorption Conf,* Fairbanks, AK, Aug 26–30, 1996.

Rotter, M., McCracken, R., Erlandson, A., and Guenet, M., *Gain Measurements on a Prototype NIF/LMJ Amplifier Pump Cavity,* Lawrence Livermore National Laboratory, Livermore, CA, UCRL-JC-124518 ABS. Prepared for *2nd Annual Intl Conf on Solid-State Lasers for Application to Inertial Confinement Fusion,* Paris, France, Oct 22–25, 1996.

Rotter, M., Doss, S., Erlandson, A., LeTouze, G., Sutton, S., Van Wonterghem, B., and Zapata, L., *Computer Modeling of Large-Aperture Laser Amplifiers for Inertial Confinement Fusion,* Lawrence Livermore National Laboratory, Livermore, CA, UCRL-JC-122025 ABS. Prepared for the *1st Biennial Tri-Laboratory Engineering Conf on Computational Modeling,* Pleasanton, CA, Oct 31–Nov 2, 1995.

Rotter, M. C., Doss, S. K., Erlandson, A. C., Jancaitis, K. S., Sutton, S., and LeTouze, G., *Modeling Pump-Induced Wavefront Distortions in Large-Aperture Laser Amplifiers,* Lawrence Livermore National Laboratory, Livermore, CA, UCRL-JC-122541 ABS & SUM. Prepared for the *Conf on Lasers and Electro-Optics (CLEO '96),* Anaheim Convention Center, Anaheim, CA, Jun 2–7, 1996. Submitted to the *Optical Society of America.*

Rubenchik, A., Kane, J., Wood-Vasey, M., Glendinning, S. G., and Remington, B. A., *On Interface Instabilities in Expanding Plasmas,* Lawrence Livermore National Laboratory, Livermore, CA, UCRL-JC-124676 ABS. Prepared for *38th Annual Mtg of the American Physical Society Div of Plasma Physics,* Denver, CO, Nov 11–15, 1996.

Runkel, M., Woods, B., Yan, M., De Yoreo, J., and Kozlowski, M., *Analysis of High Resolution Scatter Images from Laser Damage Experiments Performed on KDP,* Lawrence Livermore National Laboratory, Livermore, CA, UCRL-JC-122321. Prepared for the *Symp on Optical Materials for High Power Lasers,* Orlando, FL, Oct 30–Nov 1, 1995.

Runkel, M., Woods, B., Kozlowski, M., Yan, M., and De Yoreo, J., *Analysis of High Resolution Scatter Images from Laser Damage Experiments Performed on KDP,* Lawrence Livermore National Laboratory, Livermore, CA, UCRL-JC-122321 ABS & VG. Prepared for the *Annual Symp on Optical Materials for High Power Lasers,* Boulder, CO, Oct 30–Nov 1, 1995.

Runkel, M., and Kozlowski, M., *Large Area Damage Testing of Conventionally Grown KD*P at 351 nm on the Beamlet Laser,* Lawrence Livermore National Laboratory, Livermore, CA, UCRL-JC-124535 ABS. Prepared for *2nd Annual Intl Conf on Solid-State Lasers for Application to Inertial Confinement Fusion,* Paris, France, Oct 22–25, 1996.

Rushford, M. R., Dixit, S. N., Thomas, I. M., Martin, A. M., and Perry, M. D., *Large Aperture Kinoform Phase Plates in Fused Silica for Spatial Beam Smoothing on Nova and the Beamlet Lasers,* Lawrence Livermore National Laboratory, Livermore, CA, UCRL-JC-124511 ABS. Prepared for *2nd Annual Intl Conf on Solid-State Lasers for Application to Inertial Confinement Fusion,* Paris, France, Oct 22–25, 1996.

Rushford, M., Dixit, S., Thomas, I., and Perry, M. D., *Fabrication of Large Aperture Kinoform Phase Plates in Fused Silica for Smoothing Focal Plane Intensity Profiles,* Lawrence Livermore National Laboratory, Livermore, CA, UCRL-JC-124013. Prepared for the *1996 Diffractive Optics and Micro Optics Topical Mtg,* Boston, MA, Apr 29–May 2, 1996.

S

Saculla, M., and Letts, S., *Advances in Bouncer Pan Technology,* Lawrence Livermore National Laboratory, Livermore, CA, UCRL-JC-125136 ABS. Prepared for *11th Target Fabrication Specialists' Mtg,* Orcas Island, WA, Sept 8–12, 1996.

Sahin, S., Moir, R. W., and Sahinaslan, A., *Radiation Damage in Liquid-Protected First-Wall Materials for IFE-Reactors,* Lawrence Livermore National Laboratory, Livermore, CA, UCRL-JC-125149. Submitted to *Fusion Technol.*

Salmon, J. T., Bliss, E. S., Byrd, J. L., Feldman, M., Kartz, M. A., Toeppen, J. S., Van Wonterghem, B., and Winters, S. E., *Adaptive Optics System for Solid-State Laser Systems Used in Inertial Confinement Fusion,* Lawrence Livermore National Laboratory, Livermore, CA, UCRL-JC-122033. Prepared for the *1st Annual Int'l Conf on Solid-State Lasers for Application to Inertial Confinement Fusion,* Monterey, CA, May 30–Jun 2, 1995.

Sanchez, J. J., and Giedt, W., *Thermal Design of Cylindrical Hohlraums for the NIF,* Lawrence Livermore National Laboratory, Livermore, CA, UCRL-JC-125141 ABS. Prepared for *11th Target Fabrication Specialists' Mtg,* Orcas Island, WA, Sept 8–12, 1996.

Sanchez, J. J., and Letts, S., *High Strength Plastics May Reduce Cryogenic Requirements for the NIF,* Lawrence Livermore National Laboratory, Livermore, CA, UCRL-JC-125142 ABS. Prepared for *11th Target Fabrication Specialists' Mtg,* Orcas Island, WA, Sept 8–12, 1996.

Sangster, T. C., Cable, M. D., Kilkenny, J. D., Lerche, R. A., Nelson, M. B., Moran, M. J., Ress, D., Trebes, J. E., Turner, R. E., and Phillips, T. W., *Diagnostic Development at LLNL for the National Ignition Facility,* Lawrence Livermore National Laboratory, Livermore, CA, UCRL-JC-124452. Prepared for the *24th European Conf on Laser Interaction with Matter,* Madrid, Spain, Jun 3–7, 1996.

Schaffers, K. I., Page, R. H., Beach, R. J., Payne, S. A., and Krupke, W. F., *Gain Measurements in Dy^{3+}–Doped $LaCl_3$ µm Optical Amplifier for Telecommunications,* Lawrence Livermore National Laboratory, Livermore, CA, UCRL-JC-122120 ABS & SUM. Prepared for the *Advanced Solid State Lasers 11th Topical Mtg,* San Francisco, CA, Jan 31–Feb 3, 1996.

Scheibner, K., Haynam, C., and Worden, E., *Laser Isotope Purification of Lead for Use in Semiconductor Chip Interconnects,* Lawrence Livermore National Laboratory, Livermore, CA, UCRL-JC-122657 ABS. Prepared for the *46th Electronic Components and Technology Conf,* Orlando, FL, May 28–31, 1996.

Schirmann, D., and Tobin, M., *Target Area Conceptual Design Issue of the French Laser Magajoule Facility (LMJ),* Lawrence Livermore National Laboratory, Livermore, CA, UCRL-JC-123563 SUM. Prepared for the *American Nuclear Society 12th Topical Mtg on the Technology of Fusion Energy,* Reno, NV, Jun 16–20, 1996.

Schnittman, J. D., and Pollain, S. M., *Tetrahedral Hohlraums on the NIF,* Lawrence Livermore National Laboratory, Livermore, CA, UCRL-JC-124267 ABS. Prepared for the *26th Annual Anomalous Absorption Conf,* Fairbanks, AK, Aug 26–30, 1996.

Schroen-Carey, D., Letts, S., Buckley, S., Cook, R., and Lambert, S., *Characteristics of Barrier Layers Produced on R/F Foam Shells by Acid Chloride Interfacial Polymerization,* Lawrence Livermore National Laboratory, Livermore, CA, UCRL-JC-125127 ABS. Prepared for *11th Target Fabrication Specialists' Mtg,* Orcas Island, WA, Sept 8–12, 1996.

Schroen-Carey, D., Overturf, G. E., Letts, S. A., Cook, R. C., and Lambert, S. M., *Polymer Overcoated Resorcinol-Formaldehyde Foam Microshells for Inertial Confinement Fusion Targets,* Lawrence Livermore National Laboratory, Livermore, CA, UCRL-JC-122015 ABS. Prepared for the *10th Int'l Symp on Microencapsulation,* Austin, TX, Sept 26–28, 1995.

Sheehan, L., Kozlowski, M., Stolz, C., and Bodemann, A., *Application of Laser Conditioning to Increase the Damage Threshold of HfO_2/SiO_2 Multilayer Coatings over Large Areas,* Lawrence Livermore National Laboratory, Livermore, CA, UCRL-JC-119647. Submitted to *Appl. Opt.*

Shepard, T. D., Landen, O. L., Lindl, J. D., Rosen, M. D., and Suter, L. J., *High-Z Foil Acceleration Using Hydrodynamic Pressure of Radiatively Heated Matter,* Lawrence Livermore National Laboratory, Livermore, CA, UCRL-JC-124853 ABS. Prepared for *38th Annual Mtg of the American Physical Society Div of Plasma Physics,* Denver, CO, Nov 11–15, 1996.

Shepard, T. D., Landen, O. L., Lindl, J. D., Rosen, M. D., and Suter, L. J., *Acceleration of a High-Z Foil by Hydrodynamic Pressure of Radiatively Heated Matter,* Lawrence Livermore National Laboratory, Livermore, CA, UCRL-JC-124494 ABS. Prepared for the *26th Annual Anomalous Absorption Conf,* Fairbanks, AK, Aug 26–30, 1996.

Shepard, T. D., and Powers, L. V., *Simulation of Indirectly Driven Implosions Using a Gas-Filled Hohlraum Heated by KPP-Smoothed Laser Beams,* Lawrence Livermore National Laboratory, Livermore, CA, UCRL-JC-124493 ABS. Prepared for the *26th Annual Anomalous Absorption Conf,* Fairbanks, AK, Aug 26–30, 1996.

Shore, B. W., Feit, M. D., Perry, M. D., Rubenchik, A., and Stuart, B., *Brief Intense Laser Fields in Bulk Matter,* Lawrence Livermore National Laboratory, Livermore, CA, UCRL-JC-124040. Previously released for *Seminar on Quantum Optics and Strong-Field Phenomena in Atoms and Molecules, of 5th Intl Workshop on Laser Physics LPHY96.* Submitted to *Laser Physics.*

Shore, B. W., Perry, M. D., Britten, J. A., Boyd, R. D., Feit, M. D., Nguyen, N. T., Chow, R., and Loomis, G. E., *Design of High-Efficiency Dielectric Reflection Gratings, J. Opt. Soc. Am A* **14**(5), 1124–1136 (1997).

Skidmore, J. A., Emanuel, M. A., Freitas, B., Beach, R. J., Bibeau, C., Honea, E. C., Page, R. H., Sutton, S. B., and Payne, S. A., *High-Power Laser Diode-Pumped Yb:YAG, Tm:YAG, and Cr:ZnSe Laser Systems,* Lawrence Livermore National Laboratory, Livermore, CA, UCRL-JC-124910 ABS. Prepared for *Society of Photo-Optical Instrumentation Engineers Optoelectronics '97,* San Jose, CA, Feb 8–19, 1997.

Small, W., Heredia, N. J., Celliers, P. M., Da Silva, L. B., Eder, D. C., Glinsky, M. E., London, R. A., Maitland, D. J., Matthews, D. L., Soltz, B. A., *Laser Tissue Welding Mediated with a Protein Solder,* Lawrence Livermore National Laboratory, Livermore, CA, UCRL-JC-124046. Prepared for the *Society of Photo-Optical Instrumentation Engineers '96 Conf,* San Jose, CA, Jan 28–Feb 2, 1996.

Smolski, I., De Yoreo, J. J., Zaitseva, N. P., Lee, J. D., Land, T. A., and Rudneva, E. B., *Oriented Liquid Inclusions in KDP Crystals,* Lawrence Livermore National Laboratory, Livermore, CA, UCRL-JC-122011 Rev 1. Submitted to *Crystal Growth.*

Smolski, I., De Yoreo, J. J., Zaitseva, N. P., Lee, J. D., and Land, T. A., *Oriented Liquid Inclusions in KDP Crystals,* Lawrence Livermore National Laboratory, Livermore, CA, UCRL-JC-122011. Submitted to *Crystal Growth.*

Sommargren, G. E., *Diffraction Methods Raise Interferometer Accuracy, Laser Focus World* **32**(8), 61–71 (1996).

Soures, P. C., Tsugawa, R. T., Fearon, E. M., and Collins, G. W., *NMR Lineshapes in Solid Tritium and Deuterium-Tritium,* Lawrence Livermore National Laboratory, Livermore, CA, UCRL-JC-117391; *J. Low Temp. Phys.* **100**(1), 21-43 (1995).

Spallas, J. P., Hostetler, R. E., Sommargren, G. E., and Kania, D. R., *Fabrication of Extreme-Ultraviolet Point-Diffraction Interferometer Aperture Arrays,* Lawrence Livermore National Laboratory, Livermore, CA, UCRL-JC-119890; *Appl. Opt.* **34**(28), 6393–6398 (1995).

Stephens, R., and Collins, G., *Analysis of Performance of Integrating Sphere for IR Enhanced DT Ice Layering,* Lawrence Livermore National Laboratory, Livermore, CA, UCRL-JC-125128 ABS. Prepared for *11th Target Fabrication Specialists' Mtg,* Orcas Island, WA, Sept 8–12, 1996.

Still, C. H., Berger, R. L., Langdon, A. B., Powers, L. V., Williams, E. A., and Young, P. E., *Laser Filamentation Simulations with Nonlinear Hydrodynamics,* Lawrence Livermore National Laboratory, Livermore, CA, UCRL-JC-124472 ABS. Prepared for the *26th Annual Anomalous Absorption Conf,* Fairbanks, AK, Aug 26–30, 1996.

Still, C. H., Berger, R. L., Langdon, A. B., Powers, L. V., Willims, E. A., and Young, P. E., *Nonlinear Laser Filamentation Simulation in 3D,* Lawrence Livermore National Laboratory, Livermore, CA, UCRL-JC-124679 ABS. Prepared for *38th Annual Mtg of the American Physical Society Div of Plasma Physics,* Denver, CO, Nov 11–15, 1996.

Stolz, C., Genin, F., Kozlowski, M., Long, D., Lalarari, R., Wu, Z., and Kuo, P., *Influence of Microstructure on Laser Damage Threshold of IBS Coatings,* Lawrence Livermore National Laboratory, Livermore, CA, UCRL-JC-121627. Prepared for the *Symp on Optical Materials for High Power Lasers,* Orlando, FL, Oct 30–Nov 1, 1995. Submitted to the *Society of Photo-Optical Instrumentation Engineers.*

Stolz, C., Tench, R., Kozlowski, M., and Fornier, A., *A Comparison of Nodular Defect Seed Geometries from Different Deposition Techniques,* Lawrence Livermore National Laboratory, Livermore, CA, UCRL-JC-121628. Prepared for the *Annual Symp on Optical Materials for High Power Lasers,* Boulder, CO, Oct 30–Nov 1, 1995.

Stolz, C. J., Furr, J. S., Wu, Z. L., Krupka, R., Lu, Y., and Kuo, P. K., *Study of Defects in HfO_2/SiO_2 Multilayer Coatings Using Photothermal Microscopy,* Lawrence Livermore National Laboratory, Livermore, CA, UCRL-JC-124924 ABS. Prepared for *28th Annual Symp on Optical Materials for High Power Lasers,* Boulder, CO, Oct 7–9, 1996.

Stolz, C., Genin, F., Reitter, T. A., Bevis, R. P., von Gunten, M. K., and Hue, J., *Effect of SiO_2 Overcoat Thickness on Laser Damage Morphology of HfO_2/SiO_2 Brewster's Angle Polarizers at 1064 nm,* Lawrence Livermore National Laboratory, Livermore, CA, UCRL-JC-124875 ABS. Prepared for *28th Annual Symp on Optical Materials for High Power Lasers,* Boulder, CO, Oct 7–9, 1996.

Stone, G., Cloud, M., Salazar, M., Bush, H., Gobby, P., and Townsend, J., *Operation of Five Atmosphere Gas Filled Targets at Nova,* Lawrence Livermore National Laboratory, Livermore, CA, UCRL-JC-125133 ABS. Prepared for *11th Target Fabrication Specialists' Mtg,* Orcas Island, WA, Sept 8–12, 1996.

Stone, G. F., Rivers, C. J., Spagge, M. R., and Wallace, R. J., *Fabrication and Testing of Gas Filled Targets for Large Scale Plasma Experiments on Nova,* Lawrence Livermore National Laboratory, Livermore, CA, UCRL-JC-119390; *Fus. Tech.* **28**(12), 1820-1888 (1995).

Stout, E., Miller-Kamm, V., Spann, J., and Van Arsdall, P., *A Prototype Distributed Object-Oriented Architecture for Image-Based Automatic Laser Alignment,* Lawrence Livermore National Laboratory, Livermore, CA, UCRL-JC-124381 ABS. Prepared for *2nd Annual Intl Conf on Solid State Lasers for Application to Inertial Confinement Fusion,* Paris, France, Oct 22–25, 1996.

Strobel, G. L., and Haan, S. W., *Non-Linear Growth Factor Analysis of NIF Capsule Hydrodynamic Instabilities,* Lawrence Livermore National Laboratory, Livermore, CA, UCRL-JC-124546 ABS. Prepared for *38th Annual Mtg of the American Physical Society Div of Plasma Physics,* Denver, CO, Nov 11–15, 1996.

Suter, L. J., Kauffman, R. L., Maxon, M. S., and Grun, J. S., *Efficient Production of 2–10 keV X-Rays by Laser-Heated "Underdense Radiators",* Lawrence Livermore National Laboratory, Livermore, CA, UCRL-JC-123590 ABS. Prepared for the *24th European Conf on Laser Interaction with Matter,* Madrid, Spain, Jun 3–7, 1996.

Suter, L. J., Kauffman, R. L., Maxon, M. S., and Davis, J. F., *Efficient Production of 2–10 keV X Rays by Laser-Heated "Underdense Radiators,"* Lawrence Livermore National Laboratory, Livermore, CA, UCRL-JC-123590 ABS Rev. 1. Prepared for the *26th Annual Anomalous Absorption Conf,* Fairbanks, AK, Aug 26–30, 1996.

Suter, L. J., Thiessen, A. R., Ze, F., Kauffman, R., Price, R. H., Rupert, V. C., Slivinsky, V. W., and Wang, C., *Use of Thin Wall Imaging in the Diagnosis of Laser Heated Hohlraums,* Lawrence Livermore National Laboratory, Livermore, CA, UCRL-JC-116323. Prepared for the *11th Topical Conf on High Temperature Plasma Diagnostics,* Monterey, CA, May 12–16, 1996.

Suter, L. J., Kauffman, R. L., Maxon, M. S., and Davis, J. F., *Efficient Production of 2–10 keV X Rays by Laser Heated "Underdense Radiators,"* Lawrence Livermore National Laboratory, Livermore, CA, UCRL-JC-123590. Prepared for the *24th European Conf on Laser Interaction with Matter,* Madrid, Spain, Jun 3–7, 1996.

Suter, L. J., Kauffman, R. L., Orzechowski, T. J., Powers, L. V., Darrow, C. B., Kornblum, H., Landen, O. L., MacGowan, B. J., Phillion, D. W., Rosen, M. D., Thiessen, A. R., and Richard, A., *Radiation Drive in Gas-Filled, Lined and Pure Gold Laser-Heated Hohlraums,* Lawrence Livermore National Laboratory, Livermore, CA, UCRL-JC-123591 ABS. Prepared for the *24th European Conf on Laser Interaction with Matter,* Madrid, Spain, Jun 3–7, 1996.

Suter, L. J., Ze, F., Kauffman, R., Thiessen, A. R., Price, R. H., Rupert, V. C., Slivinsky, V. W., and Wang, C., *Use of Thin Wall Imaging in the Diagnosis of Laser Heated Hohlraums,* Lawrence Livermore National Laboratory, Livermore, CA, UCRL-JC-116323 ABS Rev 2. Prepared for the *11th Topical Conf on High Temperature Plasma Diagnostics,* Monterey, CA, May 12–16, 1996.

Suter, L. J., *Forward Emitters for Increased Coupling of Laser Produced X-Rays to Targets,* Lawrence Livermore National Laboratory, Livermore, CA, UCRL-JC-124659 ABS. Prepared for *38th Annual Mtg of the American Physical Society Div of Plasma Physics,* Denver, CO, Nov 11–15, 1996.

Sutton, S. B., and Marshall, C. D., *Thermal Recovery of NIF Amplifiers,* Lawrence Livermore National Laboratory, Livermore, CA, UCRL-JC-124528 ABS. Prepared for *2nd Annual Intl Conf on Solid-State Lasers for Application to Inertial Confinement Fusion,* Paris, France, Oct 22–25, 1996.

T

Tabak, M., *Target Physics Summary,* Lawrence Livermore National Laboratory, Livermore, CA, UCRL-JC-122327. Submitted to *J. of Fusion Engineering Design.*

Tabak, M., and Ho, D., *A Distributed Radiator Heavy Ion Target Design,* Lawrence Livermore National Laboratory, Livermore, CA, UCRL-JC-124460 ABS. Prepared for the *26th Annual Anomalous Absorption Conf,* Fairbanks, AK, Aug 26–30, 1996.

Takeuchi, K., *Final Report for "Item 1: Preliminary Refractory Testing,"* Lawrence Livermore National Laboratory, Livermore, CA, UCRL-CR-121348.

Takeuchi, K., *Final Report for "Item 3: Development of a Direct Batch Charging Method,"* Lawrence Livermore National Laboratory, Livermore, CA, UCRL-CR-121349.

Takeuchi, K., *Final Report for "Item 4: Evaluation of Improved Refractory Melter Concept,"* Lawrence Livermore National Laboratory, Livermore, CA, UCRL-CR-121347.

Takeucki, K., *Final Report for "Task 2: Construction of 1/5 Scale Continuous Melting Furnace,"* Lawrence Livermore National Laboratory, Livermore, CA, UCRL-CR-122047.

Thomas, I. M., *Laser Optical Coatings Prepared by the Sol-Gel Process,* Lawrence Livermore National Laboratory, Livermore, CA, UCRL-JC-122405. Submitted to the *Rev. of Laser Engineering,* Laser Society of Japan.

Tietbohl, G. L., and Sommer, S. C., *Design Guidelines for Mirror Support Systems in Large Lasers,* Lawrence Livermore National Laboratory, Livermore, CA, UCRL-JC-124522 ABS. Prepared for *2nd Annual Intl Conf on Solid-State Lasers for Application to Inertial Confinement Fusion,* Paris, France, Oct 22–25, 1996.

Tietbohl, G. L., Larson, D. W., Erlandson, A. C., Foley, R. J., Hackel, R. P., Hermes, G. L., Horvath, J. A., Kumpan, S. A., Murray, J. R., Remington, B. A., Sawicki, R. H., Speck, D. R., Trenholme, J. B., and Vann, C. S., *Final Report: NIF Laser Bundle Review,* Lawrence Livermore National Laboratory, Livermore, CA, UCRL-ID-122316.

Tietbohl, G. L., Larson, D. W., Erlandson, A. C., Foley, R. J., Hackel, R. P., Hermes, G. L., Horvatt, J. A., Kumpan, S. A., Murray, J. R., Remington, B. A., Sawicki, R. H., Speck, D. R., Trenholme, J. B., and Vann, C. S., *Preliminary Report: NIF Laser Bundle Review,* Lawrence Livermore National Laboratory, Livermore, CA, UCRL-ID-122317.

Tobin, M., Karpenko, V., Anderson, A., Wilemski, G., Burnham, A., Gerassimenko, M., Bernat, T., Peterson, P., Tokheim, R., Seaman, L., Curran, D., and Schirmann, D., *Target Emissions and Their Effects on the National Ignition Facility,* Lawrence Livermore National Laboratory, Livermore, CA, UCRL-JC-124526 ABS. Prepared for *2nd Annual Intl Conf on Solid-State Lasers for Application to Inertial Confinement Fusion,* Paris, France, Oct 22–25, 1996.

Tobin, M., Latkowski, J., Singh, M., and Karpenko, V., *The Impacts of Neutron Emissions on the Use of the National Ignition Facility (NIF),* Lawrence Livermore National Laboratory, Livermore, CA, UCRL-JC-124527 ABS. Prepared for *2nd Annual Intl Conf on Solid-State Lasers for Application to Inertial Confinement Fusion,* Paris, France, Oct 22–25, 1996.

Tobin, M., Sanchez, J., Pittenger, L., Dipeso, G., Serduke, F., Anderson, A., Peterson, P., Latkowski, J., and Bernat, T., *Cryogenic Target Integration and Radiation Protection of Near Target Components on NIF,* Lawrence Livermore National Laboratory, Livermore, CA, UCRL-JC-125139 ABS. Prepared for *11th Target Fabrication Specialists' Mtg,* Orcas Island, WA, Sept 8–12, 1996.

Tobin, M., Tokheim, R. E., Seaman, L., Cooper, T., Lew, B., Curran, D. R., Sanchez, J., and Anderson, A., *Calculating the Shrapnel Generation and Subsequent Damage to First Wall and Optics Components for the National Ignition Facility,* Lawrence Livermore National Laboratory, Livermore, CA, UCRL-JC-124947. Prepared for *Proceedings of the American Nuclear Society, 12th Topical Mtg on the Technology of Fusion Energy,* Reno, NV, Jun 16–20, 1996.

Tobin, M., Karpenko, V., and Peterson, R., *Implementing Direct Drive on the National Ignition Facility,* Lawrence Livermore National Laboratory, Livermore, CA, UCRL-JC-123567 SUM. Prepared for the *American Nuclear Society 12th Topical Mtg on the Technology of Fusion Energy,* Reno, NV, Jun 16–20, 1996.

Tobin, M., Karpenko, V., Foley, D., Anderson, A., Burnham, A., Reitz, T., Bernat, T., and Wavrik, R., *The Confinement of Ignition and Yield on the National Ignition Facility,* Lawrence Livermore National Laboratory, Livermore, CA, UCRL-JC-123562 SUM. Prepared for the *American Nuclear Society 12th Topical Mtg on the Technology of Fusion Energy,* Reno, NV, Jun 16–20, 1996.

Tobin, M., Kaufmann, B., Logan, G., Anderson, A., Diaz, T., Peterson, P. F., Kennedy, T. E., Hoover, T., Davis, J. F., and Alme, M. L., *Utility of the National Ignition Facility for Inertial Fusion Energy and Radiation Sciences Experiments,* Lawrence Livermore National Laboratory, Livermore, CA, UCRL-JC-123568 SUM. Prepared for the *American Nuclear Society 12th Topical Mtg on the Technology of Fusion Energy,* Reno, NV, Jun 16–20, 1996.

Tobin, M., Karpenko, V., Foley, D., Anderson, A., Burnham, A., Reitz, T., Latkowski, J., and Bernat, T., *Confinement of Ignition and Yield on the National Ignition Facility,* Lawrence Livermore National Laboratory, Livermore, CA, UCRL-JC-123562. Prepared for the *American Nuclear Society 12th Topical Mtg on the Technology of Fusion Energy,* Reno, NV, Jun 16–20, 1996.

Tobin, M., Karpenko, V., Kauffman, R., Anderson, A., Simonson, G., Kruger, H., Davis, J. F., and Hoover, T., *Utility of the National Ignition Facility for Inertial Fusion Energy and Radiation Sciences Experiments,* Lawrence Livermore National Laboratory, Livermore, CA, UCRL-JC-123568. Prepared for the *American Nuclear Society 12th Topical Mtg on the Technology of Fusion Energy,* Reno, NV, Jun 16–20, 1996.

Tobin, M., Karpenko, V., Burnham, A., and Peterson, R., *Target Area Design Issues for Implementing Direct Drive on the National Ignition Facility,* Lawrence Livermore National Laboratory, Livermore, CA, UCRL-JC-124479. Prepared for the *American Nuclear Society 12th Topical Mtg on the Technology of Fusion Energy,* Reno, NV, Jun 16–20, 1996.

Tobin, M. T., Anderson, A., Burnham, A., and Bernat, T., *Assessment of First Wall Damage from Target X-Ray Emission and Scattered Laser Light for the National Ignition Facility,* Lawrence Livermore National Laboratory, Livermore, CA, UCRL-JC-124265. Prepared for the *24th European Conf on Laser Interaction with Matter,* Madrid, Spain, Jun 3–7, 1996.

Tobin, M. T., Anderson, A., Burnham, A., Managan, R., Reitz, T., and Bernat, T., *Results of Life-Cycle Testing for the National Ignition Facility First Wall against Damage from Target Emissions and Decontamination Procedures,* Lawrence Livermore National Laboratory, Livermore, CA, UCRL-JC-124241 SUM. Prepared for the *16th Intl Atomic Energy Agency Fusion Energy Conf on Plasma Physics and Controlled Nuclear Fusion Research,* Montreal, Canada, Oct 7–11, 1996.

Tokheim, R. E., Seaman, L., and Curran, D. R., *NIF Target Area Design Support,* Lawrence Livermore National Laboratory, Livermore, CA, UCRL-CR-124257.

Turner, R. E., Landen, O. L., Kornblum, H. N., Amendt, P., Decker, C., Hammel, B. A., Morales, R., Suter, L. J., Wallace, R. J., Murphy, T. J., Gobby, P., Hauer, A. A., Knauer, J., Marshall, F. J., Bradley, D., Keck, R., Kelly, J., Kremens, R., Seka, W., and Soures, J. M., *Indirect Drive Measurements on Omega,* Lawrence Livermore National Laboratory, Livermore, CA, UCRL-JC-124665 ABS. Prepared for *38th Annual Mtg of the American Physical Society Div of Plasma Physics,* Denver, CO, Nov 11–15, 1996.

Turner, R., Anderson, A., Estabrook, K., Gerassimenko, M., and Serduke, F., *Fabrication of Low-Density Foam Shells from Resorcinol-Formaldehyde Aerogel,* Lawrence Livermore National Laboratory, Livermore, CA, UCRL-JC-125117 ABS. Prepared for *11th Target Fabrication Specialists' Mtg,* Orcas Island, WA, Sept 8–12, 1996.

Turner, R. E., Anderson, A. T., Estabrook, K., Gerassimenko, M., and Serduke, F. J. D., *Target-Induced Damage Considerations in the Design of ICF Diagnostics,* Lawrence Livermore National Laboratory, Livermore, CA, UCRL-JC-123555 ABS. Prepared for the *11th Topical Conf on High Temperature Plasma Diagnostics,* Monterey, CA, May 12–16, 1996.

V

Vann, C. S., and Post, R. F., *Reverser Architecture in a Laser Fusion Driver,* Lawrence Livermore National Laboratory, Livermore, CA, UCRL-JC-124525 ABS. Prepared for *2nd Annual Intl Conf on Solid-State Lasers for Application to Inertial Confinement Fusion,* Paris, France, Oct 22–25, 1996.

Van Wonterghem, B. M., Murray, J. E., Auerbach, J. A., Burkhart, S. C., Caird, J. A., Henesian, M., Penko, F., and Wegner, P., *High Fluence 1ω Performance Test Using 20 ns Ignition Shaped Pulses on the Beamlet Prototype Laser,* Lawrence Livermore National Laboratory, Livermore, CA, UCRL-JC-124865 ABS. Prepared for *2nd Annual Intl Conf on Solid-State Lasers for Application to Inertial Confinement Fusion,* Paris, France, Oct 22–25, 1996.

Van Wonterghem, B., Murray, J. R., Campbell, J. H., Speck, D. R., Barker, C. E., Smith, I. C., Browning, D. F., and Behrendt, W. C., *Performance of a Prototype, Large-Aperture Multipass Nd-Glass Laser for Inertial Confinement Fusion,* Lawrence Livermore National Laboratory, Livermore, CA, UCRL-JC-125150. Submitted to *Applied Optics, Optical Society of America.*

Van Wonterghem, B., Wegner, P. J., Lawson, J. K., Auerbach, J. M., Henesian, M. A., Barker, C. E., Thompson, C. E., Widmayer, C. C., and Caird, J. A., *Recent Performance Results of the National Ignition Facility Beamlet Demonstration Project,* Lawrence Livermore National Laboratory, Livermore, CA, UCRL-JC-123080 DR. Prepared for *American Nuclear Society 12th Topical Mtg on the Technology of Fusion Energy,* Reno, NV, Jun 16–20, 1996.

Van Wonterghem, B., Wegner, P. J., Lawson, J. K., Auerbach, J. M., Henesian, M. A., Barker, C. E., Thompson, C. E., Widmayer, C. C., and Caird, J. A., *Recent Performance Results of the National Ignition Facility Beamlet Demonstration Project,* Lawrence Livermore National Laboratory, Livermore, CA, UCRL-JC-123080. Prepared for *American Nuclear Society 12th Topical Mtg on the Technology of Fusion Energy,* Reno, NV, Jun 16–20, 1996.

Van Wonterghem, B., Wegner, P. J., Lawson, J. K., Auerbach, J. M., Henesian, M. A., Barker, C. E., Thompson, C. E., and Caird, J. A., *Recent 1ω Performance Results of the National Ignition Facility Beamlet Demonstration Project,* Lawrence Livermore National Laboratory, Livermore, CA, UCRL-JC-123080 ABS. Prepared for the *12th Topical Mtg on the Technology of Fusion Energy,* Reno, NV, Jun 16–20, 1996.

Von Moellendorf, U., and Tobin, M. T., *Conceptual Design Considerations for the Reaction Chamber of a Heavy Ion Driven Inertial Fusion Test Facility,* Lawrence Livermore National Laboratory, Livermore, CA, UCRL-JC-123564 SUM. Prepared for the *American Nuclear Society 12th Topical Mtg on the Technology of Fusion Energy,* Reno, NV, Jun 16–20, 1996.

W

Walton, C. C., Genin, F. Y., Chow, R., Kozlowski, M. R., Loomis, G. E., and Pierce, E., *Effect of Silica Overlayers on Laser Damage HfO_2–SiO_2 56° Incidence High Reflectors,* Lawrence Livermore National Laboratory, Livermore, CA, UCRL-JC-122320. Prepared for the *Symp on Optical Materials for High Power Laser,* Orlando, FL, Oct 30–Nov 1, 1995.

Weber, F. A., Da Silva, L. B., Barbee, T. W., Ciarlo, D., and Mantler, M., *Quantitative XRFA of Carbon in a Special Matrix by the Fundamental Parameter Method,* Lawrence Livermore National Laboratory, Livermore, CA, UCRL-JC-124249. Prepared for the *44th Annual Denver X-Ray Conf,* Colorado Springs, CO, Jul 31–Aug 4, 1995.

Weber, S. V., Dittrich, T. R., Haan, S. W., Pollaine, S. M., and Strobel, G. L., *Indirect Drive Ignition Capsules for the National Ignition Facility,* Lawrence Livermore National Laboratory, Livermore, CA, UCRL-JC-123314 ABS. Prepared for the *24th European Conf on Laser Interaction with Matter,* Madrid, Spain, Jun 3–7, 1996.

Weber, S. V., Glendinning, S. G., Kalantar, D. H., Remington, B. A., Rothenberg, J. E., Key, M. H., and Knauer, J. P., *Laser Imprint and Implications for Direct Drive Ignition with the National Ignition Facility,* Lawrence Livermore National Laboratory, Livermore, CA, UCRL-JC-123315 ABS. Prepared for the *24th European Conf on Laser Interaction with Matter,* Madrid, Spain, Jun 3–7, 1996.

Weber, S. V., Glendinning, S. G., Kalantar, D. H., Remington, B. A., Rothenberg, J. E., Key, M. H., Wolfram, E., Verdon, C. P., and Knauer, J. P., *Simulations of Laser Imprint on Nova, Vulcan, and NIF,* Lawrence Livermore National Laboratory, Livermore, CA, UCRL-JC-124490 ABS. Prepared for the *26th Annual Anomalous Absorption Conf,* Fairbanks, AK, Aug 26–30, 1996.

Weber, S. V., *Simulations of Laser Imprint for Nova and Vulcan Experiments and for Ignition Capsules,* Lawrence Livermore National Laboratory, Livermore, CA, UCRL-JC-124547 ABS. Prepared for *38th Annual Mtg of the American Physical Society Div of Plasma Physics,* Denver, CO, Nov 11–15, 1996.

Weber, S. V., Glendinning, S. G., Kalantar, D. H., Remington, B. A., Rothenberg, J. E., Key, M. H., and Knauer, J. P., *Laser Imprint and Implications for Direct Drive Ignition with the National Ignition Facility,* Lawrence Livermore National Laboratory, Livermore, CA, UCRL-JC-123315. Prepared for *24th European Conf on Laser Interaction with Matter,* Madrid, Spain, Jun 3–7, 1996.

Wegner, P. J., Van Wonterghem, B. V., Barker, C. E., Caird, J. A., Dixit, S. N., Henesian, M. A., Hunt, J. T., Seppala, L. G., and Thompson, C. E., *Third-Harmonic Performance of the Beamlet Prototype Laser,* Lawrence Livermore National Laboratory, Livermore, CA, UCRL-JC-124529 ABS. Prepared for *2nd Annual Intl Conf on Solid-State Lasers for Application to Inertial Confinement Fusion,* Paris, France, Oct 22–25, 1996.

Wegner, P. J., Van Wonterghem, B. M., Dixit, S. N., Henesian, M. A., Barker, C. E., Thompson, C. E., Seppala, L. G., and Caird, J. A., *Characterization of Third-Harmonic Target Plan Irradiance on the National Ignition Facility Beamlet Demonstration Project,* Lawrence Livermore National Laboratory, Livermore, CA, UCRL-JC-123070 ABS. Prepared for the *12th Topical Mtg on the Technology of Fusion Energy,* Reno, NV, Jun 16–20, 1996.

Wharton, K., Kirkwood, R., Afeyan, B., Back, C., Berger, R., Blain, M., Estabrook, K., Glenzer, S., Kruer, W., MacGowan, B., and Moody, J., *Measurement of Near-Wp Light as Evidence of the Electromagnetic Decay Instability,* Lawrence Livermore National Laboratory, Livermore, CA, UCRL-JC-124881 ABS. Prepared for *26th Annual Anomalous Absorption Conf,* Fairbanks, AK, Aug, 26–30, 1996.

Wharton, K., Zakharenkov, Y., Brown, C., Hammel, B., Joshi, C., Moody, J., Offenberger, A., Perry, M., Wilks, S., and Yanovsky, V., *Investigation of the Conversion of Laser Energy to Relativistic Electrons at Intensities of 1020 W/cm^2,* Lawrence Livermore National Laboratory, Livermore, CA, UCRL-JC-124295 ABS Rev. 1. Prepared for *38th Annual Mtg of the American Physical Society Div of Plasma Physics,* Denver, CO, Nov 11–15, 1996.

Wharton, K., Zakharenkov, Y., Hammel, B. A., Herman, S., Miller, J., Moody, J., Offenberger, A. A., Pennington, D., and Perry, M., *Measurements of Fast Electrons Produced in Solid Targets by Laser Intensities of 1020 W/cm^2,* Lawrence Livermore National Laboratory, Livermore, CA, UCRL-JC-123324 ABS. Prepared for the *11th Topical Conf on High Temperature Plasma Diagnostics,* Monterey, CA, May 12–16, 1996.

Wharton, K., Zakharenkov, Y., Brown, C., Hammel, B., Joshi, C., Moody, J., Offenberger, A., Perry, M., Wilks, S., and Yanovsky, V., *Investigation of the Conversion of Laser Energy to Relativistic Electrons at Intensities of 1020 W/cm^2,* Lawrence Livermore National Laboratory, Livermore, CA, UCRL-JC-124295 ABS. Prepared for the *26th Annual Anomalous Absorption Conf,* Fairbanks, AK, Aug 26–30, 1996.

Wilcox, R. B., and Browning, D. F., *A Single Frequency, Fiber Ring Laser in Yb:Silica,* Lawrence Livermore National Laboratory, Livermore, CA, UCRL-JC-124236 ABS. Prepared for the *1996 Conf on Lasers and Electro-Optics/Quantum Electronics and Laser Science Conf,* Anaheim, CA, Jun 2–7, 1996.

Wilcox, R. B., *Integrated Optic Pulse Shaping System,* Lawrence Livermore National Laboratory, Livermore, CA, UCRL-JC-116728.

Wilcox, R. B., and Browning, D. F., *A Tunable, Single Frequency, Fiber Ring Oscillator at 1053 nm,* Lawrence Livermore National Laboratory, Livermore, CA, UCRL-JC-124515 ABS. Prepared for *2nd Annual Intl Conf on Solid-State Lasers for Application to Inertial Confinement Fusion,* Paris, France, Oct 22–25, 1996.

Wilcox, R. B., and Browning, D. F., *Integrated Optic Modulator and Splitter Damage at 1053 nm,* Lawrence Livermore National Laboratory, Livermore, CA, UCRL-JC-124928 ABS. Prepared for *28th Annual Symp on Optical Materials for High Power Lasers,* Boulder, CO, Oct 7–9, 1996.

Wilemski, G., Boone, T., Cheung, L., Nelson, D., and Cook, R., *Prediction of Phase Separation During the Drying of Polymer Shells,* Lawrence Livermore National Laboratory, Livermore, CA, UCRL-JC-117329; *Fus. Tech.* **28**(12), 1773–1780 (1995).

Wilks, S. C., Freeman, R. Hartmann, F., Kerman, A., Langdon, A. B., and Woodworth, J., *Foil-Terminated Free Wave Acceleration,* Lawrence Livermore National Laboratory, Livermore, CA, UCRL-JC-124454 ABS Rev. 1. Prepared for *38th Annual Mtg of the American Physical Society Div of Plasma Physics,* Denver, CO, Nov 11–15, 1996.

Wilks, S. C., Freeman, R., Hartmann, F., Kerman, A., Langdon, A. B., and Woodworth, J., *Foil-Terminated Free Wave Acceleration,* Lawrence Livermore National Laboratory, Livermore, CA, UCRL-JC-124454 ABS. Prepared for the *26th Annual Anomalous Absorption Conf,* Fairbanks, AK, Aug 26–30, 1996.

Wilks, S. C., Kruer, W. L., and Rozmus, W., *Theory and PIC Simulations on the Competition between SBS and SRS,* Lawrence Livermore National Laboratory, Livermore, CA, UCRL-JC-124455 ABS. Prepared for the *26th Annual Anomalous Absorption Conf,* Fairbanks, AK, Aug 26–30, 1996.

Wilks, S. C., and Kruer, W. L., *Absorption Mechanisms for Ultra-Intense Laser-Plasma and Solid Target Interactions,* Lawrence Livermore National Laboratory, Livermore, CA, UCRL-JC-124456 ABS. Prepared for the *26th Annual Anomalous Absorption Conf,* Fairbanks, AK, Aug 26–30, 1996.

Williams, E. A., Glenzer, S., Back, C. A., Berger, R. L., and Estabrook, K. G., *Non-Local Transport and Plasma Heating by a Probe Laser Beam,* Lawrence Livermore National Laboratory, Livermore, CA, UCRL-JC-124677 ABS. Prepared for *38th Annual Mtg of the American Physical Society Div of Plasma Physics,* Denver, CO, Nov 11–15, 1996.

Williams, E. A., Berger, R. L., Afeyan, B. B., Cohen, B. I., Estabrook, K. G., Hinkel, D., Kruer, W. L., Langdon, A. B., Lasinski, B. F., Still, C. H., Yang, B., and Wilks, S., *Theory and Simulation of Laser Plasma Instabilities in Ignition Scale Plasmas,* Lawrence Livermore National Laboratory, Livermore, CA, UCRL-JC-123794 ABS. Prepared for the *16th Intl Atomic Energy Agency Fusion Energy Conf on Plasma Physics and Controlled Nuclear Fusion Research,* Montreal, Canada, Oct 7–11, 1996.

Williams, E. A., Cohen, B. I., Berger, R. L., Lasinski, B. F., and Langdon, A. B., *Ion Wave Parametric Instabilities,* Lawrence Livermore National Laboratory, Livermore, CA, UCRL-JC-124471 ABS. Prepared for the *26th Annual Anomalous Absorption Conf,* Fairbanks, AK, Aug 26–30, 1996.

Wolfe, C. R., and Lawson, J. K., *Characterization of Large Aperture Optical Wavefronts Using the Power Spectral Density Function,* Lawrence Livermore National Laboratory, Livermore, CA, UCRL-JC-123084 ABS & SUM. Prepared for the *Optical Society of America Topical Mtg,* Boston, MA, Apr 29–May 3, 1996.

Wood, B., Runkel, M., Yan, M., Staggs, M., De Yoreo, J., and Kozlowski, M., *Investigations of Laser Damage in Rapidly Grown KDP Crystals,* Lawrence Livermore National Laboratory, Livermore, CA, UCRL-JC-124534 ABS Rev. 1. Prepared for *28th Annual Symp on Optical Materials for High Power Lasers,* Boulder, CO, Oct 7–9, 1996.

Wood, B., Runkel, M., Yan, M., Staggs, M., De Yoreo, J., and Kozlowski, M., *Investigations of Laser Damage in Rapidly Grown KDP Crystals,* Lawrence Livermore National Laboratory, Livermore, CA, UCRL-JC-124534 ABS. Prepared for *2nd Annual Intl Conf on Solid-State Lasers for Application to Inertial Confinement Fusion,* Paris, France, Oct 22–25, 1996.

Woodworth, J. G., and Meier, W. R., *Target Production for Inertial Fusion Energy,* Lawrence Livermore National Laboratory, Livermore, CA, UCRL-JC-117396 Rev. 1; *Fusion Technol.* **31**, 280–290 (1997).

Woodworth, J. G., and Meier, W., *Target Production for Inertial Fusion Energy,* Lawrence Livermore National Laboratory, Livermore, CA, UCRL-ID-117396.

Wu, C. H., Meister, C. F., Zory, P. S., and Emanuel, M. A., *Microsecond-Long Lasing Delays in Thin P-Clad InGaAs QW Lasers,* Lawrence Livermore National Laboratory, Livermore, CA, UCRL-JC-124871. Prepared for *IEEE Lasers and Electro-Optics Society '96,* Boston, MA, Nov 18–21, 1996.

Y

Yan, M., Hutcheon, I. D., Torres, R., Staggs, M., Runkel, M., De Yoreo, J., and Zaitseva, N. P., *Investigation of Impurities and Laser Induced Damage in Rapidly Grown KDP,* Lawrence Livermore National Laboratory, Livermore, CA, UCRL-JC-124919 ABS. Prepared for *28th Annual Symp on Optical Materials for High Power Lasers,* Boulder, CO, Oct 7–9, 1996.

Yan, M., Torres, R., Hutcheon, I., Staggs, M., De Yoreo, J., and Zaitseva, N., *Impurity Segregation and Its Effects on the Optical Properties of KH_2PO_4,* Lawrence Livermore National Laboratory, Livermore, CA, UCRL-JC-123594 ABS Rev. 1. Prepared for *2nd Annual Intl Conf on Solid-State Lasers for Application to Inertial Confinement Fusion,* Paris, France, Oct 22–25, 1996.

Yan, M., *Impurity Defects in Fast Grown KDP Crystals,* Lawrence Livermore National Laboratory, Livermore, CA, UCRL-JC-122728 ABS. Prepared for the *1996 Mtg of the American Physical Society,* St. Louis, Missouri, Mar 18–22, 1996.

Yan, M., Torres, R. A., Hutcheon, I. D., De Yoreo, J. J., Zaitseva, N. P., and Rek, Z. U., *Impurity Segregation and Its Effects on the Optical Properties of KH_2PO_4,* Lawrence Livermore National Laboratory, Livermore, CA, UCRL-JC-123594 ABS. Prepared for the *10th American Conf on Crystal Growth,* Vail, CO, Aug 4–9, 1996.

Yang, T.-Y. B., Dubois, P. F., and Motteler, Z. C., *Building a Programmable Interface for Physics Codes Using Numeric Python,* Lawrence Livermore National Laboratory, Livermore, CA, UCRL-JC-123785. Prepared for the *4th Intl Python Workshop,* Livermore, CA, Jun 3–6, 1996.

Yang, T.-Y. B., Kruer, W. L., Langdon, A. B., and Johnston, T. W., *Mechanisms for Collisionless Absorption of Light Waves Obliquely Incident on Overdense Plasmas with Steep Density Gradients,* Lawrence Livermore National Laboratory, Livermore, CA, UCRL-JC-123106; *Phys. of Plasma* **3**(7), 2702–2709 (1996).

Z

Zacharias, R. A., Bliss, E. S., Davis, D. T., Decker, D. E., Miller, J. L., Toeppen, J. S., and Van Wonterghem, B., *Optics Damage Inspection for Large Laser Systems,* Lawrence Livermore National Laboratory, Livermore, CA, UCRL-JC-124380 ABS. Prepared for *2nd Annual Intl Conf on Solid-State Lasers for Application to Inertial Confinement Fusion,* Paris, France, Oct 22–25, 1996.

Zaitseva, N. P., DeHaven, M. R., Vital, R. L., Spears, H. R., Carman, M. L., Richardson, M., Atherton, L. J., and De Yoreo, J., *Rapid Growth of KH_2PO_4 Crystals in 1,000 Liter Crystallizers,* Lawrence Livermore National Laboratory, Livermore, CA, UCRL-JC-123597 ABS. Prepared for the *10th American Conf on Crystal Growth and the 9th Intl Conf on Vapor Growth & Epitaxy,* Vail, CO, Aug 4–9, 1996.

Zaitseva, N. P., DeHaven, M. R., Vital, R. L., Carman, M. L., Spears, R., Montgomery, K., Atherton, L. J., and De Yoreo, J. J., *Rapid Growth of Large-Scale (20–50 cm) KDP Crystals,* Lawrence Livermore National Laboratory, Livermore, CA, UCRL-JC-124011 ABS. Prepared for the *Nonlinear Optics: Materials, Fundamentals, and Applications,* Wailea, Maui, HI, July 8–12, 1996.

Zaitseva, N. P., De Yoreo, J., DeHaven, M., Vital, R. L., Carman, M. L., Spears, R., Montgomery, K., James, L., Atherton, L. J., and Rozsa, R., *Rapid Growth of Large-Scale (20–50 cm) KDP Crystals,* Lawrence Livermore National Laboratory, Livermore, CA, UCRL-JC-124011 ABS Rev. 1. Prepared for *2nd Annual Intl Conf on Solid-State Lasers for Application to Inertial Confinement Fusion,* Paris, France, Oct 22–25, 1996.

Zakharenkov, Y., Wharton, K., Hammel, B. A., Herman, S., Miller, J., Moody, J., Offenberger, A. A., Pennington, D., Perry, M., and Stuart, B., *Experimental Investigation of the Interaction of 100 TW Laser with Solid Targets,* Lawrence Livermore National Laboratory, Livermore, CA, UCRL-JC-123325 ABS. Prepared for the *11th Topical Conf on High Temperature Plasma Diagnostics,* Monterey, CA, May 12–16, 1996.

Zapata, L., Guenet, J., McCracken, R., Horvath, J., Rotter, M., Pollock, G., Guenet, M., Grebot, E., Seznec, S., and Erlandson, A., *Large Aperture Diagnostic System for Gain and Wavefront Measurements on NIF/LMJ Prototype Amplifiers,* Lawrence Livermore National Laboratory, Livermore, CA, UCRL-JC-124519 ABS. Prepared for 2*nd Annual Intl Conf on Solid-State Lasers for Application to Inertial Confinement Fusion,* Paris, France, Oct 22–25, 1996.

Zapata, L. E., and Erlandson, A. C., *Status Report on the Development of Large Bore Flashlamps for the National Ignition Facility,* Lawrence Livermore National Laboratory, Livermore, CA, UCRL-JC-122540 ABS & SUM. Prepared for the *Conf on Lasers and Electro-Optics (CLEO '96),* Anaheim Convention Center, Anaheim, CA, Jun 2–7, 1996.

Ze, F., Langer, S. H., Kauffman, B. L., Kilkenny, J. D., Ress, D., Rosen, M. D., Suter, L. J., Wallace, R. J., and Wiedwald, J. D., *A Comparative Study of X-Ray Emission from Laser Spots in Laser Heated Hohlraums Relative to Spots on Simple Disk Target,* Lawrence Livermore National Laboratory, Livermore, CA, UCRL-JC-124298. Submitted to *Phys. of Plasmas.*

Articles by Author

ICF Program
Lawrence Livermore National Laboratory
P.O. Box 808, L-475
Livermore, California 94551

Address Correction Requested